SCHOLARLY PUBLICATIONS

A CURRENT AWARENESS BULLETIN
OF RESEARCH OUTPUT

@DTU

(21st Edition)

SEPTEMBER 2014

BY: CENTRAL LIBRARY

DELHI TECHNOLOGICAL UNIVERSITY
(FORMERLY *DELHI COLLEGE OF ENGINEERING)*
GOVT. OF N.C.T. OF DELHI
SHAHBAD DAULATPUR, MAIN BAWANA ROAD
DELHI 110042

PREFACE

This is the Twenty first Issue of Current Awareness Bulletin started by Delhi Technological University, Central Library. The aim of the bulletin is to compile, preserve and disseminate information published by the faculty, students and alumni for mutual benefits. The bulletin also aims to propagate the intellectual contribution of Delhi Technological University (DTU) as a whole to the academia.

The bulletin contains information resources available in the internet in the form of articles, reports, presentations published in international journals, websites, etc. by the faculty and students of DTU. The publications of faculty and student which are not covered in this bulletin may be because of the reason that the full text either was not accessible or could not be searched by the search engine used by the library for this purpose.

The learned faculty and students are requested to provide their uncovered publications to the library either through email or in CD, etc to make the bulletin more comprehensive.

This issue contains the information published during September 2014. The arrangement of the contents is alphabetical. The full text of the article which is either subscribed by the university or available in the web is provided in this bulletin.

Central Library

CONTENTS

8. Curing kinetics of self-healing epoxy thermosets, Manorama Tripathi ***Devendra Kumar,*** Department of Applied Chemistry and Polymer Technology, DTU, Chitra Rajagopal and Prasun Kumar Roy

9. Delhi Technological University: Design and Development of the Littoral AUV Zyra 2.0, ***£Aayush Gupta, £Vatsal Rustagi, £Raj Kumar Saini, £Akshay Jain, £Prateek Murgai, £Aditya Rastogi, £Pronnoy Goswami, £Ayush Tomar, £Abhijit Ray, £Bhavy Dikshit, £Prithvijit Chattopadhyay, £Shubham Raina, £Mayank Gupta, £Vikas Kumar Singh, £Shubham Jain*** and ***£Chirag Gupta***, DTU

10. EFFECT OF LIME AND STONE DUST IN THE GEOTECHNICAL PROPERTIES OF BLACK COTTON SOIL, ****Ankur Mudgal, *Raju Sarkar*** and ****A.K. Sahu,*** Department of Civil Engineering, DTU

11. Effect of Multiwalled Carbon Nanotubes on the Conductivity and Swelling Properties of Porous Polyacrylamide Hydrogels, ****Sudha, *B. M. Mishra*** and ****D. Kumar***, Department of Applied Chemistry and Polymer Technology, DTU

12. Evolution from SDR to Cognitive Radio, Shilpa Jain1, ****Nidhi Taneja,*** ECE, DTU

13. Failure of Piston in IC Engines: A Review, ****R. C. Singh, *Roop. Lal, *Ranganath M S*** and ****Rajiv Chaudhary***, Mechanical Engineering, DTU

14. Flow Behaviour Of Bidisperse MR Polishing Fluid And Ball End MR Finishing, ****Mahendra Singh Niranjana,*** Mechanical Engineering, DTU and Sunil Jhab

15. Friction and Wear of Tribo-Elements in Power Producing Units for IC Engines- A Review, ****Roop Lal, *R C Sin, *Ranganath*** and ****M S S Maji***, Mechanical Engineering, DTU

16. Implemention of Distribution Energy Source as a Compensator based on Power Balance Control Algorithm, ***Nitu Dhyani, *Alka Singh*** and ***Manoj Badoni***, Electrical Engineering, DTU

17. Incorporation of SVS CBVLC Supplementary Controller for Damping SSR in Power System, ***Narendra Kumar*** and ***@Sanjiv Kumar,*** Electrical Engineering, DTU

18. Investigation of Allelopathic Potentiality of the Himalyan Lichen Parmelia reticulata Tayl. against Phalaris minor retz., Mayurika Goel, ***Archna Rani***, P. Dureja and P. Uniyal, Applied Chemistry, DTU

19. Maximum Bandwidth Enhancement of Current Mirror using Series-Resistor and Dynamic Body Bias Technique, Vandana NIRANJAN, ***@Ashwani KUMAR***, Shail Bala JAIN. DTU

20. Performance Analysis of Combined Cycle Gas Turbine for Frequency Deviation and Temperature Control, Naimul Hasana, ***B.B. Arora*** , J. N. Raic, Mechanical Engineering, DTU

21. Prevalence of Fluoride in Ground Water in Rajasthan State: Extent, Contamination Levels And Mitigation, ***Abhas Jain*** and ***Santosh Kumar Singh***, Environmental Engineering, DTU

22. Ring and Coupled Ring Oscillator in Subthreshold Region, ***Neeta Pande, *Rishi Pandel, *Tanvi Mitta***, Kirti Gupta and ***Rajeshwari Pandey***, Electronics and Communication, DTU

23. Role of Erythropoietin and other growth factors in Ex-vivo Erythropoiesis, ***Vimal Kishor Singh, *Abhishek Saini*** and Ramesh Chandra, Stem Cell Research Laboratory, Department of Biotechnology, DTU

24. Seasonal variation and sources of aerosol pollution in Delhi, India, ***Papiya Mandal, *R. Sarkar, *A. Mandal*** and T. Saud, Civil Engineering, DTU

25. Study of the Processing Pathway for Cosolvent Addition in Active Layer Preparation of Inverted Organic Solar Cell, ***Sarita S. Nair, *D. Kumar, *Abhishek Sharma*** and ***Amitava Majumdar***, Department of Applied Chemistry & Polymer Technology, DTU

26. Thiol Modified Chitosan Self-Assembled Monolayer Platform for Nucleic Acid Biosensor, Maumita Das Mukherjee, Pratima R. Solanki, Gajjala Sumana, Takaaki Manaka, Mitsumasa Iwamoto and ***Bansi D. Malhotra***, Dept of Biotechnology, DTU

27. Use of Digital Signature Standard with Station to Station Key Exchange Agreement and Cloud Manager to Enhance Security in Cloud Computing, ***Manoj Kumar*** and ***$Kranti Asiwal***, DTU

***Faculty** **@Research Scholar** **$PG Scholar**
#Alumni **£Undergraduate Student** **~ Ex Faculty**
! Teaching-cum-Research Fellow **<Ex Research Scholar** **>Ex PG Scholar**

ISSN NO. 2320-5407

Journal homepage: http://www.journalijar.com

INTERNATIONAL JOURNAL OF ADVANCED RESEARCH

RESEARCH ARTICLE

A Coupler with High Directivity and Strong Coupling Using Coupled Lines

Harish Chandra Kumawat, Dr.Priyanka Jain , Pappu Kumar Verma
Delhi Technological University, Delhi India

Manuscript Info

Manuscript History:

Received: 15 June 2014
Final Accepted: 25 July 2014
Published Online: August 2014

Key words:
High Directivity, Strong Coupling, Microstrip, Coupled line, Advance Design System

Corresponding Author

Harish Chandra Kumawat

Abstract

A new symmetrical coupler with high directivity and strong coupling is proposed using microstrip coupled lines. It can be used in a various RF combining, power splitting and sampling applications. The proposed coupler structure is very simple to fabricated using single-layer PCB. This coupler is designed using RT/duroid material having dielectric constant 2.2. The operating frequency is chosen as 2.1 GHz. The simulation has been done using Advance Design System (ADS) software. The simulated results show that it has good return loss, high directivity and good coupling.

Introduction

Microstrip coupled-line couplers are widely used for the designs of various balanced power amplifiers, mixers, modulators, measurement systems, circularly polarized antennas, beam-forming array antennas, etc [1].

Generally, traditional microstrip coupled-line couplers provide very low coupling and very poor directivity. To achieve a strong coupling and high directivity in microstrip coupled-line couplers, several methods have been studied. But these methods put extra burden such as extra connecting wires, extra capacitor and inductors on the circuit and do not provide strong coupling and high directivity together [2]-[5].

In this paper, a novel coupled-line coupler with strong coupling coefficient and high-directivity is proposed. It can be fabricated using single layer PCB.

I. COUPED LINE COUPLER

Couplers are passive devices which couple a part of the transmission power by a fixed amount out through another port, often by using two transmission lines placed close together such that energy flowing through one transmission line is coupled to the other transmission.

When two unshielded transmission lines are in close proximity, power can be coupled from one line to the other due to the interaction of the electromagnetic fields. Such lines are referred to as coupled transmission lines [6]. These coupled lines can be used to design couplers and this type of coupler is called coupled line coupler. In this paper the coupler is designed using microstrip lines.

The following quantities are commonly used to characterize a coupler

$$\text{Coupling} = C\ (\text{dB}) = -20\log S_{31}\ \text{dB}$$

$$\text{Isolation} = I\ (\text{dB}) = -20\log S_{41}\ \text{dB}$$

$$\text{Directivity} = D\ (\text{dB}) = 20\log\frac{S_{31}}{S_{41}}\ \text{dB}$$

$$\text{Insertion Loss} = IL\ (\text{dB}) = -20\log S_{21}\ \text{dB}$$

Here S_{21}, S_{31}, S_{41} are scattering parameters. S_{21} shows output from the port 2 when we apply signal on port 1. S_{31} shows output at port 3 when signal is applied on the port 1. S_{41} shows output at port 4 when we apply signal at port 1.

II. DESIGN AND SIMULATION

A. Designing of coupler

The proposed coupler has single layered structure and does not require any bonding wires, any capacitance and inductance to improve directivity or coupling. So it is easy to fabricate. For designing this coupler we have chosen a substrate RT/duroid, which have dielectric constant 2.2 and thickness 2 mm. The proposed coupler has two coupled line section one in vertical direction and other in horizontal direction.

This coupler has symmetry along the horizontal and vertical directions. So we can calculate even and odd characteristic impedance of each section of coupled by even–odd decomposition method described in [7] and [8].

In *even mode*, the currents in the strip conductors are in the same direction and equal in amplitude and in *odd mode*, the currents in the strip conductors are equal in amplitude but in opposite directions.

The designing steps for this coupler are as follows:

1) Find the power-dividing coefficient and the center frequency required for the design [1].
2) Choose even and odd mode characteristic impedance of first section of coupled line (horizontal) and electrical length of second section of coupled line (vertical) [1].
3) Calculate even and odd mode characteristic impedance of second section of coupled line (vertical) using equations given in reference number [1].
4) Convert all these electrical parameters into physical dimensions using line calculator in ADS and simulate the scattering parameters and phase information by using ADS.
5) l_n is the length of the 50Ω port and can be chosen freely as per requirements of the design[1].
6) Tune the physical dimensions including w_1, w_2, and S to obtain high directivity without affecting the coupling and matching performance.

The physical dimensions of the coupler are:
$w_1 = 2.8$ mm,
$w_2 = 1.8$ mm ,
$w_n = 5.4$ mm ,
$l_1 = 25$ mm ,
$l_2 = 14$ mm ,
$l_n = 18$ mm ,
$S = 0.4$ mm

III. RESULTS

The simulated results show that the return loss is around 60dB, coupling is 5 dB, and directivity is around 52 dB at 2.124 GHz. The phase difference between the two output ports is about 90^0 over a wide range from 1.8 to 2.4 GHz.

For this coupler we got highest directivity around 55 dB at 2.13 GHz and strongest coupling 4.965 dB at 2.199 GHz.

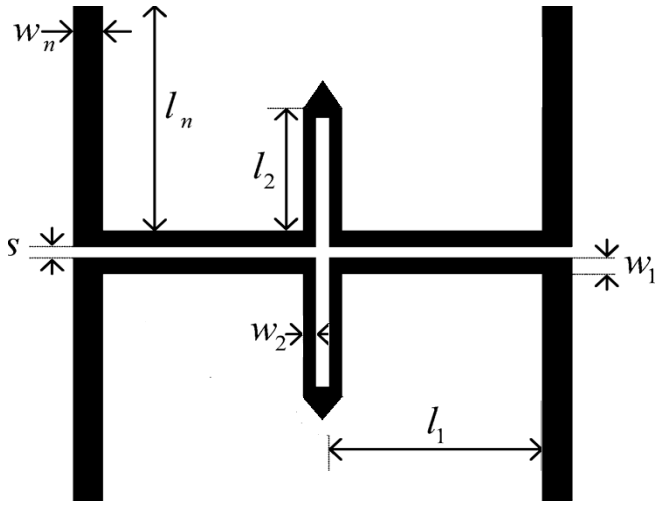

Fig. 1 Layout of the Proposed Coupler

A. Simulation of Coupler

Simulation of the coupler is done using Advance Design System (ADS) software.

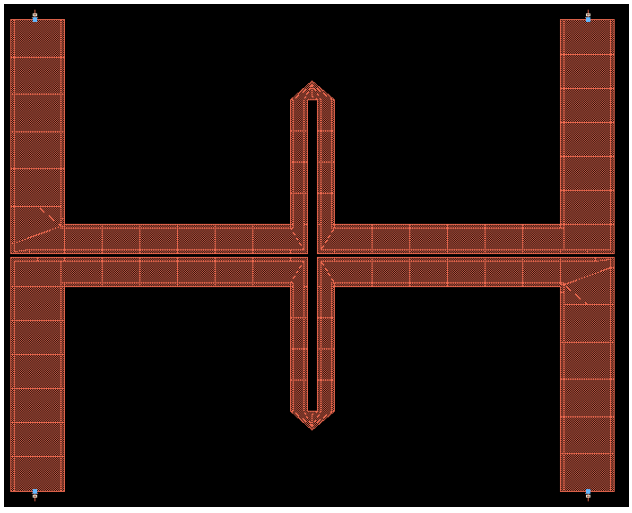

Fig. 2 Layout of Proposed Coupler in ADS

After simulation of proposed coupler using Advance Design System (ADS) software, we get following simulation results:

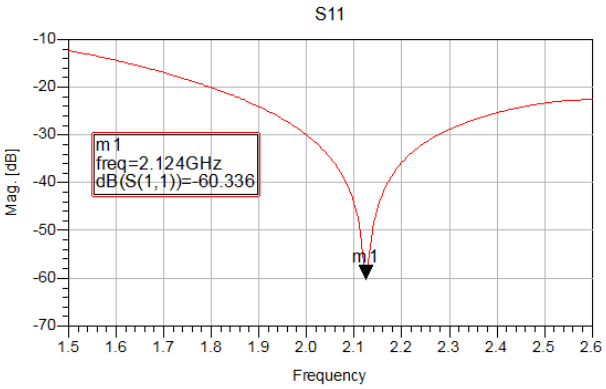

Fig. 3 Rerurn Loss of Coupler

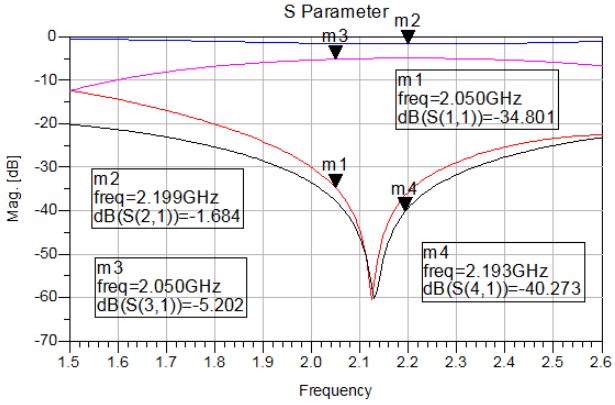

Fig. 4 S Parameters of Proposed Coupler

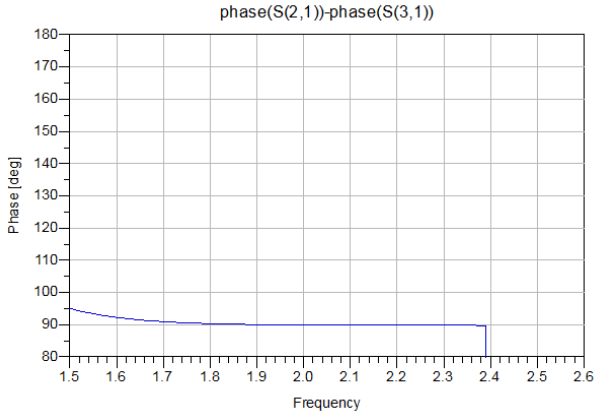

Fig. 5Phase Difference between two output ports of Proposed Coupler

IV. CONCLUSION

A new coupler using coupled-line has been proposed in this paper. The simulated results show that return loss, coupling, and directivity are good. The highest simulated return loss is around 60 dB, coupling around 5 dB and directivity is 52 dB at 2.1 GHz. This frequency is used in Universal Mobile Telecommunications System. So this coupler can be used in mobile communication. The circuit structure of this coupler is very simple and easy to fabricate.

ACKNOWLEGMENT

The authors would like to thank Dr. Priyanka Jain, Assistant Professor, Department of Electronics and Communication, Delhi technological University, Delhi for her support and encouragement.

REFERENCES

[1] Yongle Wu, Weinong Sun, Sai-Wing Leung, Yinliang Diao, Kwok-Hung Chan, and Yun-Ming Siu "Single-Layer Microstrip High-Directivity Coupled-Line Coupler With Tight Coupling" IEEE transaction on Microwave theory and Techniques, vol.61, no.2, February 2013.

[2] S. Lee and Y. Lee, "An inductor-loaded microstrip directional coupler for directivity enhancement," IEEE Microw. Wireless Compon. Lett., vol. 19, no. 6, pp. 362–364, Jun. 2009.

[3] J. Lange, "Interdigitated strip-line quadrature hybrid," IEEE Trans. Microw. Theory Techn., vol. MTT-17, no. 12, pp. 1150–1151, Dec. 1969.

[4] J.-H. Cho, H.-Y. Hwang, and S.-W. Yun, "A design of wideband 3-dB coupler with -section microstrip tandem structure," IEEE Microw. Wireless Compon. Lett., vol. 15, no. 2, pp. 113–115, Feb. 2005.

[5] M. Dydyk, "Microstrip directional couplers with ideal performance via single-element compensation," IEEE Trans. Microw. Theory Techn., vol. 47, no. 6, pp. 956–964, Jun. 1999.

[6] David M. Pozra,"Microwave Engineering" 4th ed. Jhone Wiley & Sons,Inc.,2011.

[7] J. Reed and G. J. Wheeler, "A method of analysis of symmetrical four port networks," IRE Trans. Microw. Theory Techn., vol. MTT-4, no. 4, pp. 246–252, Oct. 1956.

[8] L. K. Yeung, "A compact dual-band 90 coupler with coupled-line sections," IEEE Trans. Microw. Theory Techn., vol. 59, no. 9, pp. 2227–2232,Sep.2011.

[9] Advance Design System (ADS) software ver. 2008, by Agilent Technologies.

ISSN (Online): 2348-0866
www.IJETI.com

A Survey of Spectrum Sensing Techniques and Issues in Cognitive Radio Ad hoc Networks

Shilpa Jain[1], Nidhi Taneja[2]
[1]Electronics and Communication dept.,
Inderprastha Engineering College, Ghaziabad,U.P,India
[2]Electronics & Communication Engineering dept.,
Delhi Technological University, Delhi, India

Abstract

Since 1999, cognitive radio (CR) technology is envisaged to solve the problems in wireless networks resulting from the limited available spectrum and the inefficiency in the spectrum usage by exploiting the existing wireless spectrum opportunistically. CR networks, however, impose unique challenges due to the high fluctuation in the available spectrum as well as diverse quality-of-service (QoS) requirements. In this paper, a survey of spectrum sensing methodologies for cognitive radio ad hoc networks (CRAHNs) is presented. Spectrum management functionalities such as spectrum sensing, spectrum decision, spectrum sharing, and spectrum mobility are introduced. Various functionalities of spectrum sensing are studied from a cognitive radio perspective and multi-dimensional spectrum sensing concept is introduced. A particular emphasis is given to cooperative sensing concept and its various forms. Finally, the Challenges associated with spectrum sensing are discussed.

Keywords—*Cognitive radio ,Cognitive radio ad hoc networks, spectrum sensing, Primary user, dynamic spectrum access, multi-dimensional spectrum sensing, cooperative sensing.*

I. INTRODUCTION

The need for higher data rates is increasing as a result of the transition from voice-only communications to multimedia type applications; therefore it becomes obvious that the current static frequency allocation schemes cannot accommodate the requirements of an increasing number of higher data rate devices. As a result, *Cognitive radio* arises to be a tempting solution to the spectral congestion problem by introducing opportunistic usage of the frequency bands that are not heavily occupied by licensed users [1], [2]. In this paper, we use the definition adopted by Federal Communications Commission

(FCC):*Cognitive—radio: A radio or system that senses its operational electromagnetic environment and can dynamically and autonomously adjust its radio operating parameters to modify system operation, such as maximize throughput, mitigate interference, facilitate interoperability, access secondary markets.*‖ [2]Hence,.one main aspect of cognitive radio is that it works on this dynamic Spectrum Management principle which solves the issue of spectrum underutilization in wireless communication in a better way.

In cognitive radio terminology, *primary users* (PU) (also known as licensed device) can be defined as the users who have higher priority or legacy rights on the usage of a specific part of the spectrum. On the other hand, *secondary users* (also called cognitive radio users or unlicensed devices), which have lower priority, exploit this spectrum in such a way that they do not cause interference to PUs and they vacate the band once the PU is detected. Therefore, secondary users need to have cognitive radio capabilities, such as sensing the spectrum reliably to check whether it is being used by a PU and to change the radio parameters to exploit the unused part of the spectrum called spectrum holes or white spaces.

According to the network architecture, cognitive radio (CR) networks can be classified as the infrastructure-based CR network and the CRAHNs [3]. The infrastructure-based CR network has a central network entity such as a base station in cellular networks. Here the analysis and observations performed by each CR user feeds the central CR base-station, so that it can make decisions based on these observations on how to avoid interference with primary user networks. According to this decision, each CR user reconfigures its communication parameters, as shown in Fig. 1a. On the contrary, the CRAHN does not have any infrastructure backbone. Therefore a CR user can communicate with other CR users through ad hoc connection on both licensed and unlicensed spectrum bands. Here each user needs to have all CR capabilities and is responsible for determining its actions based on the local observation, as shown in Fig. 1b. Since the

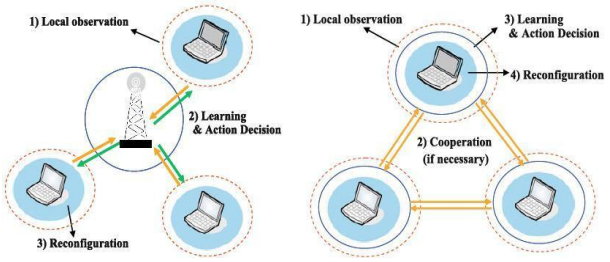

Fig. 1. Comparison between CR capabilities for: (a) infrastructure-based CR networks, and (b) CRAHNs.

CR user cannot predict the influence of its actions on the entire network with its local observation, cooperation schemes are essential, where the observed information can be exchanged among devices to get the knowledge about the network.

The goal of this paper is to point out several aspects of spectrum sensing in CRAHN. These aspects are discussed in the rest of this paper. We start by introducing the spectrum management framework for CRAHNs in Section II. In Section III, we introduce multi-dimensional spectrum sensing concept. Spectrum sensing functionalities such as PU detection, sensing control and cooperative sensing concept of cognitive network are discussed in Section IV. Finally, the research challenges associated with spectrum sensing are discussed in Section V.

II. SPECTRUM MANAGEMENT FRAMEWORK FOR COGNITIVE RADIO

CRAHN has dynamic spectrum environment which necessitates the spectrum-aware operations, which forms a cognitive cycle [3], as shown in fig. 2. The steps of the cognitive cycle consist of four spectrum management functions: spectrum sensing, spectrum sharing, spectrum decision, and spectrum mobility. Main features of spectrum management functions are as follows:

A. Spectrum sensing:

Spectrum sensing is the task of obtaining awareness about the spectrum usage and existence of primary users. A CR user can be allocated to only an unused portion of the spectrum or spectrum holes. Although spectrum sensing is traditionally understood as measuring the spectral content; but it is a more general term that involves obtaining the spectrum usage characteristics across multiple dimensions such as time, frequency, code and space. It also involves determining what types of signals are occupying the spectrum including the bandwidth, carrier frequency, modulation, waveform etc. This multi-dimensional concept is discussed in next section.

B. Spectrum sharing

Spectrum Sharing is to share the white spaces (spectrum hole) fairly among the secondary users. Since there may be multiple CR users trying to access the spectrum, their transmissions should be coordinated to prevent collisions in overlapping portions of the spectrum. For this, game theoretical approaches have also been used to analyze the behavior of selfish CR users. Furthermore, we need a CR medium access control protocol, which facilitates the sensing control to distribute the sensing task among the coordinating nodes.

C. Spectrum decision

In spectrum decision, once the available spectrum bands are identified through spectrum sensing, CR networks need to select the proper spectrum bands according to their QoS requirements. In order to design a decision algorithm that incorporates dynamic spectrum characteristics, we need to obtain a priori information regarding the PU activity. In CRAHNs, spectrum decision involves jointly undertaking route formation and spectrum selection.

D. Spectrum mobility

Spectrum mobility necessitates a spectrum handoff scheme in case of PU detection to avoid the link failure and to switch the current transmission to a new route or a new spectrum band with minimum quality degradation. Therefore we need collaboration with spectrum sensing, neighbor discovery in a link layer, and routing protocols. This functionality needs a connection management scheme to maintain the performance of upper layer protocols without the influence of spectrum switching.

Since we have limited knowledge of the network, all of the spectrum management functions are based on cooperative operations where CR users determine their actions based on the observed information exchanged with their neighbors.

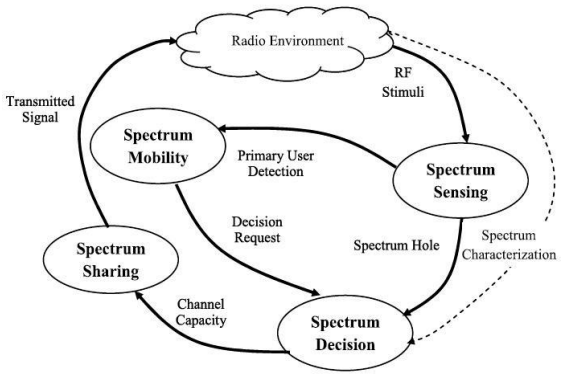

Fig. 2. Cognitive radio cycle

III. MULTI-DIMENSIONAL SPECTRUM AWARENESS

The conventional definition of the spectrum opportunity is ―a band of frequencies that are not being used by the primary user of that band at a particular time in a particular geographic area‖ [4]. This indicates methods only exploit three dimensions of the spectrum space: time, frequency, and space. However, there are other dimensions like code, angle etc, that need to be explored further for spectrum opportunity. If the code dimension is interpreted as part of the spectrum space, new opportunities for spectrum usage can be created. Likewise, the angle dimension has not been exploited well. It is assumed that the PUs and/or CR users transmit in all the directions. But, with the recent advances in multi-antenna technologies, e.g. beam forming; multiple users can be multiplexed into the same channel at the same time in the same geographical area [5]. This new dimension also creates new opportunities for spectral estimation where not only the frequency spectrum but also the angle of arrivals (AoAs) needs to be estimated. It is noticeable that the angle dimension is different than the geographical space dimension. Since in angle dimension, a primary and a secondary user can be in the same geographical area and can share the same channel. However, geographical space dimension refers to physical separation of radios in distance.

With these new dimensions, the radio space can be defined as theoretical― hyperspace occupied by radio signals, which has dimensions of frequency, time, space, angle of arrival, code , and possibly others‖ 6].[This hyperspace is also called transmission hyperspace or simply radio spectrum space, and it can be used to describe how the radio environment can be shared among multiple (PU and/or CR) systems. It is of crucial importance to define such an n-dimensional space for spectrum sensing, which includes the process of identifying occupancy in all dimensions of the spectrum space and finding spectrum space holes.

IV. SPECTRUM SENSING FUNCTIONALITIES FOR COGNITIVE RADIO

Spectrum sensing enables CR users to exploit the white spaces adaptively in all the dimensions of the radio environment. This can be done in two ways: (1) CR users find available spectrum holes over a wide frequency range for their transmission, known as out-of-band sensing, and (2) CR users monitor the spectrum band during the transmission and detect the presence of primary networks so as to avoid interference called in-band sensing. The CRAHN necessitates the following functionalities for spectrum sensing, shown in Fig. 3:

- PU detection: The CR user observes and analyzes its local radio environment. Here CR users detect the presence of PU transmissions, and accordingly identify the current spectrum availability by local observations of itself and its neighbors.

- Sensing control: In dynamic radio environment, this function enables each CR user to perform its sensing operations adaptively. It also coordinates the sensing operations of the CR users and its neighbors in a distributed manner, which prevents false alarms in cooperative sensing.

- Cooperation: To improve sensing accuracy, the observed information in each CR user is exchanged with its neighbors.

To achieve high spectrum utilization spectrum sensing needs to provide high detection accuracy. However, due to the lack of a central network entity, CR ad hoc users perform sensing operations independently of each other, which may lead to an adverse influence on sensing performance. In the following subsection, we discuss these basic functionalities required for spectrum sensing to face this challenge in CRAHNs.

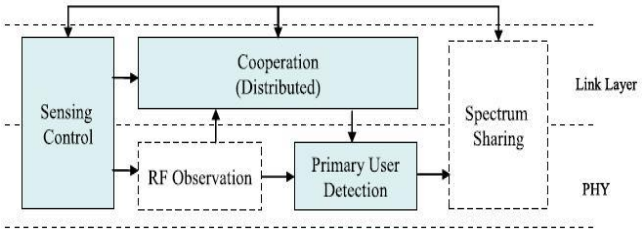

Fig. 3. Spectrum sensing structure for ad hoc CR networks.

A. *Primary user detection*

CR users do not have any real-time interaction with the PU transmitters and receivers therefore they do not know the exact information of the ongoing transmissions within the PU networks. PU detection depends on only the local radio observations of CR users. PU detection techniques for CRAHNs can be of three types [3]: primary transmitter detection, primary receiver detection, and interference temperature management (see Fig. 4). Transmitter detection is based on the detection of the weak signal from a primary transmitter through the local observations of CR users whereas the primary receiver detection [7] aims at finding the PUs that are receiving data within the communication range of a CR user. Here the local oscillator leakage power emitted by the radio frequency

(RF) front-end of the primary receiver is usually exploited, which is usually weak. This method provides the most effective way to find spectrum holes but currently it is only feasible in the detection of the TV receivers.

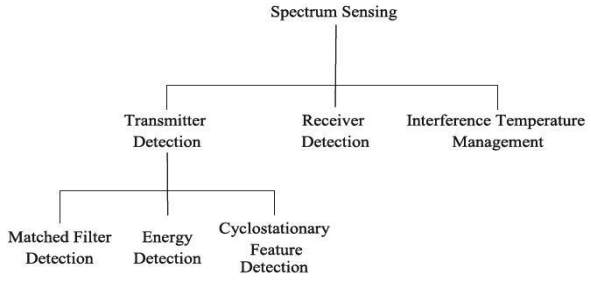

Fig. 4. Classification of spectrum sensing.

In interference temperature management scheme, the cumulative RF energy from multiple transmissions sets a maximum cap on their aggregate level that the primary receiver could tolerate, called an interference temperature limit [8]. As long as CR users do not exceed this limit by their transmissions, they can use this spectrum band. But the difficulty of this model is to accurately measure the interference temperature since CR users cannot distinguish between actual signals from the PU and the noisy signal. Therefore spectrum sensing in CRAHNs is mainly focused on primary transmitter detection.

In transmitter detection, CR users should have the capability to detect their own signal from a PU transmitter. The local RF observation used in PU detection sensing is based on the following hypothesis model:

$$r(t) = \begin{cases} n(t) & H_0 \\ hs(t) + n(t) & H_1 \end{cases} \quad (1)$$

Here s(t) is the transmitted signal of the PU, r(t) is the signal received by the CR user, h is the amplitude gain of the channel and n(t) is a zero-mean additive white Gaussian noise (AWGN). Here, H0 is a null hypothesis which states that there is no licensed user signal in a certain spectrum band. On the contrary, H1 is an alternative hypothesis, which indicates that there exists some PU signal.

Following are the three schemes used for the transmitter detection in spectrum sensing: energy detection, matched filter detection and feature detection [9].

1) Energy detection

Energy detector based approach is the most common way of spectrum sensing because of its low computational and implementation complexities [10]. In the energy detection, CR users sense the presence/absence of the PU based on the energy of the received signals. It is more generic as receivers do not need any knowledge As depictedin fig. 5, the measured signal r(t) is firstly squared and then integrated over the observation interval T. The signal is detected by comparing the output of the energy detector with a threshold λ which depends on the noise floor [10].

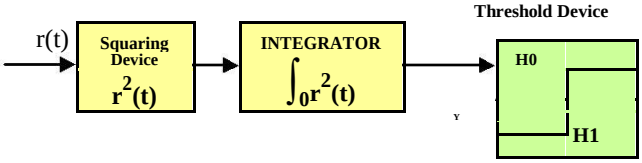

Fig. 5. Block diagram of energy detection.

Some of the challenges with energy detector based sensing include inability to differentiate interference from primary users and noise ,selection of the threshold for detecting primary users, and poor performance under low signal-to-noise ratio (SNR) values [11]. Moreover, energy detectors do not work efficiently for detecting spread spectrum signals. Energy detection also suffers from longer detection time compared to the matched filter detection. In addition, while the energy detector can only determine the presence of the signal but cannot differentiate signal types. Thus, the energy detector often results in false detection triggered by the unintended CR signals. For these reasons, in order to use energy detection, each CR user should be synchronized with the same sensing and transmission schedules ie CRAHNs need to provide the synchronization over the sensing operations of all neighbors.

2) Matched filter detection

Matched-filtering is known as the optimum method for detection of PU when the transmitted signal is known [12]. The main advantage of matched filtering is the short time to achieve a certain probability of false alarm or probability of misdetection as compared to other methods that are discussed in this section. As shown in Fig. 6, it is obtained by correlating a known original PU signal s(t) with a received signal r(t) where T is the symbol duration of PU signals. Then the output of the matched filter is sampled at the synchronized timing.

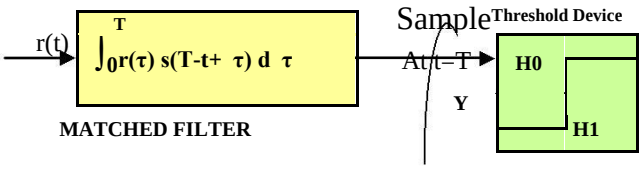

Fig. 6. Block diagram of matched filter detection.

If the sampled value Y is greater than the threshold k, the spectrum is determined to be occupied by the PU

transmission. knowledge of the characteristics of the PU signal but also the synchronization between the PU transmitter and the CR user. If this information is not accurate, then the matched filter performs poorly. For this reason, energy detection and feature detection are the most commonly used for spectrum sensing in CRAHNs. For more practical implementation, a pilot signal of PU systems is used for the matched filter detection in [13]. In ofthis themethod, P**U**s'transmitterssignalsend.the pilot signal simultaneously with data, and CR users have its perfect knowledge.

3) Feature detection

In feature detection the presence of PU signals is determined by extracting their specific features such as pilot signals, symbol rate, cyclic prefixes, spreading codes, or modulation types from its local observation. These features can be detected by analyzing a spectral correlation function since they introduce built-in periodicity in the modulated signals, which is shown in Fig. 7. This is also called cyclostationary detection [14]. Here, the spectrum correlation of the received signal r(t) is averaged over the interval T, and compared with the test statistic to determine the presence of PU signals, similar to energy detection .

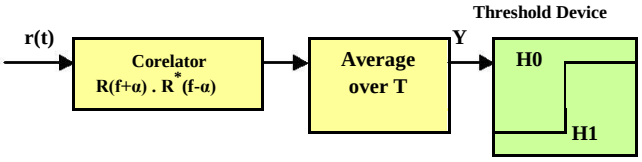

Fig. 7. Block diagram of feature detection

In [15], the enhanced feature detection scheme combining cyclic spectral analysis with pattern recognition based on neural networks is proposed .Its robustness to the uncertainty in noise power is the main advantage of feature detection. Furthermore, it can distinguish the signals from different networks. Synchronization of CR with its neighbors is not needed. Although feature detection is most effective method for spectral sensing but it is computationally complex and requires significantly long sensing time.

B. Sensing control

To find more spectrum access opportunities without interfering with PU networks is the main objective of spectrum sensing. Sensing controller controls and coordinate the sensing operations of CR users and it considers two main issues as depicted in Fig. 8.: (1) In in-band sensing, how long and frequently CR users should sense the spectrum to achieve sufficient sensing accuracy, and (2) In out-of-band sensing how quickly CR user can find the available spectrum band.

1) In-band sensing control

Maximum spectrum opportunity as well as interference avoidance are the main issues. The in-band sensing has a periodic sensing structure where CR users are allowed to access the spectrum only during the transmission period followed by sensing (observation) period. In the periodic sensing, longer sensing time leads to higher sensing accuracy, and hence to less interference. But if the sensing time becomes longer, the transmission time of CR users will be decreased. Conversely, while longer transmission time increases the access opportunities, it causes higher interference due to the lack of sensing information. Thus, a trade off between the proper sensing and transmission times is required in spectrum sensing. To optimize both sensing and transmission times simultaneously in such a way as to maximize the transmission efficiency subject to interference avoidance constraints where both parameters are determined adaptively depending on the time-varying cooperative gain, a theoretical framework is developed in [16].

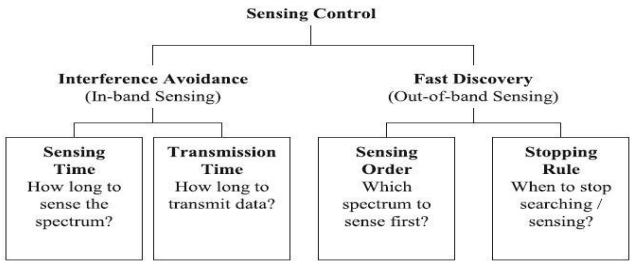

Fig. 8. Configuration parameters coordinated by sensing control.

2) Out-of-band sensing control

In out-of-band sensing, a CR user needs to find new available spectrum band and spectrum discovery time is a crucial factor to determine the performance of CRAHNs. Thus, a coordination scheme in spectrum sensing is required which not only minimizes the delay in finding them but also discovers as many spectrum opportunities as possible. Proper selection of spectrum sensing order can help to reduce the spectrum discovery time in out-of-band sensing. An n-step serial search scheme is proposed in [17] which mainly focusing on correlated occupancy channel models, where the spectrum availability of current spectrum is assumed to be dependent on that of its adjacent spectrum bands. In [18] both transmission time and spectrum searching sequence are optimized by minimizing searching delay as well as maximizing spectrum opportunities.

If the CR user senses more spectrum bands, it is highly probable to detect a better spectrum band while resulting in longer spectrum searching time. To exploit this tradeoff effectively, a well-defined stopping rule of spectrum searching is essential in out-of-band sensing. In [19], an optimal stopping time is determined to maximize the expected capacity of CR users subject to the maximum

number of spectrum bands a CR user can use simultaneously.

C. Cooperation

Each CR user needs to determine spectrum availability by itself depending only on its local observations in CRAHNs. However the observation range of the CR user is small and generally less than its transmission range. Thus, even if CR users find the unused spectrum portion, their transmission may cause interference at the PU receivers inside their transmission range, the so-called receiver uncertainty problem [3]. Furthermore, if the CR user receives a weak signal with a low signal-to-noise ratio (SNR) due to multi-path fading, or it is located in a shadowing area, it cannot detect the signal of the PUs. Thus, an efficient cooperation scheme is necessary in spectrum sensing in CRAHNs in order to prevent interference to PUs outside the observation range of each CR user [3]. A common cooperative scheme which forms clusters to share the sensing information locally for a wireless mesh networks is proposed in [20]. Here the mesh router and the mesh clients supported by it form a cluster. The mesh clients send their individual sensing results to the mesh router, which are then combined to get the final sensing result. In absence of central network entity in CRAHNs, this cooperation should be implemented in a distributed manner. In this scheme, when a CR user detects the PU activities, it should notify its observations promptly to its neighbors to evacuate the busy spectrum. Therefore, a reliable control channel is needed for discovering neighbors of a CR user as well as exchanging sensing information. Asynchronous sensing and transmission schedules make it difficult to exchange sensing information between neighbors. Thus, reliable information exchange and robust neighbor discovery are critical issues in implementing cooperative sensing in CRAHNs. This cooperation issue will also affect other spectrum management functions: spectrum decision, spectrum sharing, and spectrum mobility.

A notification protocol based on in-band signaling is proposed in [21], to disseminate the evacuation information among all CR users and thus evacuate the licensed spectrum reliably. This protocol uses the spreading code for its transmission, leading to tolerance in interference from both primary and other CR transmissions. Since it uses flooding-based routing scheme, it requires little prior information on the network topology and density. An optimal cooperative sensing strategy is proposed in [22], where the final decision is based on a linear combination of the local test statistics from individual CR users. The contribution to the cooperative decision making is indicated by the combining weight for each user's. Here, signal if CR user receives a higher-SNR signal and frequently makes its local decision consistent with the real hypothesis, then its test statistic has a larger weighting coefficient. In case of CR users in a deep fading channel, smaller weights are used to reduce their negative influence on the final decision.

Cooperative detection is theoretically more accurate since the uncertainty in a minimized single through collaboration. Moreover, multipath fading and shadowing effects can be mitigated so that the detection probability is improved in a heavily shadowed environment. However, cooperative approaches cause adverse effects on resource-constrained networks due to the overhead traffic.

V. RESEARCH CHALLENGES

- False alarm detection: each user in CRAHNs has independent and asynchronous sensing and transmission schedules; it can detect the transmissions of other CR users as well as PUs during its sensing period. But in the energy detection, which is most common method used for spectrum sensing, CR user cannot distinguish the transmission of CR and PUs, and can detect only the presence of a transmission. Therefore a false alarm is detected due to the transmission of CR users during sensing operations. this leads to an increase in spectrum opportunities. Thus, how to coordinate the sensing cooperation of each CR user to reduce these false alarms is the most important issue in spectrum sensing.

- *Cooperative sensing Optimization*: Another crucial issue introduced by Cooperative sensing is that by requesting the sensing information from several CR users, the user that initiates the cooperative sensing, improves the accuracy but also increases the network traffic. However, a high latency is introduced in collecting this information due to channel contention and packet re-transmissions.

- *Adaptable Cognitive Radio Antennas*: For dynamic communication applications, cognitive radio requires antenna researchers to design software controlled reconfigurable antennas. Switching time and the tuning ability of such antennas are important to satisfy the requirements of continuously changing communication channels. Neural Networks (NNs) arose as a perfect solution to control these antennas through Field Programmable Gate Arrays (FPGAs) [23].

Thus, CRAHNs are required to consider these factors which must be optimized for correct and efficient sensing.

VI. CONCLUSIONS

One of the exciting and promising concepts in wireless communication is the Cognitive radio, which is one of the efforts to utilize the available spectrum more efficiently through opportunistic spectrum usage. The CR devices need to incorporate the spectrum management functionalities like spectrum sensing, spectrum decision, spectrum sharing, and spectrum mobility. The main challenge in CRAHNs is to integrate these functions in the layers of the protocol stack, so that the CR users can communicate reliably in a distributed manner, over a multi-hop/multi-spectrum environment, without any infrastructure support. In this paper, the spectrum opportunity and spectrum sensing concepts are re-evaluated by considering different dimensions of the spectrum space. Various aspects of the spectrum sensing task are explained in detail. Several sensing methods are studied and Pro-active approaches are given. Estimation of spectrum usage in multiple dimensions including time, frequency, space, angle, and code; identifying opportunities in these dimensions; and developing algorithms for prediction into the future using past information can be considered as some of the open research areas.

REFERENCES

[1] I. Mitola, J. and J. Maguire, G. Q., ―Cognitive radio: making software radios more personal,‖ *IEEE Personal Commun. Mag.*, vol. 6, no. 4, August 1999, pp. 13–18.

[2] Federal Communications Commission, ―Notice of proposed rule making and order: Facilitating opportunities for flexible, efficient, and reliable spectrum use employing cognitive radio technologies,‖ ET Docket No. 03-108, February 2005.

[3] I.F.Akyildiz, W.Y. Lee, M.C. Vuran, M. Shantidev, NeXt generation/ dynamic spectrum access/cognitive radio wireless networks: a survey, Computer Networks Journal (Elsevier) 50 (2006), pp. 2127–2159.

[4] P. Kolodzy et al., ―Next generation communications: Kickoff meeting,‖ in *Proc. DARPA*, October 2001.

[5] Heli Sarvanko, Marko Höyhtyä, Marja Matinmikko and Aarne Mämmelä,―Exploiting spatial dimension in cognitive radios and networks,‖ in 6th International ICST Conference on Cognitive Radio Oriented Wireless Networks and Communications (CROWNCOM), June 2011, pp. 360 – 364.

[6] A. L. Drozd, I. P. Kasperovich, C. E. Carroll, and A. C. Blackburn, ―Computational electromagnetics applied to analyzing the efficient utilization of the RF transmission hyperspace,‖ in *Proc. IEEE/ACES Int. Conf. on Wireless Communications and Applied Computational Electromagnetics*, Honolulu, Hawaii, USA, April 2005, pp. 1077–1085.

[7] B. Wild, K. Ramchandran, Detecting primary receivers for cognitive radio applications, in: Proceedings of the IEEE DySPAN 2005, November 2005, pp. 124–130.

[8] FCC, Notice of inquiry and notice of proposed rulemaking, ET Docket No. 03-237, November 2003.

[9] D. Cabric, S.M. Mishra, R.W. Brodersen, Implementation issues in spectrum sensing for cognitive radios, in: Proceeings of the IEEE Asilomar Conference on Signals, Systems and Computers 2004 November 2004, pp. 772–776.

[10] F. Digham, M. Alouini, and M. Simon, ―On the energy detection of unknown signals over fading channels,‖ in *Proc. IEEE Int. Conf. Commun.*, vol. 5, Seattle, Washington, USA, May 2003, pp. 3575–3579.

[11] H. Urkowitz, ―Energy detection of unknown deterministic signals,‖ *Proc. IEEE*, vol. 55, April 1967, pp. 523–531.

[12] J. G. Proakis, *Digital Communications*, 4th ed. McGraw-Hill, 2001.

[13] D. Cabric, A. Tkachenko, R.W. Brodersen,‖Spectrum sensing measurements of pilot, energy, and collaborative detection,‖ in Proc. IEEE Military Communications Conference (MILCOM), October 2006.

[14] Y. Hur, J. Park, W. Woo, J.S. Lee, K. Lim, C.-H. Lee, H.S. Kim, J. Laskar, ―A cognitive radio (CR) system employing a dual-stage spectrum sensing technique: a multi-resolution spectrum sensing (MRSS) and a temporal signature detection (TSD) technique,‖ in Proc. IEEE Globecom 2006, November 2006.

[15] A. Fehske, J.D. Gaeddert, J.H. Reed, ―A new approach to signal classification using spectral correlation and neural networks,‖ in Proc. IEEE DySPAN 2005, November 2005, pp. 144–150.

[16] W.-Y. Lee, I.F. Akyildiz, Optimal spectrum sensing framework for cognitive radio networks, IEEE Transactions on Wireless Communications 7 (10) (2008) , pp. 3845–3857.

[17] L. Luo, S. Roy, Analysis of search schemes in cognitive radio, in:Proceedings of the IEEE SECON 2007, San Diego, CA, USA, June 2007, pp. 647–654.

[18] H. Kim, K.G. Shin, Efficient discovery of spectrum opportunities with MAC-layer sensing in cognitive radio networks, IEEE Transactions on Mobile Computing 7 (5) (2008) , pp. 533–545.

[19] J. Jia, Q. Zhang, X. Shen, HC-MAC: a hardware-constrained cognitive MAC for efficient spectrum management, IEEE Journal on Selected Areas in Communications 26 (1) (2008), pp. 106–117.

[20] K.R. Chowdhury, I.F. Akyildiz, Cognitive wireless mesh networks with dynamic spectrum access, IEEE Journal of Selected Areas in Communications 26 (1) (2008), pp. 168–181.

[21] X. Liu, Z. Ding, ESCAPE: a channel evacuation protocol for spectrumagile networks, in: Proceedings of the IEEE DySPAN 2007, Dublin, Ireland, April 2007.
[22] Z. Quan, S. Cui, A.H. Sayed, Optimal linear cooperation for spectrum sensing in cognitive radio networks, IEEE Journal of Selected in Signal Processing 2 (1) (2008), pp. 28–40.
[23] Y. Tawk, J. Costantine, E. Al-Zuraiqi and C. G. Christodoulou ―Cognitive radio antennas that learn and adapt using Neural Networks,‖ Radio Science Meeting (USNC-URSI NRSM), 2013 US National Committee of URSI National,January 2013, pp. 1.

Analog Integr Circ Sig Process
DOI 10.1007/s10470-014-0394-x

A very high performance compact CMOS current mirror

Bhawna Aggarwal · Maneesha Gupta · Anil Kumar Gupta · Sahil Bansal

Received: 31 January 2014 / Accepted: 19 August 2014

Abstract This paper proposes a very high performance current mirror (CM), where output current accurately copies the input current without carrying any offset component. Compact implementation of Garimella et al. CM structure has been combined with super cascode configuration to achieve the proposed very high performance CM. The proposed CM offers extremely high output resistance, very low input resistance and high degree of copying accuracy over a wide operating current range. Small signal analysis is carried out to validate the performance characteristics of the circuit. The proposed CM is simulated by Mentor Graphics Eldospice in TSMC 0.18 μm CMOS, BSIM3 and Level 53 technology, using a single supply voltage of 1.5 V. The circuit is shown to have high current copying accuracy for a range of (0–500 μA) with an error less than 0.0016 % and has no offset current at the output side. The robustness of the proposed CM against the variations in device parameters and temperature changes has been reflected in simulations by carrying Monte Carlo and temperature analysis. The simulation results show that the proposed circuit provides very high output resistance of 55.76 GΩ and a very low input resistance of 0.07 Ω.

Keywords Current mirror · Flipped voltage follower · Negative feedback · Input resistance · Output resistance · Super cascode configuration

B. Aggarwal · M. Gupta (✉)
Netaji Subhas Institute of Technology, Delhi, India
e-mail: maneeshapub@gmail.com

A. K. Gupta
National Institute of Technology, Kurukshetra, Haryana, India

S. Bansal
Maharaja Agrasen Institute of Technology, Delhi, India

1 Introduction

A CM is a type of current amplifier used to replicate the input current at its high impedance output node. It is used widely as a fundamental unit in most analog/mixed mode integrated circuits such as OTAs, CCIIs, OMAs, CFOAs, analog filters etc. for current amplification, biasing and active loading [1–5]. Thus, the efficient design of a CM helps in improving the overall performance of these integrated circuits. The major factors influencing the performance of a CM are its accuracy, input–output resistances, compliance voltage and supply voltage. A simple CM faces the problem of moderately low input resistance, low output resistance and lack of accuracy in current matching due to mismatch in drain to source voltages (v_{DS}) of basic CM pair. Nowadays, there is an increased demand of short channel MOS devices due to their high bandwidth, low power consumption and smaller chip area requirement. These problems of low output resistance and poor current transfer ratio increase with the reduction in channel length of MOS devices. This occurs as short channel MOS devices have increased output conductance and are more prone to channel length modulation effect [6, 7]. To improve the CM performance and make it compatible with the present industry trends, various high performance topologies have been suggested.

In this paper, a very high performance CM operating over a wide current range has been proposed. The proposed CM utilizes the compact implementation of Garimella et al. CM structure [8] to achieve low input and high output resistance. Moreover, super cascode technique [9] is used at the output side to remove the offset current component in output current and to increase the output resistance of the proposed CM. The CM is shown to operate over a wide current range with negligible current matching error. The paper is organized as follows: In Sect. 2, a few enhanced CM topologies reported

Published online: 10 September 2014

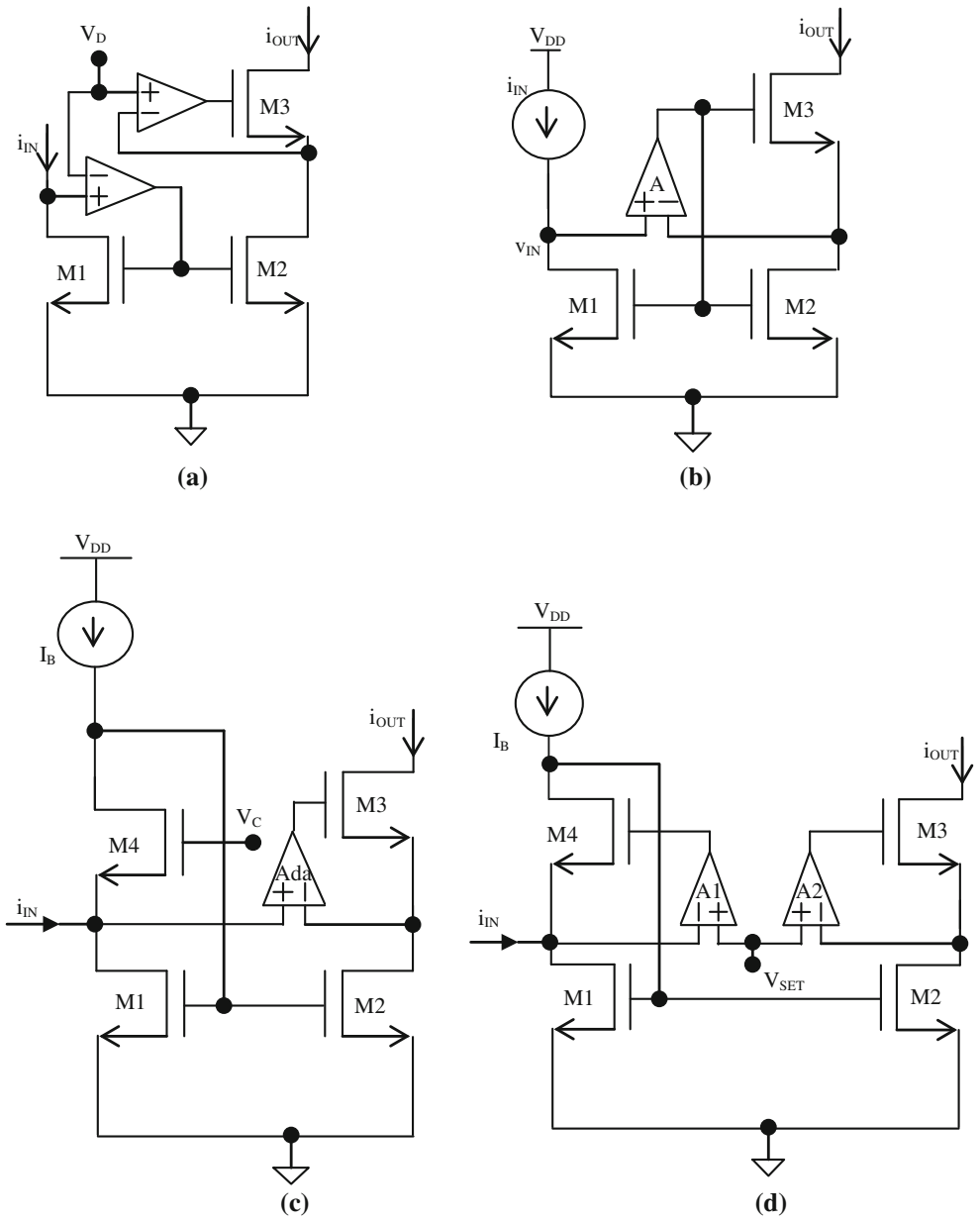

Fig. 1 **a** Active input regulated cascode CM [3] **b** High output-resistance CMOS CM [4] **c** Raimrez-Angulo structure of high performance CMOS CM [10] **d** Garimella et al. compact CM structure [8]

in literature are discussed. The proposed very high performance CM is explained in Sect. 3. In this section, small signal analysis of the proposed CM is also carried out. In Sect. 4, the simulated results of the circuit and its comparison with other circuits are presented. Finally, Sect. 5 concludes the paper.

2 High-performance CM topologies reported in literature

Various topologies were suggested and reported in literature to improve the performance characteristics of a basic CM. Improvement in the input and output resistances of a CM are based on implementation of shunt input and series output negative feedback amplifiers. A few enhanced CM topologies are shown in Fig. 1.

The active CM proposed by Nairn and Salama [1] maintains a constant voltage at the input terminal of CM with the help of an amplifier. This helps to avoid inaccuracy due to channel length modulation effect and lowers the input resistance, minimizing the loading effect on previous stage. CM with regulated cascode output stage was proposed in 1990 [2], where drain-source potential across the output MOSFET is kept constant with the help of a negative feedback loop formed by an amplifier and a

cascode MOSFET. This configuration not only improves the current matching accuracy but the output resistance of the CM as well [2, 7]. Both these configurations were combined in active input regulated cascode CM proposed by Serrano and Linares-Barranco in 1994 [3] and is shown in Fig. 1(a). In this configuration, differential amplifiers are used at both the input and output sides of the CM to achieve low input resistance and high output resistance. However, if the input voltage approaches the reference voltage (V_D), the current matching accuracy of the CM reduces. Furthermore, this scheme uses two op-amps to compare the voltages at the input and output nodes, hence it consumes more power and requires a larger chip area. A high output resistance CMOS CM is shown in Fig. 1(b). Here, amplifier A reduces current mismatch error caused due to channel length modulation effect, in the basic CM pair formed by MOSFETs M1 and M2 and reduces input voltage by means of shunt-feedback. Figure 1(c) shows Ramirez-Angulo structure [10] of high performance CMOS CM. In this circuit low input resistance is achieved with the help of single ended amplifier M4. Here, amplifier Ada provides negative feedback to ensure equal values of v_{DS1} and v_{DS2}, leading to a very high output resistance and accurate current matching. CM topology shown in Fig. 1(d) [8] was claimed by the authors to be the most compact high performance CM implementation. This configuration improves the accuracy and performance characteristics of a CM by using two nested feedback loops both at the input and output sides. The first feedback loop at the input side is formed by flipped voltage follower (FVF) implemented by MOSFETs M1, M4 and current source I_B. The second feedback loop is formed by amplifier A1 and MOSFET M4 acting as a voltage follower. The output side consists of nested feedback loops formed by cascode configuration provided by MOSFET M3 and series feedback delivered by amplifier A2. This topology has very low input resistance ($r_{in} = 1/A1g_{m1}g_{m4}r_{04}$) and very high output resistance ($r_{out} = A2r_{02}g_{m3}r_{03}$).

3 Proposed very high performance CM

The CM topology shown in Fig. 1(d) provides very low input resistance, remarkably high output resistance and operates with high degree of accuracy as nested feedbacks loops at the input and output sides forces $v_{DS1} = v_{DS2}$ [8, 11]. However, in this configuration current in MOSFET M4 is different than in MOSFET M3. This is due to the fact that at the input stage the biasing current component (I_B) has been split from signal current component (i_{IN}), though both are present together at the output stage. Hence, although the output current follows the input current with great accuracy but it has an offset term equivalent to I_B.

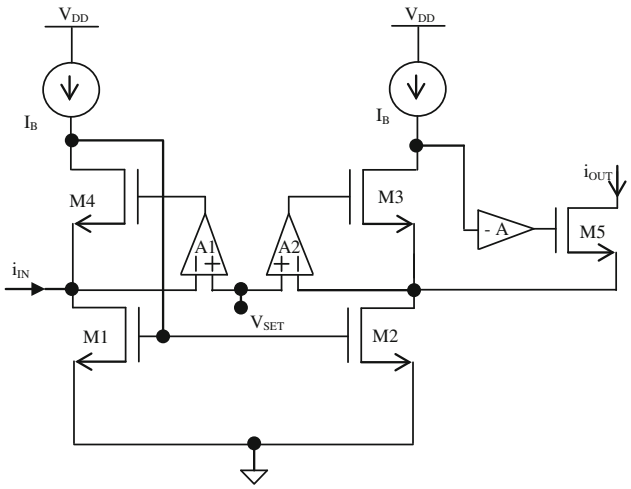

Fig. 2 Conceptual schematic of the proposed high performance CM

This offset current component can be removed, if I_B is segregated from the output current (i_{OUT}) as well. A conceptual circuit that accomplishes this task is shown in Fig. 2. In this schematic, super cascode configuration [9], is used at the output side which not only removes the offset current component present in i_{OUT} but also increases the output resistance considerably.

In the proposed circuit, the output cascode MOSFET M5 is driven by the drain of MOSFET M3 and biasing current source (I_B). To compensate the effect of polarity reversal at the drain of MOSFET M3, an inverting stage ($-$A) is used to drive the gate terminal of MOSFET M5. This inverting stage provides an additional gain-boosting, leading to further increase in output resistance. The proposed CM provides improvement in performance characteristics without increasing the voltage headroom consumption or supply voltage requirement of the original circuit.

3.1 Output resistance

The small signal model for calculating output resistance (r_{out}) of the proposed circuit is shown in Fig. 3(a). Here, v_{ij} represents potential drop across i and j nodes of the circuit shown. By analyzing this model it can be found that:

$$v_2 = -A2 \cdot v_1;\ v_4 = -A \cdot v_3 \tag{1}$$

Applying KCL at different nodes, we get:

$$g_{m3}v_{21} + \frac{v_{31}}{r_{03}} = 0 \tag{2}$$

$$i_{out} = g_{m5}v_{41} + \frac{v_{out} - v_1}{r_{05}} \tag{3}$$

$$i_{out} = \frac{v_1}{r_{02}} - g_{m3}v_{21} - \frac{v_{31}}{r_{03}} \tag{4}$$

Using Eqs. (1) and (2), we get:

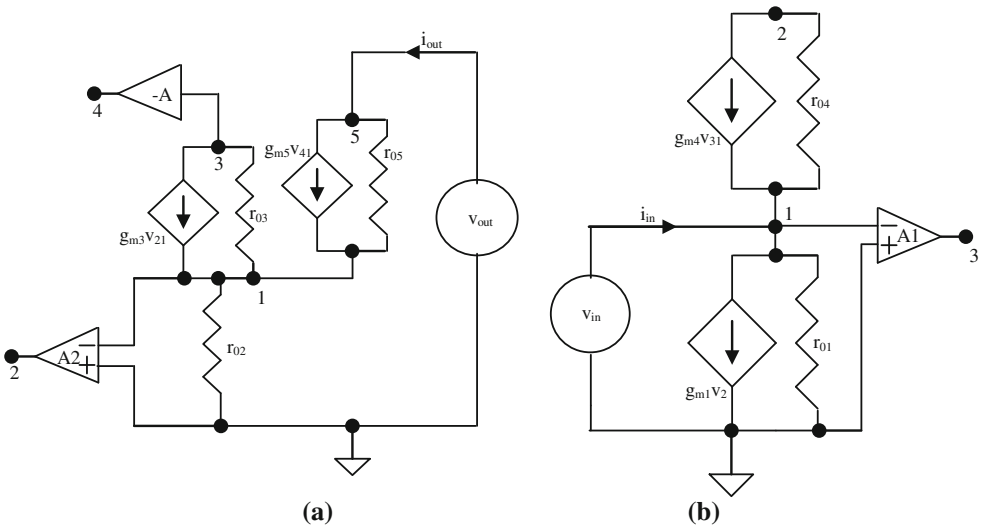

Fig. 3 **a** Small signal model for calculating output resistance of the proposed CM **b** Small signal model for calculating input resistance of the proposed CM

$$v_3 = [1 + (1 + A2)g_{m3}r_{03}]v_1 \tag{5}$$

Since,

$$r_0 g_m \gg 1 \,\&\, A \gg 1 \tag{6}$$

Thus, Eq. (5) can be simplified as:

$$v_3 \cong A2 g_{m3} r_{03} v_1 \tag{7}$$

Simplifying Eqs. (1), (3) and (7), i_{out} is obtained as:

$$i_{out} = -\frac{g_{m5}r_{05}(1 + AA2r_{03}g_{m3}) + 1}{r_{05}} v_1 + \frac{v_{out}}{r_{05}} \tag{8}$$

Using Eq. (6), Eq. (8) can be simplified as:

$$i_{out} \cong (-A)A2 g_{m3} r_{03} g_{m5} v_1 + \frac{v_{out}}{r_{05}} \tag{9}$$

Using Eqs. (2), (4) and (9), we get;

$$\frac{v_{out}}{i_{out}} = r_{05} + AA2 g_{m3} r_{03} g_{m5} r_{05} r_{02} \tag{10}$$

Using Eq. (6), Eq. (10) gets simplified as:

$$r_{out} = \frac{v_{out}}{i_{out}} \approx AA2 g_{m3} r_{03} g_{m5} r_{05} r_{02} \tag{11}$$

The output resistance of Garimella et al. [8] compact CM structure [Fig. 1(d)] is given as:

$$r_{out} = \frac{v_{out}}{i_{out}} \approx A2 g_{m3} r_{03} r_{02} \tag{12}$$

Relations Eqs. (11) and (12) show that the output resistance of the proposed CM increases by a factor equal to $Ag_{m5}r_{05}$ as compared to the output resistance of Garimella et al. compact CM structure. This proposed circuit, to the best of our knowledge, achieves the maximum output resistance reported till date.

3.2 Input resistance

The small signal model to calculate the input resistance (r_{in}) of the proposed circuit is shown in Fig. 3(b). From the model it can be analysed that:

$$v_3 = -A1 \cdot v_1 = -A1 \cdot v_{in} \tag{13}$$

Applying KCL at nodes 1 and 2, we get:

$$i_{in} = g_{m1} v_2 + \frac{v_{in}}{r_{01}} \tag{14}$$

$$g_{m4}(v_3 - v_{in}) + \frac{v_2 - v_{in}}{r_{04}} = 0 \tag{15}$$

Simplification of Eqs. (13) and (15), gives:

$$v_2 = [1 + r_{04} g_{m4}(A1 + 1)]v_{in} \tag{16}$$

Using Eq. (6), Eq. (16) gets simplified as:

$$v_2 \approx A1 r_{04} g_{m4} v_{in} \tag{17}$$

Combining Eqs. (14) and (17), we get:

$$r_{in} = \frac{v_{in}}{i_{in}} = \frac{r_{01}}{1 + A1 g_{m1} r_{01} g_{m4} r_{04}} \tag{18}$$

Using Eq. (6), Eq. (18) gets simplified as:

$$r_{in} \approx \frac{1}{A1 g_{m1} g_{m4} r_{04}} \tag{19}$$

Equation (19) shows that the input resistance of the proposed circuit is very low (less than 1 Ω). This is equivalent to what is achieved in Garimella et al. compact CM structure, as both the circuits are similar at the input side.

The complete schematic of the proposed circuit depicting the implementation of the amplifiers A1 and A2 using NMOS cascode amplifiers along with implementation of amplifier (-A) by means of common source MOSFET M6

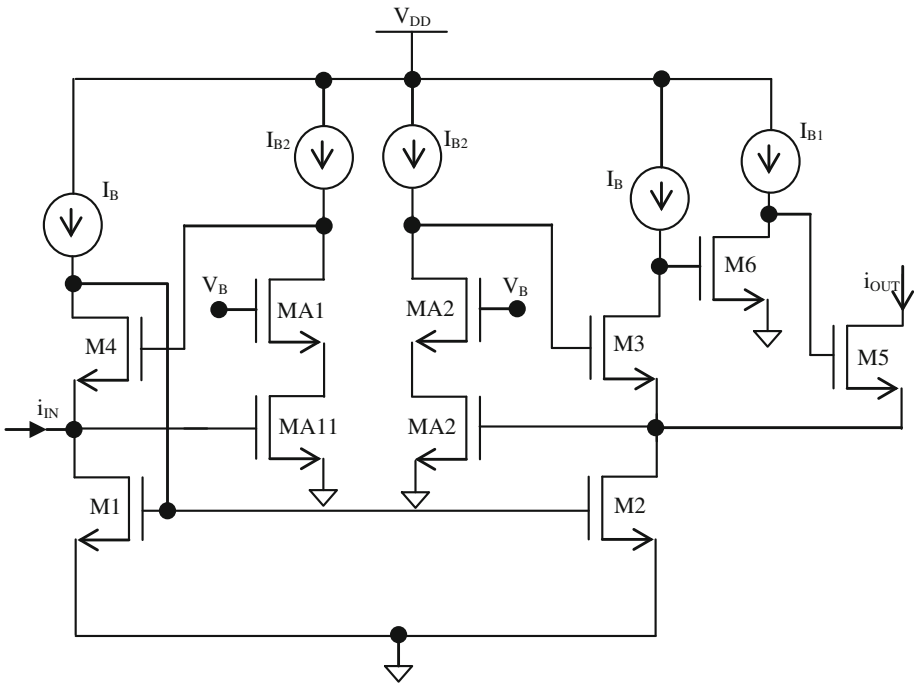

Fig. 4 The complete implementation of the proposed CM

and biasing current I_{B1} is shown in Fig. 4. Here, the MOSFETs M3, M5 and M6 and their biasing currents I_B and I_{B1} implement a super-cascode transistor. The proposed circuit removes the offset current component in the output current and boosts the output resistance considerably without increasing the supply voltage requirement. However, as additional biasing current source and MOSFETs are required, the proposed CM consumes slightly more power.

4 Simulation results

In this section, simulation results of the proposed CM have been presented. The proposed circuit has been simulated by Mentor Graphics Eldospice in TSMC 0.18 µm CMOS, BSIM3 and Level 53 technology, using a single supply voltage of 1.5 V. The design parameters for the proposed CM (Fig. 4) are summarized in Table 1.

The current transfer characteristics of the proposed CM (Fig. 4) along with that of Garimella et al. compact CM structure [Fig. 1(d)] are shown in Fig. 5. The transfer characteristic curves show that the output current in the proposed CM exactly follows the input current as compared to Garimella et al. compact CM structure, where the output current contains an additional offset term equivalent to biasing current source. This is in accordance to the explanation given in Sect. 3. The current matching error ratio of the proposed circuit is shown in Fig. 6, which is found to be less than 0.0016 % for a current range of 0–500 µA. For the specified range of i_{IN}, input voltage variations of the proposed CM and that of Garimella et al. compact CM structure are given in Fig. 7. This figure shows that the improvement is achieved in the proposed circuit while maintaining the same input compliance voltage.

Table 1 Design parameters of the proposed CM

Component name	Value
Technology	0.18 µm
V_{DD}	1.5 V
M1–M5	5 µm/0.25 µm
M6	20 µm/0.18 µm
MA11–MA22	1 µm/0.25 µm
I_B	10 µA
I_{B1}	100 µA
I_{B2}	2 µA
V_B	1.5 V
i_{IN}	0–500 µA

These simulations were carried out using the specified values of the device parameters. However, as practically this may not be the case, so in order to show the robustness of the proposed CM against variations in device parameters, the Monte Carlo analysis has been performed by applying 5 % mismatch in MOSFET's threshold voltage and aspect ratio with uniform distribution. These Monte Carlo simulations reflecting the variations in current transfer characteristic of the proposed CM are shown in Fig. 8 and 9. This analysis was also carried out to determine the deviations in input

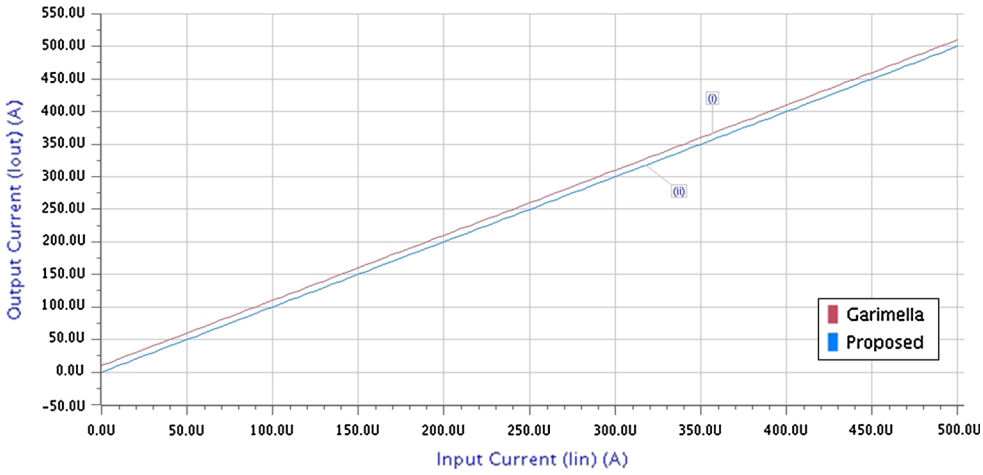

Fig. 5 Output current vs. input current transfer characteristic of (i) Garimella et al. compact CM (ii) Proposed CM

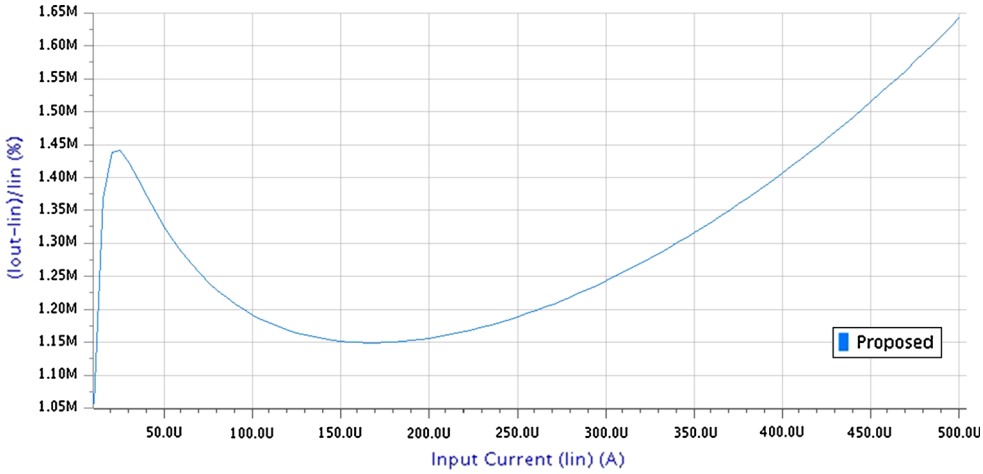

Fig. 6 Simulated current matching error ratio of the proposed CM

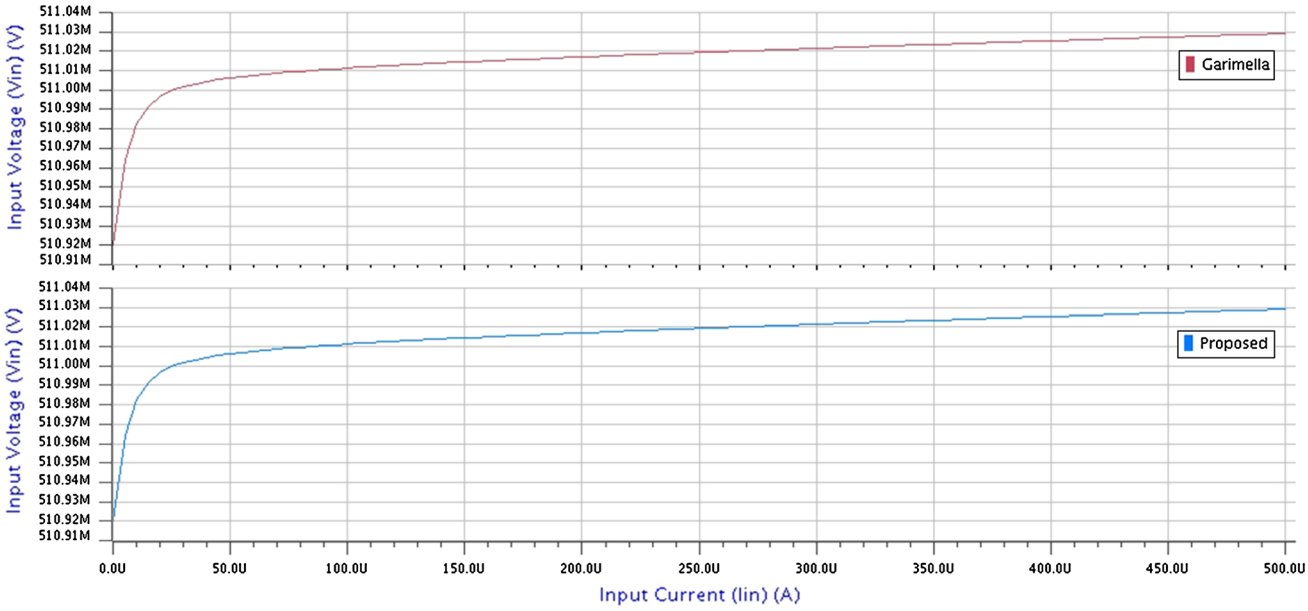

Fig. 7 Input voltage vs. input current variation of (i) Garimella et al. compact CM (ii) Proposed CM

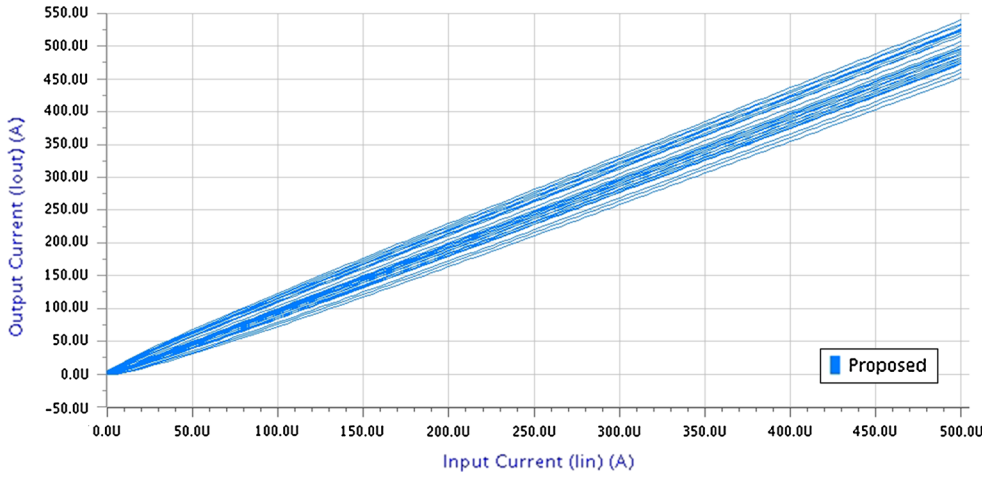

Fig. 8 Monte Carlo simulation showing variation of threshold voltage for current transfer in proposed CM

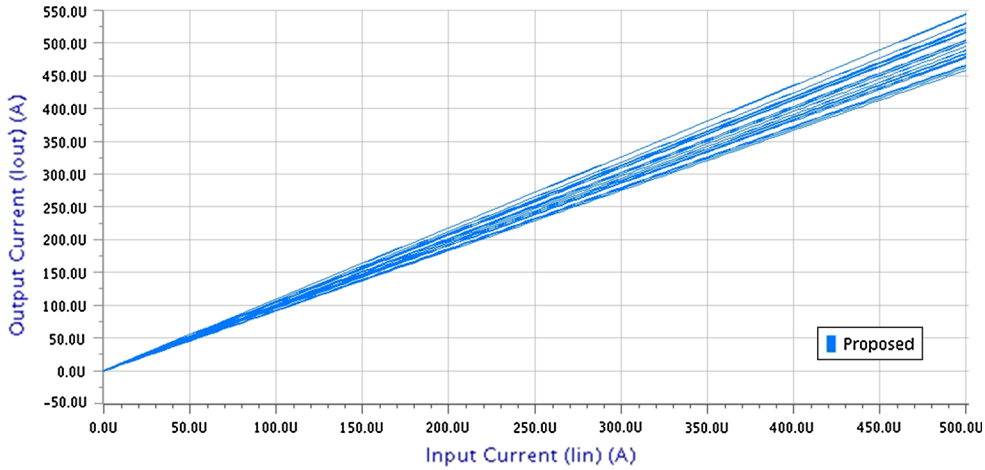

Fig. 9 Monte Carlo simulation showing variation of aspect ratio for current transfer in proposed CM

voltage of the proposed CM with respect to variations in threshold voltage and aspect ratio of the MOSFETs used. The deviation shown was from 0.495 to 0.53 V for mismatch on account of changes in threshold voltage and it ranges from 0.509 to 0.513 V for mismatch in aspect ratio. Furthermore, to investigate the effect of temperature variations on the performance of the proposed CM, the circuit has been simulated for different temperatures varying from −25 to +75 °C. The simulated results obtained for current transfer characteristic is shown in Fig. 10. Moreover, the temperature analysis carried out for calculating changes in input voltage reflected a deviation in the range of 0.509–0.514 V in the proposed CM. All these results show that the different variations caused in device parameters do not significantly affect the performance of the proposed CM. Moreover, the variation in temperature (for a range of −25 to +75 °C) has negligible effect on the performance characteristics of the proposed CM.

For the same technology, the power consumed under similar simulation conditions by the proposed CM (at $i_{IN} = 100$ μA) is 336.56 μW, while that of Garimella et al. compact CM structure is 227.55 μW. Hence it can be summarized that in the proposed circuit, performance of the CM is improved without increasing the supply voltage requirement, though the improvements are obtained at the cost of slight increase in power consumption. Moreover, the simulation results show that the proposed circuit offers considerable increment in the output resistance (r_{out} = 55.76GΩ) as compared to Garimella et al. compact CM structure (r_{out} = 4.34GΩ). The simulated value of the input resistance of the proposed circuit is found to be 0.07 Ω, which is similar to the Garimella et al. compact CM structure, as no change has been carried out at the input side compared to Garimella et al. compact CM structure.

All these values related to the proposed circuit discussed in the paper have been tabulated in Table 2. Besides, to show the efficiency of the proposed circuit, simulated results are compared with [10], [8] and [12]. These comparative results have been also summarized in Table 2, which illustrate the fact that the proposed CM has highest output resistance and accuracy. However, these

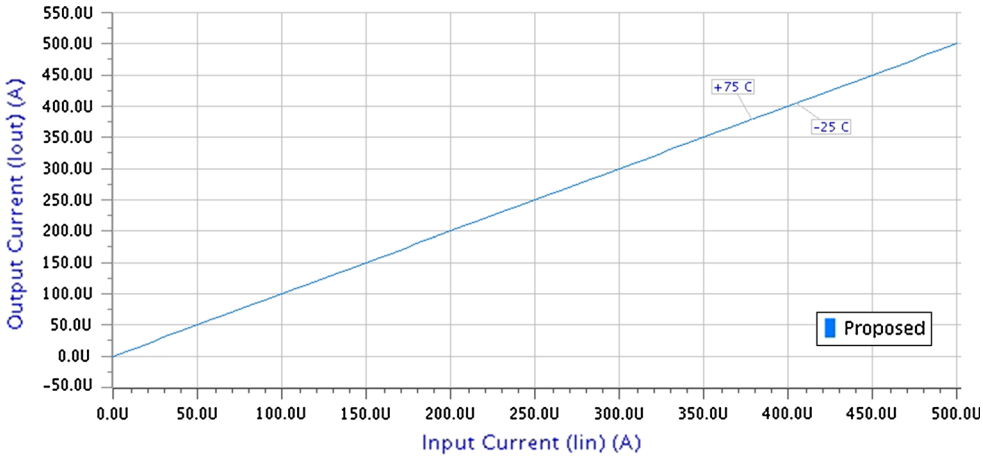

Fig. 10 Current transfer characteristic for temperature variation from −25 to +75 °C in proposed CM

Table 2 Comparative results for a few high-performance CM topologies

	[10]	[12]	[8]	Proposed
Technology	0.18 µm	0.18 µm	0.18 µm	0.18 µm
Supply voltage	1.5 V	1.5 V	1.5 V	1.5 V
Current range	0–500 µA	0–500 µA	0–500 µA	0–500 µA
% Error (at i_{IN} = 100 µA)	0.791	3.9	0.0033 (neglecting offset current)	0.0012
v_{IN} drop (in V)	0.50–0.95	1.1–1.5	0.51	0.51
Input resistance (in Ω at i_{IN} = 100 µA)	1002.8	1439	0.07	0.07
Output resistance (in Ω at i_{IN} = 100 µA)	113.03 M	253.18 M	4.34 G	55.76 G
Power (at i_{IN} = 100µA)	471.078 µW	452.94 µW	227.55 µW	336.56 µW

To get a fair comparison, all the circuits were simulated by the same technology under similar conditions by the authors

achievements are obtained at the cost of a slight increase in power consumption.

5 Conclusions

In this paper a very high performance CM has been proposed. The compact CM structure of Garimella et al. was combined with super-cascode configuration to split biasing current component from signal current component at the output stage. This technique not only allows the exact replication of input current at the output side without any offset term but also provides extremely high output resistance and exact current matching for a wide operating current range. The working of the proposed CM was shown at a supply voltage of 1.5 V using Mentor Graphics Eldospice in TSMC 0.18 µm CMOS, BSIM3 and Level 53 technology. The Monte Carlo analysis and temperature analysis of the proposed CM was shown to demonstrate the robustness of the proposed CM against the variations in device parameters and temperature changes. The results were compared with a few high performance CM topologies available in literature. The proposed CM was shown to have highest accuracy and output resistance with slight increase in power consumption.

References

1. Nairn, D. G., & Salama, C. A. T. (1990). Current-mode algorithmic analog-to-digital converters. *IEEE Journal of Solid-State Circuits, 25*(4), 997–1004.
2. Sackinger, E., & Guggenbuhl, W. (1990). A high-swing, high-impedance MOS cascode circuit. *IEEE Journal of Solid-State Circuits, 25*(1), 289–298.
3. Serrano, T., & Linares-Barranco, B. (1994). The active-input regulated-cascode current mirror. *IEEE Transactions on Circuits and Systems I: Fundamental Theory and Applications, 41*(6), 464–467.
4. Itakura, T., & Czarnul, Z. (1997). High output-resistance CMOS current mirrors for low-voltage applications. *IEICE transactions on Fundamentals of Electronics, Communications and Computer Sciences, E80-A*(1), 230–232.
5. Al-Absi, M. A. (2009). A novel highly accurate current mirror. *International Journal of Electronics, 96*(8), 781–786.
6. Sedra, A. S., & Smith, K. C. (2009). *Microelectronics circuits theory and applications* (5th ed.). New York: Oxford University Press.
7. Tiiliharju, E., Zarabadi, S., Ismail, M., & Halonen, K. (1997). A very-high impedance, high-swing cascode stage for sub-micron

analog VLSI. *IEEE Circuits and Devices Magazine, 13*(4), 49–50.
8. Garimella, A., Garimella, L., Ramirez-Angulo, J., Lopez-Martin, A. J., & Carvajal, R. G. (2005). Low-voltage high performance compact all cascode CMOS current mirror. *Electronics Letters, 41*(25), 1359–1360.
9. Torralba, A., Carvajal, R. G., Ramirez-Angulo, J., & Munoz, E. (2002). Output stage for low supply voltage, high-performance CMOS current mirrors. *Electronics Letters, 38*(24), 1528–1529.
10. Ramirez-Angulo, J., Carvajal, R. G., & Torralba, A. (2004). A low supply high-performance CMOS current mirror with low input and output voltage requirements. *IEEE Transactions on Circuits and Systems II: Express Briefs, 51*(3), 124–129.
11. Ramirez-Angulo, J., Sawant, M. S., Lopez-Martin, A., & Carvajal, R. G. (2005). Compact Implementation of high-performance CMOS current mirror. *Electronics Letters, 41*(10), 570–572.
12. Gupta, M., Aggarwal, B., & Gupta, A. K. (2013). A very high performance self-biased cascode current mirror for CMOS technology. *Analog integrated circuits and signal processing mixed signal letter (Springer), 75*(67–74), 2013.

Bhawna Aggarwal was born in 1980. She received her B.E. in Electronics & Communication Engineering from Indira Gandhi Institute of Technology, Delhi in 2002, M.E. in Electronics & Communication Engineering from Delhi College of Engineering, New Delhi in 2006 and is currently involved in Ph.D. work, in NIT Kurukshetra. Mrs. Aggarwal served as lecturer and Asst. Prof. in Maharaja Agrasen Institute of Technology, (GGSIPU), Delhi, India, for the period 2002(Aug.)–2013(Sep.). Presently, she is with Netaji Subhas Institute of Technology, New Delhi, serving as Asst. Professor in, Electronics and Communication Engineering Department. Her area of research is low power design techniques.

Maneesha Gupta received her B.E. and M.E. in Electronics & Communication Engineering from Government Engineering College, Jabalpur in the years 1981 and 1983, respectively. She received her Ph.D. in Electronics Eng. from Indian Institute of Technology (IIT), Delhi in 1990. Prof. Gupta served as lecturer in various esteemed institutes of India, for the period 1981–1998. Since 1998, she is with Netaji Subhas Institute of Technology, New Delhi and is presently serving as Professor in, Electronics and Communication Engineering Department in the same institute. Her teaching and research interests are Switched Capacitors Circuits and Analog Signal processing.

Anil Kumar Gupta received B.Tech. (ECE) from G.B.Pant University of Agriculture and Tecnology in 1972. He received M.Tech. and Ph.D. in Electrical Engineering from Indian Institute of Technology, Kanpur in the years 1974 and 1985 respectively. He served as Assistant Station Engineer in All India Radio during the period 1974–1978. Since 1985, he is with National Institute of Technology, Kurukshetra where he is presently serving as Professor, Electronics and Communication Engineering for the last thirteen years. His areas of interest are Semiconductor devices and Technology, Embedded systems, Instrumentation and VLSI Design.

Sahil Bansal received B.Tech. in Electronics & Communication Engineering from Maharaja Agrasen Institute of Technology, Delhi in 2009. Presently he is working in TCS as an Engineer in Telecom R&D. His research interests include low voltage design technique and analog circuit designing.

ATLAS: Automatic Temporal Segmentation and Annotation of Lecture Videos Based on Modelling Transition Time

Rajiv Ratn Shah
School of Computing, National University of Singapore, Singapore
rajiv@comp.nus.edu.sg

Yi Yu
School of Computing, National University of Singapore, Singapore
yuy@comp.nus.edu.sg

Anwar Dilawar Shaikh
Department of Computer Engineering, Delhi Technological University, India
anwardshaikh@gmail.com

Suhua Tang
Graduate School of Informatics and Engineering, UEC, Japan
shtang@uec.ac.jp

Roger Zimmermann
School of Computing, National University of Singapore, Singapore
rogerz@comp.nus.edu.sg

ABSTRACT

The number of lecture videos available is increasing rapidly, though there is still insufficient accessibility and traceability of lecture video contents. Specifically, it is very desirable to enable people to navigate and access specific slides or topics within lecture videos. To this end, this paper presents the ATLAS system for the VideoLectures.NET challenge (MediaMixer, transLectures) to automatically perform the temporal segmentation and annotation of lecture videos. ATLAS has two main novelties: (i) a SVM^{hmm} model is proposed to learn temporal transition cues and (ii) a fusion scheme is suggested to combine transition cues extracted from heterogeneous information of lecture videos. According to our initial experiments on videos provided by VideoLectures.NET, the proposed algorithm is able to segment and annotate knowledge structures based on fusing temporal transition cues and the evaluation results are very encouraging, which confirms the effectiveness of our ATLAS system.

Categories and Subject Descriptors

H.3.1 [**Information Storage and Retrieval**]: Content Analysis and Indexing; K.3.1 [**Computers and Education**]: Computer Uses in Education—*Distance learning*

Keywords

Lecture video segmentation; lecture video annotation; lecture video recommendation

1. MOTIVATION AND BACKGROUND

The ATLAS system presented in this paper is our solution to the ACM Multimedia 2014 Grand Challenge on automatic temporal segmentation and annotation. ATLAS stands for *automatic temporal segmentation and annotation of lecture videos based on modelling transition time*. The number of lecture video recordings on the web has increased rapidly due to the ubiquitous availability of cameras and the affordable network infrastructure. However, the accessibility and traceability of lecture video content is still a challenging task. To solve this problem, ATLAS first predicts temporal transitions (TT_1) using supervised learning on video content and temporal transitions (TT_2) by text (transcripts and/or slides) analysis using an N-gram based language model. In the next step, TT_1 and TT_2 are fused by our algorithm to obtain a list of transition times for lecture videos. Moreover, text annotations corresponding to these temporal segments are determined by assigning the most frequent N-gram token of the subtitle resource tracks (SRT) block under consideration (and similar to the N-gram token of slide titles, if available). In this way, the proposed ATLAS system improves the automatic temporal segmentation and annotation of lecture videos so that online learning becomes much easier and users can search sections within a lecture video.

ATLAS introduces new algorithms to automatically segment lecture videos based on video and text analysis. Furthermore, it automatically annotates the segments using an N-gram based language model. A color histogram of a keyframe at each shot-boundary is used as a visual feature to represent the slide transition in the video content. The relationship between the visual features and the transition time of a slide is established with a training dataset of lecture videos provided by the grand challenge organizers, using a machine-learning SVM^{hmm} technique. The SVM^{hmm} model predicts temporal transitions for a lecture video. Furthermore, our solution can help in recommending similar content to the users using text annotations as keywords for searching. The ATLAS system can determine temporal segments and annotations of lecture videos offline rather than at search time, therefore, our system is time-efficient and scales well to large repositories of lecture videos. Our initial experiments have confirmed that our system recommends reasonable temporal segmentations and annotations for lecture videos.

MM '14, November 3–7, 2014, Orlando, Florida, USA.

http://dx.doi.org/10.1145/2647868.2656407.

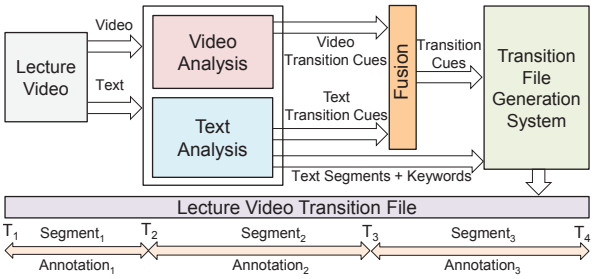

Figure 1: System Framework of ATLAS.

The paper is organized as follows. In Section 2, we review related work and Section 3 describes the ATLAS system. The evaluation results are presented in Section 4. Finally, we conclude the paper with a summary in Section 5.

2. RELATED WORK

Automatic temporal segmentation and annotation of lecture videos is a challenging task, since it depends on many factors such as speaker presentation style, characteristic of camera (*i.e.*, video quality, static or dynamic position/view, *etc*), and others. Moreover, it is a cross-disciplinary area which requires knowledge of text analysis, visual analysis, speech analysis, machine learning and others. In the last a few years, several researchers attempted to solve the problem of automatic segmentation and annotation of lecture videos. Earlier work [5, 7–9] attempted to segment videos automatically by exploiting visual, audio and linguistic features. Fan *et al.* [4] tried to match slides with presentation videos by exploiting visual content features. Chen *et al.* [3] attempted to automatically synchronize presentation slides with the speaker video. Repp *et al.* [10] proposed the segmentation and annotation of audiovisual recordings based on automated speech recognition. Recently, Bhatt *et al.* [1] and Che *et al.* [2] attempted to automatically determine the temporal segmentation and annotation for lecture videos.

3. SYSTEM OVERVIEW

Our system has several novel components which together form its innovative contributions (see Figure 1 for the system framework). The ATLAS system performs the temporal segmentation and annotation of a lecture video in three steps. First, transition cues are predicted from the visual content, using supervised learning described in Section 3.1. Second, transition cues are computed from the available texts using an N-gram based language model described in Section 3.2. Finally, transition cues derived from the previous steps are fused to compute the final temporal transitions and annotations with text, as described in Section 3.3.

3.1 Prediction of Video Transition Cues

A lecture video is composed of several shots combined with cuts and gradual transitions. Kucuktunc *et al.* [7] proposed a video segmentation approach based on fuzzy color histograms which detects shot-boundaries. Therefore, we train two machine learning models using a SVM^{hmm} [6] technique by exploiting the color histograms (64-D) of keyframes to detect the slide transitions automatically in a lecture video. As described in the later Section 4.1, we use lecture videos (V_T) with known transition times as the test set and the remaining in the dataset as the training set. We

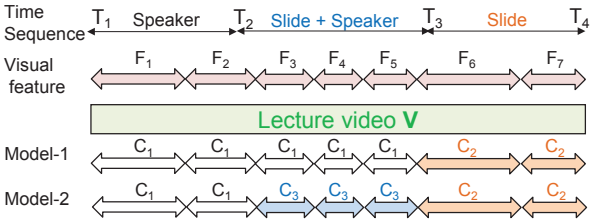

Figure 2: Slide transition models.

employ human annotators to annotate ground truths for lecture videos in the training set (see Figure 2 for an illustration of the annotation with both models).

First, a SVM^{hmm} model M_1 is trained with two classes C_1 and C_2. Class C_2 represents the segment of a lecture video when only a slideshow is visible (or the slideshow covers a major fraction of a frame) and class C_1 represents the remaining part of the video (see Model-1 in Figure 2). Therefore, whenever a transition occurs from a sequence of classes C_1 (*i.e.*, from speaker only or, both speaker and slide) to C_2 (*i.e.*, slideshow only), it indicates a temporal transition with high probability in the majority of cases. However, we find that for some videos this model detects very few transitions (less than five transitions only). We notice that there are mainly three reasons for this issue, first, when lecture videos are recorded with a single shot, second, when the transition occurs from a speaker to a slideshow but the speaker is still visible in the frame most of the time, and third, when the transition occurs between two slides only.

To resolve the above issues, we train another SVM^{hmm} model M_2 by adding another class C_3, which represents the part of a video when a slideshow and a speaker are both visible. We use this model to predict transitions from only those videos for which M_1 predicted very few transitions. We do not use this model for all videos due to two reasons. First, the classification accuracy of M_1 is better than that of M_2 when there is a clear transition from C_1 to C_2. Second, we want to focus on only those videos which exhibit most of their transitions from C_1 to C_3 throughout the video (this is the reason M_1 was predicting very few transitions), hence, a transition from a sequence of classes C_1 to C_3 is considered a slide transition for such kind of videos.

3.2 Computation of Text Transition Cues

3.2.1 *Preparation*

In the preparation step, we convert slides (a PDF file) of a lecture video to a HTML file using Adobe Acrobat software. However this can be done with any other proprietary or open source software as well. The benefit of converting the PDF to an HTML file is that we obtain the text from slides along with their positions and font sizes, which are very important cues to determine the title of slides.

3.2.2 *Title/Sub-Title Text Extraction*

Algorithm 1 extracts titles/sub-titles from the HTML file derived from slides, which represent most of the slide titles of lecture videos accurately. A small variation of this algorithm produces the text content of a slide by extracting the text between two consecutive title texts.

3.2.3 *Transition Time Recommendation from SRT File*

We employ an N-gram based language model to calculate the relevance score R for every block of thirty tokens from

Algorithm 1 Title/sub-title text extraction from slides

1: **procedure** TITLEOFSLIDES(S)
2: INPUT: A HTML file for slides (H)
3: OUTPUT: A list of title text T
4: extractFontFreq(H, $fontList$, $freq$) ▷ this function finds all font and their frequency counts in slides.
5: $titleFontSize$ = findTitleFontSize($fontList$, $freq$) ▷ this function determines the font size of the title of slides.
6: $numSlides$ = findNumSlides($titleFontSize$) ▷ this function calculates the approx number of slides.
7: T = findTitleText($titleFontSize$, $position$) ▷ this function determines the text for titles of all slides which located in top 1/3 of vertically or 2/3 of horizontally in slides.
8: **end procedure**

a SRT file. We use a hash map to keep track of all N-gram tokens and their respective term frequencies (TF). The relevance score is defined by the following equation,

$$R(B_i) = \sum_{j=1}^{N} \sum_{k=1}^{n} W_j * w(t_k),$$

$$\text{and } w(t_k) = \frac{TF(t_k|B_i) * log(TF(t_k|SRT) + 1),}{log \frac{TF(t_k|SRT)+1}{TF(t_k|B_i)}}$$

where, $TF(t_k|B_i)$ is the TF of an N-gram token t_k in a block B_i and $TF(t_k|SRT)$ is the TF of the token t_k in the SRT file. N is the N-gram count (we consider up to $N = 3$, *i.e.*, trigram), W_j is the weight for different N-gram counts such that the sum of all W_j is equal to one, and n is the number of unique tokens in the block B_i. We place more importance to a higher order N-gram count by assigning high values to W_j in the relevance score equation.

If slides of a lecture video are available then we calculate the approximate number of slides ($numSlides$) using the Algorithm 1. We consider the $numSlides$ number of SRT blocks with the highest relevance scores to determine transitions using text analysis. We infer the start time of these blocks from the hash-map and designate them as the temporal transitions derived from the available texts.

3.3 Transition File Generation

We fuse the temporal transitions derived from the visual contents and the speech transcript file by replacing two transitions less than ten seconds apart by their average transitions time and keeping the remaining transitions as the final temporal transitions for the lecture video. Next, we compare N-gram tokens of blocks corresponding to the final temporal transitions and calculate their similarity with N-gram tokens derived from the title of slides. We assign the most similar N-gram token of a block B_i as a text annotation A for a temporal segment which consists of B_i. If slides of lecture videos are not available then an N-gram token with high TF is assigned as a text annotation for the lecture segment.

4. EVALUATION

4.1 Dataset and Experimental Settings

A total of 65 videos (V) were provided with several metadata annotations such as speech transcriptions, slides, transitions, *etc.*, for the VideoLectures.NET Challenge. A transition file contains details of all transitions and corresponding title texts for a lecture video. Therefore, details in the transition file are treated as ground truth for the lecture video segmentation and annotation task. V_T is the test set for the evaluation of our approach, consisting of videos with transition files.

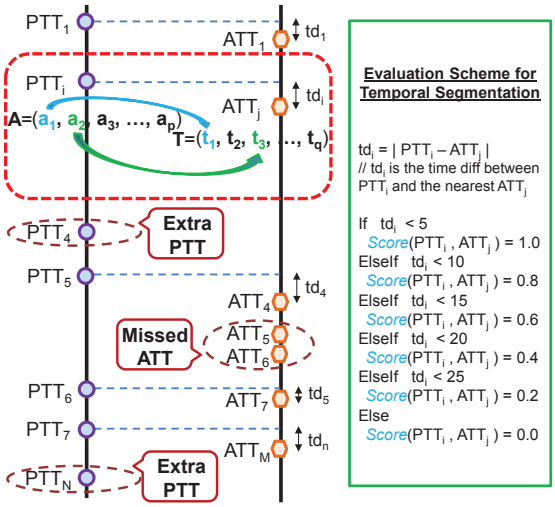

Figure 3: Mapping of PTT, ATT and their respective text to calculate precision, recall and F-1 scores.

4.2 Results

The ATLAS system determines the temporal transitions and the corresponding annotations of lecture videos, with details described earlier in Sections 3.1, 3.2 and 3.3. To evaluate the effectiveness of our approach, we compute precision, recall and F-1 scores for each video in V_T. For a few videos in V_T, precision, recall and F-measure values are very low because our SVM^{hmm} models are not able to detect transitions in lecture videos if lectures are recorded with a single shot, or without zoom-in, zoom-out, or when the slide transitions occur between two slides without any other change in the background. For example, precision and recall for the lecture video *cd07_eco_thu* are *zero*, since only a speaker is visible in the whole video except for a few seconds at the end when both the speaker and a slide consisting of an image with similar color as the background are visible. Therefore, for videos in which our machine learning techniques are not able to detect transitions, we determine transitions from analyzing the speech transcripts (and the text from slides if available) using an N-gram based language model as described in the earlier Section 3.2.

For an evaluation of the temporal segmentation, we connect one predicted transition time (PTT) with only one nearest actual transition time (ATT) from the provided transition files. It is possible that some PTTs are not connected with any ATT and vice versa, as shown in Figure 3. For example, PTT_4 and PTT_N are not connected with any ATT. Similarly, ATT_5 and ATT_6 are not connected with any PTT. We refer to these PTTs and ATTs as $ExtraPTT$ and $MissedATT$, respectively. We compute the score for each (PTT_i, ATT_j) pair based on the time difference between them, by employing a relaxed approach as depicted in Figure 3 because it is very difficult to predict exactly the same transition time at the granularity of seconds. Therefore, to evaluate the accuracy of the temporal segmentation,

Table 1: Evaluation of temporal segmentation for the lecture videos in test set V_T.

	Segmentation Accuracy with Visual Transition Cues (I)			Segmentation Accuracy with Text Transition Cues (II)			Segmentation Accuracy with Fused Transition Cues (III)		
Video Name	**Precision**	**Recall**	**F-1**	**Precision**	**Recall**	**F-1**	**Precision**	**Recall**	**F-1**
sparsemethods_01	0.536	0.728	0.618	0.245	0.185	0.211	0.393	0.638	0.486
scholkopf_kernel_01	0.434	0.451	0.442	0.186	0.255	0.219	0.258	0.506	0.341
denberghe_convex_01	0.573	0.487	0.526	0.397	0.296	0.339	0.452	0.496	0.473
bartok_games	0.356	0.246	0.291	0.156	0.938	0.268	0.169	0.831	0.281
abernethy_learning	0.511	0.192	0.279	0.340	0.625	0.441	0.379	0.600	0.465
agarwal_fgc	0.478	0.287	0.358	0.440	0.367	0.400	0.358	0.393	0.375
abernethy_strategy	0.600	0.235	0.338	0.518	0.496	0.507	0.500	0.435	0.465
cd07_eco_thu	0	0	-	0.166	0.154	0.160	0.183	0.154	0.167
szathmary_eol	0.545	0.988	0.702	0.109	0.225	0.147	0.307	0.825	0.447
2011_agarwal_model	0.350	0.088	0.140	0.366	0.331	0.348	0.366	0.331	0.348
2010_agarwal_itl	0.571	0.174	0.267	0.371	0.339	0.354	0.320	0.348	0.333
leskovec_mlg_01	0.492	0.451	0.471	0.356	0.251	0.294	0.397	0.419	0.408
taylor_kmsvm_01	0.650	0.325	0.433	0.260	0.232	0.245	0.391	0.489	0.435
green_bayesian_01	0.473	0.492	0.483	0.362	0.353	0.357	0.339	0.539	0.416
icml08_agarwal_mpg	0.200	0.012	0.023	0.363	0.352	0.357	0.500	0.121	0.190
nonparametrics_01	0.384	0.571	0.459	0.231	0.331	0.272	0.301	0.584	0.397
bubeck_games	0.655	0.465	0.543	0.280	0.452	0.347	0.379	0.574	0.456
Overall_score	**0.459**	**0.364**	**0.375**	**0.303**	**0.363**	**0.310**	**0.352**	**0.487**	**0.381**

we use the following equations to compute precision and recall, and then compute F-measure (F-1 score) using the standard formula $(2 \times \text{precision} \times \text{recall})/(\text{precision} + \text{recall})$.

$$Precision\_segmentation = \frac{\sum_{k=1}^{r} Score(PTT_i, ATT_j)}{N}$$

$$Recall\_segmentation = \frac{\sum_{k=1}^{r} Score(PTT_i, ATT_j)}{M}$$

where N is the number of ATTs, M is the number of PTTs and r is the number of (PTT_i, ATT_j) pairs.

Table 1 shows the precision, recall and F-1 scores for the temporal segmentation of the lecture videos, (I) when visual transition cues are predicted by our SVM^{hmm} models, (II) when text transition cues are predicted by our N-gram based approach, and (III) when the visual transition cues are fused with text transition cues. Furthermore, it shows that the proposed scheme (III), improves the average *recall* much and the average *F-1* slightly, compared with the other two schemes. Therefore, the transition cues determined from the text analysis are also very helpful, especially when the supervised learning fails to detect temporal transitions.

5. CONCLUSIONS

The proposed ATLAS system provides a novel and time-efficient way to automatically determine the temporal segmentation and annotation of lecture videos. First, it determines the temporal segmentation by fusing the transitions cues computed from the visual contents and the text analysis. Second, it annotates the texts corresponding to the determined temporal transitions. ATLAS can effectively segment and annotate lecture videos to facilitate the accessibility and traceability within their content. In our future work, we plan to extend the approach to apply supervised learning on all available texts using features derived from a confusion matrix based on an N-gram language model.

ACKNOWLEDGMENTS

This research has been supported by the Singapore National Research Foundation under its International Research Centre @ Singapore Funding Initiative and administered by the IDM Programme Office through the *Centre of Social Media Innovations for Communities* (COSMIC).

6. REFERENCES

[1] C. A. Bhatt, A. Popescu-Belis, M. Habibi, S. Ingram, S. Masneri, F. McInnes, N. Pappas, and O. Schreer. Multi-factor Segmentation for Topic Visualization and Recommendation: the MUST-VIS System. In *ACM Multimedia*, pages 365–368, 2013.

[2] X. Che, H. Yang, and C. Meinel. Lecture Video Segmentation by Automatically Analyzing the Synchronized Slides. In *ACM Multimedia*, pages 345–348, 2013.

[3] Y. Chen and W. J. Heng. Automatic Synchronization of Speech Transcript and Slides in Presentation. In *IEEE ISCS*, volume 2, pages 568–571, 2003.

[4] Q. Fan, K. Barnard, A. Amir, A. Efrat, and M. Lin. Matching Slides to Presentation Videos using SIFT and Scene Background Matching. In *ACM Multimedia*, pages 239–248, 2006.

[5] A. Haubold and J. R. Kender. Augmented Segmentation and Visualization for Presentation Videos. In *ACM Multimedia*, pages 51–60, 2005.

[6] T. Joachims, T. Finley, and C.-N. Yu. Cutting-plane Training of Structural SVMs. *In Machine Learning Journal*, 77(1):27–59, 2009.

[7] O. Kucuktunc, U. Gudukbay, and O. Ulusoy. Fuzzy Color Histogram-based Video Segmentation. *In Computer Vision and Image Understanding*, 114(1):125–134, 2010.

[8] M. Lin, J. F. Nunamaker Jr, M. Chau, and H. Chen. Segmentation of Lecture Videos based on Text: A Method Combining Multiple Linguistic Features. In *IEEE Hawaii ICSS*, pages 9–17, 2004.

[9] C.-W. Ngo, T.-C. Pong, and T. S. Huang. Detection of Slide Transition for Topic Indexing. In *IEEE ICME*, volume 2, pages 533–536, 2002.

[10] S. Repp, J. Waitelonis, H. Sack, and C. Meinel. Segmentation and Annotation of Audiovisual Recordings based on Automated Speech Recognition. In *Springer IDEAL*, pages 620–629. 2007.

Appl Biochem Biotechnol
DOI 10.1007/s12010-014-1179-5

Chitosan-Modified Carbon Nanotubes-Based Platform for Low-Density Lipoprotein Detection

Md. Azahar Ali · Nawab Singh · Saurabh Srivastava · Ved V. Agrawal · Renu John · M. Onoda · Bansi D. Malhotra

Received: 1 February 2014 / Accepted: 15 August 2014

Abstract We have fabricated an immunosensor based on carbon nanotubes and chitosan (CNT-CH) composite for detection of low density lipoprotein (LDL) molecules via electrochemical impedance technique. The CNT-CH composite deposited on indium tin oxide (ITO)-coated glass electrode has been used to covalently interact with anti-apolipoprotein B (antibody: AAB) via a co-entrapment method. The biofunctionalization of AAB on carboxylated CNT-CH surface has been confirmed by Fourier transform infrared spectroscopic and electron microscopic studies. The covalent functionalization of antibody on transducer surface reveals higher stability and reproducibility of the fabricated immunosensor. Electrochemical properties of the AAB/CNT-CH/ITO electrode have been investigated using cyclic voltammetric and impedimetric techniques. The impedimetric response of the AAB/CNT-CH/ITO immunoelectrode shows a high sensitivity of 0.953 Ω/(mg/dL)/cm^2 in a detection range of 0–120 mg/dL and low detection limit of 12.5 mg/dL with a regression coefficient of 0.996. The observed low value of association constant (0.34 $M^{-1}s^{-1}$) indicates high affinity of AAB/CNT-CH/ITO immunoelectrode towards LDL molecules. This fabricated immunosensor allows quantitative estimation of LDL concentration with distinguishable variation in the impedance signal.

M. A. Ali · N. Singh · S. Srivastava · V. V. Agrawal (✉) · B. D. Malhotra (✉)
Department of Science and Technology Centre on Biomolecular Electronics, CSIR-National Physical Laboratory, Dr. K. S. Krishnan Marg, New Delhi 110012, India
e-mail: ved.varun@gmail.com
e-mail: bansi.malhotra@gmail.com

M. A. Ali · R. John (✉)
Indian Institute of Technology Hyderabad, Ordnance Factory Estate, Yeddumailaram, Hyderabad, AP 502205, India
e-mail: renujohn@iith.ac.in

M. Onoda
Department of Electrical Engineering and Computer Sciences, University of Hyogo, Himeji, Hyogo 671-2280, Japan

B. D. Malhotra
Department of Biotechnology, Delhi Technological University, Shahbad, Daulatpur, Main Bawana Road, Delhi 110042, India

Published online: 09 September 2014

Keywords Low density lipoprotein · Impedance spectroscopy · Carbon nanotubes · Chitosan · Nanocomposite

Introduction

In recent years, the carbon nanotubes (CNTs) and their composites have been extensively used for biomedical applications such as biosensors, tissue engineering, intracellular analysis, cardiovascular systems, dental implants etc. [1, 2]. CNTs consisting of cylindrical graphite sheets having a diameter in nanometre scale and show many attractive properties, including excellent electrochemical behaviour [3]. CNTs can be utilized as an excellent candidate for construction of the electrochemical biosensors owing to their large surface area, high catalytic and electronic conductivity, high mechanical resistance and tunable surface properties [4]. Additionally, CNTs are being explored for application in fuel cells, solar cells and photovoltaics [5]. Due to the presence of abundant functional groups (−COOH, NH_2 etc.), CNTs provide suitable platform for biofunctionalization [6]. Acid treatment of CNTs' sidewalls plays an important role to introduce these functional groups which help towards antibody functionalization via covalent interaction [7]. The biomolecules such as antibodies, enzymes, DNA, PNA and aptamer-functionalized CNTs surface can improve the electronic properties of CNTs for fabrication of electrochemical biosensors [8]. The covalent binding of CNTs with biomolecules via diimide-activated amidation may improve stability and reproducibility of a biosensor. Thus, CNTs can be utilized for amplification of electronic signals for a desired biosensor [1–8].

The poor solubility and agglomeration of CNTs in an aqueous media is currently a major concern [9]. In this context, the biopolymers such as chitosan (CH) play an important role to reduce dispersion or agglomeration of CNTs thereby improving characteristics of the biosensor devices [10–12]. CH displays excellent film-forming ability due to good adhesion, and can be easily decorated with CNTs due to available reactive hydroxyl and amino functional groups [13, 14]. Spinks et al. have observed improved CNTs dispersion by introducing chitosan solution via sonic agitation and then centrifuge to remove CNTs aggregation [13]. The controlled decoration of CNTs with CH can create new CNT-CH nanocomposite hybrid material to develop biosensors [11]. Cao et al. have described the covalent interaction between CH and CNTs for the formation of nanocomposite material [15]. Only a few researchers have reported this CNT-CH nanocomposite for biosensor applications. Luo et al. have developed a biosensor based on CH-entrapped CNTs via electrochemical deposition method [16]. It has been found that this CNT-CH exhibits excellent electrocatalytic properties during reduction and oxidation of hydrogen peroxide. Qiu et al. have reported a glucose biosensor using porous CNT-CH film-modified electrode [17]. The controllable electrodeposition of carbon nanofiber-doped CH biocompatible layer has been used as an electrode material for the cytosensing of K562 cells [18]. A composite of CNT-CH was used as a matrix for the entrapment of lactate dehydrogenase onto a glassy carbon electrode to fabricate lactate biosensor [14]. This reported biosensor provides a fast response, excellent sensitivity, low electro-oxidation potential of NADH, and the alleviation of electrode surface fouling. Thus, chitosan can be entrapped with CNTs to reduce its agglomeration and suitable for electrode material to improve the characteristics of the biosensing device.

In this paper, we have fabricated the carboxylated CNT-CH nanocomposite-based electrode for antibody (anti-apolipoprotein B (AAB)) functionalization via a co-entrapment method. The structural and biofunctionalization have been confirmed using various spectroscopic and microscopic techniques. The antibody functionalized CNT-CH immunoelectrode has been used to detect low density lipoprotein (LDL) molecules via impedance spectroscopic

technique. The immune reaction between AAB and LDL molecules on transducer surface forms immuno-complex which changes the impedance signal during detection. In the blood stream, LDL molecules can carry 60–70 % of the total serum cholesterol. Higher levels of LDL are known to cause heart attack, stroke, hypercholesterolemia and cardiovascular disease. Thus, the estimation of LDL cholesterol is considered very important for clinical diagnostics.

Experimental Section

Reagents All chemicals including chitosan, N-hydroxisuccimide (NHS), N-ethyl-N′-(3-dymethylaminopropyl carbodiimide), anti-apolipoprotein B 100 and low-density lipoprotein (LDL) molecules are of analytical grade and have been purchased from Sigma Aldrich, USA. Five milligrammes of lyophilized LDL powder is dissolved in 2 mL of de-ionized water which containing 150 mM NaCl of pH 7.4 and 0.01 % EDTA. Bovine serum albumin (BSA, 2 mg/mL) solution is prepared in 50 mM phosphate buffer saline (PBS) of pH 7.4 containing 150 mM NaCl. AAB solution (1 mg/mL) is prepared in PBS solution (50 mM) of pH 7.4 containing 150 mM NaCl. Indium tin oxide (ITO)-coated glass slides (film thickness=~150–300 Å; a resistance of 70–100Ω/square) are procured from Vin Karola Instrument.

Fabrication of CNT-CH Immunoelectrode

The CNTs (90 %) are synthesized by catalytic chemical vapour deposition according to a previous report [19]. Five milligrammes of prepared CNTs is dispersed in 4 mL acetate buffer solution (0.05 M, pH 4.2) and sonicated for 6 h resulting in colloidal CNTs solution. A CH (0.50 %) solution is prepared by dissolving CH (50 mg) in 100 mL of acetate buffer solution. Then, 0.5 mL of CNTs colloidal solution is added to 1 mL chitosan solution and sonicated for 2 h resulting in CNT-CH nanocomposite solution. Fifty microlitres of the prepared CNT-CH nanocomposite solution is uniformly spread on ITO surface via drop casting method and is kept at 30 °C for 6 h. The $-NH_2$ groups present in chitosan are utilized to make the covalent bond formation with −COOH groups of CNTs. In addition, due to opposite charge on CH (positive) and CNTs (negative), the electrostatic interaction may also possible to form nanocomposite. This electrode has been used for biofunctionalization.

Antibody Functionalization

A co-entrapment method (two-step method) along with physical adsorption has been utilized for antibody functionalization followed by 1-ethyl-3-(3-dimethylaminopropyl)carbodiimide (EDC)-NHS coupling chemistry. The prepared AAB solution (1 mg/mL) is entrapped on CNT-CH surface for overnight in a humid chamber (at 4 °C) followed by washing with PBS containing 0.05 % in order to remove any unbound AAB. The AAB/CNT-CH/ITO surface is treated with EDC-NHS in which EDC (0.2 M) works as a coupling agent and NHS (0.05 M) works as an activator. EDC-NHS activates the −COOH group in CNTs. This results in formation of C–N bond between the −COOH group of CNT and the $-NH_2$ terminal of AAB. Lastly, 2 mg/dL of BSA solution is used for blocking the nonspecific adsorption of antibodies on AAB/CNT-CH/ITO surface. The prepared bioelectrode is stored at 4 °C when not in use. It has been found that the AAB/CNT-CH/ITO bioelectrode shows high catalytic

behaviour in phosphate buffer saline at pH 7.4 (50 mM, 0.9 % NaCl) containing $[Fe(CN)_6]^{3-/4-}$ (5 mM).

Instrumentation

The surface morphological studies have been investigated using scanning electron microscope (SEM, LEO-440). Fourier transform infrared spectroscopic (FT-IR; PerkinElmer, Model 2000) measurements is confirmed the antibody functionalization on the CNT-CH surface. The electrochemical investigations such as cyclic voltammetry and electrochemical impedance spectroscopy (EIS) have been carried out using an Autolab Potentiostat/Galvanostat (Eco Chemie, The Netherlands) in phosphate buffer saline [PBS, (50 mM, pH 7.0, 0.9 % NaCl)] containing $[Fe(CN)_6]^{3-/4-}$ (5 mM).

Results and Discussions

Morphological Studies

The high-resolution transmission electron microscopy (HR-TEM) image shows an individual CNT and the diameter of CNTs varies from 40 to 100 nm [Fig. 1(i)]. The length of this CNT is in micron range and the central core diameter of this CNT is very small (~16 nm). Inset shows CNTs with different diameters. The atomic scale image shows that CNTs are highly crystalline in nature, with an interlayer spacing of 0.34 nm (d_{002} for CNT, shown in the inset). Thus, it can be concluded that the prepared COOH-functionalized CNTs are multiwalled. The scanning electron micrograph (SEM) studies are carried out at an accelerating voltage of 20 kV [Fig. 1(ii)]. The length range of the COOH-functionalized CNTs is several micrometres, and they have an external diameter of approximately 30–110 nm. These COOH-functionalized CNTs that are likely randomly oriented on the ITO substrate.

FT-IR Studies

The FT-IR spectra of CH (spectra a) shows the bands in the region 3,200–3,500/cm due to the stretching vibration mode of OH groups [Fig. 2(i)]. The IR band at 1,602/cm corresponds to

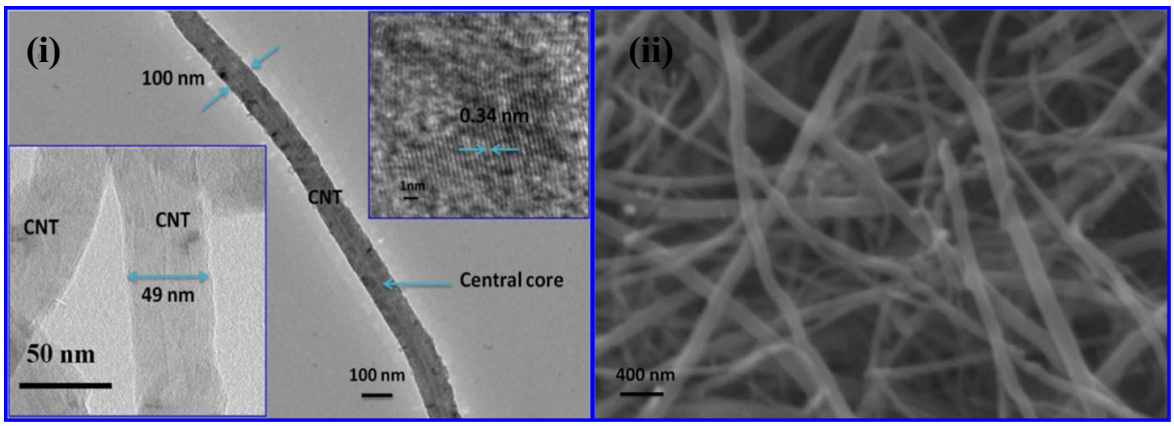

Fig. 1 The HR-TEM analysis of (*i*) an individual CNT (*inset* the CNT with different diameter and lattice fringes of the CNT). (*ii*) SEM image of CNTs

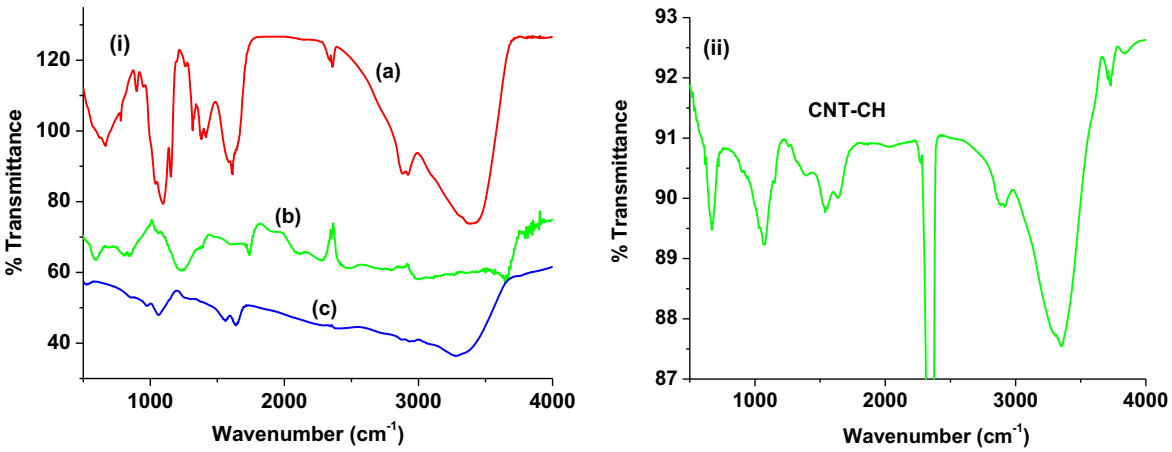

Fig. 2 (*i*) FT-IR spectra of (*a*) CH/ITO film, (*b*) CNT/ITO film and (*c*) AAB/CNT-CH/ITO film. (*ii*) FT-IR spectra of CNT-CH/ITO film

amide I group. The 1,400/cm peak is due to C–N axial deformation (amine group band), 1,317/cm peak is due to COO− group and 1,084/cm is attributed to the stretching vibration mode of the hydroxyl group. In the carboxyl functionalized CNT/ITO film (curve b), the band seen at 840 cm/^{1} is assigned to C–H bending vibration, while those seen at 1,233 and 1,600/cm correspond to stretching vibration of C–C and C=C, bond, respectively. The sharp and strong band found at 1,735/cm is attributed to C=O stretching vibration while a weak band that is seen at 1,233/^{1} due to C–O stretching indicating the carboxyl functionalization of CNTs. Curve (ii) shows the IR spectrum for CNT-CH film. Most peaks appearing in the spectra are combinations of CNT and CH indicating the formation of nanocomposite. However, after immobilization of BSA-AAB on CNT-CH/ITO film surface (curve c), the amide (I and II) bands observed at 1,557 and 3,270/cm, respectively, reveal biofunctionalization.

Electrochemical Studies

Cyclic voltammetry (CV) studies have been conducted for different electrodes in PBS (50 mM, pH 7.0, 0.9 % NaCl) solution containing $[Fe(CN)_6]^{3-/4-}$ in the potential range, −0.7 to +0.7 V verses Ag/AgCl electrode [Fig. 3(i)]. All curves show the well-defined oxidation and reduction peaks in the presence of $[Fe(CN)_6]^{3-/4-}$. The ratio of the cathodic and anodic current is close to 1, which undergoes a quasi-reversible redox process. It has been observed that the peak current for CH/ITO electrode (0.72 mA) is higher compared to that bare CNT/ITO electrode (curve a, 0.57 mA). However, the peak-to-peak potential separation (ΔE) for CH/ITO electrode (curve b, 0.54 V) is found to be lower compared to CNT/ITO electrode (0.82 V) indicating fast electron transfer towards ITO electrode. The drop casted CNTs onto the ITO electrode perhaps lead to slower electron transfer kinetics and poor dispersion ability of CNTs on electrode surface resulting in a large potential for oxidation/reduction of ferro/ferri cyanide molecules. The peak current is enhanced to 0.87 mA for the CNT-CH/ITO electrode due to nanocomposite formation (curve c). Additionally, this may be due to improved electrocatalytic properties of CNTs in presence of CH molecules on the transducer surface. The current decreases due to insulating nature of AAB and BSA loading on CNT-CH/ITO electrode surface (curve d), which perhaps obstruct (or impede) acceleration of the electrons towards the electrode. Figure 3(ii) illustrates the CV of AAB/CNT-CH/ITO immunoelectrode with scan rates varying from 20 to 160 mV/s. There is an increase in both cathodic and anodic peak currents and a slight shift in voltage have been observed with an increase in scan rate. Inset of Fig. 3(ii) shows the variation of anodic peak currents with the scan rate from 20 to

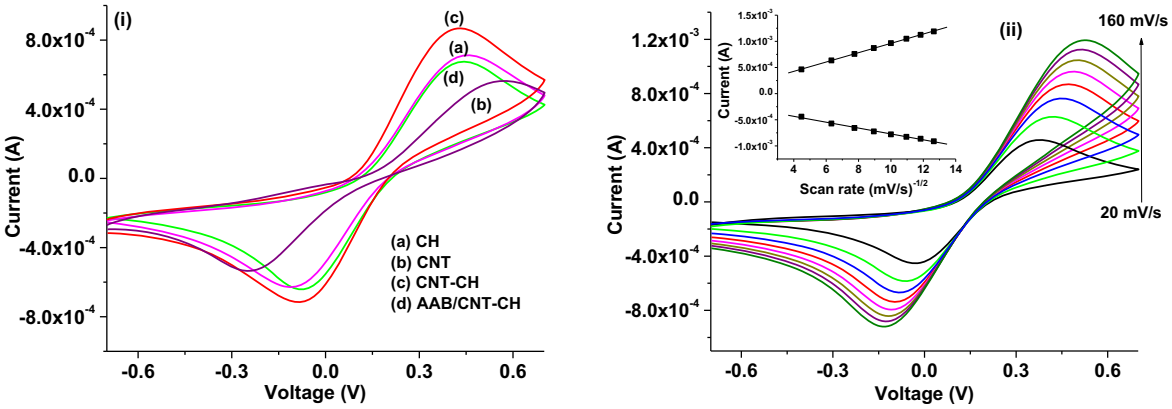

Fig. 3 (*i*) Cyclic voltammetry of different electrodes at scan rate [50 mV/s] and (*ii*) scan rate studies of the AAB/CNT-CH/ITO immunoelectrode

200 mV/s indicating a surface-controlled diffusion process. The surface concentration and diffusivity of the AAB/CysCdS/Au immunoelectrode in presence of redox species has been estimated to be 1.5 μM and 1.34×10^{-7} cm^2/s using Randles-Sevcik Eq. (1).

$$i_p = (269,000)n^{3/2}AD^{1/2}C\nu^{1/2} \tag{1}$$

where i_p is the redox peak current (A), n is the number of electrons transferred in the redox event (1), A is the electrode area (cm^2), D is the diffusion coefficient (cm^2/s), C is the surface concentration (mol) and ν is the scan rate (mV/s). The anodic and cathode current of the scan rate studies are varied according to the Eqs. (2) and (3). The values of the slope, correlation coefficient and intercept of the AAB/CNT-CH/ITO bioelectrode as follows

$$I_{pa} = 0.6\mu A + 0.89\,\mu\text{A} \times \text{sqrt(scan rate)};\ \ R^2 = 0.999 \tag{2}$$

$$I_{ca} = -0.0209\ \ \mu A - 0.56\,\mu\text{A} \times \text{sqrt (scan rate)};\ \ R^2 = 0.997 \tag{3}$$

Impedance Studies

Electrochemical impedance spectroscopy (EIS) is an efficient technique to describe the electrochemical response of a cell as a function of frequency on application of a small sinusoidal AC signal of frequencies in the ranges of 0.01–10^4 Hz. Various electrodes and impedance responses have been carried out at bias potential 0.01 V to observe the dynamics of antibody–antigen interactions. In a typical Nyquist plot, the impedance (complex value) can be described either by the modulus $|Z|$ and the phase shift φ or by the real part (Z') and the imaginary part (Z'') of the signal. Randles circuit is an equivalent circuit for modelling the EIS experimental data to represent the impedance value. It consists of an electrolyte resistance (R_s), in series with the capacitance of the dielectric layer (C_{dl}), the charge–transfer resistance (R_{ct}) and the Warburg impedance (Z_w). The linear part in this plot, observed in the low-frequency range, indicates a mass transfer-limited process, whereas the semicircle portion, observed in high frequency range, indicates a charge transfer-limited process. The parameter, R_{ct} can be extracted from the fitted circuit model. Figure 4 shows the R_{ct} value of the CH/ITO (a) to be 291 Ω whereas the R_{ct} value of the CNT-CH/ITO (b) is found to be 157 Ω. However, the charge transfer resistance for CNT/ITO electrode is calculated as 997 Ω. Thus, impedance for the CNT-CH/ITO electrode is found to be low compared to other electrodes. This is due to the

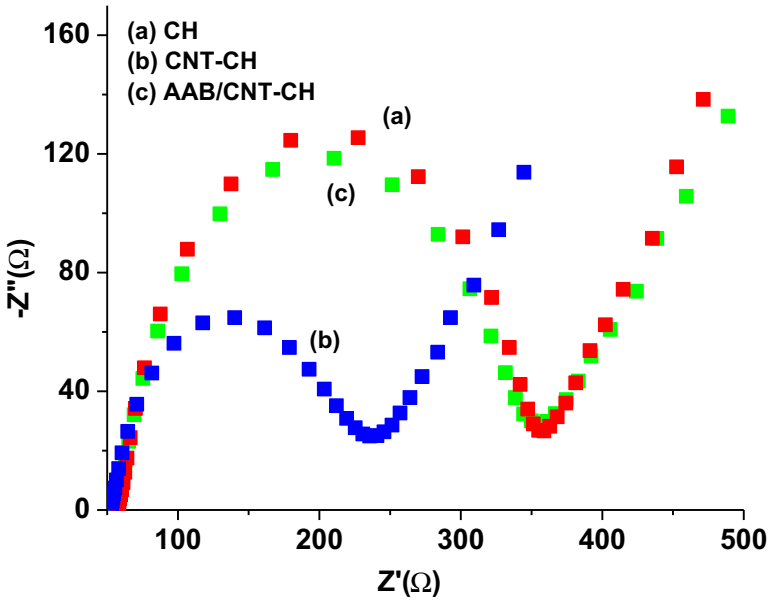

Fig. 4 The Nyquist plots of electrochemical impedance studies for different electrodes

inherent electro-catalytic and enhanced charge transfer properties of CNTs in presence CH molecules. However, the charge transfer properties after biomolecules (AAB-BSA) incorporation on CNT-CH transducer surface is found to be decreased resulting in the enhanced impedance signal (R_{ct} value=285 Ω). This is attributed to the AAB–CNT interaction which impedes the ions transfer from bulk solution to electrode through the diffusion layer and the presence of bulky protein molecules and the steric hindrance of the electron transfer. The heterogeneous electron transfer (k) of the various electrodes has been estimated using charge transfer kinetics as given in Eq. 4

$$k = \frac{RT}{n^2 F^2 A R_{ct} C} \tag{4}$$

where R is the gas constant (8.3145 J/mol), T is the temperature (298 K), n is the electron transferring constant of the redox couple (1), F is the Faraday constant (96485.3 sA/mol), A is the electrode area (0.25 cm^2) and C is the concentration of the redox couple (5 mM). The k_0 values of the AAB/CNT-CH/ITO, CNT-CH/ITO, CH/ITO and CNT/ITO electrodes are obtained as 3.31, 1.8, 3.3 and 12.6×10^{-12} cm/s, respectively.

Impedimetric Response Studies

The impedimetric response for the AAB/CNT-CH/ITO immunoelectrode has been carried out as a function of lipid (LDL) concentration [0–120 mg/dL] in PBS containing $[Fe(CN)_6]^{3-/4-}$ with incubation time of about 4 min [Fig. 5(i)]. The charge transfer resistance (R_{ct}) and double-layer capacitance (C_{dl}) are the most important electrical parameters for analysis of the antibody–antigen interactions. The availability of binding site of antibody (AAB) known as paratope has an affinity to selectively interact with specific binding sites called epitopes of antigen (LDL) resulting in immuno-complex formation. The change in LDL concentration during detection of LDL indicates a change in impedance signal. It is observed that the R_{ct} value increases linearly as LDL concentration increases (0–120 mg/dL) [Fig. 5(ii)]. The increased R_{ct} value indicates that the presence of the insulating layer of LDL on AAB/CNT-CH/ITO immunoelectrode surface due to penetration of the redox species towards the

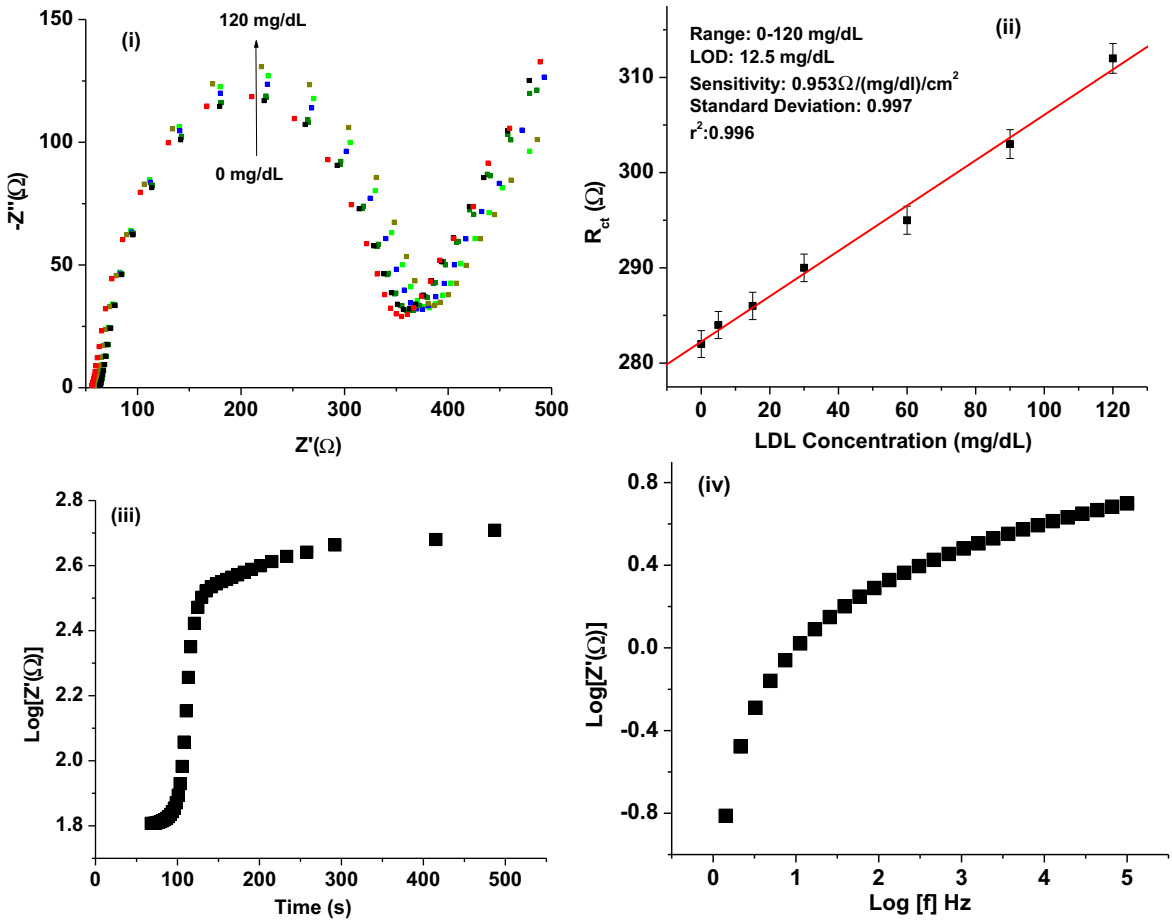

Fig. 5 (*i*) The EIS response of the AAB/CNT-CH/ITO immunoelectrode as a function of LDL concentration (0–120 mg/dL). (*ii*) Sensor calibration plot between the LDL concentration and R_{ct} value. (*iii*) Response time verses impedance plot for 60 mg/dL LDL concentration and (*iv*) Frequencies verses impedance plot for 60 mg/dL of LDL concentration

electrode, resulting in higher diameter of EIS curves. Additionally, the negative charges carried by the LDL phospholipids coating may block the electron transfer of the $[Fe(CN)_6]^{3-/4-}$ redox couple resulting in higher impedance. The immunoelectrode when treated with the 0.2 M glycine solution of pH 2.4 for about 2 min results in 95 % of the regenerated immunoelectrode. The value of R_{ct} of the AAB/CNT-CH/ITO immunoelectrode is varied with LDL concentration (0–120 mg/dL) according to Eq. (5)

$$R_{CT}(\Omega) = 282.2(\Omega) + 0.238\,\Omega/(\mathrm{mg/dL}) \times \mathrm{LDL\ \ concentration} \tag{5}$$

The sensitivity of the AAB/CNT-CH/ITO immunosensor is found as $0.953\,\Omega/(\mathrm{mg/dL})/\mathrm{cm}^2$ with regression coefficient (r^2) as 0.996. It can be seen that the impedimetric biosensor exhibits improved characteristics such as low detection limit of 12.5 mg/dL using $3\sigma_b/m$ criteria, where m is the slope of the calibration graph and σ_b is the standard deviation and response time of 130 s [Fig. 5(iii)]. This nanocomposite (CNT-CH)-based electrode for EIS measurement technique is an efficient, simple, low-cost and time-consuming technique for LDL estimation compared to other techniques such as Friedewald calculation, ultracentrification, electrophoresis etc. In addition, the prepared AAB/CNT-CH/ITO immunoelectrode has been used to investigate selectivity test for LDL (60 mg/dL) in the presence of cholesterol oleate (150 mg/dL), triglyceride (150 mg/dL), free cholesterol (150 mg/dL), and all mixed. The results indicate

that there is negligible change (reduced 98.99 %) in the impedance signal with these analytes indicating non-interference. The storage stability of the AAB/CNT-CH/ITO immunoelectrode has been determined by observing the R_{ct} value at regular intervals of time for 50 days. A plot between frequencies and impedance for 60 mg/dL of LDL concentration is shown in Fig. 5(iv). The AAB/CNT-CH/ITO immunoelectrode is stored at 40 °C when not in use. It has been observed that the immunoelectrode exhibits 97 % response up to 43 days.

Conclusions

A biosensor based on anti-apolipoprotein B functionalized CNT-CH nanocomposite has been fabricated to detect LDL molecules using EIS technique. The electrochemical, structural and morphological properties of the prepared CNT-CH nanocomposite have been investigated using EIS, CV, XRD, FT-IR and TEM techniques. The superior electrochemical properties of antibody co-entrapped CNT-CH nanocomposite improve the biosensor efficacy for detection of LDL concentration. The AAB/CNT-CH/ITO immunosensor is found to be selective for LDL and exhibits a wide detection range of LDL (0–120 mg/dL). The CNT-CH nanocomposite provides a biocompatible and favourable environment due to high surface-to-volume ratio resulting in enhanced loading capacity of AAB. Higher stability of the proposed biosensor has been observed due to covalent functionalization of AAB on CNT-CH nanocomposite surface. This AAB/CNT-CH/ITO immunosensor shows higher sensitivity and fast response. The high sensitivity combined with specificity of LDL-AAB binding, towards LDL detection using CNT-CH nanocomposite is an interesting platform that can be used to detect other lipids such as VLDL, triglyceride etc.

Acknowledgments The authors thank Director NPL, New Delhi, India, for the facilities. Md. Azahar Ali is thankful to CSIR, India for the award of Senior Research Fellowship. V. V. A. is thankful to TSDP-DST and CSIR empower project for funding. The financial support received from Department of Science and Technology, India (grant no. DST/TSG/ME/2008/18) and Indian Council of Medical Research, India (grant no. ICMR/5/3/8/91/GM/2010-RHN) is gratefully acknowledged.

References

1. Sinha, N., & Yeow, J. T.-W. (2005). Carbon nanotubes for biomedical applications. *IEEE Transaction Nanbioscience, 4*, 180–195.
2. Yang, W., Thordarson, P., Gooding, J. J., et al. (2007). Carbon nanotubes for biological and biomedical applications. *Nanotechnology, 18*, 412001.
3. Lin, Y., Lu, F., Tu, Y., et al. (2004). Glucose biosensors based on carbon nanotube nanoelectrode ensembles. *Nano Letters, 4*, 191–195.
4. Wang, J., & Lin, Y. (2008). Functionalized carbon nanotubes and nanofibers for biosensing applications. *Trends in Analytical Chemistry, 27*, 619–626.
5. Zhu, H., Wei, J., Wang, K., et al. (2009). Applications of carbon materials in photovoltaic solar cells. *Solar Energy Materials & Solar Cells, 93*, 1461–1470.
6. Balasubramanian, K., & Burghard, M. (2008). Electrochemically functionalized carbon nanotubes for device applications. *Journal of Materials Chemistry, 18*, 3071–3083.
7. Daniel, S., Rao, T. P., Rao, K. S., et al. (2007). A review of DNA functionalized/grafted carbon nanotubes and their characterization. *Sensors and Actuators B, 122*, 672–682.
8. Das, M., Dhand, C., Sumana, G., et al. (2012). Electrophoretically fabricated core-shell CNT-DNA biowires for biosensing. *Journal of Materials Chemistry, 22*, 2727–2732.
9. Vaisman, L., Wagner, H. D., & Marom, G. (2006). The role of surfactants in dispersion of carbon nanotubes. *Advances in Colloid and Interface Science, 128–130*, 37–46.

10. Li, J., Liu, Q., Liu, Y., et al. (2005). DNA biosensor based on chitosan film doped with carbon nanotubes. *Analytical Biochemistry, 346*, 107–114.
11. Liu, Y., Tang, J., Chen, X., et al. (2005). Decoration of carbon nanotubes with chitosan. *Carbon, 43*, 3178–3180.
12. Wu, Z., Feng, W., Feng, Y., et al. (2007). Preparation and characterization of chitosan-grafted multiwalled carbon nanotubes and their electrochemical properties. *Carbon, 45*, 1212–1218.
13. Spinks, G. M., Shin, S. R., Wallace, G. G., et al. (2006). Mechanical properties of chitosan/CNT microfibers obtained with improved dispersion. *Sensors and Actuators B, 115*, 678–684.
14. Tsai, Y.-C., Chen, S.-Y., Liaw, & H.-W., (2007). Immobilization of lactate dehydrogenase within multiwalled carbon nanotube-chitosan nanocomposite for application to lactate biosensors. *Sensors and Actuators B, 125*, 474–481.
15. Cao, X., Dong, H., Ming, C., et al. (2009). The enhanced mechanical properties of a covalently bound chitosan-multiwalled carbon nanotube nanocomposite. *Journal of Applied Polymer Science, 113*, 466–472.
16. Luo, X.-L., Xu, J.-J., Wang, J.-L., et al. (2005). Electrochemically deposited nanocomposite nanotubes for biosensor application. *Chemical Communications, 2169–2171*.
17. Qiu, J.-D., Xie, H.-Y., & Liang, R.-P. (2008). Preparation of porous chitosan/carbon nanotubes film modified electrode for biosensor application. *Microchimica Acta, 162*, 57–64.
18. Hao, C., Ding, L., & Zhang, X. (2007). Biocompatible conductive architecture of carbon nanofiber-doped chitosan prepared with controllable electrodeposition for cytosensing. *Analytical Chemistry, 79*, 4442–4447.
19. Ali, M.A., Srivastava, S., Solanki, P.R. (2013). Highly efficient bienzyme functionalized nanocomposite-based microfluidics biosensor platform for biomedical application. *Scientific Reports, 3*(1–9), 2661.

Struct Chem
DOI 10.1007/s11224-014-0494-3

ORIGINAL RESEARCH

Computational design of novel flavonoid analogues as potential AChE inhibitors: analysis using group-based QSAR, molecular docking and molecular dynamics simulations

Chakshu Vats · Jaspreet Kaur Dhanjal · Sukriti Goyal · Navneeta Bharadvaja · Abhinav Grover

Received: 28 March 2014 / Accepted: 11 August 2014

Abstract Acetyl cholinesterase (AChE) is an enzyme associated with the loss of cholinergic neurones in Alzheimer's disease. Acetylcholine is an important neurotransmitter found in the brain and the levels of which decrease significantly in Alzheimer's patients due to increased expression of AChE. In this study, a novel fragment-based QSAR model has been developed using twenty-seven flavonoid-derived compounds exhibiting inhibitory activity against AChE. This fragment-based method gives the advantage of studying the effect of individual fragments on the biological activity of the compound by evaluating the descriptors. The compounds were divided into training and test sets, where the test set was used for cross-validation of the model. The QSAR model exhibited good statistical values for the training set ($r^2 = 0.8070$, $q^2 = 0.7088$, F-ratio $= 31.3616$) and test set (pred_$r^2 = 0.8131$). The regression equation obtained had three descriptors describing effect of substitutions in terms of quantitative values. Evaluation of the model implied that electronegative substitution at R1 position lowers the inhibitory activity, while the presence of hydroxyl group improves the same. The presence of rings increased the activity of the compounds. The model thus generated was used to obtain six combinatorial libraries and predicts the activity of these compounds. These compounds were selected for docking and molecular dynamics simulation studies and two leads were identified against AChE.

Keywords QSAR · Acetyl cholinesterase · Alzheimer's disease · Inhibitor · Docking · Molecular dynamics simulations

Introduction

Alzheimer's is one of the leading causes of dementia affecting around 37 million people worldwide. It is also the seventh biggest cause of deaths in United States [1]. The estimated figures are expected to double every 20 years till 2040 due to rapidly ageing population around the globe. Alzheimer's is a progressive neurodegenerative disorder characterized by loss of cognition and impaired intellectual ability and functionality. The two important pathological features that characterize the disease include formation of senile plaques due to aggregation of the peptides of β-amyloid which are derived from amyloid precursor protein and neurofibrillary tangles composed of intra-neuronal cluster of paired helical filaments [2]. Other features of the disease include synaptic degeneration of acetylcholine neurotransmitter, accumulation of lysosomes and glia and mitochondria-mediated inflammation. However, none of the above mentioned factors completely describe the clinical features associated with the disorder. The actual mechanism by which amyloid-beta plaques give rise to Alzheimer's is still unknown but it has been assumed that

Electronic supplementary material The online version of this article (doi:10.1007/s11224-014-0494-3) contains supplementary material, which is available to authorized users.

C. Vats · N. Bharadvaja
Department of Biotechnology, Delhi Technological University, New Delhi 110042, India

J. K. Dhanjal · A. Grover (✉)
School of Biotechnology, Jawaharlal Nehru University, New Delhi 110067, India
e-mail: abhinavgr@gmail.com; agrover@mail.jnu.ac.in

S. Goyal
Apaji Institute of Mathematics & Applied Computer Technology, Banasthali University, Tonk 304022, Rajasthan, India

Published online: 11 September 2014

perturbance in the protein might be the initiating factor [3]. This hypothesis illustrates the triggering of neuron degeneration on accumulation of peptides of amyloid-beta. It has been shown that the toxic aggregates of the protein disrupt the calcium ion channel and initiate apoptosis [4].

Cholinergic deficit or the loss of cholinergic neurons associated with AD leads to the decreased activity of acetylcholine, a neurotransmitter responsible for memory and function [5]. This led to the development of acetyl cholinesterase inhibitors (AChEIs) as potent drugs for the treatment of AD. AChEIs prevent the degradation of AChE by inhibiting the hydrolysis of acetylcholine into choline and acetyl group thereby improving the cognition ability and memory loss [6]. Subsequently, AChEIs were introduced as the preliminary treatment against the disorder. AChEIs and memantine are being used for treatment of AD since last 15 years. All the FDA-approved Alzheimer's drugs, donepezil, tacrine, galantamine, rivastigmine and memantine, belong to these two categories only [1]. These drugs, however, are mildly efficacious and provide only symptomatic relief [7].

The paucity of these drugs and their adverse effects [8] demand major breakthrough in the advancement of new drugs preferably from natural sources. Various compounds of plant origin have been identified to be effective against AD [9]. Anisodamine from *Anisodus tanguticus*, a Chinese herb, has been found to mimic the function of choline in mouse models. Experiments also suggest the use of alkaloids like Withanolide A as probable ligands for inhibition of acetylcholinesterase [10]. Flavonoids, a group of natural compounds found in a variety of fruits and vegetables have also established a presence around the globe due to the important pharmacological functions they possess. Literature provides evidence for its free radical scavenging activity, neuroprotective role, acetyl cholinesterase inhibitory activity and anti-amyloid-beta fibril activity [11, 12]. Thus, the identification of natural products with anti-AD properties is gaining keen interest among the researchers these days.

Traditional drug development method based on random screening, chance discovery is a lengthy, expensive and intellectually inefficient method. Computer-assisted drug designing methods are fast and a viable option for screening of potential drug-like candidates. These methods are low cost and have high success rate. One such method is known as QSAR or quantitative structure activity relationship. QSAR has been long used in scientific community around the world for identification of structure–activity relationships. Previously, QSAR experiments have been performed for inhibitors targeting AChE enzyme. These experiments, however, were based on a 3-D QSAR involving CoMFA and CoMSIA studies [13–16]. With high correlation values, in the range of 0.7–0.9, these models were quite suitable for the prediction of activity of newly synthesized inhibitors based on their 3-D conformation. Although these models could predict the activity of new compounds, they could not signify the importance of the substitution of a particular group at a particular site. In order to identify the contribution of a particular group at a specific site, a novel fragment-based or group-based QSAR method has been developed. This ligand-based drug designing method is advantageous over 2-D and 3-D QSAR. Since it is a fragment-based method, descriptors can be calculated for different fragments instead of a whole molecule. This method can be applied to congeneric as well as non-congeneric inhibitors. Another advantage of this method lies in the fact that the knowledge of the effect of a particular fragment on a substitution site can be used to generate a series of compounds known as combinatorial library. This library can thus be screened for the prediction of more potent drug-like candidates. From the crystallographic structure of AChE, two different ligand binding sites have been identified, i.e. a catalytic active site (CAS) and peripheral cationic site (PAS) [17]. Therefore, in order to completely inhibit AChE, inhibition of both the sites has been advocated. A 3-D QSAR study using flavonoid inhibitors of AChE has been reported previously as well. However, the model was generated using fewer compounds and the correlation values were also low [18]. This study presents an improved model, generated using G-QSAR method and a well-trained system.

A flavonoid scaffold, developed by Li et al., possessing terminal amine groups attached with carbon spacers has been derived to fulfil the aim of designing dual binding site inhibitors of AChEIs. Varied length carbon spacers were used to enhance the dual binding inhibition by the compound. This spacer resides in the mid-gorge and allows the terminal amine groups to occupy CAS site via cation-π interaction and aromatic stacking interactions allows binding of flavonoids to PAS site [19]. In this study, a congeneric series of flavonoid analogues designed and evaluated by Li et al. were used to develop a fragment-based G-QSAR model. These derivatives having basic side chains of different lengths ranging from two to six alkanes depicted metal chelation, AChE inhibition and anti-amyloid-beta aggregation properties [20]. A viable model was obtained which predicted relationship between physiochemical properties of these compounds and their anti-AD properties. The model was then used to recognize important molecular sites and their properties to aid in the development of novel molecule using the approach of virtual combinatorial chemistry. In addition to building the QSAR model, an attempt has been made to provide detailed insights into the molecular mechanism of action of this class of compounds.

Materials and methods

Data set preparation

The structures of 27 flavonoid derivatives [20] were drawn using Marvin sketch 5.12 (Supplementary data), a ChemAxom Ltd. product. These 2-dimensional structures were converted into 3-dimensional form followed by optimization using force field batch minimization, a Vlife engine platform. The minimization was carried out to allow molecules to acquire a stable conformation. Merck molecular force field and Gasteiger charges were the preferred options for the optimization procedure. A common template, representative of all the derivatives, was prepared with the presence of a dummy atom (X) at the substitution site. The reported inhibitory activity (IC_{50}) value of these inhibitors [20] was converted into logarithmic pIC_{50} value to be used for G-QSAR model building. The study was performed using Vlife MDS, version 4.3 provided by Vlife Sciences, Pune, India on Intel® Xeon(R) CPU E31230 @ 3.20 GHz with 8.00 GB RAM [21].

Calculation of descriptors

The common scaffold (Fig. 1) prepared above was used as a template for the fragment-based QSAR model. The G-QSAR module from the VLife MDS was used for the model building. The optimized molecules were imported and their activity values were manually inserted into the worksheet. Activity data can be stored in a .qsr file with molecule names and corresponding activities in each row in this file.

Calculation of 2-D descriptors is one of the most inevitable steps. Molecular descriptors are a numerical representation of chemical information encoded by a molecule. These descriptors are obtained by certain mathematical and logical operations based on the equation and mathematical formulas for different properties. Various physico-chemical descriptors were calculated for the groups present at the substitution site in each of the molecule. The descriptor names adopt a predefined nomenclature such that the name clearly defines the substitution site and properties associated with it. For example, descriptors were named as R1-Hosoya Index, where R1 is the substitution site and Hosoya Index denotes the topological index or number of ways to arrange the edges of bonds of a graph such that no two bonds are placed together. All the columns with a constant value of the molecular descriptor were removed to eliminate the physiochemical properties which do not correlate with the biological activity.

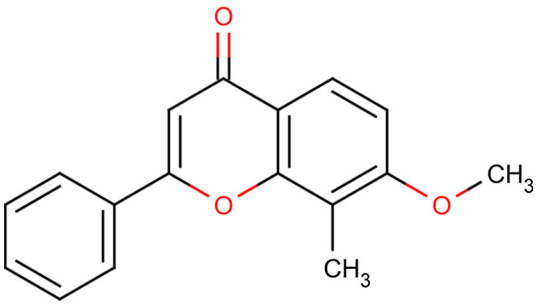

Fig. 1 Common scaffold used for preparing flavonoid derivatives

Data selection and building G-QSAR model

The dataset of the 27 derivatives was divided into test and training sets such that there was a uniform distribution of molecules with respect to activity values (pIC_{50}). This selection was done manually. 9 molecules (7d, 8b, 8d, 9b, 9c, 11c, 11d and 15d out of 27 molecules) were selected for test set and the remaining 18 formed the training set. Unicolumn statistics were calculated for both test and training sets. This is done to observe whether the test set is derived within the max–min range of training set. The mean and standard deviation data, for test and training sets give the relative point density distribution along the mean. Partial Least Square cross-validation method was selected to build G-QSAR model. This method works by removing or adding a predictor variable thereby improving the previous model. The process continues until all the significant variables were included in the model.

From variable selection and model building wizard, simulated annealing algorithm was selected. Simulated annealing was the algorithm of choice for variable (descriptor) selection. The G-QSAR model was built based upon the chosen descriptors. Simulating annealing is a probabilistic method where a temperature variable is kept for simulation of the heating process. This method derives its name from the process of annealing of metals. The temperature variable is initially set high and then decreased as the algorithm progresses. At this stage, algorithm is allowed to accept worst solutions than the current solution, with greater frequency. This ensures that the algorithm, in its initial stages, is not trapped in any local optimum. As the temperature is reduced, the acceptance of solutions becomes more stringent. This allows it to focus on the space where optimum solution can likely be found. This process of gradual cooling makes the algorithm effective enough to obtain an optimal solution in case of large number of local optimum solutions. The value of cross correlation, maximum temperature, number of iterations and variance cutoff were set as 0.5, 1000, 10 and 0.0, respectively.

Validation of the developed G-QSAR model

Certain statistical parameters have to be considered in order to establish a G-QSAR model. These include r^2, q^2, pred_r^2, F-test and standard error [22]. The r^2, coefficient of determination, is a statistical measure of how close the regression line spans the real data points. An F-test is a statistical method of comparing two different models, to identify the best fit. For the model to be robust, the value of these parameters should be above the threshold i.e. $r^2 > 0.5$, $q^2 > 0.5$ and pred_$r^2 > 0.5$. High value of F-test and low values pred_r^{2}se, q^2_se and r^2_se are desirable for a good model [23].

Cross-validation

The model was validated both internally and externally. For internal validation, leave-one-out (q^2) method was adopted. In this method, molecules in the training set were removed consecutively one by one and using the same descriptors, the model was refit. This accounted for prediction of the biological value of the removed molecule. This method is based on the formula:

$$q^2 = 1 - \left(\frac{\sum(y_i - y)}{\sum(y_i - y_{\text{mean}})}\right),$$

where, y_i is the actual and y is the predicted activity of the i^{th} molecule in the training set, and y_{mean} represents the average activity of all molecules of the training set. Model generated from the training set was then used to perform external validation using the test set compounds. The value of pred_r^2 was calculated using the following formula:

$$\text{pred\_}r^2 = 1 - \left(\frac{\sum(y_i - y)}{\sum(y_i - y_{\text{mean}})}\right),$$

where, y_{i} is the actual and y is the predicted activity of the i^{th} molecule in the test set and y_{mean} represents the average activity of all molecules in the training set. Y randomisation tests were used for testing the robustness of the model by comparing it to those derived from random data sets, obtained by shuffling molecules to form new training and test sets. Z score was calculated by the formula:

$$Z \text{ score} = \frac{(h - \mu)}{\sigma}.$$

It is used for calculating the significance of models, by comparing individual scores with the mean score of the entire data set. In this case, h represents the q^2 value calculated for the actual data set; μ is the average q^2 value and σ denotes standard deviation calculated for various iterations using models built by different data sets chosen at random.

Generation of combinatorial library

Six different combinatorial libraries were created on the basis of six different templates. The templates were differing in the length of the spacers, varying from 2 to 6. The lead grow module of VLifeMDS was used to create the libraries. Since there was only one substitution site in the template, each library consisted of 233 molecules. The prediction of activity, however, is done using the generic prediction step in the G-QSAR module. The validated G-QSAR model was used to predict the activity values of the molecules in these six libraries. A highly variable library was obtained by this method.

Preparation of protein and ligand for docking

The protein crystal structure of AChE was obtained from Protein Data Bank [PDB ID: 4M0E]. The CAS site is formed by the residues Trp84, Tyr130, Gly199, His441 and His444 and one conserved residue Phe330, is also involved in the recognition of ligands. The PAS site consists of Tyr70, Asp72, Tyr121, Trp279 and Tyr334 amino acid residues. The water molecules and non-bonded heteroatoms were removed using Accelyrs Viewerlite 5.0 [24]. In order to perform docking, protein was prepared further using Schrodinger's protein preparation wizard [25]. In this preparation process, hydrogens were added, bond lengths were optimized, disulphide bonds were created, terminal residues were capped and selenomethionine was converted to methionine. The compounds obtained from the combinatorial library with higher predicted pIC_{50} value were also prepared using LigPrep. Different chiral, stereochemical and ionization variants of these compounds were generated by this method.

In order to perform docking, a grid was created around the active site of the protein molecule using Glide module of Schrodinger [26–28]. All the small molecules were then docked against the active cleft of the protein using extra precision docking protocol of Glide. The top two complexes, ranked on the basis of their binding energies, were examined for hydrogen bonds and hydrophobic interactions using Ligplot program [29].

Molecular dynamics simulations of the docked complexes

In order to investigate the in vivo stability of the docked complexes, molecular dynamic study was performed in the presence of an explicit solvent on a fully hydrated model using explicit triclinic boundary with harmonic restraints. The simulations were performed using Desmond molecular dynamics module of Schrodinger, with optimized potentials for liquid simulations all-atom force field 2005 [30–32]. The

Table 1 Uni-column statistics

Data	Average	Maximum	Minimum	Standard deviation	Sum
Training	3.0134	3.88	1.59	0.62	54.24
Test	2.99	3.66	1.70	0.63	26.99

complexes were prepared by addition of hydrogens followed by optimization, removal of water molecules, capping of end terminals and generation of disulphide bonds using the protein preparation wizard. Prepared protein–ligand complexes were then solvated with SPC water model in a triclinic periodic boundary box. To avoid direct interaction of the protein complex with its own periodic image, the distance between the complex and the box wall was kept 10 Å. Energy of the prepared systems was minimized to 5,000 steps using steepest descent method or until a gradient threshold of 25 kcal/mol/Å was reached. It was followed by low-memory Broyden-Fletcher-Goldfarb Shanno quasi-Newtonian minimiser until a convergence threshold of 1 kcal/mol/Å was met. For system equilibration, the default parameters in Desmond were applied. The equilibrated systems were then used for simulations at a temperature of 300 K and a constant pressure of 1 atm, with a time step of 2 fs. For handling long-range electrostatic interactions, smooth particle mesh Ewald method was used whereas cutoff method was selected to define the short-range electrostatic interactions. A cut-off of 9 Å radius was used.

Results and discussion

QSAR molecular modelling

The prerequisite for generating a QSAR model is a set of congeneric series with adequate variability in the activity (pIC_{50}) values. The activity values have been derived experimentally [20]. The structures of all the 27 ligands present in the series are provided along with their activity values (Online resource 1). A QSAR model in general is generated considering three important factors: steric, electrostatic and hydrophobic interactions. The descriptors for the three energies were calculated at each lattice point around the grid after the optimization of the ligands. 67 % of the total compounds i.e. 18 were selected as training set and rest 9 as test set. Uni-column statistics (Table 1) were calculated and the two sets were found to adhere to the rule which states that maximum of the test set should be less than the maximum of training set, and minimum of test set should be greater than training set.

Interpretation of G-QSAR model

The model obtained was statistically significant with value of $r^2 = 0.80$, $q^2 = 0.70$ and pred_$r^2 = 0.81$. The values of other statistical parameters are also given in Table 2. The predicted activity data were complying with the actual data with small variations for both test and training sets, which were demonstrated in radar plots (Fig. 2a, b). The data points on the fitness plot lie near the regression line

Table 2 Statistical parameters obtained in G-QSAR model

r^2	q^2	*f*-test	r^2_se	q^2_se	pred_r^2	pred_r^2_se	Y-randomization Avg r^2	Y-randomization Avg q^2
0.8070	0.7088	31.36	0.2918	0.3584	0.8131	0.2764	0.1765	−0.447

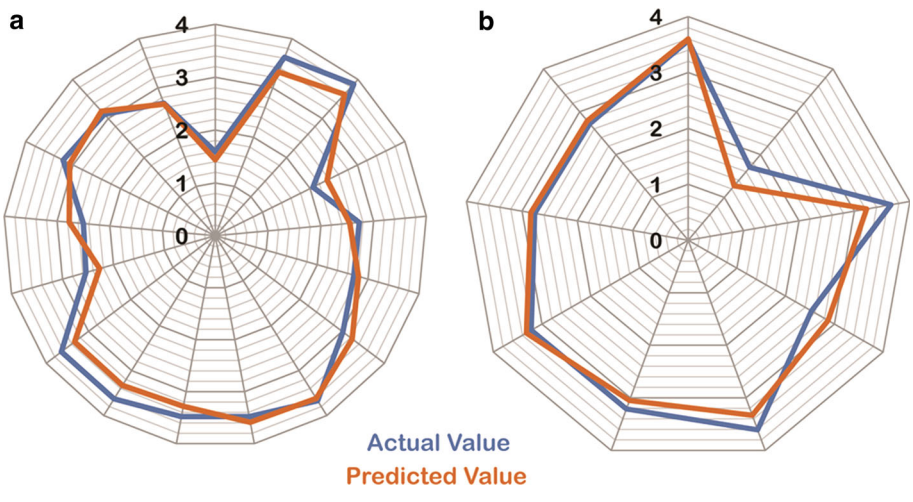

Fig. 2 *Plots* representing actual and predicted activity values of **a** training set, **b** test set

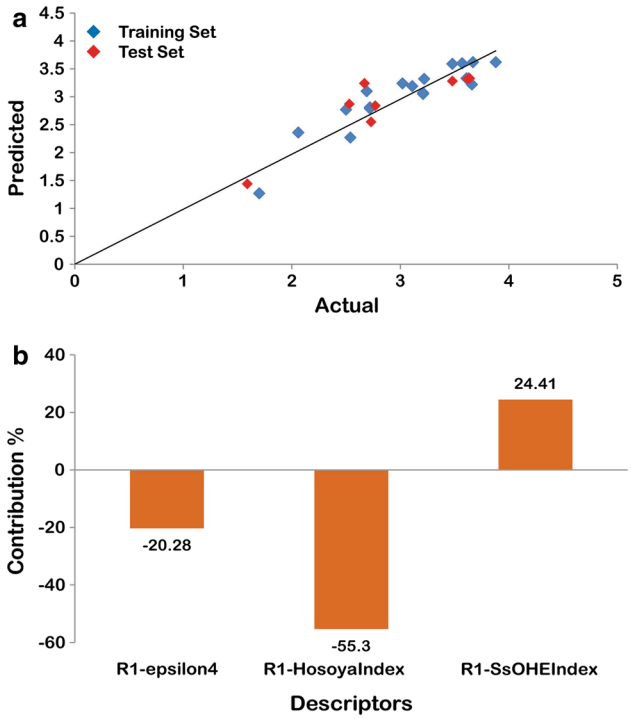

Fig. 3 **a** Fitness plot for test and training sets, **b** molecular descriptors for the G-QSAR model

indicating that the model is acceptable (Fig. 3a). Three important descriptors were calculated for the compounds namely, R1-SsOHE, R1-Hosoy Index and R1-Epsilon4 (Fig. 3b).

The model had good internal and external prediction. The model can be given by the equation:

$$\begin{aligned} \text{pIC50} = {} & (-39.014 * \text{R1} - \text{Epsilon4}) \\ & + (-0.0009 * \text{R1} - \text{Hosoya Index}) \\ & + (0.074 * \text{R1} - \text{SsOHE} - \text{Index}) + 20.82 \end{aligned},$$

with $n = 18$, Degree of freedom $= 15$, Z Score $R^2 = 7.95408$, Z Score $Q^2 = 3.24697$ and where n = no. of compounds in training set. The equation obtained had three physico-chemical descriptors which are explained below:

Hosoya Index

This descriptor signifies that the topological index or Z index of a graph is the total number of matching in it plus 1 ("plus 1" accounts for the number of matchings with 0 edges).

$$z = \sum\nolimits_k p(G,k),$$

where, $p(G,k)$ = Number of ways in which K edges from all bonds of a graph G may be chosen so that no two of them are adjacent. The descriptor has negative contribution of −55.30 indicating that less branching or smaller number of edges in the molecule graph is more favourable.

SsOHE-index

This Electro-topological descriptor gives indices for number of –OH group connected with one single bond. It had a positive value of 24.41, indicating that the presence of –OH group increases the activity of the inhibitors.

Epsilon4

Epsilon4 is the electronegativity index of the saturated carbon skeleton i.e. it indicates the electronegativity when all bonds are saturated and all atoms have made carbon. This descriptor has a negative contribution of −20.28 on the inhibitory activity of the inhibitors. This indicates that lower electronegativity is more favourable.

Y-randomization

In order to check the robustness of the model, Y-randomization test was performed using Y-randomization MLR tool of DTClab (http://dtclab.webs.com/software-tools). The test was done using multiple linear regression, which served the purpose of validation of the QSAR model as well. The model values obtained by Y-randomization were similar to the values obtained using PLS. The values for r^2 and q^2 were found to be 0.813 and 0.727, respectively, which were in accordance with the developed QSAR model. To check the effectiveness, 200 random models were generated by shuffling the activity values and keeping the descriptors constant. For a model to be robust, the averaged value of r^2 and q^2 obtained after shuffling should be low and cRp^2 should be high. Our model fulfilled these criteria with the average r^2 as 0.1765, average q^2 as −0.4476 and cRp^2 as 0.7310. This result indicated that the QSAR model was not just a chance prediction and hence is capable of predicting the activity of new compounds.

Applicability domain analysis

Applicability domain (AD) is the physico-chemical, structural or biological space on which the training set of the model has been developed. It gives information about the subspace of the chemical space in which the model can give reliable prediction. Thus, model will be applicable only to compounds falling within this domain. AD for our model was calculated using an online tool available at http://dtclab.webs.com/software-tools. AD calculation was based on distance scores and was obtained using Euclidean

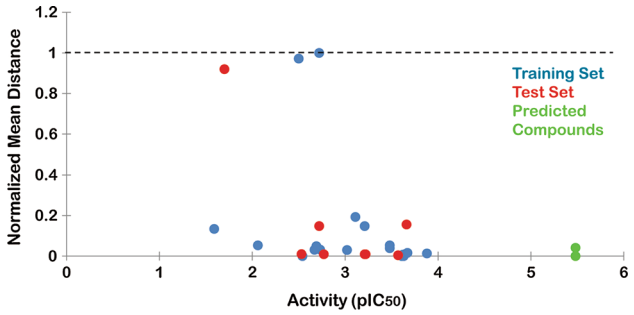

Fig. 4 Scatter plot representing applicability domain values for test set and predicted compounds

distance norms. In this method, the descriptor values were considered and normalized distance was calculated for all the compounds comprising the training and the test sets. The values for training set compounds lied between 0 and 1, where 0 represented the least diverse compound and 1 was for the most diverse compound. In case of test and external set compounds, the value should be within 0 and 1 to consider them within the AD. All the compounds were observed to be within this domain (Fig. 4).

Combinatorial library analysis

Six combinatorial libraries were generated based on the above generated model and their activities were predicted. The six different libraries were generated on different templates with different spacer sequences varying from $n = 2$ to $n = 6$. The substitution was made by different alkanes, atoms, aromatic compounds and rings. Each library consisted of 233 molecules. 40 % of the molecules had predicted values above the highest value in the congeneric series.

Docking and molecular dynamics studies

The top scoring compounds from the combinatorial library with pIC_{50} values above 3.88 were selected. In order to choose the top scoring compound, the extrapolation values were also taken into account. The compounds with extrapolation values above 1.5 were not included. This filtering gave 35 top scoring compounds from all the 6 libraries. In order to identify the potential of these compounds, molecular docking studies were performed using Glide.

Extra precision docking was performed for all the 35 compounds with AChE protein. Results were analysed and the two top scoring compounds were selected to study the interaction pattern with the 3D structure of AChE. The AD value for these two compounds was also calculated as discussed above (Fig. 4). The first compound with activity value of 5.48 contained a spacer sequence with $n = 5$ and had substitution at R1 with cyclohexane (Fig. 6a). The

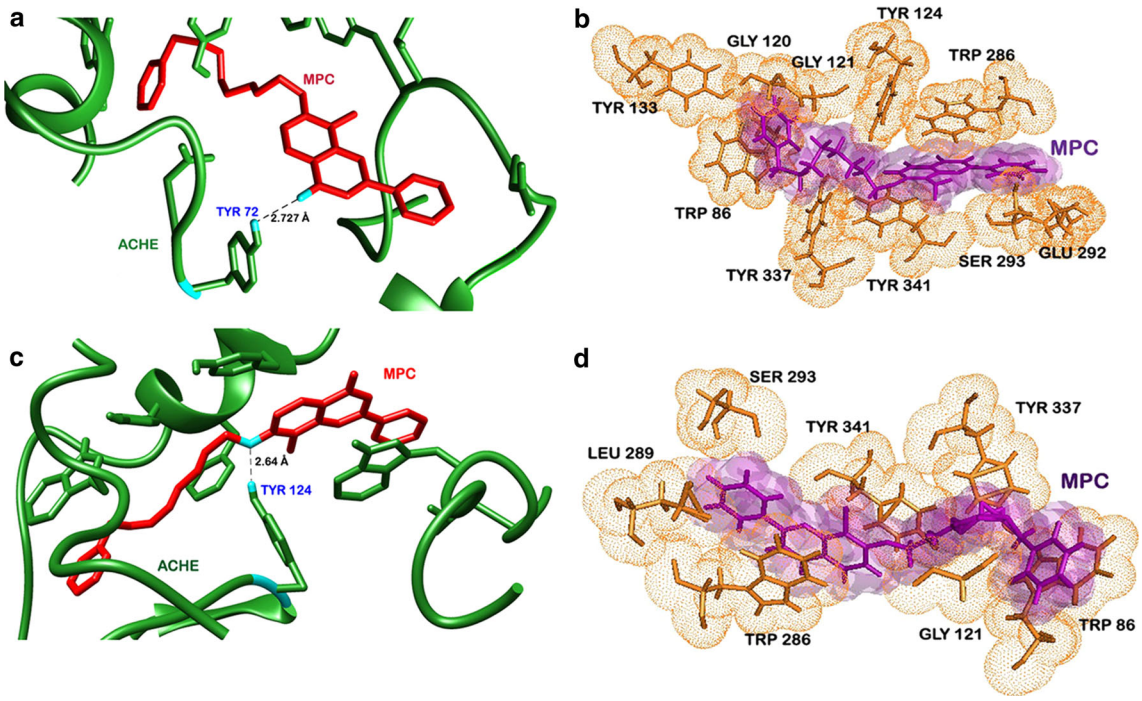

Fig. 5 **a** Pre-MD hydrogen bonds of MPC, **b** pre-MD hydrophobic interactions of MPC, **c** post-MD hydrogen bonds of MPC, **d** post-MD hydrophobic interactions of MPC

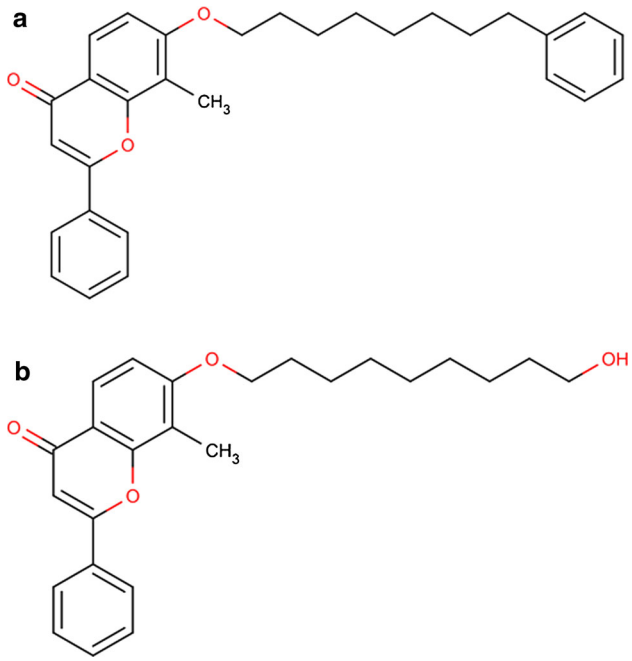

Fig. 6 Structures of the two selected compounds from the library **a** MPC, **b** MPC2

IUPAC name of the compound is 8-methyl-2-phenyl-7-[(8-phenyloctyl)oxy]-4H-chromen-4-one. For the sake of convenience, this compound would be further referred to as MPC. The glide score or the binding energy for the compound was found to be −9.82 kcal/mol. Another important energy value, i.e. van der Waal's energy was also calculated and was found to be −52 kcal/mol. These values suggested strong binding between ligand and protein. Two other important interactions namely hydrogen and hydrophobic interactions were studied using interaction networks plotted using ligplot. MPC made one hydrogen bond with Tyr 72 of AChE (Fig. 5a), one of the active site residues in PAS site, and the bond length was 2.72 Å. Many other strong hydrophobic bonds, with active site residues Gly 120, Gly 121, Leu 289, Tyr 337, Phe 338, Trp 286 and several others (Fig. 5b) were also formed. MPC was found deeply engraved in the active site of AChE.

The second compound (Fig. 6b) with $n = 2$ and activity value of 5.48 had a substitution at R1 with cyclohexane. The IUPAC name of the compound is 8-methyl-2-phenyl-7-(4-phenylbutoxy)-4H-chromen-4-one (further referred to as MPC2). The glide score or binding energy of the compound was calculated as −9.38 kcal/mol and the van der Waal's energy was observed to be −42.91 kcal/mol. In order to explore further the interaction network, ligplot was generated for the complex. MPC2 was making one hydrogen bond with Phe 295 (Fig. 7a) and its bond length was found to be 3.15 Å. Hydrophobic interactions with Trp 286, Leu 289, Val 294,

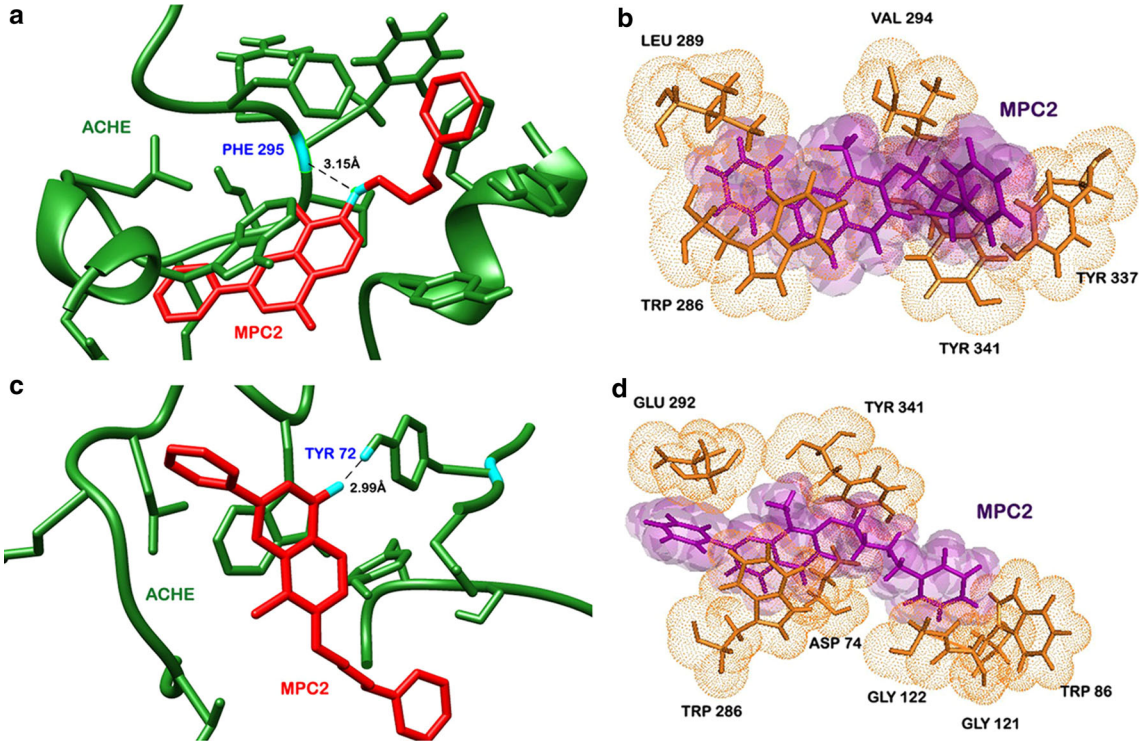

Fig. 7 **a** Pre-MD hydrogen bonds of MPC2, **b** pre-MD hydrophobic interactions of MPC2, **c** post-MD hydrogen bonds of MPC2, **d** post-MD hydrophobic interactions of MPC2

Tyr 337 and Tyr 341 were also (Fig. 7b) observed. This network of strong hydrogen and hydrophobic bonds was stably holding the ligand in place. However, in vivo conditions are different and behaviour of the ligands often changes. Therefore, to further investigate the dynamic behaviour of the ligand–protein complexes, molecular dynamics simulation studies were performed.

Both the complexes were simulated in water box for around 15 ns. A slightly different interaction pattern was observed. After MD, MPC was making one strong hydrogen bond with Tyr 124 (Fig. 5c) instead of Tyr 72 and bond length was found to be 2.64 Å. MPC was now involved in hydrophobic interactions with Trp 86, Gly 121, Trp 286, Ser 293, Tyr 337 and Tyr 341 (Fig. 5d). However, these changes did not affect the stability of the complex. The RMSD plot (Fig. 8a) showed that the complex was stable throughout with fluctuations in the range of 1–2.5 Å. Higher stability was observed from 2 to 6 ns. However, standard deviation was less than 0.8, which indicated that the complex did not deviate much from its initiation conformation. MPC2 also underwent significant changes and was now making a hydrogen bond with Tyr 72 (Fig. 7c) with bond length of 2.99 Å. Tyr 72 is an important residue of PAS site. Hydrophobic bonds with Asp 74, Trp 86, Gly 121, Gly 122, Trp 286, Glu 292 and Tyr 34 (Fig. 7d) were also formed. The changes were significant but did not interfere with the stability of the complex. RMSD of all frames in reference to the first frame was plotted. The docked complex was found to be quite stable with minor deviations (ranging between 1 and 2.5 Å) in the conformation of backbone of the protein (Fig. 8b). Thus, we can strongly suggest these two compounds to be good inhibitors of AChE.

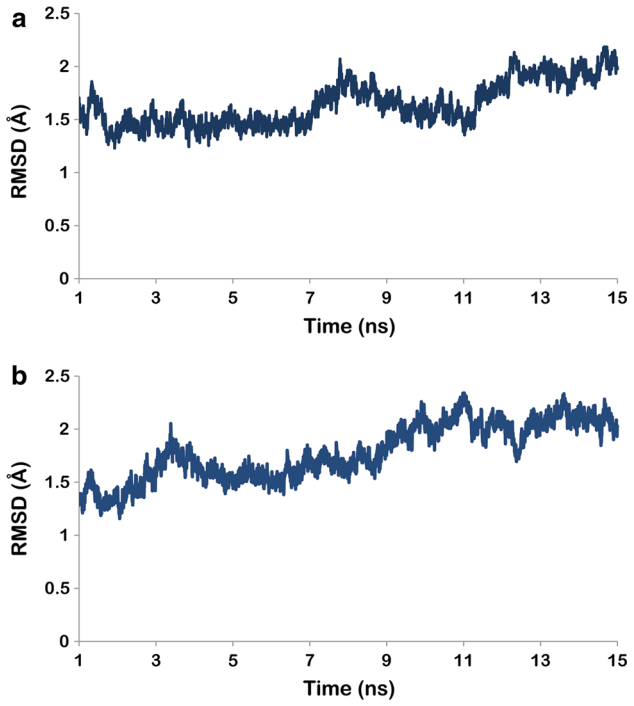

Fig. 8 RMSD trajectory for **a** MPC, **b** MPC2

Conclusion

In this study, a fragment-based QSAR model was developed based on 27 flavanoid molecules with known anti-AChE activity. The activity data and structures were obtained from the literature. The compounds were divided into training and test sets, and model was generated using PLS coupled with simulated annealing method. The statistical parameters obtained were namely r^2, q^2, *F*-test and standard error for the training set and the pred_r^2 for the test set fulfilled the conditions for a model to be considered predictive. The model equation contained three physicochemical descriptors R1-hosoyaindex, R1-SsOHE and R1-epsilon4. The second descriptor was having a positive contribution and the rest two displayed negative contribution in determining the activity of the compounds. Based on the analysis of these descriptors, six combinatorial libraries were created and their activities were predicted using the developed G-QSAR model. The compounds with an activity above 3.88 and in a valid extrapolation range were selected for further studies. Docking studies were performed for these compounds and good binding energies were obtained. This suggested that the binding between the compounds and the protein was favourable. Molecular dynamics studies were performed for the top two compounds obtained after docking to identify the stability of the complex in in vivo conditions. The RMSD reported depicts stable conformation of the protein–ligand complex. Thus, the fragment-based QSAR model developed in this study could be a useful tool in identification and development of lead molecules by taking into account specifically the properties of the substituents. The detailed analysis carried out in this study provides a substantial basis for MPC and MPC2 to be prospective lead molecules against AChE.

Acknowledgments AG would like to thank University Grants Commission, India for the Faculty Recharge position. AG is also thankful to Jawaharlal Nehru University for usage of all computational facilities.

References

1. Melnikova I (2007) Therapies for Alzheimer's disease. Nat Rev Drug Discov 6(5):341–342. doi:10.1038/nrd2314
2. Mayeux R (2006) Genetic epidemiology of Alzheimer disease. Alzheimer Dis Assoc Disord 20(3 Suppl 2):S58–S62

3. Huang Y, Mucke L (2012) Alzheimer mechanisms and therapeutic strategies. Cell 148(6):1204–1222. doi:10.1016/j.cell.2012.02.040
4. Yankner BA, Duffy LK, Kirschner DA (1990) Neurotrophic and neurotoxic effects of amyloid beta protein: reversal by tachykinin neuropeptides. Science 250(4978):279–282
5. Francis PT (2005) The interplay of neurotransmitters in Alzheimer's disease. CNS Spectr 10(11 Suppl 18):6–9
6. Stahl SM (2000) The new cholinesterase inhibitors for Alzheimer's disease, Part 2: illustrating their mechanisms of action. J Clin Psychiatry 61(11):813–814
7. Cutler NR, Sramek JJ (2001) Review of the next generation of Alzheimer's disease therapeutics: challenges for drug development. Prog Neuropsychopharmacol Biol Psychiatry 25(1):27–57
8. Allain H, Bentue-Ferrer D, Tribut O, Gauthier S, Michel BF, Drieu-La Rochelle C (2003) Alzheimer's disease: the pharmacological pathway. Fundam Clin Pharmacol 17(4):419–428
9. Kim H, Park BS, Lee KG, Choi CY, Jang SS, Kim YH, Lee SE (2005) Effects of naturally occurring compounds on fibril formation and oxidative stress of beta-amyloid. J Agric Food Chem 53(22):8537–8541. doi:10.1021/jf051985c
10. Grover A, Shandilya A, Agrawal V, Bisaria VS, Sundar D (2012) Computational evidence to inhibition of human acetyl cholinesterase by withanolide a for Alzheimer treatment. J Biomol Struct Dyn 29(4):651–662. doi:10.1080/07391102.2012.10507408
11. Schroeter H, Spencer JP, Rice-Evans C, Williams RJ (2001) Flavonoids protect neurons from oxidized low-density-lipoprotein-induced apoptosis involving c-Jun N-terminal kinase (JNK), c-Jun and caspase-3. Biochem J 358(Pt 3):547–557
12. Lou H, Fan P, Perez RG (2011) Neuroprotective effects of linarin through activation of the PI3K/Akt pathway in amyloid-beta-induced neuronal cell death. Bioorg Med Chem 19(13):4021–4027. doi:10.1016/j.bmc.2011.05.021
13. Shen LL, Liu GX, Tang Y (2007) Molecular docking and 3D-QSAR studies of 2-substituted 1-indanone derivatives as acetylcholinesterase inhibitors. Acta Pharmacol Sin 28(12):2053–2063. doi:10.1111/j.1745-7254.2007.00664.x
14. Li YP, Weng X, Ning FX, Ou JB, Hou JQ, Luo HB, Li D, Huang ZS, Huang SL, Gu LQ (2013) 3D-QSAR studies of azaoxoisoaporphine, oxoaporphine, and oxoisoaporphine derivatives as anti-AChE and anti-AD agents by the CoMFA method. J Mol Graph Model 41:61–67. doi:10.1016/j.jmgm.2013.02.003
15. Akula N, Lecanu L, Greeson J, Papadopoulos V (2006) 3D QSAR studies of AChE inhibitors based on molecular docking scores and CoMFA. Bioorg Med Chem Lett 16(24):6277–6280. doi:10.1016/j.bmcl.2006.09.030
16. Gharaghani S, Khayamian T, Ebrahimi M (2013) Molecular dynamics simulation study and molecular docking descriptors in structure-based QSAR on acetylcholinesterase (AChE) inhibitors. SAR QSAR Environ Res 24(9):773–794. doi:10.1080/1062936X.2013.792877
17. Sheng R, Lin X, Zhang J, Chol KS, Huang W, Yang B, He Q, Hu Y (2009) Design, synthesis and evaluation of flavonoid derivatives as potent AChE inhibitors. Bioorg Med Chem 17(18):6692–6698. doi:10.1016/j.bmc.2009.07.072
18. Goyal M, Grover S, Dhanjal J, Goyal S, Tyagi C, Grover A (2014) Molecular modelling studies on flavonoid derivatives as dual site inhibitors of human acetyl cholinesterase using 3D-QSAR, pharmacophore and high throughput screening approaches. Med Chem Res 23(4):2122–2132. doi:10.1007/s00044-013-0810-2
19. Fernandez-Bachiller MI, Perez C, Monjas L, Rademann J, Rodriguez-Franco MI (2012) New tacrine-4-oxo-4H-chromene hybrids as multifunctional agents for the treatment of Alzheimer's disease, with cholinergic, antioxidant, and beta-amyloid-reducing properties. J Med Chem 55(3):1303–1317. doi:10.1021/jm201460y
20. Li RS, Wang XB, Hu XJ, Kong LY (2013) Design, synthesis and evaluation of flavonoid derivatives as potential multifunctional acetylcholinesterase inhibitors against Alzheimer's disease. Bioorg Med Chem Lett 23(9):2636–2641. doi:10.1016/j.bmcl.2013.02.095
21. VLifeMDS: Molecular Design Suite. In., 3.0 edn; 2004: Vlife Sciences Technologies Pvt. Ltd., Pune, India
22. Gonzalez MP, Teran C, Saiz-Urra L, Teijeira M (2008) Variable selection methods in QSAR: an overview. Curr Top Med Chem 8(18):1606–1627
23. Golbraikh A, Tropsha A (2002) Predictive QSAR modeling based on diversity sampling of experimental datasets for the training and test set selection. J Comput Aided Mol Des 16(5–6):357–369
24. Viewerlite 5.0: Discovery Studio Visualizer. 5.0 edn
25. Sastry GM, Adzhigirey M, Day T, Annabhimoju R, Sherman W (2013) Protein and ligand preparation: parameters, protocols, and influence on virtual screening enrichments. J Comput Aided Mol Des 27(3):221–234. doi:10.1007/s10822-013-9644-8
26. Friesner RA, Banks JL, Murphy RB, Halgren TA, Klicic JJ, Mainz DT, Repasky MP, Knoll EH, Shelley M, Perry JK (2004) Glide: a new approach for rapid, accurate docking and scoring. 1. Method and assessment of docking accuracy. J Med Chem 47(7):1739–1749
27. Friesner RA, Murphy RB, Repasky MP, Frye LL, Greenwood JR, Halgren TA, Sanschagrin PC, Mainz DT (2006) Extra precision glide: docking and scoring incorporating a model of hydrophobic enclosure for protein-ligand complexes. J Med Chem 49(21):6177–6196
28. Halgren TA, Murphy RB, Friesner RA, Beard HS, Frye LL, Pollard WT, Banks JL (2004) Glide: a new approach for rapid, accurate docking and scoring. 2. Enrichment factors in database screening. J Med Chem 47(7):1750–1759
29. Wallace AC, Laskowski RA, Thornton JM (1995) LIGPLOT: a program to generate schematic diagrams of protein-ligand interactions. Protein Eng 8(2):127–134
30. Bowers KJ, Chow E, Xu H, Dror RO, Eastwood MP, Gregersen BA, Klepeis JL, Kolossvary I, Moraes MA, Sacerdoti FD (2006) Scalable algorithms for molecular dynamics simulations on commodity clusters. In: SC 2006 Conference, Proceedings of the ACM/IEEE. IEEE, pp 43–43
31. Guo Z, Mohanty U, Noehre J, Sawyer TK, Sherman W, Krilov G (2010) Probing the α-helical structural stability of stapled p53 peptides: molecular dynamics simulations and analysis. Chem Biol Drug Des 75(4):348–359
32. Shivakumar D, Williams J, Wu Y, Damm W, Shelley J, Sherman W (2010) Prediction of absolute solvation free energies using molecular dynamics free energy perturbation and the OPLS force field. J Chem Theory Comput 6(5):1509–1519

Conductance Based Fryze Algorithm for Improving Power Quality for Non-Linear Loads

Sachin Kumar Kesharvani
Department of Electrical Engineering
Delhi Technological University, Delhi
sachin.kesharvani@gmail.com

Alka Singh
Department of Electrical Engineering
Delhi Technological University, Delhi
alkasingh.dr@gmail.com

Manoj Badoni
Department of Electrical Engineering
Delhi Technological University, Delhi
manoj_badoni@yahoo.co.in

Abstract --- **In the present scenario, non-linear loads are increasing day by day, due to which harmonics are being injected in the power system. This affects a number of sensitive loads connected to the system and affects their performance. This paper discusses the simulation as well as hardware implementation results with a Distribution STATic COMpensator (DSTATCOM) for compensation of unbalanced loads and harmonic currents produced by non-linear loads. The control scheme used for the compensation is conductance-based on the generalized Fryze currents minimization theory. A proportional-integral (PI) controller is used for maintaining the dc bus voltage of the capacitor used in voltage source converter (VSC). The switching of VSC is done using Hysteresis Current Controller (HCC) based on indirect current control scheme. The hardware implementation of DSTATCOM is implemented with the help of dSPACE DS1104 R&D controller having TMS320F240 as a slave DSP. Both MATLAB-based and hardware implementation results are presented for demonstrating the steady state as well as dynamic load conditions. The conductance based Fryze control scheme is found to be very effective in reducing the THD of supply current to IEEE-519 standards.**

Keywords: **DSTATCOM; harmonics; Fryze; conductance; dSPACE; VSC; non-linear loads.**

I. INTRODUCTION

Power qualities problems occur mainly due to harmonic injection and reactive power imbalance. These are responsible for polluting the power transmission and distribution system. There are several sources of harmonics like switched mode power supplies (SMPS), rectifiers, arc furnaces, adjustable speed drives and many more non-linear loads [1]-[2]. Due to the harmonics, there is excessive heating in the system as well the performances of much sensitive equipment is adversely affected. It is also a major cause of malfunctioning and damaging the sensitive devices. Traditionally, passive filters are used to compensate the harmonics. But with these filters some demerits are associated such as resonance, performance dependency on impedance and bulky in the size and filters capability to eliminate particular harmonic [3]-[4]. Many static VAR compensators have been implemented to overcome these problems and improve power quality in distribution system. For solving the problems of current harmonics and compensating reactive power together, many types of APFs have been developed [4].

In 1976, the concept of APF was presented by Gyugyi and Strycula [1]. The APFs may be connected in two ways. The series connection of APF provides voltage compensation and the shunt connection provides current compensation of the load. This paper presents the conductance based Fryze current minimization controller based shunt APF for real time compensating the reference currents which is fed to the gate driver of the IGBTs for operating the converter [5]-[8]. This controller is better than the Instantaneous reactive power theory based controller which was introduced by H. Akagi. In which computational complication is much because of some transform like park transformation, dq-transform and dq-inverse transform [6].

II. SYSTEM CONFIGURATION

A three phase system of 110V line-to-line, 50 Hz frequency is taken as power circuit. At the point of common coupling, a three phase, 3 leg DSTATCOM is connected. The STATCOM is implemented using a universal bridge consisting of IGBTs with anti-parallel diodes. Interfacing inductors of 3.2mH are used connecting the voltage source converter to power circuit. Validation of control scheme has been done by both simulation and experimentally. LEM (LV-25) voltage sensors are used for sensing PCC voltages and LEM (LA-25) current sensors are used for sensing source and load currents. LV-25/SP5 voltage sensor having capacity of 1500V is used for sensing DC link voltage. The control scheme is implemented in dSPACE DS1104 R&D controller having TMS320F240 as a slave DSP. A three phase bridge rectifier having series RL branch on DC side with different R

978-1-4799-3140-8/14/$31.00

values and 100mH fixed inductor is used as non-linear load. The current range of above mentioned load can vary from 1amp to 6amp. PI-controller is used to regulate the voltage of dc link to its reference value of 200V.

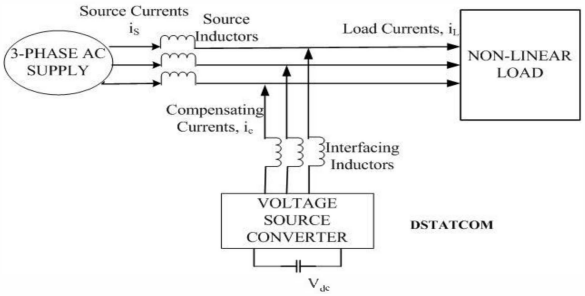

Fig. 1. DSTATCOM implemented in distribution system with the non-linear load.

Fig. 1 shows the power network in which a non-linear load is fed from three phase grid connected AC mains supply. The DSTATCOM works on the principle of shunt compensation and injects the current based on the objective to be achieved. If the controller is to be designed for harmonic compensation, then it is controlled to inject current distortion in the load current equal in magnitude but opposite in sign. Thus, it cancels the distortions coming from the load to the source at the PCC, which results in improved power quality of the source. The following equation shows the instantaneous source current and the source voltages are

$$i_s(t) = i_L(t) - i_c(t) \quad (1)$$

$$V_s(t) = V_m \sin\omega t \quad (2)$$

Where i_s, i_L, i_c, V_s and V_m are the instantaneous source current, load current, compensator current, source voltage and amplitude of the source voltage. The load current signal waveform can be analyzed by Fourier series as containing two components; first having fundament component and second term represents harmonics component.

$$\begin{aligned} i_L(t) &= \sum_{n=1}^{\infty}(I_n \sin(n\omega t + \phi n)) \\ &= I_1 \sin(\omega t + \phi 1) + \sum_{n=2}^{\infty}(I_n \sin(n\omega t + \phi n)) \\ &= \text{Fundamental component + Harmonics component} \end{aligned} \quad (3)$$

The second component of the load current is produced by the compensator in opposite phase to improve the source current quality i.e. power quality of the system.

A. DC Voltage Regulator

Some power losses occur in the voltage source converter. So for compensating these losses, active power should flow from source of the network. A dc voltage regulator is shown in the Fig. 2, in which a PI-controller is used for maintaining the voltage of dc capacitor. The output of the PI-controller i.e. G_{loss} is then used for the calculation of the active currents. G_{loss} component represents the loss component. V_{ref} is the desired DC link voltage and it is set as 200V.

Transfer function of the PI-controller is;

$$T_s = K_p + K_i/s \quad (4)$$

where, K_p is called proportional gain and K_i is called integral gain of the controller.

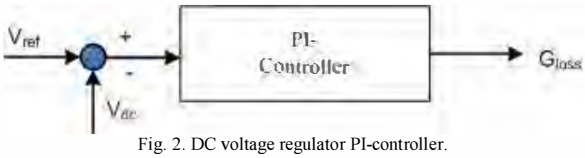

Fig. 2. DC voltage regulator PI-controller.

B. Fryze Current Minimization Algorithm

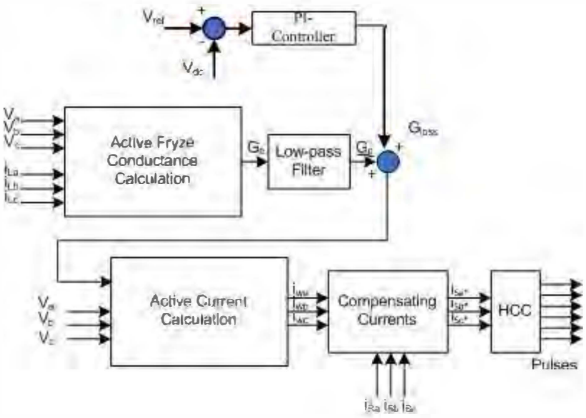

Fig. 3. Block diagram of generalized Fryze current minimization algorithm

In the Fryze current minimization control scheme [1], active Fryze Conductance Calculation is done with the PCC voltages and the load currents according to the given formula.

$$G_e = \frac{v_a.i_{La} + v_b.i_{Lb} + v_c.i_{Lc}}{{v_a}^2 + {v_b}^2 + {v_c}^2} \quad (5)$$

where, G_e is the average value of conductance v_a, v_b and v_c are the sensed phase voltages of the PCC and i_{La}, i_{Lb} and i_{Lc} are the sensed load currents. Then the average conductance value is passed through a low-pass filter of frequency 50Hz for filtering the fundamental part of the conductance. So the output of the filter i.e. $\underline{G_e}$ is added with the G_{loss} to get the net conductance G.

$$G = \underline{G_e} + G_{loss} \quad (6)$$

After that, this value is multiplied with the phase voltages v_a, v_b and v_c to get the active currents i.e. i_{wa}, i_{wb},and i_{wc}.

$$i_{wa} = (\underline{G_e} + G_{loss}).\ v_a \quad (7)$$

$$i_{wb} = (\underline{G_e} + G_{loss}).\ v_b \quad (8)$$

$$i_{wc} = (\underline{G_e} + G_{loss}).\ v_c \quad (9)$$

These active currents are passed through the hysteresis current controller (HCC) for generating six gating pulses to operate the six IGBTs of the three legs VSC. The entire scheme is shown in Fig. 3.

III. SIMULATION RESULTS

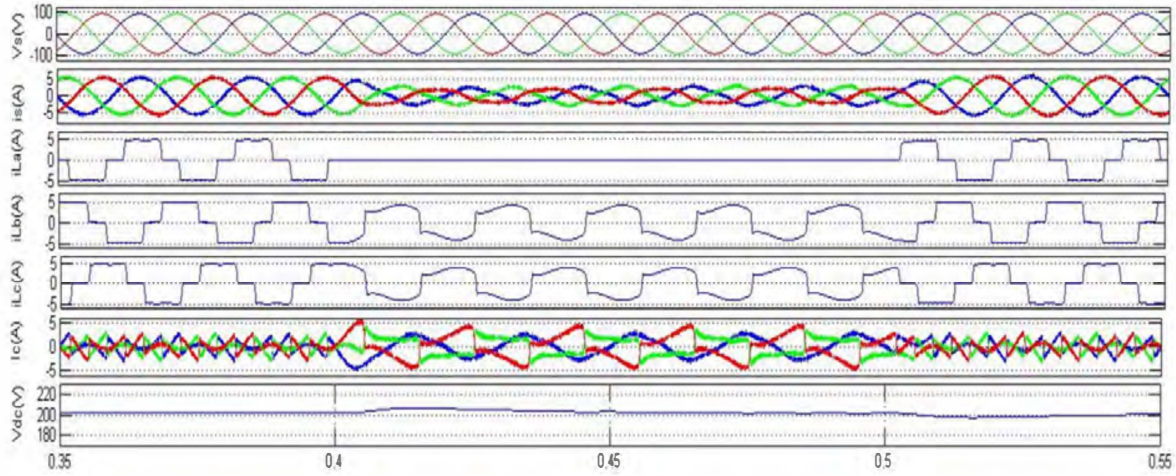

Fig. 4. Dynamic response of the system is shown with non-linear load condition. The unbalancing (load removal) is done in phase-a in DSTATCOM to the load side at 0.4sec for interval of 0.1sec and and at 0.5sec the load is reconnected. Waveforms of source voltages, source currents, load currents – phase 'a', 'b' & 'c', compensator current and DC link voltage are shown.

Fig. 4 shows the simulation results for the developed system, in which various plots of supply voltages (V_s), supply currents (i_s), phase 'a', 'b' & 'c' load currents (i_{La}, i_{Lb} & i_{Lc}), compensator currents (i_c) and dc link voltage (V_{dc}). The system is controlled by Fryze current minimization scheme. Till 0.4 the load is balanced and the load currents have THD of 27.93% with the implementation of DSTATCOM the dc link is maintain to 200V and the supply currents are observed to balanced and sinusoidal. The THD of supply current is 2.54% in steady state condition. Fig. 5 and Fig. 6 show the FFT analysis for THD of load current and supply current of phase 'a'. At t=0.4sec phase 'a' load is removed for a duration of 0.1 sec. The subplot of phase 'a' current shows a magnitude of zero during this duration. Under the sudden load change the dc link voltage of the VSC overshoots to approximately 205V but settles down quickly to its reference value of 200V. During this the dynamic load change the supply currents are still observed to be sinusoidal, balanced and reduced in magnitude as compared to the steady state condition. The compensator injects higher currents to account for the unbalance in load current. At t=0.5 sec once again the phase 'a' load of restored and hence the supply current is increase in magnitude as before.

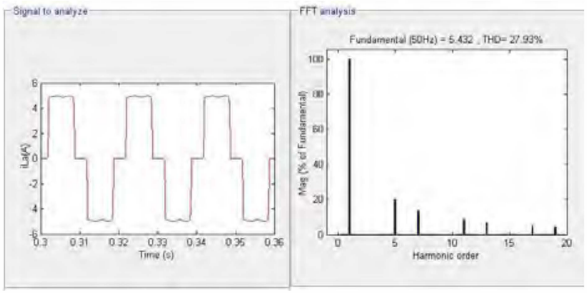

Fig. 5. FTT analysis is shown for the THD of phase 'a' load current.

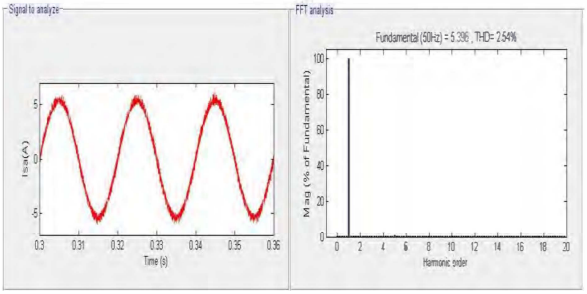

Fig. 6. FTT analysis is shown for the THD of phase 'a' source current.

IV. HARDWARE RESULTS

Results are shown with non-linear load in balanced and unbalanced conditions, which are shown on Tektronix TDS2014B CRO.

Fig. 7-15 show the results of hardware implementation for the developed prototype. Fig. 7 shows the signal plots for the phase 'a' supply current, load current and the compensator current on the CRO in steady state condition. It can be clearly observed that the supply current is sinusoidal even with non-linear load. The compensator injects highly distorted current corresponding to the harmonic component of the load current and thus improves the power quality at the supply ends.

Fig. 8 & Fig. 9 show the signal plots of source current (i_{sa}), load current (i_{la}), compensator current (i_{ca}) of the phase 'a' and dc link voltage V_{dc} under dynamic load conditions of load removal and load addition respectively. Fig. 8 shows the magnitude of the load current is reduced to zero during load removal. However, the increased compensator current during this interval maintains a reduced but sinusoidal supply current. The dc link is also found to settle in less than on cycle. The results for load addition are shown in similar manner in Fig. 9. Fig. 7-9 show the hardware implemented results which matched quite well with the simulated results as shown in Fig. 4.

Fig. 10-15 show the waveforms and THD for various currents and voltages. Fig. 10 shows the THD of source voltage of phase 'a', which is observed as 3.7%. Fig. 11 shows the THD of load current of phase 'a', which is observed as 23.9%. Fig. 12 shows the THD of source current of phase 'a', which is observed as 4.1%.

Fig. 13 shows the waveform for supply voltage and supply current of phase 'a'. It can be observed clearly that both of them are in phase. The compensator is able to achieve unity power factor also. Fig. 14 shows the voltage and load current waveform of phase 'a'. Since the non-linear load is connected in experimental set up the load current waveform is observed with harmonics. Fig. 15 shows the waveforms for supply current and compensator current of phase 'a'. The figure clearly shows the compensator injects highly distorted current to cancel the harmonics in load current.

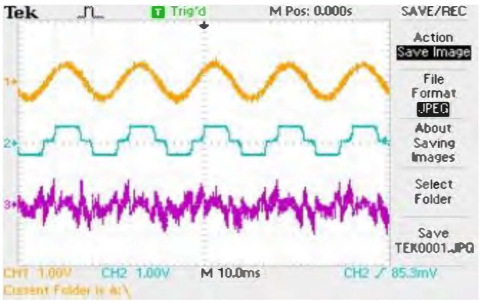

Fig. 7. Signal plots of i_{Sa}, i_{La} and i_{ca} on the CRO

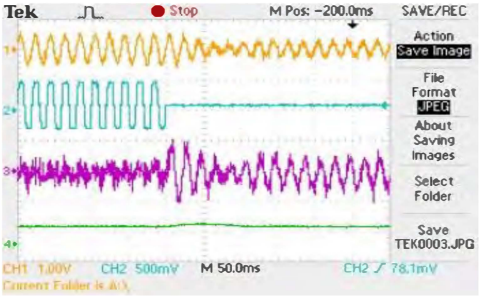

Fig. 8. Signal plots of i_{Sa}, i_{La}, i_{ca} and V_{dc} on the CRO of load removal condition.

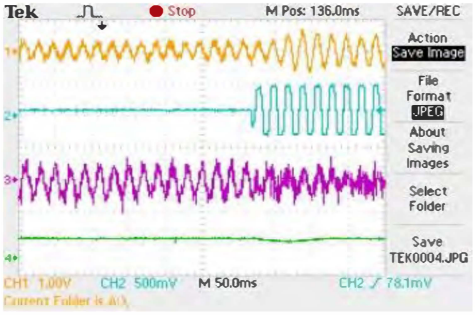

Fig. 9. Signal plots of i_{Sa}, i_{La},i_{ca} and V_{dc} on the CRO of load addition condition.

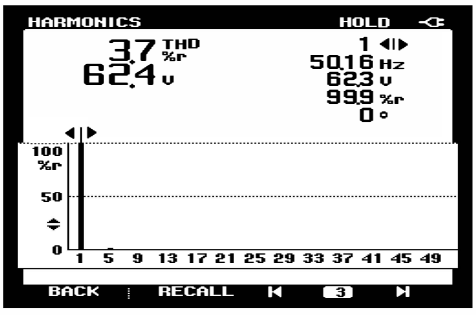

Fig. 10. THD of the supply voltage.

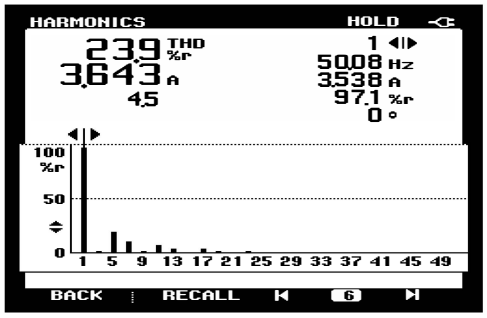

Fig. 11. THD of the phase 'a' load current.

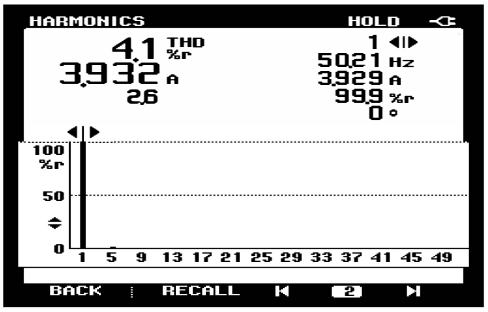

Fig. 12. THD of phase 'a' supply current.

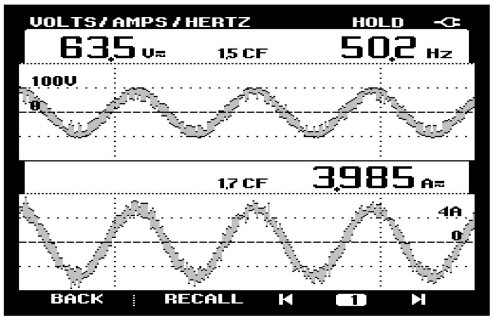

Fig. 13. Waveforms of the v_{Sa} and i_{Sa}.

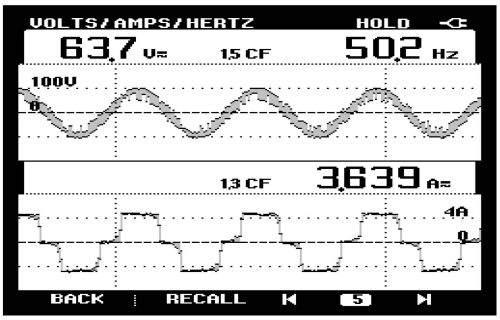

Fig. 14. Waveforms of the v_{Sa} and i_{La}.

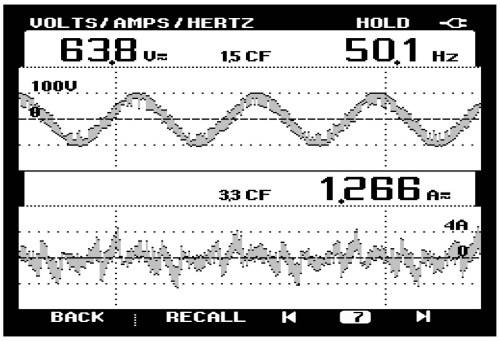

Fig. 15. Waveforms of the v_{Sa} and i_{ca}.

V. CONCLUSION

Hardware implementation of prototype DSTATCOM is implemented and realized with generalized Fryze current minimization control strategy with non-linear loads and it is observed that power quality of the system is improved satisfactorily. Reference currents are extracted by sensing the load currents from current sensors by conductance formula. The switching signals for the gate of IGBTs are derived from HCC. The voltage of dc capacitor is maintained by the help of PI controller in all the cases. The conductance based Fryze control scheme is found to be very effective in reducing the THD within 5% of supply current as per the IEEE-519 standards. Moreover, the scheme works well under dynamics of load changes, load unbalancing and removal of load too. The simulation results based on Fryze's Scheme match well with the hardware developed model of the system.

APPENDIX

PARAMETERS OF THE NETWORK SYSTEM:
The values of system parameters are; line to line source voltage = 110 V; system frequency (f) = 50 Hz; source impedances i.e. R_s = 0.15 Ω and L_s = 0.5mH; filter impedance of R_c = 0.2 Ω, L_c = 3.2mH; 3-phase diode rectifier, R load varies from 18-60Ω and L = 100mH; K_p = 0.001, K_i = 0.003; capacitance of DC link capacitor = 1640μF.

ACKNOWLEDGEMENT

The second author wishes to thank Department of Science and Technology, Ministry of Science and Technology, India for the sponsored Project No. SR/FTP/ETA-20/2010.

REFEREENCES

[1] Hirofumi Akagi, Edson Hirokazu Watanabe and Mauricio Aredes "Instantaneius power theory and applications to power conditioning" IEEE-press chapter 3-4, 2007.

[2] Bhim Singh And Jitendra Solanki, "An Implementation Of An Adaptive Control Algorithm For A Three-Phase Shunt Active Filter" IEEE Trans. on Industrial Electronics, Vol. 56, No. 8, August 2009.

[3] Zainal Salam, Tan Perng Cheng and Awang Jusoh "Harmonics Mitigation using Active Power Filter-A Technical Review" ELEKTRIKA Universiti Teknologi Malaysia, Vol.8, No.2, 2006.

[4] Maryclaire Peterson, Brij N. Singh and Parviz Rastgoufard "Active and Passive Filtering for Harmonic Compensation", 40th Southeastern Symposium on System Theory MC1.5 University of New Orleans New Orleans, LA, USA, March 16-18, 2008.

[5] Karuppanan P, and Kamala Kanta Mahapatra, "A Novel Control Strategy based Shunt APLC for Power Quality Improvements", Power, Control and Embedded Systems (ICPCES), 2010.

[6] C.N. Rowey, T.J. Summersz, R.E. Betz and D. Cornforth, "A Comparison of Instantaneous and Fryze Power Calculations on P-F and Q-V Droop in Microgrids", Universities Power Engineering Conference (AUPEC), 2010

[7] Mauricio Aredes and Luis F. C. Monteiro, "A Control Strategy for Shunt Active Filter", Harmonics and Quality of Power, 2002. 10th International Conference on 6-9 Oct. 2002.

[8] Alexandru Bitoleanu; Mihaela Popescu, "Shunt Active Power Filter; Overview on the Reference Current Methods Calculation and their Implementation", 4th International Symposium Electrical and Electronics Engineering (ISEEE), 2013.

J Therm Anal Calorim
DOI 10.1007/s10973-014-4128-1

Curing kinetics of self-healing epoxy thermosets

Manorama Tripathi · Devendra Kumar · Chitra Rajagopal · Prasun Kumar Roy

Received: 2 April 2014 / Accepted: 23 August 2014

Abstract The curing kinetics of self-healing epoxy compositions was investigated by non-isothermal differential scanning calorimetric (DSC) studies. Cycloaliphatic epoxy resin was encapsulated in urea–formaldehyde (UF) using emulsion polymerisation technique to prepare epoxy-loaded UF microcapsules. Triethylene tetramine (TETA) hardener was immobilised on a mesoporous siliceous substrate (SBA 15) and both these additives were dispersed into an epoxy resin, which was subsequently cured using TETA. DSC studies revealed the autocatalytic nature of epoxy curing, which remained unaltered due to addition of the above-mentioned fillers, responsible for introducing self-healing functionality. The kinetic parameters of the curing process were determined using both Friedman and Kissinger–Akahira–Sunose (KAS) method. The activation energy at different degrees of conversion (E_α) was found to decrease with increasing degree of cure (α). Although UF resins possess secondary amine functionalities, which have the potential to react with the epoxy groups, no significant differences in the curing kinetics of the base resin were observed. Kinetic parameters were used to predict the curing behaviour of compositions at higher heating rates using KAS method. As expected, the onset curing temperature (T_{onset}) and peak exotherm temperature (T_p) of epoxy shifted towards higher temperatures with increased heating rate; however, introduction of fillers does not affect these characteristic temperatures significantly. Also, the overall order of reaction does not vary significantly which supports the autocatalytic nature of curing reaction. The results suggests that although 2° amino groups are available with the UF resin, these do not directly participate in the curing reaction, as the primary amino groups in TETA are more easily accessible.

Keywords Curing kinetics · Autocatalytic reaction · Non-isothermal differential scanning calorimetry

Introduction

The use of epoxy composites for structural applications has seen a tremendous increase in the last few decades, primarily because of their excellent thermo-mechanical, chemical and environmental stability. One of the major issues associated with these composites arises from the inherent brittleness of the epoxy matrix which renders these materials susceptible to microcrack formation. In the context of structural engineering, microcracking can prove to be rather fatal, as coalescence of microcracks can result in catastrophic failure of the components. An ideal route to increase the lifetime of components includes the usage of self-healing compositions, and in view of the same, such polymers have attracted increasing research interests lately [1–3]. At present, the most common strategy for imparting self-healing functionality involves introduction of fragile microcapsules, which encapsulate the healing agents [4]. During crack propagation, the embedded microcapsules rupture, leading to release of the healing agent into the

Electronic supplementary material The online version of this article (doi:10.1007/s10973-014-4128-1) contains supplementary material, which is available to authorized users.

M. Tripathi · C. Rajagopal · P. K. Roy (✉)
Centre for Fire, Explosive and Environment Safety, Timarpur, Delhi 110054, India
e-mail: pkroy@cfees.drdo.in; pk_roy2000@yahoo.com

D. Kumar
Department of Applied Chemistry and Polymer Technology, Delhi Technological University, Delhi 110042, India

Published online: 12 September 2014

crack plane and undergo polymerisation, which increases the overall lifetime of the polymer.

The choice of healing agents is practically unlimited; however, most common includes dicyclopentadiene and epoxy which undergo ring-opening polymerisation and curing reactions, respectively, in the presence of suitable catalysts, which too are embedded in the matrix. Different containment structures have been explored for encapsulating healing agents and in view of their reasonable cost and fragile nature, UF microcapsules are the most commonly used [5–7]. Nevertheless, the potential of hollow tubes [8, 9] and fibres has also been explored as healing agent containers. Unlike the hydrophobic epoxy-based healing resins, encapsulation of the curing agent, i.e. amine hardener, is relatively difficult and the procedure usually adopted involves preparation of hollow microcapsules into which the amines are vacuum infiltrated [10]. Alternatively, solid latent curing agents e.g. $CuBr_2(2\text{-MeIm})_{-4}$ have also been used, but the curing necessitates certain environmental conditions, particularly elevated temperatures, which may be difficult to be made available under field conditions [11].

We hypothesise that the amine hardener can easily be immobilised on mesoporous siliceous substrates e.g. SBA 15, MCM 41, etc. Lately, the scope of porous substrates towards immobilising enzymes has been explored extensively, [12–14] but surprisingly these have not yet been employed for loading amines. In this paper, we attempt to load a representative hardener, triethylene tetramine (TETA) on SBA 15 and investigate their effect on the curing behaviour of epoxy.

In view of the enormous potential of these self-healing materials in the future, it is very important to be cognizant of the effect of these self-healing additives on the curing kinetics, as this process governs the polymer morphology, which in turn, affects its properties [15–17]. A majority of studies in this area deal with improving the efficiency of self-healing process, but surprisingly very few studies deal with the kinetics of the curing process of such compositions [11, 18]. Of particular importance is to establish the role of common encapsulating materials e.g. UF which possess 2° amino functionalities capable of reacting with epoxy resins. In fact, UF resin has also been used as an effective hardener for epoxy resins, nonetheless the curing can be effected only at higher loadings (100 phr) [19]. Moreover, the silica nanoparticles have also been reported to alter the curing kinetics of epoxy, [20] and in view of the siliceous nature of SBA-15, its contribution towards altering the curing behaviour of epoxy needs to be studied.

The aim of the present work is to study the effect of self-healing fillers on the curing kinetics of a cycloaliphatic epoxy resin with TETA hardener. For this purpose, non-isothermal DSC measurements have been carried out and empirical approaches are used to model the kinetics of the curing reactions.

Experimental

Materials

Urea, formalin (37 % formaldehyde in water), citric acid, polyvinyl alcohol (PVA) (Mw 14,000) (CDH) and triethanol amine (Merck) were used without any further purification. Tetraethyl orthosilicate (TEOS) and P-123 amphiphilic block-copolymer poly (ethylene oxide)-poly (propylene oxide)-poly (ethylene oxide), ($EO_{20}PO_{70}EO_{20}$) were purchased from Aldrich and used as silica precursor and the organic template, respectively. An amine-cured epoxy resin (Ciba Geigy, Araldite CY 230; epoxy equivalent 200 eq g^{-1}) and TETA hardener (HY 951; amine content 32 eq kg^{-1}) were used as received. Distilled water was used throughout the course of study.

Preparation of microcapsules

The preparation of epoxy-encapsulated UF microcapsules by oil-in-water (O/W) emulsion polymerisation route has been described in our previous paper [21]. In brief, urea (5 g) and formalin (10 g) were dissolved in distilled water (35 mL) under continuous stirring at room temperature. The pH of resulting solution was slowly increased to 8–9 by dropwise addition of triethanolamine, while maintaining the temperature at 343 ± 5 K for 1 h to obtain a prepolymer solution [22]. The solution was cooled and to this was added an aqueous solution of PVA (2.5 mL, 5 % w/w), which was followed by the addition of a slow stream (0.5 mL min^{-1}) of epoxy resin to form an emulsion. Post stabilisation, the pH of the emulsion was brought down to 3–4 by addition of requisite amount of aqueous citric acid solution (5 % w/v), while increasing the temperature of the solution at a rate of 1 $Kmin^{-1}$ to 323 ± 2 K. After 3 h, the obtained suspension of microcapsules was cooled down to ambient temperature, filtered, washed repeatedly with distilled water and acetone and air-dried for 24 h.

The extent of encapsulation in the microcapsules was determined by acetone extraction method as per the reported procedure [7]. For this purpose, an accurately weighed amount of microcapsules (M_{mc}) was crushed to release the encapsulated epoxy resin. The resulting powder was then repeatedly washed with acetone to extract the epoxy, filtered, dried and weighed (M_{shell}). The core content was determined gravimetrically as the ratio of encapsulated mass of epoxy to the total mass of the microcapsules.

$$\text{Core content} = \frac{M_{mc} - M_{shell}}{M_{mc}} \quad (1)$$

Assembly of mesoporous SBA-15

The preparation of SBA 15 using a polymer-templated technique has been reported in our previous paper [23]. In brief, 1.22 g of the amphiphilic block-copolymer was dissolved in 715 mL of water and 110 mL of 16 M HCl under stirring at 318 ± 1 K for 16 h. 50 mL of TEOS was introduced to this solution, and the hydrolysis was allowed to proceed for 8 h under stirring. The product obtained was washed with water and dried at 383 K prior to calcination at a controlled heating rate of 1 K min^{-1} up to 873 K.

Hardener immobilisation on SBA-15

Amine was entrapped in the pores of the mesoporous silica by physical adsorption technique. The immobilisation was achieved by placing 10 g of SBA-15 in excess of free amine and incubating the mixture at 298 K under shaking (150 rpm). After 24 h incubation, the sample was subjected to centrifugation at 600 rpm for 5 min and washed with copious amounts of ethanol. The increase in mass was used to quantify the extent of amine loading

$$\text{Immobilised amine (mg mg}^{-1}) = \frac{E_f - E_o}{E_o} \quad (2)$$

where E_f is the mass of amine immobilised SBA 15 and E_o is the mass of SBA 15 taken for immobilisation.

Characterisation methods

The surface morphology of samples was studied using a scanning electron microscope (Zeiss EVO MA15) under an acceleration voltage of 20 kV. Samples were mounted on aluminium stubs and sputter coated with gold and palladium (10 nm) using a sputter coater (Quorum-SC7620) operating at 10–12 mA for 120 s. The textural property of SBA 15 was determined by N_2 adsorption–desorption on a Surface Area Analyser (Micromeritics ASAP 2010). The identification of crystalline phases in the sample was performed by powder XRD analysis on a Philips PANalytical 1730 diffractometer using Cu Kα ($\lambda = 1.54$ Å), where the diffractograms were recorded over a range of $2\theta = 0°$–$10°$. The pore wall thickness was calculated as d (100)*2/$\sqrt{3}$—pore diameter, where d (100) is the d-spacing value of the (100) diffraction peak in XRD patterns of the silica sample [24].

Fourier transform infrared spectra of samples were recorded in the wavelength range of 4,000–600 cm^{-1} using FTIR spectroscopy on a Thermo Fisher FTIR (NICOLET 8700) analyser with an attenuated total reflectance (ATR) crystal accessory. Calorimetric studies were performed on a Differential Scanning Calorimeter (TA instruments Q20). The resin and TETA were mixed at a stoichiometric epoxide/amine ratio (100:13) at low temperatures (0–5 K). For dynamic DSC scans, samples (10 ± 2 mg) were sealed in aluminium pans and heated from 273 to 523 K at four different rates 2.5, 5, 10 and 15 K min^{-1}. Nitrogen was purged at rate of 50 mL min^{-1} to minimise oxidation of the sample during the curing process. Isothermal runs were performed on selected samples at 313 K for 1 h. Prior to the experiments, the instrument was calibrated for temperature and enthalpy using standard indium and zinc. Thermal equilibrium was regained within 1 min of sample insertion, and the exothermic reaction was considered to be complete when the recorder signal levelled off to the baseline. The total area under the exothermic curve was determined to quantify the heat of curing. The thermogravimetric analysis was performed on a Perkin Elmer simultaneous TG/DTA instrument (Diamond SDTA), for which the samples were heated from 323 to 873 K, under air atmosphere at a programmed heating rate of 10 K min^{-1}. The amount of microcapsule loading in epoxy was selected based on reported previous studies, [6] and the amount of loaded SBA-15 was decided on the basis of stoichiometric requirements. The samples have been designated as EP followed by the concentration of UF microcapsules (% w/w) and concentration of mesoporous silica. E.g. epoxy containing 10 % UF microcapsules and 2 % mesoporous silica will be referred to as EP10UF2MS and neat epoxy will be referred to as EP throughout the text.

Results and discussion

Epoxy-encapsulated UF microcapsules were prepared by oil-in-water emulsion technique, and TETA hardener (HY 951) was immobilised within the pores of mesoporous silica (SBA 15). Self-healing epoxy composites were prepared by dispersing known amount of the microcapsules and immobilised amine hardener in epoxy resin and the curing behaviour of the compositions was studied by non-isothermal calorimetry to gain insight into the effect of self-healing fillers on the curing kinetics of epoxy resin.

Epoxy-encapsulated urea–formaldehyde microcapsules

The SEM image of a representative batch of epoxy-encapsulated UF microcapsules is presented in Fig. 1. It can be seen that the microcapsules are spherical in shape, with a rough surface texture, a feature which could be attributed to the presence of protruding polymer nanoparticles [25]. The interior of the microcapsule is, however,

smooth and the thickness of the shell wall, as determined from the SEM images, was found to be $\sim 350 \pm 54$ nm (Supplementary information, Figure S1). It is to be noted that the microcapsule size could be controlled by varying the rate of agitation during the polymerisation process. In the present study, a stirring speed of 250 rpm was employed, which yielded microspheres of dimensions satisfactory for the use in self-healing application [25], i.e. (diameter $\sim 190 \pm 49$ μm). The core content of the microcapsules was determined to be 65 ± 5 %, which could be attributed to the presence of UF debris.

Fourier transform infrared spectra of urea–formaldehyde microcapsules are presented in Fig. 2. Urea–formaldehyde microcapsules exhibit characteristic broadband around 3,301 cm^{-1} which arises from the overlapping absorptions due to hydroxyl, imino and amino functionalities. Other characteristic absorptions include alkyl C–H stretching (2,962 cm^{-1}), C–H bending (1,383 cm^{-1}), aliphatic C–N (1,242 and 1,182 cm^{-1}), NH–CO–NH stretching (1,649 cm^{-1}) and C–O–C stretching (1,032 cm^{-1}) [26].

TG trace of epoxy-encapsulated UF is presented in Fig. 3. The initial mass loss of ~3.6 % ($T < 423$ K) can be attributed to the removal of water (DSC trace, Figure S2), and the subsequent loss corresponds to the removal of methanol and formaldehyde. Further heating leads to the transformation of methylene ether bridges into methylene bridges at ~473 K, a phenomenon associated with loss of formaldehyde. The subsequent mass loss at 573–663 K occurs due to pyrolytic degradation of the resultant cross-linked network.

Immobilisation of amine hardener

Detailed characterisation of the mesoporous siliceous substrate prepared by the polymer-templated route is discussed elsewhere [27]. The mesoporous nature of SBA 15

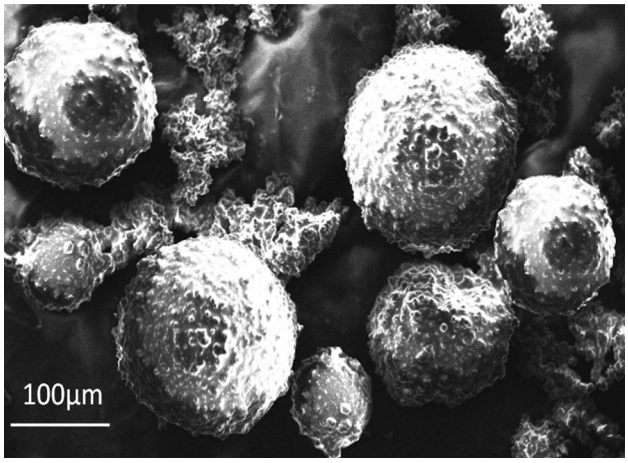

Fig. 1 SEM images of epoxy-encapsulated urea–formaldehyde microcapsules

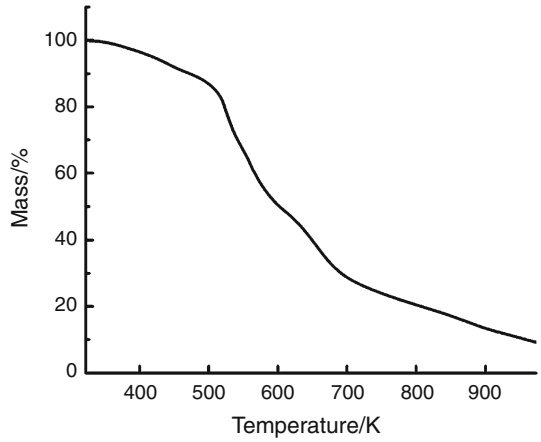

Fig. 3 TG trace of epoxy-encapsulated urea–formaldehyde microcapsules

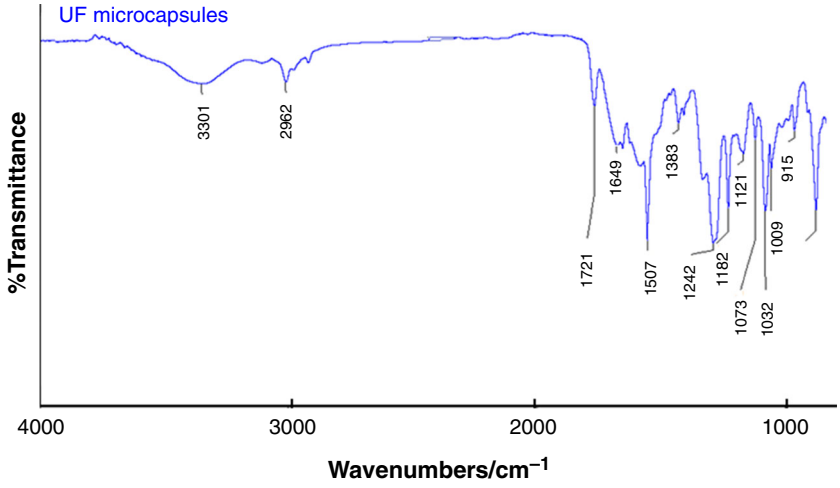

Fig. 2 FTIR spectrum of epoxy-encapsulated urea–formaldehyde microcapsules

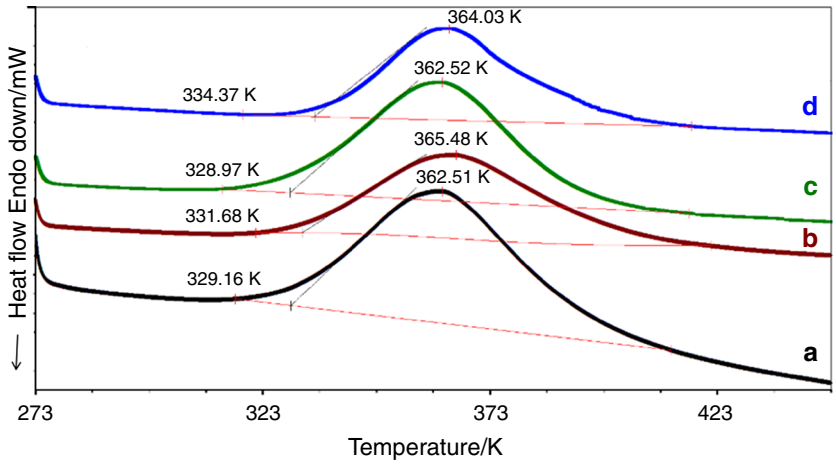

Fig. 4 Curing profile of epoxy-based compositions *a* Neat epoxy, *b* EP5UF, *c* EP10UF, *d* EP10UF2MS

was confirmed by a type II hysteresis loop evidenced in N_2 adsorption–desorption isotherm. The BET surface area was found to be 808 $m^2\ g^{-1}$ and a uniform average pore diameter of 5.4 nm was determined by the Barrett–Joyner–Halenda (BJH) method which was applied on the desorption branch of the isotherm. The XRD of SBA 15 is presented in the supplementary section (Figure S3), which was used to estimate the d (100) value of 8.84 nm and wall thickness of 4.8 nm, which match well with the values reported in the literature [24].

In view of the simplicity of the method, physical adsorption technique was used for immobilising the TETA hardener. The extent of loading was found to be 5 mg mg^{-1} as established from gravimetric studies. Chemical interactions between the siliceous substrate and the amine, particularly hydrogen bonding and acid–base interactions can be held responsible for the high loading values.

Curing behaviour

The DSC traces of neat epoxy and microcapsule filled compositions under a representative heating rate (5 K min^{-1}) are presented in Fig. 4. It is apparent from the figure that all the compositions exhibit a single exothermic peak, which is characteristic of the epoxy curing process. The presence of UF microcapsules or amine immobilised SBA-15 did not seem to affect the curing process appreciably and all the compositions exhibit similar onset cure temperature (T_{onset}) and peak cure temperature (T_{peak}) values.

Differential scanning calorimetric curves of a representative epoxy composite at various heating rates viz. 2.5, 5, 10 and 15 K min^{-1} are presented in Fig. 5. As expected, increasing the heating rate (β) leads to a systematic shift in the trace towards higher temperatures. The curing reaction is primarily a kinetic event, which is a function of both time and temperature. On being subjected to a higher heating rate, the reactants get lesser time to react at any specific temperature, leading to the observed phenomenon. The characteristic thermal parameters i.e. ΔH_{cure}, T_{onset} and T_{peak} are summarised in Table 1.

It is apparent from the data that there is no significant effect on the heat of curing (ΔH_{cure}) due to increasing heating rates. The extent of conversion (α) at any particular temperature (T_α) was estimated as the ratio of the areas under the exothermic DSC peak:

$$\alpha = \frac{\Delta H_{T_\alpha}}{\Delta H_{cure}}, \tag{3}$$

where ΔH_{T_α} is the heat of reaction of partially cured samples (till temperature T_α) and ΔH_{cure} is the total heat of reaction.

The increase in the degree of conversion with temperature for EP, and EP5UF, EP10UF and EP10UF2MS at a particular heating rate (5 K min^{-1}) is presented in Fig. 6. It can be seen that microcapsule loading does not lead to any significant effect on the curing behaviour as far as the degree of conversion is concerned. As expected [28], the trace shifts towards higher temperature with increasing heating rate, as is apparent from the data presented in Fig. 7.

Isoconversion methods

The rate of a reaction is primarily dependent on three major variables: temperature (T), extent of conversion (α) and pressure (P) as follows:

$$\frac{d\alpha}{dt} = k(T)f(\alpha)h(P) \tag{4}$$

The pressure term, ($h(P)$), is generally ignored for a majority of kinetics methods, and the reaction rate can be rewritten as

$$\frac{d\alpha}{dt} = k(T)f(\alpha) \tag{5}$$

Generally, the temperature-dependent term ($k(T)$) is assumed to exhibit Arrhenius type dependency

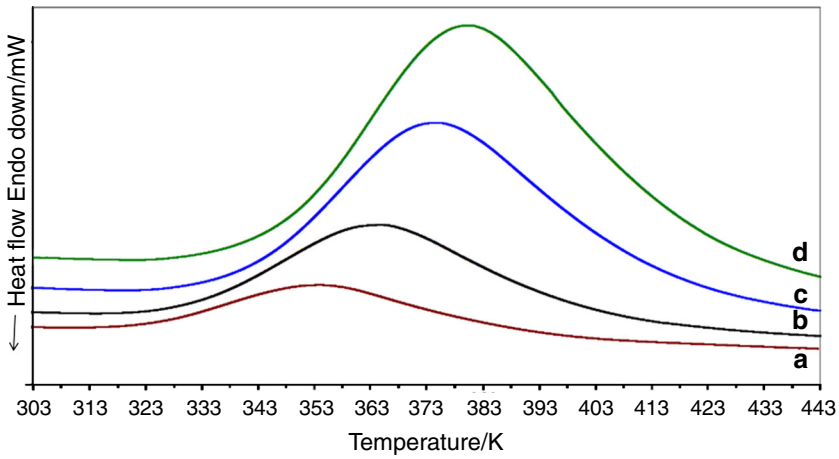

Fig. 5 Effect of heating rate on the DSC traces of microcapsule filled epoxy (EP5UF) *a* 2.5, *b* 5, *c* 10 and *d* 15 K min^{-1}

Table 1 Characteristic curing parameters of epoxy and self-healing compositions

Sample	β/K min^{-1}	T_{onset}/K	T_{peak}/K	ΔH_{cure}/J g^{-1}
Epoxy	2.5	327.1	352.2	320.3
	5	329.2	362.5	323.5
	10	338.3	375.3	342.8
	15	348.3	380.0	321.7
EP5UF	2.5	322.9	354.6	305.6
	5	331.7	365.5	311.3
	10	340.2	375.4	309.4
	15	345.5	381.1	294.3
EP10UF	2.5	321.6	353.3	319.5
	5	328.9	362.5	328.2
	10	339.3	377.9	327.8
	15	355.7	385.1	321.6
EP10UF2MS	2.5	329.4	354.4	300.5
	5	334.4	364.0	310.2
	10	342.2	374.3	312.8
	15	347.3	374.8	307.6

$$k(T) = A\exp\left(-\frac{E}{RT}\right) \tag{6}$$

Combining Eqs. 5 and 6

$$\frac{d\alpha}{dt} = A\exp\left(-\frac{E_\alpha}{RT}\right)f(\alpha) \tag{7}$$

where $f(\alpha)$ is the reaction model, T (K) is the absolute temperature, A (s^{-1}) is the pre-exponential factor, E_α (kJ mol^{-1}) is the activation energy and R the universal gas constant. For different heating rates (β_i), Friedman method directly gives Eq. 8 at specified α

$$\ln\left(\frac{d\alpha}{dt}\right)_{\alpha i} = \ln(A_\alpha f(\alpha)) - \frac{E_\alpha}{RT_{\alpha i}} \tag{8}$$

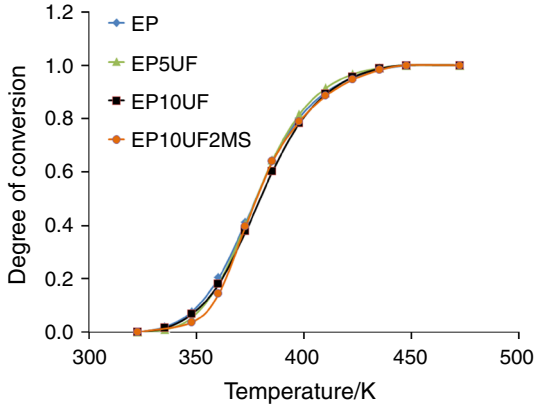

Fig. 6 Effect of temperature on the degree of conversion of epoxy and self-healing composition (β = 5 K min^{-1})

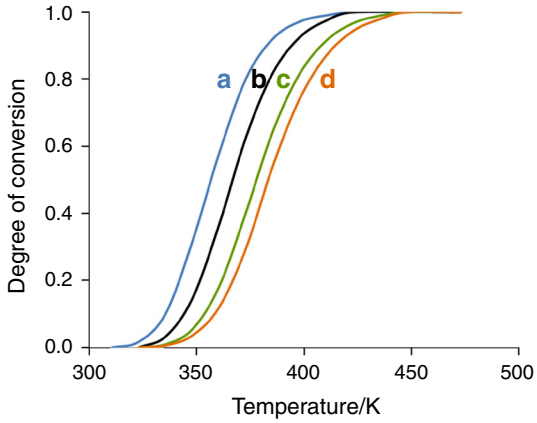

Fig. 7 Effect of temperature and heating rate on the extent of epoxy curing *a* 2.5, *b* 5, *c* 10 and *d* 15 K min^{-1}

By substituting a new parameter $C_f(\alpha) = \ln(A_\alpha f(\alpha))$, Eq. 8 may be written as

$$\ln\left(\frac{d\alpha}{dt}\right)_{\alpha i} = C_f(\alpha) - \frac{E_\alpha}{RT_{\alpha i}} \tag{9}$$

At a particular conversion (α), parameters $\left(\frac{d\alpha}{dt}\right)_{\alpha i}$ and $T_{\alpha,i}$ values can be determined experimentally at different heating rates. This can be used to arrive at E_α and $C_f(\alpha)$ from the plot of $\ln\left(\frac{d\alpha}{dt}\right)_{\alpha i}$ versus $\frac{1}{T_{\alpha,i}}$ for at least three heating rates.

Alternatively, Kissinger–Akahira–Sunose method can be used for determination of activation energy (E_α) [29]. For this method, $\left(\frac{d\alpha}{dt}\right)$ can be equated to $\frac{d(\alpha)}{dT}\beta$, and Eq. 7 can be further rearranged.

$$\frac{d\alpha}{f(\alpha)} = \frac{A}{\beta}\exp\left(-\frac{E_\alpha}{RT}\right)dT \tag{10}$$

Integrating Eq. 10 and introducing Doyle's approximation [30] lead to

$$g(\alpha) = \int_0^\alpha \frac{d(\alpha)}{f(\alpha)} = \frac{A}{\beta}\int_{T_0}^{T} \exp\frac{E}{RT}dT \cong \frac{ART^2}{\beta E}\exp\left(-\frac{E}{RT}\right) \tag{11}$$

By taking logarithm of Eq. 11, the following equation can be derived for various heating rates under a constant degree of conversion α,

$$\ln\left(\frac{\beta}{T_{\alpha i}^2}\right) = \ln\left(\frac{RA_\alpha}{E_\alpha g(\alpha)}\right) - \frac{E_\alpha}{RT_{\alpha i}} \tag{12}$$

which can further be written as

$$\ln\left(\frac{\beta}{T_{\alpha i}^2}\right) = C_k - \frac{E_\alpha}{RT_{\alpha i}}, \tag{13}$$

where $C_k(\alpha) = \ln\left(\frac{RA_\alpha}{E_\alpha g(\alpha)}\right)$

Hence, E_α can be obtained using the KAS method from the slope of $\ln\left(\frac{\beta_i}{T_{\alpha,i}^2}\right)$ against $\frac{1}{T_\alpha}$.

The linear plots (at selected conversions) used to arrive at the activation energy using KAS and Friedman method for EP5UF are depicted in the supplementary section (Figure S4). The variation of activation energy as a function of degree of conversion (α) for neat epoxy and the self-healing compositions, as determined by both the methods is presented in Fig. 8. It can be seen that the range of activation energies for all the composition is between 40 and 90 kJ mol^{-1}, irrespective of the model employed. In general, a progressive decrease in the activation energies was observed. It was interesting to note that the introduction of UF fillers or amine loaded SBA15 does not affect the activation energy-conversion profile. The reaction of the epoxy groups with amine leads to formation of a solid polymer [31], which is expected to switch the kinetically controlled process to one that of diffusion controlled, thereby expected to lead to an increase in the E_α. However, the exothermic curing process results in an increase in the energy of the reactants, indirectly lowering the energy required to cross the energy barrier. In view of the higher reactivity of the 1° amine groups with epoxy, this reaction predominates in the early stages of curing ($\alpha < 0.6$). This is followed by the reaction with 2° amines, which continues until $\alpha = 0.8$ [32]. Towards the end of the cure process, i.e. at higher temperatures, other reactions such as etherification and homopolymerisation of epoxide groups have also been reported. It is the combined result of all of the above processes which manifests in the observed $E_a - \alpha$ profile. Interestingly, the curing of epoxy has been effected by UF at higher loadings (50:50) [19]; however, our results suggests that although 2° amino groups are available on the surface of UF resin, these do not directly participate in the curing reaction, as the primary amino groups in the liquid TETA are more easily accessible.

Prediction of dynamic cure of self-healing epoxy resin

In view of its simplicity, KAS method was used to predict the curing behaviour of self-healing epoxy composites, when cured under different heating rates. For this purpose,

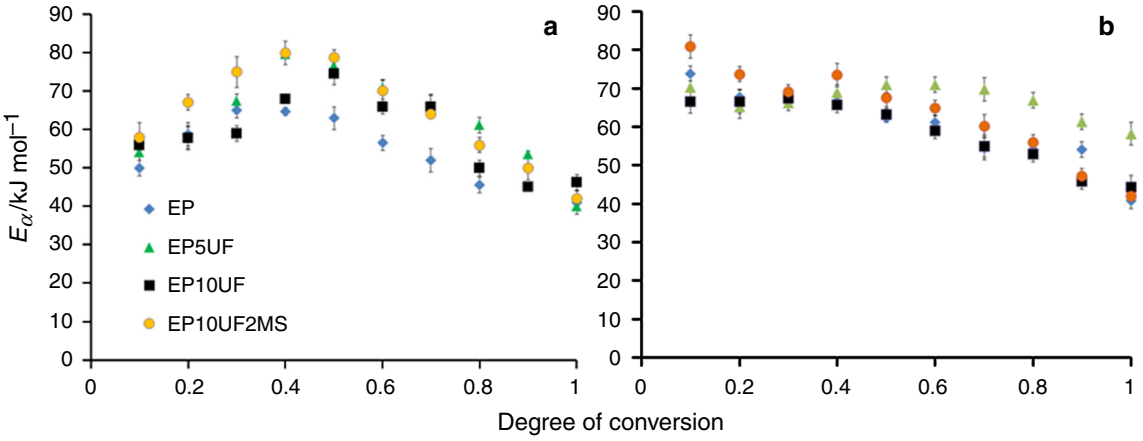

Fig. 8 Variation of activation energy (E_α) with extent of conversion **a** Friedman method **b** Kissinger–Akahira–Sunose method

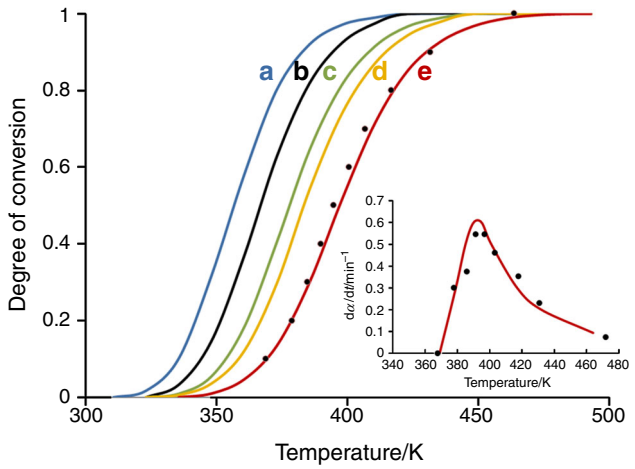

Fig. 9 Experimentally determined curing degree at different heating rates (*a*) 2.5, (*b*) 5, (*c*) 10, (*d*) 15 and (*e*) 30 K min^{-1}. *Inset* shows the experimental and KAS predicted reaction rate at 30 K min^{-1}

C_k (α) and E_α derived from the data obtained at $\beta = 2.5$, 5, 10 and 15 K min^{-1} were substituted into Eq. 13 to quantify the temperature associated with different values of α under a particular heating rate (β). The model was further validated by performing dynamic DSC run at 30 K min^{-1}, and the experimental values are presented in Fig. 9. The variation of rate of reaction $\left(\frac{d\alpha}{dt}\right)$ as a function of temperature for the specified heating rate (30 K min^{-1}) is presented in the inset of Fig. 9. It can be seen that the predicted values are in close agreement with the data obtained experimentally.

To establish the potential of the proposed self-healing system comprising of epoxy-encapsulated UF microcapsules and amine immobilised on SBA 15, curing was also effected on a mixture containing stoichiometric amounts of crushed microcapsules and SBA 15. The resulting calorimetric trace is presented in the supplementary section (Figure S5). The curve exhibits a single exothermic peak, characteristic of curing process associated with the epoxy released from the microcapsules with the hardener. However, the heat of curing (ΔH_{cure}) was found to be 170.2 J g^{-1} as compared to 342.8 J g^{-1} for neat epoxy under similar experimental conditions (10 K min^{-1}), which relates well with the core content of the microcapsules.

Conclusions

The curing behaviour of a cycloaliphatic epoxy cured with triethylene tetramine hardener and representative self-healing compositions prepared by dispersing UF microcapsules and SBA 15 immobilised amine has been systematically studied using the non-isothermal DSC technique. Curing studies were performed at different heating rates (2.5–15 K min^{-1}) and the data were used to determine the activation energy at different stages of curing, using both Friedman and Kissinger–Akahira–Sunose methods. The activation energies were found to vary from 40 to 90 kJ mol^{-1} irrespective of the method being used for estimation. The studies revealed a progressive decrease in the activation energy for all compositions, irrespective of the presence of microcapsules or SBA 15 in the composition in the concentration range studied. KAS method was further used to predict the curing behaviour at elevated heating rate 30 K min^{-1}, which was subsequently validated with dynamic DSC experiments.

References

1. Yang Y, Urban MW. Self-healing polymeric materials. Chem Soc Rev. 2013;42(17):7446–67.
2. Scheltjens G, Brancart J, Graeve I, Mele B, Terryn H, Assche G. Self-healing property characterization of reversible thermoset coatings. J Therm Anal Calorim. 2011;105(3):805–9.
3. Sharma P, Shukla S, Lochab B, Kumar D, Roy PK. Microencapsulated cardanol derived benzoxazines for self-healing applications. Mater Lett. 2014;. doi:10.1016/j.matlet.2014.07.048.
4. White SR, Sottos NR, Geubelle PH, Moore JS, Kessler MR, Sriram SR, et al. Autonomic healing of polymer composites. Nature. 2001;409(6822):794–7.
5. Kessler MR, Sottos NR, White SR. Self-healing structural composite materials. Compos A. 2003;34(8):743–53.
6. Brown EN, White SR, Sottos NR. Microcapsule induced toughening in a self-healing polymer composite. J Mater Sci. 2004;39(5):1703–10.
7. Yuan L. Preparation and characterization of poly(urea-formaldehyde) microcapsules filled with epoxy resins. Polym Degrad Stab. 2006;47:5338–49.
8. Bleay SM, Loader CB, Hawyes VJ, Humberstone L, Curtis PT. A smart repair system for polymer matrix composites. Compos A Appl Sci Manuf. 2001;32(12):1767–76.
9. Pang JWC, Bond IP. A hollow fibre reinforced polymer composite encompassing self-healing and enhanced damage visibility. Compos Sci Technol. 2005;65(11–12):1791–9.
10. Jin H, Mangun CL, Stradley DS, Moore JS, Sottos NR, White SR. Self-healing thermoset using encapsulated epoxy-amine healing chemistry. Polymer. 2012;53(2):581–7.
11. Yin T, Rong M, Zhang LM. Self-healing epoxy composites—part I: curing kinetics and heat-resistant performance. Adv Mater Res. 2013;716:383–6.
12. Hudson S, Magner E, Cooney J, Hodnett BK. Methodology for the immobilization of enzymes onto mesoporous materials. J Phys Chem B. 2005;109(41):19496–506.
13. Karimi B, Emadi S, Safari AA, Kermanian M. Immobilization, stability and enzymatic activity of albumin and trypsin adsorbed onto nanostructured mesoporous SBA-15 with compatible pore sizes. RSC Adv. 2014;4:4387–4394.
14. Yiu HHP, Wright PA, Botting NP. Enzyme immobilisation using SBA-15 mesoporous molecular sieves with functionalised surfaces. J Mol Catal B Enzym. 2001;15(1–3):81–92.
15. Chaudhary S, Parthasarathy S, Kumar D, Rajagopal C, Roy PK. Graft-interpenetrating polymer networks of epoxy with polyurethanes derived from poly(ethyleneterephthalate) waste. J Appl Polym Sci. 2014;131:40490.

16. Chaudhary S, Parthasarathy S, Kumar D, Rajagopal C, Roy PK. Poly(ethyleneterephthalate) glycolysates as effective toughening agents for epoxy resin. J Appl Polym Sci. 2014;131:39941.
17. Ramírez C, Abad MJ, Barral L, Cano J, Díez FJ, López J, et al. Thermal behaviour of a polyhedral oligomeric silsesquioxane with epoxy resin cured by diamines. J Therm Anal Calorim. 2003;72(2):421–9.
18. Tong XM, Zhang M, Yang MZ. Study on the curing kinetics of epoxy resin in self-healing microcapsules with different shell material. Adv Mater Res. 2011;306–307:658–62.
19. Ghaemy M, Yaghoob S, Karimi M. Curing kinetics of DGEBA/UF resin system used as laminates in impregnated decorative paper. Iran Polym J. 2010;19(9):661–8.
20. Rosso P, Ye L. Epoxy/Silica nanocomposites: nanoparticle-induced cure kinetics and microstructure. Macromol Rapid Commun. 2007;28(1):121–6.
21. Tripathi M, Rahamtullah, Kumar D, Rajagopal C, Roy PK. Influence of microcapsule shell material on the mechanical behavior of epoxy composites for self-healing applications. J Appl Polym Sci. 2014;131:40572.
22. Yuan YC, Rong MZ, Zhang MQ, Chen J, Yang GC, Li XM. Self-healing polymeric materials using epoxy/mercaptan as the healant. Macromolecules. 2008;41(14):5197–202.
23. Meynen V, Cool P, Vansant EF. Verified syntheses of mesoporous materials. Microporous Mesoporous Mater. 2009;125(3):170–223.
24. Naskar MK, Eswaramoorthy M. Significant improvement in the pore properties of SBA-15 brought about by carboxylic acids and hydrothermal treatment. J Chem Sci. 2008;120(1):181–6.
25. Brown EN. In situ poly(urea-formaldehyde) microencapsulation of dicyclopentadiene. J Microencapsul. 2003;20(6):719–30.
26. Salaün F, Vroman I. Influence of core materials on thermal properties of melamine–formaldehyde microcapsules. Eur Polym J. 2008;44(3):849–60.
27. Roy PK, Ullas AV, Chaudhary S, Mangla V, Sharma P, Kumar D, et al. Effect of SBA-15 on the energy absorption characteristics of epoxy resin for blast mitigation applications. Iran Polym J. 2013;22(9):709–19.
28. Wang J, Laborie M-PG, Wolcott MP. Comparison of model-free kinetic methods for modeling the cure kinetics of commercial phenol–formaldehyde resins. Thermochim Acta. 2005;439(1–2):68–73.
29. Budrugeac P, Segal E. Applicability of the Kissinger equation in thermal analysis. J Therm Anal Calorim. 2007;88(3):703–7.
30. Doyle CD. Kinetic analysis of thermogravimetric data. J Appl Polym Sci. 1961;5(15):285–92.
31. Ghumara R, Adroja P, Parsania PH. Synthesis, characterization, and dynamic DSC curing kinetics of novel epoxy resin of 2,4,6-tris(4-hydroxyphenyl)-1-3-5-triazine. J Therm Anal Calorim. 2013;114(2):873–81.
32. Prime RB. Thermal characterization of polymeric materials. New York: Academic; 1997.

Delhi Technological University: Design and Development of the Littoral AUV Zyra 2.0

Aayush Gupta,Vatsal Rustagi,Raj Kumar Saini,Akshay Jain,Prateek Murgai,Aditya Rastogi
Pronnoy Goswami,Ayush Tomar,Abhijit Ray,Bhavy Dikshit,Prithvijit Chattopadhyay
Shubham Raina,Mayank Gupta,Vikas Kumar Singh,Shubham Jain,Chirag Gupta

***Abstract*—The Delhi Technological University Autonomous Underwater Vehicle project team's main objective is to design and develop an autonomous underwater vehicle for the AUVSI and ONR International Robosub-2014 competition. The competition is held at the TRANSDEC facility, part of SPAWAR Systems Center Pacific in San Diego, California. The paper presents the design and development of a modular littoral autonomous underwater vehicle called 'Zyra 2.0' having four degrees of freedom for performing the following tasks underwater target localization and homing, buoy detection, path following, obstacle detection and obstacle manipulation tasks. The development of the AUV has been divided into five departments namely mechanical design and fabrication, embedded and power systems, control and software, image processing, underwater acoustics. A fully functional AUV has been tested in a self created arena with different tasks spread out in a shallow water environment.**

I. Introduction

Autonomous Underwater Vehicle are powerful and complex systems which are capable of performing underwater (shallow and deep sea) tasks. The range encompasses bathymetry calculation, detection of faults in oil pipelines, recovery and monitoring of submerged installations and even complex tasks like collecting data which aids in understanding global warming. The aim is to design and develop an Autonomous Underwater Vehicle which will serve as a technology demonstrator which is highly compact, multirole and can be used for various missions with the independence of choosing payload. Zyra 2.0 is the product of completely refined mechanical assembly, control systems, embedded systems, vision system and acoustics module. The mechanical model of Zyra 2.0 is designed to be in hydrodynamically stable equilibrium both below and above water surface. The mechanical system consist of main pressure hull, front and back lids, frame, electronics rack. The focus of embedded and the power systems department is mainly on the implementation of acoustic positioning module, actuator board and the designing of a power distribution board for diverting power to various modules on the AUV [1]. Dynamic control is achieved by retrieval of coordinates using various PID control algorithms [2],[3]. The software is designed to run in decentralized multi-threaded agent architecture, with the threads handling pressure sensor, acoustics, cameras, control system, IMU, each performing input and output operations in continuous loops. The mission plan model is also taken care by the control department as it is responsible for the artificial intelligence of the vehicle [4],[5]. The vision system is designed to perform tasks like buoy detection, bin detection, path detection, entry gate detection. The image processing software consists of various colour filters, edge and line detection algorithms. For the target(sound source or pinger) localization the AUV employs a three dimensional array of hydrophones forming a passive SONAR system. The data acquired through hydrophones is passed through a amplifier, filter and detector circuit before it is converted into its digital form

for further processing. The localization task is a sequential task in which first we calculate a set of values of TDOA(Time Difference of Arrival) using the hydrophone signals and using these values we estimate the bearing and the position vector of the sound source with respect to the AUV. For the experimental testing of the AUV an arena is created in a shallow water area and the tasks of entry gate detection, buoy detection, path detection and sound source are spread throughout the arena.

II. Mechanical Design

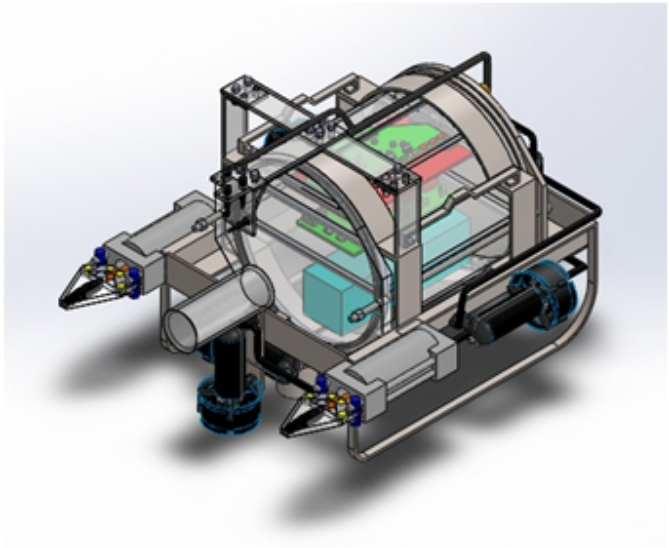

Fig. 1. Solidworks Assembly of Zyra 2.0

Zyra 2.0 is the product of indigenously designed mechanical assembly to embedded and control systems. It has a custom made LiPo battery pack, a novel power distribution board, redesigned actuator control board, battery monitor, leak sensor, an acoustic signal processing module and improved software. The fabrication material chosen for pressure hull is Virgin Cast Acrylic (Clear) because of its excellent workability, strength, shock resistance and comparatively low density. Simulation is done on hull at underwater depth of 10 m and Factor of safety is found out to be more than 5.1.

The body shall be propelled by four thrusters and has a net positive buoyancy. The frame is so designed to ensure easy mounting of thrusters, sensors, grabbers etc. The profile of the vehicle makes it highly manoeuvrable. The front lid is made

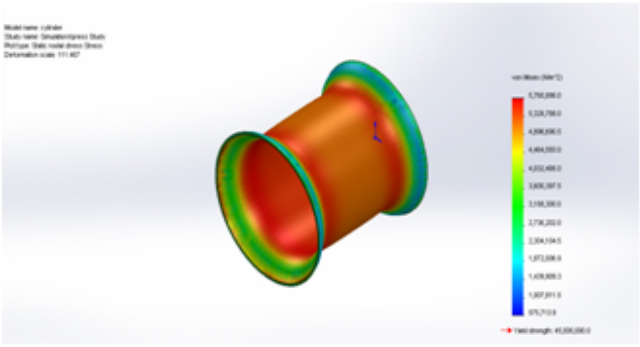

Fig. 2. Solidworks simulation of the main hull-Von Mises Stress distribution

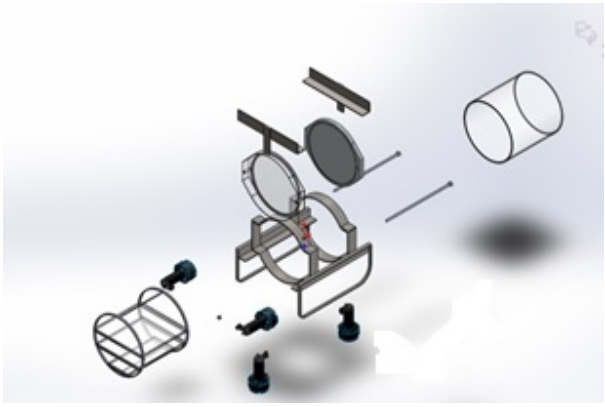

Fig. 3. Exploded view of assembly

of virgin cast acrylic .Its transparency ensures clear and unobstructed view for the forward camera that is mounted inside the hull.Back-lid will be made of aluminium.Its smooth surface will ensure easy and efficient installation of connectors and aluminium being a good thermal conductor will also help as a heat sink.

A. Electronics Hull

The main hull of Zyra 2.0 is of cylindrical shape. The shape of the vehicle has been decided after calculations, keeping various hydrodynamic parameters in mind to improve the overall performance of the robot. Main frame is designed to ensure easy installation of thrusters, grabber, hydrophone array etc. The main consideration while designing it was that unwanted stresses on hull are uniformly and efficiently transmitted to the whole frame and prevent cracks. Some of its components are made up of Stainless Steel GR316 and others are of

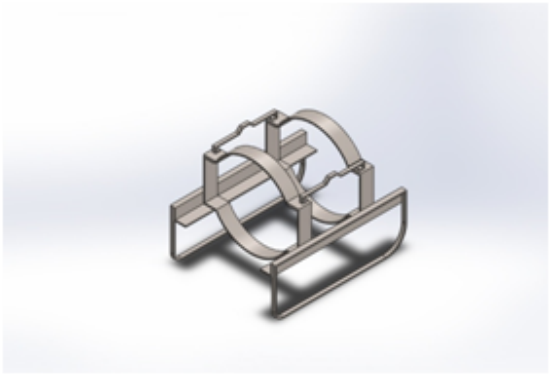

Fig. 4. Solidworks model of main frame

Aluminium. The reason for this approach is to have a suitable combination of weight, buoyancy, resistance to corrosion along with low maintenance, high strength and ease of fabrication. The hull is waterproofed using Toggle Clamps instead of Rods for faster opening and closing of the rear lid.

B. Vehicle Dynamics

Thrusters: Four strap-on BTD-150 thrusters from Seabotix Inc. are used to manoeuvre the vehicle. Two thrusters facilitate motion in the horizontal direction as well as yaw motion when operated in differential mode, while other two facilitate the vertical motion. These thrusters provide a two blade bollard thrust of 2.9 kgf and require power in the range of 80-110 watts depending on the conditions outside. All electronic components are housed in-

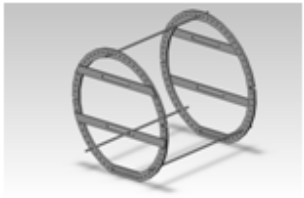

Fig. 5. Solidworks model of electronics frame

side the electronics hull. Components are placed in racks inside the main hull so as to facilitate easy removal of component in case of a technical fault. The rack is so designed to ensure easy addition of new shelves later as per requirements and least length of wires. Battery is placed at lower most shelf to ensure lower centre of gravity and improve stability and resist roll.

C. Degrees OF Freedom

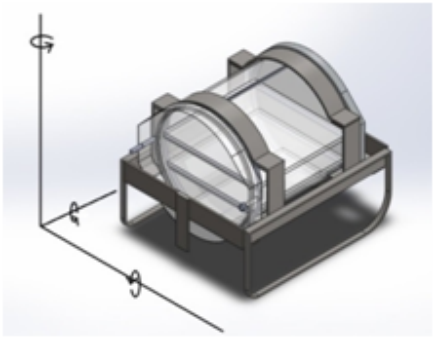

Fig. 6. Zyra 2.0's Degrees of Freedeom

The four thrusters are installed in such a way that the vehicle has four degrees of freedom namely heave, yaw, pitch and surge.

D. Stability

The AUV is designed in such a way so that the centre of gravity and centre of buoyancy lie in the same vertical line.Fig.7 displays the stability parameters.

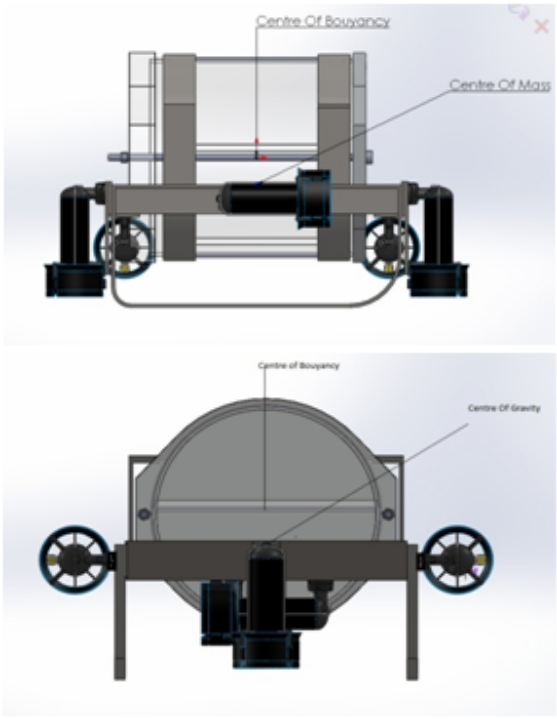

Fig. 7. Centre of buoyancy and gravity in same vertical line

TABLE I
CHARACTERISITICS OF ZYRA 2.0

Property	Value
Dimensions	70cm x 40cm x 50 cm
Diameter of Hull	30cm
Dry Weight	35Kg
Length of Hull	37cm
Propulsion	2 horizontal + 2 vertical thrusters
Velocity	0-1.5m/s

E. Robustness

Fig.2 displaying Von Mises Stress Distribution and Fig.8 showcase the robustness of the mechanical design.

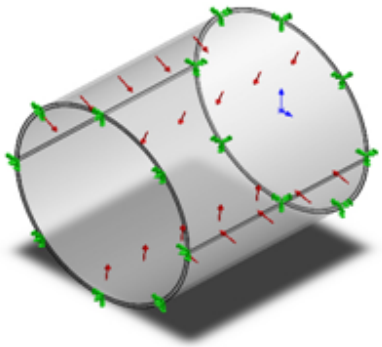

Fig. 8. Depicts the fixture and face of pressure application

III. EMBEDDED AND POWER SYSTEMS

As discussed before for the AUV Zyra 2.0 the focus of electronics department is primarily on implementation of SONAR and signal processing module, actuator board for control of four SeaBotix thrusters. A new power distribution board is designed for voltage regulation and to provide power directly to all the systems through one particular board which would eliminate the need of further bucking of voltage and hence concentrates the heat dissipating unit in one particular section of hull which can be placed near the metal ends to allow heat exchange with the water.

A. Power Systems

The electrical power system is comprised of lithium polymer (LiPo) battery, encased within the main electronics hull. The battery is rated at 18000 mAh at 18.5V. The battery protection board monitors voltage of each cell and shuts off the power if the voltage drops to 16V, also the overcharge and current drawn is monitored by the same. It is connected to a Power Distribution Board (PDB) which is responsible for diverting power to various modules on the bot. The PDB is equipped with fuses in case of battery/circuit failure, multiple capacitors to smooth out ripples, and eliminates high frequency noise. The PDB divides the power and provides regulated power supply to sensitive electronics. It provides Zyra 2.0 with clean, isolated, and regulated power at 5V, 12V, and 18.5V.

B. Actuator Control

The actuator board used for Zyra 2.0 is custom designed. It takes in care the electromagnetic interference from the thrusters which distorts the motor control signal coming from the microcontroller unit LPC-2148(ARM). This microcontroller is responsible for taking in signals from the central processing board through packetized serial interface. The microcontroller is capable of processing at 30MIPS.

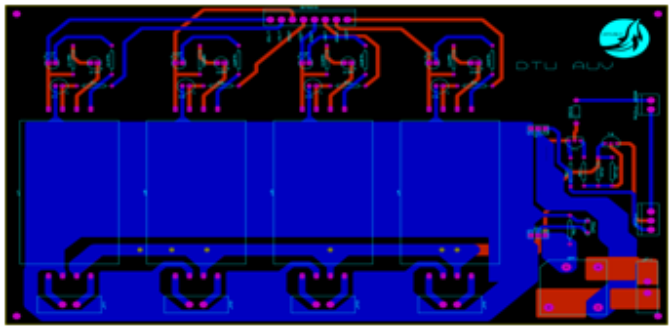

Fig. 9. Schematic for Actautor board

The motor controllers from Dimension Engineering are capable of functioning at ultra-high fre-

quency of 32 KHz thus making it inaudible for human ears and eliminate the irritating humming noise. The controllers can be configured to use either in tank style differential drive or analog voltage control. The microcontroller unit receives signals specifying direction and speed of the Zyra 2.0which in turn actuate the required thrusters. A hermetically sealed switch is responsible for killing the power to the propulsion system.A normally open reed switch is responsible for killing power to the propulsion system. The advantage is it can be easily operated from outside the main hull.

Along with hard kill a soft kill is also incorporated in the code. Analog voltage is used to control the speed of thrusters with another signal to specify the direction of motion. PWM motor controller of dsPIC30F2010 is used to generate variable duty cycle PWM signal which is filtered and smoothed into an analog signal (0V-5V) via a high capacitance, RC filter. The added advantage of mounting syren-10 on the actuator board is that any particular controller can be replaced in case it gets damaged and thus prevailing re-usability of the board. Learning from past experiences, the

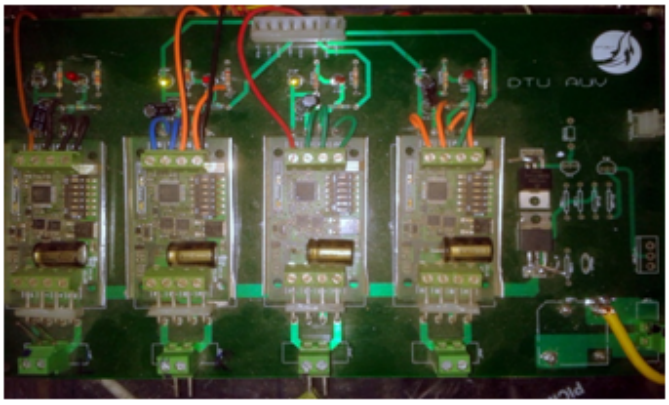

Fig. 10. Actuator Board

propulsion system of Zyra 2.0 have been completely redesigned.The communication of Master Computer and Micro-controller have been changed from RS-232 protocol to TTL. Instead of the fact that RS-232 is noise tolerant, the communication to UART is done using USB-TTL chips.

C. Electronics Rack

Modularity of the vehicle has been the priority while developing the vehicle. Electronics Rack is designed such that it holds all the electronics and can be removed from Zyra 2.0 without disturbing the rest of the system

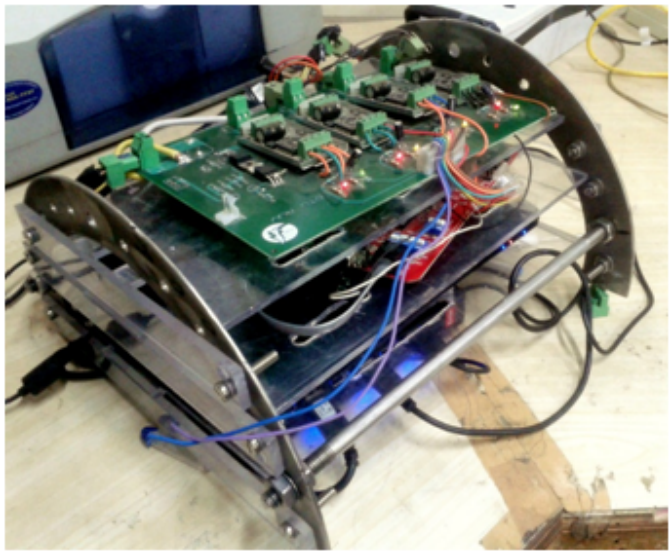

Fig. 11. Electronics rack for Zyra 2.0

The level of various racks can be varied according to payload.

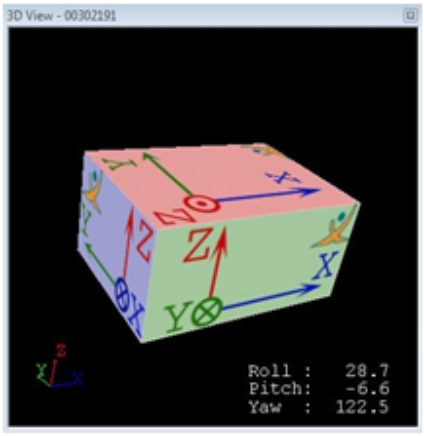

Fig. 12. Orientation data received from IMU used as an input in Control system module.

IV. Mission Module

Mission plan module of Zyra 2.0 is responsible for the artificial intelligence of the vehicle. It is at the highest level in the software hierarchy, coordinating the global state of the AUV and the state of each subsystem. It makes calls to sensor modules like vision, sound etc. determine the position and

TABLE II
COMMERICIAL OFF THE SHELF(COTS) PRODUCTS USED IN ZYRA 2.0

Devices	Model
Kontron Motherboard	986LCD-M/mITX
Battery	Li-Po 18.5V , 18000mAh
Motor Controller	Syren 10
Camera	Microsoft LifeCam-3000 and Logitech HD Pro C920
Propulsion	SeaBotic BTD-150
Pressure Sensor	Applied Measurements Pi9933
IMU	XSENS MTi-28A
Actuator Controller	LPC-2148(ARM)
Servo HiTec	HS5646WP
Hydrophones	Reson TC-4013

orientation of the AUV and to identify targets in the arena. The mission plan module coordinates the state of the AUV as it goes through the entire mission arena. It has a scheduler/ timing module which times each operation and is capable of making smart decisions of leaving a task and moving to the next one based on mission time elapsed and pre-written contingency plans. Once the AUV determines what type of action is to be performed, it calls the control module which commands the actuators to function precisely.

V. CONTROL MODULE

Control module is called by the mission plan module as and when required to change the orientation and position and orientation of the AUV based on the operation being performed and input from vision, acoustic, depth and other sensor modules. Control module maintains the orientation of AUV using continuous PID loops running simultaneously. It relies on the mechanical stabilization for both roll and pitch movement, and thus, only the yaw, depth and horizontal movement of AUV is controlled by this module. The PID control algorithm has been coded in Qt Creator 3.0. This method has proven to be more efficient, less processor intensive and easily implementable. The system attempts to maintain its state using dynamic feedback from the IMU, pressure sensor and the acoustic and vision modules. User interfaces have been specifically developed to tune and adjust the PID parameters easily.

This year we have shifted all our codes to open source softwares. We have integrated all the codes in Qt SDK 5.2 using Qt Creator 3.0.The Computer

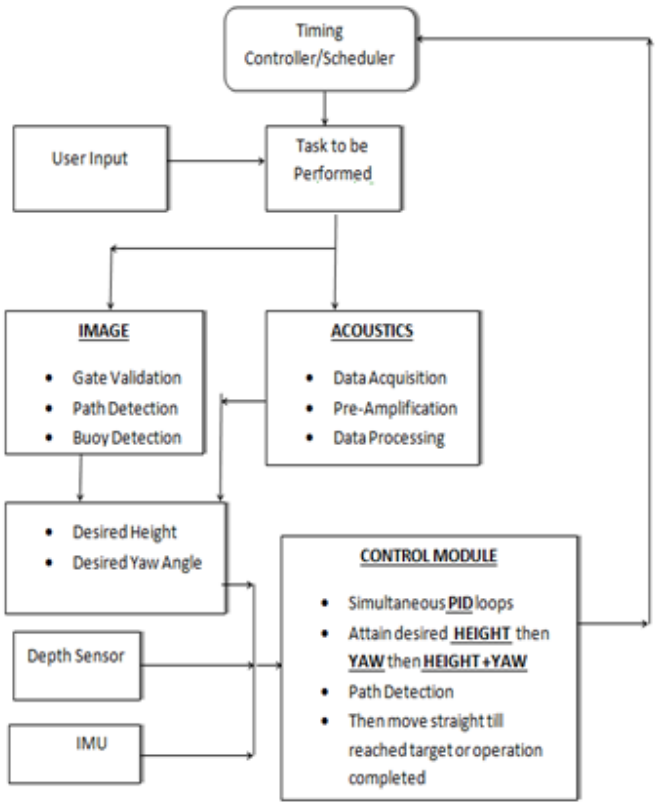

Fig. 13. Various software modules working in tandem to achieve mission control

Vision module is developed using OpenCV library of C++.

The Computer Vision module was developed using the OpenCV library of C++ integrated with Qt SDK using Ubuntu 12.04. The high parallelism during execution of programs on multi-core processors in Ubuntu (Linux) gives the vision module the re-

quired real-time computational power. The module incorporates concepts involving the various image processing algorithms for particle analysis, image segmentation, binary morphology, Hough transformation and Machine Vision. The major change this year is that the navigation system works on absolute yaw (angle) control and we have used the User Datagram Protocol (UDP) for communication of the AUV. The previous generation vehicles had a less accurate navigation system partly based on heuristics.

We have used an Android phone as our IMU (Inertial Measurement Unit) using an application for Android operating System to get the orientation of the AUV as an alternative of our IMU. The Android phone uses the UDP communication for sending and receiving data packets between the Android phone and the single board computer.

VI. Software and Machine Vision

The software team is responsible for mission planning, machine vision and developing several software tools to enhance the debugging and operability of the vehicle. This year the team has shifted all the codes to open source softwares keeping in mind the following objectives: 1)Enhancing the parallel processing capability and modularity. 2)Reducing mission task execution time. 3)Development of debugging and replacement modules in case of critical hardware failure.

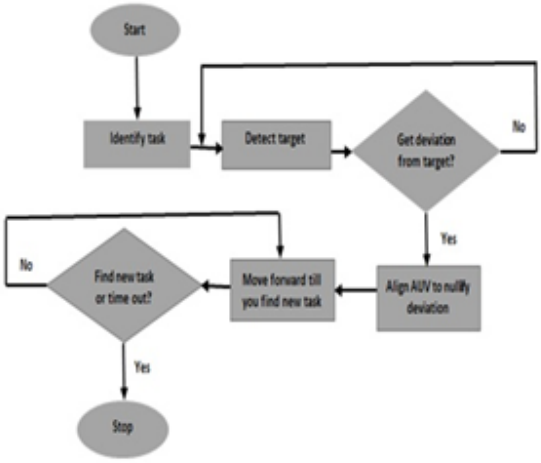

Fig. 15. Generalized flow chart for target detection using Image Processing

A. Software stack on SBC

The software stack has been built on Ubuntu Core GNU/Linux distribution, using Ubuntu 12.04. The vehicles computer is composed of Kontron Motherboard 986LCD-M/mITX, 4 GB of RAM and an Intel Atom Processor clocked at 1.60GHz . The entire software stack has been written in C/C++. The software stack performs mission planning, image processing, and handling the communication between the hardware modules, power board and inertial measurement unit.

B. Middleware

The objective of the middleware is to formulate a neat and clean interface for various processes to interact with each other. The inter process communication for various processes and multiple sensor modules on the on-board computer operate on the shared memory managed on Qt SDK 5.2 using QSharedMemory Class. A central mission control module then takes the decisions according to the sensor values received from these processes.

C. Vision

The team has integrated all the codes in Qt SDK 5.2 using Qt Creator 3.0. The Computer Vision module is developed using OpenCV library of C++. We are using two cameras (Logitech C920) one facing downwards and the other forward facing camera. These cameras are USB 2.0 enabled and interfaced to the SBC. The front facing camera is used for localization while the bottom camera is used for orienting the vehicle along the path placed at the bottom.

1) Image Preprocessing: Images tend to get degraded as the vehicle goes underwater. Since as the depth increases, the amount of light on objects decreases and light distribution becomes non-uniform. To tackle this issue, the input images are converted to YCbCr color space and Contrast Limited Adaptive Histogram Equalization (CLAHE) is performed on the Luminescence(Y) channel of the image which improves the local contrast, at the same time limiting the amplification which can over-amplify the noise too. Normalized cross correlation techniques and Pyramidal Mean Shift filter is also used to enhance the target image before further processing.

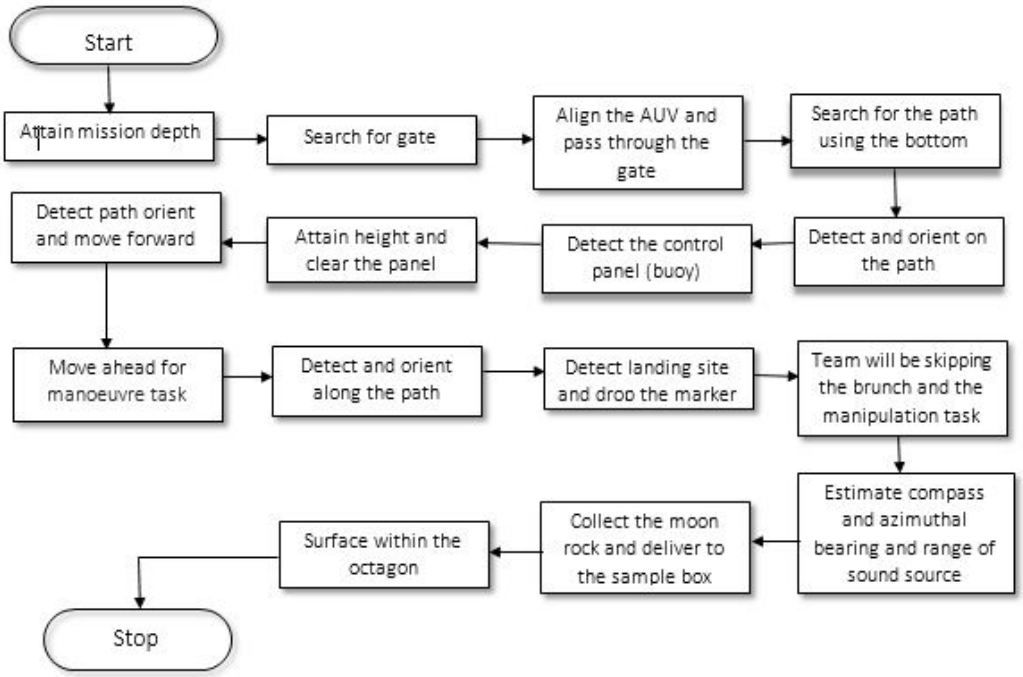

(a)

Fig. 14. ROBOSUB Mission Controller's Approach .

The AUV is capable of doing the tasks described below. Fig.15 gives the generalized flow chart for target detection using vision module.

D. Gate Validation

Starting with the Gate Detection, our vision algorithm receives video feed from the front facing camera and gives the heading relative to the AUV as the output. To accomplish this the Cr channel from the image in YCbCr is taken. Over this image, Canny Edge Detection is performed and perpendicular Hough Lines are found. The center of the symmetry of the resulting image thus gives the correct heading relative to the vehicle.

E. Path Detection

For Path Detection video feed from the downward facing camera is analyzed and heading relative to the AUV is given as output. The captured image is converted to HSV and segmented for specific color. Further, morphological operations are performed to remove any unnecessary noise. Contours are then found on the resulting image to find the connected components. Smaller contours are removed pertaining to noise. A minimum bounding rectangle is formed over the detected contours and the angle of the edge having the longest length is taken as the angle of the path.

F. Buoy Detection

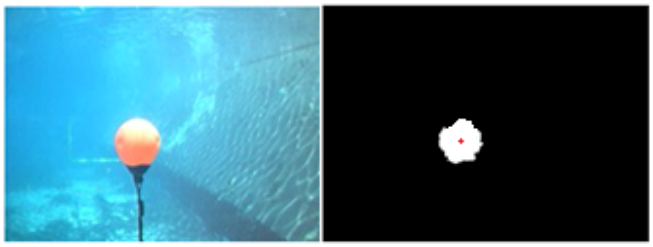

Fig. 18. Original Image and Processed Image for Buoy Detection

Algorithm for buoy detection is similar to path detection. Video feed from the front camera is taken and the captured image is converted to HSV and segmented for specific color. Over the resulting binary image, morphological operations are performed to remove any unnecessary noise. On the resulting image, the center of the largest blob is found using central moments. The position of the center gives the relative heading for the AUV.

(a) (b) (c)

Fig. 16. Visual comparison: (a) Input image, (b) Cr channel from YCbCr space and (c) Gate detected after applying the algorithm

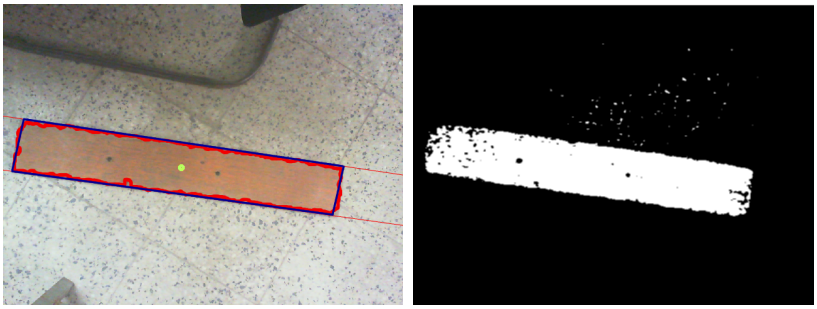

(a) (b)

Fig. 17. Visual comparison: (a) Original image with path detected and heading calculated, (b) Corresponding binary image.

VII. UnderWater Acoustics

Zyra 2.0 has an acoustic navigation system which employs a three dimensional array of hydrophones for data acquisition to calculate azimuthal and compass bearing and estimate hyperbolic location of the sound source in far-field approximation using Time difference of arrivals (TDOAs). Fig.19 shows

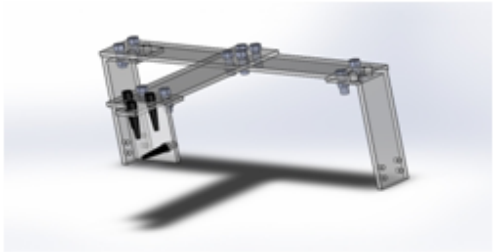

Fig. 19. 3-D hydrophone array

a tetrahedral array of hydrophones which has been used for the localization of the sound source. Such a symmetric array eases calculation while making time difference of arrival(TDOA) calculations and helps in reducing symmetric noise at different hydrophones.

The localization task has been broken down into two parts as follows :

A) TDOA(Time Difference of Arrival Estimation)

B) Position Estimation

A. TDOA Estimation

The Generalized cross-correlation technique using phase transform (GCC-PHAT) is employed to calculate the time difference of arrival corresponding to the correlation peak. Estimated TDOAs give bearing estimation for far field approximation. The mathematics of the method is discussed as belows: Let $S_1(t)$ and $S_2(t)$ be two signals at two different hydrophones and Δ be the Fast Fourier transform of the signals, then

$$X_1(f) = \Delta(S_1(t))$$

$$X_2(f) = \Delta(S_2(t))$$

GCC-PHAT is defined as:

$$GPHAT = \frac{X_1(f)[X_2(f)]^*}{|X_1(f)[X_2(f)]^*|}$$

where * is the complex conjugate of a function

$$TDOA = argmax(\Delta^{-1}(GPHAT))$$

In environments of high levels of reverberation GCC-PHAT helps to improve robustness and accu-

racy in calculating the time difference of arrival as we can see from Fig.20 that GCC-PHAT enhances the peak and whitens the region around it.

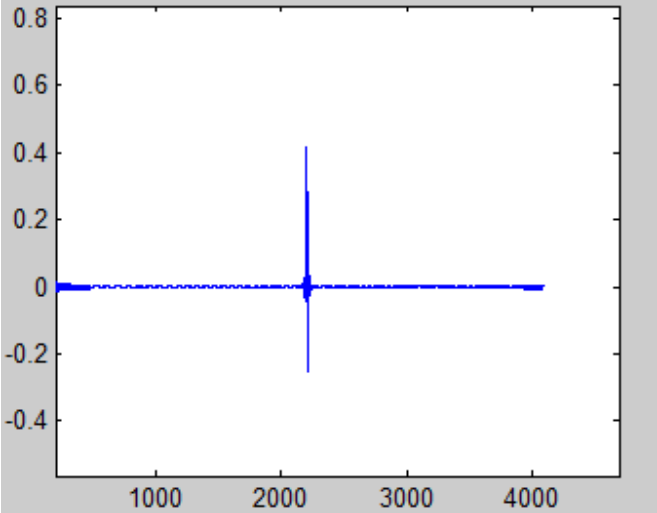

Fig. 20. Typical GCC-PHAT function

B. Position Estimation

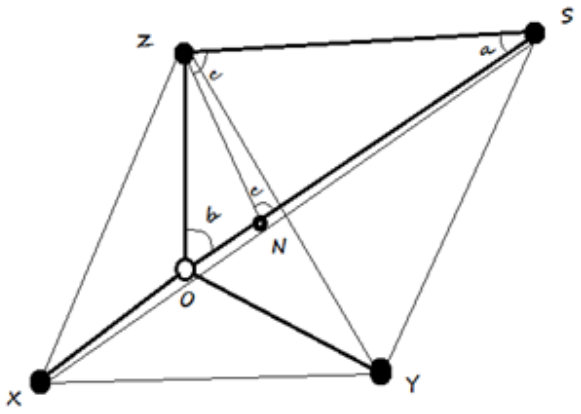

Fig. 21. Geometrical model of the localization system

We have to note a few terminologies here. X, Y and Z are my sensor positions respectively on the x,y and z cartesian axes. The point S represents my sound source. Since TDOA measurements require 2 hydrophones, we will be dealing with source hydrophone triangles such as ΔOZS.

$\angle(ZOS) = b$ is my bearing, we have defined $\angle(ZSN) = a$ and $\angle(ZNS) = c.ZN$ has been drawn such that $ZS = NS$.

The path difference $x = c\tau$ where c is the speed of sound and τ is the TDOA. We define OZ=OX=OY=d.

We define (vectorially), $OS = rs$ and $ZS = rz$ and in a similar fashion we define r_x and r_y.

The basic TDOA equations are:-

$$||r_i| - |r_j|| = X_{ij}$$

Where i and j run over x ,y and z and x is my path difference. Note that X_{ij} is symmetric due to the modulus on the left hand side.

A little manipulation with the parallelogram law of addition and TDOA equations would show us that for that triangle OZS we can derive the quadratic in $|r_s|$ as :

$$A = 4sin^2(a/2)$$

$$B = \pm 4sin^2(a/2)X_{zs}$$

$$C = (X_{zs})^2 - d^2$$

In $A^2x + Bx + C = 0$, x is the dummy varaible(different from X_{ij}) , where

$$x = |r_s|$$

Now clearly ON is the path difference that is $ON = X_{zs}$.

Determine ZN = f by cosine rule and finally using sine rule in triangles OZN and NZS.

$$sin(a/2) = \sqrt{1 - \frac{d}{f}sin^2(b)}$$

The discriminant of the quadratic gives us the condition that :

$cos(a/2)\epsilon -\frac{d}{X_{zs}}, \frac{d}{X_{zs}}$ or in a better sense $\frac{d}{X_{zs}} < 1$.

The idea is to find $|rs|$ from the quadratic and calculate $p = |rs|sin(b)$ and z- coordinate of source using $z(s) = |rs|cos(b)$.

And finally for X_{xs} or for X_{ys} using the fact that,

$$|r_y| = \sqrt{|r_s|^2 - 2dy(s) + d^2}$$

And that $y(s) = psin\psi$, ψ being measured in the XY plane from X axis we find out by using this in the TDOA equation in triangle OYS.

$$sin\psi = \frac{d^2 - {X_{ys}}^2 \pm |r_s|X_{ys}}{2dp}$$

The beauty of this method lies in the fact that we haven't used any approximations for calculating the exact positions .

Although there is the possibility of multiple roots from the quadratic yet only one of the solutions will be feasible satisfying all other conditions . Any error if encountered will be on part of the TDOA analysis method, it will only be multiplied by a scalar constant while calculating the overall error.

VIII. Conclusion and Current Progress

In this paper the development of the AUV Zyra 2.0 is presented to perform various shallow water tasks. The idea and logic behind the mechanical design ,embedded and power systems design, control algorithms and software platforms , image processing techniques and the geometric mathematics involved in the localization process of the pinger have been explained in detail.Zyra 2.0 is now in the testing phase. Prior to vehicle assembly, the mechanical systemswere thoroughly leak tested, and the electrical systems were bench tested.

Acknowledgment

The authors would like to thank the sponsors, namely ONGC, Yamaha, Samtec, NIOT, Seabotix and National Instruments for their financial and technical support. Further thanks to our faculty advisors P.B.Sharma and Prof. R.K.Sinha. We are grateful to Mr. Anil for providing his pool for testing. Without these individuals support,the development of the AUV would not have been possible.

References

[1] Sinha, R.K. Delhi Technological. University and Ahmed,S. , Bahuguna,P. , Kumra,R. , Agarwal,V., Saxena,V. , Mittal,V. ; Gupta,P. , Tutwani,M. , *Vehicle for Automation Research and Underwater Navigation*, 3rd ed.

[2] Ming Chen , Qiang Zhan and Sanlong Cai *Control System Design of an Autonomous Underwater Vehicle*, 3rd ed. IEEE Conference on Robotics, Automation and Mechatronics, Dec. 2006.

[3] Daniel Moussette , Ashish Palooparambil and Jarred Raymond *Optimization and Control Design of an Autonomous Underwater Vehicle*, 3rd ed. WORCESTER POLYTECHNIC INSTITUTE Thursday, April 29, 2010.

[4] Ann Marie Polsenberg, MIT , Drew Gashler *Developing an AUV Manual Remote Control System*, 3rd ed. WORCESTER POLYTECHNIC INSTITUTE Thursday, April 29, 2010.

[5] Robert Pavish *Dynamic control capabilities developments of the Bluefin Robotics AUV fleet*, 3rd ed. Cambridge 2009

Int. J. of GEOMATE, Dec., 2014, Vol. 7, No. 2 (Sl. No. 14), pp. 1033-1039
Geotech., Const. Mat. and Env., ISSN:2186-2982(P), 2186-2990(O), Japan

EFFECT OF LIME AND STONE DUST IN THE GEOTECHNICAL PROPERTIES OF BLACK COTTON SOIL

Ankur Mudgal[1], Raju Sarkar[2] and A.K. Sahu[2]

[1]Civil Engineering Department, Galgotia's College of Engineering & Technology
[2]Department of Civil Engineering, Delhi Technological University, New Delhi

ABSTRACT: In the present study Black Cotton Soil was stabilized with a mixture of lime and Stone Dust. First an optimum value of lime was determined on the basis of some geotechnical properties of mixture of lime and Black Cotton Soil. Then Stone Dust was mixed upto 25% by weight with an increment of 5% in the optimized mixture of lime-Black Cotton Soil. California bearing ratio, unconfined compression strength and maximum dry density values were determined of these modified mixes. Morphology of the soil and admixture has been studied by Scanning electron microscope (SEM), while mineralogical composition has been determined by X-Ray diffraction technique (XRD).

Keywords: *Black Cotton Soil, Geotechnical properties, California bearing ratio (CBR), scanning electron microscopic (SEM) and X-ray diffraction (XRD)*

1. INTRODUCTION

Every year many civil engineering structures like buildings, embankments, roads and dams constructed on expansive soils got damaged due to highly expansive behavior of such soils. The main reason behind such behavior of expansive soils is the presence of mineral called montmorillonite. It has high water content capacity and swells significantly when it comes in contact with water. In India expansive soils are also known as Black Cotton Soils as cotton is cultivated in majority of the areas where this black soil is found. It covers around 20% of total land area of India. It is largely found in southern, western and central parts of India, covering Andhra Pradesh, Karnataka, Gujarat and some parts of Madhya Pradesh. The construction on Black Cotton Soil has always been a big challenge to geotechnical engineers. Many researchers have worked to improve or stabilize its expansive behavior with various admixtures. They have used waste materials as admixtures and showed their best results in soil stabilization. Modak et. al [1] studied the combined effect of lime and fly ash in Black Cotton Soil and concluded that with increasing the percentage of lime and fly ash in Black Cotton Soil, California bearing ratio (CBR) and maximum dry density (MDD) values are also increases. Nadgouda and Hegde [2] found optimum value of CBR and MDD at 3.5 % lime addition in Black Cotton Soil. Ijimdiya et. al [3] stabilized the Black Cotton Soil by groundnut shell ash (GSA) and observed that unconfined compressive strength increased from 91 kN/m^2 without adding GSA to a maximum value of 211 kN/m^2 at 8% GSA, whereas the optimum value of CBR was found on the addition of 6.3% of GSA.

Calcium oxide (CaO) known as quicklime is a widely used chemical compound. It is a white, caustic and alkaline crystalline solid at room temperature. As a commercial product, lime often also contains magnesium oxide, silicon oxide and smaller amounts of aluminium oxide and iron oxide (refer Table I for a typical chemical composition).

Lime in the form of quicklime (calcium oxide - CaO), hydrated lime (calcium hydroxide $–Ca(OH)_2$), or lime slurry can be used to treat soils. Quicklime is manufactured by chemically transforming calcium carbonate (limestone-$CaCO_3$) into calcium oxide. Hydrated lime is created when quicklime chemically reacts with water (refer Table II for comparison). It is hydrated lime that reacts with clay particles and permanently transforms them into a strong cementitious matrix. Usually, limes used for soil treatment are "high calcium" limes, which contain no more than 5 percent of magnesium oxide or hydroxide. Lime, either alone or in combination with other materials, can be used to treat a range of soil types (Sarkar et. al [4]).

Again, the annual generation of quarry dust is roughly around 200 million tons in India (Soosan et. al [5]). Limited researches are available regarding the utilization of Stone Dust with lime for stabilization of expansive soils. So, in the present study, lime and Stone Dust was used as admixtures for Black Cotton Soil. The maximum dry density (MDD) and optimum moisture content (OMC), California bearing ratio (CBR) and unconfined compression strength (UCS) characteristics were studies. The present study aims towards showing how these two above materials can be utilized in Black Cotton Soil in an optimum way to assure a win-win condition for both soil stabilization and quarry waste disposal.

2. MATERIAL USED

2.1 BLACK COTTON SOIL

Table I Chemical composition of lime (Sarkar et. al. [5])

Properties	Test value (%)
Minimum Array (Acidimetric)	95.00
Maximum Limits of Impurities	
Chloride (Cl)	0.10
Sulphate (SO_4)	0.50
Iron (Fe)	0.10
Lead (Pb)	0.02
Loss on Ignition	10.0

Table II Index properties of quicklime and hydrated lime (Sarkar et. al [5])

Properties	Quicklime	Water	Hydrated lime
Molecular weight	56	18	78
Specific gravity	3.3	1	2.2
Relative weight	1	0.32	1.32
Relative volume	1	-	1.99

For the present study, Black Cotton Soil sample were collected from Gwalior-Jhansi road, near Tekanpur BSF area (National Highway No. - 7), Gwalior.The top layer of the soil was removed with the help of shovel up to a depth of 0.5 m before collecting the soil sample. The geotechnical properties of Black Cotton Soil sample used in this study are given in Tables III.

2.2 STONE DUST

Bulk quantities of Stone Dust were procured from stone crusher plant of Aman vihar Industrial area, New Delhi.

2.3 LIME

The lime was procured from the local market. The chemical composition of lime is mentioned in Table I.

3. EXPERIMENTAL INVESTIGATIONS

3.1 INTRODUCTION

Bulk quantities of Black Cotton Soil in wet state were collected from the sites of Gwalior-Jhansi road. The samples were collected personally and procured freshly at the beginning of the study and stored properly.

Table III Geotechnical properties of Black Cotton Soil

The collected soil samples were characterized in the geotechnical laboratory of Delhi Technological University. Tests were conducted to determine physical and geotechnical properties of soil samples. The specific gravity tests were performed on Black Cotton Soil, lime and Stone Dust. The standard Proctor tests were also performed on soil samples alone as well as their mixes with an increasing percentage of lime by weight (3, 6, 9 and 12 percentage) and maximum dry density (MDD) was calculated to determine the optimum percentage of lime to be mixed with the soil. After determining optimum percentage of lime (=9%), Stone Dust was mixed by 5, 10, 15, 20 and 25% by weight in the lime-Black Cotton Soil mix to determine MDD and OMC, unconfined compression strength (UCS) and California bearing ratio (CBR) value of the new mix. The details of the experimental program are summarized in Table IV. The tests were performed conforming to Indian standard specifications listed in Table V.

Properties	Value
Specific Gravity	2.61
Percentage passing IS Sieve 75 micron (%)	58.0
Liquid Limit (%)	57.0
Plastic limit (%)	31.4
Plasticity index (%)	26.5
Differential Free Swell (%)	41.0
Unified Soil Classification System (USCS)	CH
Maximum dry density (kN/m^3)	16.1
CBR (soaked) (%)	1.50
Unconfined compression strength, (kN/m^2)	166.2

3.2 DETAILS OF TESTS CONDUCTED

3.2.1 Specific gravity

The specific gravity of the soil was determined as per Indian standard specifications [6].

3.2.2 Grain size distribution

The grain size distribution of soil was carried out as per the Indian standard specifications [7].

3.2.3 Atterberg limit test

All the tests for Atterberg limits were conducted as per the Indian standard specifications [8]. Liquid limit tests were carried out using Casagrande's equipment.

3.2.4 Differential free swell (DFS) index

Differential free swell index of soil sample was determined by Indian standard specification [9]. Free swell index is used for the classification of the

expansive soils on the basis of degree of expansiveness.

3.2.5 Compaction characteristics

Light (standard Proctor) test were carried out to determine the maximum dry density (MDD) and optimum moisture content (OMC) of soil and treated soil as per Indian standard specifications [10].

Table IV Experimental program

Material	Details of experiments
Black Cotton Soil	a) Specific gravity
	b) Atterberg limit tests
	c) Differential free swell test
Black Cotton Soil alone and mixed with lime and Stone Dust	d) Standard Proctor test
	e) California bearing ratio test
	f) Unconfined compression strength test

Table V: Standard codes used to perform laboratory tests

Laboratory tests	Standard/Procedures
Specific gravity	IS: 2720 (Part 3) – 1980
Grain size analysis	IS: 2720 (Part 4) – 1985
Atterberg limit test	IS: 2720 (Part 5) – 1985
Differential free swell index	IS: 2720 (Part 40) – 1977
Standard Proctor compaction test	IS: 2720 (Part 7) – 1980
California Bearing Ratio test	IS: 2720 (Part 16) – 1987
Unconfined compressive strength test	IS: 2720 (Part 10) – 1973

3.2.6 California Bearing Ratio (CBR) test

California bearing ratio (CBR) tests were conducted on soil and treated soils as per Indian standard specifications [11]. The California bearing ratio test is a penetration test that measures the subgrade strength of soils used for roads and pavements (Sarkar et. al [4]). The results obtained by CBR tests are used with empirical curves to determine the thickness of pavement and its component layers. It is the most widely used method for the design of flexible pavements.

3.2.7 Unconfined Compression Strength (UCS) test

Unconfined compression strength tests were conducted on soil and treated soils as per Indian standard specifications [12]. The UCS test evaluates the compressive strength of cohesive soil in unconfined state and very necessary for the determination of load carrying capacity of foundation, embankment etc.

3.3 TEST RESULTS AND DISCUSSION

3.3.1 Specific Gravity

The specific gravity of Black Cotton Soil, lime and Stone Dust were found 2.61, 3.22 and 2.75, respectively.

3.3.2 Atterberg limit test

The liquid limit of Black Cotton Soil was found to be 57% and plastic limit was found 31.43 %. According to Unified Soil Classification System (USCS), soil can be classified as highly compressible soil (CH).

3.3.3 Differential free swell test

The differential free swell index of Black Cotton Soil was found 41%.

3.3.4 Compaction behavior

Light compaction tests were conducted on the natural and treated soil in the investigation to determine MDD and OMC value. Fig. 1 shows the variation of MDD with percentage of lime. It is observed that MDD value is increases from 16.1 kN/m^3 to 16.6 kN/m^3 when no lime is added and 9% lime is added, respectively, and it decreases afterwards. Lime causes the soil particles to coagulate, aggregate, or flocculate. Thus soil becomes more easily workable and its strength and stiffness increases up to a certain value. The MDD values are 16.2 kN/m^3, 16.4 kN/m^3, 16.6 kN/m^3 and 16.5 kN/m^3 for the soil mixed with 3%, 6%, 9% and 12% lime, respectively.
Figure 2 shows the variation of MDD with percentage of Stone Dust in soil-lime (=9%) mix. It is observed that MDD of lime stabilized soil increases upto addition of 20% Stone Dust and further addition of Stone Dust decreases the MDD value. This can be due to the mixing of heavy particles of Stone Dust in significant amount. Beyond addition of 20% Stone Dust in lime stabilized soil, the strength decreases since large Stone Dust content segregates the particles and maximum dry density decreases.

3.3.5 California Bearing Ratio (CBR) test

Soaked CBR tests were conducted on Black Cotton Soil and soil mixed with admixtures as per Indian Standards. Sample was prepared in cylindrical mould and compacted in five layers. Then the compacted sample along with mould was submerged in water for 72 hours. After removing from water, the CBR test was performed under a constant strain rate of 1.25 mm/min. Fig. 3 shows the variation in CBR with percentage of lime.

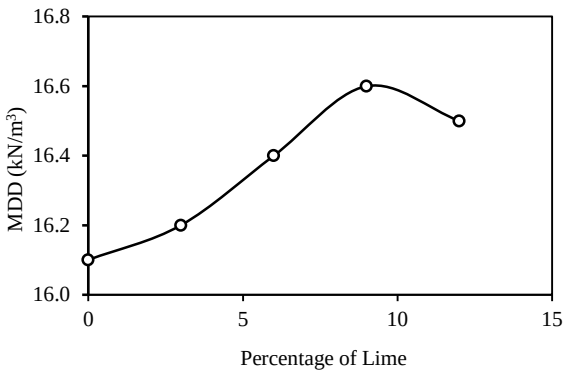

Fig. 1 Variation of MDD with percentage of lime

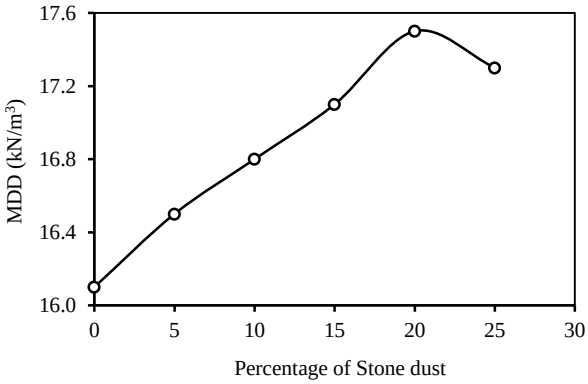

Fig. 2 Variation of MDD with percentage of Stone Dust in soil-lime (=9%) mix

The CBR value is 1.5% when no lime is added in the soil. The CBR values are 3.9%, 7.6%, 12.8% and 12.0% for the soil mixed with 3%, 6%, 9% and 12% lime, respectively. It is noted that as observed in case of variation of MDD with percentage of lime (Fig. 1), the CBR value is also increases upto 9% addition of lime in soil and then decreases.

Figure 4 shows the variation of CBR with percentage of Stone Dust in soil-lime (=9%) mix. It is observed that the soaked CBR value attains highest value when 20% of Stone Dust was added in lime stabilized soil and then decreases.

As mentioned above, addition of Stone Dust in the soil-lime (=9%) mix up to 20%, increases the CBR value since silica in all the finer particles of soil and Stone Dust are used up to this value and addition of more Stone Dust actually becomes counterproductive thereafter.

3.3.6 Unconfined Compression Strength (UCS) test

Unconfined compression tests were conducted on soil and treated soils as per Indian Standards. Samples were prepared in split mould at MDD and optimum moisture content (OMC). The cylindrical specimen of soil and treated soil were tested under normal vertical load. The UCS value of every sample was determined by dividing the maximum load at which the failure takes place and the corrected cross sectional area of the specimen. Fig. 5 shows the variation of UCS with percentage of lime. It is observed that the UCS value increases upto the 9% addition of lime and then decreases. The UCS value is 154 kN/m^2 when no lime is added in soil. The UCS values are 159 kN/m^2, 164 kN/m^2, 169 kN/m^2 and 166 kN/m^2 for the soil mixed with 3%, 6%, 9% and 12% lime, respectively. The optimum value of MDD of soil occurred at 9% lime addition.

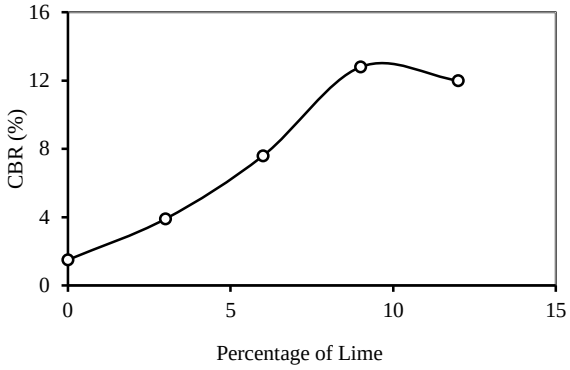

Fig. 3 Variation of CBR with percentage of lime

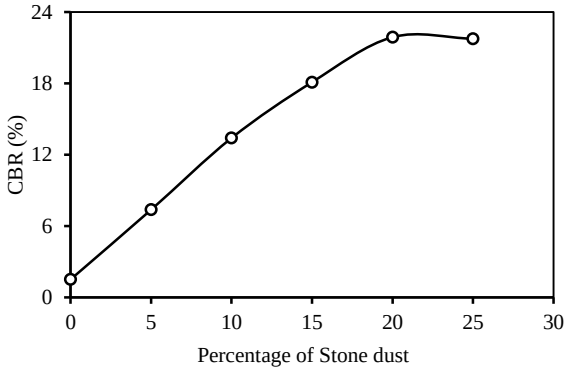

Fig. 4 Variation of CBR with percentage of Stone Dust in soil-lime (=9%) mix

Figure 6 shows the variation of UCS with percentage of Stone Dust in soil-lime (=9%) mix. It is observed that UCS value increased from 154 kN/m^2 to 182 kN/m^2 when no Stone Dust is added and 20% of Stone Dust is added, respectively, and it decreases afterwards. It is due to the addition of Stone Dust beyond 20% gives the negative effect to the UCS value of lime stabilized soil.

3.4 MORPHOLOGY

The morphology of the Black Cotton Soil and admixtures were analyzed by Scanning Electron Microscopic (SEM) Hitachi S 3700. Samples were taken after 28 days of curing. Referring Fig. 7(a)-(e), it is clearly visible that from the micrograph Black Cotton Soil, lime and stone dust have undergone pozzolanic reaction, stone dust and lime particles accumulated over the Black Cotton Soil and forming the various cementitious compounds.

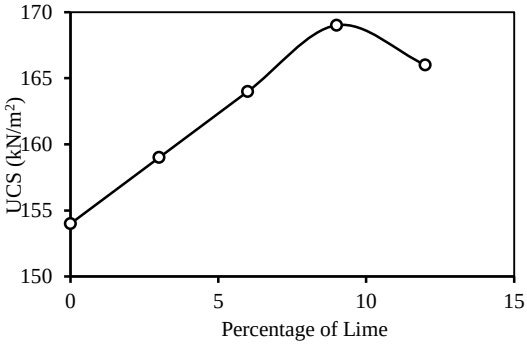

Fig. 5 Variation of UCS with percentage of lime

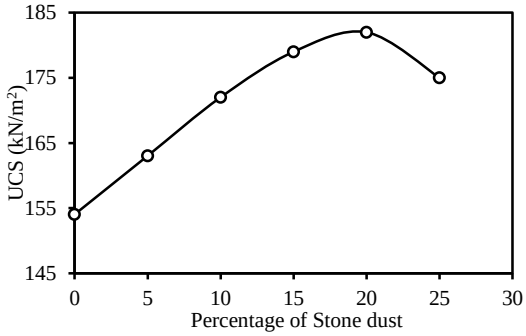

Fig. 6 Variation of UCS with percentage of Stone Dust in soil-lime (=9%) mix

3.5 MINERALOGICAL CHARACTERIZATION

The pozzolanic reaction between soil and admixtures, results in the change in mineralogical phases of soil. Hence, the mineralogical analysis of the treated soil becomes very essential. Therefore, XRD-analysis was conducted on the treated soils. Test was conducted with the help of X-Ray diffractometer, Hitachi, which employ a Cu-Kα radiation (step of 0.05° 2θ and range of 0°-70° 2θ). Sulphate present in the soil reacts with calcium (from lime) and alumina (from stone dust and clay) forms the mineral ettringite. This ettringite mineral improves the soil strength and reduce the swelling tendency of the soil. The description of the sequence given by (Hunter in 1988) as

$$6Ca + 2Al(OH)^{-}_{4} + (OH)^{-} + 3(SO_4)^{2-} + 26H_2O \longrightarrow Ca_6[(Al(OH)_6)]_2(SO_4)_3 . 26H_2O$$

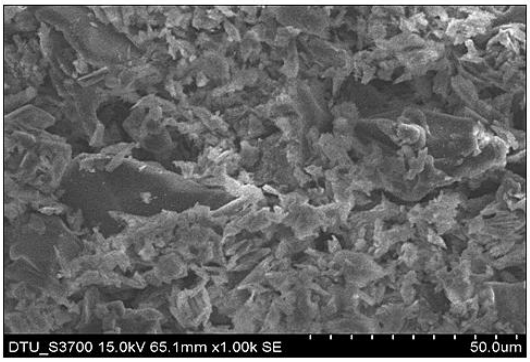

7(a)

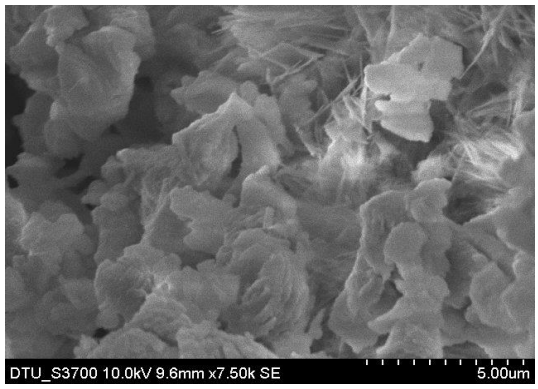

7(b)

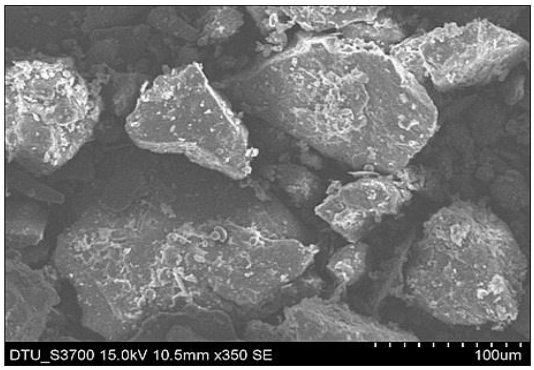

7(c)

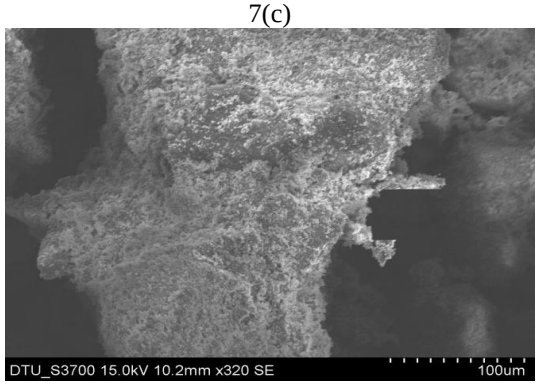

7(d)

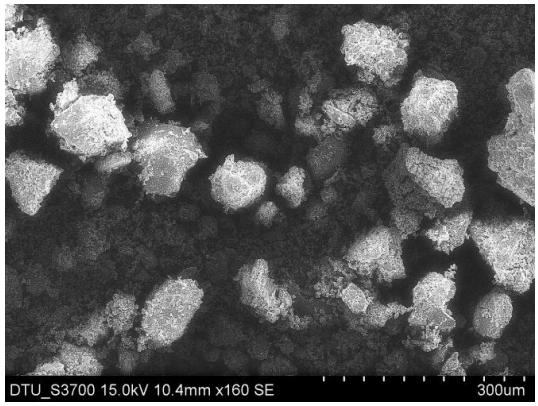

7(e)

Figure 7 Scanning electron micrographs of (a) Black Cotton Soil (b) Lime (c) Stone Dust (d) Black Cotton Soil + 9 % (e) Lime Black Cotton Soil + 9 % Lime + 25% Stone Dust

Figure 8(a)-(c) shows the X-Ray Diffraction patterns of Black Cotton Soil, Stone Dust and Black Cotton Soil mixed with Lime (9%) and Stone Dust (25%), respectively.

4. CONCLUSION

Black Cotton Soil and admixtures were identified by experimental studies. The changes in their physical properties were studied with the help of laboratory tests. The following conclusions can be obtained by test results data.

1. It is observed that MDD of lime stabilized (=9%) Black Cotton Soil increases up to the addition of 20% Stone Dust and further increase of the agent decreases the value.
2. Similarly, for UCS and CBR, the strength increases upto 20% addition of Stone Dust in lime stabilized soil. The reason of this effect is the pozzolanic reactions of lime with the amorphous silica and alumina present in soil and Stone Dust.
3. SEM Pictures of cured sample clearly shows coarser bonded particles of Black Cotton Soil , Lime and Stone Dust
4. X-Ray diffraction of samples shows the presence of montmorillonite, vermiculite (minerals of smectite group), in Black Cotton Soil, whewellite and Quartz in Stone Dust and dolomite calcite in lime.

5. REFERENCES

[1] Modak, P.R., Nangare, P.B., Nagrale, S.D., Nalawade, R.D, and Chavhan, V.S. (2012). Stabilization of Black Cotton Soil using admixtures, International Journal of Engineering and Innovative Technology, Vol. 1 No.5, pp. 11-13

[2] Nadgouda, K.A. and Hegde, R.A. (2010). The effect of lime stabilization on properties of Black Cotton Soil, proceeding, Indian Geotechnical Conference-2010 (GEOtrendz), Bombay, pp. 511-514

[3] Hunter D. (1988). Lime induced heave in sulphate bearing clay soils, ASCE. J. Geot. Eng. 114, 150-167

[4] Haldar, M. K. and Das, S. K. (2012). Effect of sand stone dust for quartz and clay in triaxialporcelain composition, Indian Academy of Sciences, Vol. 35 No. 5, pp. 897–904

[5] Ijimdiyaa, T.S., Ashimiyu, A.L. and Abubakar, D.K. (2012). Stabilization of Black Cotton Soil using groundnut shell ash, Electronic Journal of Geotechnical Engineering (EJGE), Vol. 7 No.4, pp. 3645-3652

[6] Sarkar, R., Abbas, S.M., and Shahu, J.T., (2012). A comparative study of geotechnical behavior of lime stabilized pond ashes from Delhi region, International Journal on GEOMATE, Japan, 03(01), 273-279

[7] Lekha, B M., Goutham, S., and Shankar, A U., (2013). Laboratory investigation of soil stabilized with nano chemical, Indian Geotechnical Conference, Roorkee.

[8] IS: 2720 (Part 3) (1980). Methods of Test for Soils: Determination of Specific Gravity, Bureau of Indian Standards, New Delhi, India

[9] IS: 2720 (Part 4) (1985). Methods of Test for Soils: Determination of Grain Size Analysis, Bureau of Indian Standards, New Delhi, India

[10] IS: 2720 (Part 5) (1985). Methods of Test for Soils: Determination of Liquid and Plastic Limit, Bureau of Indian Standards, New Delhi, India.

[11] IS: 2720 (Part 40) (1977). Methods of Test for Soils: Determination of Free Swell Index of Soils, Bureau of Indian Standards, New Delhi, India

[12] IS: 2720 (Part 7) (1980). Methods of Test for Soils: Determination of Water Content-Dry Density Relation Using Light Compaction, Bureau of Indian Standards, New Delhi, India

[13] IS: 2720 (Part 16) (1987). Methods of Test for Soils: Determination of CBR Value, Bureau of Indian Standards, New Delhi, India

[14] IS: 2720 (Part 3) (1980). Methods of Test for Soils: Determination of Unconfined Compression Strength, Bureau of Indian Standards, New Delhi, India.

Int. J. of GEOMATE, Dec., 2014, Vol. 7, No. 2 (Sl. No. 14), pp.1033-1039.
MS No. 140204 received on April 2, 2014 and reviewed under GEOMATE publication policies.

C**orresponding Author: Raju Sarkar**

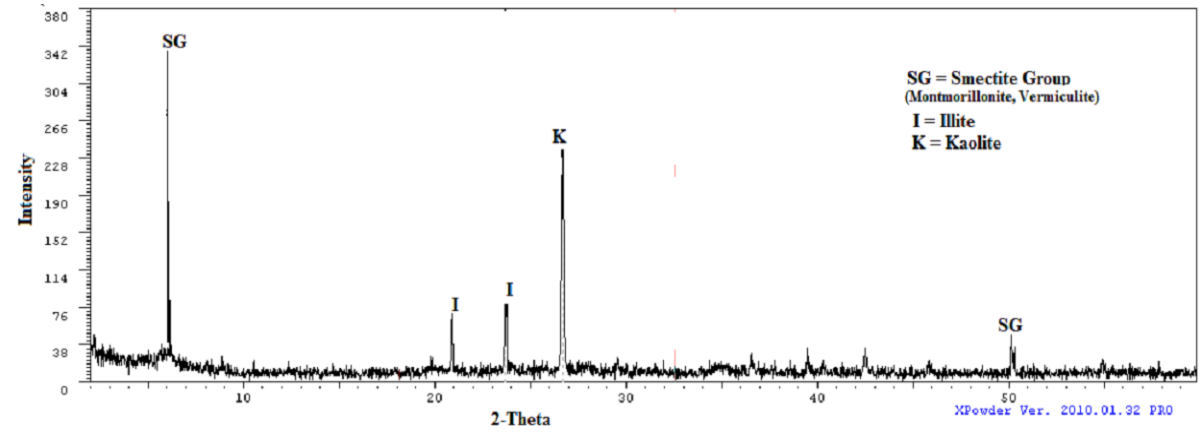

(a)

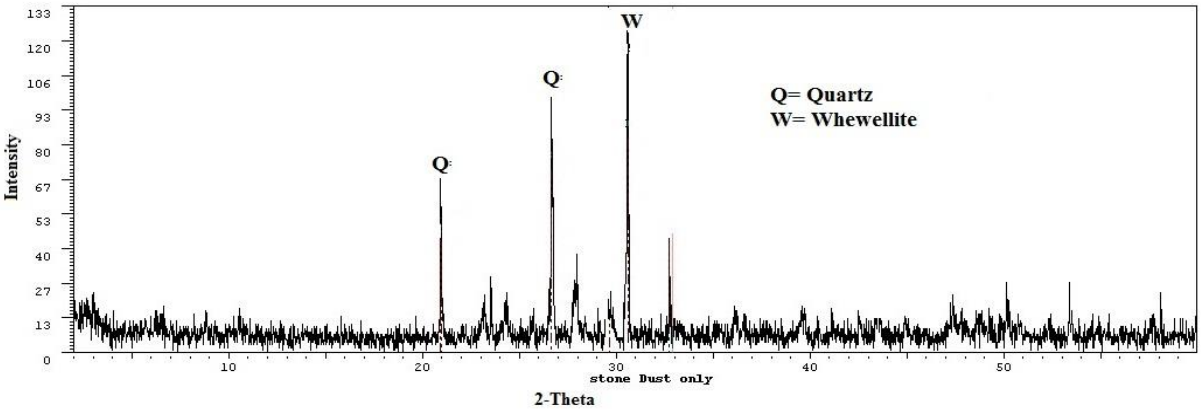

(b)

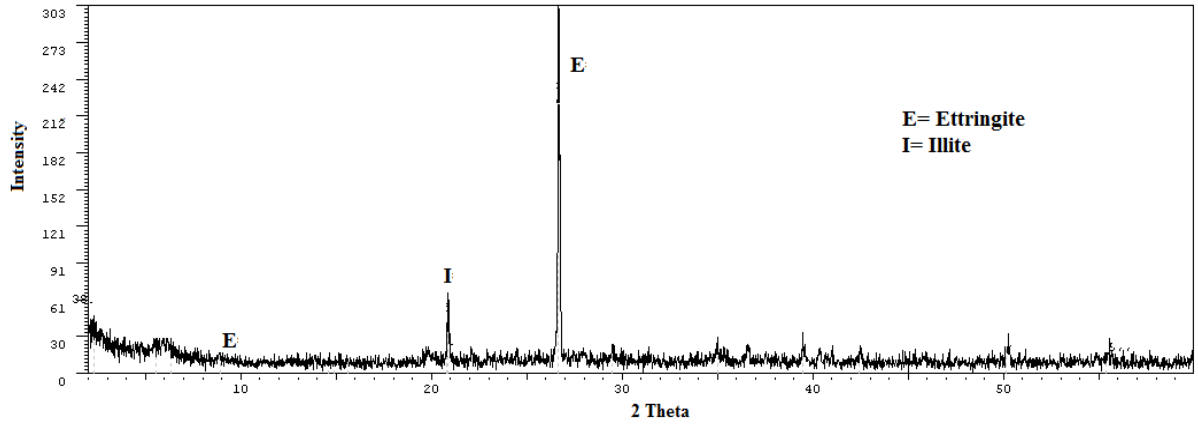

(c)

Figure 8 X-Ray Diffraction patterns of (a) Black Cotton Soil (b) Stone Dust (c) Black Cotton Soil + 9% Lime + 25% Stone Dust

Particulate Science and Technology: An International Journal

Publication details, including instructions for authors and subscription information:
http://www.tandfonline.com/loi/upst20

Effect of Multiwalled Carbon Nanotubes on the Conductivity and Swelling Properties of Porous Polyacrylamide Hydrogels

Sudha[a], B. M. Mishra[a] & D. Kumar[a]

[a] Department of Applied Chemistry and Polymer Technology, Delhi Technological University, (Formerly Delhi College of Engineering), Shahbad Daulatpur, Delhi, India

Accepted author version posted online: 02 Sep 2014.

To cite this article: Sudha, B. M. Mishra & D. Kumar (2014): Effect of Multiwalled Carbon Nanotubes on the Conductivity and Swelling Properties of Porous Polyacrylamide Hydrogels, Particulate Science and Technology: An International Journal, DOI: 10.1080/02726351.2014.948974

To link to this article: http://dx.doi.org/10.1080/02726351.2014.948974

Effect of Multiwalled Carbon Nanotubes on the Conductivity and Swelling Properties of Porous Polyacrylamide Hydrogels

Sudha[1,], B. M. Mishra[1], D. Kumar[1]

[1]Department of Applied Chemistry and Polymer Technology, Delhi Technological University, (Formerly Delhi College of Engineering), Shahbad Daulatpur, Delhi, India

Address correspndence to Sudha, Department of Applied Chemistry and Polymer Technology, Delhi Technological University, (Formerly Delhi College of Engineering), Shahbad Daulatpur, Main Bawana Road, Delhi-110042, India. E-mail: sudha1320@gmail.com

Abstract

MWCNTs were added to polyacrylamide (PAM) hydrogels in different proportions to tune their electrical and mechanical properties. The choice of MWCNTs as a reinforcement is justified by the fact that these are highly conducting, fairly stable and flexible particles. A series of MWCNT/PAM hydrogels were prepared by "*freezing method*". The characteristic absorption peaks at 1480 and 1213 cm^{-1} in the FTIR spectra reveal that MWCNTs are embedded in the PAM hydrogels. Powder X-ray diffractograms and TGA thermograms show that the MWCNT/PAM hydrogels are crystalline, more thermally stable and have a higher electrical conductivity than a traditional PAM hydrogel. Scanning electron micrographs reveal about reduced pore size, homogeneous and denser texture. The swelling properties of all these hybrid hydrogels were found to be better than those of the parent PAM hydrogel. The Li-Tanaka equation was employed to produce the swelling parameters. The D_c of PAM hydrogel is 10 times higher than the literature value. 0.8% MWCNTs reinforced PAM hydrogel has excellent $\square_c$ and electrical conductivity (0.76 mS/cm) with improvements in all properties. Lower D_c of 0.8% MWCNTs/PAM hydrogel reveal that extent of crosslinking is much important than density of the system for a better collective diffusion of the respective solvent.

KEYWORDS: Collective diffusion coefficient, multiwalled carbon nanotubes, conductivity, hydrogels.

1. Introduction

Polymeric gels are important as they have potential to design systems with well-defined and controlled electrical and mechanical properties. Fundamentally speaking, a gel is a kind of colloid having 99 % liquid by weight and are the result of immobilization of the liquid because of the surface tension between it and a macromolecular network of fibres constructed from a small amount of gelating substance present. These macromolecular networks could be any material or particles for example organic polymers or proteins. On a special note, by taking water as a dispersion medium in polymer gels, they offer a degree of flexibility which is very similar to biological tissues. These polymeric gels are named as "Hydrogels". These kind of polymeric gels are three-dimensional water swollen structures composed mainly of hydrophilic homo-polymers or copolymers. They absorb large quantities of water while remain insoluble in aqueous solutions due to chemical or physical cross-linking of individual polymer chains. Also, crosslinks provide the network structure and physical integrity to form a stable hydrogel in which the absorbed water is hard to remove even under external pressure. Shibayama and Tanaka (1993) reported that the volume transition in hydrogels is the consequence of opposing forces within the polymer network that entirely depends on the chemical composition of the gel. These opposing forces could be the combination of four fundamental interactions: Van der Waals, hydrophobic, electrostatic and hydrogen bonding. Understanding the swelling and shrinking properties of hydrogels are of great importance due to its widespread

applicability. Swelling of chemically crossed linked gel is a kinetically controlled process and can be understood by considering the osmotic pressure versus the restraining force. The total free energy of a chemical gel consists of bulk and shear energies. In fact, in a swollen gel, the bulk energy can be characterized by the osmotic bulk modulus K, which is defined in terms of the swelling pressure and the volume fraction of polymer at a given temperature. On the other hand, the shear energy which keeps the gel in shape can be characterized by the shear modulus G. Here, the shear energy minimizes the non-isotropic deformations in the gel. A theory of the swelling of gel networks was first derived from the theory of elasticity as reported by Tanaka et al. (1973). Hydrogels are commonly used for a great deal of applications: sustained drug delivery system by Verheyen et al. (2010), materials responsive to specific molecules (glucose or antigens used as biosensors), diapers, contact lenses, medical electrodes, water gel explosives, breast implants, paints, coatings, adhesives, recyclable absorbents, bioreactors containing immobilized enzymes, bioassay systems, display devices, actuators, valves, sensors, artificial muscles for robotic devices, chemical memories, optical shutters, molecular separation systems and toys (Roy et al. 2011 and Tajima et al. 2011) etc.

Hydrogels became fascinating since Shibayama and Tanaka (1993) discovered in that by cooling a clear polyacrylamide (PAM) gel, he could make it cloud up and eventually became opaque and after warming the gel restored its clarity. A phase transition in a polymer network was identified, similar to that observed in the inter-conversion of the liquid and vapour phases of water at the critical point. Therefore, small change in solvent amount or temperature causes hydrogel to abruptly swell (or shrink) to many times its

original size. Though, hydrogels as a type of biocompatible polymers have applications in biological and medical fields reported by Lira et al. (2009) but hybrid hydrogel is a better option for its wide utility. Composite/hybrid hydrogels normally forms core-shell structures having many exciting properties like optical, magnetic, conducting properties etc. Preliminary investigations have already shown that carbon nanotube (CNT) reinforced composites hydrogel have potential for biosensors, actuators, and tissue engineering (Jagur-Grodzinski 2006; Joshi et al. 2005; Shi et al. 2005 and Kawaguchi et al. 2006). It has also been reported by MacDonald et al. (2005) that bulk CNT/hydrogel composites have improved selectivity in protein electrophoresis separation owing to the hydrophobic effect of the CNTs. Thus, a combination of CNTs with hydrogels are taken into account to view synergetic effect.

In general, an adequate dispersion of nanotubes into a polymeric matrix is a challenge, prompting the use of specialized methods including in-situ polymerization techniques (Huang et al. 2006; Mitchell et al. 2002 and Fukushima et al. 2006), surface modification of CNT (Zhu et al. 2006; Mitchell and Krishnamoorti 2007; Hobbie and Fry 2007; Abdalla et al. 2007), surfactants (Shanmugharaj et al. 2007; Gong et al. 2000) and spraying CNTs solution onto a polymeric powder (Gojny and Schulte 2004) so that CNTs may be successfully dispersed in both organic solvents (Zhang et al. 2006) and aqueous solution (Chen et al. 1998). Surface functionalized MWCNTs are considered for drug delivery to the target sites, including chemotherapy drugs into solid tumours (O'Connell et al. 2001; Liu and Wang 2007) and biochemical sensing by Bianco et al. (2005). Li et al. (2003) added CNTs into gelatine and found that the hybrid hydrogels with CNTs have

the ability to separate the protein. In addition, CNTs have the actuator property and could be used as artificial muscles (Li et al. 2003; Baughman et al. 1999; Minett et al. 2002). Keeping these aspects in view, we aimed to synthesize MWCNT/PAM hydrogels. Here, we report the successful synthesis and instrumental analysis of MWCNT/PAM hybrid hydrogels by a "*freezing method*" in the present paper. These hydrogels were then characterized by powder X-ray diffraction (XRD), scanning electron micrograph (SEM), thermo-gravimeter (TGA) and Four probe conductivity measurement techniques. Swelling time constants (c) and collective diffusion coefficients (D_c) were measured by employing the Li-Tanaka model. It was observed that water chains diffuse in the MWCNTs/PAM gel according to Fickian diffusion during the swelling process.

2. Experimental Analysis

All chemicals of analytical grade were used. N,N′-methylene bisacrylamide (MBA) and N,N,N′,N′-tetramethylethylenediamine (TEMED) were purchased from Sisco Research Lab. Pvt. Ltd. Mumbai, India. Acrylamide monomer and potassium persulphate (KPS) were supplied by CDH Chemicals India. MWCNTs used were procured from Cheap Tubes Inc., Brattleboro, VT, USA (100 µm length and 40-50 nm diameter). All chemicals were used as received without further purification. Double distilled and demineralized water from Millipore was used throughout the studies.

2.1 *Preparation of PAM and MWCNT/PAM composite hydrogels*

PAM superabsorbent polymer was prepared by mixing 10:1 weight ratio of acrylamide monomer and cross-linker MBA in 10 ml of distilled water at an ambient temperature.

The solution mixture was stirred for 10 min in the nitrogen atmosphere. Then initiator (KPS, 0.1g) and 100 □l of TEMED were added in the solution and stirred vigorously for 1 min. The mixture was carefully transferred in vials for solidification. The hydrogel solution gets solidified within 5 min. The PAM hydrogels were taken out from the vials and washed several times by distilled water.

MWCNT/PAM composite hydrogels were also prepared in a similar manner as reported above except the dispersion of different concentrations (0.2%, 0.4%, 0.8%, 2%, 4%) of MWCNTs in wt% in PAM using sonication for 15 min.

2.2 *Measurement of water content in MWCNT/PAM hydrogel*

The swelling ratio is the criterion for describing water absorption capacity of hydrogels. The measurement for the swelling ratio of MWCNT/PAM was conducted using distilled water as an absorbent with 0.2 mm diameter of hydrogels.

2.2.1 *Dehydration and Rehydration studies*

The swollen samples were allowed to dehydrate (weight loss) completely. The weight of the samples during drying was measured after 30 min. (W_{dt}) and the water content calculated using following equation:-

$$\text{Water Content } \% = \frac{W_{dt} - W}{W} \times 100 \quad \text{---------- (1)}$$

Where, W is the initial weight of hydrogel.

Upon completion of the dehydration measurement, MWCNT/PAM composite hydrogels were immersed in distilled water to observe the rehydration behaviour. The weight of the samples during rehydration increased and was measured half hourly (W_{rt}). The water content during rehydration was obtained from the equation given below:-

$$\text{Water Content } \% = \frac{W_{rt} - W}{W} \times 100 \qquad \text{----------(2)}$$

2.3 *Characterization*

The FT-IR spectra of the samples were recorded in transmission mode with KBr pressed pellets using a Perkin–Elmer spectrometer (Model No.2000, UK). TGA thermograms of the samples were recorded using a TGA Q50, TA instruments in the nitrogen atmosphere up to 650°C at a heating rate of 10°C/min. Powder XRD pattern of samples were recorded using a Rigaku miniflex diffractometer employing $CuK_{\alpha 1}$ radiation at a scan rate of 1°/min and step size 0.02 from 2θ range 5-60°. Scanning electron micrographs were obtained with a Hitachi scanning electron microscope (Model S-3700N) at an acceleration voltage of 10 kV. The fractured surfaces of samples were plasma coated with a thin layer of gold to provide electrical conduction and reduce surface charging. Electrical conductivity of these hydrogels was measured by Four probe method. Small pieces of gels cut from the strip were pressed between two aluminium foils and connected to Four probe (Optochem International, New Delhi) for conductivity measurements. Redox properties of composite materials were studied by cyclic voltammetry (Autolab PGSTAT 302 Potentiostate/Galvanostate, USA)

2.4. Theoretical Calculations

Calculation model of diffusion coefficient:

The swelling phenomena and its kinetics have long been studied. The swelling kinetics of a spherical gel was formulated by Tanaka and Fillmore on the basis of a cooperative diffusion theory by Tanaka et al. (1973) by making some assumptions:

(1) Constant diffusion coefficient in porous medium during the measurement process.

(2) Homogeneous porous medium.

(3) Swelling capacity caused by water diffusion into the hydrogel, convective mass caused by density and volume changes of the hydrogel.

(4) The natural convection effect of gas in porous medium is neglected.

Where; the shear modulus was considered to be negligible in comparison with the osmotic compressive modulus. By including a non-negligible shear modulus, Peters and Candau (1998) developed a general model to characterize the swelling kinetics of spherical, cylindrical and disc-like polymer gels. Later, Li and Tanaka proposed a two-process mechanism after realizing that neither gel swelling and shrinking can be considered to be a pure diffusion process. They predicted that the shear modulus (G) is related to the longitudinal osmotic modulus (M) and osmotic bulk modulus (K) by

$$R = \frac{G}{M} = \frac{G}{K + \frac{4G}{3}} \qquad \text{----------(3)}$$

According to Li and Tanaka, the swelling or shrinking follows;

$$\frac{W_t - W}{W_t} = \sum_{n=1}^{n=t} B_n e^{-t/\tau_n} \quad \text{----------(4)}$$

Where W and W_t are the swelling or solvent uptake at time t = 0 and at time t = t (i.e., at equilibrium) respectively; $\left[\frac{W_t - W}{W_t}\right]$, the relative swelling capacity at time t; B_n, a complicated function of R; and τ_n, the relaxation time related to n^{th} mode. When t >> 1 or $\tau_1 >> \tau_n$ ($n \geq 2$) or $B_1 >> B_n$ ($n \geq 2$), all high order terms ($n \geq 2$) in Equation (4) can be dropped. In this case, the swelling and shrinking follows first-order kinetics, (Wu and Yan 1994) i.e.,

$$\ln\left[\frac{W_t - W}{W_t}\right] = \ln B_1 - \frac{t}{\tau_c} \quad \text{----------(5)}$$

where B_1 is related to R by;

$$B_n = \frac{2(3 - 4R)}{\alpha_n^2 - (4R - 1)(3 - 4R)} \quad \text{----------(6)}$$

and τ_c is related to the collective diffusion coefficients (D_c) by

$$\tau_c = \frac{3a^2}{D_c \alpha_1^2} \quad \text{----------(7)}$$

with α_1 being a function of R, i.e.,

$$R = \frac{1}{4}\left[1 + \frac{\alpha_1 J_0(\alpha_1)}{J_1(\alpha_1)}\right] \quad \text{----------(8)}$$

and a being half of the disc thickness in the final swelling equilibrium state, where J_0 and J_1 are the zeroth- and first order Bessel functions. The t-dependence of $\left[\frac{W_t - W}{W_t}\right]$ can lead first to B_1 and τ_c, and then to R and D_c on the basis of Equation (5) – (8).

3. Results and Discussion

3.1 *Dehydration and Rehydration Studies*

PAM and MWCNT/PAM hydrogels were dried naturally at room temperature and the % water content of the hydrogels is reported at different time intervals.

Figure 1 shows that the % water content decreases with increase in concentration of MWCNTs and time. The initial dehydration rate for PAM hydrogel is slightly higher in comparison to the nano-composite hydrogels. It seems that there may be a retardation in the diffusion of water through the three dimensional network due to the presence of MWCNTs in the porous hydrogel network. It is also observed that the maximum weight loss occurs in first 5-6 h indicating fast surface evaporation and poor forces of water retention thereafter. But overall, the percentage loss of water is more in case of 0.8% MWCNT reinforced hydrogel. It may be possibly due to the maximum dispersion of MWCNTs at this optimum concentration.

Rehydration tests were carried out in distilled water as described earlier. The degree of rehydration for the PAM and MWCNT/PAM composite hydrogels are shown in Figure 2.

The water holding capacity of hydrogel is reduced by the incorporation of MWCNTs inside acrylamide network. Since, the voids or spaces in the network are occupied by MWCNTs; there is less space available for water molecules to bind. Also, the network junction movement is retarded by the presence of rigid MWCNTs network inside the hydrogels. It is concluded that although the water uptake or swelling capacity of hydrogels decreases with the incorporation of MWCNTs, yet the decrease is small and

not phenomenal. Such a phenomenon is very important for the composites and 0.8% MWCNT loaded hydrogel has a comparable swelling property as PAM hydrogel. The basic swelling property of the matrix is retained at a maximum in MWCNT based composite hydrogels particularly 0.8% MWCNT loaded hydrogel. Hence, it is clear that MWCNT has impended minimum hindrance to the network properties of hydrogel matrix at the optimum loading of MWCNTs.

As has been pointed out by Peters and Candau, both *Do* and *R* can be measured from the kinetics of the hydrogel swelling or shrinking. Given that from experimental values for $\square_c$ and B_1 (shown in Figure S1 to S6 in supplementary data); we can obtain *Do* and *R* from literature simultaneously (Li and Tanaka 1990). Table-1 shows all B_1, R, $\square_c$ values for the different concentrations of MWCNTs in PAM hydrogel which have disc like shape with 0.2 mm diameter. The collective diffusion constant for PAM hydrogel measured by dynamic light scattering was 2.4×10^{-7} cm^2/s by Tanaka (1973) and 4.0×10^{-7} cm^2/s by Peters and Candau. Finally, we would like to point out that the D_c for PAM hydrogel is 10 times higher than the value given by Tanaka through dynamic light scattering. For MWCNTs reinforced PAM hydrogel, the $\square_c$ is higher for 0.8% MWCNTs reinforced PAM hydrogel than traditional hydrogels. The D_c for MWCNTs reinforced PAM is higher than PAM hydrogel showing that the mobility of water molecules in cross-linked MWCNTs are higher than simple PAM hydrogel.

Interestingly, a comparison within the MWCNTs reinforced PAM hydrogels, D_c of 0.8% MWCNTs/PAM is lesser than others; showing a better crosslinking between MWCNTs

and PAM, due to which diffusion of water molecule become less. Therefore, the extent of crosslinking is much important than density of the system for a better collective diffusion of the respective solvent.

3.2 *Fourier transform infrared spectra (FT-IR)*

In Figure 3, the absorption peak at 3310 cm^{-1} attributes to the N–H bending, 2984 cm^{-1} to a $–CH_2$ stretching, 1647 cm^{-1} to a C=O bending of PAM. Also, the absorption peak at 1480 cm^{-1} is attributed to the benzene ring stretching of MWCNT.

In addition to these characteristic bands, the presence of MWCNTs in the composites results in the appearance of a band at 1213 cm^{-1} (due to a C–H bending) whose intensity increases with MWCNT content. The spectra show that the structural changes of PAM are occurred with reinforcements loading because of the molecular interaction of MWCNTs with different reaction sites of PAM. Therefore, the FT-IR spectra confirm that the MWCNTs were reinforced within the PAM matrix.

3.3 *Thermo-gravimetric Analysis (TGA)*

Figure 4 shows a clear variation in thermal stabilities of PAM and MWCNT/PAM composite hydrogels by two step transitions. MWCNT/PAM composite hydrogels exhibit good thermal stability in comparison to PAM hydrogel. Thermograms show a small weight loss around 230°C which may be due to the loss of volatiles and oligomers. Then, they begin to degrade after 330°C, but nano-composite hydrogel degradation completes at lower temperature than PAM hydrogels. It is also observed that the percentage weight

loss decreases with increase in MWCNT concentration within the composites at higher temperature, which is above 400°C. But, 0.8% MWCNT incorporated PAM is much more stable than the other hydrogels and show less percentage weight loss. It may be because of the proper cross linking between the PAM network and MWCNTs. Hence, it appears that thermal stability of hydrogel increased by incorporation of MWCNTs perhaps due to the resistance to heat by MWCNTs present inside the polyacrylamide network.

3.4 *Powder X-ray diffraction*

Crystallinity and orientation of conducting materials have been found of interest, because highly ordered systems could display a metal-like conducting state (Vohrer et al. 2004). Figure 5 shows PXRD patterns for MWCNT, PAM, 0.8% and 4% MWCNTs reinforced into the PAM matrix.

In Figure 5a, the characteristic peak of MWCNTs at 26.13° is strong and sharp corresponding to (022) reflections. In Figure 5b, the broad peak observed at 2θ angle of 22° which is in agreement with the earlier data reported by Li et al. (1993) and the crystalline peaks appeared at 2θ = 29.57° and 30.60° corresponding to PAM patterns. Figure 5c & 5d show the diffraction peak at 26.18° which is attributed due to the presence of MWCNT alone. The X-ray pattern of MWCNT/PAM composites gives crystalline peaks for both pure PAM and MWCNT. It reveals that MWCNTs are reinforced into PAM resulting in the betterment of crystallinity, strength, and conducting

behaviour of hydrogels. The strength of MWCNT/PAM composite was further supported by network like structure as shown in SEM micrographs.

3.5 *Scanning electron micrographs*

Figure 6 shows two pictures of transparent PAM hydrogel and dark black colour MWCNT/PAM hydrogel after reinforcement of MWCNTs in to PAM matrix.

The SEM micrographs of PAM and MWCNT/PAM composite hydrogels are shown in Figure 7. It can be seen from the micrograph that the surface of PAM is glossy and no impurity accretes, while the fractured surface shows the presence of open spaces or pores.

After the introduction of MWCNTs, the composite hydrogel exhibits a much more compact, reduced pore size and homogeneous texture with network-like structure which suggests that the MWCNT component combines successfully with the primary hydrogel and fills up the existent voids. Such a microstructure is beneficial for enhancing the mechanical toughness for hydrogels. The PAM three-dimensional network is formed during polymerization reaction while MWCNTs were reinforced within the PAM network. It can be seen that a porous structure is formed in MWCNT/PAM hydrogels and the pores are interconnected to each other. Based on the porous structures of MWCNT/PAM hydrogels, the hydrogel is expected to have infiltration, swelling and drug release properties. A hydrogel with porous microstructure is expected to give rise to faster volume change, since the effective diffusion distance can be controlled by the average distance between neighbouring pores to obtain quick response gels. The

swelling/deswelling of such gels is faster than any other responsive gels of comparable dimensions having random interconnectivity.

3.6 *Electrical conductivity*

Electrical conductivity data of PAM and MWCNTs/PAM hydrogels are presented in Table-2. It is very difficult to measure the precise value of conductivity by the standard Four probe method due to very soft hydrogel samples, therefore the approximate values have been reported here. In order to avoid water evaporation and consequent de-swelling (shrinking) the measurements were done in closed chamber. As we know that the conductivity stems from both ionic and electronic components of the polymer, however, pure PAM is completely insulating (no ionic conductivity), although conductivity of MWCNT/PAM composite is found at maximum of the order of 10^{-4} S/cm. Therefore, the contribution of ionic counterpart is almost negligible to the total conductivity of the hydrogel; the observed conductivity in each of the samples is mainly electronic and accounted for the presence of MWCNTs. It may be concluded that the presence of MWCNTs can increase an effective conductivity of the composite materials by facilitating interconnect channels of MWCNTs in PAM matrix. The maximum conductivity is reported only in case of 0.8% MWCNT reinforced composite hydrogel.

3.7 *Cyclic voltammetry*

Electrochemical characterization of PAM and PAM/MWCNT composite hydrogels was carried out using cyclic voltammetry in 0.1M HCl solution. A sterile needle was inserted in the centre of swollen cylindrical hydrogel carefully and was used as a working

electrode. Cyclic voltammetry was done in a conventional three electrode cell with standard Ag/AgCl and platinum electrode as reference and counter electrodes, respectively. Cyclic voltammograms of the hydrogels were recorded with the scan rate of 0.05 V/s and potential was applied from -0.25 to 1.25V.

Cyclic Voltammetry of the composite hydrogel shows the characteristic redox response commonly observed for conventional CNTs at electrode surface. Figures 8(a) and 8(b) show a comparison between the cyclic voltammograms of PAM and PAM/MWCNT composite hydrogels under standard conditions.

However, the cyclic voltammogram of composite hydrogels is not well defined with a general blurring of redox responses. Such behaviour is indicative of increased resistance or sluggish electron transfer as MWCNT lies inside the PAM network. Cyclic voltammetric responses indicate that ion transport in and out of entire composite hydrogel is significantly more difficult than for the compact films.

4. Conclusion

MWCNT/PAM hybrid hydrogels are being prepared by a novel "*freezing method*" to modulate the original properties of hydrogel which is accomplished by loading of MWCNTs in the PAM matrix. The results obtained in this work are consistent with the theoretical predictions available in the literature. The swelling properties of all these hybrid hydrogels were found better than the corresponding PAM hydrogel. The Li-Tanaka equation was employed to produce the swelling parameters. The D_c of PAM

hydrogel (2.4×10^{-6} cm^2/s) is 10 times higher than the literature value (2.4×10^{-7} cm^2/s). 0.8% MWCNTs reinforced PAM hydrogel has excellent $\square_c$ and electrical conductivity (0.76 mS/cm) with improvements in all other properties. Lower D_c value of 0.8% MWCNTs/PAM hydrogel than other samples reveal that extent of crosslinking is much important than density of the system for a better collective diffusion of the respective solvent. The FT-IR, powder XRD and SEM spectroscopic analysis indicates the presence of MWCNTs, which establishes proper interconnect channels in PAM matrix. These hydrogels can be used for the selective drug delivery on the basis of flexible porosity. These hydrogels are also good candidates in applications of excellent conducting, heat dissipating and mechanical stable hydrogels for industrial uses. All these results show that MWCNTs can be an ideal reinforcement to modify the performance of the hydrogels at large scale.

Acknowledgements

Authors are thankful to Prof. P B Sharma, Vice-Chancellor, Delhi Technological University (formerly Delhi College of Engineering), Delhi for encouragement and support. A financial support to one of the author, Sudha is also acknowledged gratefully.

References

Abdalla, M., D. Dean, D. Adibempe, E. Nyairo, P. Robinson, and G. Thompson. 2007. The effect of interfacial chemistry on molecular mobility and morphology of multiwalled carbon nanotubes epoxy nanocomposites. *Polymer*. 48:5662-5670.

Baughman, R. H., C. X. Cui, A. A. Zakhidov, Z. Iqbal, J. N. Barisci, and G. M. Spinks. 1999. Carbon nanotube actuators. *Science*. 284(5418):1340-1344.

Bianco, A., K. Kostarelos, and M. Prato. 2005. Applications of carbon nanotubes in drug delivery. *Curr. Opin. Chem. Biol.* 9:674-679.

Chen, J., M. A. Hamon, H. Hu, Y. S. Chen, A. M. Rao, and P. C. Eklund. 1998. Solution properties of single-walled carbon nanotubes. *Science*. 282:95-98.

Fukushima, T., A. Kosaka, Y. Yamamoto, T. Aimiya, S. Notazawa, and T. Takigawa. 2006. Dramatic effect of dispersed carbon nanotubes on the mechanical and electro-conductive properties of polymers derived from ionic liquids. *Small*. 2:554-560.

Gojny, F. H., and K. Schulte. 2004. Functionalisation effect on the thermo-mechanical behaviour of multi-wall carbon nanotube/epoxy-composites. *Compos. Sci. Technol.* 64:2303-2308.

Gong, X., J. Liu, S. Baskaran, R. D. Voise, and J. S. Young. 2000. Surfactant assisted processing of carbon nanotube/polymer composites. *Chem. Mater.* 12:1049-1052.

Huang, G., Y. Zhang, J. Ouyang, W. R. G. Baeyens, and J. R. Delanghe. 2006. Application of carbon nanotube-matrix assistant native polyacrylamide gel electrophoresis to the separation of Apolipoprotein Ai and Complement C3. *Anal. Chim. Acta*. 557:137-145.

Hobbie, E. K., and D. J. Fry. 2007. Rheology of concentrated carbon nanotube suspensions. *J. Chem. Phys.* 126:1-7 124907.

Jagur-Grodzinski J. 2006. Polymers for tissue engineering, medical devices, and regenerative medicine. Concise general review of recent studies. *Polym. Adv. Technol.* 17:395-418.

Joshi, P. P., S. A., Merchant, Y. Wang, and D. W. Schmidtke. 2005. Amperometric biosensors based on redox polymer-carbon nanotube-enzyme composites. *Anal. Chem.*77:3183-3188.

Kawaguchi, M., T. Fukushima, T. Hayakawam, N. Nakashima, Y. Inoue, and S. Takeda. 2006. Preparation of carbon nanotube-alginate nanocomposite gel for tissue engineering. *Dent. Mater. J.* 25:719-725.

Li, H., D. Q. Wang, H. L. Chen. B. L. Liu, and L. Z. Gao. 2003. novel gelatin-carbon nanotubes hybrid hydrogel. *Macromol. Biosci.* 3: 720-724.

Li Q., L. Cruz, and P. Philips, 1993. Granular-role model for electronic conduction in polymer. *Phys. Rev. B.* 47:1840-1845

Li, Y., and T. Tanaka. 1990. Kinetics of swelling and shrinking of gels. *J. Chem. Phys.* 44:1365-1371.

Lira, L. M., K. A. Martins, and S. I. Cordoba de Torresi. 2009. Structural parameters of polyacrylamide hydrogels obtained by the equilibrium swelling theory. *Eur. Polym. J.* 45:1232-1238.

Liu, Y., and H. Wang. 2007. Nanomedicine: Nanotechnology tackles tumours. *Nat. Nanotechnol.* 2:20-21.

MacDonald, R. A., B. F. Laurenzi, G. Viswanathan, P. M. Ajayan, and J. P. Stegemann. 2005. Collagen-carbon nanotube composite materials as scaffolds in tissue engineering. J. Biomed. *Mater. Res. Part A.* 74:489-496.

Minett A., J. Fràysse, G. Gang, G. T. Kim, and S. Roth. 2002. Nanotube actuators for nano-mechanics. *Curr. Appl. Phys.* 2:61–64.

Mitchell, C. A., and R. Krishnamoorti. 2007. Dispersion of single-walled carbon nanotubes in poly(ε-caprolactone). *Macromolecules.* 40:1538-1545.

Mitchell, C. A., J. L. Bahr, S. Arepalli, J. M. Tour, and R. Krishnamoorti. 2002. Dispersion of functionalized carbon nanotubes in polystyrene. *Macromolecules.* 35:8825-8830.

O'Connell, M. J., P. Boul, L. M. Ericson, C. Huffman, Y. H. Wang, and E. Haroz. 2001. Reversible water-solubilisation of single walled carbon nanotubes by polymer wrapping. *Chem. Phys. Lett.* 342:265–271.

Peters. A., and S. J. Candau. 1998. Chemical and morphological analysis of surface enrichment in a biodegradable polymer blend by phase-detection imaging atomic force microscopy. *Macromolecules.* 21:2278-2283.

Rajendran, S., B. V. Apparao, and Palaniswamy, N. 1998. Synergistic and antagonistic effects existing among polyacrylamide, phenyl phosphonate and Zn^{2+} on the inhibition of corrosion of mild steel in a neutral aqueous environment. Electrochim. Acta. 44:533-537.

Roy, P. K., V. Swami, D. Kumar, and C. Rajagopal. 2011. Removal of toxic metals using superabsorbent poly-electrolytic hydrogels. *J. Appl. Polym. Sci.* 122(4):2415-2423.

Shanmugharaj, A. M., J. H. Bae, K. Y. Lee, W. H. Noh, S. H. Lee, and S. H. Ryu. 2007. Physical and chemical characteristics of multiwalled carbon nanotubes functionalized with amino silane and its influence on the properties of natural rubber composites. *Compos. Sci. Technol.* 67:1813-1822.

Shi, J., Z. Guo, B. Zhan, H. Luo, Y. Li, and D. Zhu. 2005. Actuator based on MWNT/PVA hydrogels. *J. Phys. Chem. B.* 109:14789-14791.

Shibayama, M., and T. Tanaka. 1993. *Volume phase-transition and related phenomena of polymer gels*. In: Dusek K, editor. Advances in polymer science. Berlin: Springer-Verlag. pp. 1-62.

Tajima, H., Y. Yoshida, and K. Yamagiwa. 2011. Experimental study of swelling and shrinking kinetics of spherical poly (N,N-diethylacrylamide) gel with continuous phase transition. *Polymer*. 1-7.

Tanaka T., L. Hocker, and G. Benedek. 1973. Spectrum of light scattered from a viscoelastic gel. *J. Chern. Phys.*59:5151-5160.

Verheyen, E., L. Delain-Bioton, S. V. Wal, N. Morabit, W. E. Hennink, and C. F. V. Nostrum. 2010. Protein macromonomers for covalent immobilization and subsequent triggered release from hydrogels. *J Controlled Release*. 148:e18-e19.

Vohrer U., I., Kolaric, M. H., Haque, S. Roth, and U. Deltaff-Weglikowska, 2004. Carbon nanotube sheets for the use as artificial muscles. *Carbon*. 42:1159-1164.

Wu, C., and C.Y. Yan. 1994. Studies of the swelling and drying kinetics of thin gelatin gel films by in situ interferometry. *Macromolecules*. 27:4516-4520.

Zhang, Q., D. R. Lippits, and S. Rastogi. 2006. Dispersion and rheological aspects of SWNTs in ultrahigh molecular weight polyethylene. *Macromolecules.* 39:658–666.

Zhu, B., S. Xie, Z. Xu, Y. Xu. 2006. Preparation and properties of the polyimide/multi-walled carbon nanotubes (MWNTs) nanocomposites. *Compos. Sci. Technol.* 66:548-554.

Table 1. Experimental collective diffusion coefficient for MWCNTs reinforced PAM hydrogels from Li-Tanaka equation

Sample (Content of MWCNTs in PAM)	τ_c (min.)	B_1	R	$D_c \times 10^{-5}$ ($cm^2 s^{-1}$)
4%	88±5	0.598	0.15	33.6
2%	100±5	0.623	0.22	34.2
0.8%	117±5	0.706	0.42	31.2
0.4%	100±5	0.622	0.20	37.2
0.2%	97±5	0.613	0.18	38.4
0.0%	73±5	0.643	0.26	24.6

Table 2. Four Probe Conductivity of PAM and MWCNTs reinforced PAM hydrogels

S. No.	% of MWCNT reinforced	Electrical conductivity (S/cm)
1	0.0	2.3×10^{-9}
2	0.2	3.4×10^{-8}
3	0.4	6.8×10^{-8}
4	0.8	7.6×10^{-4}
5	2.0	6.2×10^{-6}
6	4.0	8.5×10^{-6}

Fig. 1. Dehydration of PAM and MWCNTs reinforced hydrogels against time

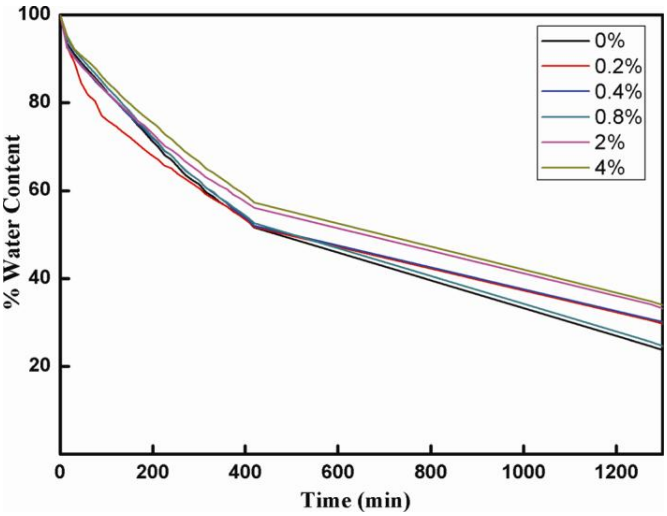

Fig. 2. Rehydration of PAM and MWCNTs reinforced hydrogels against time

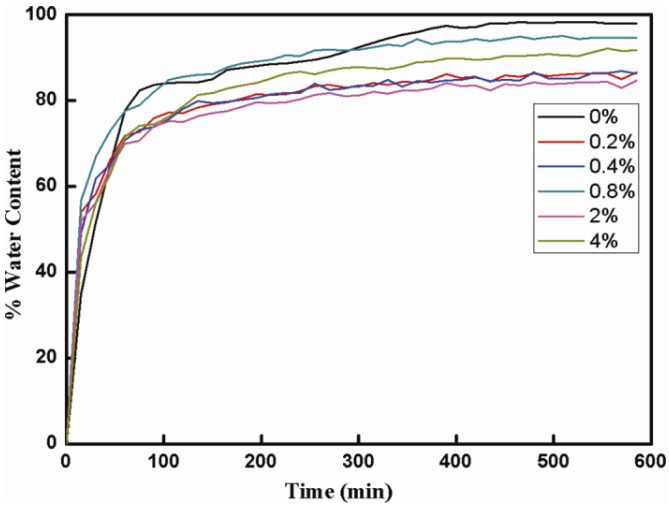

Fig. 3. FT-IR spectra of 0.8% MWCNT reinforced dry composite hydrogel

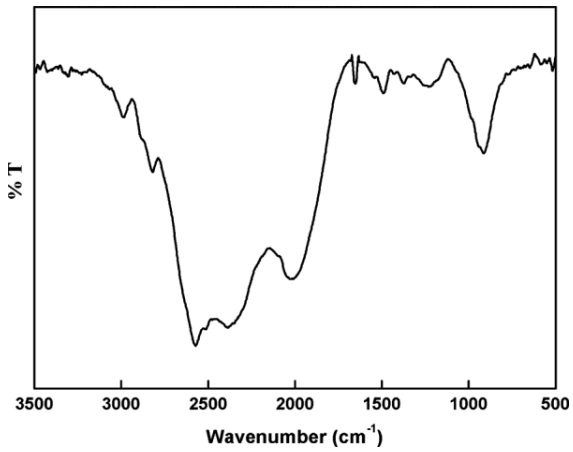

Fig. 4. TGA thermo-grams of PAM and MWCNTs reinforced hydrogels with variation in weight percentage of MWCNTs

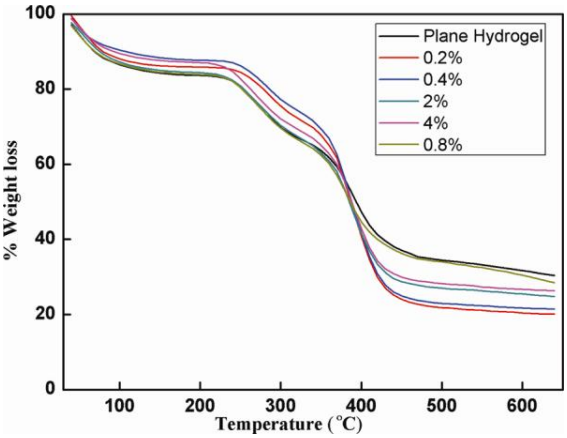

Fig. 5. Powder X-Ray diffraction pattern of (a) MWCNT (b) PAM (c) 0.8% reinforced MWCNT (d) 4% reinforced MWCNT hydrogels

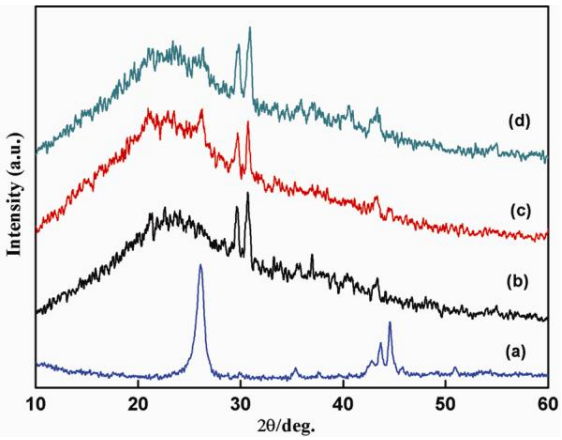

Fig. 6. Pictures of (a) MWCNT/PAM and (b) PAM hydrogel

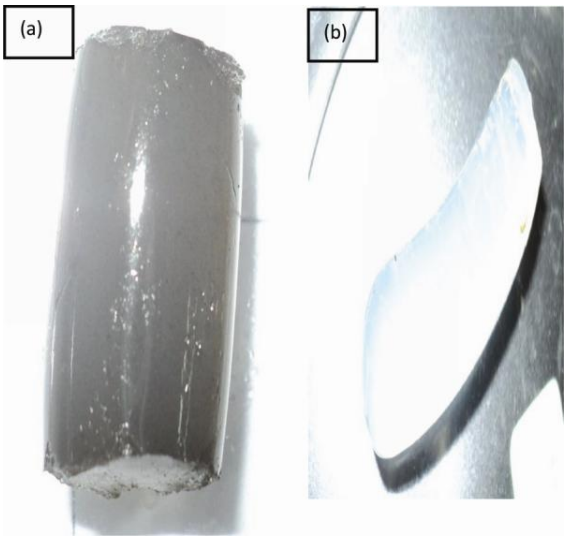

Fig. 7. Scanning electron micrographs of (a) PAM hydrogel (b) 0.8% loaded MWCNT hydrogel (c) Fractured surface micrograph of 0.8% MWCNT loaded hydrogel and (d) 4% loaded MWCNT hydrogel

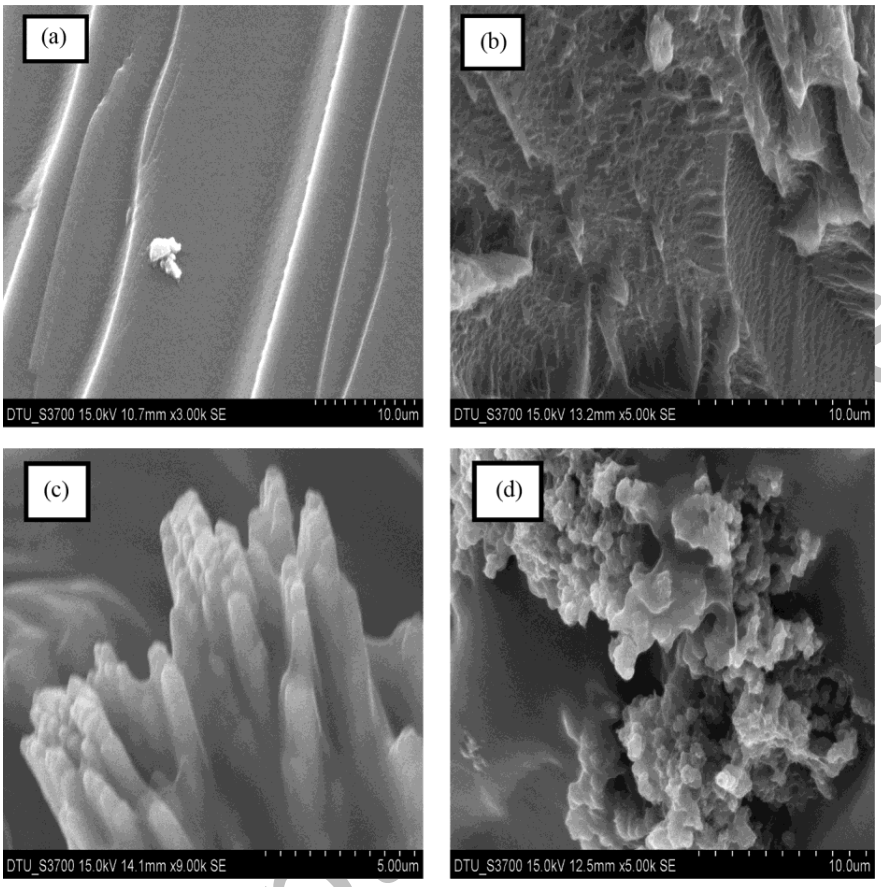

Fig. 8. Cyclic Voltammograms of (a) PAM and (b) 0.8% MWCNT reinforced composite hydrogels with sweeping potential from -0.25 to 1.25V

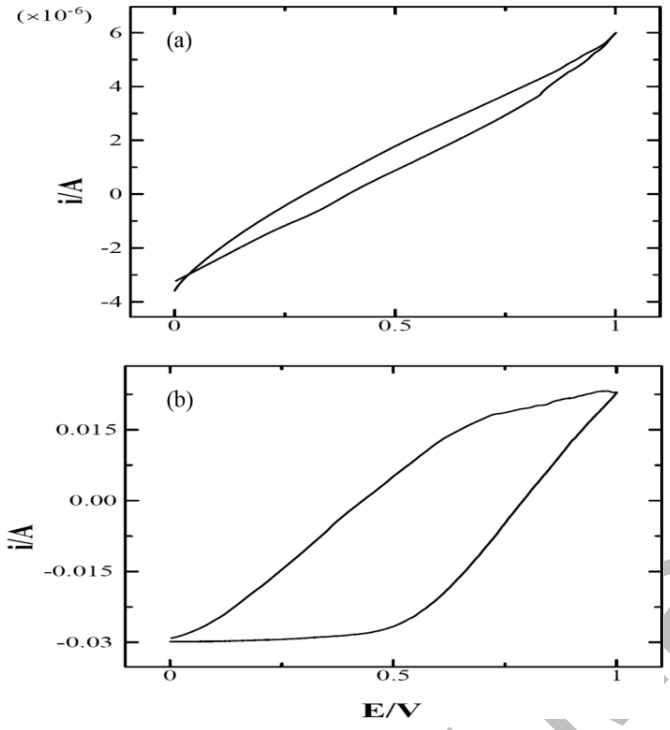

Evolution from SDR to Cognitive Radio

Shilpa Jain[1], Nidhi Taneja[2]
[1]Electronics and Communication dept.,
Inderprastha Engineering College, Ghaziabad,U.P,India
[2]Electronics & Communication Engineering dept.,
Delhi Technological University, Delhi, India

Abstract
Software Defined Radio (SDR) is a flexible radio architecture which can be configured to adapt various waveforms, frequency bands, bandwidths, modes of operations and wireless standards simply by altering the physical layer behavior through changes in its software. This paper presents a detailed survey of the existing hardware and software platform for SDRs. However, an SDR can switch functions and operations only on demand; it is not capable of reconfiguring itself into the most effective form without its user even knowing it. Therefore, Cognitive radio (CR) came into existence which extends the software radio with radio-domain model-based reasoning and would be trainable in a broad sense, instead of just programmable. In this paper a survey of spectrum sensing methodologies for cognitive radio is presented. These cognitive technologies may be considered as an application on top of a basic SDR platform.

Keywords— Software Defined Radio, Cognitive radio, radio frequency

I. INTRODUCTION

In a remarkably visionary article published in 1993 [1],Joseph Mitola III envisioned a very different kind of radio: A digital radio that could be reconfigured in fundamental ways just by changing the software code running on it. He dubbed this as software-defined radio. A few years later Mitola‟s vision turned into reality. In the mid-1990s military radio systems came into existence in which software controlled most of the signal processing digitally, enabling one set of hardware to work on many different frequencies and communication protocols. SPEAKeasy I and SPEAKeasy II radios [2], which allowed units from different branches of armed forces of U.S. military to communicate, were the first known examples of this type of radio.

In the late 1990s SDR started to spread from the military domain to the commercial sector. Cellular networks were considered as the most obvious and potentially most lucrative market that SDR could penetrate. The benefits it could bring to this industry included a general-purpose and therefore more economic hardware platform, easier bug fixes through software upgrades, and increased functionality and interoperability through the ability to support multiple standards.

The reconfigurability offered by SDR technology can be achieved only on demand; it is not capable of reconfiguring itself into the most effective form without its user even knowing it. In his licentiate thesis Mitola introduced Cognitive radio (CR) [3],[4] as “a really smart radio that would be selfaware, RF-aware, user-aware, and that would include language technology and machine vision along with a lot of high-fidelity knowledge of the radio environment”. Cognitive radio clearly goes hand in hand with SDR; together, they can achieve functionality considered impossible only a decade ago. These cognitive technologies may be considered as an application on top of a basic SDR platform. Consequently, before continuing any further with respect to CR, we first provide an overview of SDR technology in Section II. This is followed by a detailed survey of various hardware and software platforms for SDR in Section III. An introduction of Cognitive radio is presented in section IV. Finally, various Spectrum sensing functionalities especially of non-cooperative types are discussed in Section V.

II. SOFTWARE DEFINED RADIO

A Software Defined Radio (SDR) the baseband operation characteristics of the radio, such as coding, modulation/demodulation, error correction coding, comp type and frequency band, can be changed at will, simply by loading new software. The multiple radio devices using different modulations can be replaced by a single radio device that can perform the same task. However, there are a number of challenges in the transition from hardware radio to software defined radio. First, transition from hardware to software processing results in a substantial increase in computation, which in turn results in increased power consumption. This reduces battery life and is one of the key reasons why softwaredefined radios have not been deployed yet in end-user devices, but rather in base stations and access points, which can take advantage of external power resources. Second, the AD/DA conversion should be moved as close as possible to the antenna so that all signal processing can be done digitally and an ideal SDR can be realized. Taken together, this means that highbandwidth, high-frequency RF transmissions require very high sampling rates. Indeed, it is only recently that sufficiently fast DSPs and wideband AD/DA chipsets have become available at affordable cost to make it feasible to contemplate AD conversions of the IF rather than the baseband signal. SDR is currently used to build radios that support multiple interface technologies such as GSM, CDMA and WiFi with a single modem by reconfiguring it in software [5].

A. Real SDR Model

The dominant implementation architecture used for RF Front-Ends (FEs) is the super-heterodyne architecture [6],[7].The figure 1 shows the model of real SDR system. The antenna receives the analog radio signal. An intermediate step before conversion is needed in the receiver. This conversion to an intermediate frequency is required since SDRs must deal with radio frequency signals. This step transforms the received high-frequency signal into a so called Intermediate Frequency (IF) by a tuner. Following this the IF is filtered and digitized. The filtering is done to prevent aliasing frequency signals into the band of frequencies that are being digitized. The stream is received and processed in a combination of software and hardware. These hardware and software process the waveform. An output waveform is sent as a digital signal to be converted by DAC into an analog signal. A similar transformation can be made to shift the IF back for transmission. The analog signal is generally amplified and transmitted into air by a radio antenna.

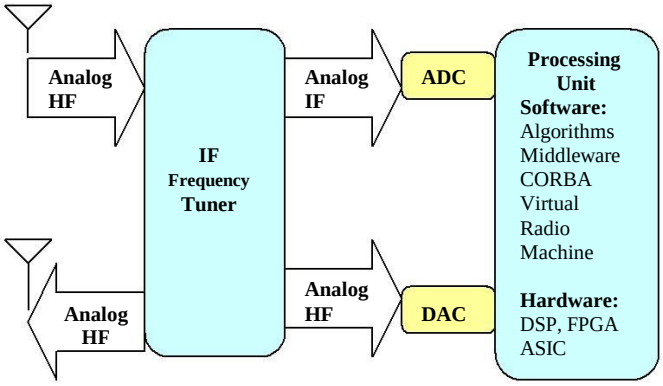

Fig. 1. Real SDR Model

B. SDR Receiver

The figure 2 shows a block diagram of a SDR receiver. The RF tuner converts analog RF to analog IF signals.

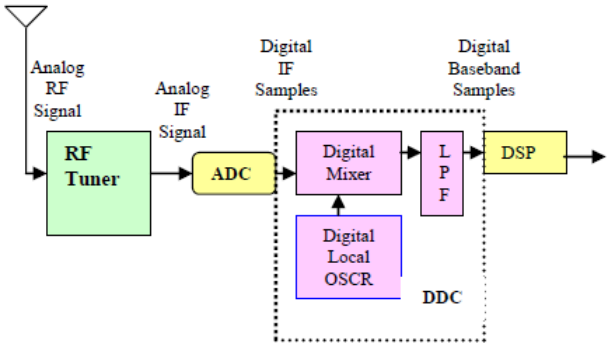

Fig. 2. SDR Receiver

The A/D converter that follows digitizes the IF signal thereby converting it into digital samples. These samples are fed to the next stage which is the digital down converter (DDC) shown within the dotted lines. The DDC is typically a single monolithic chip or FPGA IP, and it is a key part of the SDR system.

The digital mixer and local oscillator translate the digital IF samples down to baseband. The FIR low pass filter limits the signal bandwidth and acts as a decimating low pass filter. The digital baseband samples are then fed to a block labeled DSP, which performs tasks such as demodulation, decoding and other processing tasks.

C. SDR Transmitter

The input to the transmitter side of an SDR system is a digital baseband signal, typically generated by a DSP stage after processing, is shown in figure 3.The digital hardware block in the dotted lines is a DUC (digital upconverter) that translates the baseband signal to the IF. The D/A converter that follows convert the digital IF samples into the analog IF signal. Next, the RF upconverter converts the analog IF signal to RF frequencies. Finally, the power amplifier boosts signal energy to the antenna.

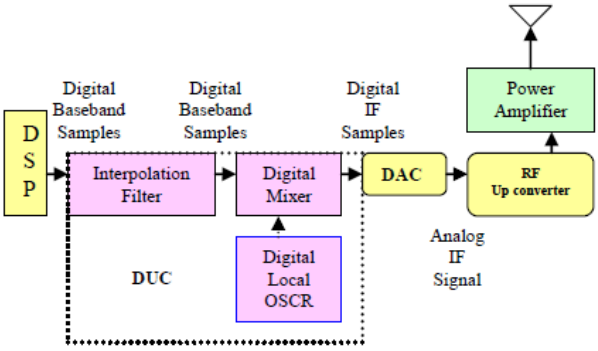

Fig. 3. SDR Transmitter

D. SDR Modules and Hardware

The main hardware alternatives that can be used to implement a SDR are:

- ASICs (Application-Specific Integrated Circuits).
- FPGAs (Field-Programmable Gate Arrays).
- DSPs (Digital Signal Processors).
- GPPs (General-Purpose Processors).

Table.1 shows the comparison between DSP, ASICs, GPPs and FPGAs. DSPs are microprocessors with architecture, instructions and features suited specifically for signal processing applications. DSP and GPPs are essentially serial in operation. The main strengths of DSPs and GPPs are their flexibility and easy configurability. Field Programming Gate Arrays (FPGA) contains DSP blocks that can be re-configured to work as parallel multiplier/adder or MAC. FPGA are extremely flexible and fast as they provide high computing power due to quasi-parallel processing nature The ASICs are non-reprogrammable that contradicts the principle of SDR, but

still used as a part for special characteristics.

Table 1 COMPARISON OF ASIC, DSP, FPGA & GPP

Comparison Parameters	High- Speed DSPs	Multiple ASICs	GPP	FPGAs
Power Consumption	Very High	Very Low	Moderate	Low
Size	Modest	Large	Moderate	Low
Cost	Moderate / High	High	Moderate	Moderate /Low
Field Upgradable	High	None	Some	High

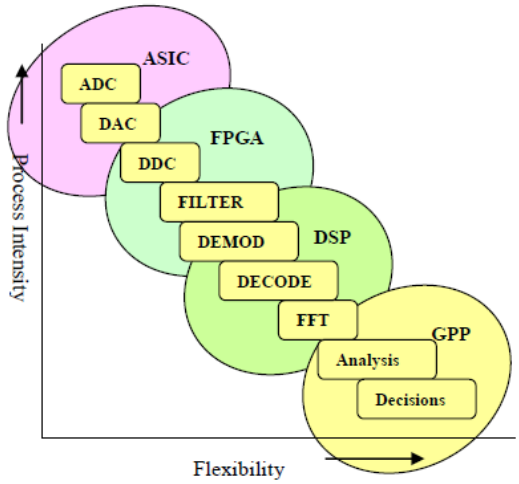

Fig. 4. ASIC, FPGA, GPP and DSP Platform for different SDR Modules

The graph of Processing Intensity vs. Flexibility as shown in figure 4 highlights some of the popular signal processing tasks associated with SDR system [8]. Processing intensity is the degree of highly repetitive operations. The upper left area indicates dedicated functions like ADC & DDC that requires specialized hardware structures like ASIC and FPGA, to complete the operations in real time. Flexibility defines how easily the functionality can be changed or customized for any specific applications. The lower right area shows functions like analysis and decision making which are highly variable & often subjective, therefore requires programmable GPP for this purpose. Intermediate area shows modules like filter, Modulator/Demodulator, Encoder/Decode which needs programmability as well as fast computation and can be implemented through DSPs or GPPs.Software Defined Radio platforms

There are various hardware platforms and the software architectures that are used for defining the software radios [8], [9]. This section presents a survey of the current SDR hardware platforms followed by the software architectures.

E. SDR Hardware Platforms

Table II shows a detailed survey of existing SDR hardware platforms (Front end) and their performance.

1) Universal Software Radio Peripheral 2 (USRP2)

It is a product of Matt Ettus (Ettus Research LLC) [10]. The USRP2 platform is a second generation of Universal Software Radio Peripheral [10]. USRPs are commonly used with the GNU Radio software suite to create complex software-defined radio systems.

2) Rice Wireless Open-Access Research Platform (WARP)

The wireless open-access research platform of Rice University is a scalable and extensible programmable platform, built for prototyping advanced wireless networks [11]. It has programmability of both physical and network layer protocols on a single platform.

3) Berkeley Emulation Engine 3 (BEE3)

BEE3 is new generation of Berkeley Emulation Engine-2 [12].It is jointly developed by Microsoft Research, UC Berkeley and BEE cube Inc. It is useful for most computationally intensive real-time applications, high-speed multiple FPGA, real-world prototyping and development platform.

4) Kansas University Agile Radio (KUAR)

The KUAR hardware [13] has been promoted through the defense advanced research projects agency (DARPA) as next generation (XG) program. The complete system was developed in Simulink and implemented in Xilinx VHDL by generating the VHDL code from Simulink model(s) using a Modelsim of Mentor Graphics.

5) Small Form Factor Software Defined Radio (SSF-SDR)

The Xilinx Inc. in collaboration with Lyrtech and Texas Instruments incorporated a SFF-SDR development platform for developing the handheld and mobile radios [14].

6) Intelligent Transport System (ITS)

National Institute of Information and Communications Technology (NICT) of Japan, developed a software-defined radio platform so-called NISTITS. It is specially designed for mobile communication, wireless LAN and digital terrestrial TV [15].

F. SDR Software Platforms

1) GNU Radio

It is an open source software development toolkit that provides the signal processing runtime and processing blocks to implement software radios using readily-available, low-cost external RF hardware and commodity processors [10]. The radio applications are written in Python, while the performance critical signal processing components are implemented in C++.

GNU Radio Companion (GRC) is a graphical tool for creating signal flow graphs and generating flow-graph source code. Thus, the developer is able to implement real-

time, high throughput radio systems in a simple-to-use, rapid-application development environment

TABLE II. A SURVEY OF SDR HARDWARE PLATFORMS [13-21]

TABLE II. A SURVEY OF SDR HARDWARE PLATFORMS [13-21]

	USRP2	**KUAR**	**WRAP v2.2**	**SSF-SDR**	**BEE3**	**NICT-ITS**
Architecture (GPP,DSP, FPGA)	FPGA (Xilinx Spartan III) GPP (AeMB Processor)	FPGA (XilinxVirtex11) GPP (Pentium M)	FPGA (XilinxVirtex-4) GPP(PowerPC)	FPGA (Xilinx Virtex-4)	4FPGAs (Xilinx Virtex-5) Quad-Core OpenSPARC	FPGA (Xilinx Virtex-4) GPP(ARM 11)
RF Bandwidth	100 MHz	30 MHz	30 MHz	22 MHz	100 MHz	5 MHz
RF Range	24 GHz & 5 GHz (multi M/G Hz)	24 GHz & 5 GHz ISM/UNII	24 GHz & 5 GHz ISM/UNII	0.2-1.0, 1.6-2.2 GHz, 2.5/3.5 GHz (WiMAX)	Ultra-wide-band (muiti-GHz)	2 GHz ,5 GHz and VUHF
RF Channels	2	16	4	2	16	5
Connectivity	Gig Ethernet (National Semiconductor)	USB 2.0, Gig Ethernet	USB 2.0, Gig Ethernet(Marvel)	RS232/ USB 2.0, Gig Ethemet	RS232/USB Gig Ethemet Broadcom	RS232/USB Ethemet
ADCs	14-bit ,100 MS/s (LTC2284)	14-bit ,105 MS/s (LTC2284)	14-bit,65MS/s (AD9248)	14-bit, 125MS/s (ADS5500)	8-bit,3GS/s (BEE3-ADC-D3G)	12-bit, 170MS/s (ADCs N/C)
DACs	16-bit,400MS/s (AD9777)	16bit, 100MS/s (AD9777)	16-bit,160MS/s (AD9777)	16-bit,500MS/s (TI DAC5687)	I2-bit, 2GS/s (BEE3-DAC-D2G)	12-bit, 500MS/s (DAC N/K)
Power	6 volt	12 volt	12 volt	12 volt	12 volt	3.3 volt
Price	$ 1400.00	$4,000.00	$6,500.00	99,900.00	$20,000.00	N/A

2) Open-Source SCA Implementation *Embedded (OSSIE)*
It is a Virginia Tech‟s open source, the core framework is based on the JTRS software communications architecture (SCA); the CORBA based communication model for SDR [16]. The OSSIE is an object-oriented SCA operating environment, where signal processing components are written in C++. The operating environment, often referred to as the core framework, implements the management, configuration, and control of the radio system. Every OSSIE‟s component is considered having two parts: one part realizing the signal processing and another managing the SCA infrastructure. The OSSIE waveforms are described in an XML that is used to describe component properties and interconnections between components in a waveform.

3) Wireless Open-Access Research Platform for Network
It is an SDR framework that is built around client server architecture in Python [17]. The WARPnet uses PCAP (packet capture) API to communicate with the WARP board directly. To allow the Python-based client/server to access PCAP, the Pcapy module is required. With WARPLab, one can interact with WARP nodes directly from the MATLAB workspace and signals generated in MATLAB can be transmitted in real-time over-the-air using WARP nodes.

4) Cognitive Radio Open Source System (CROSS)
It is open source cognitive radio architecture [18]. It consists of five core components categories (modules); cognitive radio shell (CRS), cognitive engine (CE), policy engine (PE), service management layer (SML), and softwaredefined radio host platform. The CROSS is a modular cognitive radio system framework that uses socket connections for inter-component communication. The cognitive radio shell library and API are implemented in C++, the other modules can be implemented in any language that supports a TCP/IP socket interface.

III. COGNITIVE RADIO

The need for higher data rates is increasing as a result of the transition from voice-only communications to multimedia type applications; therefore it becomes obvious that the current static frequency allocation schemes cannot accommodate the requirements of an increasing number of higher data rate devices. As a result, *Cognitive radio* [19] arises to be a tempting solution to the spectral congestion problem by introducing opportunistic usage of the frequency bands that are not heavily occupied by licensed users. In this paper, we use the definition adopted by Federal Communications Commission (FCC) [20]: "*Cognitive radio: A radio or system that senses its*

operational electromagnetic environment and can dynamically and autonomously adjust its radio operating parameters to modify system operation, such as to mitigate interference, maximize throughput, facilitate interoperability and access secondary markets." [20]. Hence, one major feature of cognitive radio is its dynamic Spectrum Management principle which solves the issue of spectrum underutilization in wireless communication in a better way.

In cognitive radio terminology, *primary users* (PU) (also known as licensed device) can be defined as the users who have higher priority or legacy rights on the usage of a specific part of the spectrum and the *secondary users* (also called cognitive radio users or unlicensed devices), which have lower priority, exploit this spectrum in such a way that they do not cause interference to PUs and they vacate the band once the PU is detected. Therefore, secondary users need to posses cognitive radio capabilities, such as sensing the spectrum reliably to check whether it is being used by a PU and to change the radio parameters to exploit the unused part of the spectrum called spectrum holes or white spaces, as shown in figure 5. Such kind of reconfiguring to adapt various waveforms, frequency bands, wireless standards, bandwidths, and modes of operations by altering the physical layer behavior can be easily achieved by SDRs, through changes in its software. Therefore SDR provides an ideal platform for the realization of Cognitive radio. Hence, Cognitive radio extends the software radio with radio-domain model-based reasoning.

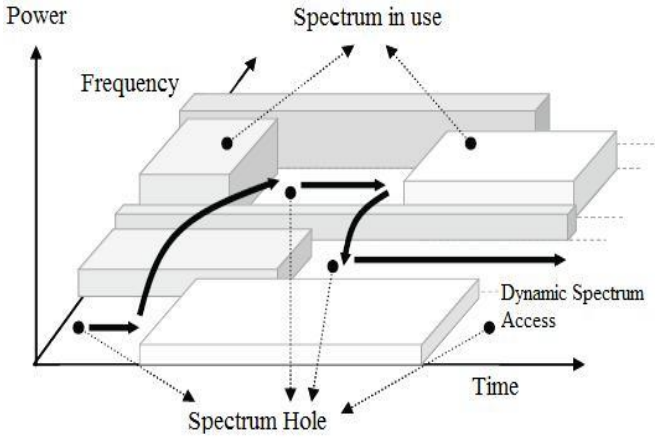

Fig. 5. Spectrum hole concept

Cognitive radio has four major functions [5]. They are Spectrum Sensing, Spectrum decision, Spectrum Sharing and Spectrum Mobility. Spectrum Sensing is to identify the presence of licensed users and unused frequency bands i.e. white spaces in those licensed bands. Spectrum decision is to identify how long the secondary users can use those white spaces. Spectrum Sharing is the fair sharing of white spaces (spectrum hole) among the secondary users (CRs). Spectrum Mobility is to maintain unbroken communication during the transition to better spectrum.

IV. SPECTRUM SENSING FUNCTIONALITIES FOR COGNITIVE RADIO

The major challenge of the cognitive radio is that the secondary user needs to detect the presence of primary user and to quickly quit the frequency band if the corresponding primary radio emerges in order to avoid interference to primary users.

Spectrum sensing can be classified [21] as shown in figure 6 as:

A. Spectrum Sensing for Spectrum opportunities

1) Primary transmitter detection: Based on the received signal at CR users the detection of primary users is performed. This approach includes Matched filter (MF) detection, Energy detection (ED), Covariance detection, Waveform detection and Cyclostationary detection.

2) Cooperative and collaborative detection: The primary signals for spectrum opportunities are detected reliably by interacting or cooperating with other users, and the method can be implemented as either centralized access to spectrum coordinated by a spectrum server or distributed approach implied by the spectrum load smoothing algorithm or external detection.

B. Spectrum Sensing for Interference Detection

1) Interference temperature detection: In this approach, CR system works as in the ultra wide band (UWB) technology where the secondary users coexist with primary users and are allowed to transmit with low power and are restricted by the interference temperature level so as not to cause harmful interference to primary users.

2) Primary receiver detection: In this method, the interference and/or spectrum opportunities are detected based on primary receiver's local oscillator leakage power.

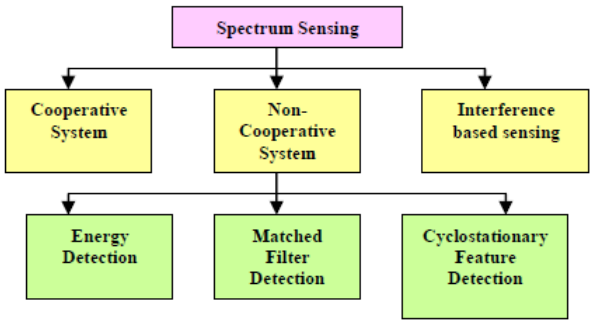

Fig. 6. Classification of Spectrum Sensing techniques

A. Primary Transmitter Detection: In this we are going to discuss about few primary transmitter detection techniques. They are:

1) *Energy Detection(ED):* In this technique there is no need of prior knowledge of primary signal energy [22].

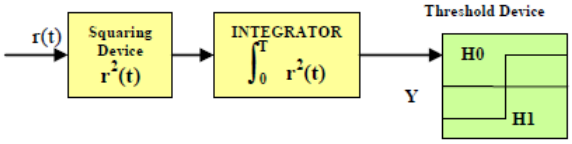

Fig. 7. Block Diagram of Energy Detection

Where H0 = Absence of User.
H1 = Presence of User.

As depicted in figure 7, the measured signal r(t) is first squared and then integrated over the observation interval T. The output from the integrator block is then compared to a predefined threshold level λ_E. By this comparison we discover the presence or absence of the primary user. The threshold value can be fixed or variable based on the channel conditions.

Here we consider two hypotheses:

H0: y(k) = n(k)

H1: y(k) = h * s(k) + n(k)

where y (k) is the sample to be analyzed at each instant k and n (k) is the noise of variance σ2. Let y(k) be a sequence of received samples kϵ{1, 2….N} at the signal detector, then a decision rule can be summarized with two probabilities:

a) Probability of detection *PD: It* is the probability of detecting a signal on the considered frequency when it is truly present. It can be written as

$PD = \Pr(M > \lambda E | H1)$

b) Probability of false alarm *PF* : It is the probability that the test incorrectly decides that the considered frequency is occupied when it actually is not, and it can be formulated as

$PF = \Pr(M > \lambda E | H0)$

where Pr is the probability of reception and the decision metric for the energy detector can be written as

$$M = \sum_{n=0}^{N} |y(n)|^2$$

PF should be kept as small as possible to prevent underutilization of transmission opportunities. The decision threshold λE can be selected for finding an optimum balance between PD and PF .

2) Matched Filter: A Matched Filter (MF) is a linear filter designed to maximize the output signal to noise ratio for a given input signal [23]. When secondary user has a priori knowledge of primary user signal, matched filter detection is applied. The block diagram for the Matched filter detection technique is shown in the figure 8.

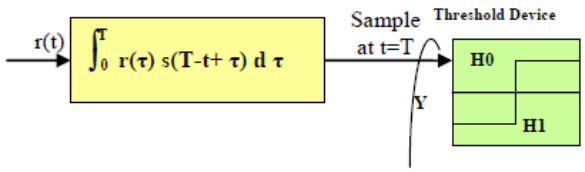

Fig. 8. Block Diagram of Matched Filter detecter

Matched filter operation is equivalent to correlation in which the unknown signal is convolved with the filter whose impulse response is the mirror and time shifted version of a reference signal. The operation of matched filter detection is expressed as:

$Y[n] = \Sigma\, h[n-k]\, x[k]$

Where „x" is the unknown signal (vector) and is convolved with the „h" which is the impulse response of the matched filter that is matched to the reference signal for maximizing the SNR. Detection by using matched filter is useful only in cases where the information about primary users signaling features such as bandwidth, operating frequency, modulation type and order, pulse shaping, and frame format are known to the cognitive users in advance.

3) Cyclostationary detection: In feature detection the presence of PU signals is determined by extracting their specific features such as pilot signals, symbol rate, cyclic prefixes, spreading codes, or modulation types from its local observation. These features can be detected by analyzing a spectral correlation function since they introduce built-in periodicity in the modulated signals, which is shown in figure 9. This is also called Feature detection [24]. Here, the spectrum correlation of the received signal r(t) is averaged over the interval T, and compared with the test statistic to determine the presence of PU signals, similar to energy detection.

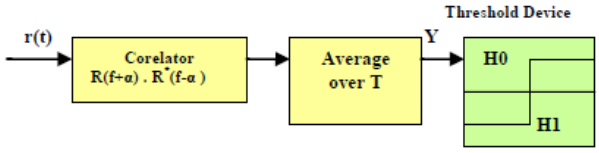

Fig. 9. Block diagram of feature detection

V. COMPARISON OF VARIOUS SENSING TECHNIQUES

Comparison of different techniques of *Primary Transmitter Detection* is shown in figure 10. ED is the simplest one and also does not need prior knowledge of primary signal energy but ED needs long sensing time to achieve a given probability of detection. Its detection performance is also subject to the uncertainty of noise power and ED cannot be used to detect spread spectrum signals. Whereas Matched Filter detection needs less detection time because it requires few samples to meet a given probability of detection constraint but it requires a prior knowledge

of every primary signal therefore if the information is not accurate, MF performs poorly. Also the most significant disadvantage of MF is that a CR would need a dedicated receiver for every type of primary user. In Cyclostationary detection method, its robustness to the uncertainty in noise conditions is its main advantage. Furthermore, it can distinguish the signals from different networks and also synchronization of CR with its neighbors is not required. Although feature detection is most effective method for spectral sensing but it is computationally complex and requires significantly long sensing time. Also its cyclostationary features may be completely lost due to channel fading [25].

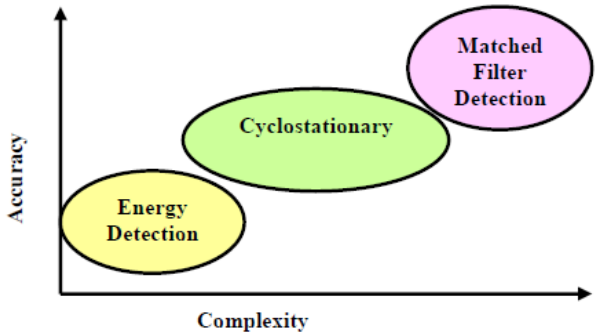

Fig. 10. Sensing accuracy and complexity of various sensing methods

CONCLUSION AND FUTURE WORK

In this paper firstly we presented a survey of SDR Hardware architectures and Software platforms. Then a comparison of different technological choices available for implementing SDR like ASICs, FPGAs, GPP and DSPs is done We found that FPGA is more advantageous as compared to other platforms because it provides reconfiguration, parallel processing, flexible memory structures, parallel and pipelined dataflow, flexible I/O and high speed. Next, we introduced Cognitive radio, which utilizes the available spectrum more efficiently through opportunistic spectrum usage. SDR provides an ideal platform for the realization of Cognitive radio. Finally we discussed and compared various aspects of Primary transmitter detection spectrum sensing techniques and we observed that cyclostationary-based methods perform worse than energy detector based sensing methods when the noise is stationary. However, in case of non-stationary noise energy detector based schemes fail while cyclostationarity-based algorithms are not affected.

Estimation of spectrum usage in multiple dimensions including time, frequency, space, angle, and code; identifying opportunities in these dimensions; and developing algorithms for prediction into the future using past information can be considered as some of the open research areas.

REFERENCES

[1] J. Mitola III, “Software radios: Survey, critical evaluation and future directions,” *IEEE Aerospace and Electronic Systems Magazine*, vol. 8, pp. 25–36, Apr. 1993.

[2] R. I. Lackey and D. W. Upmal, “SPEAKeasy: The military software radio,” *IEEE Communications Magazine*, vol. 33, pp. 51–61, May 1995

[3] J. Mitola, “The software radio architecture,” *IEEE CommunicationsMagazine*, pp. 26–38, May 1995.

[4] J. Mitola III, “Software radio architecture: a mathematical perspective,” *IEEE Journal on Selected Areas in Communication.* vol. 17, no. 4, April 1999.

[5] J. Mitola III, “Cognitive radio for flexible mobile multimedia communications,” in *Proceedings of the IEEE International Workshop on Mobile Multimedia Communications*, San Diego, CA, USA, vol. 1, pp. 3–10, Nov. 1999.

[6] J. Mitola III, “Cognitive radio: An integrated agent architecture for software defined radio.” PhD thesis, Royal Institute of Technology (KTH), Stockholm, Sweden, May 2000.

[7] Enrico Buracchini, “The software radio concept,” *IEEE Communications Magazine*, vol. 38, no. 9, Sept. 2000.

[8] Parul Gupta, Shivkumar Kalyanaraman, Pradipta Dey, Qing Wangz, Jian Wen Chenz, Yong Hua Lin “Software Radio: A Review of Design Considerations and Digital Hardware Choices”, IBM Research Lab.

[9] Ahmad Ali Tabassam, Farhan Azmat Ali, Sumit Kalsait2, Muhammad Uzair Suleman, “Building Software-Defined Radios in MATLAB Simulink – A Step Towards Cognitive Radios,” IEEE 13th International Conference on Modelling and Simulation (UKSim), pp. 492-497, March 30 -April 1 2011.

[10] C. Clark, Software Defined Radio: with GNU Radio and USRP, McGraw-Hill Professional, Nov. 2008.

[11] P. Murphy, A. Sabharwal, and B. Aazhang, “Design of WARP: Wireless open-access research platform,” in *Proc. of European Signal Processing Conference*, June 2006.

[12] C. Chang, J. Wawrzynek, and R. W. Brodersen, “Bee2: a high-end reconfigurable computing system,” in *Proc. of IEEE Magazine, Design and Test of Computers*, vol. 22, no. 2. April 2005.

[13] G. J. Minden, et al, “KUAR: A flexible software defined radio development platform,” in *Proc. of IEEE Dynamic Spectrum Access Networks Symposium*, April 2007.

[14] L. Belanger, "Advanced SDR platform eases multiprotocol radio development," RF Design Magazine, January 2007.
[15] H. Harada, "Software defined radio prototype toward cognitive radio communication systems," IEEE Symposium on New Frontiers in Dynamic Spectrum Access Networks (DySPAN-05), Maryland, Nov. 2005.
[16] *C. R. A. González et al.,*"Open-source SCA-based core framework and rapid development tools enable software-defined radio education and research," *IEEE Communication. Magazine.*, vol. 47, no. 10, pp. 48–55, Oct. 2009.
[17] C. Hunter, J. Camp, P. Murphy, A. Sabharwal, and C. Dick, "A Flexible Framework for Wireless Medium Access Protocols," Invited Paper in *Proc. of IEEE Signals, Systems and Computers Conference*, Asilomer, Pacific Grove, CA, Nov. 2006.
[18] T.R Newman, S.M.S. Hasan, D. Depoy, T. Bose, and J.H. Reed "Designing and deploying a building-wide cognitive radio network testbed," *IEEE Communications Magazine*, vol. 48, no 9, Sept. 2010.
[19] I. Mitola, J. and J. Maguire, G. Q., "Cognitive radio: making software radios more personal," *IEEE Personal Commun. Mag.*, vol. 6, no. 4, August 1999, pp. 13–18.
[20] Federal Communications Commission, "Notice of proposed rule making and order: Facilitating opportunities for flexible, efficient, and reliable spectrum use employing cognitive radio technologies," ET Docket No. 03-108, February 2005.
[21] Takeshi Ikuma and Mort Naraghi-Pour (2008), "A Comparison of Three Classes of Spectrum Sensing Techniques", IEEE GLOBECOM proceedings.
[22] Sabita maharjan, Kimtho Po, and Jun-ichi Takada,"Energy Detector Prototype for Cognitive Radio System," Technical report of IEICE.
[23] R. Tandra and A. Sahai, "Fundamental limits on detection in low SNR under noise uncertainty," in *Proc. IEEE Int. Conf. Wireless Networks, Commun. and Mobile Computing*, vol. 1, Maui, HI, June 2005, pp. 464– 469.
[24] Y. Hur, J. Park, W. Woo, J.S. Lee, K. Lim, C.-H. Lee, H.S. Kim, J. Laskar, "A cognitive radio (CR) system employing a dual-stage spectrum sensing technique: a multi-resolution spectrum sensing (MRSS) and a temporal signature detection (TSD) technique," in Proc. IEEE Globecom 2006, November 2006.
[25] P. D. Sutton, J. Lotze, K. E. Nolan, and L. E. Doyle, "Cyclostationary signature detection in multipath rayleigh fading environments," in *Proc IEEE Int. Conf. Cognitive Radio Oriented Wireless Networks and Commun. (Crowncom),* Orlando, Florida, USA, Aug. 2007

OPEN ACCESS

International
Journal
Of Modern Engineering Research (IJMER)

Failure of Piston in IC Engines: A Review

R. C. Singh[1], Roop. Lal[2], Ranganath M S[3], Rajiv Chaudhary[4]
[1]*Associate Professor,* [2]*Assistant Professor, Mechanical Engineering, Delhi Technological University, Delhi, India*

Abstract: *Piston in the internal combustion (IC) engine is robust, dynamically loaded tribo-pair that reciprocates continuously at varying temperature. Study has been made by various researchers on piston design, dynamics, fatigue and wear at the interface with other element in contact along with their effects on IC engines. It was found that the friction coefficient increases with increasing surface roughness of liner surface and thermal performance of the piston increases with increased coating thickness. The free material liberated due to deep scoring between the piston and liner snowballs, leads to seizure failure.*

Keywords: *Piston, Tribo-pair, IC Engines, Fatigue, Wear.*

I. INTRODUCTION

The current trend in the land transportation and power production is to develop IC engines of enhanced "power-capacity" and "reduced emissions" (to follow specified international intrinsic norms). Piston, piston rings and cylinder liner are important components of an IC engine. The prime function of piston is to transmit the motion produced by liberation of chemical energy of fuel to mechanical works. Piston rings dynamically seal the gap between the moving piston and the cylinder liner surface in order to prevent the escape of the combustion gases from the combustion chamber into the crankcase and the leakage of the oil from the crankcase into the combustion chamber.

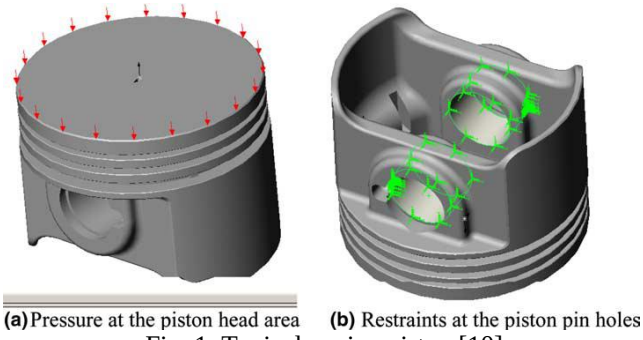

Fig. 1. Typical engine piston [10]

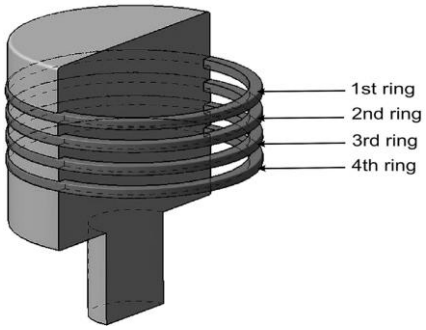

Fig. 2. Schematic illustration of a worn ring piece [25]

The manufacturing of cylinders includes boring, honing and plateau honing which has received much attention by manufacturers in recent times. The process of the surface changes which occurs during running of the engine is related to the wearing action caused by the piston ring on the bore. This action takes place of "transitional topography" where the surface generated exhibits the influence of the piston ring which modifies the machined surface. This has been made possible by improving the design of piston and reducing the failure i.e. scuffing, sculling, seizure of piston etc. The piston is one of the continuous moving parts of engine, is of pivotal importance. Piston has high dynamic loaded speed and heavy reciprocating weight develop high inertia forces, which are undesirable. The following factors may be considered for proper functioning of piston in IC Engine:

1. The piston should have enormous strength and heat resistance properties to withstand gas pressure and inertia forces. They should have minimum weight to minimize the inertia forces.
2. The material of the piston should have good and quick dissipation of heat from the crown to the rings and bearing area to the cylinder walls. It should form an effective gas and oil seal.
3. Material of the piston must possess good wearing qualities, so that the piston is able to maintain sufficient surface-hardness unto the operating temperatures.
4. Piston should have rigid construction to withstand thermal, mechanical distortion and sufficient area to prevent undue wear. It has even expansion under thermal loads so should be free as possible from discontinuities.

5. Piston should form tribo-pairs and have high reciprocation speed without noise, minimum work of friction and have little or no tendency towards corrosion and pitting-up.

II. LITERATURE REVIEW

Sunden and R. Schaub [12] presented a selection of some of the more practically orientated principles of the successful manufacture of grey cast iron piston rings greater than 175 mm in diameter, and shown that when considered with the sciences of strength of materials and diesel engineering, the subject of piston rings becomes an embodiment of the wider subject of tribology. A brief description of the most important topics of practical piston ring manufacture, and an indication of the vast size and complicated nature of an industry which concerns itself with one of the cheapest components of a diesel engine has been given. P. C. Nautiyal, et al, [23] investigated a large part of the top piston ring wear of an IC engine which takes place in boundary lubrication around top dead centre (TDC) position. A quantitative assessment of the frictional behavior using actual piston ring and cylinder liner under conditions close to TDC was made. The factors responsible for wear under these conditions have been identified as surface temperature, peak combustion pressure, total energy on the wearing surfaces and other physical properties of the material under sliding. T. H. C. Childs and F. Sabbagh [30] carried out tests to study the wear mechanisms responsible, particularly the relative importance of high cycle metal fatigue and chemical reaction film wear. Two types of cast iron used as piston rings (a grey and a carbidic iron) were used as pins and a cylinder bore material was used as the ring. Specific loads were varied from 20 to 400 M Pa and the sliding speed was 0.4 m s^{-1}. The wear mechanisms in the two types of test were possibly different, as the engine tests produced worn surfaces which when examined by an optical microscope were bright, whereas the pin-on-ring test surfaces were covered by patchy non-metallic films. Wear rates, friction coefficients, percentage metallic contact and plasticity index were measured in the pin-on-ring tests. Specific wear rates did not correlate with any parameters of contact stress severity.

D. J. Picken and H. A. Hassaan [6] paper described the theory and use of a method for estimating the service life of an internal combustion (i.c.) engine based on experimental evidence and the law of adhesive wear. A simple computer program described, which predicted the overhaul life of an IC engine from its design data and a typical sample of its particular running conditions. The use of the program for an engine generator set operating on biogas at a farm site used as an example. It was considered that the work reported showed that the limit of engine life occurred when the wear of the cylinder liner at the upper position of the piston ring became excessive. Based on this, and assuming marginal lubrication in this area was possible to do a calculation which predicted engine life for any given application. J. E. Willn [13] discussed various methods of characterizing and describing surface finish more accurately for specification purposes. Later, it was hoped that some part of the characterization may also form a correlation with the performance of the ring and bore surfaces with respect to scuffing failure. Complete surface finish characterization was a pre-requisite to ring and liner scuffing tests from which it could be possible to form some correlation between performance and some feature of the surface profile. Meanwhile, a practical and more precise method of specifying finish was required for insuring consistent results in production. Then established random analysis techniques offer a means of characterizing profiles which describe the variations more fully than the simple values of center line average or root mean square. In the majority of cases, the specimen profiles which were examined, varied randomly in amplitude but not in frequency. A. V. Sreenath and N. Raman [2] studied about the conformance between the liner and rings of an internal combustion engine and found that it depend upon mainly on the linear wear (dimensional loss) during running-in. Running-in wear studies, using the factorial design of experiments, on a compression ignition engine showed that at certain dead centre locations of piston rings the linear wear of the cylinder liner increases with increase in the initial surface roughness of the liner. The linear wear of the cast iron liner and rings decreased with increasing load but the mass wear increased with increasing load. Statistical analysis of the linear wear data showed that, during running-in, the initial surface roughness of the liner had a significant effect on running-in wear at and around such dead centre positions of rings where more than one compression ring slide over. It was observed that metal to metal contact occurs at the dead centre positions of rings during running-in. K. J. Stout and T. A. Spedding [17] considered the methods of producing engine bores and the surface profiles obtained by these methods were examined and attempted to characterize their surface topography made. The effects of wear studied and from a consideration of the surface topography of the initial machining process a characterization technique was proposed. The random part of the bored surface has a similar skewness and kurtosis to the honed surface which was due to the similarity of the effects of shearing and deformation on the surface during the two finishing operations.

William G. Agnew [33] reviewed the combustion research conducted by one automotive research laboratory of General Motors. Wieslaw Grabon et al, [32] carried out experiments on a reciprocating tester. The lubricant was supplied into the inlet side of the contact zone. The construction of tribological tester allowed to

measure the friction force between specimen and counter-specimen. Tribological behaviors of cylinder liners with and without oil pockets were compared. Specimens were cut from plateau honed cylinder liners made of grey cast iron. Counter-specimens were cut from grey cast iron piston rings. The results suggested that hydrodynamic oil pocket effect was of prime importance. The positive effect of additional cylinder liner surface texturing on frictional resistance under worse lubrication conditions was smaller. Height and slope of piston ring surface topographies decreased due to wear. S. Mezghani et al, [27] investigated the various aspects of the wear modeling that caused running- in problems in honed surfaces and its implications on ring-pack friction performance. Plateau honing experiments under different conditions were carried out on an instrumented vertical honing machine. The plateau honing experiments characterized the surface modifications during running-in wear of cast-iron engine bores using advanced characterization method. The predictions were in good agreement with the measurement data of plateau and valleys surface-height parameters. The simulation model of piston ring-pack contact developed to predict friction of cylinder surfaces after plateau honing showed that smooth surfaces lead to better friction performances despite the increases of the ratio between plateau and valleys height (non-plateaued surface). E.P. Becker and K.C Ludema [9] used a laboratory simulator to identify the important variables influencing cylinder bore wear. The same characteristics of wear were observed in the simulator as in running engines, even though the simulator did not attempt to duplicate all the conditions found within an engine. A new picture of wear in cylinders was presented, consistent with the data and previous work on boundary lubrication. The qualitative model accounted for the evolution of the cylinder running surface in terms of composition and texture changes. The model was used to determine the relative importance of the many variables that can influence wear behavior, including contributions from lubricant chemistry, material properties, and mechanical loading. J. Galligan et al, [14] developed a bench test in the first part of this work and the time to failure of ring bore contacts lubricated with a fully formulated motor oil. It was found that failure times correlated well with load, frequency, test temperature and quantity of oil, but that the effect of surface finish, though present, was more difficult to quantify. The main findings in this respect were that there is an optimum finish for long life, and that liner surfaces which were initially highly polished lived which are more dispersed than those with standard finishes. The time to failure in a bench test designed to simulate scuffing failure in the bores of IC engines was shown to be linearly related to load, frequency, temperature and quantity of oil. If the first three of these exceed a critical value, or if the quantity of oil falls below a critical value, scuffing was almost instantaneous. The time to scuff was related to liner surface finish as measured by the rms slope of the top half of its profile.

S.G. Chung et al,[29] employed three types of fixed piston samplers at Nakdong River Delta. The retrieved samples were equally divided into 100 mm long pieces. Quality was evaluated using suction, shear wave velocity, and consolidation tests. The constant rate of strain consolidation test, rather than the incremental loading test, produced a better correlation with the nondestructive test results. The results suggested that the difference in sample quality was principally caused by the mechanical disturbance attributed to the different penetration mechanisms (methods) of the sampling tubes. The tip angle of sampling tubes significantly affected sample quality, whereas the length-to-diameter ratio had a relatively insignificant effect. The three methods used are in the following order: oil-operated, mechanical, and hydraulic samplers. The difference in sample quality was primarily caused by the mechanical destructuration that occurs because of different penetration mechanisms. Sample quality tends to vary with the in-situ void ratio of the clay. M. Priest, C.M. Taylor [18] reviewed the nature of the surfaces encountered in the piston assembly, valve train and journal bearings of the internal combustion engine. The mathematical models of engine tribology endeavouring to cope with the extreme complexities for the incorporation of surface topography potentially were discussed. U.I. Sj¨odin, U.L.-O. Olofsson [31] investigated the wear interaction between piston ring and piston groove in a radial piston hydraulic motor in regard to mass loss and changes in form and surface roughness. A test rig was developed to simulate the tilting movements of pistons .The results showed that wear on the piston ring groove can be up to 10 times greater than the wear on the piston ring. Factorial design analysed that the form of the piston groove significantly influences the amount of wear, the dominant wear mechanism was mild wear.The most important design variable was the length of the support surface. The preferred design was a piston groove without any support plane. Zenon Krzyzak and Pawel Pawlus [36] analysed the surfaces of a large number of piston skirts surfaces under the "zero-wear" condition were analysed. The amplitude of worn piston skirt surfaces decreased, the ordinate distribution became asymmetric, summit density increased and lay direction changed from circumferential to axial during wear. The relationship between microgeometry parameters was studied using correlation and regression analysis. It was decided to determine the local wear of piston skirts based on the changes in amplitude parameters. An increase in the initial surface height caused and increase in piston skirt wear. The local linear wear of piston skirts was bigger on the thrust side than on the anti-thrust side of the cylinder . The worn piston skirt surfaces were observed to be smoothed. The ordinate distribution became asymmetric during "zerowear". The ratio of average slopes in axial and circumferential directions can monitor

piston skirt wear. Piston skirt wear was proportional to initial profile height. Change of height parameter during wear process was bigger on the thrust side than on the anti-thrust side of the cylinder. A. Skopp, et al, [1] compared the tribological behaviour of TinO2n−1 and TiO1.95−x coatings under lubricated conditions with uncoated specimen of grey cast iron. The interaction of the pairs with prototype engine oils based on esters and polyglycols were studied under mixed/boundary lubrication using the BAM test method. Lubricants were factory fill engine oils, ester-containing lubricants with low-SAP (sulphur–ash–phosphor) and/or bio-notox properties as well as polyglycole-based lubricants. The ester and polyglycole-based engine oils respond both to bio-no-tox criteria and were polymer-free. They followed different strategies to reduce zinc, phosphorus and sulphur to assure a low ash content. Based on the piston ring/cylinder liner simulation BAM test outside of engines under conditions of mixed/boundary lubrication, it is reasonable that thermally sprayed TiOx-based cylinder liner coatings can substitute commonly used uncoated grey cast iron liner materials. The coefficient of friction was more determined by the lubricants or by an individual interaction between lubricants and a specific material or tribopairing.

L. Ceschini, et al, [16] carried out both bench tests and laboratory dry sliding tests on components for hydraulic motors involved in a boundary lubricated sliding contact, with the aim of investigating the tribological behavior and improve the durability of the components. Bench tests were carried out on a rotating shaft, consisting of a quenched and tempered 36CrNiMo4 steel, coated by a Ni7Al layer deposited by Air Flame Spray, sliding against a carburized E470 steel contacting element. Failure analysis of real components after bench tests identified the main wear mechanism as two body abrasion. Laboratory dry sliding tests allowed the investigation of the influence of normal load and sliding distance on friction and wear behavior. Those tests also used in the subsequent steps of the work for ranking candidate alternative materials for the investigated tribo system. Rohollah Ghasemi and Lennart Elmquist [25] investigated the relationship between the deformation of the matrix and the closing tendency of flake graphite.

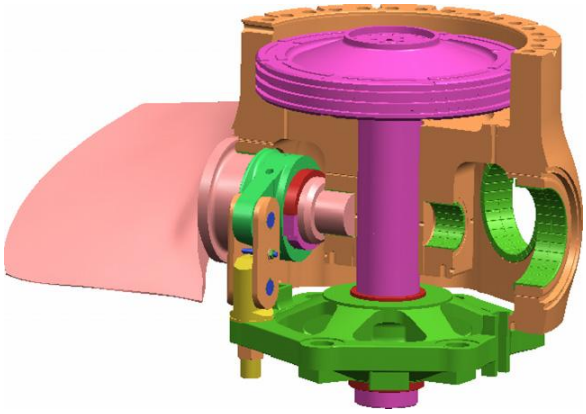

Fig. 3. Blade-control system for one blade.[35]

Two representative piston rings, which belonged to the same two-stroke marine engine but were operated for different periods of time, were studied. Initial micro structural observations indicated a uniform distribution of graphite flakes on unworn surfaces, where as worn surfaces demonstrated a tendency towards a preferred orientation. SEM and EDS analysis indicated substantial deformation of the matrix in the area around the flakes.

An insignificant corrosion attack was observed on both worn piston ring surfaces. As the orientation of the graphite flakes deviated more from the sliding direction, there was a higher chance of them maintaining their intrinsic self-lubricating nature and continuously supplying graphite to the sliding surface. C.W. Huanga and C.H. Hsuehb [5] selected Piston-on-three-ball tests by the International Organization for Standardization to establish ISO 6872 for the evaluation of the biaxial strength of dentistry–ceramic materials. The formula adopted in ISO 6872 for the fracture load-biaxial strength relationship was an approximate equation originally derived for piston-on-ring tests of mono layered discs. This formula was modified and extended to the case of multilayered discs subjected to piston-on-ring loadings recently. The purpose of their study was to evaluate the adequacy of applying the formula for piston-on-ring to piston-on-three-ball tests for both mono layered and multilayered discs. Finite element analyses were performed to simulate both piston-on-three-ball and piston-on-ring tests. Different degrees of friction between the specimen supporting surface and the loading fixture were considered in the simulations. The results depended on friction when the disc was supported by a ring, however the results became insensitive to friction when the disc was supported by three balls. The maximum tensile stress on the surface of the disc decreased when the friction increased. The results of finite element analyses demonstrated how the friction between the specimen supporting surface and the loading fixture affects the

biaxial strength evaluation in piston-on-ring and piston-on-three-ball tests. Results demonstrated that Hsueh et al.'s formulae predict well the biaxial tensile strength for mono layered systems.

Dacheng Li, et al, [7] proposed a capacity-regulation system based on a novel rotary control valve for reciprocating refrigeration compressor and designed for the first time. The regulation system was mainly composed of a rotary control valve and an adaptive regulation system. The parameters for the design and control of the rotary control valve are theoretically determined. To verify the feasibility and effectiveness of the proposed system, a three-cylinder reciprocating compressor was adopted as a test device. Experimental results showed that the technology was able to realize continuous stepless capacity regulation for the compressor within the range of (0)10e100%, and power consumption decreased correspondingly with the load reduction. S. Mezghania, et. al, [27] developed a prediction friction model in the hydrodynamic contact regime between the ring and cylinder liner taking into account the real topography of the cylinder liner. The properties of groove texture were related to the oil consumption. The friction performance in the piston ring/cylinder liner contact was associated with the plateau formation. Piston ring-pack friction reduction strategies through the cylinder liner groove texture optimization were analyzed. In their study, the groove texture (grooves balance, honing angle, etc.) have been demonstrated to greatly affect friction performance. This model aimed to solve the average Reynolds equation, which depends on the real surface topographies of the cylinder liner, and describes the influence of surface irregularities on the lubricant flow under hydrodynamic lubrication conditions, considering lubricant film rupture and cavitations. Muhammet Cerit [19] determined the temperature and the stress distributions in a partial ceramic coated spark ignition (SI) engine piston. Effects of coating thickness and width on temperature and stress distributions were investigated including comparisons with results from an uncoated piston. It was observed that the coating surface temperature increase with increasing the thickness in a decreasing rate. Surface temperature of the piston with 0.4 mm coating thickness was increased up to 82 °C. The normal stress on the coated surface decreases with coating thickness, up to approximately 1 mm for which the value of stress was the minimum. The optimum coating thickness was found to be near 1 mm under the given conditions. Results indicated that temperature distributions developed at the ceramic coated piston surface can be considerably higher than those of the uncoated piston surface. Thermal analysis results indicated that the coated section of the piston, which is close to the crevice and wall quenching regions, cause an increase in the temperature. As a result of increase in temperature, a slight amount of decrease in carbon monoxide emission may be expected since CO oxidation reactions strongly depend on temperature. The von Misses stress decreased with increased coating thickness. The shear stress which causes lateral cracks increased with the coating thickness increase and reached its maximum level at the inner edge of the coated region at the interface of the substrate. Finally, it was found that the optimum coating thickness for the ceramic coating was slightly below 1 mm.

C. Friedrich a, et al, [4] conducted experiments with coating development and model wear test results from PVD coatings on piston rings for combustion engines. Piston rings were examples for the application of thin films on commonly used mechanical components. The PVD CrxN coatings were deposited by RF magnetron sputtering and characterized by their fundamental mechanical properties like thickness, hardness, residual stress and adhesion, which are important for the tribological behavior of the coating substrate compound. The contact mechanics of the tribological system piston-ring–cylinder were determined by high mechanical loading and changing geometry caused by the sliding kinematics. Therefore, the range of thickness was about 7 mm. The selected rings were made of steel DIN 1.4112 (DIN X 90 Cr Mo V 18) with a bore diameter of 97.5 mm. The results of the coating substrate characterization — high hardness, moderate compressive residual stresses and sufficient adhesion on metallic substrates — provide good behaviour of coatings in this tribological application. This was confirmed by the results of the tribological test procedures which have been performed with ring-on-disc model-wear tests and a short-stroke test rig. The wear of piston rings was investigated with respect to PVD hard coatings as a surface finish with an adjustable profile of mechanical properties. Dhananjay Kumar Srivastava et al,[8] closely related the performance of a combustion engine with the friction force and wear between cylinder liner and piston rings. This friction force was significantly reduced by optimizing the surface topography of cylinder liners. The experiments were carried out for evaluating wear and friction in simulated engine conditions using Cameron–Plint wear testers, Pin-on-disk testers, SRV testers, etc. A non-firing engine simulator was developed in order to simulate engine conditions to a closer extent compared to these machines. This simulator operated at similar linear speed, stroke, and load as real engine and simulated almost all engine operating conditions, except firing pressures. Energy dispersive analysis (EDS) was carried out of liner and top ring for evaluating materials transfer. Coefficient of friction between three different liner segments and ring was evaluated using an SRV wear tester. Coefficient of friction in the piston ring–liner interface increases with increasing average surface roughness for liner. Surface profile and SEM tests were conducted on liner and rings at different stroke position, which reveal that highest amount

wear takes place at TDC location. Even at the BDC location, the wear was higher than the mid-stroke position because of failure of hydrodynamic lubrication regime. The major elements of liner material were iron, manganese, chromium and silicon. During the experiment, concentration of silica went up. In the ring, the hard chrome plating weared out with time and the base metals got exposed towards the end of the experiment. YujunLi et al, [34] developed a novel vibration-based fault diagnostic method to identify the vital components of a diesel engine that have abnormal clearance. The advantage of this method was that it does not require the comparison of current operating parameters to those collected as the baseline.The proposed method employs the timing of impacts caused by two contacting components as the prime diagnostic feature. To extract the features that distinguish the components with abnormal clearance from those with normal clearance, the characteristics of the vibrations generated by a diesel engine typically used in manufacturing were analyzed in this research.

F.S. Silva [10] analysed the fatigue-damaged pistons from petrol/diesel engines, as well as automobiles including trains. The study of damages initiation in the piston at the crown, ring grooves, pin holes and skirt was assessed. An assessment was made through the Case studies as well as the analysis of the thermal/mechanical fatigue damages the pistons. The stress distribution during the combustion was determined through the linear static stress analysis, using ''cosmos works''. Stresses at the piston crown, pin holes, grooves and skirt was also determined. For the confirmation of the crack initiation sites, a fractographic study was also done. The fatigue was a problem for the engine pistons, however, it was not responsible for being the largest part of the damaged pistons. The limitation of weight reduction promoted thinner walls, which cause higher stresses. The priority of fuel consumption reduction and more power was in contradiction as another constraint. Z.W. Wang et al, [35] predicted the failure conditions in the piston rods, in Kaplan turbines and the stresses were analyzed. The pressure oscillations over the turbine blades transfered the forces to the piston rods. The analysis of the dynamic stresses were done at thirteen operating conditions using CFD analyses of the flow, along with the analysis of the stresses to the dynamic loads.

The predicted position of the maximum stress concentration was in good agreement with the actual fracture position. The excessive dynamic stresses at the rated output resulted the crack to grow ending to fracture, in the AGC mode, The mean and dynamic stresses were smaller than that of the retainer ring structure due to the pre tightening force in the structure. G. Floweday et al, [11] Studed diesel engine piston failures, during a bench dynamometer engine durability test, which was aimed to evaluate the effects of various fuels on the life of the fuel system components in diesel engine cars. During the test, a number of pistons, cylinder heads and turbocharger failures were experienced. The study aimed at finding the reasons of the piston failures during the tests. Investigation of the fractured pistons revealed that due to excessive thermo-mechanical loading, thermo-mechanical fatigue initiation took place as a result of silicon phase cracking and subsequent micro-crack formation. Micro cracks with progressive formations lead to flaws upto sufficient magnitude for initiating the propagation by high cycle fatigue mechanisms.

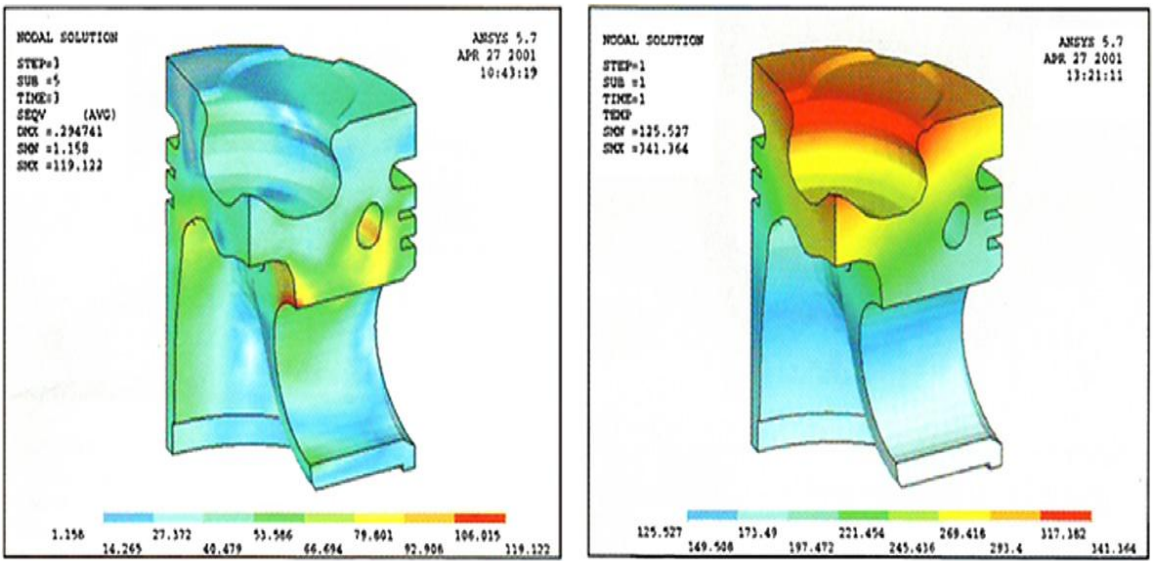

Fig. 4. Contour plot showing the distribution of stress (left) and temperature (right) in a diesel piston due to the combined thermal and pressure loads experienced in an engine. (Reprinted with permission from SAE R-345_2004 SAE International).[11]

Over-fuelling along with the combination of elevated and poorly controlled post intercooler air temperature caused the excessive thermo-mechanical piston loading. No evidence was found supporting the failures to be related with the test fuel formulations. The piston failure may be attributed to, minor over-fuelling and associated thermo-mechanical overload of the pistons, because of the use of neutral injector codes in the engine ECUs, as it deactivates the ECU's function of recalibration of the fuel injector. The damage of the Surface and hairline cracking of the reference fuelled engine piston, the indications of reduced radiation thermal loading as well as spray penetration with the test fuels gave strong indication that fuel formulations were not contributing to the piston failures. Roop Lal et al, [26] made studies on cylinder liner and piston rings interface. Published data on friction and wear was collected from various researchers and concluded. The oil film thichness played important roll and finally affected the performance of engine. Surface roughness of tribo pair material at the junction producing friction and it varied throughout the stroke length of piston. Loss of power in lubrication had the shear force due to boundary conditions. The tribological performance in IC engine could understood when friction and wear were considered. The necessaity to study the factors influencing reliability and performance along with wear was expressed . From the view point of tribo element it was very important to know the specific load, speeds and temperatures for the major components of engine like piston assembly, valve train, the journal bearing and lower viscocity engine oil for lubrication.

O.P. Singh et al, [22] investigated experimentally the seizure failure of piston with numerical simulation of thermal elasto-hydrodynamic lubrication (EHL).

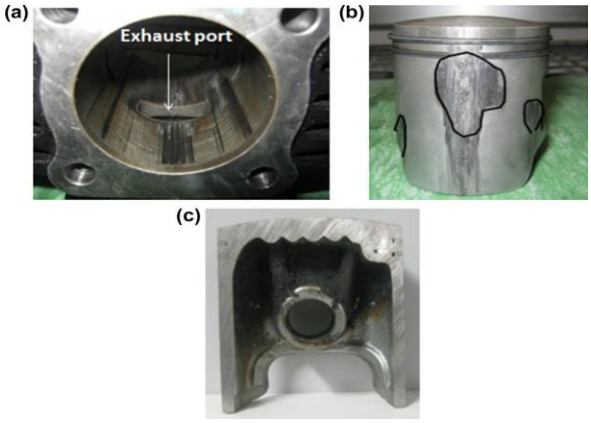

Fig. 5. (a) Seized cylinder liner, (b) seized piston and (c) cut section of the piston showing burnt oil under the crown and skirt. [22]

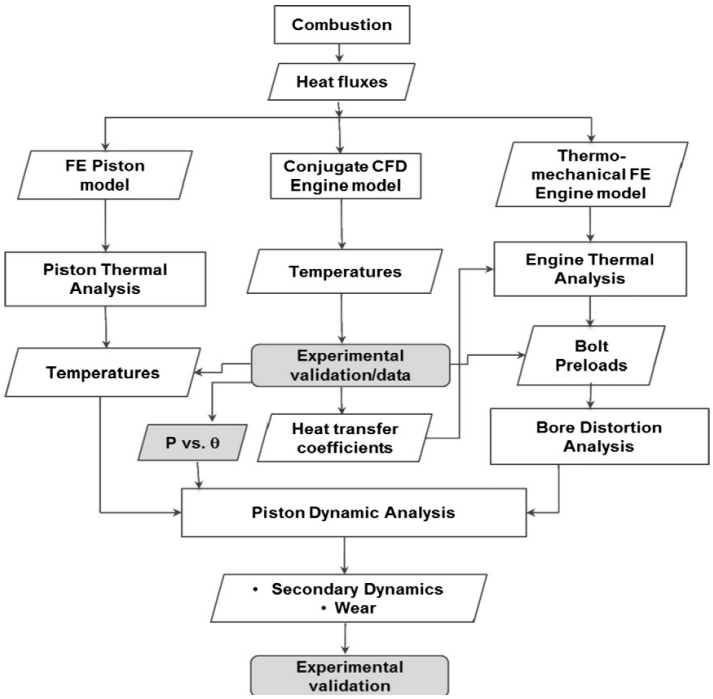

Fig. 6. Flow chart showing steps used in the numerical model of piston hydrodynamic simulation.[22]

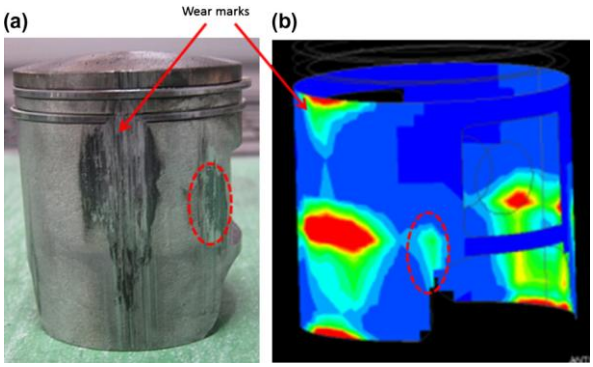

Fig. 7. Correlation of seized marks obtained from the test results and the cumulative wear plot from numerical simulation.[22]

A metallurgical investigation of the piston, rings and liner was done in terms of chemical composition, chemical analysis and hardness. The results indicated large decrease in clearances between the piston and liner at 28°C after TDC. The variation in frictional power over the cycle exhibited sudden increase in magnitude at that location after TDC. The predicted wear mark locations compared well with the test results. The overheating happened to be the root cause of the current piston seizure. Pistons coated with molybdenum material, although enhanced the piston life, but with the problem of skinning off the coating under severe conditions of temperatures and pressures. B. Zhang et al, [3] performed the design as well as experimental validation of a double acting free piston expander in which a slider-based control scheme was used for realizing a full expansion process for the expander. A model was developed for determining the geometric parameters of the expander along with the auxiliary compressor. The results showed that the expander worked stably in a wide range of pressure differences/ratios. R. Mikalsen and A.P. Roskilly [24] reviewed the history of free-piston I C engines, from the air compressors and gas generators used in the mid-20th century Salient features of the free-piston engine has been presented and the effects on engine operation has been discussed, along with comparative advantages and disadvantages with the conventional engines has been discussed.

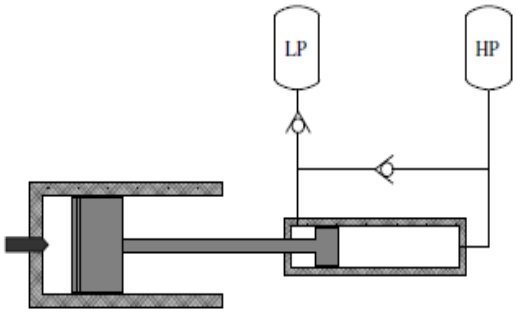

Fig. 8. Single piston hydraulic free-piston engine [24]

Muhammet Cerit and Mehmet Coban [20] improved the performance of a diesel engine, by finding out both temperature and thermal stress distributions on an aluminum piston crown with zirconia coating in a plasma sprayed magnesia-stabilized environment. Effects of the coating thickness varying between 0.2 to 1.6 mm has been investigated, and the results has been compared with that of an uncoated piston, using finite element method. Higher combustion chamber temperature was developed by means of TBC, resulting increase in thermal efficiency of the engine. The engine performance improved with reduction in the piston (substrate) surface temperature. The thermal performance of the piston also increased with increase in coating thickness. From the analysis it was found that the calculated stress values was lower than the allowable stress values of the materials.

III. SUMMARY

Experiments revealed that friction coefficient increases with increasing surface roughness of liner surface. The linear wear of the cast iron liner and rings decreased with increasing load but the mass wear increased with increasing load.

The thermal stress is related to coating thickness. It increases with the coating thickness on the SUBS. The greatest value of the normal stress which produces spalling of the ceramic is produced on the bond coat. It is nearly twice the value of the maximum normal stress on the substrate. The thermal performance of the piston

increases with increased coating thickness. Stress values obtained from FEA were compared with the mechanical properties of the aluminum alloy and zirconia material and it was concluded that calculated stress values were lower than the allowable stress values of the materials.

The ratio of average slopes in axial and circumferential directions can monitor piston skirt wear. The free material liberated due to deep scoring between the piston and liner snowballs, changes its phase from solid to molten state and finally makes its way into the rings. It locks the rings and thus leading the complete engine seizure failure.

Surface thermal damage and hairline cracking of the reference fuelled engine piston, as well as the indications of marginally reduced radiation thermal loading and spray penetration associated with the test fuels gave strong indication that the fuel formulations did not contribute to the piston failures. The fractographic and microstructural analyses reveal regarding selection of correct material for piston fabrication.

The piston failures were determined to have occurred due to Surface thermal damage of the piston bowl lip, Crack initiation by thermal micro-cracking and erosion of primary silicon particles, leading to threshold flaw size, Propagation by thermo-mechanical high and low cycle fatigue and Brittle fast fracture at the critical crack length. Subsequent fuel and flame impingement resulting in piston burn through and loss of engine compression.

The main causes contributing to the piston wear and failures was the use of neutral injector codes in the engine ECUs which deactivated the ECU's function of automatic recalibration of the fuel injector flow rates, resulting in minor over-fuelling and associated thermo-mechanical overload of the failed pistons. Further poorly controlled post intercooler air temperatures and an elevated set point, resulting in overheating of the piston and other combustion chamber components.

REFERENCES

[1] A. Skopp a,1, N. Kelling a,1, M. Woydta,1, L.-M. Berger b,, Thermally sprayed titanium sub oxide coatings for piston ring/cylinder liners under mixed lubrication and dry-running conditions, Wear 262 (2007) 1061–1070

[2] A. V. Sreenath And N. Raman, Running-In Wear Of A Compression Ignition Engine: Factors Influencing The Conformance Between Cylinder Liner And Piston Rings, Wear, 38 (1976) 271 – 289

[3] B. Zhang, X. Peng , Z. He, Z. Xing, P. Shu, Development of a double acting free piston expander for power recovery in trans critical CO2 cycle, Applied Thermal Engineering 27 (2007) 1629–1636

[4] C. Friedrich a,, G. Berg a, E. Broszeit a, F. Rick b, J. Holland b, PVD CrxN coatings for tribological application on piston rings, Surface and Coatings Technology 97 (1997) 661–668

[5] C.W. Huanga,, C.H. Hsuehb,c, Piston-on-three-ball versus piston-on-ring in evaluating the biaxial strength of dental ceramics, Dental materials 2 7 (2 0 1 1) e117–e123

[6] D. J. Picken; H. A. Hassaan, A Method for Estimating Overhaul Life of Internal Combustion Engines including Engines Operating, J. agric. Engng Res,28. (1983), 139-147

[7] Dacheng Li a,, Haiqi Wub, Jinji Gao b, Experimental study on stepless capacity regulation for reciprocating compressor based on novel rotary control valve, International journal of refrigeration 36 (2013) 1701 e1715

[8] Dhananjay Kumar Srivastava a, Avinash Kumar Agarwal a,, Jitendra Kumar b, Effect of liner surface properties on wear and friction in a non-firing engine simulator, Materials and Design 28 (2007) 1632–1640

[9] E.P. Becker a,, K.C Ludema b, A qualitative empirical model of cylinder bore wear, Wear, 225-229 (1999) 387-404

[10] F.S. Silva , Fatigue on engine pistons – A compendium of case studies, Engineering Failure Analysis 13 (2006) 480–492

[11] G. Floweday a, S. Petrov b, R.B. Tait b,, J. Press c, Thermo-mechanical fatigue damage and failure of modern high performance diesel pistons, Engineering Failure Analysis 18 (2011) 1664–1674

[12] H. Sunden and R. Schaub †, Piston rings for slow and speed diesel engines, Tribology International February 1979

[13] J. E. Willn, Characterisation Of Cylinder Bore Surface Finish A Review Of Profile Analysis, Wear - Elsevier Sequoia S.A., Lausanne - Printed in the Netherlands

[14] J. Galligan a, A.A. Torrance a,), G. Liraut b , A scuffing test for piston ring bore combinations: Pt. II. Formulated motor lubrication, Wear 236 (1999) 210–220

[15] Jarosław Milewski, Łukasz Szabłowski, Jerzy Kuta, Control strategy for an Internal Combustion engine fuelled by Natural Gas operating in Distributed Generation, Energy Procedia 14 (2011) 1478 – 1483

[16] L. Ceschini, A.Marconi, C.Martini n, A.Morri, Tribological behavior of components for radial piston hydraulic motors: Bench tests, failure analysis and laboratory dry sliding tests, Wear 305 (2013) 238 –247

[17] K. J. Stout And T. A. Spedding, The Characterization Of Internal Combustion Engine Bores, Wear, 83 (1982) 311 – 326

[18] M. Priest, C.M. Taylor, Automobile engine tribology — approaching the surface, Wear 241 (2000) 193–203

[19] Muhammet Cerit , Thermo mechanical analysis of a partially ceramic coated piston used in an SI engine, Surface & Coatings Technology 205 (2011) 3499–3505

[20] Muhammet Cerit and Mehmet Coban,Temperature and Thermal Stress analysis of a ceramic-coated aluminium alloy piston used in a diesel engine, International Journal of Thermal Sciences 77, (2014) 11-18

[21] Mustafa Canakci , Combustion characteristics of a turbocharged DI compression ignition engine fueled with petroleum diesel fuels and biodiesel, Bio resource Technology 98 (2007) 1167–1175

[22] O.P. Singh a,, Yogesh Umbarkar b, T. Sreenivasulu a, E. Vetrivendan a, M. Kannan a, Y.R. Babu a, Piston seizure investigation: Experiments, modeling and future challenges, Engineering Failure Analysis 28 (2013) 302–310

[23] P. C. Nautiyal, S. Singhal and J. P. Sharmat, Friction and wear processes in piston rings,Tribology International,1983
[24] R. Mikalsen, A.P. Roskilly , A review of free-piston engine history and applications, Applied Thermal Engineering 27 (2007) 2339–2352
[25] Rohollah Ghasemi, Lennart Elmquist. The relationship between flake graphite orientation, smearing effect, and closing tendency under abrasive wear conditions, Wear 317 (2014)153–162.
[26] Roop Lal, R C Singh, Ranganath M S and S Maji, Friction and Wear of Tribo-Elements in Power Producing Units for IC Engines- A Review, International Journal of Engineering Trends and Technology (IJETT) – Volume 14 Issue 5, 2014
[27] S. Mezghani a, n, I.Demirci a, M.Yousfi a,b, M.ElMansori a, Running-in wear modeling of honed surface for combustion engine cylinder liners, Wear 302 (2013) 1360–1369
[28] S. Mezghania, I. Demircia,, H. Zahouanib, M. El Mansoria, The effect of groove texture patterns on piston-ring pack friction, Precision Engineering 36 (2012) 210– 217
[29] S.G. Chung, J.M. Lee, W.Y. Jang, Comparing the Quality of Samples obtained by Three Types of Fixed Piston Samplers for Soft Sensitive Clay, Accepted manuscript, Engineering Geology, Accepted date: 21 June 2014
[30] T. H. C. Childs and F. Sabbagh, Boundary-Lubricated Wear Of Cast Irons To Simulate Automotive Piston Ring Wear Rates, Wear, 134 (1989) 81 – 97
[31] U.I. Sjodin, U.L.-O. Olofsson, Experimental study of wear interaction between piston ring and piston groove in a radial piston hydraulic motor, Wear 257 (2004) 1281–1287
[32] Wieslaw Grabon a, WaldemarKoszela a, PawelPawlus a,n, Slawomir Ochwat b a, Improving tribological behaviour of piston ring–cylinder liner frictional pair by liner surface texturing, Tribology International 61 (2013) 102–108
[33] William G. Agnew, Fifty Years Of Combustion Research At General Motors, Proc.Energy Combust. Scie. VoI 4, pp 115-155, 1978
[34] YujunLi a, PeterW.Tse a,, XinYang b, JianguoYang b, EMD-based fault diagnosis for abnormal clearance between contacting components in a diesel engine, Mechanical Systems and Signal Processing 24 (2010) 193–210
[35] Z.W. Wang a,, Y.Y. Luo a, L.J. Zhou b, R.F. Xiao a, G.J. Peng a, Computation of dynamic stresses in piston rods caused by unsteady hydraulic loads, Engineering Failure Analysis 15 (2008) 28–37
[36] Zenon Krzyzak, Pawel Pawlus, 'Zero-wear' of piston skirt surface topography, Wear,260 (2006) 554-561

Available online at www.sciencedirect.com

ScienceDirect

Procedia Materials Science 6 (2014) 798 – 804

Procedia Materials Science

www.elsevier.com/locate/procedia

3rd International Conference on Materials Processing and Characterisation (ICMPC 2014)

Flow Behaviour Of Bidisperse MR Polishing Fluid And Ball End MR Finishing

Mahendra Singh Niranjan[a*], Sunil Jha[b]

[a*]*Department of Mechanical Engineering, Delhi Technological University, New Delhi 110042, India.*

[b]*Department of Mechanical Engineering, Indian Institute of Technology Delhi, Hauz Khas, New Delhi 110016, India.*

Abstract

Bidisperse MR polishing fluid samples has been prepared with varying percentage of small sized magnetic contents of carbonyl iron powder (CIPs) HS grade within same vol% of total magnetic contents. Magnetorheological behaviours of bidisperse MR polishing fluid for comparison with monodisperse MR polishing fluid using physica MCR-301 rheometer is presented in this paper. The flow behaviour of MRP fluid has been evaluated by steady state rheograms at different magnetic field strength. The yield shear stress and viscosity of bidisperse MRP fluid for all experiments were found maximum at 16 vol% CIPs CS grade, 4 vol% CIPs HS grade, 25 vol% abrasives and 55 vol% base fluid. The results indicate that the yield shear stress and viscosity of bidisperse MRP fluid has been found improved as compare to monodisperse MRP fluid for all magnetic field strength. The morphology of the prepared samples has been studied using scanning electron microscope. After characterization, the experiment was performed with bidisperse MRP fluid on mild steel work-piece using ball end MR finishing tool for 30 minutes with a set of given machining parameters. Percentage reduction in surface roughness (%ΔRa) was calculated and found superior results as compared to existing one.

Selection and peer review under responsibility of the Gokaraju Rangaraju Institute of Engineering and Technology (GRIET)

Keywords: Magnetorheological; Abrasives; Bidisperse; Rheology; Nanofinishing; MRPF

1. Introduction

Magnetorheological (MR) fluids are smart fluids which changed reversibly from fluid to solid like in a very short time interval in external magnetic field and shows changed magnetorheology.

* Corresponding author. Tel.: +91-11-27871438 ; fax: +0-000-000-0000 .

E-mail address: mahendraiitr2002@gmail.com

Selection and peer review under responsibility of the Gokaraju Rangaraju Institute of Engineering and Technology (GRIET)
doi:10.1016/j.mspro.2014.07.096

The MR fluids consist of ferro/ferri magnetic contents in base fluid. Daniela et al. (2010) has studied the magnetorheology for extremely bidisperse magnetic fluids with same magnetic solid contents and found enhanced relative viscosity with addition of nano particles as compared to available conventional MR fluid. The major constituent of MR fluid is carbonyl iron powder (CIP) which is produced by thermal decomposition of iron pentacarbonyl Fe(co)5 and spherical shaped grains are obtained. It has outstanding magnetization behavior which is relevant for the applications such as inductive electronic components and magnetorheological fluids. Bong et al. (2009) used nano sized carbonyl iron particles (CIPs) as an additive for conventional MR fluids. The flow behaviour of MR fluid with and without nano magnetic contents was studied in the presence of magnetic field. On introduction of nano sized carbonyl iron particles in conventional MR fluids, the yield behaviour was found improved with strengthened structure. Patel (2011) has studied the mechanism of structural micro cavities formation in conventional MR fluid. These micro cavities were formed by association with large magnetic contents and were filled with nano magnetic contents in the presence of external magnetic field. These nano magnetic contents along with large magnetic particles restrict the aggregation of large contents and causes field induced phase separation in MR fluid. Hence it became important to study the stability against sedimentation and redispersibility of conventional MR fluid for its potential application. It was observed that 3% volume fraction nano magnetic particles are sufficient for stability of MR fluids having iron more than 30%. Iglesias et al. (2012) has evaluated the performance of extremely bidisperse MR fluids using steady state rheograms with various combinations of magnetic contents under applied magnetic field. Yield shear stress was observed high with improved stability and redispersibility.

The MR fluids along with abrasive particle can have potential application in ultra fine finishing of metals. Kordonski and Jacobs (1996) stated that the MR finishing is controlled way finishing techniques and can be applied on variety of geometries by changing the MR fluid's yield shear stress under applied magnetic field. In this process, the surfaces are selectively finished and nano level surface finish is achieved on optical lenses. Sidpara and Jain (2012) have done experimental study to see the effect of process parameter on surface roughness and material removal rate (MRR) in MR finishing of silicon blank. Sidpara and Jain (2012) analysed the mechanism of material sheared in MR finishing with the help of mathematical model of forces acting on work-piece. Two different theories were used and validation of model has been done with experimental results. Sidpara and Jain (2013) analysed the forces on free form surface after measuring the forces experimentally and effect of various parameters on tangential, normal and axial forces was studied. Kim et al. (2004) has used MR finishing to get nano level surface finish on three dimensional optical components. Seok et al. (2007) has done experimental study for the fabrication of curved surfaces and Finite element method was used to investigate the effect of magnetic field around the tool assembly on machined surface profile. Sidpara et al. (2009) has done magnetorheological characterization of magnetorheological polishing (MRP) fluid with and without externally applied magnetic field for obtaining rheograms to study the shear stress (τ) and viscosity (η) in a shear strain range (γ). Singh et al. (2011) has designed and developed a novel computer controlled ball end magnetorheological finishing (BEMRF) tool to finish three dimensional and flat surfaces. This newly developed BEMRF process can be applied on ferrous as well as non ferrous workpiece materials. There is no restriction on relative movement of finishing tool on the workpiece surface.

To further improve the efficiency of finishing action as well as overall effectiveness in MR finishing, an attempt has been made to use bidisperse magnetorheological polishing (MRP) fluid with the developed BEMRF process.

2. Preparation of samples

MR polishing fluid samples has been prepared with 20 vol % carbonyl iron powder of CS and HS grade, 25 vol % SiC abrasives and 55 vol % viscoplastic base fluid. The carbonyl iron powder (CIPs) HS grade was considered from 0 to 6 vol % within 20 vol% total magnetic solid contents and other composition was kept same. In this way, four samples of MRP fluid were prepared as shown in table 1. The samples were prepared with micron size carbonyl iron powder (CIPs, standard CS and HS grade, BASF, Germany). The average particle sizes (d50 value) of CS and HS grade CIPs are 6-7μm and 1.8–2.3μm respectively. The average particle size of SiC abrasives with 800 mesh size is 19μm.

Table 1. MR polishing fluid compositions.

Sample Number	MR polishing fluid Compositions
Sample 1 (Monodisperse)	20 vol% CIP of CS grade, 25 vol% SiC abrasive and 55 vol% base fluid.
Sample 2 (Bidisperse)	18 vol% CIP of CS grade, 2 vol% CIP of HS grade, 25 vol% SiC abrasive and 55 vol% base fluid
Sample 3 (Bidisperse)	16 vol% CIP of CS grade, 4 vol% CIP of HS grade, 25 vol% SiC abrasive and 55 vol% base fluid
Sample 4 (Bidisperse)	14 vol% CIP of CS grade, 6 vol% CIP of HS grade, 25 vol% SiC abrasive and 55 vol% base fluid

3. Characterization

The morphology of uniform mixture of 20 vol% carbonyl iron powder (CIPs) CS grade, and 25 vol% SiC abrasives (sample 1 in powder form) and 16 vol% CIPs CS grade, 4 vol % CIPs HS grade and 25 vol% SiC abrasives (sample 3 in powder form) has been studied by scanning electron microscope. The carbonyl iron powder (CIPs) CS and HS grade has been seen spherical in shape and in different sizes while abrasive particles are seen irregular in shapes with sharp edges.

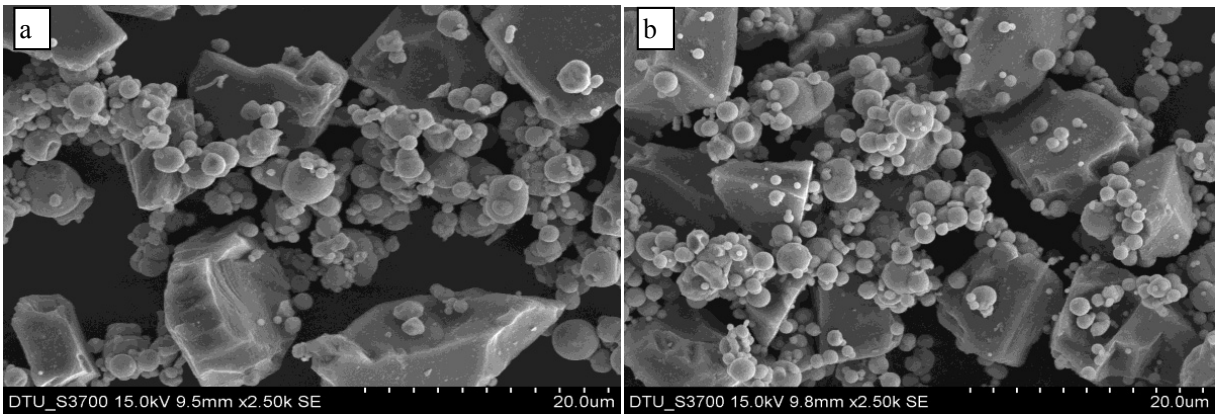

Fig. 1. Scanning Electron Micrograph of (a) Monodisperse magnetic abrasives (sample 1); (b) Bidisperse magnetic abrasives (sample 3)

The magnetorheological characterization plays an important role in the magnetic fluid application. Magnetorheometer (Physica MCR-301, Anton Paar), magnetorheological cell (plate-plate) with diameter of 20 mm and gap of 1 mm was used for all experiments to study flow behaviour of prepared MR polishing fluid samples at 25^0C and 60% relative humidity at different magnetic field strength. Then flow behaviour of prepared MRP fluid was evaluated with the help of obtained steady state rheograms under different magnetic field strength. The built-in coil of magnetorheological cell develop the magnetic field at different current values shown in table 2 which is applied to the sample to study the flow behaviour of MR polishing fluid.

Table 2. Magnetic field and magnetic field strength at different current.

Current I (A)	Magnetic field B (Tesla)	Magnetic field strength H (kA/m)
0.00	0.00	0.00
1.00	0.43	81.91
2.00	0.80	142.20
3.00	1.08	186.50
4.00	1.20	206.50

4. Experimentation

The experiment was conducted with bidisperse magnetorheological polishing (MRP) fluid having maximum yield shear stress and viscosity (sample 3) on ball end magnetorheological finishing (BEMRF) tool. The experiment was performed for 30 minutes on mild steel work-piece at 334 RPM, 4A current and 0.80 mm gap between tool and work-piece. The surface roughness before and after experiment was measured at same point with data length of 4 mm and cut-off evaluation length 0.25 mm by Talysurf.

5. Results and Discussion

Fig.2 shows shear stress as well as viscosity vs shear rate in shear rate range 0 to 1000 sec-1 for prepared four MRP fluid samples at current of 1A. The flow behavior of prepared MRP fluid is strongly magnetic field dependent and found maximum for sample 3 among all MRP fluid samples. The yield shear stress was observed to be 9.885 kpa and viscosity 98.99 kpa-s for sample 3 and minimum yield shear stress was observed 0.432 kpa and viscosity 4.331 kpa-s for sample 1 at current of 1A.

It shows that as the vol % of small sized magnetic contents of carbonyl iron particles (CIPs) HS grade increases within fixed total magnetic contents, the shear stress and viscosity increases and reaches maximum value at 4 vol % of CIPs HS grade then after decreases with further increase the vol % of CIPs HS grade. That is optimum value of 4 vol % CIPs HS grade is sufficient to fill structural micro cavities completely formed with large magnetic particles and abrasives.

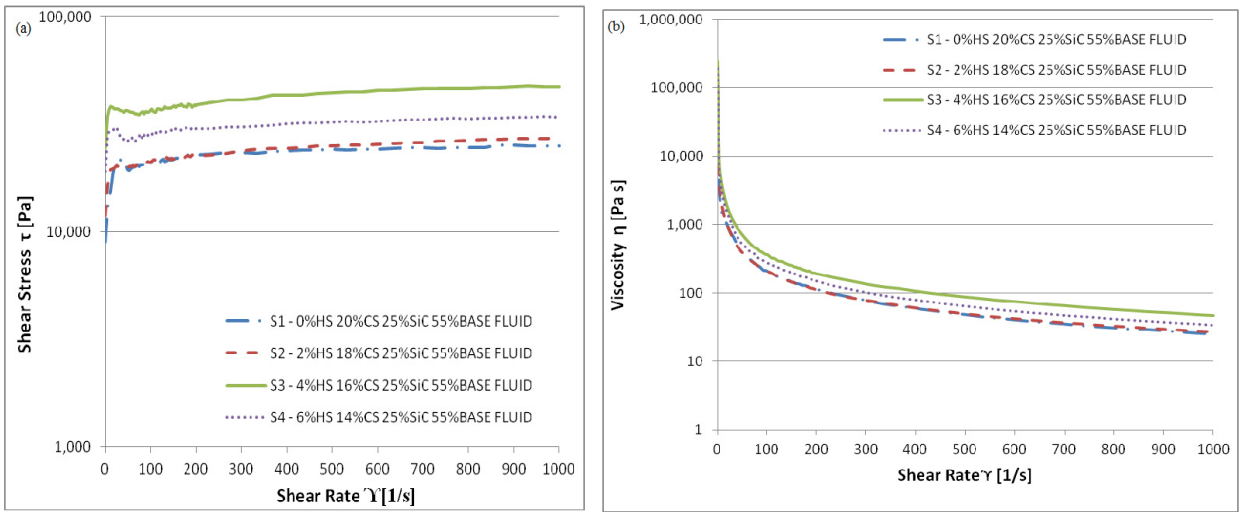

Fig. 2. (a) Shear Stress vs Shear Rate ; (b) Viscosity vs Shear Rate of synthesized MRP fluids for samples at current of 1 A.

The flow behavior of prepared MRP fluid was measured at higher level of current 2A as shown in fig.3. The yield shear stress and viscosity increases with increase the magnetic field and found to be maximum for sample 3 among all MRP fluid samples. The yield shear stress was observed to be 24.54 kpa and viscosity 246.6 kpa-s for sample 3 and minimum yield shear stress was observed 8.984 kpa and viscosity 90.03 kpa-s for sample 1 at current of 2A.

.

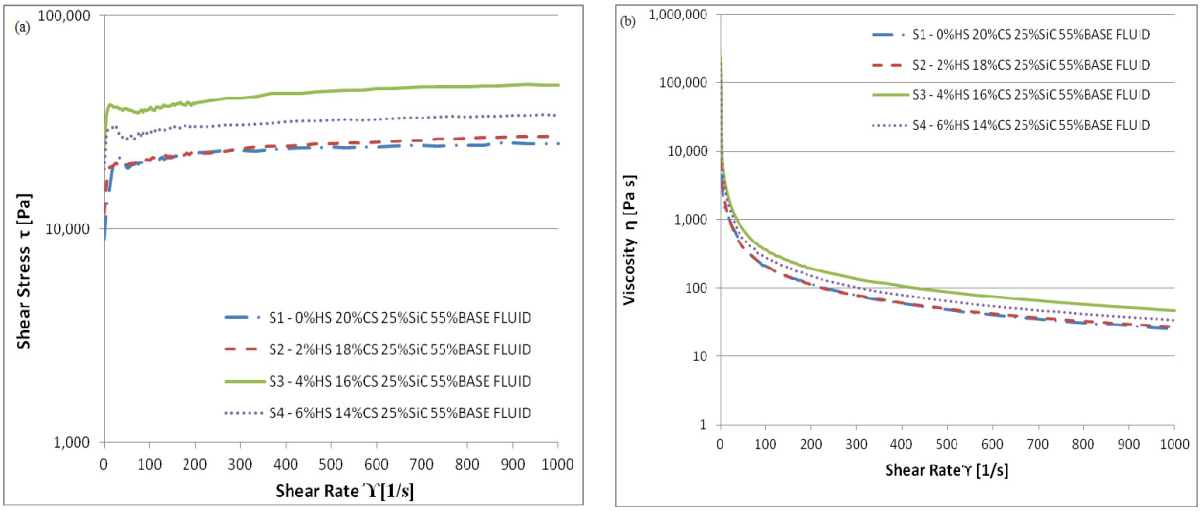

Fig. 3. (a) Shear Stress vs Shear Rate ; (b) Viscosity vs Shear Rate of synthesized MRP fluids for samples at current of 2 A.

The flow behaviour of prepared MRP fluid was again measured at higher level current of 4A as shown in fig.4. It is seen that the flow behavior for sample 2 and sample 3 is almost same at the higher current of 4 A. The yield shear stress was observed to be 43.67 kpa and viscosity 440.7 kpa-s for sample 3 and minimum yield shear stress was observed 15.81kpa and viscosity 158.7 kpa-s for sample 1 at current of 4A.

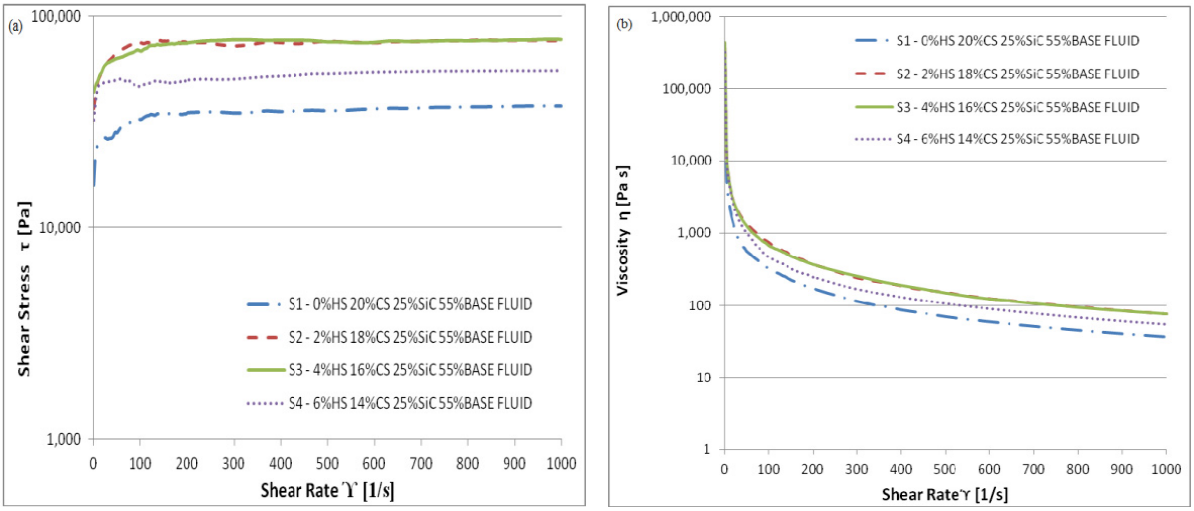

Fig. 4. (a) Shear Stress vs Shear Rate ; (b) Viscosity vs Shear Rate of synthesized MRP fluids for samples at current of 4 A.

The improvement of yield shear stress and viscosity in bidisperse MRP fluid at all magnetic field strength level is obtained due to increased in interaction strength in CIPs CS grade dispersed with small sized CIPs HS grade added. Hence bidisperse MRP fluid demonstrate high yield behaviour as well as high shear stress under shear rate range in the externally applied magnetic field and strengthened structure was obtained. After characterization, experiment was conducted with prepared MRP fluid having maximum yield shear stress and viscosity (sample 3) and improvement in surface roughness was measured from initial surface roughness 0.2115μm in R_a (centre line average value), 0.2665 μm in R_q (root mean square value), 1.3869 μm in R_z (peak to valley height value) to final surface roughness 0.1406 μm in R_a, 0.1967 μm in R_q, 1.1043 μm in R_z.

Fig. 5. (a) Surface roughness profile before finish; (b) Surface roughness profile after finish using bidisperse MRP fluid (sample 3)

Fig.5 (a) and (b) indicates the surface roughness profile before and after MR finishing for a period 30 minutes with bidisperse MRP fluid (sample 3). Then $\%\Delta R_a$ was calculated and found to be 33.52% in R_a, 26.19% in R_q and 20.37% in R_z. It was observed that the $\%\Delta R_a$ has been found better by finishing work-piece surface with bidisperse MRP fluid (sample 3) than the monodisperse MRP fluid (sample 1).

6. Conclusions

In this study, bidisperse magnetorheological polishing fluid samples were prepared. The morphology of prepared samples has been seen with the help of scanning electron micrograph. The flow behaviour of MRP fluid samples has been studied by magnetorheometer at different magnetic field strength and steady state rheograms has been drawn. The magnetorheometery results show that the yield shear stress and viscosity were found maximum for bidisperse MRP fluid (sample 3) for all experiments as compare to monodisperse MRP fluid. After characterization, the experiment was conducted on mild steel workpiece at given machining conditions using bidisperse MRP fluid (sample 3) on BEMRF tool and percentage reduction in surface roughness was calculated and found better.

References

Bong, J.P., Kang, H.S., Hyoung, J.C., 2009. Magnetic carbonyl iron nano particle based magnetorheological suspension and its characteristics. Materials Letters. 63, 1350-1352.

Daniela, S.R., Doina, B., Vekas, L., 2010. Flow behaviour of extremely bidisperse magnetisable fluids. Journal of Magnetism and Magnetic Materials. 322, 3166-3172.

Iglesias, G.R., Lopez, L.M.T., Duran, J.D.G., Gonzalez, C.F., Delgado, A.V., 2012. Dynamic characterization of extremely bidisperse magnetorheological fluids. Journal of Colloid and Interface Science. 377, 153-159.

Kim, W., Lee, S.H., Min, B.K., 2004. Surface finishing and evaluation of three-dimensional silicon microchannel using magnetorheological fluid. Journal of Manufacturing Science and Engineering. 126, 772-778.

Kordonski, W.I., Jacobs, S.D., 1996. Magnetorheological finishing. International Journal of Modern Physics. B 10, 2857-2865.

Patel, R., 2011. Mechanism of chain formation in nano fluid based MR fluids. Journal of Magnetism and Magnetic Materials. 323, 1360-1363.

Seok, J., Kim, Y.J., Jang K.I., Min B.K., Lee, S.J., 2007. A study on the fabrication of curved surfaces using magnetorheological fluid finishing. International Journal of Machine Tools and Manufacture. 47, 2077-2090.

Sidpara, A., Das, M., Jain, V.K., 2009. Rheological characterization of magnetorheological finishing fluid. Journal of Materials and Manufacturing Processes. 24/12, 1467 – 1478.

Sidpara, A., Jain, V.K., 2012. Nano level finishing of single crystal silicon blank using magnetorheological finishing. Tribology International. 47, 159-166.

Sidpara, A., Jain, V.K., 2012. Theoretical analysis of forces in magnetorheological fluid based finishing process. International Journal of Mechanical Sciences. 56, 50-59.

Sidpara, A., Jain, V.K., 2013. Analysis of forces on the free form surface in magnetorheological fluid based finishing process. International Journal of Machine Tools and Manufacture. 69, 1-10.

Singh, A.k., Jha, S., Pandey, P.M., 2011. Design and development of nanofinishing process for 3D surfaces using ball end MR finishing tool. International Journal of Machine Tools and Manufacture. 51, 142-151.

Friction and Wear of Tribo-Elements in Power Producing Units for IC Engines- A Review

Roop Lal[#1], R C Singh[*2], Ranganath M S[*2], S Maji[*3]

[#1] *Assistant Professor,* [*2] *Associate Professor,.* [*3] *Professor,.*
Department of Mechanical Engineering,
Delhi Technological University, Delhi, India

***Abstract*— Piston rings are vital components in the internal combustion (IC) engines having reciprocative motion. The oil film thichness plays important roll and finally affects the performance of engine. Surface roughness of tribo pair material at the junction produce friction and it varies throughout the stroke length of piston. Loss of power in lubrication has the shear force due to boundary conditions. The tribological performance in IC engine can be understood when friction and wear are considered. It is also necessary to study the factors influencing reliability and performance along with wear . From the view point of tribo element it is very important to know the specific load, speeds and temperatures for the major components of engine like piston assembly, valve train, the journal bearing and lower viscocity engine oil for lubrication. This paper explains the studies made on Cylinder liner and Piston rings interface. Published data on friction and wear have been collected from various researchers concluded from their experiments and experiences.**

***Keywords*— Piston Rings, Friction, Cylinder liner, IC Engines, Wear**

I. INTRODUCTION

Piston rings are important elements in the internal combustion (IC) engine. Their prime function is to facilitate smoth running of reciprocating part and dynamically seal the distance between the moving piston and the cylinder liner interface to prevent the escape of the combustion gases from the combustion chamber into the crankcase and at the same time the leakage of the lubricating oil from the crankcase into the combustion chamber. During the running of an IC engine, the hydrodynamic oil film at the interface between the different rings and liner is encouraged preferred. Thin lubricating film reduces both engine wear and friction. The performance, durability and exhaust emissions are greatly affected by the phenomena of lubrication at the junction rings and liner. The frictional force at the rings is determined by the load on the ring, the material surface properties and the lubrication conditions as determined by the velocity gradient viscosity and availability of the oil. The load on the ring comprises the ring pre-tension and the gas forces acting on the back-side of the ring. The total tension of the piston rings in the ring pack determines the friction losses at power producing unit. Wear of the cylinder liner is caused to a great extent by the action of the piston rings. Practical observations and theoretical analyses correlate well in terms of the strongest wear of the cylinder liners taking place in the vicinity of the top reversal point of the top piston ring, where the thermal, chemical, erosive, adhesive and abrasive conditions are the severest. A high sulphur content of the fuel can increase the proportion of tribochemical wear of the cylinder liner dramatically, particular at low cylinder surface temperatures. High wear of the cylinder liner is furthermore associated with the top reversal point of the next to top piston ring, and to a less extent with the bottom reversal points of the piston rings. Carbon deposits above the ring pack on the piston may significantly increase the cylinder liner wear near the TDC region. This paper explains the studies made on Cylinder liner and Piston rings interface. Published data on friction and wear have been collected from various researchers concluded from their experiments and experiences.

II. LITERATURE REVIEW

Researchers continuously involve in study of the lubrication charecteristics and different zones of lubrication at the motion of piston ring with respect to cylinder liner. Many researchers had considered that the entire surface of the ring was enveloped in an oil film, but much experimental research has discovered that not all the entire surface was soaked. Dong-Chul Han and Jae-Seon Lee, [7] analysed the piston ring lubrication with a new boundary condition. They considered a partially lubricated ring, with the following conditions; oil starvation was applied to the inlet region and the open-end assumption to the outlet region. The algorithm confirmed flow continuity and the pressure was allowed to go down to the saturation pressure. Using these new boundary conditions, the actual effective width participating in ring lubrication was determined and the minimum film thickness and flow rate for the ring pack were calculated. The effective width was expected to be about 20 to 30 percent of the whole width of the ring, and the minimum film thickness was less than the result obtained by using the Reynolds cavitation boundary condition. Ming-Tang Ma et al., [18] developed a model for piston-ring lubrication in IC engines with circular and non-circular cylinder bores considering the influences of many factors, such as level of bore distortion, ring conformability, axial motion of the ring, and circumferential variation of the ring face profile. An improved method for determining oil availability in a ring pack was also developed by considering the effect of relative locations of rings on the piston and oil accumulation in front of the ring. The performance of piston rings in the fully flooded lubrication condition was simulated through solving the Reynolds equation, whereas a flow-continuity approach was developed

and used to predict the behaviour of piston-rings in the more realistic lubrication conditions which are usually encountered in conventional engines. The computerized model offered engine designers a useful tool and was used to investigate the effects of the following variables on the tribological performance: E.P. Becker and K.C Ludema, [8] formulated qualitative empirical model of cylinder bore wear. In their investigation, they used a laboratory simulator to identify the important variables influencing cylinder bore wear.

1. bore distortion/ring conformability,
2. composite surface roughness,
3. relative ring (groove) positions,
4. constant ring eccentricity,
5. constant ring twist,
6. axial motion of ring,
7. circumferential variation in ring face profile,
8. circumferential ring gap position.

The same characteristics of wear were observed in the simulator as in running engines, even though the simulator did not attempt to duplicate all the conditions found within an engine. Data were collected showing the influence of several parameters. In particular, a strong effect from ring material was observed. A new picture of wear in cylinders was presented, consistent with the data and previous work on boundary lubrication. This qualitative model took care of the evolution of the cylinder running surface in terms of composition and texture changes. The model also used to determine the relative importance of the many variables that can influence wear behavior, including contributions from lubricant chemistry, material properties, and mechanical loading. M. Priest et al., [16] studied the predictive wear modelling of lubricated piston rings in a diesel engine, Their works review the nature of the surfaces encountered in the piston assembly, valve train and journal bearings of the internal combustion engine and how mathematical models of engine tribology are endeavouring to cope with the extreme complexities the incorporation of surface topography potentially brings. Key areas for future research and the implications for design are highlighted.

Simon C. Tung and Hong Gaob [24] investigated the friction and wear performance of coatings on nitrided stainless steel (NSS) piston rings and chrome plated stainless steel rings sliding against cast iron cylinder liner segments in fully-formulated engine oils by using a high frequency reciprocating tribometer. The ring coatings include thermal-sprayed CrN and physical vapor deposited (PVD) diamond-like-carbon (DLC). The tribological characteristics of piston ring coatings were determined by applying several advanced piston ring coatings and energy-conserving lubricants containing friction modifiers. The impacts of E85 ethanol fuel (a fuel blend of 85% ethanol and 15% unleaded gasoline) on scuffing of the chrome-coated piston ring and cast iron cylinder liner segment were studied with different fuels varying in their degree of acidity. The tribological characteristics due to surface interactions between piston ring coatings and energy-conserving engine oils containing molybdenum dithiocarbamate (MoDTC) or an organic friction modifier were compared and analyzed. The test results showed that the DLC coating produces the lowest wear on the cylinder liner segment and has a similar ring wear to nitrided and CrN coated piston rings.With MoDTC present in the engine oil, friction and wear were effectively reduced. The acidic fuel promoted the occurrence of scuffing. Zenon Krzyzak and Pawel Pawlus [27] performed an analysis of the surfaces of a large number of piston skirts after engine operation. Changes of piston skirts surfaces under the "zero-wear" condition were analysed. The amplitude of worn piston skirt surfaces decreased, the ordinate distribution became asymmetric, summit density increased and lay direction changed from circumferential to axial during wear. The relationship between microgeometry parameters was studied using correlation and regression analysis. It followed from the study that one can fairly precisely describe a piston skirt surface topography using the following parameters: Sq, SSk (or Sp/St), Str and Sdq. The parameters St±3σ , Sku, Sds, SSc and *P_ax*/*P_ay* are recommended for detailed description. It was decided to determine the local wear of piston skirts based on the changes in amplitude parameters. An increase in the initial surface height caused and increase in piston skirt wear. The local linear wear of piston skirts was bigger on the thrust side than on the anti-thrust side of the cylinder.

M. Hahna et al., [15] investigated a cylinder that was run in a road test motor. The relevant piston ring positions that fully describe the tribosystem defined at the combustion chamber (CC), top dead centre (TDC), stroke and bottom dead centre (BDC). Transmission electron microscopy (TEM) and energy-filtered transmission electron microscopy (EFTEM) were used to analyse these contact zones in terms of microstructure and chemistry. Nanocrystalline surface layers up to a thickness of 100 nm occurred in all areas of contact whereas subsurface zones revealed differing microstructural changes. Thus the influence of thermal impact and different mechanical load conditions in a motor cylinder were evident. EFTEM elemental mappings verified the incorporation of elements that stem from lubrication or combustion residues. L. Garaa et al., [13] performed cylinder liner surface roughness and wear measurements through an experimental study of a single cylinder diesel engine operating at a steady state. A replication method was used to evaluate wear and surface roughness on a cylinder liner, where measurements were made at different locations on the cylinder liner before and after each test. Replicated surface profiles were measured by a WYKONT 1100 optical surface profilometer. It was found that surface roughness decreased with time and the rate of decrease was higher during the run-in period. A unique wear volume calculation method that includes bearing ratio parameters was proposed, and reasonable results for wear volume were obtained. Cylinder bore wear rates measured by this replication method were consistent with long-term wear observed in different tests of diesel engines.

B.E. Slattery et al., [3] investigated of wear induced surface and subsurface deformation in a linerless Al–Si engine. The wear mechanisms of a linerless eutectic Al–Si engine subjected to extensive dynamometer testing have been thoroughly investigated using scanning and transmission electron microscopy, focused ion beam milling, optical surface profilometry, X-ray photoemission spectroscopy, and nano-indentation techniques. The as-prepared chemically etched cylinder, which consisted of silicon particles initially exposed 1.1µm from the aluminum matrix, exhibited sufficient wear resistance to operate under ultra mild wear conditions. Silicon particles were found to decrease to an equilibrium height of nearly 0.6–0.7µm. Under these particles, plastically deformed regions of aluminum and ultra-fine grain formations were observed, suggesting that the silicon particles support a significant portion of the load and that the aluminum matrix deforms to accommodate the exerted pressures. Oil deposits were abundant on the worn surface and were shown to fill/protect uneven areas on the aluminum matrix. These amorphous structures were found to consist of combustion byproducts, elements from the oil, and nano-sized aluminum and silicon debris. Staffan Johanssona et al., [25] considered new materials, coatings and high-tech machining processes that previously were too expensive and therefore only used in complex applications. The reciprocating tribometer at Volvo Technology was updated to better evaluate the frictional difference between material combinations/ surfaces; it was possible to evaluate a number of operational parameters in each experiment. The components that were studied were a piston ring running against a cylinder liner. Friction, wear and change in surface morphology were studied in the experiments and design of experiments were introduced based tribometer test the interaction of dynamic viscosity, velocity and contact pressure can be studied within one experiment. The results show differences in friction which could be explained as the surface creating beneficial contact conditions for oil film build-up. It is also apparent that surface roughness is important regardless of material properties. To better understand the correlations between friction and surface roughness a future study should include a study of similar materials with different roughness values.

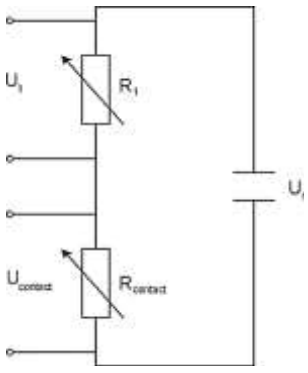

Fig 1: Circuit diagram of electrical resistance measurement between piston ring and cylinder liner.[25]

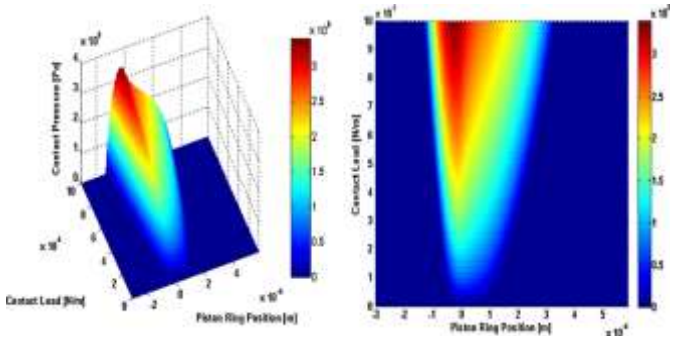

Fig 2: The contact pressure as a function of piston ring position and contact load.[25]

J.C. Walker et al., [12] explained the influence of start–stop transient velocity on the friction and wear behavior of a hyper-eutectic Al–Si automotive alloy. In order to determine the effect of a start–stop velocity cycles on the lubricated friction and wear behavior of a hyper-eutectic Al–Si liner, an Interrupted reciprocating laboratory tribometer test programme was developed based upon the European Urban Cycle standard. Refined cast iron piston ring segments were slid at 23Hz frequency, 4MPa Nominal contact pressure and 25 mm stroke length against a conformal honed Alusil cylinder liner segment. Regular velocity interruptions at 60s intervals did not significantly inhibit the dynamic friction behaviour between the liner and the cast-iron piston ring segment, indicating that lubricant additive function was not significantly inhibited. However contact potential and FIB–SIMS depth profiles indicated that anti-wear tribo-film thickness was reduced as a result of start–stop cycling. Mass loss from the piston ring was also notably higher as a result of the interruption of elasto-hydrodynamic lubrication causing boundary conditions at re-start and subsequent 2-body abrasion by harder protruding Si particles. Specific wear rates for the Al–Si liner as a result of start–stop velocities were surprisingly lower compared to uninterrupted tests and was believed to be due to faster running-in of the piston ring surface. These results were discussed in terms of the viability of Al–Si as engine materials running start–stop technology.

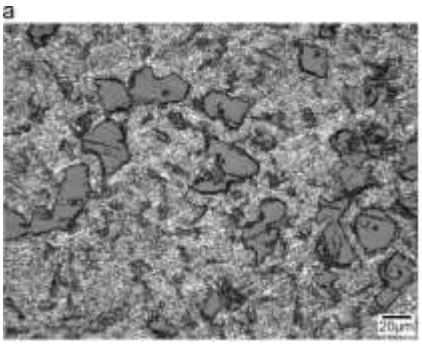

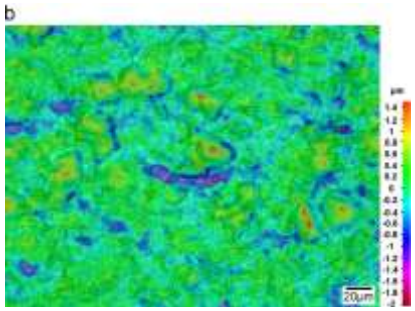

Fig 3: (a) Optical micrograph of the Alusil liner and (b) corresponding
Colour depth map from the same area.[12]

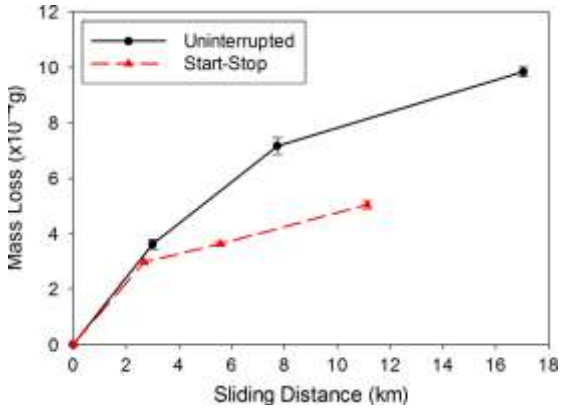

Fig 4: Mass loss vs sliding distance forun-interrupted and start–stop tests[12]

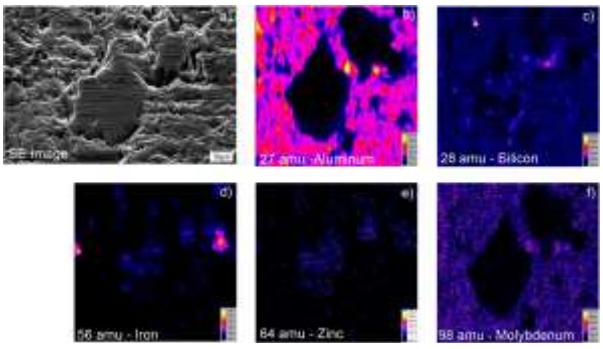

Fig 5: Secondary electron image (a) of surface tribo-films formed on start–stop surface in the mid-stroke region and(b–f)FIB–SIMS chemical maps of aluminium, silicon, iron, zinc and molybdenum, respectively.[12]

M. Priest et al., [17] applied a new model to the piston ring pack of a diesel engine. With the overall aim of evaluating the correlation between theory and experiments, the analysis was divided into two discrete parts. First, the model was used to predict the lubrication performance of measured ring packs before and after periods of running, at constant speed and load, in a Caterpillar 1Y73 single-cylinder diesel engine: the objective being to establish the change in tribological behaviour with observed wear in the engine. Secondly, the model was used interactively to predict the lubrication and wear of the top compression ring from the same engine. This research presented advances in the understanding of piston ring profile evolution with time and its dependence on complex interactions between lubrication and wear.

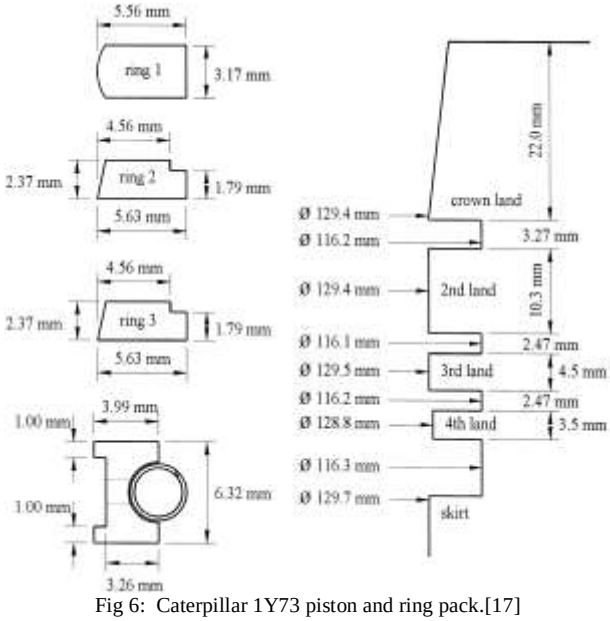

Fig 6: Caterpillar 1Y73 piston and ring pack.[17]

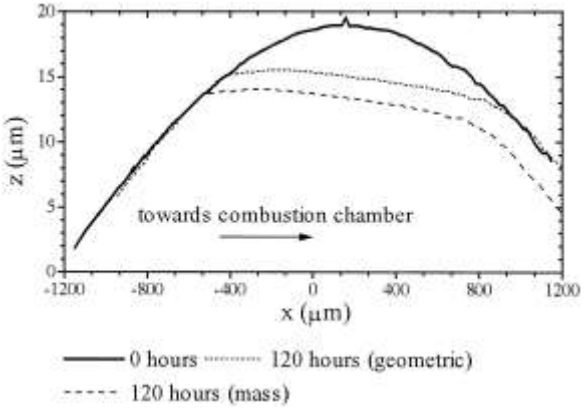

Fig 7: Measured profiles of the new and worn ring.[17]

S. Mezghania et al.,[23] developed a numerical model to investigate the effects of groove characteristics on the lubrication condition and friction at the interface between the piston ring and cylinder liner.

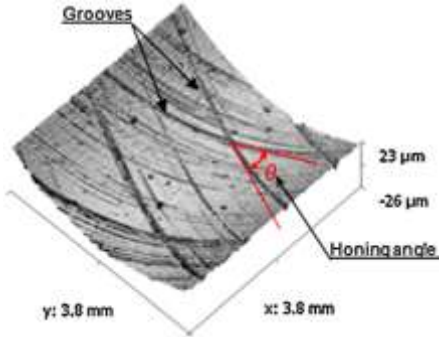

Fig 8: Plateau honed surface of thermal engine cylinder.[23]

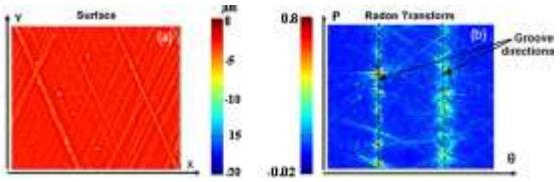

Fig 9: Plateau honed surface (a) and its radon transform (b).[23]

This model was used to solve the average Reynolds equation, which depends on the real surface topographies of the cylinder liner, and describes the influence of surface irregularities on the lubricant flow under hydrodynamic lubrication conditions, considering lubricant film rupture and cavitations. Numerical results helped to determine the optimum lateral groove characteristics to reduce friction and then noxious emissions.

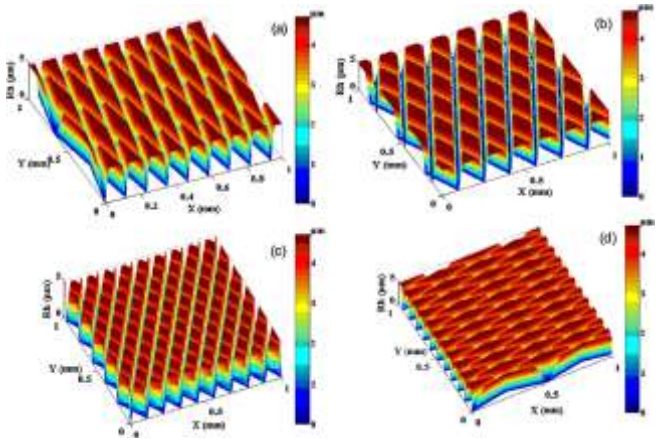
Fig 10: Simulated honed surface with different honing angles: (a) 20◦, (b) 50◦, (c) 120◦ and, (d) 160◦.[23]

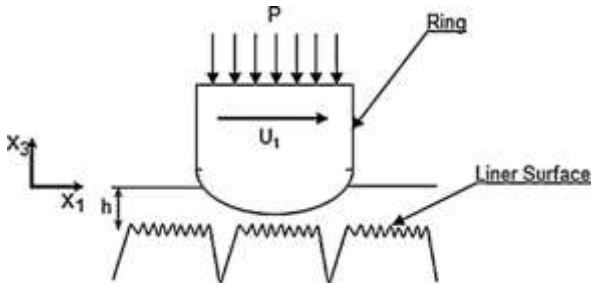

Fig 11: Piston–liner contact description[23]

Luiz G.D et al.,[14] analysed numerically the influence of film thickness and properties on the stress state of thin film-coated piston rings under contact loads.The systems were compared based on the stress distribution, particularly in terms of the intensity and position of the peak stresses in the film and at the film/substrate interface. Results show that (a) in terms of radial stresses in the ring, the stiffer (or thicker) the film, the lower the compressive stresses at the interface immediately under the film-sleeve contact, and the higher the tensile stresses deeper at the ring, while (b) in the coating, the more compliant the material, the more compressive the axial stresses observed. C. Friedrich et al., [4] worked on PVD CrxN coatings for tribological application on piston rings. They concluded from the results: the wear protection of piston rings by PVD coating systems was possible as an alternative to the surface materials used up to now; and as a consequence of the reduced wear rates, the coating thickness can be lower. Carlos Eduardo Pinedo,[5] used selective plasma nitriding on piston rings for performance improvement. Plasma nitriding proved that selective nitriding is possible using a simple mounting system, leading to homogeneous properties on both inner and outer diameter surfaces. Only a diffusion zone, without grain boundaries nitrides, composes the nitrided microstructure. The surface hardness is increased up to 1100 HV0.1. The mechanical tests showed that the performance of selective plasma nitrided rings is superior to the gas nitrided counterpart. The wear rate is 30% higher for the plasma nitrided rings, but acceptable for practical purposes.

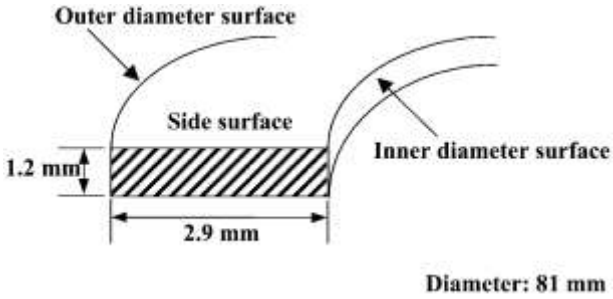

Fig 12: Typical gasoline ring dimensions [5]

R C Singh et al., [22] presented performance behaviors of a commercial diesel engine fueled with diesel and Jatropha based biodiesel (B100) at various loads (up to 100%) and compared using standard (conventional) and three new face profile designs (I, II & III) of piston rings. Face profiles of piston rings had considerable impact on engine's brake thermal efficiency (BTE), brake specific fuel consumption (BSFC), and mass flow rate, irrespective of fuels used. BTE of engine fueled with diesel increases 2-8% with new face profile design (III) of piston rings in comparison to standard (conventional) piston rings. BTE enhanceed 8-16% when engine is fueled with biodiesel using face profile design (III) on piston rings. Corresponding to increase in BTE, recorded reduction in BSFC (biodiesel) was 28-34%. Industrial application of the results of this study was useful in saving and conservation of fuels. Dhananjay Kumar Srivastava et al., [6] explained the effect of liner surface properties on wear and friction in a non-firing engine simulator. In their study, a production grade cylinder liner was used and the experiments were conducted using a custom-made non-firing engine simulator. The wear and surface property behaviour were evaluated at several locations in the liner and found that after running-in an engine, surface of cylinder liner exhibits plateau-honed-like characteristic. Energy dispersive analysis (EDS) was carried out of liner and top ring for evaluating materials transfer. Coefficient of friction between three different liner segments and ring was evaluated using an SRV wear tester. Coefficient of friction in the piston ring–liner interface increased with increasing average surface roughness for liner.

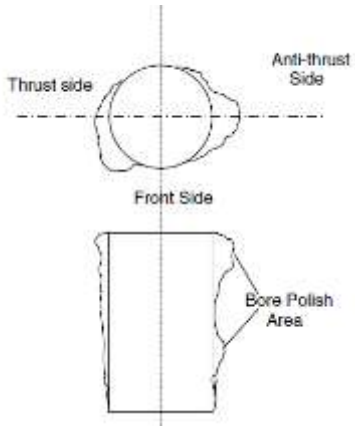

Fig 13: Exaggerated diagram of typical cylinder liner wear [6]

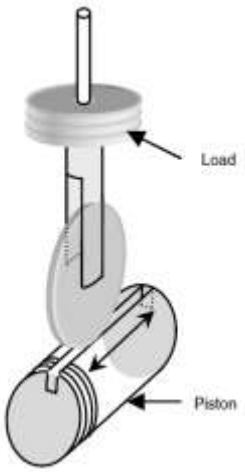

Fig 14: Loading mechanism on the piston [6]

Hanbey Hazar,[10] coated the surface of a piston in a diesel engine with molybdenum nitride (MoN) by using the arc PVD method, and its surface behaviour was subsequently analyzed. Analyses of microhardness, SEM, X-ray and surface roughness were carried out in order to examine surface characteristics of pistons. It is found that the hardness of coated piston is 2000±400 HV while hardness uncoated piston 123 HV. The results showed less deformation and fewer scratches due to wear on the MoN-coated piston as compared to uncoated one. Atul Dhara et al., [2] carried out an investigation of a motored engine in order to validate the sensor and instrumentation and it can be directly employed in a firing engine also. The oil film thickness was measured at different speeds at three different locations, i.e. close to TDC, mid stroke position and close to BDC position and the results were accordingly presented. Lubricating oil film thickness was found to vary between 0.2 and 8_min the motored engine. At a particular position, lubricating oil film thickness varied significantly in upward and downward stroke of the engine due to reversal in direction of piston tilt.

III. SUMMARY

After the detailed study of the published data the following points have been summarized:

i. Lubrication at ring/liner contacts mainly depend on the oil quality, quantity behavior of tribo materials, contour, sliding relative velocity and deformation at the interection due to dynamic action of piston rings.
ii. The frictional loss at the interaction of piston ring and cylinder liner reflect the energy consumption, responsible for wear, and depend on the lubricated conditions of the sliding tribo-pairs.
iii. A steady level of mild wear develops after an initial phase of running-in of the engine. The wear mechanism during running-in depend on two-body abrasion theory. Maximum wear takes place near the top dead centre and the bottom dead centre of the piston motion.
iv. The physics of phase change, gas dynamics, and material scuffing is complex due to the free material liberated from deep scoring between the piston and liner snowballs that changes its phase from solid to molten state and finally makes its path into the inter space of rings. On cooling molten melal locks the rings and thus leading the complete seizure of engine.
v. The lubricating oil film thickness varies significantly in upward and downward stroke of the engine due to reversal in direction of piston tilt in the two strokes. The lubricating oil film thickness increases with increasing engine speed when shifting of lubrication regime from boundary/mixed lubrication to hydrodynamic regime.
vi. Increase the speed of sliding increases the rate of wear as well as the increase in the average roughness, while it is inversely associated with the sliding distance. In a lubricated, the tribology behavior of alloys at sliding distance to steady-state conditions depends on the type of surface preparation.
vii. Building plateau-honed liner at the time of production can control initial wear of the engine and thus reduce the amount of wear debris generation during the initial running-in period. Building-in plateau honedliner surface at the production stage will reduce the initial wear due to running-in. Fatigue will last a problem for long because efforts on fuel consumption reduction and power increase will push to the limit weight reduction that means thinner walls and higher stresses.
viii. The wear rate for plasma nitriding is lower than that found for gas nitrided rings, but still acceptable by the manufacturer and for the application. Plasma

nitriding is an alternative process for piston ring production.

ix. When the piston's surface is coated with the arc PVD method, pistons can be used without any need to apply any additional process on the surface after the coating. Surface hardness of the coated piston is higher than the uncoated one and this has positive effects on its resistance against wear. The surface of the coated piston is harder than that of the uncoated one and this contributes to the piston's load capacity.

x. The friction performance in the piston ring/cylinder liner contact is associated with the plateau formation. Both oil consumption and ring-pack failure through scuffing are complex phenomena rather difficult to predict numerically. Engine testing, then will allow the verification of this optimal spatial morphology and will also permit the quantification of the effects of the proposed liner groove texture characteristics on oil consumption and scuffing tendency.

REFERENCES

[1] A Riyadh A. Al-Samarai , Haftirman , Khairel Rafezi Ahmad , Y. Al-Douri, Effect of Roughness of Hypo-and Hyper-Eutectic Al-Si Piston Alloy on Wear Characteristics under Lubrication, Procedia Engineering 53 (2013) 616 – 623

[2] Atul Dhara, Avinash Kumar Agarwal Vishal Saxenab, Measurement of dynamic lubricating oil film thickness between piston ring and liner in a motored engine, Sensors and Actuators A 149 (2009) 7–15

[3] B.E. Slattery, A. Edrisya, T. Perryb, Investigation of wear induced surface and subsurface deformation in, a linerless Al–Si engine, Wear 269 (2010) 298–309

[4] C. Friedrich, G. Berg, E. Broszeit, F. Rick J. Holland, PVD CrxN coatings for tribological application on piston rings, Surface and Coatings Technology 97 (1997) 661–668

[5] Carlos Eduardo Pinedo, The use of selective plasma nitriding on piston rings for performance improvement, Materials and Design 24 (2003) 131–135

[6] Dhananjay Kumar Srivastava, Avinash Kumar Agarwal, Jitendra Kumar, Effect of liner surface properties on wear and friction in a non-firing engine simulator, Materials and Design 28 (2007) 1632–1640

[7] Dong-Chul Han and Jae-Seon Lee, Analysis of the piston ring lubrication with a new boundary condition Tribology International Vol. 31, No. 12, pp. 753–760, 1998, Ó 1999 Elsevier Science Ltd.

[8] E.P. Becker , K.C Ludema, A qualitative empirical model of cylinder bore wear, Wear 225–229 _1999. 387–404

[9] F.S. Silva ,Fatigue on engine pistons A compendium of case studies, Engineering Failure Analysis 13 (2006) 480–492

[10] Hanbey Hazar , Characterization of MoN coatings for pistons in a diesel engine, Materials and Design 31 (2010) 624–627

[11] I. Sherrington and E.H. Smith Experimental methods for measuring the oil-film thickness between the piston-rings and cylinder-wall of internal combustion engines Tribology International 0301-679X/85/060315-06 $03.00 © 1986 Butterworth & Co (Publishers) Ltd

[12] J.C. Walker n, T.J.Kamps, R.J.K.Wood, The influence of start– stop transient velocity on the friction and wear behavior of a hyper-eutectic Al–Si automotive alloy, Wear 306(2013)209–218

[13] L. Garaa, Q. Zoua, B.P. Sangeorzana, G.C. Barbera, H.E. McCormickb, M.H. Mekaric, Wear measurement of the cylinder liner of a single cylinder diesel engine, using a replication method Wear 268 (2010) 558–564

[14] Luiz G.D.B.S. Lima , Luiz C.S. Nunes , Roberto M. Souza, N.K. Fukumasu , André Ferrarese , Numerical analysis of the influence of film thickness and properties on the stress state of thin film-coated piston rings under contact loads, Surface & Coatings Technology 215 (2013) 327–333

[15] M. Hahna, R. Theissmannb, B. Gleisinga,W. Dudzinskic, A. Fischera, Microstructural alterations within thermal spray coatings during highly loaded, diesel engine tests, Wear 267 (2009) 916–924

[16] M. Priest, D. Dowson, C.M. Taylor, Predictive wear modelling of lubricated piston rings in a diesel engine, Wear 231 _1999. 89–101

[17] M. Priest, C.M. Taylor, Automobile engine tribology — approaching the surface, Wear 241 _2000. 193–203

[18] Ming-Tang Ma, I. Sherrington, E. H. Smith and N. Grice Development of a detailed model for piston-ring lubrication in IC engines with circular and non-circular cylinder bores, Tribology International Vol. 30, No. 11, pp. 779–788, 1997 Ó 1998 Elsevier Science Ltd

[19] Murat Kapsiz , Mesut Durat, Ferit Ficici, Friction and wear studies between cylinder liner and piston ring pair using Taguchi design method, Advances in Engineering Software 42 (2011) 595–603

[20] O.P. Singh , Yogesh Umbarkar, T. Sreenivasulu , E. Vetrivendan , M. Kannan , Y.R. Babu , Piston seizure investigation: Experiments, modeling and future challenges, Engineering Failure Analysis 28 (2013) 302–310

[21] P. C. Nautiyal, S. Singhal and J. P. Sharmat, Friction and wear processes in piston rings, 0301-679X/83/010043-07 $03.00 © TRIBOLOGY international February 1983 Butterworth & Co (Publishers) Ltd

[22] R C Singh, R Chaudhary, R K Pandey and S Maji, Experimental studies for the role of piston rings' face profiles on performance of a diesel engine fueled with diesel and jatropha based biodiesel, Journal of Scintific and Industrial Research, Vol. 71, 2012, pp. 57-62

[23] S. Mezghania, I. Demircia,, H. Zahouanib, M. El Mansoria, The effect of groove texture patterns on piston-ring pack friction, Precision Engineering 36 (2012) 210– 217

[24] Simon C. Tung , Hong Gaob, Tribological characteristics and surface interaction between piston ring, coatings and a blend of energy-conserving oils and ethanol fuels, Wear 255 (2003) 1276–1285

[25] Staffan Johanssona, Per H. Nilssona, Robert Ohlssonb, Bengt-Göran Rosénc, Experimental friction evaluation of cylinder liner/piston ring contact, Wear 271 (2011) 625–633

[26] T. H. C. Childs And F. Sabbagh, Boundary-Lubricated Wear Of Cast Irons To Simulate, Automotive Piston Ring Wear Rates, International Conference On Wear Of Materials, Denver, Wear, 134 (1989) 81 – 97

[27] Zenon Krzyzak, Pawel Pawlus, 'Zero-wear' of piston skirt surface topography, Wear 260 (2006) 554–561

Implemention of Distribution Energy Source as a Compensator based on Power Balance Control Algorithm

Nitu Dhyani
Department of Electrical Engineering, DTU
Delhi Technological University, Bawana Road
Delhi, India
nitudhyani@gmail.com

Alka Singh and Manoj Badoni
Department of Electrical Engineering, DTU
Delhi Technological University, Bawana Road
Delhi, India
alkasingh.dr@gmail.com
manoj_badoni@yahoo.co.in

***Abstract*—This paper represents a method for evaluating the reference current for the Distribution Static Compensator (DSTATCOM) using power balance control technique under static and dynamic conditions has been discussed. In this paper, three phase three wire VSC (Voltage Source Converter) based DSTATCOM is used for power factor correction, voltage regulation at point of common coupling, load balancing of non linear load. The proposed algorithm is simulated in MATLAB environment using SIMULINK and Sim-Power System (SPS) toolbox. A hardware prototype of DSTATCOM has been developed using dSPACE DS1104 R&D controller having TMS320F240 as slave DSP. Both MATLAB based simulation and hardware test results are presented under steady state and dynamic conditions. It is found that the developed algorithm is effective for improving various power quality features such as unity power operation, harmonic compensation and load balancing.**

***Keywords*—DSTATCOM; unit templates; power quality; DC link voltage; PI controller; harmonic compenstaion; load balancing etc.**

I. INTRODUCTION

The power quality issue [1] has become very prominent due to proliferation of power electronic equipment. These equipments cause various power quality problems on both utility and customer side. In recent years, there is a great emphasis on use of more automated and modern equipments which are electronically controlled and energy efficient. These equipments are also more sensitive to deviation in power supply and power quality problems. The non-linear loads draw non linear current and degrade electric power quality and this leads to low power factor, low efficiency, overheating of transformer, malfunction of sensitive devices, voltage sag and swell, current harmonics, voltage harmonics, flicker, poor power factor, increase losses, power interruption, reduced overall efficiency [2].

To overcome these power quality issues, earlier passive filters [3-4] were used to reduce the harmonics and improve the power factor. But passive filters have limitations of fixed compensation, large size and resonance. The increased presence of harmonics has lead to the development of dynamic and adjustable power quality solution named as active filters [5]. Distribution static compensator [6] is the shunt connected active power filter which injects the current at the point of common coupling. Fig. 1 shows the system configuration and design. For proper operation of DSTATCOM, it is necessary to maintain dc link voltage at a value such that pulse width modulation (PWM) control is not lost.

Various control algorithms have been reported in the literature such has p-q theory [7-8], synchronous d-q reference frame method [9], neural network algorithm [10] to extract the reference current of the compensator. Most of these methods require various transformations and are difficult to implement. In this paper, power balance control technique is used to extract the reference source current for indirect current control and it controls the DSTATCOM for power factor correction (PFC) mode and zero voltage regulation (ZVR) mode along with the load balancing and harmonic elimination. The model is simulated in MATLAB environment using SIMULINK and Sim Power System(SPS). The proposed control algorithm has been implemented using dSPACE DS1104 on developed hardware prototype of DSTATCOM for load compensation.

II. SYSTEM CONFIGURATION

The basic block diagram of distribution static compensator is shown in Fig. 1. The distributed energy source is used as a DSTATCOM comprising three leg voltage source converter along with dc capacitor to provide an effective current control. Three phase VSC is realized using six IGBT (insulated gate bipolar transistor) switch with anti parallel diodes. A hysteresis carrier less PWM current control [12] is employed for generating switching signals. The three phase load is consists of reactive load or unbalanced load or non linear load. The non linear load is a three phase diode rectifier and resistance in series with the inductor at the output terminal. An interfacing inductor is used at the ac side to reduce the ripples in the compensator current. The DSTATCOM is operated to compensation of non-linear load, unbalanced load to correct the power factor at the source side or to regulate the PCC voltage. The power balance control algorithm is implemented on a developed hardware prototype of distribution static compensator using dSPACE DS1104 R&D controller having TMS320F240 as slave DSP for load compensation.

978-1-4799-3140-8/14/$31.00

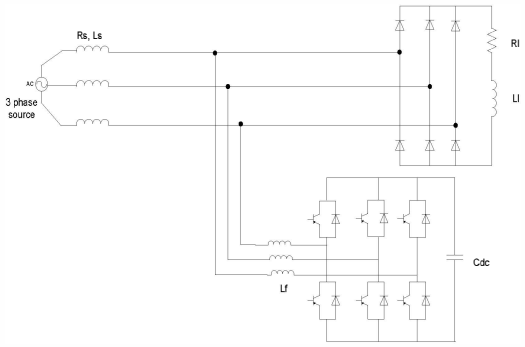

Fig. 1. System configuration.

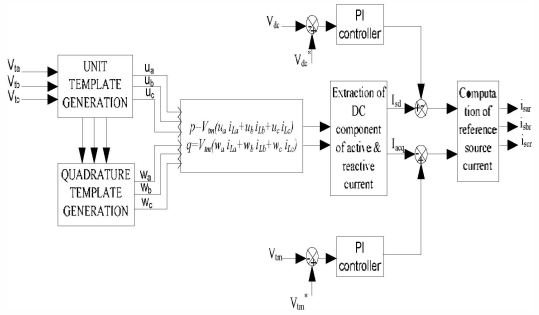

Fig. 2. Block diagram of control algorithm

III. CONTROL ALGORITHM

The control algorithm used for distribution static compensator is based on power balance theory is shown in Fig. 2. The reference currents are extracted by sensing the load current (i_{la}, i_{lb}, i_{lc}), load voltage (v_{la}, v_{lb}, v_{lc}), source voltage (v_{sa}, v_{sb}, v_{sc}), source current (i_{sa}, i_{sb}, i_{sc}), dc link voltage (V_{dc}), voltage at PCC (V_{tm}) through current sensors and voltage sensors.

The amplitude of PCC voltage is calculated from equation 1.

$$V_{tm} = \sqrt{\frac{2}{3}\left(v_{ta}^2 + v_{tb}^2 + v_{tc}^2\right)} \quad (1)$$

where, v_{ta}, v_{tb} and v_{tc} are terminal voltages at point of common coupling.

Unit vector templates in phase with PCC voltage are obtained from the equation 2.

$$u_a = \frac{v_{sa}}{V_{tm}} \quad ; \; u_b = \frac{v_{sb}}{V_{tm}} \; ; \; u_c = \frac{v_{sc}}{V_{tm}} \quad (2)$$

Unit vectors in quadrature with the PCC voltage are obtained from the equation 3.

$$w_a = (u_c - u_b)/\sqrt{3};$$
$$w_b = u_a/\sqrt{2} + (u_b - u_c)/\sqrt{6}\ ; \quad (3)$$
$$w_c = (u_b - u_c)/\sqrt{6} - u_a/\sqrt{2}$$

The instantaneous active and reactive load power is calculated from equation 4.

$$p_{load} = V_{tm} \times (u_a\, i_{La} + u_b\, i_{Lb} + u_c\, i_{Lc})$$
$$q_{load} = V_{tm} \times (w_a\, i_{La} + w_b\, i_{Lb} + w_c\, i_{Lc}) \quad (4)$$

The total load power calculated has two components. The first one is the DC component and second one is AC component is shown in equation 5.

$$p_{load} = \overline{p} + \tilde{p}$$
$$q_{load} = \overline{q} + \tilde{q} \quad (5)$$

The DC component is extracted by filtering the load power through low pass filter.

For obtaining the power factor correction, it is assumed that source supplies the load active power (p_{load}) and power loss (p_{loss}) in the converter. The reactive power requirement of the load is fed locally from distribution static compensator. The DC component ($\overline{p}$) of load active power is extracted by filtering it through low pass filter from which required active load current (I_{sd}) is calculated as shown in equation 6.

$$I_{sd} = \frac{2}{3} \times \frac{\overline{p}}{V_{tm}} \quad (6)$$

For the regulation of DC link bus voltage (V_{dc}), a PI controller is employed. The output of this PI controller is considered as loss component of power in the converter is shown in equation 7.

$$i_{loss(n)} = i_{loss(n-1)} + k_{pd}\,\{V_{de} - V_{de(n-1)}\} + k_{id}\, V_{de(n)} \quad (7)$$

where, $V_{dc(n)} = V_{dcr} - V_{dc(n)}$ denotes the error between sensed DC voltage and reference DC voltage. k_{pd} and k_{id} are proportional and integral gains of DC bus voltage PI controller.

The amplitude of active power component of the reference source current is calculated from equation 8 and 9.

$$i_{sdr} = I_{sd} + i_{loss} \quad (8)$$

$$i_{sdar} = u_a \times i_{sdr}\ ;$$
$$i_{sdbr} = u_b \times i_{sdr}\ ; \quad (9)$$
$$i_{sdcr} = u_c \times i_{sdr}\ ;$$

Thus in PFC mode only active component are calculated for generating reference current.

For zero voltage regulation, another PI controller is employed over the amplitude of AC terminal voltage at point of common coupling. The AC terminal voltage is filtered through low pass filter to obtain DC component. The output of this PI controller is shown in the equation 10.

$$i_{acq}(n) = i_{acq}(n\text{-}1) + k_{pq}\,\{V_{ae} - V_{ae}(n\text{-}1)\} + k_{iq}\, V_{ae}(n) \quad (10)$$

where, $V_{ae(n)} = V_{tmr} - V_{tm(n)}$ denotes the error between sensed

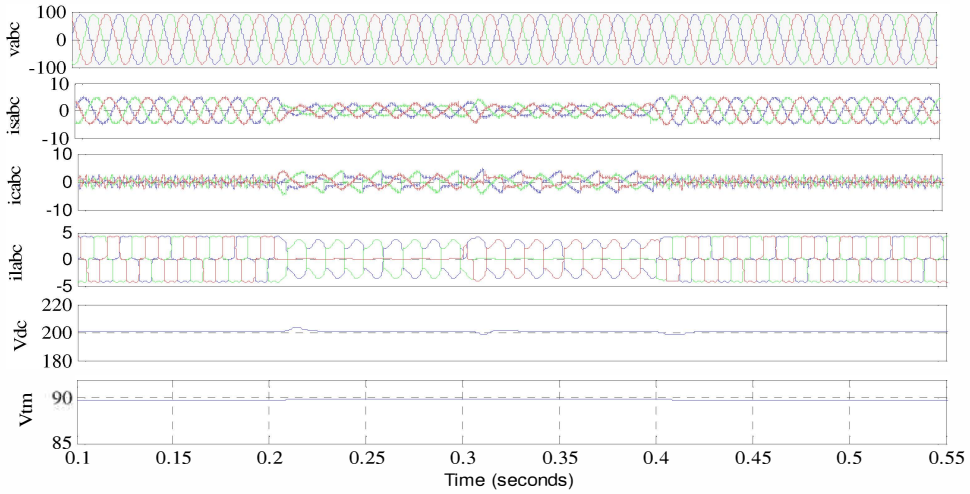

Fig. 3. Performance of DSTATCOM in PFC mode for non-linear load under balance /unbalance condition.

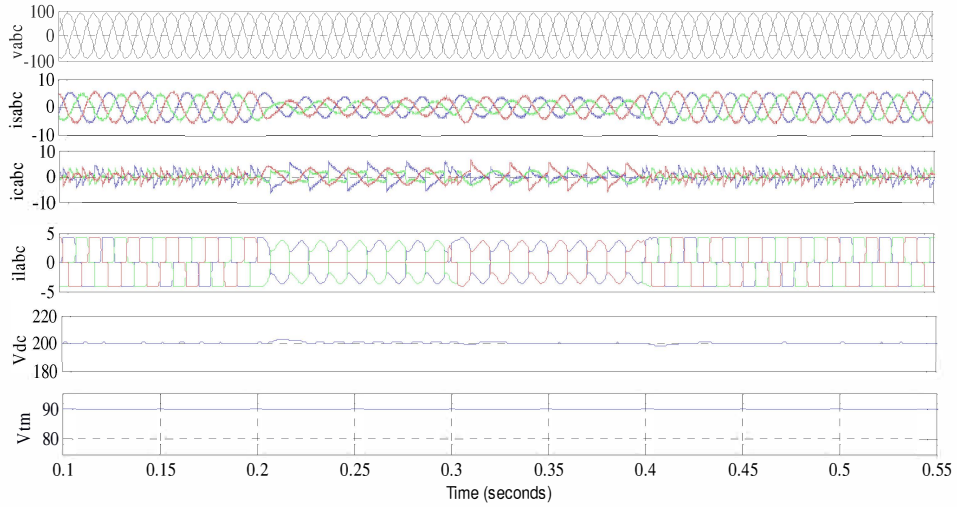

Fig. 4. Performance of DSTATCOM in ZVR mode for non-linear load under balance/unbalance condition.

AC voltage and reference AC voltage at point of common coupling. k_{pq} and k_{iq} are proportional and integral gains of AC voltage PI controller. The amplitude of reactive load current I_{sq} is calculated from equation 11.

$$I_{sq} = \frac{2}{3} \times \frac{\bar{q}}{V_{tm}} \tag{11}$$

The reactive power component of the source current are calculated as shown in equation 12 and 13.

$$i_{sqr} = i_{acq} + I_{sq} \tag{12}$$

$$\begin{aligned} i_{sqar} &= w_a \times i_{sqr} ; \\ i_{sqbr} &= w_b \times i_{sqr} ; \\ i_{sqcr} &= w_c \times i_{sqr} ; \end{aligned} \tag{13}$$

Hence in ZVR mode of operation the total reference currents for all the three phases are obtained by respectively adding the amplitude of active and reactive component of the load current as are shown in equation 14.

$$\begin{aligned} I_{sar} &= i_{sdar} + i_{sqar} \\ I_{sbr} &= i_{sdbr} + i_{sqbr} \\ I_{scr} &= i_{sdcr} + i_{sqcr} \end{aligned} \tag{14}$$

Thus, the desired reference currents can be generated depending on mode of operation for the three phases and are compared with the sensed actual source currents and is fed through hysteresis current controller to generate switching signals for DSTATCOM.

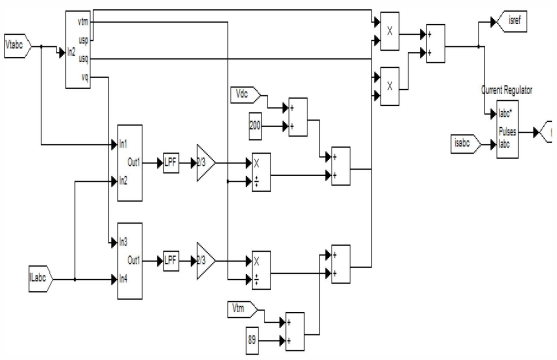

Fig. 5. MATLAB based simulation model

IV. MATLAB BASED MODEL AND SIMULATION RESULTS

A model of distribution static compensator and its controller is developed in MATLAB environment using SIMULINK and Sim Power System (SPS) toolboxes is shown in Fig. 5. The performance of distribution static compensator is evaluated in MATLAB environment using SIMULINK and SPS toolboxes. The DC voltage of DSTATCOM is selected 200V for the source voltage of 110V. For self supporting DC bus voltage of DSTATCOM, a capacitor of 1640µF is used. The VSC is connected through 3.4mH inductor to the network. A non linear load is a three phase diode rectifier with resistance of 35Ω and inductor 100mH in series. The simulation results are taken for both power factor correction (PFC) and zero voltage regulation (ZVR) for the same load conditions. The results are obtained for two different cases.

Case A. Performance of DSTATCOM in PFC mode

Fig. 3 shows the performance of DSTATCOM under steady state and dynamic condition for power factor correction, harmonic reduction and load balancing. The simulation result shows that DC link voltage reaches it steady state value at t=0.06s and remains in steady state till t=0.2s. In the non linear load, phase c and phase b are removed at t=0.2s and t=0.25s respectively. It is observed that there is rise in DC link voltage and it regain its steady state value within few cycles. Similarly, phase c and phase b are added at t=0.3s and t=0.4s respectively. It is observed that there is dip in DC link voltage and it regain its steady state value within few cycle. The source voltage ($v_{sa,}$ $v_{sb,}$ v_{sc}), source current ($i_{sa,}$ $i_{sb,}$ i_{sc}), compensator current ($i_{ca,}$ $i_{cb,}$ i_{cc}), load current ($i_{la,}$ $i_{lb,}$ i_{lc}), DC bus voltage (V_{dc}), PCC voltage (V_{tm}) are shown in Fig. 3. It is observed that the source currents are balanced, harmonic free

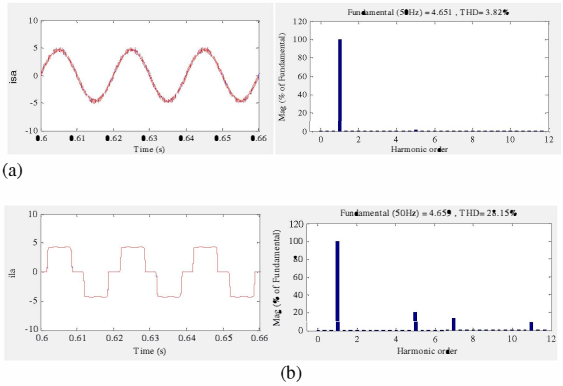

Fig. 6. THD waveform in PFC mode (a) THD of source current in phase a. (b) THD of load current in phase a.

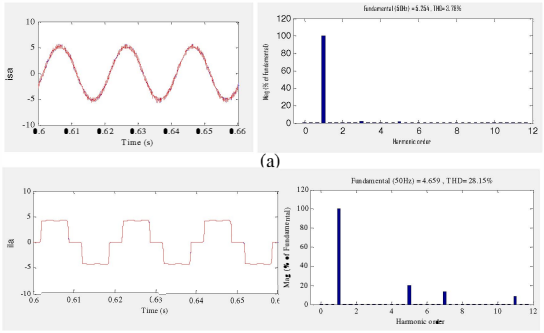

Fig. 7. THD waveform in ZVR mode (a)THD of source current in phase a. (b) THD of load current in phase a.

and in phase with PCC voltage irrespective of balanced or unbalanced load conditions as the loads are compensated by DSTATCOM. The DC bus voltage is also regulated to its reference value. Fig. 6 shows the waveform THD and harmonic spectra of source current and load current. The THD of source current is 3.82% when load current THD is 28.15%.

Case B. Performance of DSTATCOM in ZVR mode

The performance of DSTATCOM in ZVR is evaluated for the same load conditions as in PFC mode. The results are shown in Fig. 4. It is observed that the PCC voltage regulates to reference value under both balanced and unbalanced conditions. DC voltage is also maintained to its reference voltage by the controller. It is seen that non linear load is compensated by DSTATCOM and make the source currents harmonic free and balanced when the non linear load is unbalanced. Fig. 7 shows THD and harmonic spectra of source current and load current. The THD of source current is 3.78% when the THD of load current is 28.15%.

V. HARDWARE RESULTS

The system details for hardware implementation are mentioned in the Appendix. The same parameters chosen for simulation are considered for hardware implementation. A prototype of DSTATCOM is developed using 'Semikron' three leg VSC with six IGBTs. Five current sensors (LEM LA25) and four voltage sensors (LEM LV 25) are used for sensing various current and voltage signals. The proposed control model is implemented using dSPACE DS1104 processor. The test results recorded using fluke 43B power analyzer. The performance of DSTATCOM is tested for different non-linear load conditions in PFC mode.

Fig. 8 shows the waveform of source current, load current and compensator current with DC link voltage under steady state condition. Fig. 9 shows the dynamic condition of DSTATCOM in which load from phase 'c' is removed. The load current in phase 'c' becomes zero. This results in sudden increase in DC link voltage which settle down to its reference value very quickly by controllers action. During phase removal DSTATCOM supplies increased compensator current to make supply current in phase 'c' sinusoidal and thus the source current reduces slightly and remain balanced. In Fig. 10 phase 'c' is added to remove unbalancing thus the i_{lc} increases. This results in sudden dip in the DC link voltage which settle down to its reference value very quickly. This causes reduction in compensator current and increase in source current. The source current remains in balanced condition. The non-linear loads current are compensated by DSTATCOM to make the source current harmonic free and balanced even though the non-linear load is unbalanced.

Fig. 11(a) shows the source voltage and source current waveform which are sinusoidal. Fig. 11(b) shows the THD of source current in phase 'a' which is 4.7%. The THD of load current in phase 'a' is 23.9% which is shown in Fig. 11(c). The THD of PCC voltage is shown in Fig. 11(d) which is 3.1%. These results show the effective performance of control algorithm.

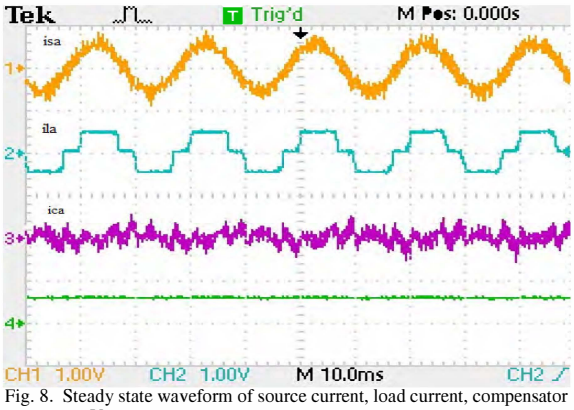

Fig. 8. Steady state waveform of source current, load current, compensator current and V_{dc}

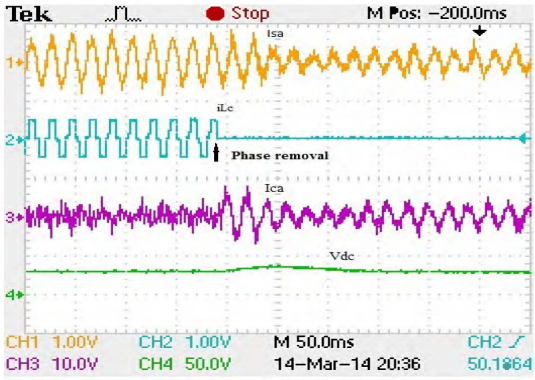

Fig. 9. Waveform of source current, load current, compensator current and DC link voltage when load is removed in phase 'c'.

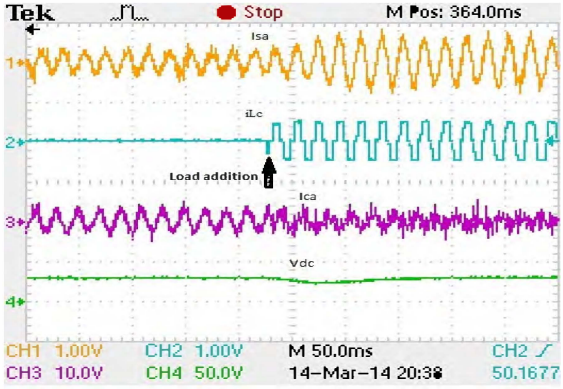

Fig. 10. Waveform of source current, load current, compensator current and DC link voltage when load is added in phase 'c'.

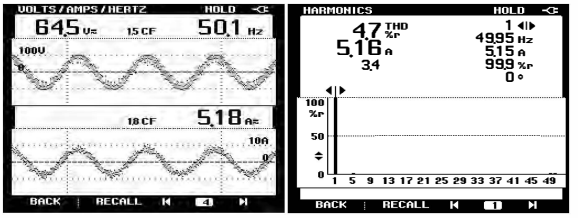

(a) (b)

(b) (d)

Fig. 11. (a) waveform of source voltage and source current. (b) THD of source current. (c) THD of load current (d) THD of source voltage.

VI. CONCLUSION

This paper discusses power balance theory for control of distributed energy source used as a compensator. The results are illustrated for non-linear load in both steady state and dynamic load conditions. MATLAB model is implemented in Sim Power System and three phase reference supply currents are evaluated using power balance theory. Prototype model is developed using the same simulation parameters. Simulation as well as hardware implemented results show THD of less than 5% in the supply current with non linear load currents. Extensive simulation and hardware result have been shown which prove that DSTATCOM can be controlled using power balance control algorithm for mitigating various power quality problems.

APPENDIX

Data for Simulation and Hardware Implementation

The simulation model and hardware prototype has same parameters: AC line voltage is 110V; frequency 50 Hz; DC capacitor value is 1640µF; DC link reference voltage 200V; interfacing inductor 3.4mH; 3 phase non-linear load (3 phase diode rectifier and R=16Ω & L=100mH); k_{pd}= 0.3, k_{id}= 0.05, k_{pq}= 0.011, k_{iq}= 0.0008; five current sensors (LEM LI 25); two voltage sensors (LEM LV 25).

ACKNOWLEDGMENT

The second author wishes to thank the department of Science and Technology, India for the sponsored project no. SR/FTP/ETA-20/2010.

REFERENCES

[1] R. C. Dugan, M. F. McGranaghan, and H. W. Beaty, *Electrical Power Systems Quality.* New York: McGraw-Hill, 1996.

[2] C. Sankaran, *Power Quality.* Boca Raton, FL: CRC Press, 2002.

[3] N.G. Hingorani, "Introducing custom power," *Spectrum, IEEE*, vol. 32, pp. 41-48, 1995.

[4] J.C. Das, "Passive filters - potentialities and limitations," *Industry Applications, IEEE Transactions on*, vol. 40, pp. 232-241, 2004.

[5] B. Singh, K. Al-Haddad, and A. Chandra, "A review of active filters for power quality improvement," *Industrial Electronics, IEEE Transactions on*, vol. 46, pp. 960-971, 1999.

[6] K. R. Padiyar, "FACTS Controllers in Power Transmission and *Distribution,*" New Age International (P) Limited, Publishers, New Delhi, 2007.

[7] H. Akagi, Y. Kanazawa and A. Nabae, "Instantaneous reactive power compensators comprising switching devices without energy storage component," *IEEE Trans. Ind. Appl*, Vol -20,No.3, pp.625-631, May/June 1984.

[8] H. Akagi, E. H. Watanabe, and M. Aredes, *Instantaneous Power Theory and Applications to Power Conditioning.* Piscataway, NJ: IEEE Press, 2007.

[9] A. Chandra, B. Singh, and B. N. Singh, "An Improved Control Algorithm of Shunt Active Filter for Voltage Regulation, Harmonic Elimination, Power-Factor Correction, and Balancing of Nonlinear Loads," *IEEE Trans. Power Electronics,* vol. 15, pp. 495-507, May 2000.

[10] Y. Wang, J. Gu, and C. Chen, ''An improved Adaline algorithm for online tracking of harmonic components,'' *Int. J. Power and Energy System.*, vol. 23, no. 2, pp. 117--127, 2003.

[11] B. Singh, K. Al-Haddad, and A. Chandra, "A new control approach to three-phase active filter for harmonics and reactive power compensation," *IEEE Transaction on Power Systems*, vol. 13, no. 1, pp. 133–138, Feb. 1998.

[12] W. M. Grady and S. Santoso, "Understanding power system harmonics," IEEE Power Engineering Review, vol. 21, no. 11, pp. 8-11, 2001.

Available online at www.sciencedirect.com

ScienceDirect

APCBEE Procedia 9 (2014) 140 – 144

Procedia APCBEE

www.elsevier.com/locate/procedia

2013 5th International Conference on Chemical, Biological and Environmental Engineering (ICBEE 2013)
2013 2nd International Conference on Civil Engineering (ICCEN 2013)

Investigation of Allelopathic Potentiality of the Himalyan Lichen *Parmelia reticulata* Tayl. against *Phalaris minor* retz.

Mayurika Goel[a], Archna Rani[b*], P. Dureja[a] and P. Uniyal[c]

[a]*Division of Agricultural Chemicals, Indian Agricultural Research Institute, New Delhi, India*
[b]*Department of Applied Chemistry, Delhi Technological University, (Delhi College of Engineering), New Delhi, India*
[c]*Department of Botany, University of Delhi, Delhi, India*

Abstract

Allelopathic potentiality of hexane , ethyl acetate and methanol extracts of the Himalyan lichen, *Parmelia reticulate* Taylor, at different concentrations (50, 25 and 12.5µg ml^{-1}) was studied on germination and early seedling growth of highly devastating weed *Phalaris minor*. The experiments were carried out in portray maintained in natural environment. Current investigation has revealed concentration dependent allelopathic phenomenon of the lichen extracts on *P. minor*. Hexane and ethyl acetate extracts at 50 µg ml^{-1} exhibited maximum detrimental effect on seed germination (56 % as compared to control i.e. 90%). Hexane extract at 50 µg ml^{-1} showed maximum inhibition of early seedling growths, determined in terms of shoot and root lengths of the test weed. It reduced shoot and root lengths to 2.5cm (control 10.7 cm) and 0.9 cm (control 3.4cm) respectively, indicating semipolar nature of constituents responsible for bioactivity.

Selection and peer review under responsibility of Asia-Pacific Chemical, Biological & Environmental Engineering Society

Keywords: Allelopathic, Parmelia reticulate Taylor, Phalaris minor

1. Introduction

After severe setback arising from the detrimental effects associated with the use of conventional synthetic crop protectants, efforts to explore allelochemicals have gained momentum. Because of natural origin, these products can be relatively broad spectrum, bioefficacious, biodegradable and environmentally safe [1].

* Corresponding author, fax: +91-11-27871023.
E-mail address: archnar8@yahoo.co.in

2212-6708
Selection and peer review under responsibility of Asia-Pacific Chemical, Biological & Environmental Engineering Society
doi:10.1016/j.apcbee.2014.01.025

Lichens, in this context, are catching the attention of scientists worldwide as new significant sources of bioactive substances [2-5]. Lichens are symbiotic organisms composed of a fungal partner (mycobiont) in association with one or more photosynthetic partners (photobiont) [6]. They commonly grow on rock surfaces, poorly developed soils such as those found in arid lands and boreal arctic regions and as epiphytes on trees and shrubs [7]. The lichen-forming fungi produce antibiotic secondary metabolites and provide protection from animals and pathogenic microorganisms [8]. Their metabolites are structurally unique and highly active in comparison to plant metabolites [8]. The distribution pattern of secondary metabolites is greatly affected by varying conditions of climate, availability of nutrients, substrates, pH, temperature, light, humidity, stress, topography and varied altitude of the area [9-14]. Lichen metabolites have been shown to be toxic and feeding deterrent to insect larvae [15]. Several lichen extracts have been used for various remedies in folk medicine, and screening tests with lichens have shown the frequent occurrence of metabolites with antibiotic, anti-mycobacterial, antiviral, antitumor, analgesic and antipyretic properties [16, 17]. In spite of possessing remarkable bioactivity the agrochemical potential of lichens have not been explored to its fullest. In accordance with these facts, a comprehensive investigation has been initiated aiming at the survey, collection and chemical and biological screening of lichens from the under collected habitats of Kilberi forest ranges (Northern Himalayas) in the Uttaranchal State (Uttarakhand) [18, 19]. In this paper we report herbicidal activity of solvent extracts of *P. reticulata* Tayl. *in vitro* against *Phalaris minor.*

2. Experimental

2.1. Materials

Samples of *Parmelia reticulata* Tayl. were collected from bark of trees, shrubs and on rocks of Kilberi forest ranges (Northern Himalayas) in the Uttaranchal State (Uttarakhand), India and air-dried. A specimen was deposited in the herbarium of the Department of Botany, University of Delhi, Delhi, India (voucher number DUH 13531). Laboratory grade reagents were procured locally. The solvents used were of analytical grade (AR). Seeds of *P. minor* Retz. were collected from Division of Agronomy, Indian Agricultural Research Institute, New Delhi.

2.2. Solvent extraction of lichen material

The lichen thalli were washed thoroughly with water to remove dust particles and dried at room temperature. The air-dried mass was powdered with a mortar and pestle. The powdered material (50 g) was subjected to soxhlet extraction using hexane followed by ethyl acetate and finally with methanol (500 ml) 6 h for each. The solvent was evaporated *in vacuo*, and the dried residues obtained were stored at 4^0C for further biological screening.

2.3. In vitro Biological screening

The effect of different solvent extracts at concentrations 50, 25 and 12.50 µg ml^{-1} on germination and early seedling growth of *P. minor* was evaluated. The experiments were carried out in portray maintained in natural environment in the National Phytotron Facility, India Agricultural Research Institute (IARI). The concentrations of each solvent extract were prepared containing 1% Tween 20 and minimum amount of acetone to dissolve the extract and the volume was made up to 5 ml in water. Thirty seeds of equal size were soaked overnight in above solutions of different extracts. These soaked seeds were removed from the aqueous solutions and dried in the air, to give a uniform layer of the extract on the seed coat. These coated seeds were

placed in the portrays maintained in natural environment of growth room at 18^0C and 12 hours daily light periods. Seeds were considered germinated, if a radical protruded at least 1 mm. Root and shoot lengths of the seedlings were measured after 15 days. Each bioassay was replicated 3 times in a complete randomized design. The control treatments for all sets contained the same quantities of 1% Tween 20 and distilled water. The allelopathic efficacy of lichen extracts was calculated in terms of percentage inhibition of seed germination, and root/shoot lengths as shown in equation (1).

$$\%\ Inhibtion = \frac{Root\ /\ shoot\ length\ in\ control(cm) - Root\ /\ shoot\ length\ in\ treatment(cm)}{Root\ /\ shoot\ length\ in\ control(cm)} \times 100 \qquad (1)$$

3. Results and Discussion

The effect of hexane, ethyl acetate and methanol extract of *P. reticulata* on seed germination, shoot length and root length of *P. minor* is shown in table 1and figure 1a-c.

Table 1. Effect of hexane, ethyl acetate and methanol extracts of *P. reticulata* on seed germination, shoot length and root length of *P. Minor*

Extract	Concentration (μg ml^{-1})	% Germination (% Inhibition)	Shoot length (cm) (%Inhibition)	Root length (cm) (%Inhibition)
Hexane	**Control**	**90 ± 1.86 (0.00)**	**10.7 ±0.08 (0.00)**	**3.4 ± 0.16 (0.00)**
	50	56 ± 2.64 (37.77)	2.5 ±0.08 (76.63)	0.9±0.14 (73.52)
	25	57 ± 1.73 (36.66)	4.7 ±0.11 (56.07)	1.4±0.17 (58.82)
	12.5	79 ± 1.00 (12.22)	6.0 ±0.15 (43.92)	2.6±0.16 (23.52)
Ethyl acetate				
	50	56 ± 0.81 (26.66)	4.6 ± 0.09 (57.00)	1.5 ± 0.12 (55.88)
	25	63 ± 1.24 (25.55)	5.4 ± 0.09 (49.53)	1.8 ± 0.12 (47.05)
	12.5	77 ± 1.73 (15.55)	7.4 ± 0.12 (30.84)	1.9 ± 0.10 (44.11)
Methanol				
	50	66 ± 1.73 (26.66)	6.3 ± 0.11 (41.12)	1.5 ± 0.11 (55.88)
	25	67 ± 2.64 (30.00)	6.8 ± 0.09 (36.44)	2.7 ± 0.17 (20.58)
	12.5	76 ± 2.64 (14.44)	7.3 ± 0.11 (31.77)	2.9 ± 0.13 (14.70)

Mean percentage seed germination, shoot length and root length used for calculation, is an average of three replicates and standard deviation ranged from 0.81 to 2.64, 0.08 to 0.15 and 0.10 to 0.17 respectively. Values given in parentheses indicate % inhibition in terms of seed germination, shoot length and root length as compared to the control.

The above results revealed that the allelopathic efficacy of lichen extracts depends upon i) the solvent used for extraction: In general, hexane extract exhibited maximum allelopathic effect followed by ethyl acetate and methanol extracts and ii) the treatment dose: the detrimental effects of extracts are more prominent at higher

concentrations. The percentage inhibition of seed germination, shoot and root lengths by hexane, ethyl acetate and methanol extracts at different concentration was observed in the range of 12.22-37.77%, 43.92-76.63%, 23.52-73.52%; 15.55-26.66%, 30.84-57.00, 44.11-55.88% and 14.44-26.66, 31.77-41.12, 14.70-55.88% respectively. Furthermore, at maximum concentration of 50 µg ml^{-1} the percentage inhibition of seed germination, shoot and root lengths was found to be 37.77, 76.63, 73.52% by hexane extract; 26.66, 57.00, 55.88% by ethyl acetate; and 26.66, 41.12, 55.88% by methanol extract.

From comparative analysis of the data it is also evident that the extracts are more effective in reducing the early seedling growth than in suppressing the seed germination. It may be attributed to the hard impermeable seed coat which protects the seeds from outer incompatible environment. It is therefore, the weed is highly competitive and can cause significant yield losses under favourable conditions.

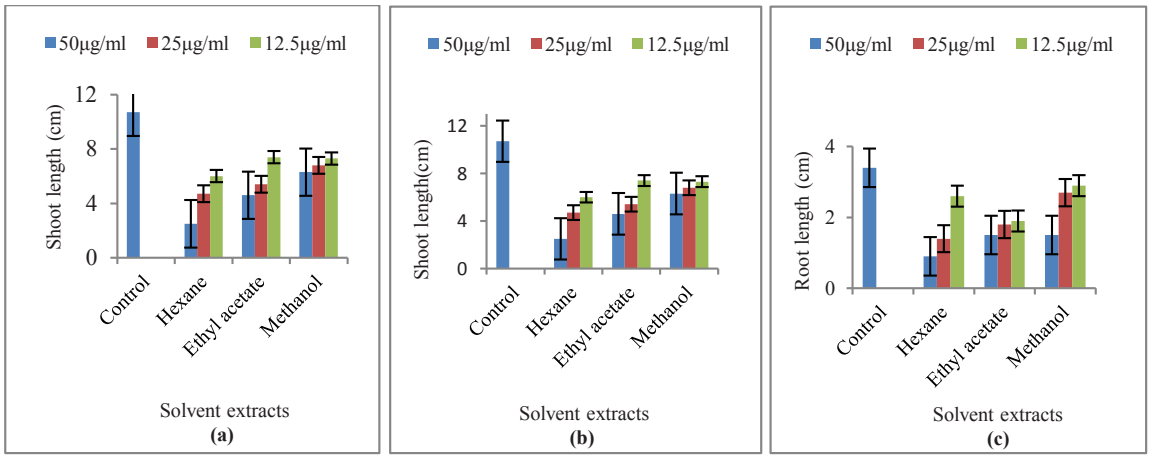

Fig. 1. Effect of hexane, ethyl acetate and methanol extract of *P. reticulata* on (a) seed germination *(b)* shoot length and (c) root length of *P. minor*

Thus, the current investigation established that hexane extract at 50 µg ml^{-1} concentration possesses highest *in vitro* allelopathic efficacy against *P. minor* indicating the semipolar nature of constituents responsible for bioactivity.

4. Conclusions

Weeds are any undesirable plants grown in field along with the main crop plants. After microbial phytopathogens, weeds are the next main agricultural yield limiting factors in most parts of the world. In particular, *Phalaris minor* Retz has been identified as a serious weed of wheat and barley fields in India, USA, Canada, Africa, Australia, France, Pakistan, Iran, Iraq and Mexico [20, 21]. Furthermore, a rice- wheat crop rotation also stimulated its emergence, growth and development [22]. Due to morphological similarity of *P. minor* with wheat, manual weeding at early stages is difficult. Synthetic herbicides are the preferred methods for its management due to their efficacy and cost effectiveness, even though, their increased use poses serious environmental hazards and public health concerns [23-25]. It provides a compelling justification for the current investigation aimed to explore newer natural resources of safer crop protectants. The results obtained highlight the potentiality of lichens as a reservoir of future agrochemicals.

References

[1] Cutler HG, Cutler SJ. *Biological active natural products: Agrochemicals,* Boca Raton, Florida, USA: CRC Press Inc.; 1999.

[2] Kowalski M, Hausner G,Michele D. Piercey-Normore. Bioactivity of secondary metabolites and thallus extracts from lichen fungi. *Mycoscience* 2011; 52 (6): 413-418.

[3] Eisenreich W, Knispel N, Beck A. Advanced methods for the study of the chemistry and the metabolism of lichens. *Phytochemistry Reviews* 2011; 10 (3): 445-456.

[4] Shukla V, Joshi GP, Rawat M S M. Lichens as a potential natural source of bioactive compounds: a review. *Phytochemistry Reviews* 2010; 9:303- 314.

[5] Boustie J, Tomasi S, Grube M. Bioactive lichen metabolites: alpine habitats as an untapped source. *Phytochemistry Reviews* 2011; 10(3): 287-307

[6] Nash TH. *Lichen Biology*, Cambridge: Cambridge University Press, 1996

[7] Taylor TN, Hass H, Wand R, Kerp H. The oldest fossil lichen. *Nature* 1995; 378: 244.

[8] (a) Lawrey, JD. Biological Role of Lichen Substances. *The Bryologist* 1986; 89(2): 111-122. (b) Lawrey J D. Lichen secondary compounds: evidence for a correspondence between antiherbivore and antimicrobial function. *The Bryologist* 1989; 92:326-328.

[9] Bjerke JW, Lerfall K, Elvebakk A. Effects of ultraviolet radiation and PAR on the content of usnic and divaricatic acids in two arctic-alpine lichens. *Photochem Photobiol Sci* 2002; 1 (9): 678-85.

[10] Bjerke JW, Joly D, Nilsen L, Brossard T. Spatial trends in usnic acid concentrations of the lichen Flavocetraria nivalis along local climatic gradients in the Arctic (Kongsfjorden, Svalbard). *Polar Biology* 2004; 27(7): 409-417.

[11] Bjerke JW, Elvebakk A, Domínguez E, Dahlback. A Seasonal trends in usnic acid concentrations of Arctic, alpine and Patagonian populations of the lichen *Flavocetraria nivalis*. *Phytochemistry* 2005; 66(3):337-44

[12] Rubio C, Fernández E, Hidalgo ME, and Quilhot W. Effects of solar UV-B radiation in the accumulatio of rhizocarpic acid in a lichen species from alpine zones of Chile. *Bol. Soc. Chil. Quím* 2002; 47(1): *67-72.*

[13] Vicente C, Ruiz JL, Estevez M.P. Mobilization of usnic acid in *Evernia prunastri* under critical conditions of nutrient availability. *Phyton: international journal of experimental botany* 1980; 39: 15-20.

[14] Hager A, Brunauer G, Türk R, Stocker-Wörgötter E. Production and Bioactivity of Common Lichen Metabolites as Exemplified byHeterodea muelleri (Hampe) Nyl. *Journal of Chemical Ecology* 2008; 34(2): 113-120

[15] Emmerich, R., Giez, I., Lange, OL, Proksch, P. Toxicity and antifeedant activity of lichen compounds against the polyphagous herbivorous insect *Spodoptera littoralis*. *Phytochemistry*1993; 33: 1389-1394.

[16] (a)Podterob A P. Chemical composition of lichens and their medical applications. *Pharmaceutical Chemistry Journal* 2008; 42(10): 582-588; (b)Huneck S. The significance of lichens and their metabolites. *Naturwissenschaften* , 1999; 86(12): 559-570,

[17] (a) Kosanić M, Ranković B, Vukojević J. Antioxidant properties of some lichen species. *Journal of Food Science and Technology* 2011; 48(5): 584-590. (b) Shrestha G, Larry L. St. Clair. Lichens: a promising source of antibiotic and anticancer drugs. *Phytochemistry Reviews* 2013; 12(1): 229-244.

[18] Goel M, Dureja P, Rani A, Uniyal P L, Laatsch H. Isolation, characterization and antifungal activity of major constituents of the Himalayan Lichen *Parmelia reticulata* Tayl. *J. Agric. Food Chem* 2011; *59* (6): 2299-2307.

[19] Goel M, SharmaP K, Dureja P, Rani A, Uniyal P L.Antifungal activity of extracts of the lichens *Parmelia reticulata, Ramalina roesleri, Usnea longissima* and *Stereocaulon himalayense*. *Arch Phytopathology Plant Protect.* 2011; *44*(13): 1300-1311.

[20] Holm L,Pacho JV, Herberger JP, Plucknett DL. A geographical atlas of world weeds, New York:Wiley 1979.

[21] Shad R, Siddiqui S, Problems Associated with Phalaris minor and Other Grass Weeds in India and Pakistan. *Experimental agriculture* 1996; 32: 151-160.

[22] Chhokar RS, Sharma RK, Singh RK and Gill SC. Herbicide resistance in littleseed canarygrass (*Phalaris minor*) and its management. *Global Issues. Paddock Action." Edited by* Unkovich M. *Proceedings of 14th Agronomy Conference, Adelaide, South Australia,* September 2008*, 21-25.*

[23] Gupta PK, Herbicides and fungicides chapter 39 in Reproductive and Developmental Toxicology (editor Gupta RC) : Academic Press; *2011*; *503-521*

[24] Bradberry SM, Watt BE, Proudfoot AT, Vale JA. Mechanisms of toxicity, clinical features, and management of acute chlorophenoxy herbicide poisoning: a review. *J Toxicol Clin Toxicol*. 2000; 38(2):111-22.

[25] Aktar W, Sengupta D, and Chowdhury A. Impact of pesticides use in agriculture: their benefits and hazards. *Interdiscip Toxicol*. 2009; 2(1): 1–12.

Maximum Bandwidth Enhancement of Current Mirror using Series-Resistor and Dynamic Body Bias Technique

Vandana NIRANJAN, Ashwani KUMAR, Shail Bala JAIN

Dept. of Electronics & Communication Engineering, Indira Gandhi Delhi Technical University for Women, Kashmere Gate, Delhi-110006, India

vandana7379@gmail.com, drashwnikumar@yahoo.com, shail_jain@rediffmail.com

Abstract. *This paper introduces a new approach for enhancing the bandwidth of a low voltage CMOS current mirror. The proposed approach is based on utilizing body effect in a MOS transistor by connecting its gate and bulk terminals together for signal input. This results in boosting the effective transconductance of MOS transistor along with reduction of the threshold voltage. The proposed approach does not affect the DC gain of the current mirror. We demonstrate that the proposed approach features compatibility with widely used series-resistor technique for enhancing the current mirror bandwidth and both techniques have been employed simultaneously for maximum bandwidth enhancement. An important consequence of using both techniques simultaneously is the reduction of the series-resistor value for achieving the same bandwidth. This reduction in value is very attractive because a smaller resistor results in smaller chip area and less noise. PSpice simulation results using 180 nm CMOS technology from TSMC are included to prove the unique results. The proposed current mirror operates at 1 Volt consuming only 102 μW and maximum bandwidth extension ratio of 1.85 has been obtained using the proposed approach. Simulation results are in good agreement with analytical predictions.*

Keywords

Body effect, dynamic body bias, cascode current mirror, low voltage, high bandwidth, low power.

1. Introduction

The current mirrors (CM) are most commonly used in signal processing and conditioning analog circuits. Low voltage current mirrors having simple circuitry are very attractive for analog integrated circuit applications where large bandwidth and low power consumption are required. The current design trend of industry to reduce the supply voltage to sub-volt supplies and minimum gate size, places challenge to analog circuit designers. The shrinking sizes of semiconductor devices in CMOS technology entail the simultaneous reduction of supply voltage and threshold voltage of MOS transistor. Since the threshold voltage of a MOS transistor is not reduced at the same rate as the power supply, it becomes increasingly difficult to design wideband current mirror circuits because of the reduced voltage headroom. Analog signal processing circuits now operating from single 1.5 V supplies and dropping, are constantly demanding higher bandwidth and speed performances of current mirrors. The current mirror bandwidth performance degrades as power supply voltage is reduced. For a given bias point, the DC accuracy requirement fixes the power-speed ratio of the current mirror circuit and the tradeoff between the bandwidth, the accuracy and the power consumption is set by technology constants [1], [2].

Various techniques have been reported for bandwidth extension of low voltage current mirrors [3–8]. Throughout the bibliography many references [9–13] can be found considering series-resistor technique [3]. This technique improves the bandwidth of a current mirror by inserting a series-resistor between the gates of the primary pair transistors of current mirror. By appropriately choosing the resistor value, zero cancels a dominant pole thereby enhancing current mirror's bandwidth. The added resistor however increases the overall noise of the circuit owing to the additional thermal noise. Also, bandwidth enhancement is much smaller if the current gain is large. Hence this technique is not suitable for low noise high frequency applications. For full monolithic integration, resistor can be made of polysilicon or a diffusion resistor. The main drawback of integrated resistor is the large tolerance of its absolute values. Even with mature process, the passive and active components can have more than 10% variations. Although a MOS transistor can be used for active implementation of series-resistor but this results in penalty of extra power consumption and increase in chip area. Under very low supply voltages, the reduction of voltage headroom poses an important limitation on the power consumption in additional passive component/circuitry for improving bandwidth. Hence other techniques must be investigated.

In this work, we have proposed a new approach for bandwidth enhancement of a low voltage CMOS current mirror. The proposed approach is based on boosting the transconductance of a MOS transistor using dynamic body bias technique, while maintaining low power consumption. This approach also results in reduction of threshold voltage

(V_{TH}) of MOS transistor utilizing body effect. We have used the proposed approach along with series-resistor technique in a low voltage cascode current mirror circuit for maximum bandwidth enhancement. The parasitic resistance and capacitance due to dynamic body biasing introduces a zero in the transfer function of the proposed current mirror. This zero cancels one of the poles thereby enhancing the bandwidth of the proposed current mirror.

The dynamic body bias technique is implemented using triple well CMOS technology which is compatible with standard CMOS process. Triple well process can be achieved at the slightly higher cost process but without increase in any chip area. A triple well structure reduces the cross-talk in mixed systems-on-chip designs and is more robust to process and well junction capacitance variations [14]. The paper is organized as follows: Section 2 introduces conventional current mirror where series-resistor technique has been used for enhancing its bandwidth. Section 3 introduces dynamic body bias technique and circuit implementation of proposed current mirror. Bandwidth analysis is carried out using small signal analysis to predict its maximum theoretical bandwidth. Simulation results are presented in Section 4. Conclusions are summarized in Section 5.

2. Conventional Current Mirror

In modern sub-micron CMOS process the g_m/g_{ds} ratio is less than 100 and consequently a significant gain error results when more of the current amplifier stages are cascaded. This gain error is usually reduced by increasing the output impedance using different cascode topologies [15]. Fig. 1 shows a low voltage cascode current mirror. Here, the input voltage (V_{in}) depends solely on the biasing conditions of M1 and minimum V_{in} required to pump input current (I_{in}) into the input port of the mirror is given as [16].

$$V_{inmin} = V_{TH1}\,. \tag{1}$$

The other important factors that establish its capability to operate in a low-voltage environment are the minimum supply voltage and output voltage given by the following expressions

$$V_{DDmin} = V_{TH1} + V_{DSsat5}\,, \tag{2}$$

$$V_{outmin} = V_{DSsat2} + V_{DSsat3}\,. \tag{3}$$

Transistors M2 and M3 form output transistor cascode pair and due to the independent biasing of the transistor M3, provided by M4, the output voltage swing is not affected. Hence the output impedance of the structure can be increased to have high gain structures at low voltage levels. The input resistance of the mirror is decided by the transconductance (g_{m1}) of M1.The expression for input and output resistances is given as

$$R_{in} \cong \frac{1}{g_{m1}}, \tag{4}$$

$$R_{out} \cong g_{m3}\,.r_{o2}.r_{o3}\,. \tag{5}$$

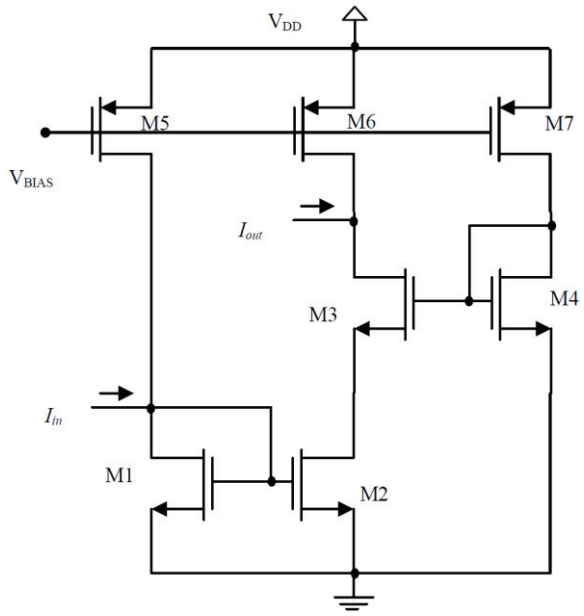

Fig. 1. Low voltage cascode current mirror.

Cascode current mirror suppress the effect of channel-length modulation and improves input-output isolation as there is no direct coupling from the output to input. The simple circuit structure of current mirror in Fig. 1 ensures a higher bandwidth. Its DC gain and -3dB frequency is given by the following expression [13]

$$Gain = \frac{g_{m2}}{g_{m1}}, \tag{6}$$

$$\omega_0 = \sqrt{\frac{g_{m1}(g_{m3})}{2\,C_{gs1}C_{gs3}}}\,. \tag{7}$$

From (7) we observe that the ratio between gate transconductance and gate-to-source capacitance of a MOS transistor dominates the frequency behavior. Thus g_m and C_{gs} are the main parameters that have major influence over the current mirror bandwidth.

The series-resistor technique to improve the bandwidth performance of low voltage cascode current mirror is shown in Fig. 2. Henceforth throughout this paper, we have considered current mirror in Fig. 2 as conventional current mirror under study. The introduction of R to the primary pair transistors of the current mirror results in a zero which cancels one of the poles when $R = 1/g_{m1}$ is selected, thereby enhancing its bandwidth. The expressions for DC gain and -3dB frequency is given as [13]

$$Gain_{CCM} = \frac{g_{m2}}{g_{m1}}, \tag{8}$$

$$\omega_{0,CCM} = \sqrt{\frac{g_{m1}(g_{m3})}{C_{gs1}C_{gs3}}}\,. \tag{9}$$

Comparing (7) and (9) we obtain

$$\omega_{0,CCM} = \sqrt{2}\,\omega_0\,. \tag{10}$$

Thus from (6), (8) and (9), it is evident that series-resistor technique enhances the bandwidth by factor $\sqrt{2}$ without compromising DC gain.

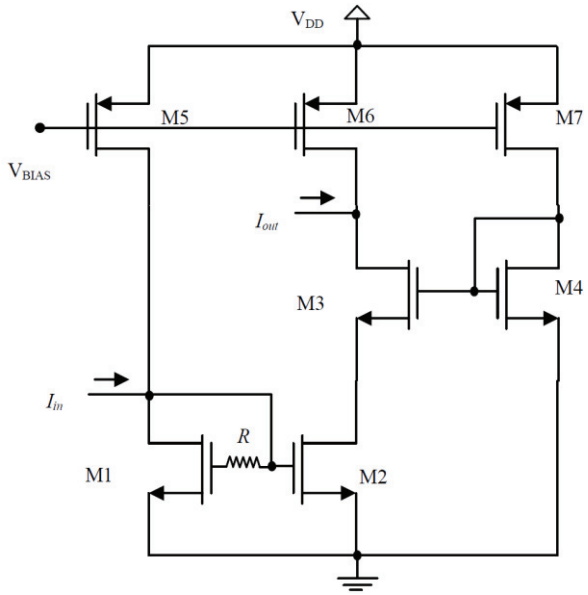

Fig. 2. Conventional current mirror.

We observe from Fig. 2 that in conventional CM, M3 suffers from body effect. In most of the current mirror analysis, generally body effect is neglected either for the sake of simplicity or due to its negligible effect, at higher power supply voltage. Some inaccuracy nevertheless arises due to the body effect present in a MOS transistor. Due to body effect, the ideal square-law behavior of MOS transistor in saturation region of operation approaches more closely to an ideal linear transfer function. As a result, high-order harmonics introduced to the drain current expression results in an error in its transconductance [17]. Due to this effect, there is non-negligible attenuation, which may not be neglected in the submicron circuits operating at low power supply voltage.

With the progressive reduction of MOS transistors minimum dimension and their associated supply voltages, use of body effect is becoming an attractive opportunity for improving the performance of low voltage analog integrated circuits [18]. In this paper we have utilized body effect in M3 using dynamic body bias technique for improving bandwidth and output resistance of conventional CM.

3. Proposed Current Mirror

In this section, we have briefly discussed dynamic body bias technique and a small signal model of MOS transistor biased with this technique is proposed. The circuit implementation of proposed current mirror using dynamic body biasing is suggested. Bandwidth analysis of proposed CM shows that the dynamic body bias technique has enhanced its bandwidth and output resistance.

3.1 Dynamic Body Bias Technique

For low voltage low power design, various techniques have been reported in the literature to overcome the difficulties introduced by the relatively high threshold voltage of a MOS transistor. One such reported technique in literature is bulk-driven technique, where input signal is applied at body/bulk terminal instead of gate terminal, after biasing the gate terminal to a sufficient voltage; thus the threshold voltage in this setup is removed from signal path. Unfortunately, the transconductance of a bulk-driven MOS transistor is substantially smaller and the equivalent input referred noise is higher than that of a conventional gate-driven MOS transistor, which may result in lower gain bandwidth and worse frequency response [19]. Another circuit technique which provides an important solution to the threshold voltage scaling limitation is body bias technique, which modulates the threshold voltage of a MOS transistor electronically using body effect, without any technology modification. Body effect enables a variety of effective body bias techniques [20].

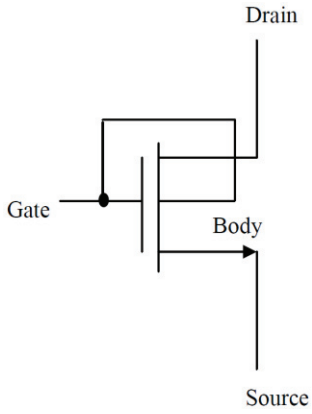

Fig. 3. MOS transistor using dynamic body bias technique.

In this work, our proposed approach is based on using both bulk/body and gate terminals of a MOS transistor as signal input. This concept, first presented in [21] is shown in Fig. 3. Due to gate and body terminals shorted together, threshold voltage (V_{TH}) of the transistor becomes function of input signal. With change in input, bias voltage at body terminal also changes dynamically as input changes hence known as dynamic body bias technique. The relation between input signal and V_{TH} is described using the following equation [22]

$$V_{TH} = V_{TH0} + \gamma\left(\sqrt{\psi_s + V_{SB}} - \sqrt{\psi_s}\right). \qquad (11)$$

where V_{TH} is threshold voltage due to body effect i.e. applied V_{SB} , V_{TH0} is the threshold voltage when V_{SB} is zero and mainly depends on the manufacturing process. γ is typically equal to 0.4 $V^{0.5}$ and depends on the gate oxide capacitance, silicon permittivity, doping level and other parameters. ψ_s is surface potential in strong inversion and typically is 0.6 V. ψ_s in (11) is assumed to $|\ 2\Phi_F\ |$, where Φ_F is Fermi potential.

In dynamic body bias technique, $V_{GS} = V_{BS}$ is maintained all the time and same bias voltage is applied at gate and body terminals. Here source-body junction gets slightly forward biased when input signal increases. Although source-body junction parasitic diode is slightly forward biased but any substantial conducting pn junction current is

absent as V_{TH} decreases due to the body effect as predicted by (11). The potential in the channel region is strongly controlled by the gate and body terminals, leading to a high transconductance owing to faster current transport.

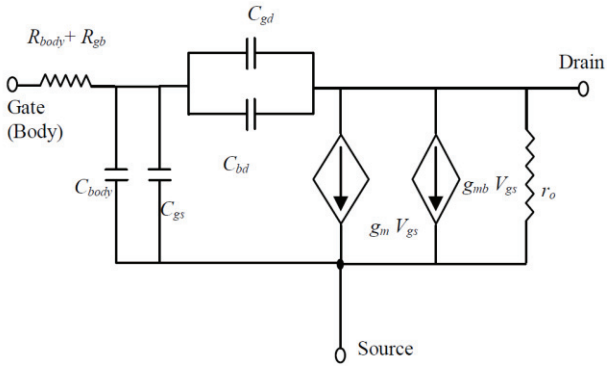

Fig. 4. Proposed small signal model of MOS transistor using dynamic body bias technique.

The proposed small signal equivalent circuit of MOS transistor using dynamic body biasing is shown in Fig. 4. It has two transconductances, the gate transconductance g_m and body transconductance g_{mb}. The relation between both transconductances is [22]

$$\frac{g_{mb}}{g_m} = \eta \approx (0.2 - 0.4) \tag{12}$$

where η is the specific parameter and its value depends on bias conditions and on the technology used. Dynamic body bias increases the effective transconductance from g_m to $(g_m + g_{mb})$ as $V_{SB} = V_{GS}$ is maintained all the time and both transconductance contributes to the conduction current. The effective transconductance is obtained as

$$g_{m,eff} = g_m(1 + \eta)\ . \tag{13}$$

Due to higher effective transconductance, the input referred noise power spectral density is also reduced, defined as

$$v_{noise}^2(f) = \frac{i_{ni}^2}{(g_m + g_{mb})^2} \tag{14}$$

where i^2_{ni} is the total drain current generated by noise sources.

The bulk of a MOS transistor has finite resistance and additional parasitic capacitance. The effective input capacitance from Fig. 4 is defined as

$$C_{eff} \approx C_{gs} + C_{body} \tag{15}$$

where C_{body} is body capacitance and C_{gs} is gate capacitance. The effective input resistance from Fig. 4 is defined as

$$R_{eff} \approx R_{gb} + R_{body} \tag{16}$$

where R_{gb} is gate-body contact resistance and R_{body} is bulk/body resistance.

Dynamic body bias technique is implemented using triple well CMOS technology hence latch-up is absent. This technique exhibits merits over other body bias techniques in terms of higher transconductance-to-drain current ratio and elimination of additional circuitry for bias voltage generation.

3.2 Circuit Implementation

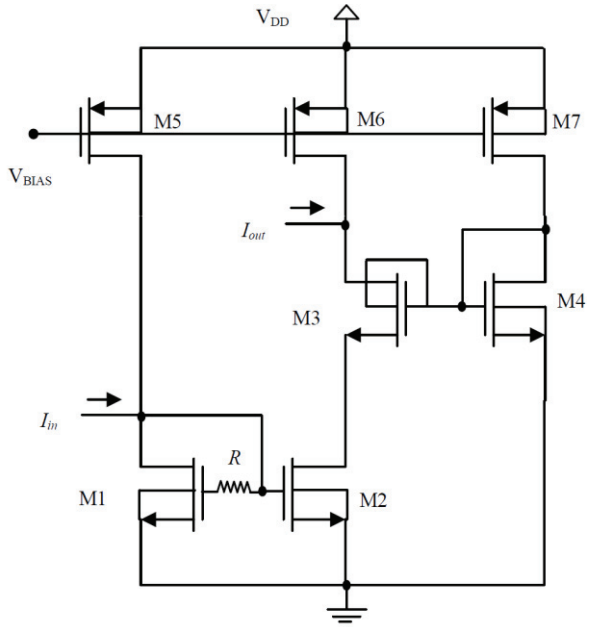

Fig. 5. Proposed current mirror.

The current mirrors using MOS transistors operating in saturation mode have higher transconductance than those based on MOS transistors operating in triode or sub-threshold mode. This leads to higher bandwidth and better input and output impedances. A convenient way to bring MOS transistor into saturation is by using body effect [23]. Fig. 5 shows the circuit implementation of proposed CM in which we have applied dynamic body bias technique in M3 and thus for any variation in load, M3 always remains in saturation, utilizing body effect. For remaining transistors, body and source terminals are connected together.

A current mirror may be characterized as having output impedance which affects the accuracy of the current replicated in the current mirror. High output impedance in current mirrors is required for accurate replication of currents. It can be seen from (4), (5) and (13) that due to dynamic body bias in M3, input resistance of proposed CM remains unaffected whereas output resistance is increased, given as

$$R_{out} \cong g_{eff}\ .\ r_{o2}.r_{o3}\ . \tag{17}$$

3.3 Bandwidth Analysis

The small signal model for bandwidth calculation of proposed CM is shown in Fig. 6. In the small signal analysis of proposed current mirror, short channel effects like drain-induced barrier lowering, hot carriers effects, velocity saturation are neglected for the sake of simplicity of hand calculations with the goal to give an idea on the order of magnitude of bandwidth improvement rather than finding

an exact value. The notations used in the analysis are as follows: C_{gsi} is gate-source capacitance, V_{gsi} is gate-source voltage and g_{mi} is gate transconductance for Mi where i = 1 to 4. Here, g_{mb3} is body transconductance, C_{eff} is total input capacitance and R_{eff} is total input resistance of M3. R is series-resistor between gates of M1 and M2.

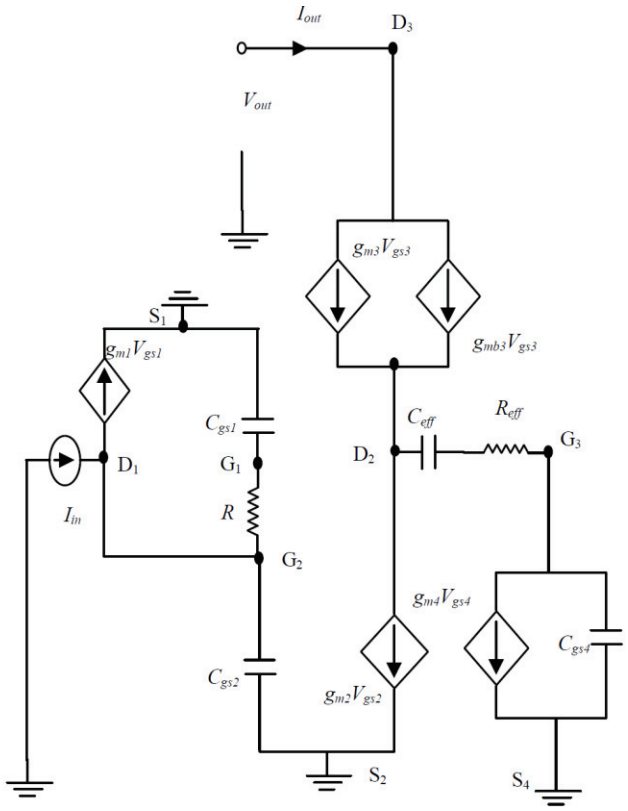

Fig. 6. Small signal model for calculating bandwidth of proposed CM.

Neglecting output conductance and capacitance in Fig. 6, equation for node D1 is given as

$$I_{in}(s) = g_{m1}V_{gs1} + s\,C_{gs2}V_{G2} + \frac{V_{G2}-V_{G1}}{R}. \quad (18)$$

Since both R and C_{gs1} are in series we get

$$\frac{V_{G2}-V_{G1}}{R} = V_{G1}s\,C_{gs1}. \quad (19)$$

Simplifying (19) we get

$$V_{G1} = \frac{V_{G2}}{(1+sRC_{gs1})}. \quad (20)$$

Substituting (19) in (18) we get

$$I_{in}(s) = V_{G1}\left(g_{m1} + s\,C_{gs1}\right) + s\,C_{gs2}V_{G2}. \quad (21)$$

Substituting (20) in (21) we get

$$V_{G2} = V_{gs2} = I_{in}(s)\left[\frac{(1+sRC_{gs1})}{g_{m1}+s\,C_{gs1}+s\,C_{gs2}(1+sRC_{gs1})}\right] \quad (22)$$

Writing equation at node S3

$$g_{m2}V_{gs2} = (g_{m3}+g_{mb3})V_{gs3} + \frac{V_{gs3}}{R_{eff}+\frac{1}{sC_{eff}}} \quad (23)$$

Because of mirror action $V_{gs1} = V_{gs2}$ and substituting (22) in (23) we get

$$I_{in}(s)\left[\frac{g_{m2}(1+sRC_{gs1})}{g_{m1}+s\,C_{gs1}+s\,C_{gs2}(1+sRC_{gs1})}\right] = \left(g_{m3}+g_{mb3}+\frac{1}{R_{eff}+\frac{1}{sC_{eff}}}\right)V_{gs3} \quad (24)$$

Writing equation for node D3 we get

$$I_{out}(s) = g_{m3}V_{gs3} + g_{mb3}V_{gs3}. \quad (25)$$

Simplifying (25) we get

$$V_{gs3} = \frac{I_{out}(s)}{g_{m3}+g_{mb3}}. \quad (26)$$

Substituting (26) in (24) we obtain transfer function as

$$\frac{I_{out}(s)}{I_{in}(s)} = \frac{g_{m2}(1+sRC_{gs1})(g_{m3}+g_{mb3})}{\left[g_{m1}+s\,C_{gs1}+s\,C_{gs2}(1+sRC_{gs1})\right]\left(g_{m3}+g_{mb3}+\frac{1}{R_{eff}+\frac{1}{sC_{eff}}}\right)} \quad (27)$$

Simplifying and rearranging (27) we get

$$\frac{I_{out}(s)}{I_{in}(s)} = \left[\frac{g_{m2}(g_{m3}+g_{mb3})\,RC_{gs1}\left(s+\frac{1}{RC_{gs1}}\right)}{RC_{gs1}C_{gs2}\left\{s^2+s\left(\frac{C_{gs1}+C_{gs2}}{RC_{gs1}C_{gs2}}\right)+\frac{g_{m1}}{RC_{gs1}C_{gs2}}\right\}}\right] \times \left[\frac{R_{eff}C_{eff}\left(s+\frac{1}{R_{eff}C_{eff}}\right)}{\{C_{eff}+R_{eff}C_{eff}(g_{m3}+g_{mb3})\}\left[s+\frac{g_{m3}+g_{mb3}}{C_{eff}+R_{eff}C_{eff}(g_{m3}+g_{mb3})}\right]}\right]. \quad (28)$$

Assuming M1 and M2 to be matched and substituting $C_{gs1} = C_{gs2}$ in (28), we get

$$\frac{I_{out}(s)}{I_{in}(s)} = \left[\frac{g_{m2}(g_{m3}+g_{mb3})\,RC_{gs1}\left(s+\frac{1}{RC_{gs1}}\right)}{RC_{gs1}{}^2\left\{s+\frac{1}{RC_{gs1}}\right\}^2}\right] \times \left[\frac{R_{eff}C_{eff}\left(s+\frac{1}{R_{eff}C_{eff}}\right)}{\{C_{eff}+R_{eff}C_{eff}(g_{m3}+g_{mb3})\}\left[s+\frac{g_{m3}+g_{mb3}}{C_{eff}+R_{eff}C_{eff}(g_{m3}+g_{mb3})}\right]}\right] \quad (29)$$

We observe from (29) that the introduction of R in the circuit has resulted in a zero at Z_R = -1/ RC_{gs1} and dynamic body bias technique has resulted in a zero at Z= -1/ $R_{eff}\,C_{eff}$.

Substituting $R = 1/g_{m1}$ in (29) then zero cancels one of the poles and simplified transfer function is written as

$$\frac{I_{out}(s)}{I_{in}(s)} = \left[\frac{g_{m2}(g_{m3}+g_{mb3})}{C_{gs1}\left(s+\frac{g_{m1}}{C_{gs1}}\right)}\right] \times \left[\frac{R_{eff}\left(s+\frac{1}{R_{eff}C_{eff}}\right)}{\{1+R_{eff}(g_{m3}+g_{mb3})\}\left[s+\frac{g_{m3}+g_{mb3}}{C_{eff}\{1+R_{eff}(g_{m3}+g_{mb3})\}}\right]}\right]. \quad (30)$$

Assuming $R_{eff}(g_{m3}+g_{mb3}) >> 1$, (30) can be further simplified as

$$\frac{I_{out}(s)}{I_{in}(s)} = \left[\frac{g_{m2}(g_{m3}+g_{mb3})}{C_{gs1}\left(s+\frac{g_{m1}}{C_{gs1}}\right)}\right]\left[\frac{\left(s+\frac{1}{R_{eff}C_{eff}}\right)}{(g_{m3}+g_{mb3})\left(s+\frac{1}{R_{eff}C_{eff}}\right)}\right]. \quad (31)$$

We observe from (31) that zero cancels one of the poles and transfer function becomes

$$\frac{I_{out}(s)}{I_{in}(s)} = \left(\frac{g_{m2}}{g_{m1}}\right)\frac{\frac{g_{m1}}{C_{gs1}}}{\left(s+\frac{g_{m1}}{C_{gs1}}\right)}. \quad (32)$$

Comparing (32) with standard equation of first order transfer function given as

$$T(s) = \frac{K}{1+\frac{s}{\omega_0}} \quad (33)$$

where ω_0 is -3dB frequency. DC gain and -3dB frequency of proposed CM is obtained as

$$Gain_{PCM} = \frac{g_{m2}}{g_{m1}}, \quad (34)$$

$$\omega_{0,PCM} = \frac{g_{m1}}{C_{gs1}}. \quad (35)$$

On the basis of analytical predictions for bandwidth from (35) and comparing it with (9), it is observed that the proposed approach enhances the bandwidth of current mirror. It is evident from the analysis that the bandwidth enhancement mechanism of dynamic body bias technique and series-resistor techniques differs fundamentally. This suggests that both techniques can be employed simultaneously for maximum bandwidth enhancement. From (5) and (17) we see that output resistance is also improved using the proposed approach as effective transconductance of M3 has increased. The dynamic body bias technique does not affect the current mirror's DC gain as evident from (8) and (34).

4. Simulation Results

Conventional current mirror in Fig. 2 and proposed current mirror in Fig. 5 have been designed in 180 nm CMOS technology from TSMC. The current mirror (CM) circuits have been simulated at V_{DD} = 1 V and V_{BIAS} = 0.35 V. All the transistors have the same channel length L = 180 nm and width parameters are given in Tab. 1.

MOS transistor	Type	W(µm)
M1	NMOS	8.3
M2,M3	NMOS	9
M4	NMOS	0.36
M5	PMOS	0.36
M6,M7	PMOS	9

Tab. 1. Width parameters for various transistors.

Fig. 7 shows simulated frequency response of conventional and proposed current mirror for R = 1 kΩ. -3dB frequency of conventional CM and proposed CM is obtained as 344.224 MHz and 538.987 MHz respectively with 0 dB peaking. Thus dynamic body bias technique boosts the bandwidth by a factor of 1.56 (R = 1 kΩ). Fig. 8 shows transfer characteristics. The approx. range of proposed CM is 0 to 250 µA. The simulated static power consumption of proposed CM is 0.102e-4 W.

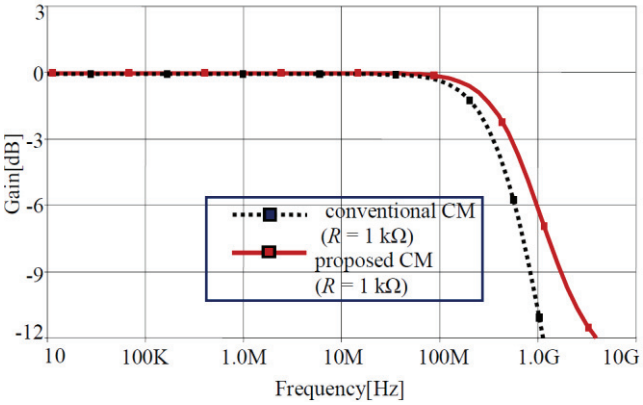

Fig. 7. Frequency response of conventional and proposed current mirror.

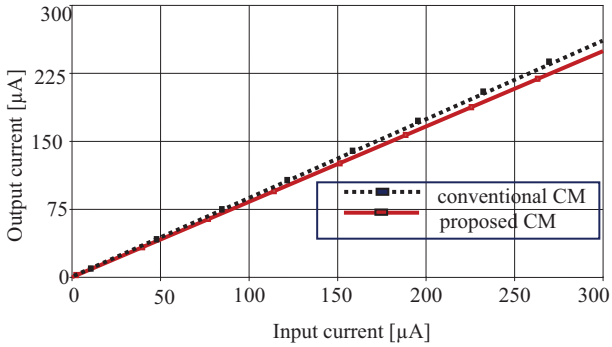

Fig. 8. Transfer characteristics of proposed current mirror.

The parasitic capacitances in CMOS circuits introduce zeros which results in peaks in frequency response. To maximize the bandwidth and avoid ringing in time domain response, the series-resistor is sized based on the criterion of the critical damping. Fig. 9 shows frequency behavior of conventional CM when R is varied from 1 kΩ to 60 kΩ, detailed in Tab. 2.

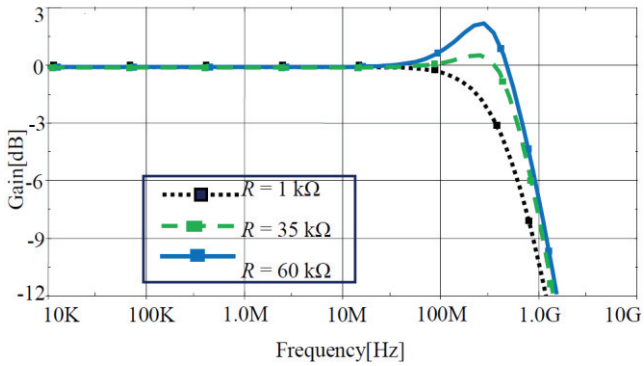

Fig. 9. Variation in frequency response of conventional current mirror with R.

R (kΩ)	Conventional CM (MHz)	Peaking (dB)	Proposed CM (MHz)	Peaking (dB)	BWER (bandwidth extension ratio)
1	344.224	0	538.987	0	1.565
5	370.186	0	608.429	0	1.643
10	417.881	0	765.741	0	1.832
15	471.719	0	875.195	0	1.855
20	526.081	0	941.204	0.245	1.789
25	565.759	0	964.296	0.766	1.704
30	586.706	0.221	976.053	1.263	1.663
35	601.100	0.580	976.053	1.727	1.623
40	608.429	0.961	976.053	2.148	1.604
45	615.848	1.331	976.053	2.528	1.585
50	615.848	1.658	976.053	2.835	1.585
55	615.848	1.947	976.053	>3	1.585
60	615.848	2.216	976.053	>3	1.585

Tab. 2. Comparison of -3dB frequency of conventional and proposed current mirror(CM) for different values of *R*.

It is observed from the table that the bandwidth increases as value of R increases and there is no peaking in frequency response up to $R = 25$ kΩ. The maximum bandwidth obtained without peaking and with peaking for conventional CM is 565.759 MHz and 615.848 MHz respectively.

Fig. 10 shows frequency behavior of proposed CM when R is varied from 1 kΩ to 50 kΩ, detailed in Tab. 2. It is observed from the table that the bandwidth increases as value of R increases and there is no peaking in frequency response up to $R = 15$ kΩ. The maximum bandwidth obtained without peaking and with peaking for proposed CM is 875.195 MHz and 976.053 MHz respectively.

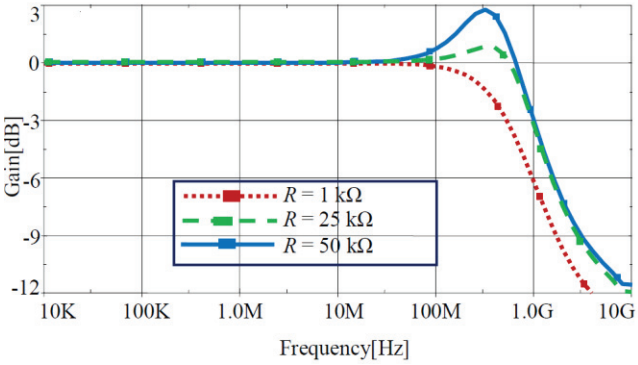

Fig. 10. Variation in frequency response of proposed current mirror with *R*.

It is seen from Tab. 2 that about 600 MHz bandwidth in conventional CM is obtained when $R = 45$ kΩ is used. In proposed CM the same bandwidth of about 600 MHz is achieved for $R = 5$ kΩ only. This reduction in value of R is very attractive because a smaller resistor results in smaller chip area and less noise. Further resistors with a smaller parasitic capacitance, such as non-silicide poly resistors, may be preferred over diffusion resistors for reducing peaking and achieving higher bandwidth.

It is observed from Tab. 2 that maximum bandwidth which can be achieved using dynamic body bias technique, without peaking, in the proposed CM is 875.195 MHz for $R = 15$ kΩ. For conventional CM, bandwidth of 471.719 MHz is obtained for $R = 15$ kΩ. Thus maximum BWER of 1.85 is obtained using dynamic body bias technique without peaking.

A current mirror having excellent static performance is more preferable for biasing applications. For signal processing applications, current mirrors lie along the signal path of a circuit and must have good dynamic performance. Fig. 11 shows simulated responses of the proposed and conventional current mirror to a step change in I_{in} from 25 µA to 175 µA. From this plot, it is evident that the step response of the proposed CM is much faster than that of the conventional CM.

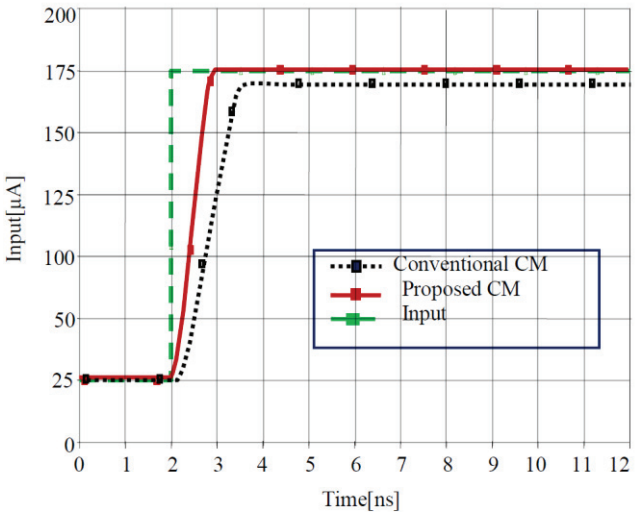

Fig. 11. Transient response of proposed current mirror.

Fig. 12 shows simulated frequency response of CM in Fig. 1, i.e. without any bandwidth extension technique and -3dB frequency of 340.341 MHz is obtained.

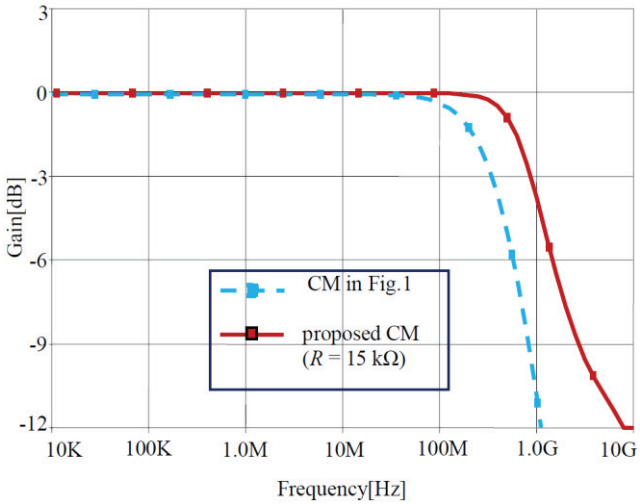

Fig. 12. Frequency response of proposed current mirror and current mirror (Fig. 1) without any bandwidth extension technique.

Tab. 4 compares the bandwidth extension ratio (BWER) achieved using series-resistor technique and combination of series resistor and dynamic body bias technique for $R = 15$ kΩ, without peaking (as observed in Tab. 2). It

is evident from Tab. 4 that BWER of 1.38 is obtained using series-resistor technique and BWER of 2.57 is obtained when both dynamic body bias technique and series-resistor technique are used simultaneously in low voltage cascode current mirror shown in Fig. 1.

Parameters	Conventional current mirror (Fig. 2)	Proposed current mirror(Fig. 5)
Supply voltage (V)	1	1
CMOS technology (nm)	180	180
Simulated maximum bandwidth without peaking (MHz)	565.759 (for R = 25 kΩ)	875.195 (for R = 15 kΩ)
Range (μA)	262	250
Input resistance (kΩ)	1.381	1.381
Output resistance (kΩ)	561.382	817.331
Power dissipation (W)	0.104e-4	0.102e-4

Tab. 3. Comparison of simulated parameters for conventional and proposed current mirror.

Parameter	Current mirror in Fig. 1	Bandwidth extension using only series-resistor technique (Fig. 2)	Bandwidth extension using both dynamic body bias technique and series-resistor technique simultaneously (Fig. 5)
-3dB frequency (MHz)	340.341	471.719	875.195
BWER obtained for CM in Fig. 1 without peaking for R = 15 kΩ		1.38	2.57

Tab. 4. Comparison of BWER using series-resistor and proposed technique.

5. Conclusion

In this paper, the authors have revealed a new approach of enhancing the bandwidth of a low voltage CMOS current mirror using dynamic body bias technique. The unique feature of this biasing technique is that no additional circuitry is required for bias voltage generation. The proposed approach boosts the bandwidth of the current mirror by a factor of 1.85 and output resistance by factor 1.45 at low supply voltage of 1 volt. The proposed approach does not add any noise owing to higher transconductance of MOS transistor. In emerging CMOS technologies, analog integrated circuits containing passive components are less preferred. It is due to the difficulty faced in fabricating high quality passive devices with tightly-controlled values or a reasonable physical size. This proposed approach reduces the value of series-resistor for achieving same bandwidth performance. This reduction in value of R is very attractive because a smaller resistor results in smaller chip area and less noise. It is pertinent to mention that the dynamic body bias technique virtually has no effects on the overall power consumption of the proposed current mirror and therefore any improvement is not at the expense of increased power consumption. The proposed approach is particularly attractive for low voltage CMOS current mirrors for higher bandwidth performance without degrading overall noise.

References

[1] RAMÍREZ-ANGULO, J., CARVAJAL, R. G., TORRALBA, A. Low supply voltage high-performance CMOS current mirror with low input and output voltage requirements. *IEEE Transactions on Circuits and Systems—II: Express Briefs*, 2004, vol. 51, no. 3, p. 124-129.

[2] PETERSON, K. D., GEIGER, R. L. Area/bandwidth tradeoffs for CMOS current mirrors. *IEEE Transactions on Circuits and Systems*, 1986, vol. CAS-33, no. 1, p. 667-669.

[3] VOO, T., TOUMAZOU, C. High-speed current mirror resistive compensation technique. *IEE Electronics Letters*, 1995, vol. 31, no. 4, p. 248–250.

[4] VOO, T., TOUMAZOU, C. Precision temperature stabilized tunable CMOS current-mirror for filter applications. *IEE Electronics Letters*, 1996, vol. 32, no. 2, p. 105–106.

[5] BENDONG, S., YUAN, F. A new inductor series-peaking technique for bandwidth enhancement of CMOS current-mode circuits. *Analog Integrated Circuits and Signal Processing*, 2003, vol. 37, p. 259–264.

[6] YUAN, F. Low voltage CMOS current-mode circuits: topology and characteristics. *IEE Proc-Circuits Devices Systems*, 2006, vol. 153, no. 3, p. 219–230.

[7] ITAKURA, T., IIDA, T. A feedforward technique with frequency dependent current mirrors for low-voltage wideband amplifier. *IEEE Journal of Solid State Circuits*, 1996, vol. 31, no. 6, p. 847 to 850.

[8] RAJ, N., SINGH, A. K., GUPTA, A. K. Low-voltage bulk-driven self-biased cascode current mirror with bandwidth enhancement. *IEE Electronics Letters*, 2014, vol. 50, no. 1, p. 23–25.

[9] TIKYANI, M., PANDEY, R. A new low-voltage current mirror circuit with enhanced bandwidth. In *Proceedings of the International Conference on Computational Intelligence and Communication Networks*. 2011, p. 42–46.

[10] GUPTA, M., MALHOTRA, A., MALIK, A. Low-voltage current mirror with extended bandwidth. In *Proc. of the IEEE 5th India International Conference on Power Electronics*, 2012, p. 1–5.

[11] SHARMA, S., RAJPUT, S. S., MANGOTRA, L. K., JAMUAR, S. S. FGMOS current mirror: behaviour and bandwidth enhancement. *Analog Integrated Circuits and Signal Processing*, 2006, vol. 46, no. 3, p. 281–286.

[12] GUPTA, M., SINGH, U., SRIVASTAVA, R. Bandwidth extension of high compliance current mirror by using compensation methods. *Active and Passive Electronic Components*, vol. 2014, Article ID 274795, 8 pages.

[13] GUPTA, M., AGGARWAL, P., SINGH, P., JINDAL, N. K. Low voltage current mirrors with enhanced bandwidth. *Analog Integrated Circuits and Signal Processing*, 2009, vol. 59, p. 97–103.

[14] NIRANJAN, V., KUMAR, A., JAIN, S. B. Triple well subthreshold CMOS logic using body-bias technique. In *Proceedings of the IEEE International Conference on Signal Processing, Computing and Control*, 2013, p. 1–6.

[15] RAZAVI, B. *Design of Analog CMOS Integrated Circuits.* 2nd ed., Tata McGraw-Hill Publishing Company Limited, 2002.

[16] KOLIOPOULOS, C., PSYCHALINOS, C. A comparative study of the performance of the flipped voltage follower based low voltage current mirror. In *Proceedings of the IEEE International Symposium on Signals, Circuits and Systems*, 2007, p. 1–4.

[17] ZHU, X., SUN, Y. Low-distortion low-voltage operational transconductance amplifier. *IEE Electronics Letters*, 2008, vol. 44, no. 25, p. 1434–1436.

[18] MONSURRÒ, P., PENNISI, S., SCOTTI, G., TRIFILETTI, A. Exploiting the body of MOS devices for high performance analog design. *IEEE Circuits and Systems Magazine*, Fourth Quarter, 2011, p. 8–23.

[19] KHATEB, F., DABBOUS, S. B. A., VLASSIS, S. A survey of non-conventional techniques or low-voltage low-power analog circuit design. *Radioengineering*, 2013, vol. 22, no. 2, p. 415–427.

[20] NIRANJAN, V., GUPTA, M. Body biasing - a circuit level approach to reduce leakage in low power CMOS circuits. *Journal of Active and Passive Electronic Devices*, 2011, vol. 6, no. 1-2, p. 89–99.

[21] ASSADERAGHI, F., SINITSKY, D., PARKE, S. A., ET AL. Dynamic threshold voltage MOSFET (DTMOS) for ultra low voltage VLSI. *IEEE Transactions on Electron Devices*, 1997, vol. 44, no. 3, p. 414–422.

[22] TSIVIDIS, Y. P. *Operation and Modeling of the MOS Transistor*. New York: Mc-Graw Hill, 1987.

[23] LEDESMA, F., GARCIA, R., RAMIREZ ANGULO, J. Comparison of new and conventional low voltage current mirrors. In *Proceedings of the 45th Midwest Symposium on Circuits and Systems*, 2002, p. 49–52.

About Authors ...

Vandana NIRANJAN was born in 1979 and received her B.Tech. in Electronics & Communication Engineering from Government Engineering College, Bhopal, India in 2000 and her M.Tech degree in Semiconductor Devices & VLSI Technology from Indian Institute of Technology (IIT), Roorkee in March 2002. She joined the Department of Electronics and Communication Engineering, Indira Gandhi Delhi Technical University for Women, New Delhi, in July 2002 as Asst. Professor. At present she is pursuing research in the area of MOSFET body bias techniques. Her teaching interest includes VLSI circuit design and low voltage CMOS analog integrated circuits. She is a member of IEEE and Women in Engineering, USA.

Ashwani KUMAR was born in 1969 and received his B.E. in Electronics & Communication Engineering from Delhi College of Engineering, Delhi University in the year 1991 and his M.E. in Electronics & Communication Engineering from Delhi College of Engineering, Delhi University in the year 1993. He received his Ph.D. in the field of Signal Processing from Delhi College of Engineering, Delhi University in the year 2000. From October 1991 to January 2008, he has rich industry experience as Senior Program Manager in Centre for Development of Telematics, Delhi, Telecom Technology Centre of Government of India Centre, Ministry of Communication and Information Technology, Government of India. Since February 2008, he joined Indira Gandhi Delhi Technical University for Women, New Delhi as Professor. At present he is the Head of the Electronics and Communication Engineering Department. He has published a large number of papers in national and international journals. His teaching and research interests are signal processing and low voltage analog circuits. He is a member of IEEE, USA.

Shail Bala JAIN was born in 1950 and received her B.E in Electronics & Communication Engineering from Delhi College of Engineering, Delhi University and her M.Tech. in Electronics and Communication Engineering from Indian Institute of Technology (IIT), Delhi. She received her Ph.D in the field of Signal Processing from Delhi University. From 1971 till Oct. 2002 she has 31 years of teaching experience in the Department of Electronics and Communication Engineering, Delhi College of Engineering. At present she is a Professor, Electronics and Communication Engineering, Indira Gandhi Delhi Technical University for Women, New Delhi. A life fellow of IETE and a senior member of IEEE, USA, she is co-author of two books, (i) Linear Integrated Circuits, (ii) Electronics Devices and Circuits. She has published a large number of papers in national and international journals. Her field of interest is integrated circuits and signal processing.

INTERNATIONAL JOURNAL OF ENGINEERING RESEARCH & INFORMATICS

ISSN NO: 2348-6481

Vol. 1, Issue 7, Agust 2014

Performance Analysis of Combined Cycle Gas Turbine for Frequency Deviation and Temperature Control

Naimul Hasan[a], B.B. Arora[b] , J. N. Rai[c]

[a] Associate Professor,Department of Electrical Engineering, Jamia Millia Islamia,New Delhi,India

[b]Associate Professor, Department of Mechanical Engineering, Delhi Technological University,Delhi,India

[c]Research Scholar,Department of Electrical Engineering, Jamia Millia Islamia,New Delhi,India

Email ID of Corresponding author:jnrai.phd@gmail.com

***ABSTRACT:*A combined cycle power plant combines a gas turbine and a steam turbine and to achieve high energy efficiency. The subject of this project is to develop a single-shaft combined cycle plant model and analyse its response to frequency and electrical load deviations. Stability of frequency control and the consequences of overheat control are investigated. In our analysis, a SIMULINK model for a single-shaft combined cycle power plant was developed along with the transfer function model of load frequency and temperature control loop. This work observes the effect of frequency and temperature on the stability of the power plant. Since most of the loads are induction type load and the induction motor speed is directly proportional to frequency, the frequency has to be kept within certain limits. Low temperature causes lower efficiency of the heat recovery boiler and temperature higher than allowed, reduces the life of the equipment. Consequently, the temperature has to be regulated for safe operation of the power plant.**

Keywords: Energy Efficiency, Frequency Control, SIMULINK, Temperature Control

I INTRODUCTION

The energy mix of the electricity grid in India has changed greatly over the last few decades. An increasing proportion of combined cycle gas turbine (CCGT) units are now being utilized for auxiliary services, such as frequency response.

Combined Cycle is based on a simple principle, burning gas in a gas turbine produces not only power – which can be converted to electric power by a coupled generator but also very hot flue gases. Diverting these flue gases through a water-cooled heat exchanger generates steam, which can be turned into electric power with a coupled steam turbine and generator. This set-up consisting of Gas Turbine, is called a combined cycle power plant. Such type of power plant is being increasingly installed in places where there is access to significant quantities of natural gas. Such a power plant produces high power outputs at high efficiencies and with low emissions.

Power output of the steam turbine is typically 1/3 of the total output of the total power output of the combine cycle power plant. It is this "extra" electricity produced without additional fuel consumption, makes a combined cycle plant much more efficient than a simple cycle gas turbine power plant.

The steam portion of combined cycle plants takes approximately 2.5 to 3 hours to heat up. This is much slower than a peak load plant that can be at full load in about10 – 25 minutes. Combined cycle systems are handy allowing for many different configurations to satisfy the requirements of individual applications. There are two major groupings of combined cycle systems:

1) Oil or natural gas fired systems for power generation.

2) Combined cycle cogeneration systems and coal or oil fired integrated gasification combined cycle (IGCC) power generation systems.

II LITERATURE SURVEY

The Combined Cycle is based on simple principle that is, burning gas in a gas turbine produces not only power – which can be converted to electric power by a coupled generator but also fairly hot exhaust gases. Diverting these gases through a water- cooled heat exchanger produces steam, which can be turned into electric power with a coupled steam turbine and generator. This set-up of Gas Turbine, waste-heat boiler, steam turbine and generators is called a combined cycle.

During the last few decades there has been nonstop growth of combined cycle gas turbine due to their increased efficiency and their low emissions. The dynamic response of such power plants to load and frequency perturbation is rather problematic. The rotor speed and frequency have a direct effect on air and fuel supply, which introduces a negative effect on system stability[1]. This fact raises further issues relative to the response of combined cycle gas turbine (CCGT) during frequency drops or variations at load power.

ISSN NO: 2348-6481

Vol. 1, Issue 7, Agust 2014

In addition, combined cycle power plants work on the temperature restrictions (above a relatively low power level) so as to attain the best efficiency in the steam generator [1].Temperature should be maintained (apart from the first few seconds of the disturbance) below certain limits for the protection of the plant infrastructure.Gas turbines are the fundamental machineries of combined cycle units. Several researchers have studied the dynamic performance of gas turbines [6]. The dynamic simulations of the gas turbines used in these researches are mainly based on the heavy duty gas turbine model developed by Rowen [5].

As for the steam side of combined cycle units, Kunitomi K. proposed the non-linear mathematical model of heat recovery steam generator (HRSG) and steam turbine in a three-pressure combined cycle unit. This model contains several parameters and nonlinear characteristic curves [9], so it is difficult to obtain the accurate model and use it for dynamic characteristics analysis.Kakimoto and Baba analysed dynamic behaviour in the event of a frequency drop for a single-shaft combined cycle plant operating independently i.e. not connected to a grid[7].Mantzaris and Vournas extended the results of Kakimato and Baba by closely examining the air flow control[6-8].

However, an extensive blackout happened in Malaysia in 1996 [2]. Following a frequency drop of about 1.5 Hz, many combined cycle and gas turbine plants sequentially tripped out. The total generation loss was 5760 MW. Because of its importance, several studies were made on responses of combined cycle power plants to frequency drops [3]–[4]. Some models were developed based on models in and to represent practical plants, and then used to calculate responses to frequency changes[5-7]. In this paper, we analyse dynamic behaviour of a combined cycle power plant for frequency drops. Several dynamic models have been proposed [5]–[9]. We can utilize some of them and build a model for a single-shaft combined cycle plant. We perform MATLAB simulations to see how the combined cycle plant behaves when the plant frequency drops.

Objective of the Present Study:

1. A supervisory control of the combustion control unit has been implemented.
2. Present a stability analysis of control loops with and without a low value select function. Inputs to the LVS are the fuel demand signal determined by the speed governor and an overheat control parameter. During the operation of the unit, only one of the control branches is active, the one whose control parameter has the lowest value.
3. Proposing a method to alleviate the plant response to frequency transients during full load operation.

III CCGT: THERMODYNAMIC MODEL

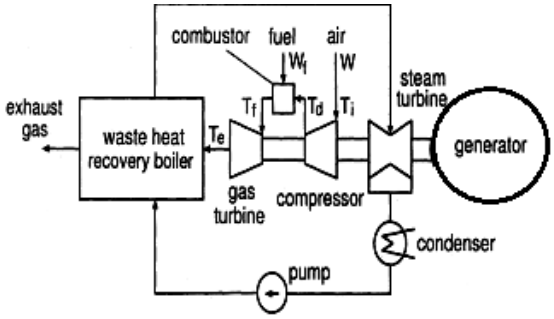

Figure 1: Single-shaft combined cycle plant

Figure 1 shows a single-shaft combined cycle plant. The plant consists of a compressor, combustor, gas turbine, waste heat recovery boiler, steam turbine, and a generator. The compressor compresses air, and sends it to the combustor. The combustor burns air with fuel, and makes high temperature and pressure combustor gas. This combustor gas drives the gas turbine. The waste heat recovery boiler collects some energy of exhaust gas, and drives the steam turbine. Plant power output is the combination of the gas turbine and the steam turbine power outputs.

Since the air is adiabatically compressed, compressor discharge temperature T_d (K) is given as follows:

$$T_d = T_i\left(1+\frac{x-1}{\eta_c}\right) \qquad (1)$$

$$x = (P_{ro}W)^{\gamma-1/\gamma} \qquad (2)$$

Where T_i (K) is compressor inlet temperature and equals ambient temperature, η_c is compressor efficiency, x is compressor temperature ratio, P_{ro} is design compressor pressure ratio, W is airflow in per unit of its rated value, and γ is ratio of specific heats. The airflow depends on the ambient temperature and the atmospheric pressure P_a

IJERI
ISSN NO: 2348-6481
Vol. 1, Issue 7, Agust 2014

$$W = W_a \frac{P_a}{P_{ao}} \frac{T_{io}}{T_i} \qquad (3)$$

Where subscript "o" denotes rated value, and W_a is the air flow at P_{ao} and T_{io}. We assume $P_a = P_{ao}$ .Gas turbine inlet temperature T_f (K) is given by

$$T_f = T_d + (T_{fo} - T_{do}) \frac{W_f}{W} \qquad (4)$$

Where W_f is fuel flow in per unit of its rated value. The fuel flow is a negligible amount compared with the airflow. Gas turbine exhaust temperature T_e(K) is described as follows:

$$T_e = T_f \left[1 - \left(1 - \frac{1}{x} \right) \eta_t \right] \qquad (5)$$

Where η_t is turbine efficiency. The exhaust gas flow is practically equal to the airflow.

IV. OPERATIONAL ZONES

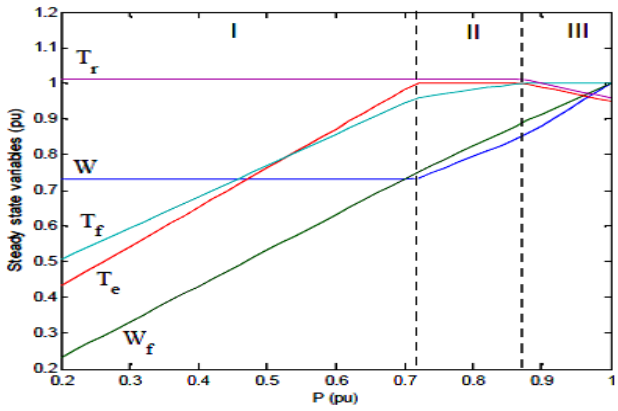

Figure 2: Operational Zones

In steady state and for initialization purposes, one required parameter is the plant output P (in percent of rated), which is equal to the sum of the normalized generation of the two turbines, i.e.: Eg + Es = P.

Figure 2 shows the operational zone for steady state parameters with plant output (P). Therefore, it is necessary to define one more parameter in order to determine the operating point of the system in steady state. Depending upon which parameter we define we can distinguish three operating regions for plant.

- **Operational Zone I :**

The exhaust temperature is lower than the nominal value (light loading of the plant). Since exhaust temperature is lower than reference temperature, so the input of the air control branch is negative in steady state and the airflow gate opening obtains its minimum value.

- **Operational Zone II:**

As the production of plant is increased (with airflow set at its minimum value), it is obvious that the exhaust temperature will continue to rise as the fuel flow rises as seen in figure 2. When T_e reaches the nominal value (maximum allowable temperature), the plant enters region II. The exhaust temperature tends to exceed the reference value and thus air control loop is activated and the exhaust temperature is fixed at its nominal level. Thus, operational zone II is the zone where the temperature control is active to keep the exhaust temperature T_e at its nominal value, while the combustion temperature T_f is below its rated value (intermediate loading). In this area, T_e is equal to nominal.

- **Operational Zone III:**

It has been added to check the effect of heavy loads. T_f(Turbine inlet temperature) tends to exceed its nominal value. In this case the supervisory combustion temperature control designed in this paper is activated to change the exhaust temperature reference so as to control T_f to its nominal value. Supervisory control, sets T_f at its nominal value and decreases the exhaust temperature below nominal, by adjusting the reference temperature.

ISSN NO: 2348-6481

Vol. 1, Issue 7, Agust 2014

V. SIMULINK MODEL

Figure 3 shows a SIMULINK model of the combined cycle plant. It consists of several blocks. There are four blocks related with speed/load control, temperature control, fuel control, and air control. Remaining blocks describe gas turbine, waste heat recovery boiler/steam turbine, rotor shaft, and temperature transducer.

In the above model inlet temperature at compressor T_i has been fed to the temperature discharge block and linked to air flow block. The various thermodynamic equations involving calculation of air flow parameter W has been fed in the embedded function block.

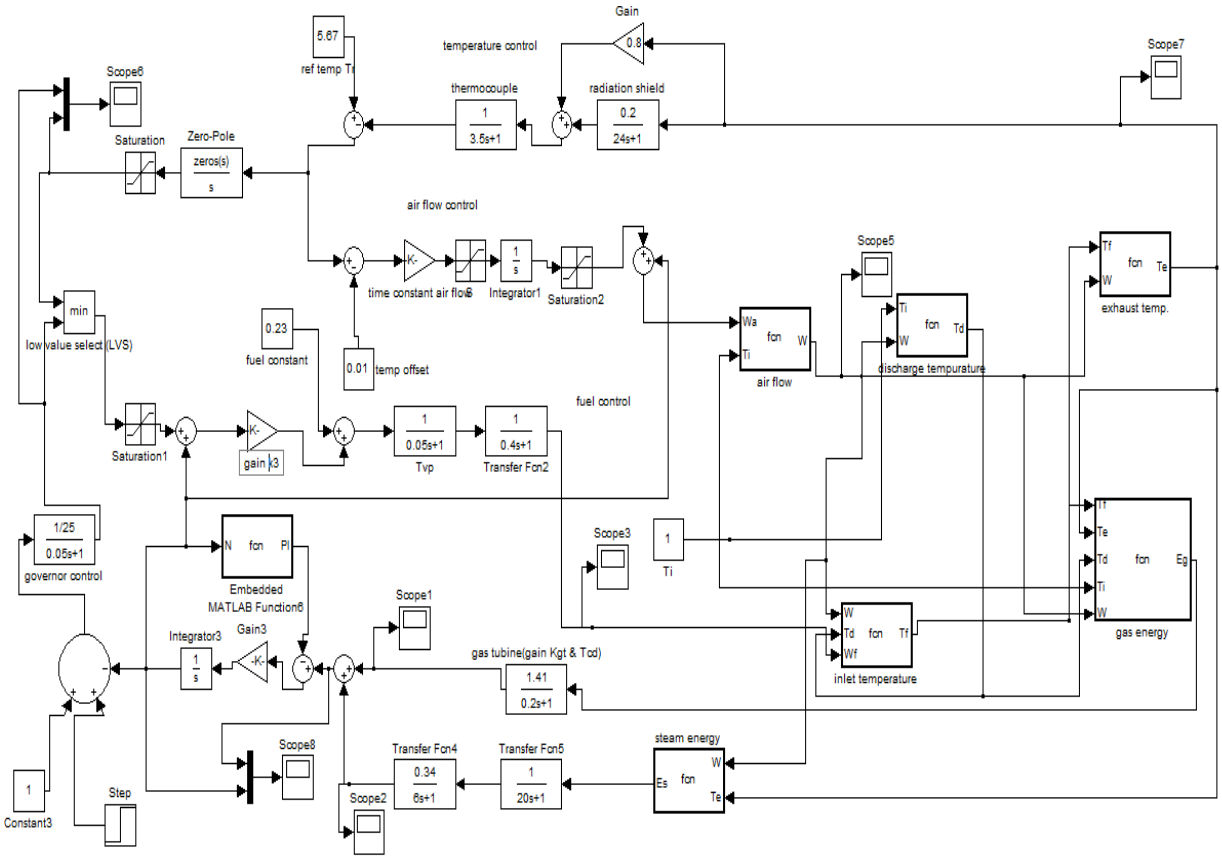

Figure 3: SIMULINK MODEL OF CCGT

VI TEMPERATURE AND AIR CONTROL SECTION

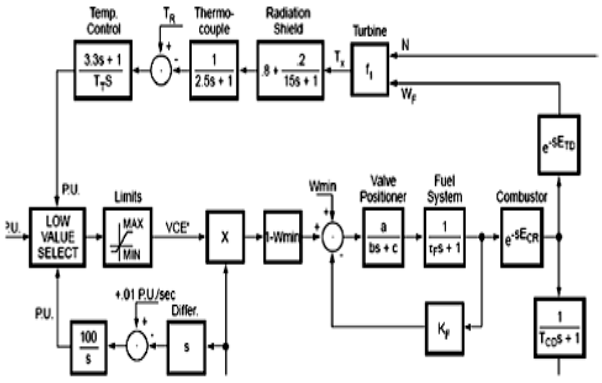

Figure 4: Temperature and air control section

IJERI
ISSN NO: 2348-6481
Vol. 1, Issue 7, Agust 2014

Figure 4 shows the temperature and air control section. Once the air flow gets calculated, the gas turbine inlet temperature T_f is calculated with the help of output from fuel flow W_f control block, discharge temperature T_d and air flow parameter. This part comes under the gas turbine section wherein this inlet temperature gets used in calculation of energy produced by burning of gas E_g.

There are aspects that are essential to complete the gas turbine model: the exhaust temperature measuring device and the inlet guide vanes (IGV) system. The actual exhaust gas temperature varies together with the changes in: rotor speed, fuel flow, ambient temperature, and IGV orientation. The expression used to calculate the exhaust gas temperature can be derived from, and it combines all of these factors together[7-8].The exhaust gas temperature is commonly measured by thermocouple. In order to get the actual exhaust gas temperature, we must take the temperature thermocouple and radiation shield into account. Two time constants (T_{rs}, T_{tc}) represent time lag of thermocouple module and radiation shield module respectively. The IGVs' dynamic is modelled as an inertia module, and T_V represents the time constant of this module[10].This E_g now gets suitably converted into gas turbine power P_g. In the branch of P_g calculation, the signal is fed into a compressor dynamic module, and T_{cd} represents the compressor discharge time lag. Then the gas turbine power output is calculated. The formulation used to calculate P_{GT} is derived from literatures [7-8].

The energy of exhaust gas is used again in waste heat recovery boiler and adds to the energy of steam. The HRSG model has constant efficiency over its normal operating range. Its steam production depends on the quantity and temperature of the turbine exhaust gas. Because of large time constants in HRSG, the dynamic behaviour of steam turbine can be neglected. The response of the steam turbine mechanical power follows changes in gas turbine exhaust energy with basically two time lags for the high pressure contribution and the low pressure contribution. Two time constants (T_m, and T_h) are used to represent the dynamics of the HRSG. The gain K_{st} between gas turbine exhaust energy and steam turbine output is modelled as a constant gain here for simplification. The net power output P_m is the summation of P_g and P_s. This value determines the rotor speed in the model. The value of rotor speed is connected to the fuel flow control block and the air flow control, which is the core requirement of this system of CCGT[11].

VII POWER AND SPEED SECTION

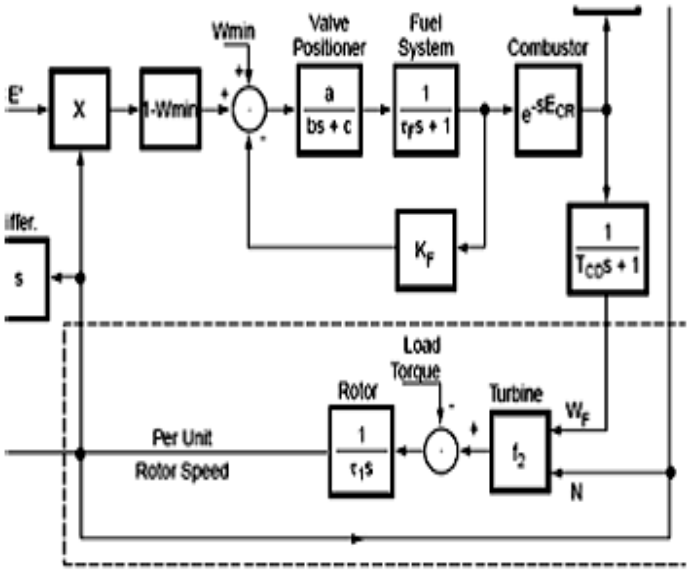

Figure 5: Power and speed section

By comparing measured rotor speed with reference speed, speed deviation is used as the control command of the speed controller. In figure5, a droop controller is adopted to regulate the unit, the droop setting value R generally range from 3% to 6%.

Deviation between measured exhaust gas temperature and reference exhaust gas temperature is fed into the temperature controller to generate a control signal. The control signal is compared with the one from speed controller, and the smaller value is used as the final control command of the fuel valve.Compressor inlet guide vane control is designed to maintain the temperature of combustion chamber. It ensures high gas turbine efficiency under full load and partial load operation. The IGV must be closed to reduce the air/fuel ratio, and the temperature in the combustion chamber can be stabilized in an acceptable range.

In figure 5, the speed and load controller is the primary controller. Fuel demand signal F_g from the speed and load controller is compared with fuel demand signal F_t from the exhaust gas temperature controller in a low value selection module, and the smaller value is considered as the actual fuel demand. This reduces fuel supply to prevent rapid increasing of speed when the power system frequency suddenly increase, and also slowly increases fuel supply to prevent blade damage caused by overheat of the unit combustion chamber. Fuel pumps speed is linked to the rotor speed, and speed signal must be taken into account to generate the actual fuel supply. Fuel demand signal changes the fuel supply by changing the position of the fuel control valve (T_{vp} represents the time constant of the fuel control valve).

IJERI
ISSN NO: 2348-6481
Vol. 1, Issue 7, Agust 2014

VIII ANALYSIS of SPEED and TOTAL POWER vs TIME

The result shown in the following graphs whether for unit step(figure 6), impulse (figure 7) or random input(figure 8) shows that the combined power P_T= Pm(Pg+Ps) increases with time and as a result due to increase in shaft torque, the speed shows a suitable increase with time. Speed increase is not so steep in the beginning but rises somewhat exponentially.

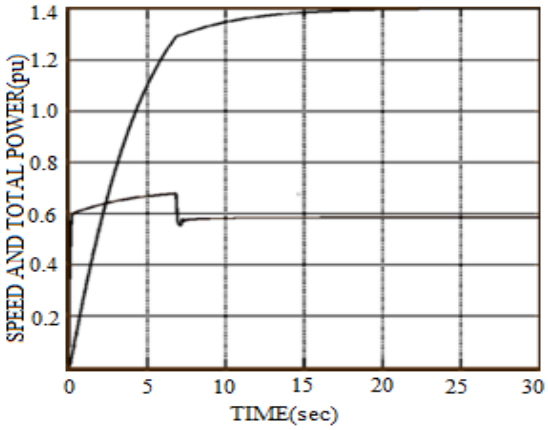

Figure 6. For unit step input

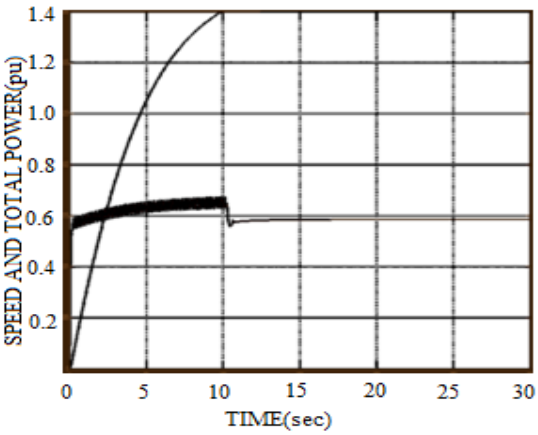

Figure 7. For impulse input

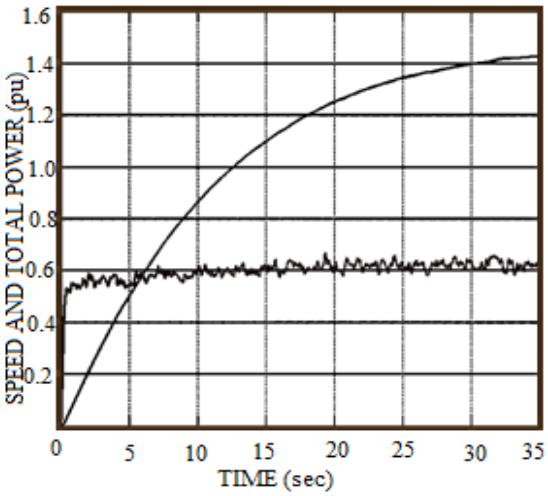

Figure 8. For random input

IJERI
ISSN NO: 2348-6481
Vol. 1, Issue 7, Agust 2014

IX ANALYSIS of FUEL FLOW vs TIME

When a step load (figure 9) increase is applied, speed has to increase to maintain the frequency. This is observed as a sharp increase in speed and power curves. Fuel supply is increased, leading to an increase in T_e values as shown in the figure 12. After sometime, we observe a dip in the T_e graph indicating that $T_e > T_r$ .Air flow is increased to curb the rise of T_e. A positive slope in W graph confirms this. Fuel supply is reduced in order to decrease T_e. Fuel supply becomes constant near 1.5 sec. Hence $T_e < T_r$ occurs after 1.5 sec so fuel supply again rises to increase speed to a stable value with a positive increase in air flow supply. Figures 10 and Figure 14 show the results for the impulse input. Figures 11 and Figure 13 show for the random input.

Air flow effect for step input is shown in figure 15, for pulse input in figure 16 and for random input is shown in figure 17.

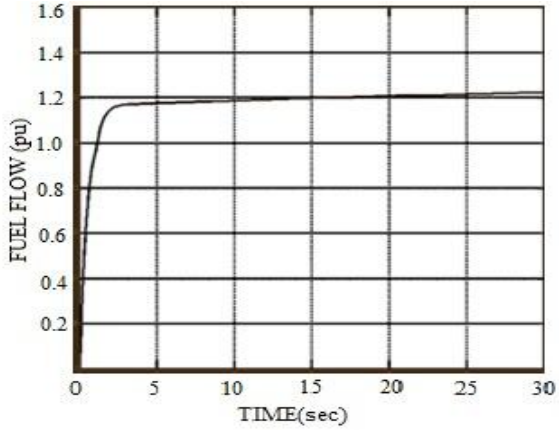

Figure 9. For unit step input

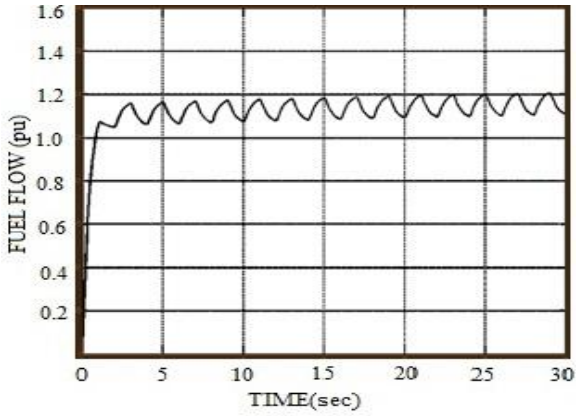

Figure 10. For impulse input

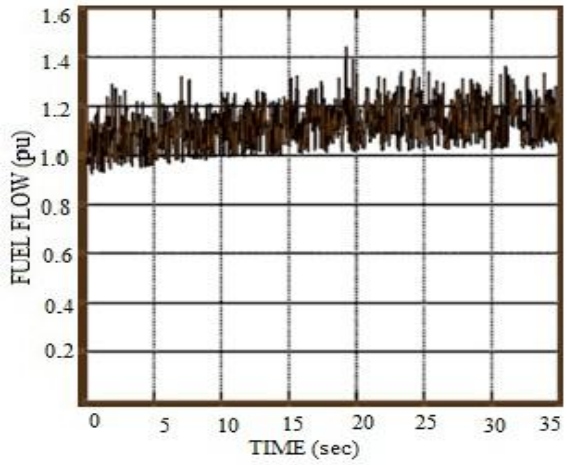

Figure 11 For random input

IJERI
ISSN NO: 2348-6481
Vol. 1, Issue 7, Agust 2014

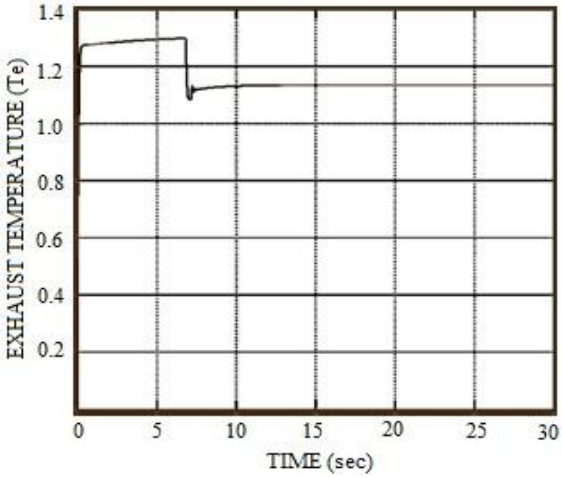

Figure 12. Te vs Time for unit step

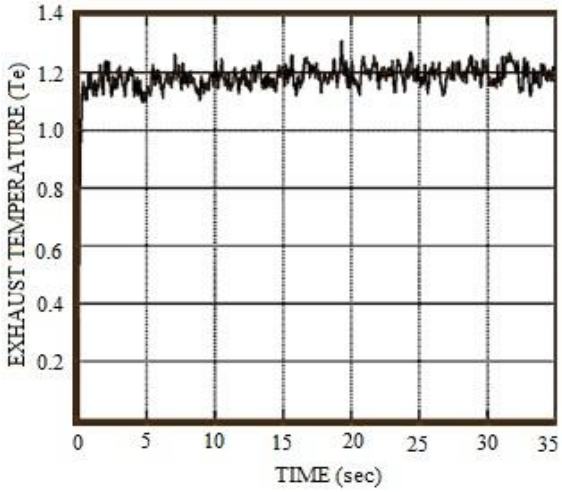

Figure 13. Te vs Time for random input

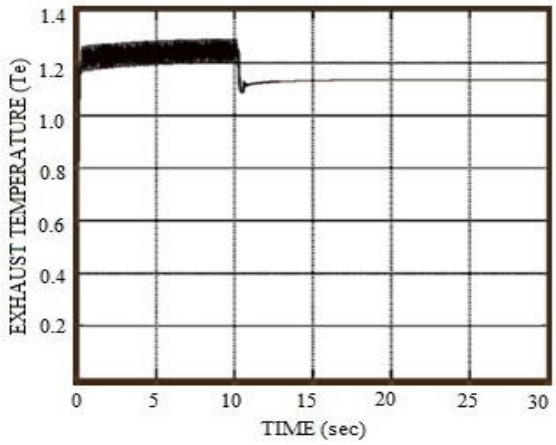

Figure 14. Te vs Time for impulse input

IJERI
ISSN NO: 2348-6481
Vol. 1, Issue 7, Agust 2014

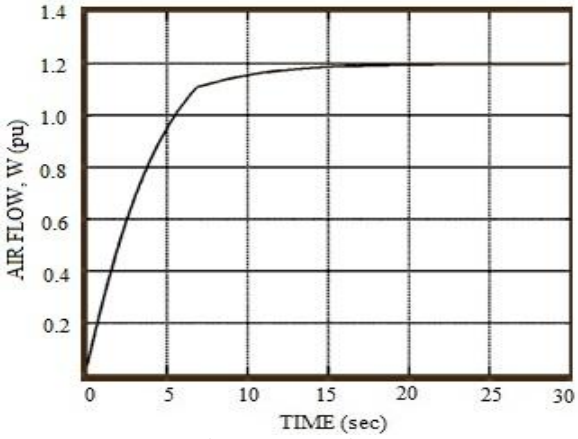

Figure 15. Air flow W vs time for unit step input

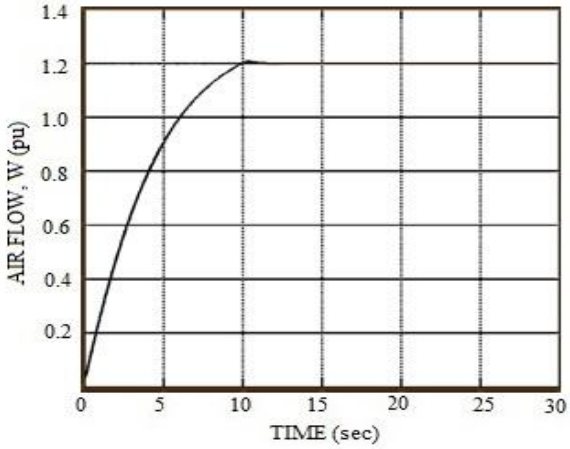

Figure 16. Air flow vs time for pulse input

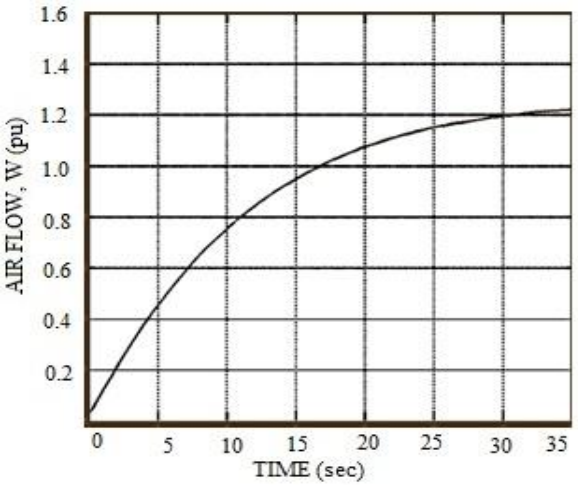

Figure 17. Air flow vs time for random input

As there is a feedback of speed to air flow control block, the air flow plots (figures 15,16 and 17) shows a similar nature to that of speed plot. The values and nature of responses are different due to the different parameters involved in the air flow block.

IJERI
ISSN NO: 2348-6481
Vol. 1, Issue 7, Agust 2014

X. CONCLUSION

In this paper the model and the stability of a single shaft combined cycle plant, as well as its various control loops i.e. air control loop, fuel control, temperature control loop and speed control loop have been developed and monitored. The model consists of equations describing the steady-state turbine characteristics, simple dynamic models of the fuel system turbine dynamics, and temperature transducer, and the models of the temperature control, acceleration control, and governor as they are designed and implemented on actual units.
Analysis of the performance of such a plant in frequency disturbances can be summarized as follows:

- A speed control loop is essential for the plant stability, as the frequency feedback in fuel flow and air flow render the plant very sensitive to turbulences.
- Low value select (LVS) function plays a very important role in the response. It enables the temperature control in case of overheat, which restricts the fuel supply. Otherwise it enables the speed control loop, which is essential for plant stability.
- Without LVS a significant perturbation is observed in turbine power output in the beginning of the simulation, resulting in disturbance in the fuel flow and air flow. Exhaust temperature also gets disturbed, although due to the control loops they die out as time elapses.
- The plant is unsteady, without the frequency control mechanism, To achieve steady state after a disturbance, a necessary condition is for the LVS to switch back to speed control.
- Air control helps in increasing the power output, to correct frequency errors without creating overheat.
- Since the simulation response is relatively slow, some blocks with small time constants can be ignored in order to reduce the order of the model and hence simplifying calculations.

XI. REFERENCES

[1] CIGRE, 2003, "Modeling Gas Turbines and Steam Turbines in Combined-Cycle Power Plants", International Conference on Large High Voltage Electric Systems, Technical Brochure.

[2] "Large-scale blackout in Malaysia," in Kaigai Denryoku (Foreign Power): Japan Electric Power Information Center, Inc., 1996, pp.103–104.

[3] T. Inoue, Y. Sudo, A. Takeuchi, Y. Mitani, and Y. Nakachi, "Development of a combined cycle plant model for power system dynamic simulation studies," Trans. Inst. Elect. Eng. Jpn., vol. 119-B, no. 7, pp.788–797, 1999.

[4] S. Suzaki, K. Kawata, M. Sekoguchi, and M. Goto, "Combined cycle plant model for power system dynamic simulation study," Trans. Inst.Elect. Eng. Jpn., vol. 120-B, no. 8/9, pp. 1146–1152, 2000.\

[5] W. I. Rowen, "Simplified mathematical representations of heavy-duty gas turbines," Trans. Amer. Soc. Mech. Eng., vol. 105, pp. 865–869, Oct.1983.

[6] Wei Siliang, Liu Shangming, Ni Weidou, "Simulation of Gas Turbine with Droop Control System under Matlab/Simulink", Power Engineering,Vol. 21, No. 6, 2001, pp. 1555-1559

[7] Kakimoto, N., Baba, K., 2003, "Performance of Gas Turbine-Based Plants During Frequency Drops", IEEE Transactions on Power Systems.Vol. 18, No. 3, pp. 1110 – 1115.

[8] John Mantzaris and Costas Vournas∗"Modelling and Stability of a Single-Shaft Combined Cycle Power Plant", Int. J. of Thermodynamics Vol. 10 (No. 2),pp-71-78,June 2007,ISSN 1301-9724.

[9] Kunitomi, K., Kurita, A., Tada, Y., Ihara, S., Price, W.W., Richardson, L.M, Smith, G., 2003,"Modeling Combined-Cycle Power Plant for Simulation of Frequency Excursions", IEEE Transactions on Power Systems, Vol. 18, No. 2,pp. 724-729.

[10] F. P. de Mello and D. J. Ahner, "Dynamic models for combined cycle plants in power system studies," IEEE Trans. Power Syst., vol. 9, pp.1698–1708, Aug. 1994.

[11] A. J. Raja, B. Dr. C. Christober Asir Rajan and C. Y. Thiagarajan, "Frequency Excursion and Temperature control of Combined Cycle Gas Plant Including SMES", International Journal of Computer and Electrical Engineering, Vol.2, No.6, December, 2010.

IJERI
ISSN NO: 2348-6481
Vol. 1, Issue 7, Agust 2014

Appendix-1

Table 1. System Parameters

Symbol	Description	Value
T_i	Compressor inlet temperature	30 $^{\circ}C$
T_{do}	Compressor discharge temperature	390 $^{\circ}C$
T_{fo}	Gas turbine inlet temperature	1085 $^{\circ}C$
T_{eo}	Gas turbine exhaust temperature	535 $^{\circ}C$
P_{ro}	Compressor pressure ratio	11.5
γ	Ratio of specific heat	1.4
η_c	Compressor efficiency	0.85
η_t	Turbine efficiency	0.85
R	Speed Regulation	0.04
T_t	Temperature control integration rate	0.469
$T_{c\max}$	Temperature control upper limit	1.1
$T_{c\min}$	Temperature control lower limit	0
$F_{d\max}$	Fuel control upper limit	1.5
$F_{d\min}$	Fuel control lower limit	0
T_v	Valve position time constant	0.05
T_{fu}	Fuel system time constant	0.4
T_w	Air control time constant	0.4669
T_{cd}	Compressor volume time constant	0.2
K_0	Gas turbine output coefficient	0.0033
K_1	Steam turbine output coefficient	0.00043
T_g	Governor time constant	0.05
K_4	Gain of radiation shield	0.8
K_5	Gain of radiation shield	0.2
T_3	Radiation shield time constant	15
T_4	Thermocouple time constant	2.5
T_5	Temperature control time constant	3.3
K_3	Ratio of fuel adjustment	0.77
K_6	Fuel valve lower limit	0.23
T_m	Tube metal heat capacitance time constant of waste heat recovery boiler	5
T_b	Boiler storage time constant of waste heat recovery boiler	20
T_i	Turbine rotor time constant	18.5

Gas Turbine Model – Frame 6, MS9000 series units, 50Hz application (rotational speed 3000 rpm).

Scientific Online

OPEN JOURNAL OF WATER POLLUTION AND TREATMENT
In Press

OPEN JOURNAL OF WATER POLLUTION AND TREATMENT

Prevalence of Fluoride in Ground Water in Rajasthan State: Extent, Contamination Levels And Mitigation

Abhas Jain*, Santosh Kumar Singh

Department of Environmental Engineering, Delhi Technological University, New Delhi-110042, India.
***Corresponding author**: abhasjain01@gmail.com

Abstract:
Ground water is one of the major sources of water supply in Rajasthan due to absence of dependable surface water sources in the most parts of the state. Due to the scanty rainfall and over exploitation of ground water, in 2011, out of the 243 blocks, only 25 are safe from the ground water availability point of view, rest are declared dark zones. More than 80% of the water supply schemes depend on ground water and a number of tube wells, open wells and hand pumps have been dug over the past few decades. In most cases, the source either becomes dry or starts giving low yield and chemical quality gets degraded, resulting in failure of the water supply scheme. As a result, in most of the districts, ground water quality does not conform to BIS or WHO standards as it contains excessive fluorides, nitrates, chloride and total dissolved solids (TDS). The problem of fluoride in ground water has primarily existed in the western districts of the state since ages but with increasing demand for drinking water and over exploitation of ground water, it has spread to almost all the 33 districts. People in some of the districts consume water with fluoride level up to 6 mg/L. Though in some of the districts, people learnt rain water harvesting and used rain water for drinking to avoid ill effects of fluoride. Constant efforts by the government have resulted in increased awareness about the problem. In addition to promoting treatment of fluoride at source, government is now shifting its attention to surface water sources to supply safe drinking water. The state of Rajasthan is a classic example of the socio-cultural-environmental aspects of drinking water and the fight of the community against the scarcity and poor quality of ground water. This paper is an attempt to look at the problem of fluoride in Rajasthan as regards its extent, effects and various practices at the level of the government and community.

Keywords:
Fluorosis; Fluoride; Rajasthan

1. INTRODUCTION

Ground water has been an important source of drinking water in India as well as in Rajasthan. Due to the different soils and presence of indigenous rocks, the groundwater contains a variety of dissolved ions

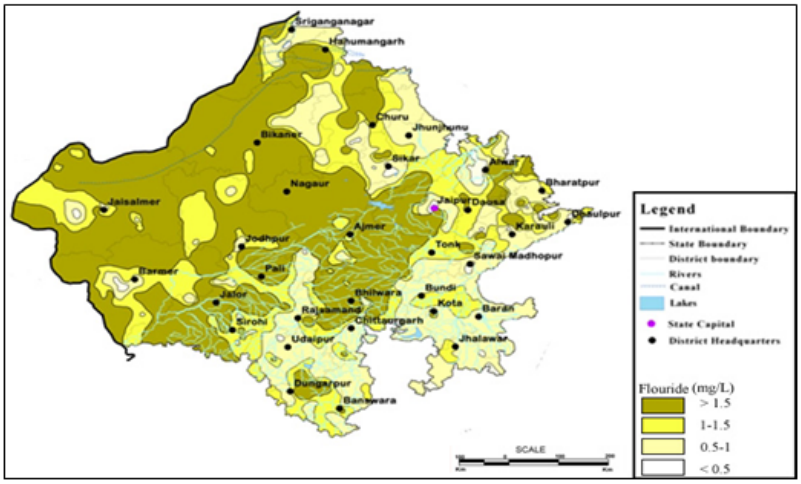

Figure 1. Map of Rajasthan showing Fluoride variation in the state [2].

Table 1. Sources of Fluoride in groundwater [3].

Minerals	Chemical composition	Rocks of these minerals
Fluorite (Fluorspar)	CaF_2	Pegmatite Pneumatolitic deposits as vein deposit
Flurapatite (Apatite)	$Ca(F_2Cl)PO_4$	Pegmatite & metamorphosed limestone.
Mica Biotite Muscovite	$K(MgFe^{+2})_3(AlSi_3)O_{10}(OHF)_2$ $KAl_2(AlSi_3O_{10})(OHF)_2$	Basalts Permatites, Amphiboites
Amphiboles Hornblende Tremolite Actinolite	$NaCa_2(MgFe+2)_4(AlFe+3)(SiAl)_8O_{22}(OHF)_2$ $Ca_2(MgFe+2)_5(Si_8O_{22})(OHF)_2$	Gneisses, schists, shales, Clay Aklaline rocks *etc.*
Topaz	$Al_2SiO_4(OHF)_2$	Acid, Igneous rocks, schists, gneisses *etc.*
Rock Phosphate	$NaCa_2(MgFe^{+2})_4(AlFe^{+3})(SiAl)_8O_{22}(OHF)_2$	Limestone, fossils *etc.*

in different concentrations. The concentration of the dissolved ions determines the suitability of water for different purposes.

In nature, fluoride occurs mainly as Sellaite (MgF_2), fluorspar (CaF_2), cryolite (Na_3AlF_6) and fluorapatite $3Ca_3(PO_4)_2Ca(F,Cl_2)$). As fluorspar it is found in sedimentary rocks and as cryolite in igneous rocks. These fluoride minerals are nearly insoluble in water. Hence fluorides will be present in groundwater only when conditions favor their dissolution or high fluoride containing effluents are discharged to the water bodies from industries [1]. Fluorine always occurs in combined form of minerals as fluoride. It is high reactivity and represents about 0.06 to 0.09% of the earth crust (WHO, report 1994). The presence of fluorine in ground water is mainly a natural phenomenon, and mainly influenced by local and regional geological conditions, as the fluoride minerals are nearly insoluble in water. Hence fluorine is present in ground water only when the conditions favor their solution.

The main source of fluorine in groundwater is basically from the mafic minerals shown in **Table 1** and concentration of fluoride in these rocks given in **Table 2**.

These minerals are commonly associated with the country rocks through which the ground water percolates under variable temperature conditions. Besides these minerals, alkali rocks, hydrothermal solutions may also contribute to higher concentration of fluoride in groundwater.

Table 2. Value of Fluorides in various rock types [3]

Rocks	Flouride range (in ppm)	Average (in ppm)
Basalts	20-1060	360
Granites and Gniesses	20-2700	870
Shales and Clasy	10-2700	800
Line stones	0-1200	220
Sandstones	10-880	180
Phosphorite	24000-41500	31000
Coal (ash)	40-480	80

Table 3. Fluoride afftected states [5]

Percentage extent	Affected States
50-100%	Andhra Pradesh, Tamil Nadu, Uttar Pradesh, Gujarat, Rajasthan
30-50%	Bihar, Haryana, Karnataka, Maharashtra, Madhya Pradesh, Punjab, Orissa, West Bengal
< 30 %	J & K, Delhi, Kerala

It was reported that the main source of fluorine in ordinary soil consists of clay minerals [4]. The weathering and leaching process, mainly by moving and percolating water, play an important role in the incidence of fluoride in groundwater. The features related to the release of fluoride into water by fluoride bearing minerals may be due to i) The chemical composition of water ii) The presence and accessibility of fluoride minerals to water or iii) The contact time between the source minerals.

2. EXTENT OF THE PROBLEM

The occurrence of high fluoride content in ground water has now become one of the most important health related geo-environmental issues in many countries of the world. The international status of fluoride problem is also alarming. The following countries have been identified for the problem of fluorosis: Pakistan, Bangladesh, Argentina, United States of America, Morocco, Middle East countries, Japan, South African Countries, New Zealand, and Thailand *etc.*

As mentioned in the **Table 3**, in India, this problem has reached alarming proportions affecting at least 17 states [6]. Our country is also confronting the same problem where the high fluoride concentration in ground water resources and the resultant disease “Fluorosis” is evenly distributed in nearly 150 districts of 15 states. It has been observed that about 25 million people in 8700 village in India are using ground water having fluoride content more than 1.5 mg/l. **Table 3** give information about percentage extent of fluoride level in different states.

3. FLUORIDE IN GROUNDWATER OF RAJASTHAN

Rajasthan is located in the North-West part of India. The status of availability and utilization of water in Rajasthan is quite critical. Rajasthan is the largest State of the country. It has about 10.5% area; 5.5% population and 18.7% livestock of the country but has only 1.16% surface water and 1.72% ground water of the country [7]. The ground water condition in the Rajasthan is quite alarming. The stage of ground

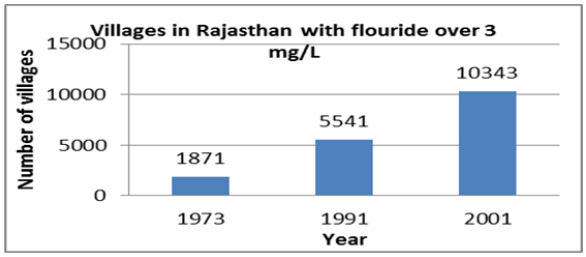

Figure 2. Increase in Fluoride in villages of Rajasthan above 3 mg/L [10].

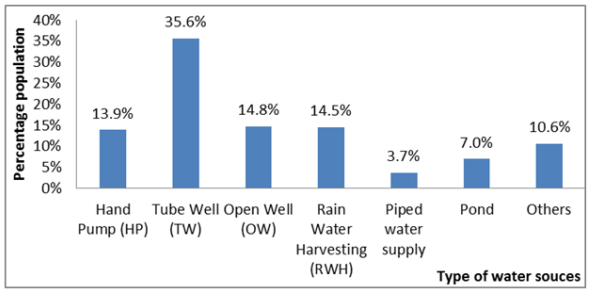

Figure 3. Water sources and its usage in excess Fluoride regions in Rajasthan [2].

water exploitation, which was just 35% in the year 1984, has reached a level of 125% in 2004. Only 25 of the 243 blocks in the State are categorized as "safe" with respect to groundwater availability [8].

A recurring feature in the state is the uncertainty of rainfall, which only aggravates the drought and famine conditions. The situation is worst in the eastern part of Rajasthan, which is adjacent to the Thar Desert. With ever growing population and water demand, the water availability (per capita) is also dwindling year after year. As per present estimation, per capita water availability is about 640 cum per year against international standards of 1000 cum per year. It is apprehended that this may further reduce to 440 cum by the year 2025 [9].

Fluorides in drinking water of Rajasthan are found to originate from various rocks. These rocky belts extend from Delhi to Gujarat. The geological distribution of rocks in Rajasthan reveals that th'e fluoride yielding ores occupies large areas of eastern and southeast parts of the state. Also, Rajasthan has mica mines, where the ground water is rich in fluorides.

As seen in **Figure 2**, the number of villages affected by fluoride has increased over time. In 1973, there were 1,871 villages with fluoride levels over 3mg/l. By 2001, this number had risen to 10,342 villages, an increase of more than five times. This makes Rajasthan the most severely affected state in India, with millions crippled as the result of consuming excessive amounts of fluoride [10]. All the 32 districts have been declared as fluoride prone areas. Among all the districts worst affected are Nagaur, Jaipur, Sikar, Jodhpur, Barmer, Ajmer, Sirohi, Jhunjhunu, Churu, Bikaner, Ganganagar *etc.* [11] People in some of these districts in Rajasthan are consuming water with fluoride concentrations up to 24 mg/l. Rajasthan has more than 51 per cent of the affected villages in the country [2]. **Table 3** in the last gives the detail about the district with fluoride re than 1.5 mg/L and 3 mg/L **Figure 3** shows the major water sources for drinking, cooking and other household demands (HP- Hand Pump,, TB-Tube Well, OW- Open Well, RWH- Rain Water Harvesting, PWS- Piped Water Supply).

Table 4. Effect of prolonged use of drinking water on human health, related to fluoride content [13]

F^- concentration, (mg/L)	**Health outcome**
<0.5	Dental caries
0.5–1.5	Optimum dental health
1.5–3.0	Dental fluorosis/ mottled enamel
3.1-6.0	Osteoporosis
20-80 mg/day or more in water or air	Crippling skeletal fluorosis
50 mg/l in food or water	Thyroid change
100 mg/l in food or water	Growth retardation
More than 125 mg/lin food or water	Kidney change
2.5 – 5.0 gm in actual dose	Death

4. EFFECTS OF FLUORIDE ON HUMAN HEALTH

Presence of Fluoride in drinking water has a profound effect on teeth and bones. Fluoride displaces hydroxide ions from hydroxyapatite, $Ca_5(PO_4)_3OH$, which is the principal mineral constituent of teeth (in particular, the enamel) and bones, to form the harder and tougher compound fluoroapatite, $Ca_5(PO_4)_3F$. Up to some extent this strengthens the enamel. However, fluoroapatite, comparatively is less soluble than hydroxyapatite and at high fluoride concentration the conversion of a large amount of the hydroxyapatite into fluoroapatite makes the teeth and (after prolonged exposure) the bones denser, harder and more brittle. As given in **Table 4**, this causes mottling in the teeth. This condition is also known as **dental fluorosis** [12].

Under prolonged exposure of higher fluoride concentrations, dental fluorosis progresses to skeletal fluorosis (**Table 4**). Fluoride is thus considered beneficial in drinking water if the levels are about 0.7 mg/L but harmful once if the level exceeds 1.5 mg/L which is the World Health Organization limit being followed in most of the nations [9] and is also the Australian recommended limit [14]. The difference between desirable doses and toxic doses of fluoride is ill-defined, and fluoride may therefore be considered as an essential mineral with a narrow margin of safety [13].

5. MITIGATION OF FLUORIDE PROBLEM IN RAJASTHAN

The people of western Rajasthan have been practicing rain water harvesting, by collecting rainwater from roof tops or pucca surfaces or collecting it in small surface ponds. The salinity in ground water has been the major cause of this practice and not much was known about fluoride in particular, (**Table 5**) except for the fact that they knew about the ill effects of the ground water on body which the rain water didn't have. In the last few decades, thousands of tube wells and hand pumps have been dug in all the districts to provide drinking water to rural areas.

The other districts didn't know about the wise water practice of rain water harvesting and hence fell victim to the ill effects of fluoride as the ground water quality has gradually deteriorated throughout the state. The government with support of NGOs like UNICEF and others took up the issue and launched massive community awareness programme and implemented ways and methods to provide safe drinking water. Efforts were made to treat fluoride through user friendly methods. The Nalgonda technique (using lime and alum to treat fluoride) developed by NEERI [15] proved to be too cumbersome and failed. The

Table 5. Details of Fluoride affected villages (and habitations) in Rajasthan [3]

	Name of districts	Total			F> 1.5			F > 3		
No		Villages	Habitations	Total	Villages	Habitations	Total	Villages	Habitations	Total
1	Ajmer	985	952	1931	654	371	1025	352	232	584
2	Alwar	1946	2449	4395	537	342	879	155	68	223
3	Banswara	1431	3175	4606	293	551	844	35	60	95
4	Bharatpur	1345	549	1894	529	81	610	152	11	163
5	Barmer	1623	2780	4403	597	221	818	181	68	249
6	Bhilwara	1566	963	2534	678	318	996	392	227	619
7	Bikaner	580	366	946	84	2	86	7	0	7
8	Bundi	826	332	1158	42	9	51	3	0	3
9	Chittorgarh	2173	904	3077	115	48	163	14	9	23
10	Churu	926	199	1125	240	8	248	27	1	28
11	Dholpur	551	983	1534	142	157	299	22	18	40
12	Dungarpur	846	681	1527	127	225	362	30	55	85
13	S.Ganganagar/ Hanumangarh	4437	4190	8627	425	418	844	149	129	273
14	Jaipur/Dausa	3140	7518	10758	1187	1795	3172	491	739	1230
15	Jaisalmer	518	1172	1690	300	184	484	96	65	161
16	Jalore	666	823	1489	369	107	476	115	45	160
17	Jhalawar	1448	124	1572	42	5	47	15	3	18
18	Jhunjhuinu	824	208	1032	96	3	99	15	1	16
19	Jodhpur	860	2801	3661	314	99	413	59	8	67
20	Kota/Baran	1881	288	2169	44	0	44	17	0	22
21	Nagaure	1374	1972	3346	778	147	925	322	42	364
22	Pali	904	651	1555	242	83	330	69	34	103
23	Swaimadhopur/ Karoli	1464	2191	3655	452	263	725	121	69	190
24	Sikar	931	2401	3332	331	471	792	125	144	269
25	Sirohi	446	92	544	176	5	181	43	1	44
26	Tonk	1019	881	1900	516	209	724	199	71	270
27	Udaipur/ RajSamand	3179	5561	8740	431	497	923	74	81	155
	Total	**37889**	**45311**	**8200**	**9741**	**6619**	**16560**	**3280**	**2181**	**5461**

only alternative available was to depend on surface water sources, which was too expensive and was likely to take years to cover each and every village. Also, there were not many dependable surface sources. Then came the adsorption method of fluoride using Activated Alumina. It was developed by IIT-Kanpur with UNICEF support. The government launched Rajasthan Integrated Fluoride Mitigation Programme (RIFMP). The habitations having more than 5 mg/L fluoride in ground water were targeted in RIFMP Phase-I and those having 3-5 mg/L were addressed to in the phase-II. In both the phases, Domestic De-fluoridation Units (DDFUs) based on adsorption by activated alumina were distributed through NGOs, who were supposed to educate people and train them in using the DDFUs. Despite huge effort, phase-I and phase-II couldn't bring the desired success except for increased awareness in almost all the rural areas of Rajasthan. The major issues linked with the failure were; regeneration of AA, free distribution of DDFUs to BPL and on payment to APL, the people looking at the government for piped water supplies *etc.* On the basis of learning from the phase-I and II, the government launched the phase-III wherein the hand pump and tube well attached large size DDFUs have been installed through private agencies who would operate and maintain the units for 10 years in addition to educating the people. This has brought

appreciable success. Under the GoI supported NRDWP, rain water harvesting and ground water recharge have also been taken up in a big way. But using rain water for drinking hasn't been popular in most of the districts due to the habit and socio cultural reasons. Installation of large size RO plants has also been taken up wherein a private agency installs and operates and maintains the units and the villagers are required to pay 10 paisa per liter for the treated drinking water. The mega RO plant at Matasukh (Nagaur), treating about 10 MLD saline water from coal mines, is one of its own kind in the country.

After all the experience and learning the government of Rajasthan aims at covering the whole state by providing safe drinking water from surface sources. The spot treatment of ground water is likely to continue as an interim measure till all the villages start getting water supply from major projects depending on surface water.

Bisalpur dam, IGNP canal, River Chambal and a number of other dams are the major surface sources of water for most of the major projects.

6. CONCLUSION

Rajasthan is a typical example of age old practice of indigenous water management suitable to the natural scarcity and hardships in relation to availability of water. The issue of fluoride is quite complex due to the technical, socio-cultural, environmental factors associated to it. The people, who used to manage their water systems on their own in ancient times, are now looking at the government for piped water supplies, and reluctant to pay too. The traditional sources and systems are being abandoned with time. Education and awareness regarding water and its linkage to health is still a long way to go. But, it's now being understood at all levels, that water is more of a social issue and the new water systems must be in tune with the habits and socio-cultural aspirations of the people. A good and balanced mix of appropriate technology with adequate community participation can only be an effective answer to combat fluoride.

References

[1] M. Mohapatra, S. Anand, B. Mishra, D. E. Giles, and P. Singh, "Review of fluoride removal from drinking water," *Journal of Environmental Management*, vol. 91, no. 1, pp. 67–77, 2009.

[2] "Report on Fluorosis Prevalence and related issues based on 50 villages surveyed in 8 Tehsils of Nagaur District, Rajasthan, Project Monitoring Supervision Consultants (PMSC) Rajasthan Rural Water Supply & Fluorosis Mitigation Project (Nagaur)."

[3] J. Hussain, K. Sharma, and I. Hussain, "Fluoride In Drinking Water In Rajasthan And Its Ill EffectsOn Human Health," *Journal of Tissue Research*, vol. 4, no. 2, pp. 263–273, 2004.

[4] J. Smet *et al.*, "Fluoride in drinking water," in *Endemic Fluorosis in Developing Countries? Causes, Effects and Possible Solution: Report of a Symposium Held in Delft, The Netherlands*, Netherlands-Organization for Applied Scientific Research, 1990.

[5] D. Ozha, K. Mathur, and F. Golani, "Scourge of High Fluoride in Ground Waters of Arid Rajasthan and Strategy of Its Mitigation," *Asian Journal of Experimental Sciences*, vol. 17, no. 1-2, pp. 43–49, 2003.

[6] RGNDWM, "Prevention and Control of fluorosis in India. Water Quality and Defluoridation Techniques," 1993.

[7] M. Dhingra, “Fight Fluorosis and Save Our Children. Jaipur: Hindustan Times,” 2001.
[8] “JICA Report, Fluoride project in Nagaur and other districts,” 2002.
[9] W. H. Organization, *Guidelines for Drinking Water Quality, ?Health Criteria and Other Supporting Information*, vol. 2. World Health Organization, 1984.
[10] Hindu, “MDG and Indias Drinking Water: Racing Ahead at What Cost?,” 2008.
[11] S. Chandra *et al.*, “Endemic fluorosis in Rajasthan,” in *Indian Association of Preventive and Social Medicine, Rajasthan Chapter, Conference, SP Medical College, Bikaner*, pp. 123–131, 1998.
[12] W. H. Organization, *Guidelines for Drinking Water Quality*, vol. 3. World Health Organization, 1985.
[13] C. Dissanayake, “The fluoride problem in the ground water of Sri Lankaenvironmental management and health,” *International Journal of Environmental Studies*, vol. 38, no. 2-3, pp. 137–155, 1991.
[14] NHMRC, “Australian Drinking Water Guidelines,” 2004.
[15] NHMRC, “NEERI Manual, Technical Digest,” 1978.

Ring and Coupled Ring Oscillator in Subthreshold Region

Neeta Pandey[1], Rishi Pandey[2], Tanvi Mittal[3], Kirti Gupta[4], Rajeshwari Pandey[5]

1,2,3,5 – Department of Electronics and Communication
Delhi Technological University, Delhi, INDIA

4 – Department of Electronics and Communication
Bharati Vidyapeeth's College of Engineering, Delhi

[1]n66pandey@rediffmail.com, [2]rishipandey777@gmail.com, [3]tanvi.mittal1@gmail.com, [4]kirtigupta22@gmail.com, [4]rajeshwaripandey@gmail.com

***Abstract*— In this paper, the implementation of oscillators in the subthreshold region is proposed. The ring and coupled ring oscillators are implemented. The technique of swapped body biasing technique has been introduced for coupled ring oscillators to enhance their performance. The functionality of the oscillators in subthreshold region is verified through simulations using 180 nm TSMC CMOS technology parameters. A comparison in performance of the oscillators is carried out. It is found that coupled ring oscillator based on the swapped body biasing shows the best performance with the frequency of oscillation, power and propagation delay as 19.79 MHz, 973 nW and 12.84 ns respectively.**

Keywords—*Subthreshold region, Ring oscillator, Coupled Ring Oscillator, Swapped Body Biasing*

I. INTRODUCTION

Now-a-days, with the emergence of portable devices, biomedical applications, and radio frequency identification the demand for low power VLSI circuits is on the rise. Different techniques are adopted to achieve low power operation. The operation of CMOS circuits in subthreshold region is one of the most suited solutions for the ultra-low power devices. In subthreshold regime, the energy is minimized by using the subthreshold leakage current as the circuit drive current [1].

Oscillator is an essential component in phase-locked loop (PLL) [2,3] for providing the timing basis in clock control, data recovery, and synchronization. It is also an integral part of voltage controlled oscillator which is employed in a wide variety of applications such as disk-drive read channels [4], on-chip clock distribution [5], integrated frequency synthesizers [6,7], clock and data recovery circuit [8,9] and microprocessor clock generation [10]. This paper proposes the implementation of two ring oscillators in subthreshold region. The first implementation uses a chain of odd numbers of CMOS inverters operating in subthreshold region. In the second implementation, a coupled ring oscillator [10] capable of producing quadrature outputs is proposed.

The paper first briefly presents the operation of a MOSFET in subthreshold region in section II. The implementation of the ring oscillator in subthreshold region is presented in the next two sections. The section III presents the implementation of ring oscillator followed by the implementation of coupled ring oscillator in section IV. The simulation section V verifies the functionality of both the ring oscillators and compares their performance by using CMOS 180nm technology parameters.

In section V, the simulation results are presented along with the description of the metrics used to evaluate design performance. The conclusion drawn from the results appear in section VI.

II. CMOS LOGIC DESIGN IN SUBTHRESHOLD REGION

A. Origin of Weak Inversion Logic Circuits

In the state of weak inversion at the silicon surface in a metal-insulator-silicon (MIS) structure, the majority carriers repel away from the surface, leaving a depletion charge of fixed atoms. Though the density of minority carriers is increased with respect to the distant bulk, but it is still negligible in the overall charge balance, and does not affect the capacitance-voltage curves of the MIS diode significantly. These minority carriers are the only mobile charge available at the surface which move by diffusion producing a drain current as soon as some voltage is applied between the source and the drain of a MOS transistor structure [4].

When the characteristics of MOS transistors were measured at this low current level, they showed the unusual exponential dependency of the drain current on the gate voltage. Weak inversion then came to the attention of the digital design community under the name "subthreshold current" which is actually nothing but the leakage current which keeps flowing through a MOS transistor when it is supposed to be blocked, by imposing $V_{GS} = 0$ V [4].

Though extensive designing of analog circuits in subthreshold region has been done, it is comparatively new in digital design domain. Subthreshold digital circuits are suitable for applications which require extremely low power consumption but do not need high performance. Therefore, subthreshold circuits can also be applied to applications where the circuits remain idle for an extended period of time. This type of applications appears almost in every design, including the high performance microprocessors. For example, when the

978-1-4799-3140-8/14/$31.00

microprocessor goes into deep sleep, a specific module will poll the input devices (e.g. keyboard or mouse) at a regular period of time[5].

Since a CMOS inverter unit is the most basic unit in digital design, we extend a brief discussion over its operation in subthreshold region. In the subthreshold, the power supply voltage V_{DD} is made less than its threshold voltage V_{th}.In this case, the drain current I_{ds} region is exponentially related to the gate voltage V_s as shown in Equation (1)[5]:

$$I_{ds} = I_o \exp\frac{(VGS-Vth)}{Vtm}\left[1 - \exp\frac{-Vds}{Vtm}\right] \quad (1)$$

B. *Voltage Transfer Characteristics*

The voltage transfer characteristics (VTC) of the inverter gate running in subthreshold mode is closer to ideal compared to the VTC in normal strong inversion region [5]. Also, the much improved VTC yields better noise margin.

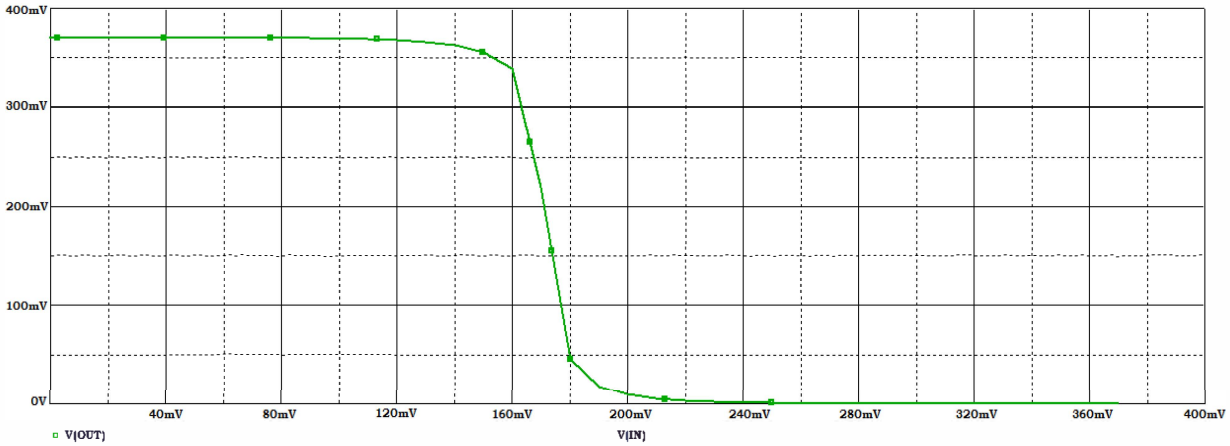

Fig. 1. Voltage Transfer Charactersistic of CMOS Inverter in subthreshold region

III. RING OSCILLATOR

Ring oscillator (RO) is one of the most commonly used components in many integrated systems. The unique features of RO include ease of design with the state-of-art integrated circuit technology (CMOS, BiCMOS), ability to oscillate at lower values of voltage, high frequency oscillations can be achieved, electrically tunable with wide tuning range; attainment of multiphase outputs. There are many methods to implement RO. The two most common are presented in the paper.

The first method implements the RO as a cascade of odd number of inverter stages, connected in a close loop chain. The Fig. 2 shows a ring oscillator employing seven inverters. The frequency of oscillation of an RO varies with propagation delay τ_d of the individual inverter stage and the number of inverter stages used in the ring structure. There must be a phase shift of 2π and unity voltage gain at the oscillation frequency to achieve self-sustained oscillation. In a RO with m inverter stages, a phase shift of π/m is provided by each stage while the remaining phase shift of π is provided by the dc inversion. The signal undergoes m delay stages in a time of $m\tau_d$ to provide a phase shift of π and for another time in a time period of $2m\tau_d$ to obtain the remaining phase of π [6]. Therefore, the frequency of oscillation f_o can be found out using [6]:

$$f_o = \frac{1}{2m\tau d} \quad (2)$$

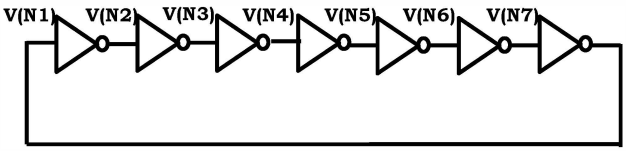

Fig. 2. Proposed ring oscillator in subthreshold region with 7 inverter stages

IV. COUPLED RING OSCILLATOR

A coupled ring oscillator (CRO) is designed by coupling two ring oscillators in such a way that only four distinguished nodes are formed. These four nodes generate quadrature outputs for a completely symmetrical coupling [10]. The implementation of a coupled ring oscillator employing 8 inverter stages is shown in Fig. 3. The circuit has four outputs (0^0, 90^0, 180^0, 270^0) having a phase difference of 90^0.

In this paper, the authors present two implementations of CRO. The first implementation proposes the use of conventional CMOS inverters operating in subthreshold region. The CMOS inverter using traditional body biasing is used in the CRO shown in Fig. 3. In the second implementation, the performance of the conventional CMOS inverter has been improved by using Swapped Body Biasing (SBB) technique [7]. In SBB technique, the substrate of the NMOS devices are tied to the power supply voltage V_{DD} whereas those of the PMOS devices are tied to ground.

Swapping the bulk terminals of the two MOSFETs increases the drive currents in the subthreshold operation from an exponential current increase, but degrades output node voltages when V_{DD} is greater than the zero bias threshold voltage [7]. Thus, SBB technique provides improved performance under subthreshold supply voltages. A CMOS inverter implemented using SBB technique is shown in Fig. 4.

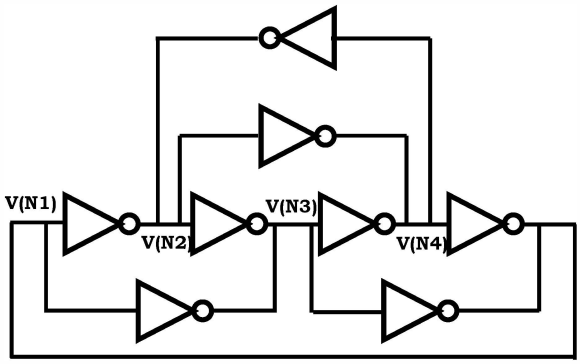

Fig. 3. Coupled Ring Oscillator two coupled 3-stage ring oscillator

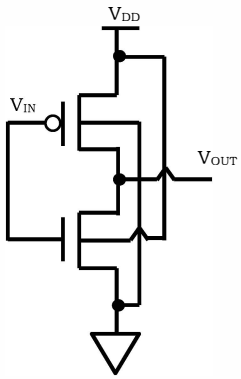

Fig.4. A CMOS inverter based on swapped body biasing technique

V. Simulation Results

In the first sub-section, the functionality of the proposed ring oscillators in subthreshold region (Fig. 2 and 3) is verified. The CRO implemented using the conventional CMOS inverter (implementation 1) and the inverters based on the swapped body biasing technique (implementation 2) are taken in simulation. Then in the second section, the results of the comparison in performance of the ring oscillator and coupled ring oscillator (implementation 1 and 2) are presented. All the simulations are carried with SPICE using 180 nm TSMC CMOS technology parameters as mentioned in Table I. A power supply and load capacitor of 0.37 V and 1 fF have been taken in simulations respectively.

A. Functional verification

The ring oscillator shown in Fig. 2 is simulated. The waveform obtained at the output is shown in Fig. 5. It can be seen that the ring oscillator conforms to the functionality. The two implementations of coupled ring oscillator shown in Fig. 3 are simulated. The waveforms obtained at the four output nodes of the coupled ring oscillator (implementation 2) are shown in Fig. 6. The waveform for the coupled ring oscillator (implementation 1) is not shown for the sake of brevity.

B. Performance Comparison

The simulation results for the ring oscillator and the coupled ring oscillator (implementation 1 and 2) are listed in Table II. It can be observed that the coupled ring oscillators increases the frequency of oscillation by 17.6 MHz (from 2.19 MHz to 19.79 MHz) while simultaneously showing the power reduction of 917 nW. Also, the implementation 2 of coupled ring oscillator outperforms the ring oscillator, reducing the propagation delay by 37.69 ns. With reference to coupled ring oscillator implementation 1, implementation 2 increases the frequency of operation by 16.99 MHz and reduces the delay by 77.99 ns.

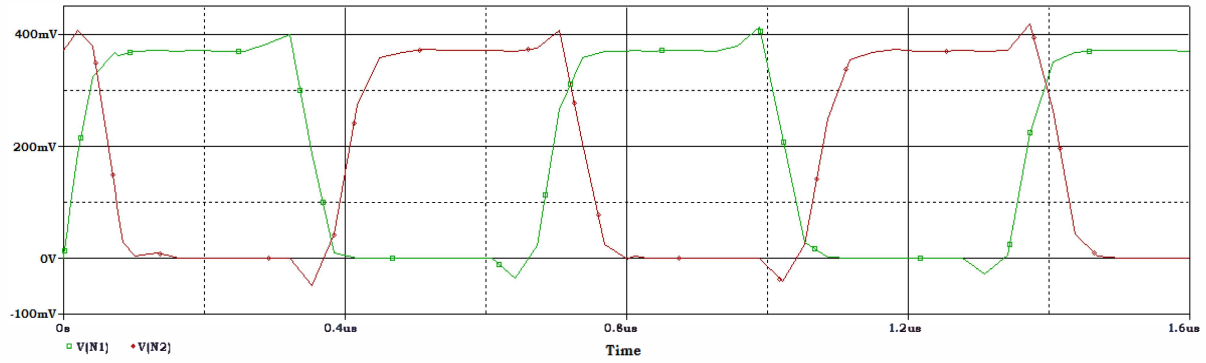

Fig. 5. Output Waveform of Ring Oscillator

TABLE I. 180NM TSMC CMOS MODE AND PARAMETERS

MOS Transistor	Parameters
NMOS	LEVEL = 7: TNOM = 27; TOX = 4.1E-9; DEV .1%; XJ = 1E-7; NCH = 2.3549E17; VTH0 = 0.3750766; K1 = 0.5842025; K2 = 1.245202E-3; K3 = 1E-3; K3B = 0.0295587; W0 = 1E-7; NLX = 1.597846E-7; DVT0W = 0; DVT1W = 0; DVT2W = 0; DVT0 = 1.3022984; DVT1 = 0.4021873; DVT2 = 7.631374E-3; U0 = 296.8451012; UA = -1.179955E-9; UB = 2.32616E-18; UC = 7.593301E-11; VSAT = 1.747147E5; A0 = 2; AGS = 0.452647; B0 = 5.506962E-8; B1 = 2.640458E-6;KETA = -6.860244E-3 A1 = 7.885522E-4; A2 = 0.3119338; RDSW = 105; PRWG = 0.4826; PRWB = -0.2; WR = 1; WINT = 4.410779E-9; LINT = 2.045919E-8; XL = 0; XW = -1E-8; DWG = -2.610453E-9; DWB = -4.344942E-9; VOFF = -0.0948017; NFACTOR = 2.1860065; CIT = 0; CDSC = 2.4E-4; CDSCD = 0; CDSCB = 0; ETA0 = 1.991317E-3; ETAB = 6.028975E-5; DSUB = 0.0217897; PCLM = 1.7062594; PDIBLC1 = 0.2320546; PDIBLC2 = 1.670588E-3; PDIBLCB = -0.1; DROUT = 0.8388608; PSCBE1 = 1.904263E10; PSCBE2 = 1.546939E-8; PVAG = 0; DELTA = 0.01; RSH = 7.1; MOBMOD = 1; PRT = 0; UTE = -1.5; KT1 = -0.11; KT1L = 0; KT2 = 0.022; UA1 = 4.31E-9; UB1 = -7.61E-18; UC1 = -5.6E-11; AT = 3.3E4; WL = 0; WLN = 1; WW = 0; WWN = 1; WWL = 0; LL = 0; LLN = 1; LW = 0; LWN = 1; LWL = 0; CAPMOD = 2; XPART = 0.5; CGDO = 6.7E-10; CGSO = 6.7E-10; CGBO = 1E-12; CJ = 9.550345E-4; PB = 0.8; MJ = 0.3762949; CJSW = 2.083251E-10; PBSW = 0.8; MJSW = 0.1269477; CJSWG = 3.3E-10; PBSWG = 0.8; MJSWG = 0.1269477; CF = 0; PVTH0 = -2.369258E-3; PRDSW = -1.2091688; PK2 = 1.845281E-3; WKETA = -2.040084E-3; LKETA = -1.266704E-3; PU0 = 1.0932981; PUA = -2.56934E-11; PUB = 0; PVSAT = 2E3; PETA0 = 1E-4; PKETA = -3.350276E-3;
PMOS	LEVEL = 7: TNOM = 27; TOX = 4.1E-9; XJ = 1E-7; NCH = 4.1589E17; VTH0 = -0.3936726; K1 = 0.5750728; K2 = 0.0235926; K3 = 0.1590089; K3B = 4.2687016; W0 = 1E-6; NLX = 1.033999E-7; DVT0W = 0; DVT1W = 0; DVT2W = 0; DVT0 = 0.5560978; DVT1 = 0.2490116; DVT2 = 0.1; U0 = 112.5106786; UA = 1.45072E-9; UB = 1.195045E-21; UC = -1E-10; VSAT = 1.168535E5; A0 = 1.7211984; AGS = 0.3806925; B0 = 4.296252E-7; B1 = 1.288698E-6; KETA = 0.0201833; A1 = 0.2328472; A2 = 0.3; RDSW = 198.7483291 PRWG = 0.5; PRWB = -0.4971827; WR = 1; WINT = 0; LINT = 2.943206E-8; XL = 0; XW = -1E-8; DWG = -1.949253E-8; DWB = -2.824041E-9; VOFF = -0.0979832; NFACTOR = 1.9624066; CIT = 0; CDSC = 2.4E-4; CDSCD = 0; CDSCB = 0; ETA0 = 7.282772E-4; ETAB = -3.818572E-4; DSUB = 1.518344E-3; PCLM = 1.4728931; PDIBLC1 = 2.138043E-3; PDIBLC2 = -9.966066E-6; PDIBLCB = -1E-3; DROUT = 4.276128E-4; PSCBE1 = 4.850167E10; PSCBE2 = 5E-10; PVAG = 0; DELTA = 0.01; RSH = 8.2; MOBMOD = 1; PRT = 0; UTE = -1.5; KT1 = -0.11; KT1L = 0; KT2 = 0.022; UA1 = 4.31E-9; UB1 = -7.61E-18 UC1 = -5.6E-11; AT = 3.3E4; WL = 0; WLN = 1; WW = 0; WWN = 1; WWL = 0; LL = 0; LLN = 1; LW = 0; LWN = 1; LWL = 0; CAPMOD = 2; XPART = 0.5; CGDO = 7.47E-10; CGSO = 7.47E-10 CGBO = 1E-12; CJ = 1.180017E-3; PB = 0.8560642; MJ = 0.4146818; CJSW = 2.046463E-10; PBSW = 0.9123142; MJSW = 0.316175; CJSWG = 4.22E-10; PBSWG = 0.9123142; MJSWG = 0.316175; CF = 0; PVTH0 = 0.456598E-4; PRDSW = 8.4838247; PK2 = 1.338191E-3; WKETA = 0.0246885; LKETA = -2.016897E-3; PU0 = -1.5089586; PUA = -5.51646E-11; PUB = 1E-21; PVSAT = 50; PETA0 = 1E-4; PKETA = -3.316832E-3;

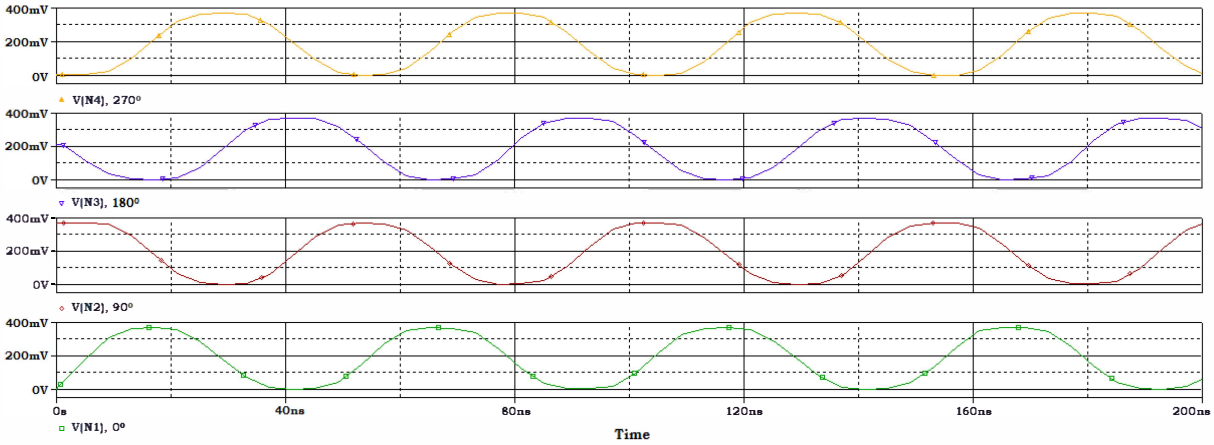

Fig. 6. Output Waveform of Coupled Ring Oscillator using SBB

TABLE II. PERFORMANCE COMPARISION OF OSCILLATORS

Performance Parameters	Ring Oscillator	Coupled Ring Oscillator	
		Implementation 1	Implementation 2
Frequency of oscillation (MHz)	2.19	2.80	19.79
Propagation Delay (ns)	50.53	90.83	12.84
Power Dissipation (W)	5.6×10^{-8}	1.14×10^{-7}	9.73×10^{-7}

VI. CONCLUSION

This paper proposes the implementation of oscillators in the subthreshold regime. The ring and coupled ring oscillators are implemented. An improved structure based on swapped body biasing technique is proposed. The feasibility of the oscillators in subthreshold region is studied through simulations using 180 nm TSMC CMOS technology parameters. A comparison in performance of the oscillators shows that coupled ring oscillators based on the swapped body biasing technique outperforms others.

REFERENCES

[1] Massimo Alioto, "Understanding DC Behavior of Subthreshold CMOS Logic Through Closed-Form Analysis", IEEE Transactions on Circuits and Systems-I: Regular Papers, Vol. 57, No. 7, July 2010.

[2] B. Razavi, "A 2-GHz 1.6-mW phase-locked loop", IEEE J. Solid-State Circuits, Vol. 32, pp.730-735, 2007.

[3] A. M. Ali Hasan, "Analysis and design of high performance ring voltage controlled oscillator", International Journal of Computer Applications(0975-8887), Vol. 70, No. 20, May 2013.

[4] Alice Wang, Benton H. Calhoun, Anantha P. Chandrakasan, book on "Sub-threshold Design for UltraLow-Power Systems".

[5] Hendrawan Soeleman and Kaushik Roy, "Digital CMOS Logic Operation in the SubThreshold Region" in CM Great Lakes Symposium on VLSI 2000: 107-112.

[6] M.K. Mandal & B.C. Sarkar, " Ring Oscillators: Characteristics and applications", Indian Journal of Pure & Applied Physics Vol. 48, February 2010, pp. 136-145.

[7] Jabulani Nyathi, Brent Bero and Ryan McKinlay, "A Tunable Body Biasing Scheme for Ultra-Low Power and High Speed CMOS Designs" in International Symposium on Low Power Electronics and Design - 2006. October 4-6,2006.

[8] C. K. K. Yang, R. Farjad-rad, M. A. Horowitz, "A 0.5-m CMOS 4.0-Gbit/s serial-link transceiver with data recovery using oversampling", IEEE Journal of Solid-State Circuits, Vol. 33, pp.713-722, 2008.

[9] M. Alioto, G. Palumbo, "Oscillation frequency in CML and ESCL ring oscillators", IEEE Trans. Circuits Syst. I, Vol. 48, pp.210-214, 2010.

[10] Behzad Mesgarzadeh and Atila Alvandpour, "A Wide-Tuning Range 1.8 GHz Quadrature VCO Utilizing Coupled Ring Oscillators" in IEEE International Symposium on Circuits and Systems 2006.

Environ Chem Lett
DOI 10.1007/s10311-014-0479-x

ORIGINAL PAPER

Seasonal variation and sources of aerosol pollution in Delhi, India

Papiya Mandal · R. Sarkar · A. Mandal · T. Saud

Received: 12 January 2014 / Accepted: 22 August 2014

Abstract Urbanization and industrialization in Delhi are growing very rapidly. As a consequence, aerosol emissions are increasing, thus leading to poor ambient air quality for human health. The precise sources and chemical composition of carbonaceous aerosols are not well known. In India, carbonaceous aerosols represent a major part, of around 50 %, of $PM_{2.5}$: the particulate matter with aerodynamic diameter lower than 2.5 μm. Here, we investigated carbonaceous aerosol in $PM_{2.5}$ fraction monthly in the industrial area of Delhi in 2011. Results show annual average concentrations of $PM_{2.5}$ of 145.59 μg/m^3, of organic C of 41.12 μg/m^3 and of elemental C of 13.25 μg/m^3. Organic C and elemental C were higher in post-monsoon and winter seasons. Organic and elemental C were correlated in pre-monsoon with R^2 of 0.83, and in winter with R^2 of 0.79, implying the existence of similar emission sources. The organic/elemental C ratios in $PM_{2.5}$ ranged from 2.71 to 5.29 with an annual average of 3.28, indicating that vehicle exhaust, coal smoke and biomass burning are the sources of carbonaceous fractions in Delhi.

P. Mandal (✉)
Zonal Laboratory, CSIR-NEERI, New Delhi 110 028, India
e-mail: papiya.mandal1942@gmail.com; p_mandal@neeri.res.in

P. Mandal · R. Sarkar · A. Mandal
Department of Civil Engineering, Delhi Technological University, New Delhi 110 042, India

T. Saud
Centre for Atmospheric Science, Indian Institute Technology Delhi, New Delhi 110 016, India

Keywords Particulate matter · Organic carbon · Elemental carbon · Aerosol · Seasons · Urban air pollution

Introduction

Atmospheric aerosols are gaining considerable importance in present-day scenario in urban cum industrial areas due to growing anthropogenic activities as well as in terms of their effects on human and climate. Recent interest has centered on fine particles ($PM_{2.5}$) and chemical species, particularly carbonaceous fractions (Fenger 2009), since they act as both air pollutants and climate agents (Yu et al. 2007, 2004, 2001). The secondary sources contribute particles below 1 μm via conversion of natural and anthropogenic trace gases into solid and liquid particles. Therefore, researchers are focusing on chemical composition of atmospheric aerosol. Carbonaceous aerosols are the single largest absorber of solar radiation, and their heterogeneous reactions change the dynamics of atmospheric boundary layer which reduces visibility and also create health hazard (Yang et al. 2011). Elemental and organic C are the most important carbonaceous fine fractions in industrial cum urbanized areas of India. Elemental C is a primary pollutant, emitted as by-product of all combustion processes such as industrial emission, traffic, outdoor fires and household biomass fuels. Organic C is emitted directly or formed in situ in the atmosphere. It is a major component in scattering light and cooling the atmosphere. Primary organic C (POC) is directly emitted to the atmosphere, while secondary organic C (SOC) is formed through atmospheric oxidation of volatile organic compounds and subsequent gas-to-particle conversion processes (Plaza et al. 2006). Delhi is a humid subtropical climate city in northern India with an area of 1,484 km^2. Atmospheric pollution and its associated risk to

Published online: 02 September 2014

human health are of particular concern in Delhi. Rapid urbanization, industrialization, steep rise of vehicular registration (more than five million, with an annual average growth rate of 5.85 %, as reported by the Economic Survey of Delhi 2005–2006) and power plants lead to serious deterioration of air quality in Delhi. The concentrations of organic and elemental C in $PM_{2.5}$, tracking their changes with seasons, provide valuable information for constraining their emission sources, understanding atmospheric transport/transformation mechanisms as well as assessing the impact of human activity on the atmospheric environment. The description of the monitoring location is described in the paper by Mandal et al. 2013. The primary objectives of the paper are (1) to examine the seasonal variation pattern of $PM_{2.5}$, organic and elemental C in Delhi, (2) quantification of primary and SOC and (3) identification of most probable sources of emission of C fractions of Delhi.

Methodology

Measurement of $PM_{2.5}$

The samples were collected by APM 550 samplers (Envirotech Pvt. Ltd., India: http://www.envirotechindia.com/apm-550.html) for 8–10 days in a month on Whatman Micro fiber quartz filter papers on 12 hourly basis at a flow rate of 1 m^3/h. The filter papers were pre-baked in a muffle furnace at 550 °C for 6 h to remove organic impurities and kept in desiccators for 24 h before and after the sampling. The concentrations of $PM_{2.5}$ (in $\mu g/m^3$) were measured by gravimetric method.

Organic C/elemental C determination

Organic and elemental C were analyzed by Carbon Analyser (Atmoslytic Inc., USA). The principle of the analyzer is based on the preferential oxidation of organic and elemental C at different temperatures. A 0.5-cm^2 punch from the filter was analyzed for eight carbon fractions following the Interagency Monitoring of Protected Visual Environments (IMPROVE) thermal/optical reflectance (TOR) protocol (Fung et al. 2002; Chow et al. 2004). The principal function of the analyzer is to pyrolyze the sample and then to char the organic C compounds into elemental C. The method analyzes for organic C fractions (OC1, OC2, OC3 and OC4 at 140, 280, 480 and 580 °C), pyrolyzed carbon fraction (OP) and elemental C fractions (EC1, EC2 and EC3 at 580, 740 and 840 °C), respectively. The IMPROVE protocol software defines organic C as OC1 + OC2 + OC3 + OC4 + OP and elemental C as EC1 + EC2 + EC3 − OP.

Results and discussion

Variation of $PM_{2.5}$, organic, elemental and total C

The higher concentrations of $PM_{2.5}$, organic, elemental and total C in the month of December 2011 were found to be 190.56 ± 32, 52.91 ± 13.81, 18.92 ± 5.88 and 71.83 ± 19.33 $\mu g/m^3$, respectively, whereas lower concentrations observed in the month of July were 73.88 ± 12.55, 16.01 ± 3.64, 3.16 ± 0.83 and 19.17 ± 3.98 $\mu g/m^3$, respectively (Table 1). The trends of $PM_{2.5}$, organic and elemental C concentrations were decreasing from January to March 2011, while sharp increasing trends were observed during the months of April and May, 2011. The average monthly $PM_{2.5}$ concentration ranged 70.88–190.56 $\mu g/m^3$ with annual mean of 145.59 ± 25.22 $\mu g/m^3$ (Table 1). The high concentration of $PM_{2.5}$ could be due to traffic, commercial and industrial activities in the surroundings of sampling sites. The comparison of organic and elemental C in $PM_{2.5}$ with the reported values in Asia is presented in Table 2. In the present study, the reported organic and elemental C concentrations were high as compared to other Asian cities. The monthly averages of organic and elemental C ranged 16.01–55.36 and 3.16–18.92 $\mu g/m^3$, respectively (Table 1). The annual mean of organic and elemental C was 41.12 ± 9.17 and 13.25 ± 3.11 $\mu g/m^3$, respectively. The concentrations of organic, elemental and total C showed similar trend to $PM_{2.5}$ mass. Figure 1 shows the seasonal variation of organic and elemental C in $PM_{2.5}$ in Delhi. The contribution of $PM_{2.5}$ was attributed to high emissions from bursting of fire crackers during Diwali festival (post-monsoon), biomass burning and unfavorable metrological conditions (stability of atmospheric boundary layer, low-average mixing height and slow dispersion) during winter season as compared to pre-monsoon and monsoon seasons. The annual mean concentration of $PM_{2.5}$ was above the permissible limit of National Ambient Air Quality Standard (annual mean 40 $\mu g/m^3$) of Central Pollution Control Board 2009. As shown in Table 1, the average concentrations of $PM_{2.5}$, organic and elemental C during winter were 180.26 ± 29.10, 51.07 ± 11.42 and 17.77 ± 4.72 $\mu g/m^3$, respectively, while they were 145.44 ± 23.29, 40.20 ± 8.71 and 11.71 ± 2.23 $\mu g/m^3$ during pre-monsoon, respectively. The average concentrations of $PM_{2.5}$, organic and elemental C during monsoon were 78.67 ± 21.81, 19.99 ± 2.93 and 6.30 ± 0.85 $\mu g/m^3$, respectively, while they were 176.83 ± 25.48, 54.26 ± 14.75 and 16.96 ± 4.57 $\mu g/m^3$ during post-monsoon, respectively. The lower concentrations of carbonaceous aerosol occurred in monsoon, whereas higher concentrations occurred in post-monsoon and winter seasons, respectively. The higher elemental C concentration was due to increased soot particles from vehicles and industrial emissions. The seasonal organic C concentrations ranked in the ascending order of monsoon, pre-monsoon,

Table 1 Average concentration (μg/m^3) of organic C, elemental C, total C, total carbonaceous aerosols, $PM_{2.5}$, organic C/elemental C and total carbonaceous aerosol/$PM_{2.5}$ ratios

Season	Month	Organic C	Elemental C	Total C	Total carbonaceous aerosols	$PM_{2.5}$	Organic carbon/elemental C	Total carbonaceous aerosol/$PM_{2.5}$ (%)
Winter	December ($n = 10$)	52.91 ± 13.81	18.92 ± 5.88	71.83 ± 19.33	103.58 ± 27.57	190.56 ± 32	2.85 ± 0.34	51.81 ± 5.93
	January ($n = 8$)	52.07 ± 12.35	18.20 ± 4.64	70.28 ± 16.49	101.52 ± 23.84	180.31 ± 29.88	2.89 ± 0.44	55.83 ± 5.24
	February ($n = 8$)	50.56 ± 9.42	17.20 ± 3.98	67.76 ± 13.25	98.10 ± 18.88	176.89 ± 30.88	2.98 ± 0.30	55.54 ± 5.81
	March ($n = 10$)	48.73 ± 10.11	16.77 ± 4.40	65.50 ± 14.12	94.74 ± 20.13	173.30 ± 23.64	2.96 ± 0.37	54.19 ± 4.50
	Average ($n = 36$)	51.07 ± 11.42	17.77 ± 4.72	68.84 ± 15.79	99.48 ± 22.61	180.26 ± 29.10	2.92 ± 0.36	54.34 ± 5.37
Pre-monsoon	April ($n = 8$)	39.53 ± 5.92	11.79 ± 1.75	51.32 ± 7.57	75.03 ± 11.11	139.33 ± 16.65	3.36 ± 0.19	53.74 ± 2.85
	May ($n = 8$)	41.40 ± 9.31	12.13 ± 1.85	53.53 ± 11.02	78.37 ± 16.60	154.50 ± 29.64	3.39 ± 0.36	50.93 ± 7.19
	June ($n = 8$)	39.67 ± 10.90	11.21 ± 3.11	50.88 ± 13.85	74.68 ± 20.37	142.50 ± 23.57	3.56 ± 0.40	51.63 ± 5.87
	Average ($n = 24$)	40.20 ± 8.71	11.71 ± 2.23	51.91 ± 10.81	76.03 ± 16.03	145.44 ± 23.29	3.43 ± 0.32	52.10 ± 5.30
Monsoon	July ($n = 8$)	16.01 ± 3.64	3.16 ± 0.83	19.17 ± 3.98	28.77 ± 6.14	73.88 ± 12.55	5.29 ± 1.56	38.92 ± 5.13
	August ($n = 8$)	18.09 ± 4.56	6.19 ± 1.60	24.28 ± 5.93	35.14 ± 8.64	70.88 ± 21.13	2.94 ± 0.46	41.46 ± 4.74
	September ($n = 8$)	25.88 ± 0.57	9.55 ± 0.11	35.43 ± 0.46	50.95 ± 0.80	91.25 ± 31.76	2.71 ± 0.09	43.02 ± 1.12
	Average ($n = 24$)	19.99 ± 2.93	6.30 ± 0.85	26.29 ± 3.46	38.29 ± 5.19	78.67 ± 21.81	3.65 ± 0.70	41.14 ± 3.66
Post-monsoon	October ($n = 8$)	53.17 ± 14.94	16.37 ± 4.61	69.54 ± 18.73	101.44 ± 27.62	175.35 ± 25.55	3.30 ± 0.60	54.39 ± 7.96
	November ($n = 8$)	55.36 ± 14.56	17.55 ± 4.53	72.91 ± 18.79	106.12 ± 27.50	178.30 ± 25.40	3.16 ± 0.33	51.31 ± 7.71
	Average ($n = 16$)	54.26 ± 14.75	16.96 ± 4.57	71.22 ± 18.76	103.78 ± 27.56	176.83 ± 25.48	3.23 ± 0.47	52.85 ± 7.83
Annual	($n = 100$)	41.12 ± 9.17	13.25 ± 3.11	54.37 ± 11.96	79.04 ± 17.43	145.59 ± 25.22	3.28 ± 0.45	50.23 ± 5.34

Values are represented as average ± standard deviation

winter and post-monsoon, while elemental C took a pattern of monsoon, pre-monsoon, post-monsoon and winter. The seasonal total C concentrations ranked in the order of post-monsoon < winter < pre-monsoon < monsoon. This can be attributed to coarse loose soil intrusion into ambient air due to dust raising winds and turbulent atmosphere during monsoon. Winter season leads to frequent accumulation of atmospheric pollutants in lower atmospheric layer. The total carbonaceous aerosol is the sum of elemental and organic matter (1.6 × organic C) (Turpin and Huntzicker 1995). The annual average concentrations of total carbonaceous aerosol were 50.23 % of $PM_{2.5}$ with seasonal variation in the descending order of winter, post-monsoon, pre-monsoon and monsoon (Table 1).

Estimation of primary and secondary organic C

The separation and quantification of primary and SOC are difficult as no simple direct analytical technique is available (Yu et al. 2007, 2004), although there are many methods for quantification of total organic C. Generally, SOC formation is low when photochemical activity is low, indicates low ratios of organic and elemental C. SOC contributes organic C significantly in pre-monsoon season due to favorable climatic condition (higher temperature and more intense solar radiation). The minimum ratio of organic/elemental C was obtained to estimate SOC (Castro et al. 1999). The equations to estimate secondary organic C are given below.

$$\text{Secondary organic C} = \text{Total organic C} - \text{Primary organic C}$$

$$\text{Primary organic C} = \text{Elemental C} \times (\text{organic/elemental C})_{\text{minimum}}$$

The minimum organic/elemental C during the study period was 1.25. The seasonal fluctuation of primary and SOC and elemental C in $PM_{2.5}$ is illustrated in Fig. 2. The distribution of SOC in pre-monsoon, monsoon, post-monsoon and winter seasons were 49.36, 47.09, 46.42 and 41.87 % of total C, respectively. Secondary organic aerosol = 1.6 × SOC (Turpin and Huntzicker 1995) plays an important role on physical and chemical properties of atmosphere, relating to haze, visibility, climate and health. The annual average concentration of secondary organic aerosol was 39.93 μg/m^3, covering 27.42 % of $PM_{2.5}$ mass, indicated that secondary organic aerosol contributed a major fraction of $PM_{2.5}$ mass in Delhi.

Relationship between organic and elemental C

The strong correlation between organic and elemental C was observed in pre-monsoon ($R^2 = 0.83$), followed by winter ($R^2 = 0.79$) and post-monsoon ($R^2 = 0.71$) seasons. The weak correlation was in monsoon ($R^2 = 0.57$) season.

Table 2 Comparison of organic and elemental C in $PM_{2.5}$ with the reported values in Asia

Country	Sample site	Sampling period	Major source	Analytical method	Concentration in μg/m^3		References
					OC	EC	
China	Shanghai (Hainan Road)	March 1999–March 2000	Traffic	Thermal/optical reflectance	15.43	6.77	Ye et al. (2003)
	Beijing	July–August 2001, December 2001, June–July 2002	Urban	Elemental analyzer	20.44	20.1	Dan et al. (2004)
Japan	Sapporo	November 1991–October 1992	Urban	Combustion method	4.06	4.51	Ohta et al. (1998)
Korea	Seoul	October–November 2001	Urban	Thermal/optical reflectance	18	8.13	Kang et al. 2004
	Sihwa	February 1998 and 1999	Industrial	Thermal/optical reflectance	9.8	1.8	Park et al. (2001)
India	Delhi	January 2011–December 2011	Urban/industrial	Thermal/optical reflectance	41.12	13.25	This study

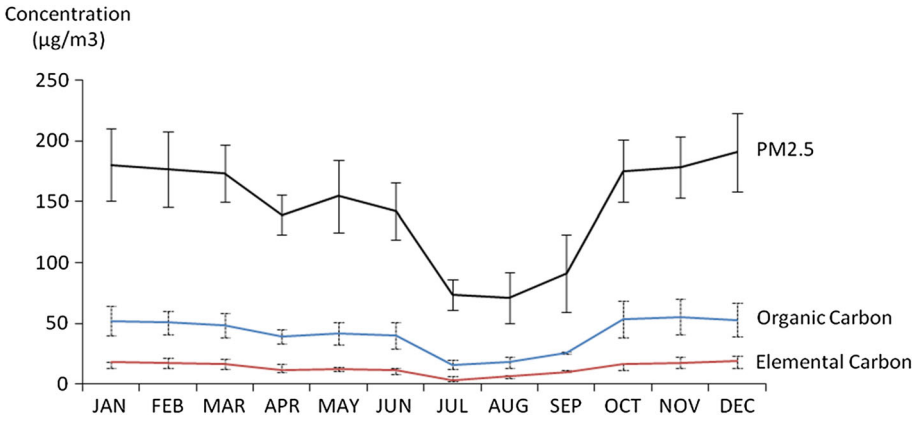

Fig. 1 Monthly variation of organic C, elemental C and $PM_{2.5}$ in the year 2011: Organic C, elemental C and $PM_{2.5}$ concentrations varied from 19.99 to 54.26, 6.30 to 17.77 and 78.67 to 180.26 μg/m3, respectively

The measurements of organic and elemental C provide an idea to identify the possible sources of carbon emissions. Elemental C is a good marker for the diesel–fuel engine exhaust emissions (Gray and Cass 1998; Funasaka et al. 1998). Total carbonaceous aerosol represents a mixture of various emission sources; hence, organic/elemental C ratios could be used to distinguish different origin and transformation characteristics (Chu 2005). The organic/elemental C ratios vary for vehicular exhaust (2.5–5.0) (Schauer et al. 2002), coal smoke (2.5–10.5) (Chen et al. 2006), kitchen emissions (4.3–7.7) (See and Balasubramanian 2008) and biomass burning (3.8–13.2) (Zhang et al. 2007) etc., respectively.

The organic/elemental C ratios in the study period varied from 2.71 to 5.29 with an annual average of 3.28, indicated multiple emission sources such as vehicular exhaust, coal smoke, biomass burning. The concentrations of OC1, OC2, OC3, OC4, OP and EC1 during winter season represented the mixture of coal combustion, motor vehicle exhaust and biomass burning (Fig. 3). The concentrations of EC2 and EC3 during pre-monsoon and monsoon seasons were indicated the emission from diesel vehicle exhaust as it contains lots of high temperature component of elemental C (Watson et al. 1994). Carbon fraction (OC1) represents biomass burning, whereas carbon

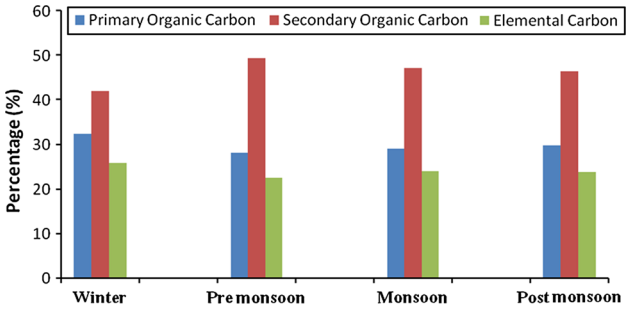

Fig. 2 Seasonal variation of primary and SOC and elemental C

fractions OC2, OC3, OC4, OP and EC1 represent gasoline motor vehicle exhaust or coal combustion (Cao et al. 2005).

Conclusion

The seasonal variation of PM2.5, organic and elemental C concentrations in Delhi, India, were varied from 78.67 to 180.26, 19.99 to 54.26 and 6.30 to 17.77 μg/m^3, respectively. The trends of organic and elemental C concentrations were low in warm seasons as compared to cold season, which

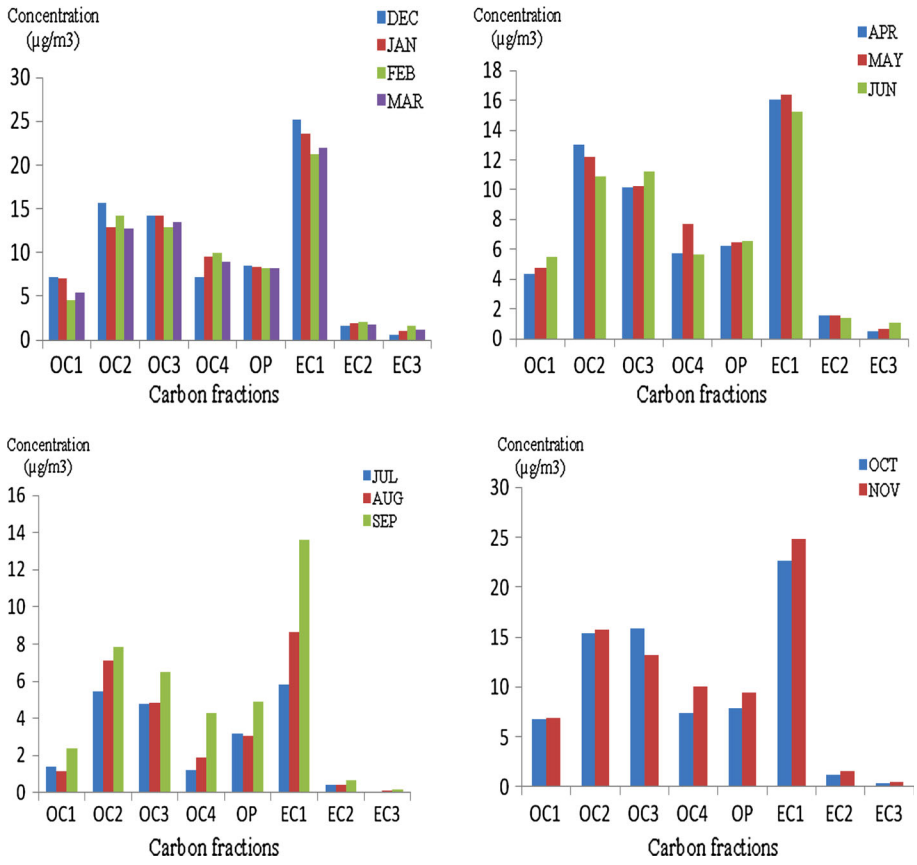

Fig. 3 Seasonal variation of carbon fractions in the year 2011: organic C = OC1 + OC2 +OC3 + OC4 + OP and elemental C = EC1 + EC2 + EC3 − OP. The analysis of carbon fractions indicated the multiple emission sources, e.g., motor vehicle exhaust, industrial emission and biomass burning

implied that meteorological conditions were a main governing factor. The annual average concentration of organic C was 75 % of total C. The annual average concentration of SOC was 60.34 % of organic C. The average ratio of organic and elemental C in Delhi was 3.28 which indicated mixed emission sources of carbonaceous aerosol. The emission sources were vehicle exhaust, coal combustion, biomass combustion, etc. Efficient emission control strategies of mixed emission sources are necessary to minimize emission of carbonaceous aerosol in the ambient air.

Acknowledgments The authors are thankful to Director, CSIR-NEERI for giving permission to publish the work.

References

Cao JJ, Lee SC, Zhang XY, Chow JC, An ZS, Ho KF, Watson JG, Fung K, Wang YQ, Shen ZX (2005) Characterization of airborne carbonate over a site near Asian dust source regions during spring 2002 and its climatic and environmental significance. J Geophys Res 110:D03203. doi:10.1029/2004JD005244

Castro LM, Pio CA, Harrison RM, Smith DJT (1999) Carbonaceous aerosol in urban and rural European atmospheres: estimation of secondary organic carbon concentrations. Atmos Environ 33(2771): 2781

Chen YJ, Zhi GR, Feng YL, Fu JM, Feng JL, Sheng GY et al (2006) Measurements of emission factors for primary carbonaceous particles from residential raw-coal combustion in China. J Geophy Res Lett 33:L20815. doi:10.1029/2006GL026966

Chow JC, Watson JG, Kuhns HD, Etyemezian V, Lowenthal DH, Crow DJ, Kohl SD, Engelbrecht JP, Green MC (2004) Source profiles for industrial, mobile, and area sources in the big bend regional aerosol visibility and observational (BRAVO) study. Chemos 54(185):208

Chu SH (2005) Stable estimate of primary OC/EC ratios in the EC tracer method. Atmos Environ 39(1383):1392

CPCB (2009) National ambient air quality standards in India. http://cpcb.nic.In/uplo/Publication/Publication_514_airqualitystatus2009.Pdf

Dan MO, Zhuang G, Li X, Tao H, Zhuang Y (2004) The characteristics of carbonaceous species and their sources in $PM_{2.5}$ in Beijing. Atmos Environ 38(3443):3452

Economic Survey of Delhi (2005–2006) Published by the Planning Department, Government of NCT of Delhi, Delhi Secretariat, New Delhi

Fenger J (2009) Air pollution in the last 50 years—from local to global. Atmos Environ 43(13):22

Funasaka K, Miyazaki T, Kawaraya T, Tsuruho K, Mizuno T (1998) Characteristics of particulates and gaseous pollutants in a highway tunnel. Environ Poll 102(171):176

Fung KK, Chow JC, Watson JG (2002) Evaluation of OC/EC speciation by thermal manganese dioxide oxidation and the IMPROVE method. J Air Waste Manag Asso 52(11):1333–1341

Gray AH, Cass GR (1998) Source contributions to atmospheric fine carbon particle concentration. Atmos Environ 32(3805):3822

Kang CM, Lee HS, Kang BW, Lee SK, Sunwoo Y (2004) Chemical characteristics of acidic gas pollutants and PM2.5 species during hazy episodes in Seoul, South Korea. Atmos Environ 38(4749): 4760

Mandal P, Saud T, Sarkar R, Mandal A, Sarma SK, Mandal TK, Bassin JK (2013) High seasonal variation of atmospheric C and particle concentrations in Delhi, India. Environ Chem Lett. doi:10.1007/s10311-013-0438-y

Ohta S, Hori M, Yamagata S, Murao N (1998) Chemical characterization of atmospheric fine particles in Sapporo with determination of water content. Atmos Environ 32:1021–1025

Park SS, Kim YJ, Fung K (2001) Characteristics of $PM_{2.5}$ carbonaceous aerosol in the Sihwa industrial area, South Korea. Atmos Environ 35(657):665

Plaza J, Ǵomez-Moreno FJ, Ńũnez L, Pujadas M, Arínano B (2006) Estimation of secondary organic aerosol formation from semi-continuous OC-EC measurements in a Madrid suburban area. Atmos Environ 40(6):1134–1147

Schauer JJ, Kleeman MJ, Cass GR, Simoneit BRT (2002) Measurement of emissions from air pollution sources 5. C1–C32 organic compounds from gasoline-powered motor vehicles. Environ Sci Technol 36(6):1169–1180

See SW, Balasubramanian R (2008) Chemical characteristics of fine particles emitted from different gas cooking methods. Atmos Environ 42(8852):8862

Turpin BJ, Huntzicker JJ (1995) Identification of secondary organic aerosol episodes and quantitation of primary and secondary organic aerosol concentrations during SCAQS. Atmos Environ 29(13):3527–3544

Watson JG, Chow JC, Lowenthal DH, Pritchett LC, Frazier CA, Neuroth GR, Robbins R (1994) Differences in the carbon composition of source profiles for diesel-and gasoline-powered vehicles. Atmos Environ 28(2493):2505

Yang F, Huang L, Duan F, Zhang W, He K, Ma Y, Brook JR, Tan J, Zhao Q, Cheng Y (2011) Carbonaceous species in $PM_{2.5}$ at a pair of rural/urban sites in Beijing, 2005–2008. Atmos Chem Phy 11:7893–7903

Ye B, Ji X, Yang H, Yao X, Chan CK, Cadle SH, Chan T, Mulawa PA (2003) Concentration and chemical composition of $PM_{2.5}$ in Shanghai for a 1-year period. Atmos Environ 37:499–510

Yu S, Zender CS, Saxena VK (2001) Direct radiative forcing and atmospheric absorption by boundary layer aerosols in the southeastern US: model estimates on the basis of new observations. Atmos Environ 35:3967–3977

Yu S, Dennis R, Bhave PV, Eder B (2004) Primary and secondary organic aerosols over the United States: estimates on the basis of observed organic carbon (OC) and elemental carbon (EC), and air quality modeled primary OC/EC ratios. Atmos Environ 38:5257–5268

Yu S, Bhave PV, Dennis RL, Mathur R (2007) Seasonal and regional variations of primary and secondary organic aerosols over the continental United States: observation-based estimates and model evaluation. Environ Sci Technol 41:4690–4697

Zhang YX, Shao M, Zhang YH, Zeng LM, He LY, Zhu B (2007) Source profiles of particulate organic matters emitted from cereal straw burnings. J Environ Sci 19(2):167–175

Study of the Processing Pathway for Cosolvent Addition in Active Layer Preparation of Inverted Organic Solar Cell

Sarita S. Nair,[1] D. Kumar,[1] Abhishek Sharma,[2] Amitava Majumdar[2]
[1] *Department of Applied Chemistry & Polymer Technology, Delhi Technological University, Shahbad Daulatpur, Delhi-110042, India*
[2] *Moserbaer India Ltd., 66, Udyog Vihar, Greater Noida, Uttar Pradesh-201306, India*

Investigation on processing pathway for co-solvent addition in active layer preparation of an inverted organic solar cell indicated that the composite films cast out of simple marginal solvent (like cyclohexanone) addition in poly(3-hexyl thiophene)-[6,6]-phenyl C_{61}-butyric acid methyl ester (P3HT-PCBM) solution were not effectively crystallized. A comparison of one step direct marginal solvent addition to the P3HT-PCBM solution with the modified two step process consisting of primary P3HT crystallization in first step by marginal solvent addition to a solution of only P3HT in good solvent (like *ortho*-dichloro benzene) followed by mixing of PCBM solution revealed improvement in P3HT crystallization in the latter method. Grazing incidence X-ray diffraction measurements supported favorable vertical concentration gradient in the P3HT-PCBM composite film. This modification of active layer morphology with the two step individually mixed cyclohexanone addition into the active layer spin coating solution results in an improved power conversion efficiency of 3.39%, an improvement of more than 10% compared to the conventional one step blended co-solvent addition method. POLYM. ENG. SCI., 00:000–000, 2014.

INTRODUCTION

The ability of organic semiconducting molecules (donor/acceptor mixture) to function as the active layer in a polymer solar cell has been widely acknowledged [1]. Largely accepted among the solution processed organic solar cells (OSCs) is the bulk heterojunction (BHJ) composite structure of semiconducting poly(3-hexyl thiophene) (P3HT) donor polymer (having high mobility) and the soluble fullerene [6, 6]-phenyl C_{61}-butyric acid methyl ester (PCBM) acceptor [2]. Problems associated with the commercialization of polymer solar cells (in conventional BHJ architecture) are related to the chemical instability caused by packing the active layer between a high work function metal at the bottom as anode and a low work function metal at the top as cathode. The problems of vertical phase separation and device instability of conventional architectures suggest moving to an inverted configuration as a reliable alternative. Preference given to the inverted configuration with reversed polarity is because of the air stability that this architecture offers, with rapidly oxidizing low work function metals replaced by more stable high work function metals such as silver (Ag) or gold (Au) [3]. This inverted architecture has the added advantage of favorable vertical phase separation for charge carrier transport which was adversely affecting the normal device configuration [4]. Also with the recent bridging of the efficiency gap between normal and inverted architectures, inverted device with better lifetime is pursued more [5].

Figure 1 demonstrates a recognized layer sequence in inverted and normal architecture of polymer solar cells. However, in both of these architectures, morphology of photoactive organic thin film has a decisive part to play for effective performance of the solar device. Prior art recommends the semiconductor mixture, necessitated to overcome the exciton decay, as a complex combination appearing out of partial miscibility and simultaneous incompatibility of the two components in the composite [6]. Segregated nanoscale phases as well as bi continuous interpenetrating network of donor–acceptor domains are the two things that are desired for efficient charge separation of the photo-generated excitons and their transport to the respective electrodes [7]. Factors restricting the high device efficiency have been the existing discrepancy between the hole and electron mobility. Hole mobility is adversely affected in donor–acceptor composite films, as thin film coating technique such as spin coating on account of fast solvent evaporation do not support well-organized growth of P3HT crystals [8]. Earlier reports have suggested that solubility of acceptor molecules does influence the crystallinity of donor in the composite. The unstructured areas thus created in the composite material due to the presence of acceptor confines the charge carrier mobility due to the hopping movement among the amorphous (insufficiently crystallized) polymer chains. So, this limited structural development supposed for crystallizable polymer like P3HT in the presence of PCBM limits the hole transport and hence low efficiency [9]. To overcome these issues, few reports in literature also concentrated on mixing directly the preorganized crystalline fibrillar poly(3-alkyl thiophene) (P3AT) with the acceptor. However, such devices dealt with low efficiency in turn, due to larger phase separation between the donor and acceptor domains in the composite mixture. For this reason, they suggested mixing back some amount of low molecular weight amorphous P3HT into the filtered P3HT nanofibers solution so as to have the connectivity between its crystalline domains and hence, to have an interpenetrating network structure for improved device efficiency [10].

Numerous processing methods initiated toward controlling the active layer morphology and hence, to improve the device efficiency includes thermal annealing [11], solvent annealing [12], solvent–non-solvent mixture method [13], etc. Post treatments such as thermal and solvent annealing though successful to some extent for modifying the morphology of the active layer are difficult to put into practice for large scale production considering their incompatibility with flexible substrates and the possible danger of explosive solvent vapors. The method of solvent–non solvent mixture has been growing even with flexible

Correspondence to: D. Kumar; email: dkumar@dce.ac.in and drdkumar@yahoo.co.uk
DOI 10.1002/pen.24014
Published online in Wiley Online Library (wileyonlinelibrary.com).

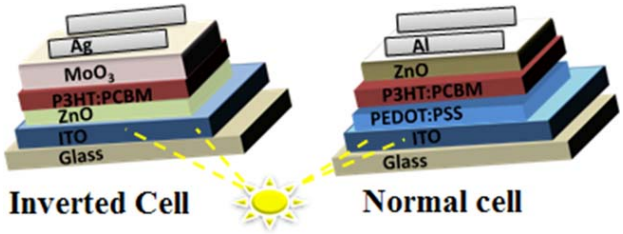

FIG. 1. Schematic representation of the layer sequence in inverted and normal architecture of polymer solar cell. [Color figure can be viewed in the online issue, which is available at wileyonlinelibrary.com.]

substrates, and unlike a single solvent, combination solvents can offer improved solubility of the components in the composite mixture [14]. Alkane dithiols have been the best recognized category of "processing additive," effectual in modifying the morphology in quite a lot of polymer classifications including classical P3HT donor polymer as well as for group of some low band gap polymers. An outcome of the competent study on processing additives (carried out by Peet et al.) was a remarkable enhancement in the photovoltaic device efficiency, attributable to the change in the morphology of the active layer via incorporating 1,8-octane dithiol additive. The additive was found to selectively dissolve the fullerene phase, in a way providing independence for the poly[2,6-(4,4-bis(2-ethylhexyl)−4*H*-cyclopenta[2,1-b;3,4-b′]-dithiophene)-*alt*−4,7-(2,1,3 benzothiadiazole)] (PCPDTBT) polymer to crystallize sufficiently in the composite mixture [15]. Thereafter, there were continued efforts directed on the same track by numerous other researchers providing a means for exploring other solvent mixtures such as 1,8-diiodooctane/chlorobenzene for active layer preparation [16].

Nevertheless, we are still far away from the optimal composite morphology and from the realm of commercialization. Systematization over the morphology of the composite in the solvent mixture method was complicated as the P3HT crystallization and requisite phase separation of components take place in a single stage. As different solvents present different solubility to P3HT polymer and PCBM acceptor consequently, the solvent mixture method can offer wide range of arrangements among the components of the composite. Hence, this approach can be effective in modifying the donor–acceptor interface areas and charge carrier mobility in P3HT-PCBM composites depending on the employed solvent system [17, 18]. However, since there have not been many reports upon utilization of solvent–co-solvent mixture approach for modifying the active layer (P3HT/PCBM) morphology in an inverted device so, we considered in detail two processing techniques for the aforesaid co-solvent addition (before spin coating step) for active layer preparation in the inverted device. The aim was to enhance the P3HT reorganization or self-assembly by nullifying the effect of the acceptor component to enhance the device performance. Our main concern was to have an efficient P3HT crystallization while, simultaneously maintaining effectual connectivity between these crystalline P3HT domains via amorphous P3HT segments spread in between them, to promote PCBM diffusion thereafter for achieving interpenetrating donor–acceptor networks.

We evaluated one step conventional process of direct marginal solvent addition to the P3HT-PCBM solution in good solvent (like *o*-dichloro benzene) with the two step process of crucial P3HT crystallization in first step by marginal solvent addition (like cyclohexanone) to a solution of only P3HT in good solvent followed by mixing of PCBM solution in good solvent to the same, and ultimately mild thermal annealing of both of the casted films for further phase separation of domains in the composite film.

EXPERIMENTAL

Materials and Method

In this experiment, we fabricated inverted BHJ polymer solar cells with a constituent layer structure of indium tin oxide (ITO)/zinc oxide (ZnO)/P3HT:[6,6]-phenyl-C_{61}-butyric acid methyl ester (PCBM) blend (P3HT:PCBM)/MoO_3/Ag (realized by means of procuring P3HT and PCBM from Sigma Aldrich). Zinc acetate dihydrate ($C_4H_{10}O_6Zn$), 2-methoxy ethanol ($C_3H_8O_2$), and ethanolamine (C_2H_7NO) employed in zinc oxide (ZnO) preparation were also purchased from Sigma Aldrich.

Inverted polymer solar cells were assembled over the patterned ITO-coated glass substrate with less than 20 Ω/sq sheet resistance. ITO glass substrates were cleaned via ultrasonication for 20 min each sequentially in a boiling soap solution, deionized water, acetone, and isopropanol, followed by drying with nitrogen and then 26 min of UV–ozone exposure. A 30 nm thin ZnO film was deposited on the cleaned substrate from a solution prepared by mixing zinc acetate dihydrate, ethanolamine, and 2-methoxy ethanol yielding a 0.50M ZnO solution. Subsequent curing of the coated film at 250°C for 10 min in air was carried out to partly crystallize the ZnO. For active layer fabrication, P3HT and PCBM (1:0.6 weight ratio) were dissolved in 1 ml of good solvent, i.e., 1,2 *ortho*-dichloro benzene (*o*-DCB) by means of continuous stirring overnight at 50°C yielding a 30 mg ml^{-1} blend solution, following which an active layer was spin coated over the ZnO coated substrate using the prepared solution. Thereafter, the substrates were transferred to nitrogen ambient and annealed at 85°C for 30 min. Molybdenum oxide (MoO_3) and silver (Ag) layers were thermally deposited in a vacuum chamber at a base pressure of 5×10^{-6} mbar. MoO_3 layer (hole transporting layer, HTL) of 7 nm thickness was deposited at a deposition rate of 0.5 Å s^{-1}. This was followed by deposition of 150 nm Ag as a top electrode, at a deposition rate of 1.0 Å s^{-1}.

The performance of devices of area 0.09 cm^2 was measured under illumination from a solar simulator AM 1.5G with intensity of 100 mW cm^{-2}. To study the effect of co-solvent addition on the active layer preparation, spin-coating solutions were prepared by two different methods and a comparison was made. Co-solvent used for this study is cyclohexanone solvent with a boiling point of 155.6°C. The choice of cyclohexanone co-solvent was made keeping in mind the solubility index of the solvent that suggests more solubility to PCBM than P3HT. The amount of co-solvent for active layer preparation was optimized to be 5%, as an amount higher than 5% results in gel formation in precursor solution over a period of time at room temperature and lesser than 5% co-solvent did not result in significant improvement. For each of these modifications, 5% of the co-solvent was added and the solution was stirred for 2 h in nitrogen ambient prior to any further processing. For convenience, we named the composite films as BLND (i.e., blended addition,

 DOI 10.1002/pen

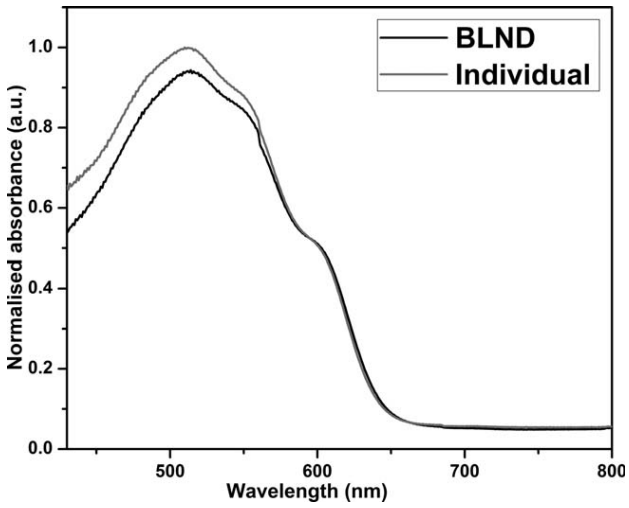

FIG. 2. Absorption spectra of P3HT-PCBM composite films casted out of solutions modified with blended cyclohexanone addition and individually mixed cyclohexanone addition.

for films prepared from solution with cyclohexanone added directly to P3HT:PCBM blended solution in *o*-DCB solvent) and individual (i.e., individually mixed, for films prepared from solutions with first cyclohexanone added to a P3HT only solution in *o*-DCB, followed by stirring for 2 h and subsequent mixing of PCBM solution in *o*-DCB to the above solution).

Measurements

The current density (J)–voltage (V) characteristics of the as prepared photovoltaic devices were measured using a Keithley (Model 2420) source meter under illumination intensity of 100 mW cm^{-2} from a solar simulator (Model SS150AAA Photo Emission Technology Inc.) with AM 1.5 G filter. Device preparation was carried out in nitrogen ambient (which was maintained inside a glove box from Jacomex with $\Delta P = 3.0$ mbar and oxygen level of 0.3 ppm). The UV–visible absorption measurements were performed using a Perkin Elmer lambda 35 UV–visible spectrophotometer. Surface morphology was characterized using an atomic force microscope (AFM), VEECO DI-3100, with Nanoscope (III) in tapping mode. Grazing incidence X-ray diffraction (GI-XRD) measurements employing Cu-Kα radiation were done at three grazing incidence angles of 0.11°, 0.13°, and 0.3° using a Rigaku ultima IV X-ray diffractometer ($\lambda = 1.54$ Å).

RESULTS AND DISCUSSION

UV–Visible Absorption Measurements

Figure 2 shows the comparative UV–visible absorption spectra of the P3HT-PCBM composite films prepared via two methods (blended addition and individually mixed addition), to investigate the effect of co-solvent addition pathway on the variation in UV–visible radiation absorption by the polymer chains in the composite mixture. Spectra of both the films include an absorption peak at around 512 nm, with shoulders at 550 and 610 nm, clearly confirming the presence of strictly controlled P3HT chains in the composite mixture. The absorptions at 512, 550, and 610 nm fit with an intra-chain π–π^* transition, extensive conjugated chain absorption, and inter-chain transition, respectively of the highly ordered solid state P3HT [19]. An increase in the intensity of the absorption at 512 and 550 nm observed for the case of individually mixed modified (Individual) sample as compared to blended (BLND) co-solvent modified composite sample film suggests a more efficient growth of P3HT crystals in the former. This improved crystallization of P3HT can be expected due to the diminishing disturbance of PCBM by the side of P3HT crystallization in individually co-solvent modified sample. Growth of P3HT crystals in P3HT only solution is known to take place by its self-organization ability from random coil conformation to rod-like conformation, easing of the chain entanglement [20]. This same criterion applies to the crystallization of P3HT in the composite (P3HT:PCBM) film also; however this transition is limited by the extent of co-precipitating (or co-existing) PCBM content.

The coil to rod transition was found to be more favorable with an individual co-solvent modified sample consistent with the increased absorptions observed at 512 and 550 nm, corresponding to more enhanced intra-chain transition and extended conjugation length of P3HT chains. So, sufficient P3HT precipitation must have taken place in individual co-solvent modified solution, prior to the addition of PCBM solution. The crystallization step then would have been followed by diffusion of PCBM to the disordered phases of some completely dissolved (un-precipitated) polymer in the *o*-DCB/cyclohexanone mixture to form an interpenetrating network, allowing us to achieve the best possible P3HT crystallization in the composite mixture. However, such a process would have resulted in a bit larger sized P3HT domains, causing larger phase separation between the components of the composite mixture as suggested by Kozub et al. [21]. Again, a decreased P3HT absorption in the blended cyclohexanone added sample film reveals that though the cyclohexanone addition must have influenced the precipitation order changeover to P3HT first; however probability of PCBMs presence in the disordered regions of completely dissolved P3HT chains in *o*-DCB during the crystallization process could have hindered the maximum possible intra-chain transition of P3HT chains [22].

Grazing Incidence X-ray Diffraction Measurements

To verify the crystalline ordering in the active composite of inverted OSC, GI-XRD measurements were performed on spin coated films of P3HT:PCBM composite (modified by co-solvent addition). GI-XRD measurements were attempted using the lab source instrument following some recent reports of GI-XRD measurements from lab sources for stronger scattering films [23]. Measurements were employed at three grazing incidence angles, i.e., 0.11°, 0.13°, and 0.3°, to verify the vertical phase separation through the composite film. It is well known that for an electromagnetic radiation such as an X-ray, the refractive index of solid material being less than unity, results in bending of the X-ray on its way to the surface due to refraction. So, using a fixed grazing incidence angle of 0.11°, i.e., smaller than the critical angle for P3HT, total reflection occurs and only a short-lived beam transverses just few nanometers below the surface, giving diffraction mainly from the surface of the composite film. At grazing incidence angle slightly higher than the critical angle for external reflection (i.e., 0.13°), the X-ray

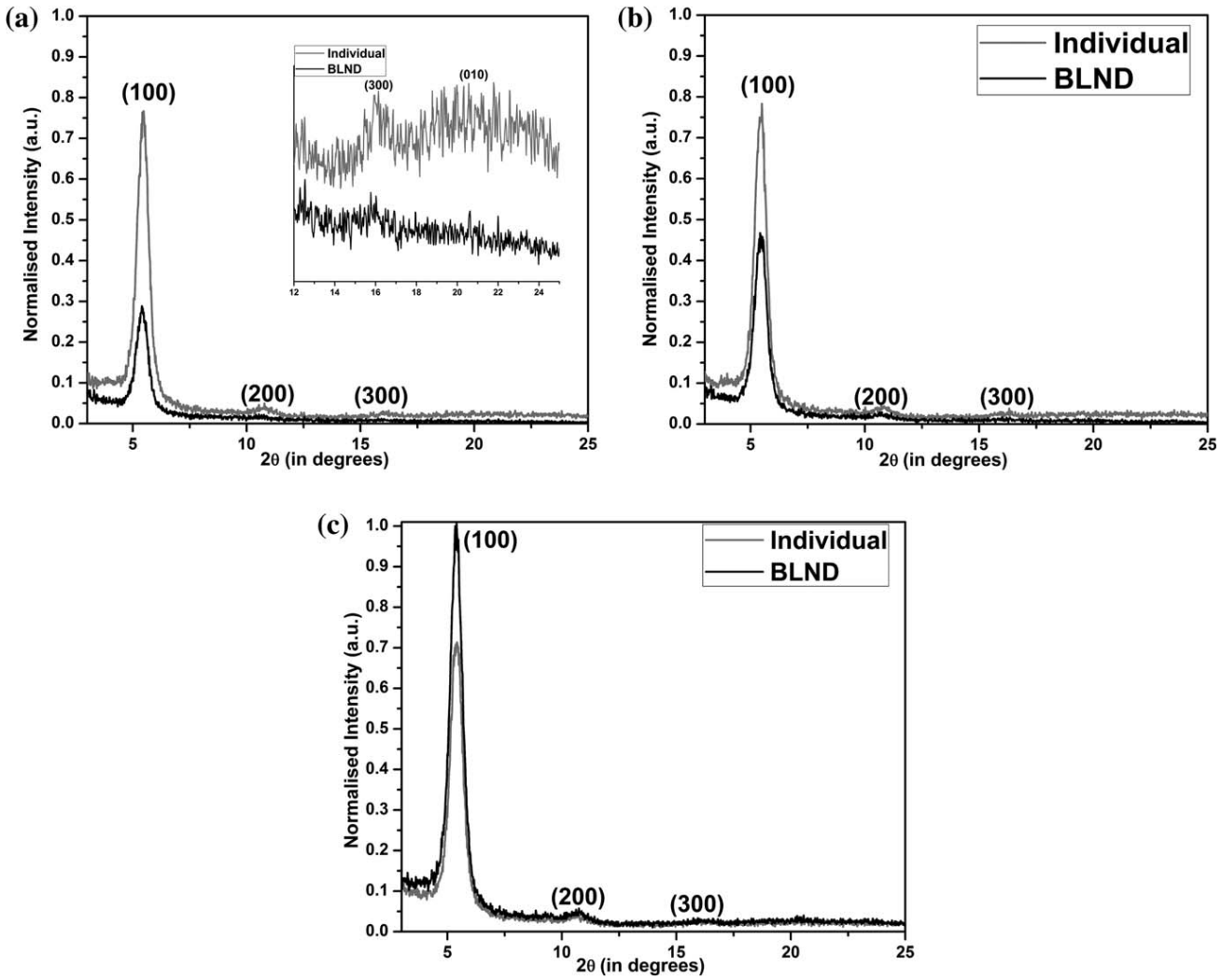

FIG. 3. (a) Normalized GI-XRD profiles of P3HT: PCBM composite films casted from solution modified with cyclohexanone solvent by two different approaches at grazing incidence of 0.11° and inset shows the enlarged view of diffraction intensity profile with 2Θ ranging 12° to 25°, (b) GI-XRD profiles of films at grazing incidence of 0.13°, (c) GI-XRD profiles at incidence of 0.3°

diffuses deeper in the film providing diffraction from the depth of the film. The probed depth for an organic material increases rapidly with a small increase in the incidence angle near the critical angle region. Again, keeping incidence angle well above the critical angle (i.e., at 0.3°) provides diffraction from the whole volume (bulk) of the composite film [24, 25]. So, by varying the probe depth with the incidence angle, X-rays can be used to check the surface, underlying interfaces, and bulk material.

For both the BLND and individual mixed films at 0.11° incidence angle, three diffraction peaks marked as (h00) where, $h = 1$–3 corresponds to layered intra-chain P3HT orientation along α axis of crystallographic plane and (010) peak indexed the inter-chain π–π stacking orientation of P3HT backbone along b-axis of crystallographic plane (Fig. 3a) [26]. The intensities of the (100) reflection peaks at $2\Theta = 5.426°$ for BLND co-solvent modified films and at $2\Theta = 5.440°$ for individually mixed films suggest improved crystallite orientation along a-axis of the crystallographic plane in case of the latter. Better P3HT crystallization observed in individually mixed co-solvent modified sample is possibly due to the negligible interruption by PCBM crystallites during P3HT crystallization in the solvent: co-solvent mixture.

Table 1 sums up the interlayer distances and crystallite sizes of P3HT domains determined of the (100) diffraction peak in the GI-XRD patterns at three grazing incidence angles. An additional inference from the study of the π–π stacking (010) peak intensity also highlighted the better part played by the polythiophene backbone in individual mixed co-solvent modified sample to form superior π–π stacked domains as compared to the inter-chain stacking in BLND composite film [27] (inset of Fig. 3a). So, surface of individual mixed co-solvent modified composite film have more number of well crystallized P3HT domains. At an incidence angle of 0.13° (Fig. 3b), individually mixed co-solvent casted film still dominates blended co-solvent casted film in terms of more number of well crystallized P3HT chains. However, the differences in diffraction intensities (related to the crystallinity and number of P3HT crystallites) that existed at the

 DOI 10.1002/pen

TABLE 1. Summary of interlayer distances (d) and the size of the coherent P3HT domains resolved of the (100) peak at three grazing incidences 0.11°, 0.13°, and 0.3° in the XRD pattern.

S. no.	Device	Grazing incidence angle (in degree)	2Θ value (in degree)	Interlayer distance d_{100} (Å)	FWHM	Grain size (nm)
1.	BLND	0.11°	5.426	16.27	0.608	13.00
2.	BLND	0.13°	5.448	16.21	0.632	12.45
3.	BLND	0.3°	5.356	16.48	0.654	12.02
3.	Individually mixed	0.11°	5.440	16.23	0.580	13.70
4.	Individually mixed	0.13°	5.422	16.18	0.616	12.77
5.	Individually mixed	0.3°	5.375	16.43	0.638	12.33

surface of BLND and individual mixed co-solvent sample film were reversed when bulk of these films were probed (Fig. 3c, at incidence angle of 0.3°). This effect may be due to the presence of greater fraction of PCBM in the bulk of individually mixed co-solvent casted film as compared to blended co-solvent modified film.

To compare the vertical phase separation in both the co-solvent modified composite films, a comparison of the set of P3HT diffraction peaks at 0.11°, 0.13°, and 0.3° grazing incidence angles was made. Generally, the intensity of the diffraction peaks should increase with the increase in the grazing incidence angle and maximum P3HT intensity is observed at angle slightly larger than the critical angle. In individually mixed co-solvent modified composite film, P3HT crystallization was more at the surface than in the bulk of the film, as it gets more room to build up efficiently and the minimum hindrance from PCBM was perceived. As we enter into the bulk film, slightly reduced P3HT diffraction peak intensities may be due to reduced polymer crystallization or the increasing PCBM interruption. As the concentration of P3HT in both the processing methods is same (number of P3HT crystallites also be the same) so, slightly reduced intensity of the (100) reflection peak in the bulk of individually mixed co-solvent casted film may be due to the lesser fraction of oriented P3HT crystallites in the bulk. So, there is a redistribution of the P3HT through the film with more oriented P3HT crystallites at the surface and lesser of them in the bulk. However, in blended co-solvent modified films lesser P3HT crystallites at the surface as compared to the bulk were observed. These results point to a concentration gradient in the active layer of inverted OSC prepared via co-solvent addition. In other words, individually mixed co-solvent modified films have more number of crystallized P3HT and lesser PCBM domains at the surface, i.e., next to HTL (i.e., MoO_3 in present inverted device case), while the bulk (in the neighborhood of bottom contact or electron transport layer (ETL), which is ZnO in our case) comprises of less number of P3HT crystallites and more PCBM domains. This upright phase separation or concentration gradient is an added advantage to the inverted architecture. This favorable concentration gradient or upright phase separation is more prominent for individually mixed co-solvent modified casted film, which may in turn benefit the device, prepared thereof with individually mixed co-solvent casted film. Using the Scherrer formula, we could successfully work out the size of P3HT crystallites near the surface as 13.0 and 13.7 nm for BLND and individual mixed films, respectively, while in the bulk of the film, crystallite size was of the order of 12.0 and 12.33 nm, respectively for blended and individually mixed co-solvent modified films [28]. Larger crystal size of crystallizable polymer in active layer produced via modified co-solvent addition method can also be vital for the charge transport, which may be a contributing feature for high photocurrent generation in the OSC [29].

Surface Morphology

The surface morphology study of the P3HT:PCBM composite films were done using tapping mode AFM. Figure 4a and b depicts the topographical AFM image of individually mixed and BLND co-solvent modified films, respectively. All films were of homogeneous morphology, as the preliminary optical scans on micrometer scale did not have any micrometer sized flaws of dust, scratch, or overgrown PCBM aggregates. AFM topographic images show greater crowding at the surface of individual mixed co-solvent casted film with the consistently formed crystalline continuous P3HT phases as compared to partially crystallized broken phases in its counter film which is in agreement with the GI-XRD results that predicted more number of P3HT crystallites at the surface for individual mixed co-solvent casted film. The continuous and well crystallized P3HT domains have higher hole mobility and hence are crucial for increasing the efficiency of the device [30]. Further, decreased surface roughness (1.36 nm) in case of individual mixed sample is related to well-organized and unhindered P3HT crystallization and decreased PCBM domains at the surface as compared to BLND film which in contrast have higher root mean square roughness (2.01 nm) (Fig. 4c and d) owing to much unsystematic restricted P3HT crystallite growth on account of greater fraction of disordered PCBM phase at the surface [31]. Analysis of the collected root mean square roughness data and the topographic images from the spin-casted films of BLND and individually mixed sample reveals that the individually mixed co-solvent modified sample surface has denser and ordered P3HT crystallites with lesser PCBM segment. The root mean square roughness values correlate with the surface composition predicted by the GI-XRD measurement. Uniform and homogenous active composite layer is a prerequisite for photon harvesting, as the non-uniform active layer may end up causing a short circuit or exciton recombination. So, this modified method of co-solvent addition can prove to be beneficial for fabricating smoother and uniform films.

Photoluminescence Emission

Figure 5 shows the photoluminescence (PL) emission spectra of P3HT:PCBM composite films casted from solutions modified

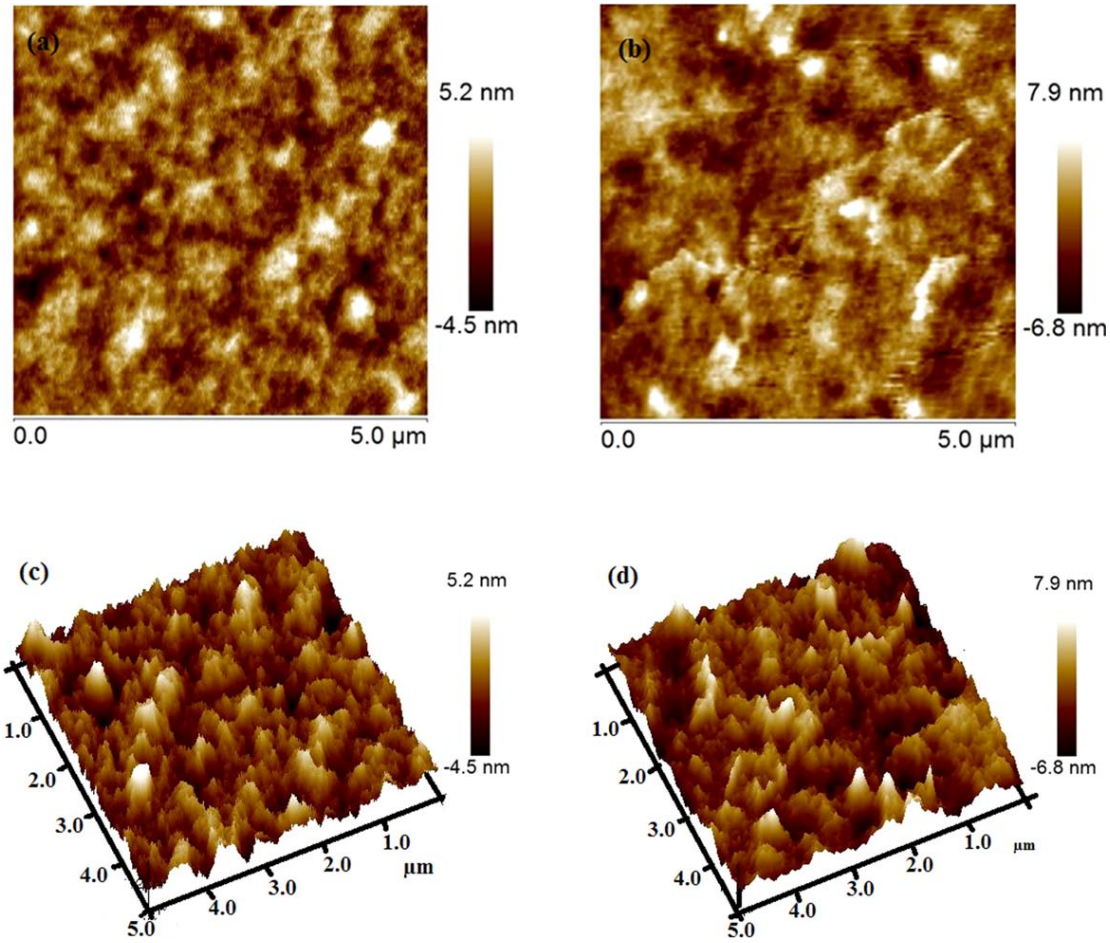

FIG. 4. Tapping mode AFM image scans (5 µm × 5 µm) of P3HT:PCBM composite films modified via (a) individually mixed cyclohexanone addition, (b) blended cyclohexanone addition approaches, and (c, d) are AFM height images of individually mixed and blended co-solvent modified film, respectively. [Color figure can be viewed in the online issue, which is available at wileyonlinelibrary.com.]

by individually mixed co-solvent addition and blended co-solvent addition. To remark on the possible effect of two methods of co-solvent addition on the nanomorphology of the donor–acceptor domains in the composite layer and on the charge transfer mechanism, PL measurements were completed. PL, a reflection of photoinduced charge transfer between the donor and acceptor phase is thought to be quenched in an intimately mixed donor–acceptor composite. The recent breakdown in the weakly coupled H-aggregate model (used for describing coupling interaction in aggregates) for P3HT nanowhiskers with its PL ratio (PL_{0-0}/ PL_{0-1} i.e. ratio of PL peak intensity of zero-phonon transition to the vibrational replicas) reaching value as high as two exceeding Huang–Rhys parameter (HR) limit, suggests that allowed zero phonon (0–0) transition is not because of disorder structure of the macromolecule but due to the intra-chain excitons coupling interaction expected for a J-type of aggregate. The same behavior of intra-chain excitons coupling interaction can be relatively linked to the P3HT aggregate formation in individually mixed co-solvent casted film as its PL spectra presents larger PL 0–0/0–1 ratio (though not of the order of two but of 0.973) as compared to 0.96 in blend co-solvent added sample. And, also a slight reduction in PL 0–2/0–1 intensity observed in individually mixed co-solvent casted film further recommends intramolecular interaction (through bonds coupling) in the P3HT chains. Exciton bandwidth "*W*" of aggregate being proportional to HR (PL 0–2/0–1 ratio) is also slightly reduced in individually mixed film resulting in efficient charge transfer to PCBM. A further confirmation of intra-chain structural order (or J-aggregate formation) in individually mixed co-solvent casted film is the small reduction in stoke's shift by 5 nm (difference in nanometer between peak excitation and peak emission wavelength) similar to that of P3HT nanofibers [32]. So, decrease in PL emission in individually mixed sample is because of weaker radiative transition of the lowest lying excitons in this film. Reduced PL intensity in individually mixed modified film provides an indication of larger critical exciton dissociation at the interface between the domains of the composite when compared to incomplete quenching or higher PL intensity in blended co-solvent modified casted film. Higher PL intensity in blended co-solvent mixed casted film recommends a coarser P3HT:PCBM mixture or inopportune phase separation between the domains of larger sizes. Not all the excitons generated in one polymer reach at the interface of the other polymer within the same film [33]. This verifies the adverse

 DOI 10.1002/pen

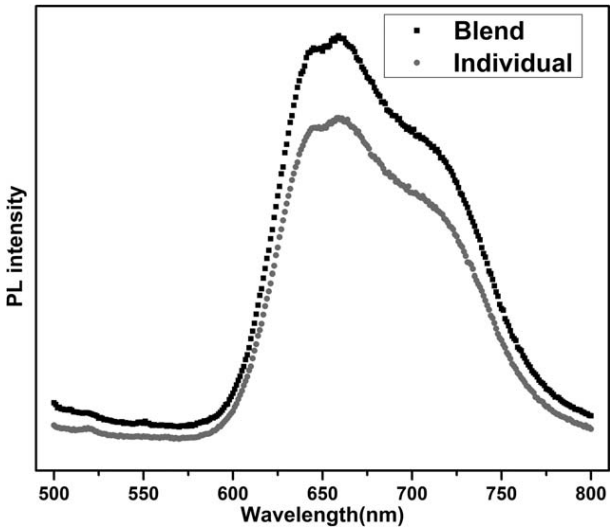

FIG. 5. PL spectra of P3HT:PCBM composite films casted of solutions modified by individual mixed and blended cyclohexanone addition approach.

decrease of efficiency in blended co-solvent casted device, suggesting more carrier recombination in such devices and hence reduced short circuit current density (J_{sc}). Individually mixed co-solvent casted film offers just the precise equilibrium phase

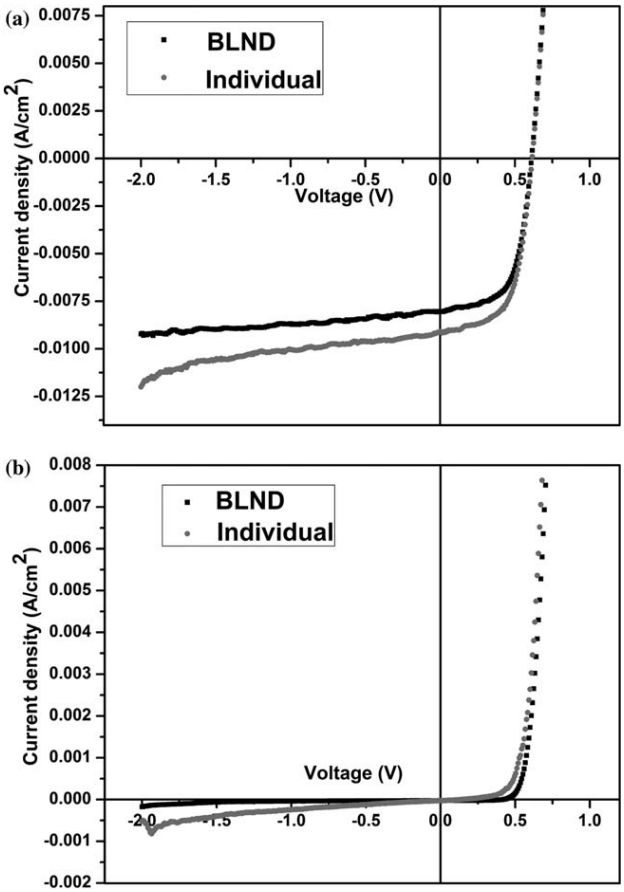

FIG. 6. (a) Current density–voltage (J–V) characteristic of devices fabricated with active layer modified by blended cyclohexanone addition and individually mixed cyclohexanone addition under AM 1.5 G white light illumination (b) as prepared devices tested in dark.

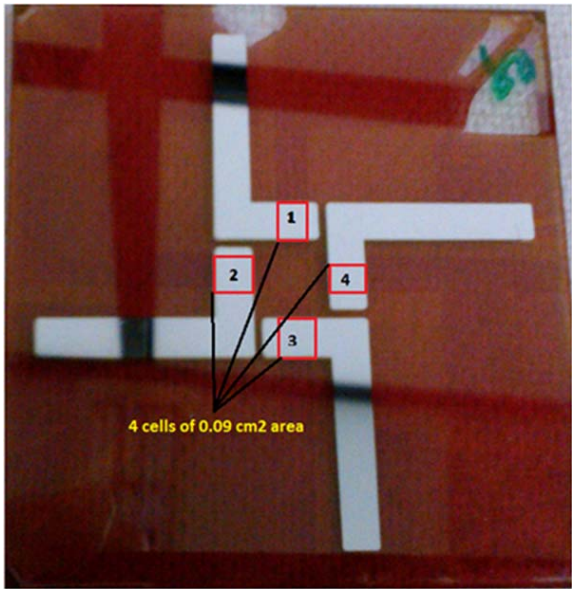

FIG. 7. Representative prototype of an inverted organic solar cell primed on 5 cm × 5 cm ITO/glass substrate comprising 4 cells each of 0.09 cm^2 area. [Color figure can be viewed in the online issue, which is available at wileyonlinelibrary.com.]

separation for efficient charge separation and transport. Phase separation is still less coarser in individual mixed sample assuring close contact of donor and acceptor domains to undergo charge transfer. Again, grain size relaxation and substantial quenching is as of the novel long-range excitons quenching mechanism [34]. Unusual PL quenching observed in case of bit larger grain sized (~13.7 nm) individually mixed co-solvent casted film can be thought of to be driven by self-quenching mechanism. The more ordered and planar P3HT chains formed in this case provides secure dissipation pathway for the as formed inter-chain excitons to discharge its energy at a diffusion length beyond the normal excitons diffusion length (8–10 nm) in organic polymer and hence diminishing the probability of radiative decay (PL) as such [35].

Photovoltaic Properties

Figure 6b shows the current density–voltage characteristic of the devices in dark (primed with co-solvent modified active layer taking up two different routes, i.e., blended addition and individually mixed solution addition). Details of the two processing pathways for co-solvent addition are given in the earlier sections. Solar cell devices fabricated in both the schemes demonstrated diode like characteristics. Practically, larger increase of the forward and reversed biased current at higher voltages for the solar device with individually mixed co-solvent modified active layer in comparison to blended co-solvent modified device relates to the shrinking interfacial charge injection barriers between the active layer and electrodes, which can be a result of greater crystalline P3HT phase and lesser PCBM (hole blocker) domains at the interface of HTL in individually mixed co-solvent modified device. Figure 6a illustrates the current density–voltage characteristics of the illuminated solar devices prepared via adopting two different approaches of modification in the (1:0.6) P3HT:PCBM composite layer with cyclohexanone solvent.

TABLE 2. Summary of photovoltaic device parameters for ITO/ZnO/ P3HT:PCBM/MoO_3/Ag polymer solar cell under AM 1.5G white light illumination, with different processing conditions for the active layer preparation.

Substrate[b]	Cell no.	Device	V_{oc} (V)	J_{sc} (A cm^{-2})	FF	%E	R_{sh} (Ω cm^2)	R_s (Ω cm^2)
1	1	BLND[a]	0.61	8.04 $E-03$	0.61	3.01	700	12
1	2	BLND	0.61	8.14 $E-03$	0.62	3.09	600	12
1	3	BLND	0.62	7.94 $E-03$	0.61	3.00	1167	12
1	4	BLND	0.62	7.62 $E-03$	0.64	3.01	1391	12
2	1	Individual[a]	0.61	9.01 $E-03$	0.61	3.39	1008	12
2	2	Individual	0.61	9.16 $E-03$	0.60	3.37	355	12
2	3	Individual	0.61	8.78 $E-03$	0.62	3.33	750	11
2	4	Individual	0.62	8.99 $E-03$	0.60	3.32	700	12

[a]Individual and BLND devices refers to the different processing conditions.
Individual = Individually cyclohexanone added mixed primed device.
BLND= P3HT: PCBM Blended cyclohexanone added primed device.
[b]Substrate is a 5 cm $\times$ 5 cm ITO glass substrate with inverted cell layer sequence comprising 4 cells each of area 0.09 cm^2.

Figure 7 represents an inverted polymeric solar cell primed on 5 cm $\times$ 5 cm ITO/glass substrate comprising of 4 cells each of 0.09 cm^2 area. In combination, a summarized report of all the device parameters is presented in Table 2. Individually mixed co-solvent addition approach proved to be favorable for getting better device performance. A particular case of individually mixed co-solvent modified device had short circuit current density (J_{sc}) of 9.01 $E-03$ A cm^{-2}, open circuit voltage (V_{oc}) of 0.61 V, and fill factor (FF) of 0.61, resulting in an efficiency of 3.39%. While on the contrary, a device modified with blended co-solvent addition had device parameters J_{sc} 8.04 $E-03$ A cm^{-2}, V_{oc} 0.61 V, and FF 0.61, resulting in an efficiency of 3.01%. A 10% increase in the efficiency in devices primed with individually mixed co-solvent approach compared to blended co-solvent addition approach is an outcome of the apparent increase in the device current that can be attributable to improved crystallization of P3HT in the photoactive layer avoiding PCBM interference to a great extent. Improved crystallinity of P3HT donor can benefit the device performance in two ways; firstly, enhanced crystallinity brings about greater optical absorption of the solar spectrum by the photoactive layer and further this improved crystallinity can result in efficient hole transport and its collection at the anode [36]. We attribute the increase in efficiency of our device primed with individually mixed co-solvent casted active layer to the increased size of the P3HT crystallites on the surface following the report by Chiu et al. They also related the enhancement in efficiency of their device via annealing to the increased crystallite size of the components in the composite mixture up to a limit of successful exciton dissociation [37]. As discussed in the previous section, P3HT crystallites of the order of 13.7 nm is still small enough for successful exciton dissociation following the long distance exciton quenching relaxation favored in highly crystalline and planar chains. Again, an increase in the shunt resistance of the device with the individually mixed co-solvent casted active layer further results in lesser recombination losses and leakage current verifying the smoother film observed by AFM and also reflected from additional quenched PL intensity.

CONCLUSION

PCE of a typical device, primed with this co-solvent modified active layer was found to improve from 3.01 to 3.39% by changing the co-solvent addition method from conventional blended mixture addition to individually mixed method. Improvement in the device efficacy is related to improved characteristic surface morphology as seen in AFM images, proven by improved crystallization of donor polymer supported by the UV–visible spectroscopy, GI-XRD, and PL data. Fine coverage with homogenously distributed well grown P3HT crystallites evident in the individually mixed co-solvent casted film promoted the enhanced photo absorption and charge transport properties which in turn must have benefited the device made thereof in terms of increased J_{sc} and PCE. GI-XRD results also supported more favorable upright concentration gradient in the aforesaid film which favors ease of charge transport.

ACKNOWLEDGMENTS

Authors are thankful to Prof. P B Sharma, Vice-Chancellor, Delhi Technological University (formerly Delhi College of Engineering), Delhi for encouragement and support. A financial support to one of the authors, Sarita is also acknowledged gratefully. The authors are also grateful to Mr. Sujit Pillai and Ishwar Dayal Sharma of the Materials Characterization Lab at Moserbaer India Ltd. for their assistance in performing the experiment and characterization.

REFERENCES

1. G. Li, R. Zhu, and Y. Yang, *Nat. Photon.*, **6**, 153 (2012).
2. A.C. Mayer, S.R. Scully, B.E. Hardin, M.W. Rowell, and M.D. McGehee, *Mater. Today*, **10**, 28 (2007).
3. F. Zhang, X. Xu, W. Tang, J. Zhang, Z. Zhuo, J. Wang, J. Wang, Z. Xu, and Y. Wang, *Sol. Energy Mater. Sol. Cells*, **95**, 1785 (2011).
4. E. Pavlopoulou, G. Fleury, D. Deribew, F. Cousin, M. Geoghegan, and G. Hadziioannou, *Org. Electron.*, **14**, 1249 (2013).
5. S.K. Gupta, A. Sharma, S. Banerjee, R. Gahlot, N. Aggarwal, Deepak, and A. Garg, *Sol. Energy Mater. Sol. Cells*, **116**, 135 (2013).
6. L.M. Chen, Z. Hong, G. Li, and Y. Yang, *Adv. Mater.*, **21**, 1434 (2009).
7. B.C. Thompson and J.M.J. Frechet, *Angew. Chem. Int. Ed.*, **47**, 58 (2008).

8. G. Li, V. Shrotriya, Y. Yao, J. Huang, and Y. Yang, *J. Mater. Chem.*, **17**, 3126 (2007).
9. L. Li, H. Tang, H. Wu, G. Lu, and X. Yang, *Org. Electron.*, **10**, 1334 (2009).
10. S. Berson, R.D. Bettignies, S. Bailly, and S. Guillerez, *Adv. Funct. Mater.*, **17**, 1377 (2007).
11. Y. Kim, S.A. Choulis, J. Nelson, D.D.C. Bradley, S. Cook, and J.R. Durrant, *J. Mater. Sci.*, **40**, 1371 (2005).
12. C.W. Chu, H. Yang, W.J. Hou, J. Huang, G. Li, and Y. Yang, *Appl. Phys. Lett.*, **92**, 103306 (2008).
13. F.C. Chen, H.C. Tseng, and C.J. Ko, *Appl. Phys. Lett.*, **92**, 103316 (2008).
14. K. Kawano, J. Sakai, M. Yahiro, and C. Adachi, *Sol. Energy Mater. Sol. Cells*, **93**, 514 (2009).
15. J. Peet, J.Y. Kim, N.E. Coates, W.L. Ma, D. Moses, A.J. Heeger, and G.C. Bazan, *Nat. Mater.*, **6**, 497 (2007).
16. J.K. Lee, W.L. Ma, C.J. Brabec, J. Yuen, J.S. Moon, J.Y. Kim, K. Lee, G.C. Bazan, and A.J. Heeger, *J. Am. Chem. Soc.*, **130**, 3619 (2008).
17. J.H. Kim, J.H. Park, J.H. Lee, J.S. Kim, M. Sim, C. Shim, and K. Cho, *J. Mater. Chem.*, **20**, 7398 (2010).
18. J.S. Kim, J.H. Lee, J.H. Park, C. Shim, M. Sim, and K. Cho, *Adv. Funct. Mater.*, **21**, 480 (2011).
19. N. Kiriy, E. Jähne, H.J. Adler, M. Schneider, A. Kiriy, G. Gorodyska, S. Minko, D. Jehnichen, P. Simon, A.A. Fokin, and M. Stamm, *Nano Lett.*, **3**, 707 (2003).
20. S. Malik, T. Jana, and A.K. Nandi, *Macromolecules*, **34**, 275 (2001).
21. D.R. Kozub, K. Vakhshouri, L.M. Orme, C. Wang, A. Hexemer, and E.D. Gomez, *Macromolecules*, **44**, 5722 (2011).
22. J. Liu, S. Shao, H. Wang, K. Zhao, L. Xue, X. Gao, Z. Xie, and Y. Han, *Org. Electron.*, **11**, 775 (2010).
23. D.J. Gundlach, J.E. Royer, S.K. Park, S. Subramanian, O.D. Jurchescu, B.H. Hamadani, A.J. Moad, R.J. Kline, L.C. Teague, O. Kirillov, C.A. Richter, J.G. Kushmerick, L.J. Richter, S.R. Parkin, T.N. Jackson, and J.E. Anthony, *Nat. Mater.*, **7**, 216 (2008).
24. G. Renaud, R. Lazzari, and F. Leroy, *Surf. Sci. Rep.*, **64**, 255 (2009).
25. N.D. Treat, M.A. Brady, G. Smith, M.F. Toney, E.J. Kramer, C.J. Hawker, and M.L. Chabinyc, *Adv. Energy Mater.*, **1**, 82 (2011).
26. F.C. Chen, C.J. Ko, J.L. Wu, and W.C. Chen, *Sol. Energy Mater. Sol. Cells*, **94**, 2426 (2010).
27. D.H. Kim, Y.D. Park, Y. Jang, S. Kim, and K. Cho, *Macromol. Rapid Commun.*, **26**, 834 (2005).
28. M.-S. Su, C.-Y. Kuo, M.-C. Yuan, U.-S. Jeng, C.-J. Su, and K.-H. Wei, *Adv. Mater.*, **23**, 3315 (2011).
29. S. Jeong, S.H. Woo, H.K. Lyu, and Y.S. Han, *Sol. Energy Mater. Sol. Cells*, **95**, 1908 (2011).
30. A. DeSio, T. Madena, R. Huber, J. Parisi, S. Neyshtadt, F. Deschler, E.D. Como, S. Esposito, and E. Hauff, *Sol. Energy Mater. Sol. Cells*, **95**, 3536 (2011).
31. K.S. Chen, H.L. Yip, C.W. Schlenker, D.S. Ginger, and A.K.Y. Jen, *Org. Electron.*, **13**, 2870 (2012).
32. M. Baghgar, J. Labastide, F. Bokel, I. Dujovne, A. McKenna, A.M. Barnes, E. Pentzer, T. Emrick, R. Hayward, and M.D. Barnes, *J. Phys. Chem. Lett.*, **3**, 1674 (2012).
33. R. Koeppe and N.S. Sariciftci, *Photochem. Photobiol. Sci.*, **5**, 1122 (2006).
34. S.R. Scully and M.D. McGehee, *J. Appl. Phys.*, **100**, 034907 (2006).
35. A.L. Ayzner, C.J. Tassone, S.H. Tolbert, and B.J. Schwartz, *J. Phys. Chem. C*, **113**, 20050 (2009).
36. P.W.M. Blom, V.D. Mihailetchi, L.J.A. Koster, and D.E. Markov, *Adv. Mater.*, **19**, 1551 (2007).
37. M.Y. Chiu, U.S. Jeng, C.H. Su, K.S. Liang, and K.H. Wei, *Adv. Mater.*, **20**, 2573 (2008).

Appl Biochem Biotechnol
DOI 10.1007/s12010-014-1177-7

Thiol Modified Chitosan Self-Assembled Monolayer Platform for Nucleic Acid Biosensor

Maumita Das Mukherjee · Pratima R. Solanki · Gajjala Sumana · Takaaki Manaka · Mitsumasa Iwamoto · Bansi D. Malhotra

Received: 11 February 2014 / Accepted: 15 August 2014

Abstract A self-assembled monolayer (SAM) of thiol modified chitosan (SH-CHIT), with thioglycolic acid (TGA) as a modifier to bestow thiol groups, has been prepared onto gold (Au)-coated glass plates for fabrication of the nucleic acid biosensor. The chemical modification of CHIT via TGA has been evidenced by Fourier transform infrared spectroscopy (FT-IR) studies, and the biocompatibility studies reveal that CHIT retains its biocompatible nature after chemical modification. The electrochemical studies conducted onto SH-CHIT/Au electrode reveal that thiol modification in CHIT amino end enhances the electrochemical behavior indicating that it may be attributed to delocalization of electrons in CHIT skeleton that participates in the resonance process. The carboxyl group modified end of DNA probe has been immobilized onto SH-CHIT/Au electrode using *N*-ethyl-*N*′-(3-dimethylaminopropyl) carbodimide (EDC) and *N*-hydroxysuccinimide (NHS) chemistry for detection of complementary, one-base mismatch and non-complementary sequence using electrochemical and optical studies for *Mycobacterium tuberculosis* detection. It has been found that DNA-SH-CHIT/Au bioelectrode can specifically detect 0.01 μM of target DNA concentration with sensitivity of 1.69×10^{-6} A μM^{-1}.

M. D. Mukherjee
Amity Institute of Applied Sciences, Amity University, Noida, Uttar Pradesh, India

P. R. Solanki
Special Centre for Nanoscience, Jawaharlal Nehru University, New Delhi, India

G. Sumana · B. D. Malhotra
Department of Science and Technology Centre on Biomolecular Electronics, Biomedical Instrumentation Section, Materials Physics and Engineering Division, CSIR- National Physical Laboratory, New Delhi 110012, India

T. Manaka · M. Iwamoto
Department of Physical Electronics, Tokyo Institute of Technology, 2-12-1 O-okayama Meguro-ku, Tokyo 152-8552, Japan

B. D. Malhotra (✉)
Department of Biotechnology, Delhi Technological University, Main Bawana Road, Shahbad Daulatpur, Delhi 110042, India
e-mail: bansi.malhotra@gmail.com

Published online: 10 September 2014

Keywords Thiol modified chitosan · DNA biosensor · Surface plasmon resonance · *Mycobacterium tuberculosis*

Introduction

In recent years, there is an increased interest towards the development of nucleic acid biosensors for clinical monitoring of the infectious diseases, especially those resulting from life-threatening pathogens. In addition to the clinical monitoring, the change in the DNA redox properties (oxidation of guanine), redox indicator-based indirect electrochemistry, considered to be an important alternative for development of nucleic acid hybridization biosensors which offer advantages in terms of reusability and sensitivity. Besides this, electrochemical biosensors do not require additional labeling step and can be easily integrated with electronics for fabrication of miniaturized devices for diagnosis of infectious diseases and the detection of pathogenic biological species of environmental and clinical interests [1, 2].

Tuberculosis is presently the chronic pulmonary bacterial infectious disease, caused by *Mycobacterium tuberculosis*. According to the World Health Organization (WHO), nearly two billion people in the present world's population have been exposed to the tuberculosis pathogen. It is the world's greatest infectious killer of women of reproductive age and is the leading cause of death among people with HIV/AIDS [3, 4]. The resurgence of TB and increased risk for TB in HIV-infected persons has intensified the requirement for a rapid, cost-effective method for diagnosis. Conventional diagnostic methods such as polymerase chain reaction (PCR) and restriction fragment length polymorphism (RFLP) are time consuming and require trained expertise. There is, thus, an urgent need for sensitive, specific, stable, cost-effective, and reusable method for *M. tuberculosis* detection. In this context, affinity biosensors have emerged as promising alternative for microbial detection using nucleic-acid-based detection of complementary target sequences [5–8].

Lately, there is an enhanced interest to minimize denaturation of biomolecules and to achieve rapid electron transfer at desired surfaces. Among the various strategies used for modification of the electrode surfaces, self-assembled monolayer (SAM) exhibit unprecedented flexibility to tailor interfacial properties and present biologically relevant groups. The SAMs are considered to be more suitable for biosensing, since they are easy to form and have increased stability, reusability, ordered arrangement, and high reproducibility. SAMs of functionalized silanes, alkanes, or polymers have been found to be useful for anchoring proteins, enzymes, and DNA for fabrication of biosensors as these may provide the interface between the transducer and the analyte for faster signal detection [9–11].

Chitosan (CHIT) and its derivatives have been found to be suitable for immobilization of desired biomolecules because of the excellent film-forming ability, high permeability, mechanical strength, biocompatibility, and low cost. Moreover, chemical modification of the amino groups of CHIT provides hydrophilic environment for biomolecules. Recently, CHIT and their composites deposited using sol-gel technique; spin coating and electrochemical deposition have successfully been applied for the development of biosensors [12]. However, using these techniques, the constant thickness, and uniformity is very difficult to achieve resulting in complexity in getting the reproducibility.

In this manuscript, we report the thiolation of chitosan (SH-CHIT) at amino ($-NH_2$) ends, with thioglycolic acid (TGA) via amide bond formation, and its self-assembled monolayer has been fabricated on gold (Au) surface using Au-SH affinity interaction. The SH-CHIT/Au electrode has been utilized for the fabrication of DNA biosensor for *M. tuberculosis* using

surface plasmon resonance (SPR) technique utilizing the advantage of CHIT-SAM onto Au surface. Besides this, electrochemical transducer has been used to detect the hybridization event as SH-CHIT/Au electrode shows improved electrochemical properties compared to CHIT/Au, which may be attributed to the conjugation of electrons in SH-CHIT skeleton [13–15].

Materials and Method

Low molecular weight chitosan (Mw 2.4×10^6), *N*-ethyl-*N*′-(3-dimethylaminopropyl) carbodimide (EDC), *N*-hydroxysuccinimide (NHS), thioglycolic acid (TGA), oligonucleotide probe sequence specific to *M. tuberculosis*, complementary target, one-base mismatch, and non-complementary DNA sequences have been purchased from Sigma-Aldrich, USA. All the solutions and glassware are autoclaved prior to being used, and desired reagents (molecular biology grade) have been prepared in de-ionized water (Milli Q 10 TS). The 50-nm-thick Au-coated BK-7 glass plates (24 mm diameter) are procured from Autolab, The Netherlands. Pre-cleaned (with piranha solution, H_2SO_4: H_2O_2=7:3, for about 5 min followed by rinsing in de-ionized water) Au-coated glass plates have been used as substrates for deposition of thiolated chitosan SAM. The sequence of DNA probes used for the DNA hybridization detection is as follows:

Probe : Carboxyl-GAA-CAA-CCC-GCT-GTC-GGG-GT

Complementary : AC-CCC-GAC-AGC-GGG-TTG-TTC

One-base mismatch : AC-CCC-GTC-AGC-GGG-TTG-TTC

Non-complementary : CG-GCG-CAG-TGG-ATA-GCT-GCA

Fabrication of the Thiol Modified Chitosan Film onto Au Electrode

For the fabrication of SH-CHIT SAM, Au-coated BK-7 glass plates have been immersed in 0.1 M TGA in water, along with 50 mM EDC, 1.0 g of CHIT, and 4 mL of acetic acid, and kept overnight at room temperature [16, 17]. TGA is reacted with CHIT in dilute solution for covalent binding of the acids with amine groups of CHIT, resulting in amide bond formation. CHIT is reacted in the presence of a carbodiimide to facilitate amide-forming condensation reaction. For each synthetic reaction, pH is adjusted to 4.5–5.0. After the coupling reaction, electrodes are rinsed with water to remove physically adsorbed SH-CHIT from the Au surface and then dried under a stream of nitrogen.

Immobilization of ssDNA Probe on SH-CHIT/Au Electrode and Hybridization with Complementary Target Analyte

Carboxyl (−COOH) functionalized 20-mer probe DNA (ssDNA) is immobilized onto SH-CHIT/Au surface using EDC-NHS carbodiimide chemistry (DNA-SH-CHIT/Au). One milliliter of 100 μM of −COOH-ssDNA is activated with EDC (100 mM) in presence of 200 mM NHS for about 24 h at room temperature (25 °C). This activated DNA is covalently immobilized onto SH-CHIT/Au surface using −OH functionality of CHIT via ester bond formation between −COOH of DNA and −OH of CHIT (Scheme 1). The electrode is rinsed

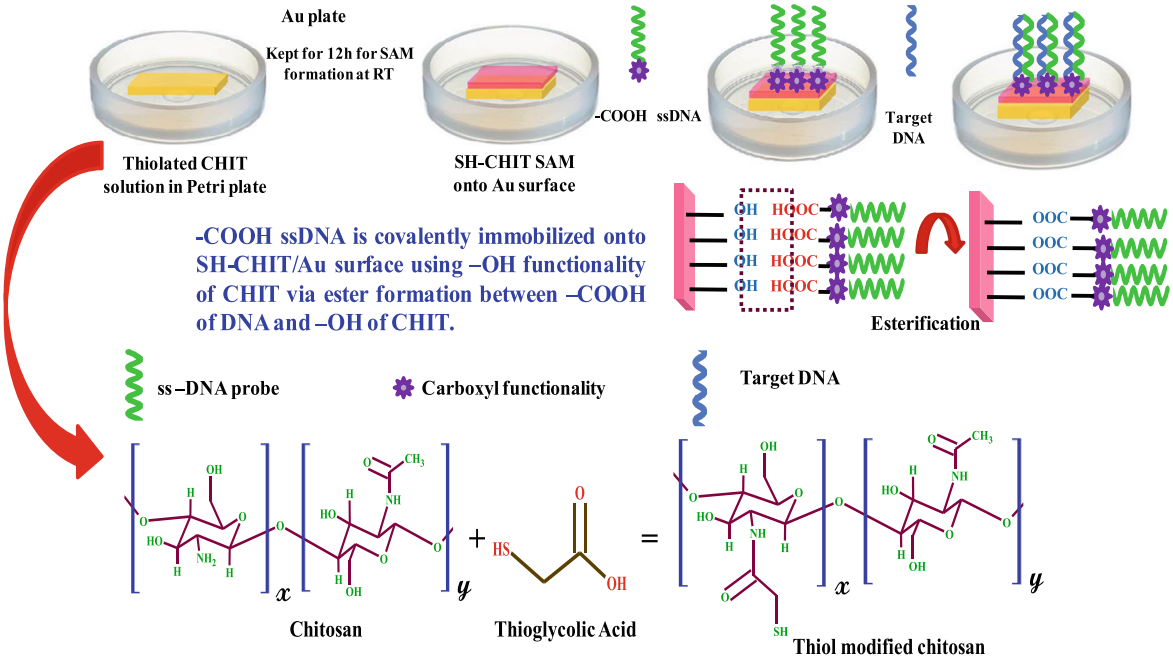

Scheme 1 Chemical modification of CHIT with TGA, fabrication of SH-CHIT SAM onto Au surface using SH-Au affinity interaction and immobilization of carboxyl functionalized DNA onto SH-CHIT/Au surface

three times with phosphate buffer (pH 7.0) to remove any unimmobilized ssDNA. The hybridization is performed at 25 °C by incubating DNA-SH-CHIT/Au bioelectrode with complementary target and non-complementary and one-base mismatch DNA sequences of different concentration for about 60 s. The electrode is washed with phosphate buffer (pH 7.0) to remove any unhybridized DNA.

For the hybridization studies, a stock solution of 100 μM of target DNA has been prepared and dilution is made in buffer solution up to the desired concentration i.e. 0.01 μM. Five microliters of the target DNA solution was added to DNA-SH-CHIT/Au electrode, and their electrochemical response was studied by differential pulse voltammetry (DPV) technique in PBS (50 mM, pH 7.0, 0.9 % NaCl) using methylene blue (MB) as redox indicator.

Characterization

CHIT/Au, SH-CHIT/Au, and DNA-SH-CHIT/Au electrodes have been characterized by Fourier transform infrared spectroscopy (FT-IR, PerkinElmer, Spectrum BX II), contact angle measurements (CA-Dataphysics, Germany, model: OCA 15EL), and high-resolution transmission electron microscopy (HR-TEM, Tecnai-G2 F30 STWIN with field emission gun electron source) studies. Electrochemical analysis has been conducted using Autolab Potentiostat/Galvanostat (Eco Chemie, AD Utrecht, The Netherlands) using a three-electrode system with Au as working electrode, platinum wire as auxiliary electrode, and Ag/AgCl as reference electrode in PBS (50 mM, pH 7.0) containing 5 mM $[Fe(CN)_6]^{3-/4-}$ as redox probe. The hybridization experiments using SPR have been carried out using an Autolab SPR, Eco Chemie (Netherlands), based on the traditional Kretschmann configuration. In SPR experiments, linearly *p*-polarized light from a laser (670 nm) is directed to a prism onto the gold electrode, and the intensity of reflected light is measured over a range of 4,000 millidegrees (m°) at 25 °C as a function of time. An index matching fluid (SPR oil) has been used for coupling the gold-coated glass electrode with the plane. In this experiment, a gold-coated glass electrode is coupled with the plane face of the prism.

Results and Discussion

Fourier Transformed Infrared Studies

The chemical modification of CHIT with TGA has been confirmed by FT-IR studies (film thickness 100 nm) and is depicted in Fig. 1a. Evidence of conversion of the amine group of CHIT is seen from the observed decrease of the amine N-H bend signal at 1,596 cm^{-1} in SH-CHIT. Coupled with the loss of amine signal indicates the formation of amide in SH-CHIT, with the appearance of amide I and amide II band signals at 1,657 and 1,562 cm^{-1}, respectively. It can be seen that the C-O-C stretch near 1,100 cm^{-1} remains essentially unchanged in SH-CHIT/Au and CHIT/Au electrodes [18].

Scanning Electron and Transmission Electron Microscopic Studies

The scanning electron microscopic (SEM) analysis of SH-CHIT/Au electrode shows uniform and rough surface morphology (Fig. 1b) indicating the homogeneous SAM formation onto Au surface. The transmission electron microscopic (TEM) images of SH-CHIT/Au electrode (Fig. 1b) show featureless grains with individual grain size of 1–2 μm. The corresponding EDX clearly reveals the presence of elements like carbon, nitrogen, oxygen, phosphorous, and sulfur. The existence of sulfur is attributed to the thiolation of the CHIT polymeric chain as also confirmed by FT-IR data.

Contact Angle Measurement

Contact angle (CA) technique based on sessile drop method has been used to explain the hydrophilic/hydrophobic nature of the surface as the quality of the monolayer can be estimated from the wetting measurement; the shape of the liquid drop is affected by the free energy of the surface. Figure 2a shows CA studies of blank Au (i), SH-CHIT/Au (ii), and DNA-SH-CHIT/Au (iii) electrodes, respectively. The change in CA value indicates the modification of CHIT film onto bare Au surface and immobilization of ssDNA onto SH-CHIT/Au film [19]. The CA value obtained as 64° for blank Au surface reveals both clean as well as hydrophobic nature of the surface. The value decreases to 50° after SH-CHIT SAM formation which may be attributed to the hydrophilic nature of CHIT due to presence of the OH groups. Further, the CA value decreases to 32° after DNA immobilization revealing the presence of hydrophilic phosphate backbone of DNA bound onto the SH-CHIT/Au electrode.

Biocompatibility Studies Using Bacterial and Plant Systems

The biocompatibility of SH-CHIT solution of 0.1 mg mL^{-1} concentration has been investigated with both the bacterial and plant systems. For the bacterial system (Fig. 2b), a culture is grown overnight in a nutrient broth medium at 30 °C in a rotary shaker at 150 rpm. One hundred microliters of the culture is spread on a nutrient agar plate, and wells (2 mm diameter) are made with the sterile core borer. Ten microliters of the SH-CHIT solution is added to the wells and kept for incubation at 30 °C. After ~48 h of incubation, no zone of inhibition is seen in the plate, indicating biosafety of the compound. For plant germination (Fig. 2c), wheat (i) and mustard (ii) seeds are immersed in solution of SH-CHIT solution and placed on soft agar for germination. After incubation at 30 °C in the dark for 4 days (for wheat seeds) and 7 days (for mustard seeds), germination is checked and compared with that of the controlled seeds. The observations pertaining to the effect of SH-CHIT solution on seed germination reveal

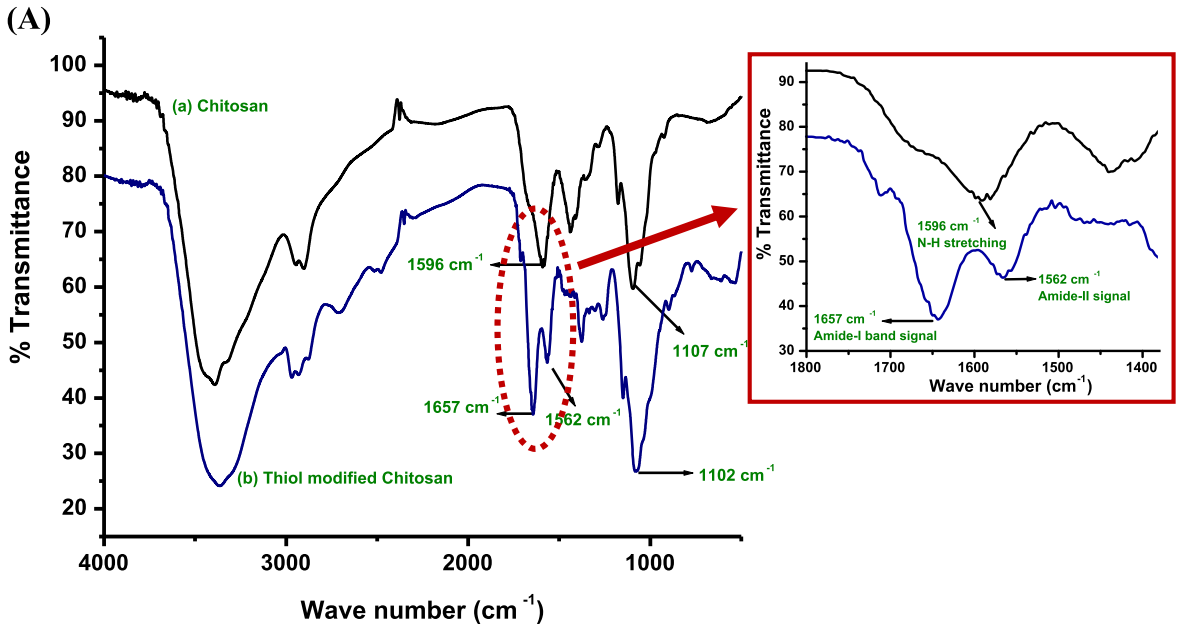

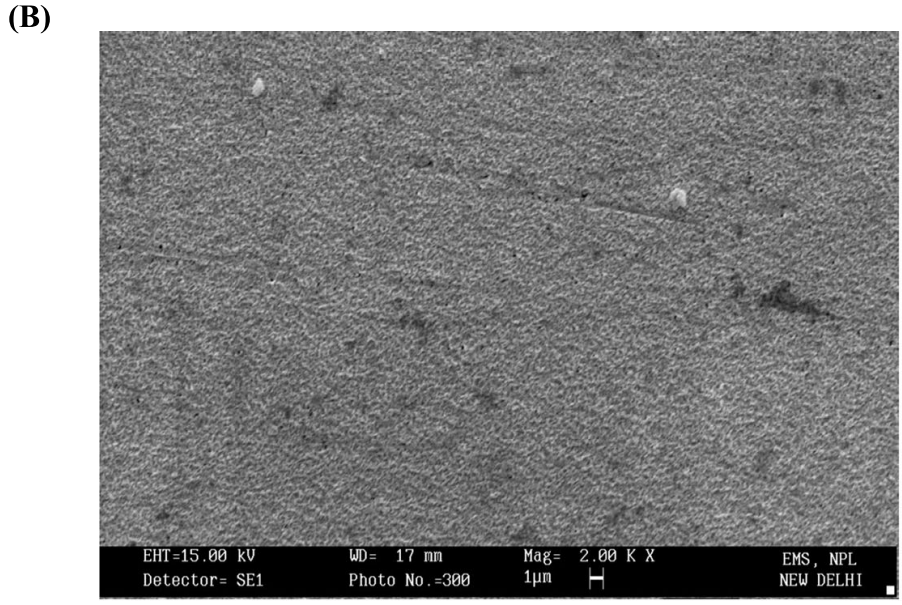

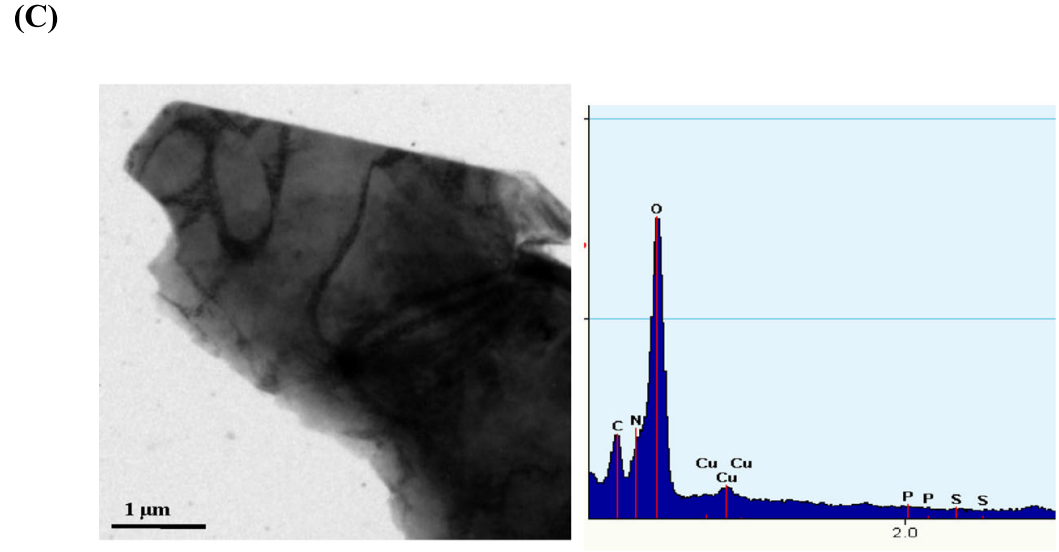

Fig. 1 **a** FT-IR spectra of *a* CHIT onto gold surface and *b* thiol modified CHIT onto gold surface. **b** SEM image of SH-CHIT/Au surface. **c** TEM and corresponding EDX of SH-CHIT solution

appropriate seed germination in wheat and mustard seeds, indicating once again the biocompatible nature of this nanocomposite.

Electrochemical Studies

Figure 3a shows results of cyclic voltammetric (CV) studies of (i) SH-CHIT/Au, (ii) CHIT/Au, and (iii) DNA-SH-CHIT/Au electrodes in PBS (50 mM, pH 7.0, 0.9 % NaCl) containing

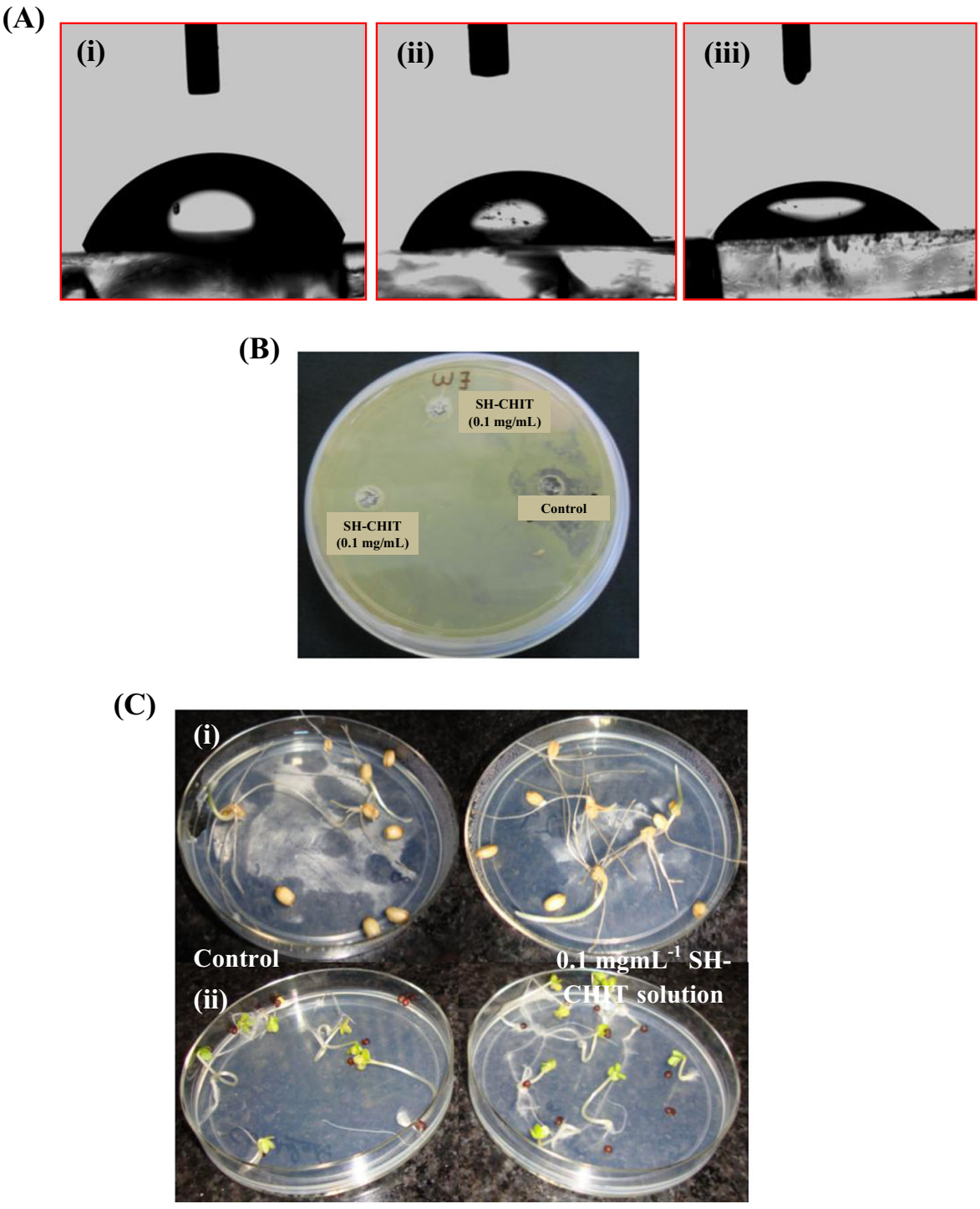

Fig. 2 **a** Contact angle of *i* blank Au, *ii* S-CH/Au, and *iii* DNA-S-CH/Au bioelectrodes; Snapshot of the agar plates containing **b** *Pseudomonas* sp. after 48 h of incubation, revealing no inhibition zone formation in the plate using SH-CHIT solution and **c** wheat (*i*) and mustard (*ii*) seeds after 4 and 7 days of incubation, respectively, revealing proper seed germination, showing the biocompatibility of SH-CHIT solution even after thiolation

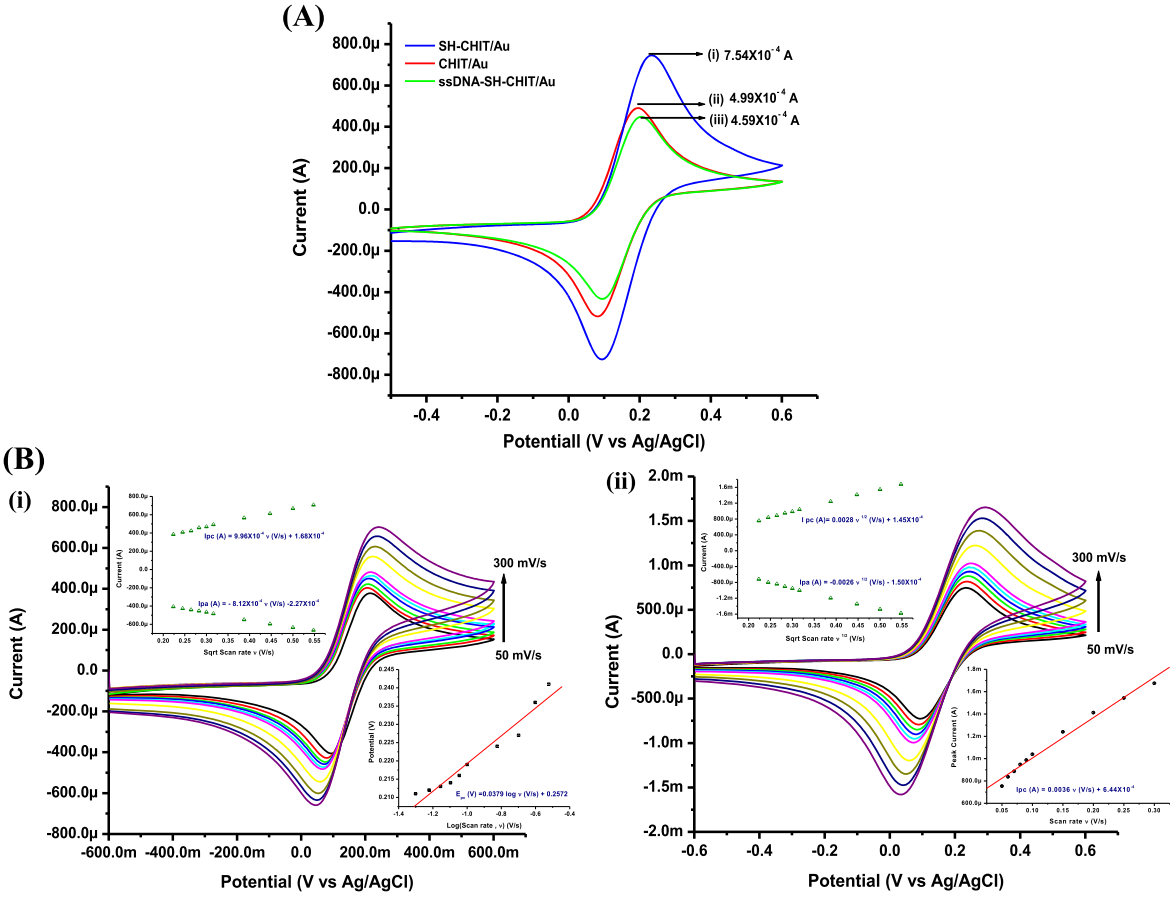

Fig. 3 Cyclic voltammetric studies of **a** SH-CHIT/Au (*i*), CHIT/Au (*ii*), and DNA-SH-CHIT/Au (*iii*) electrodes. **b** CHIT/Au (*i*) and SH-CHIT/Au (*ii*) electrodes as a function of scan rate (50–300 mV/s) in PBS (50 mM, pH 7.0, 0.9 % NaCl) containing 5 mM $[Fe(CN)_6]^{3-/4-}$ (*inset* plot of peak current vs. $\nu^{1/2}$ (V/s) and peak potential vs. scan rate ν (V)) in PBS (50 mM, pH 7.0, 0.9 % NaCl) containing 5 mM $[Fe(CN)_6]^{3-/4-}$

5 mM $[Fe(CN)_6]^{3-/4-}$ in the potential range of −0.6 to 0.7 V at a scan rate of 50 mV/s. CV of CHIT/Au shows a well-defined redox behavior (curve ii) at 0.197 V (E_{pc}), and the anodic peak potential (E_{pa}) at 0.082 V with cathodic peak current of 4.99×10^{-4} A. This may be due to cationic CHIT that accepts electrons from ferricyanide species resulting in enhanced redox current. The magnitude of current response for SH-CHIT/Au electrode (curve i) increases (7.54×10^{-4} A) in comparison to that of CHIT/Au electrode. This may be due to the fact that after thiolation, two pairs of electrons are in conjugation with CHIT skeleton and participate in resonance which is absent in pristine CHIT with one lone pair fixed onto $-NH_2$ group. Moreover, peak-to-peak separation of 0.13 V for SH-CHIT/Au electrode suggests that the redox behavior approaches towards perfectly reversible system. After immobilization of ssDNA onto SH-CHIT/Au surface, the peak current value decreases to 4.59×10^{-4} A, which may be attributed to repulsion between negatively charged DNA and $[Fe(CN)_6]^{3-/4-}$ moieties present in PBS, resulting in inhibited electron transfer kinetics. CVs of both CHIT/Au and SH-CHIT/Au electrodes as a function of scan rate (50–300 mV/s) in PBS (50 mM, pH 7.0, 0.9 % NaCl) containing 5 mM $[Fe(CN)_6]^{3-/4-}$ have been studied to estimate number of ionic species per unit area (Γ) and found that 0.27×10^{-8} and 0.765×10^{-8} mol.cm^{-2}, respectively (Fig. 3b). The higher Γ for SH-CHIT/Au electrode indicates that large number of redox moieties are available for oxidation leading to higher faradic current wherein, the presence of delocalized electrons due to thiolation, results in increased electron transport between redox species and electrode [20–24].

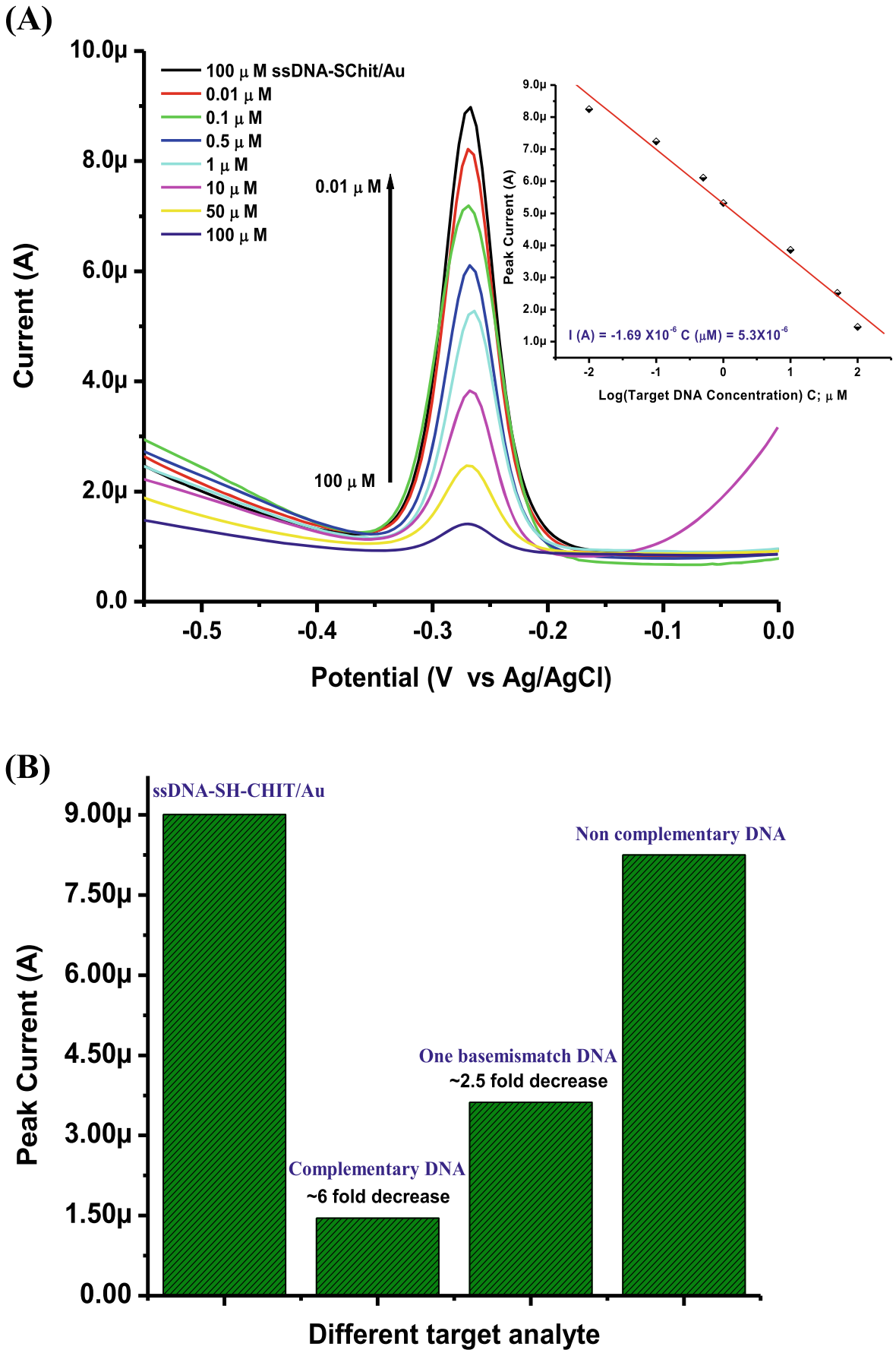

Fig. 4 **a** DPV response of ssDNA-SH-CHIT/Au bioelectrode after hybridization with complementary target DNA in PBS containing MB as indicator. **b** Bar diagram of selectivity studies of ssDNA-SH-CHIT/Au, with complementary, one-base mismatch and non-complementary target DNA of 100 μM concentration

Electrochemical Response Studies

The electrochemical response of ssDNA-SH-CHIT/Au bioelectrode after hybridization with 0.01–100 μM of complementary target DNA (dsDNA) has been studied by differential pulse voltammetry (DPV) technique in PBS (50 mM, pH 7.0, 0.9 % NaCl) using methylene blue (MB) as redox indicator. The magnitude of current with respect to MB changes after hybridization of probe with target (Fig. 4a). It has been observed that magnitude of current response decreases with increased complementary DNA concentration (inset, Fig. 3b). This may be due to enhanced number of target DNA molecules onto ssDNA-SH-CHIT/Au

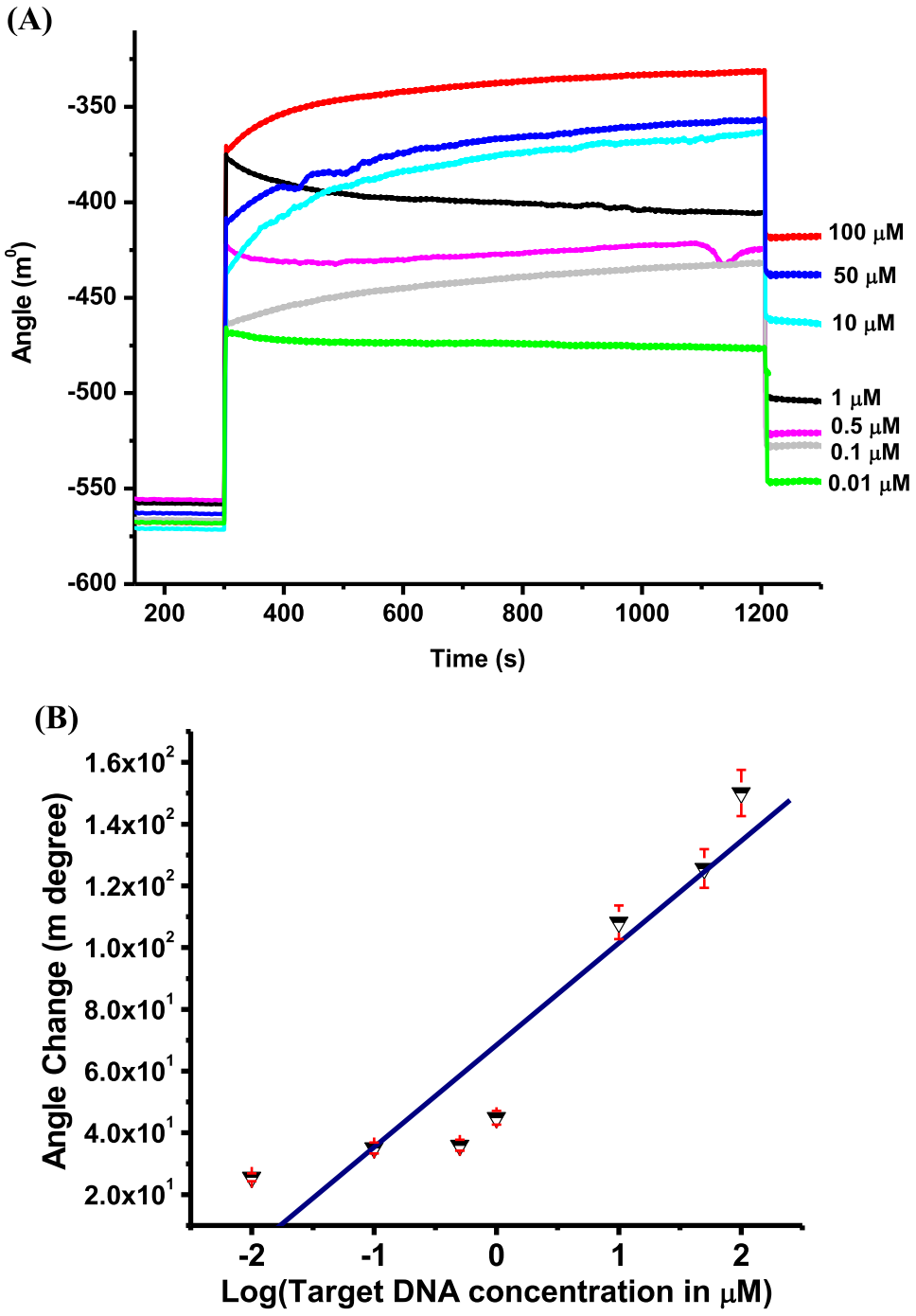

Fig. 5 **a** SPR sensorgrams for covalent immobilization of ssDNA onto SH-CHIT/Au. **b** Linearity curve of target DNA concentration in micromolar against angle in SPR angle in millidegrees

bioelectrode resulting in steric inhibition of MB packing between double helix of the hybrid. It has been observed that decrease in the MB peak with respect to target concentration follows Eq. 1.

$$\mathrm{I(A)\ dsDNA} = -1.69 \times 10^{-6} \times \log\left[\text{DNA concentration in } \mu\mathrm{M}\right] + 5.3 \times 10^{-6} \quad (1)$$

The detection limit of ssDNA-SH-CHIT/Au bioelectrode is 0.01 μM with sensitivity of 1.69×10^{-6} A μM^{-1}.

The selectivity of ssDNA-SH-CHIT/Au bioelectrode has been investigated by examining the interaction of ssDNA-SH-CHIT/Au bioelectrode (Fig. 4b) with the complementary, one-base mismatch and non-complementary DNA sequence. When ssDNA-SH-CHIT/Au bioelectrode is incubated with non-complementary target DNA, negligible change in the signal is observed reflecting the expected absence of hybridization. However, after incubation with the complementary target analyte and one-base mismatched sequence, the magnitude of MB signal decreases down to ~sixfold and ~2.5-fold, respectively. The results demonstrate that only complementary target DNA hybridizes with the probe DNA (ssDNA) leading to significant decrease in the DPV signal. The observed negligible change in the signal observed for the non-complementary sequence shows high selectivity of the hybridization detection [25–27].

Surface Plasmon Resonance Studies

The DNA probe solutions (100 μM) are immobilized onto the SH-CHIT/Au surface and used for hybridization studies with the complementary DNA sequences using SPR technique. During SPR measurements, the baseline is corrected for about 300 s using the autoclaved de-ionized water to remove any unbound DNA molecules. After the baseline correction, complementary DNA sequences are allowed for the association phase for about 900 s. On completion of the association phase, the unbound solution is discarded and the electrode is washed with de-ionized water (dissociation phase; 200 s). The change in the SPR angle before and after the association phase corresponding to the amount of DNA hybridized has been monitored, while keeping all other parameters constant. After completion of the dissociation phase, the surface is fully regenerated by washing with HCl solution (5.0 mM) for 120 s (data not shown).

Figure 5a shows results of SPR studies of ssDNA-SH-CHIT/Au bioelectrode for detection of hybridization with the complementary target DNA having concentration from 0.01 to 100 μM. It is observed that change in the SPR angle decreases with decrease in the complementary DNA concentration, resulting in lesser availability of the complementary

Table 1 Various biosensing parameters of SH-CHIT/Au electrode in comparison with those based on other CHIT-based nanocomposites

Matrix	Analyte	Transducer used	Detection limit	Reference
Covalently cross-linked chitosan	Catechol	Amperometric	10 nM	29
Chitosan/layered double hydroxides organic-inorganic composite	Catechol	Amperometric	0.36 nM	30
Chitosan/tetrakis(2-hydroxyethyl) orthosilicates composite	H_2O_2	Amperometric	4×10^{-7} mol/L	31
Chitosan-coupled carbon nanotubes on polyaniline-modified gold electrode	GOD	Amperometric	0.1 mM	32
Thiol modified chitosan	DNA	SPR and electrochemical	0.01 μM	Present work

DNA towards probe or presence of less mass loading onto the surface. The change in SPR signal of ssDNA-SH-CHIT/Au bioelectrode has been measured from 25.64 to 150.00 m° after hybridization with the complementary target (100 μM) indicating complete saturation of the electrode. The change in the SPR angle varies linearly with increased concentration (Fig. 5b). The control experiment using de-ionized water has been conducted, and no significant change in SPR angle is observed (data not shown). Table 1 shows the various biosensing parameters of SH-CHIT/Au electrode in comparison with those reported in the literature based on other CHIT-based nanocomposites

Conclusions

Thiol modified CHIT by TGA has been used to fabricate SAM onto Au surface using SH-Au affinity interaction which in turn helps to capture the DNA hybridization event using SPR. FT-IR studies confirm thiol incorporation into the CHIT skeleton, and biocompatibility studies indicate that the biocompatible nature of CHIT remains intact after thiol modification. Cyclic voltammetric studies have revealed that these SH-CHIT/Au electrode exhibits enhanced electrochemical properties due to the delocalized electrons that participate in resonance. The ssDNA-SH-CHIT/Au bioelectrode exhibits high sensitivity (1.69×10^{-6} A μM^{-1}) towards hybridization detection (0.01–100 μM complementary DNA) using DPV and SPR technique. SH-CHIT/Au platform can be used for fabrication of other electrochemical DNA biosensor for the detection of clinically important analyte such as cholera, *Neisseria gonorrhoeae*, etc.

Acknowledgments We thank Prof. R.C. Budhani, Director, National Physical Laboratory, India for the facilities. Maumita Das Mukherjee is thankful to Amity University, Noida for allowing her to perform the experiments. The financial support received at NPL, from Department of Science and Technology, India under the projects GAP 081132 and GAP 080232 is greatly acknowledged.

References

1. Leegsma-Vogt, G., Rhemrev-Boom, M. M., Tiessen, R. G., Venema, K., Korf, J., Jeffrey, M., Halliday, W. G., & Taylor, K. C. (2004). *Biomedical Materials and Engineering, 14*, 455–464.
2. Singh, R., Verma, R., Sumana, G., Srivastava, A. K., Sood, S., Gupta, R. K., & Malhotra, B. D. (2012). *Bioelectrochemistry, 86*, 30–37.
3. Das, M., Sumana, G., Nagarajan, R., & Malhotra, B. D. (2010). *Applied Physics Letters, 96*, 133706.
4. Das, M., Dhand, C., Sumana, G., Srivasrava, A. K., Nagarajan, R., Nain, L., Iwamoto, M., Manaka, T., & Malhotra, B. D. (2011). *Biomacromolecules, 12*, 540–547.
5. Chun, A. L. (2009). *Nature Nanotechnology, 4*, 698–699.
6. Thanyani, S. T., Robert, V., Siko, D. R. G., Very, P., & Verschoor, J. A. (2008). *Journal of Immunological Methods, 332*, 61–72.
7. Russell, D. G. (2001). *Nature Reviews Molecular Cell Biology, 2*, 569–577.
8. Good, M. C., Greenstein, A. E., Young, T. A., Ng, H. L., & Albert, T. (2004). *Journal of Molecular Biology, 339*, 459–469.
9. Wang, L., & Wang, E. (2004). *Electrochemistry Communications, 6*, 49–54.
10. Shan, D., Han, E., Xue, H., & Cosnier, S. (2007). *Biomacromolecules, 8*, 3041–3046.
11. Francia, G. D., Ferrara, V. L., Manzo, S., & Chiavarini, S. (2005). *Biosensors and Bioelectronics, 21*, 661–665.

12. Kaushik, A., Solanki, P. R., Ansari, A. A., Ahmad, S., & Malhotra, B. D. (2008). *Electrochemistry Communications, 10*, 1364–1368.
13. Guggi, D., Langoth, N., Hoffer, M. H., Wirth, M., & Schnurch, A. B. (2004). *Journal of Pharmacognosy, 278*, 353–360.
14. Solanki, P. R., Arya, S. K., Nishimura, Y., Iwamoto, M., & Malhotra, B. D. (2007). *Langmuir, 23*, 7398–7403.
15. Solanki, P. R., Prabhakar, N., Pandey, M. K., & Malhotra, B. D. (2008). *Biomedical Microdevices, 10*, 757–767.
16. Zhu, X., Su, M., Tang, S., Wang, L., Liang, X., Meng, F., Hong, Y., & Xu, Z. (2012). *Molecular Vision, 18*, 1973–1982.
17. Schnürch, A. B., Hornof, M., & Zoidl, T. (2003). *International Journal of Pharmaceutics, 260*, 229–237.
18. Cathell, M. D., Szewczyk, J. C., Bui, F. A., Weber, C. A., Wolever, J. D., Kang, J., & Schauer, C. L. (2008). *Biomacromolecules, 9*, 289–295.
19. Arya, S. K., Prusty, A. K., Singh, S. P., Solanki, P. R., Pandey, M. K., Datta, M., & Malhotra, B. D. (2007). *Analytical Biochemistry, 363*, 210–218.
20. Singh, A., Sinsinbar, G., Choudhary, M., Kumar, V., Pasricha, R., Verma, H. N., Singh, S. P., & Arora, K. (2013). *Sensors and Actuators B: Chemical, 185*, 675–684.
21. Zhao, G., Xu, J., & Chen, H. (2006). *Electrochemistry Communications, 8*, 148–154.
22. Yang, M., Yang, Y., Yang, H., Shen, G., & Yu, R. (2006). *Biomaterials, 27*, 246–255.
23. Zhuang, Q., Hen, J., Chen, J., & Lin, X. (2008). *Sensors and Actuators B: Chemical, 128*, 500–506.
24. Hu, G., Zhang, D., Wu, W., & Yang, Z. (2008). *Colloids and Surfaces B: Biointerfaces, 62*, 199–205.
25. Liao, J. C., Mastali, M., Li, Y., Gau, V., Suchard, M. A., Babbitt, J., Gornbein, J., Landaw, E. M., McCabe, E. R. B., Churchill, B. M., & Haake, D. A. (2007). *Journal of Molecular Diagnostics, 9*, 158–168.
26. Ulianas, A., Heng, L. Y., Lau, H. Y., Ishak, Z., & Ling, T. L. (2014). *Analytical Methods, 6*, 6369–6374.
27. Siddiquee, S., Yusof, N. A., Salleh, A. B., Bakar, F. A., & Heng, L. Y. (2010). *Bioelectrochemistry, 79*, 31–36.

International Journal of Applied Information Systems (IJAIS) – ISSN : 2249-0868
Foundation of Computer Science FCS, New York, USA
Volume 7– No.8, September 2014 – www.ijais.org

Use of Digital Signature Standard with Station to Station Key Exchange Agreement and Cloud Manager to Enhance Security in Cloud Computing

Manoj Kumar
Associate Professor
Delhi Technological University
New Delhi-110042, India

Kranti Asiwal
M.Tech Student
Delhi Technological University
New Delhi-110042, India

ABSTRACT
Cloud computing provides IT as service. Cloud computing is a budding paradigm having high availability, performance, least cost and many others. Cloud is an IT environment based on which it remotely provides IT resources to users. As cloud computing is an internet based computing solution, there are lots of security breaches and vulnerabilities like authenticity, data security, confidentiality and privacy which should be dealt properly to get high performance. Different combinations are used by different researchers to tackle these security breaches and vulnerabilities, same way we have chosen a combination of authentication technique and key exchange with cloud manager. In this paper we have proposed a model to enhance security of cloud by using Station to Station key agreement for generating session key with a fixed timestamp between User and Cloud Server and then send request for any service by using Digital Signature Standard, the request message would be encrypted by using that session key which was shared earlier and once a session key is used then that session key would not be used again. So the user requires a new key for each session. All of these issues related to authentication and authorization are handled by a cloud manager present between cloud server and user.

General Terms
Cloud Security

Keywords
Cloud Computing, Digital Signature Standard, Station to Station key exchange.

1. INTRODUCTION
Cloud Computing is virtual pool of resources and it provides these resources over the internet on pay per usage basis to users. Companies can reduce cost by providing service over internet.

Services provided by cloud are-

1) Platform as a service
2) Software as a service
3) Infrastructure as a service

Since cloud computing is a utility available on internet so security is main concern. So for Security problems we have used authentication technique, verification technique and a manager which will manage everything to enhance security.

As for secure connection between user and server one to one connection is preferable for security purpose that's why session key is generated by Station To Station (STS) key exchange agreement. Station To Station key exchange agreement will establish session keys between user and server for a fixed timestamp and only for single use that means once a session key is used by user for any service then again it won't be used again. After establishment of session key it is used in Digital Signature Standard so as intruders will be unable to decrypt the message sent by user; this message is the request from user to server for a service. All request-response management, session key generation and management are handled by Cloud Manager.

2. PROBLEM STATEMENT
Cloud computing technology provides services over internet so privacy and security is main concern that's why security issues like authentication, confidentiality, privacy should be handled properly. To deal with these problems a scheme where one to one medium is generated by Station To Station for privacy, encryption algorithm are used by cloud manager for data encryption and thus it provides confidentiality and Digital Signature Standard is used as an authentication technique.

3. RELATED WORK
Prashant Rewagad and Yogita Pawar [1]: They have proposed three way architecture to make use of digital signature and diffie hellman key exchange with advance AES to protect confidentiality of data stored in cloud.

Uma Somani, Kanika Lakhani and Manish Mundra [2]: A scheme has been proposed by them in which Digital Signature with RSA algorithm is used to encrypt data while transferring over network.

Siani Pearson, Yun Shen and Miranda Mowbray [5]: They have described Privacy Manager in Cloud Computing for increasing privacy and privacy management.

Siani Pearson [6]: He has described privacy challenges that engineers face while working on cloud computing.

Mandeep Kaur and Manish Mahajan [8]: They have proposed a plan to use different encryption algorithms like – AES, DES, RSA & BLOWFISH to ensure security of data in cloud for the perspective of different users.

4. PROPOSED MODEL

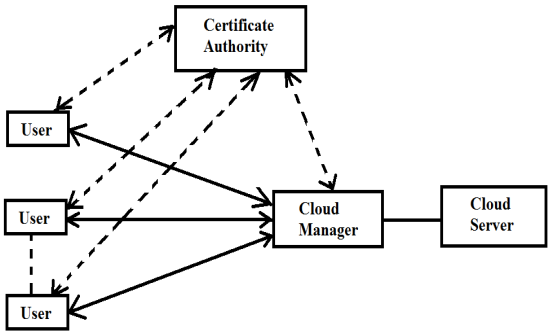

Figure 1: Proposed Model Entities layout

4.1 Parts of model

We are enhancing security of cloud by using Station to Station key agreement with Digital Signature Standard and Cloud Manager.

This model is working on 3 important parts:-

1. Cloud Manager
2. Station to Station key exchange agreement
3. Digital Signature Standard

4.1.1 Cloud Manager:

As its name suggests cloud manager manages everything of cloud server or things related to cloud server.

Cloud manager reduces risk for cloud computing users of their private data being stolen or being misused, and also assists the cloud provider to conform to privacy law.

Cloud Manager acts as a third party to issue session key between user and cloud server, cloud manager will verify user credentials signed by user and then send with request message for using any service from cloud.

After providing any of service to a user from the cloud server cloud manager will remove that session key on which that service was used from session key allocated list managed by cloud manager.

Every time a user requests a file from cloud the cloud manager will decrypt that file where all information regarding all files are present and will check from there that which algorithm has been used on user's required file so as to de-obfuscate i.e. decrypt that file and provide to user.

4.1.1.1 Services provided by Cloud Manager

4.1.1.1.1 Random Obfuscation

When any user stores its file/data on cloud, cloud manager will randomly choose one of the available asymmetric Encryption/Decryption methods to encrypt data provided by user and store it in data storage of cloud. Randomly chosen encryption method information is stored in one file where all of the information of all files is stored and that is encrypted with cloud manager public key.

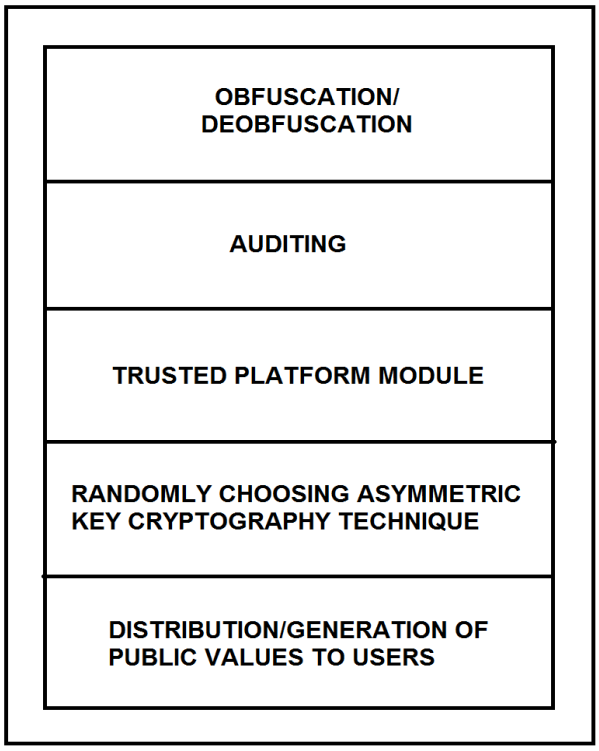

Figure 2: Services Provided by Cloud Manager

After every de-obfuscation, again cloud manager will randomly choose encryption algorithm to obfuscate and store it.

With respect to the privilege of user cloud manager will provide data to him/her i.e. if user is owner then read/write only file is provided and if user is normal user then read only data is provided so that no unwanted changes can be done.

4.1.1.1.2 Auditing

It also act as an auditor by keeping all information regarding what service is provided to users and when, what users did with that service? All information is audited.

4.1.1.1.3 Trusted Platform Module

It is a hardware that checks integrity of cloud manager. It decreases the risk of unsecured access, so increases confidentiality by providing a tamper resistant hardware based security. Protected data cannot be used by other platforms. So trusted computing can be done and it yields trust in integrity of the privacy management and of involved platforms.

4.1.1.1.4 Random Encryption Method

This method is used for obfuscation and de-obfuscation. Cloud manager have a list of asymmetric encryption methods from which it will randomly choose for encryption and save that information in a file which is maintained by it.

4.1.1.1.5 Public Value Generation and Broadcast

Cloud Manager provide values of g, P, q and B to users at the time of registration and broadcast new g, P, q and B values after timestamp is reached. So new public key values and private key values are regenerated by users and their new certificates are created by certificate authority (digital certificates are renewed). g, P, q and B are used in Digital Signature Standard as well as in Station to Station key exchange agreement.

- $(2^{L-1} < P < 2^{L})$. L is a multiple of 64.
- q is prime divisor of P-1.
- A random number h is chosen. 0<h<P-1, $g=h^{(P-1)/q}$ modB.
- A value B is also chosen pseudo-randomly or randomly so as to be used in Station to Station Key Exchange Agreement.

A timestamp is set for all these values and when this time expires then these values are regenerated and broadcasted to all users.

4.1.1.2 Files maintained by Cloud Manager

4.1.1.2.1 Audit File

This contains all auditing information.

4.1.1.2.2 Session key allocation file

This file maintains the information about session keys provided to users and their timestamps.

4.1.1.2.3 Data Files obfuscation information

This file has information of files for obfuscation and corresponding encryption methods used.

4.1.1.2.4 Public values File

This file has all values which are public and their timestamps. From this file values are broadcasted to users (Here g, P, q and B are public values, which are broadcasted time to time).

4.1.2 Station To Station Key Exchange Agreement

Station To Station (STS) key exchange agreement is commonly known as Station To Station (STS) protocol. Digital signatures with public key certificates are used to establish session key. It is based on diffie hellman algorithm, as in diffie hellman algorithm man in middle attack can take place but Station To Station key exchange agreement prevents man in middle attack problem. As session keys are created for a fixed timestamp it will increase security level.

4.1.3 Digital Signature Standard

Digital Signature Algorithm is used in Digital Signature Standard (DSS) based on Elgamal scheme with some ideas from Schnorr scheme. DSS signatures are faster than RSA Signatures. DSS signatures are smaller than other Signatures. Message send by user to cloud manager is encrypted by using session key already created by Station To Station key agreement.

4.2 Steps for getting a service from cloud

4.2.1 Registration

- User can register to cloud by providing required information and user name and password.
- After successful registration g, P, q and B values and hashing technique used for creating digests are provided by cloud manager to user.
- Then a random number x is chosen by user and that would be its private key and from that $z = g^{x} \text{mod} B$ is generated, that is its public key (x and z values are renewed time to time when new values of g, P, q and B are received from Cloud Manager).

4.2.2 Station to Station Key Exchange Agreement

Algorithm:

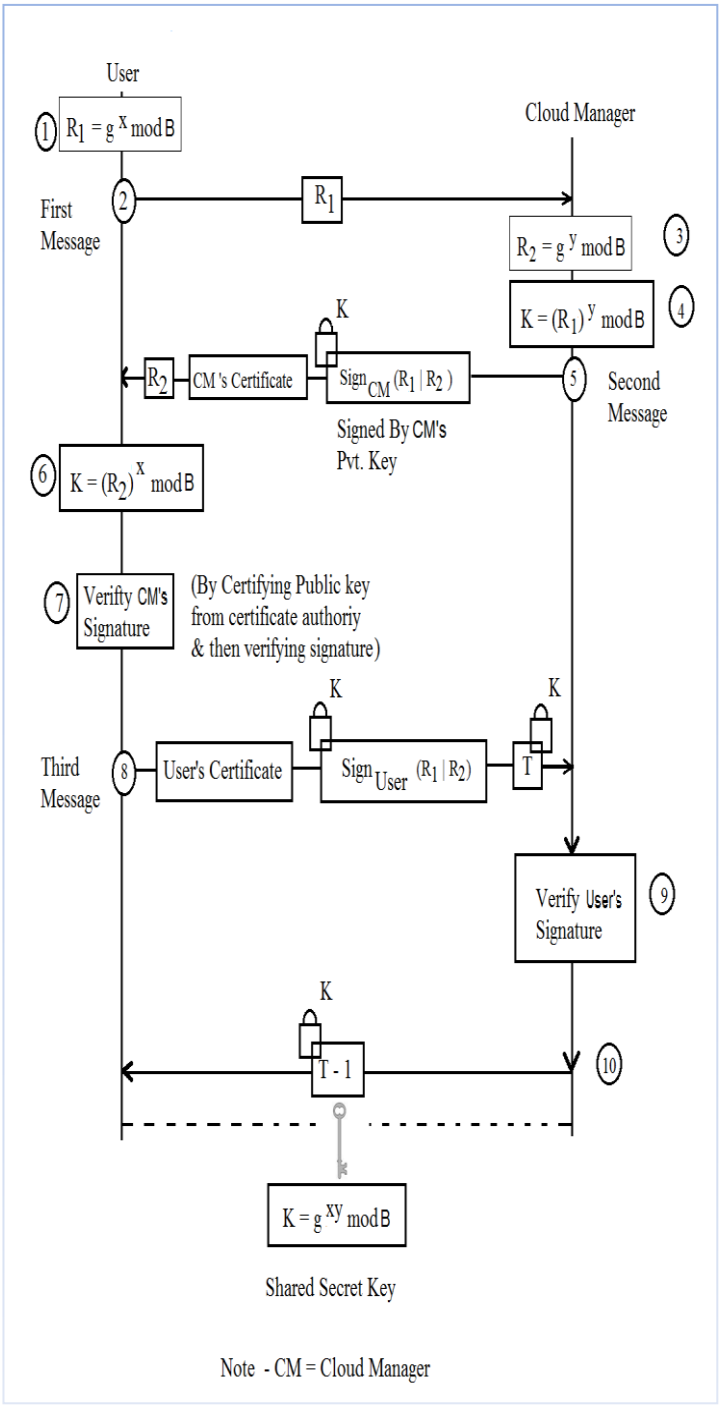

Figure 3: Station to Station Key Exchange Agreement

a) A random number x that is user's private key is already been chosen at the time of registration with a time stamp and will renew it time to time when new g, P, q and B values are received then x is also renewed.

b) New user will calculate $R_1 = g^x \text{mod} B$ & send this R_1 to cloud manager.

c) After getting R_1, cloud manager will choose a random number y & find out R_2.

d) Now cloud manager will find out key (session key) $K = (R_1)^y \text{mod} B$.

e) After calculating R_2 & the session key, cloud manager concatenates R_1 and R_2 and then signs the result with the private key. Cloud manager now sends R_2, the signature & his own public key certificate to user. Signature is encrypted with session key.

f) Now after getting R_2 user will calculate session key & verify cloud manager signature by the certificate authority

g) After that user will create a signature by concatenate $R_1|R_2$ and encrypt that signature by K & send user's certificate also & send an encrypted timestamp value to cloud manager.

h) Cloud manager will verify Digital signature of user & if it is verified then it will send the encrypted T-1. That means key K is been set for T-1 time.

4.2.3 Digital Signature Standard

Algorithm:

Signing:-

a) User chooses a random number n ($1 \leq n \leq q$).

b) User calculates the first signature

$r = (g^n \text{mod} P) \text{mod} q$.

c) User will create digest of Message h(M) by already shared hashing technique with users.

d) Now user will calculate 2nd signature

$S = (((h(M)+xr)n^{-1}) \text{mod} q)$

e) Now user will send r, s , session key encrypted M & session key encrypted z(public key of user) to cloud manager.

(Cloud manager won't store value of z.)

Verifying:

a) Cloud manager checks whether r or s is less than or greater than zero or not because if any of value will be equal to zero then n must be chosen again.

b) Calculates digest using same hash algorithm as used by user because that's already been discussed.

c) Cloud manager calculates $V = \left(\left(g^{h(M)s^{-1}} z^{rs^{-1}} \text{mod} P\right) \text{mod} q\right)$.

d) If r is congruent to V then message request is accepted.

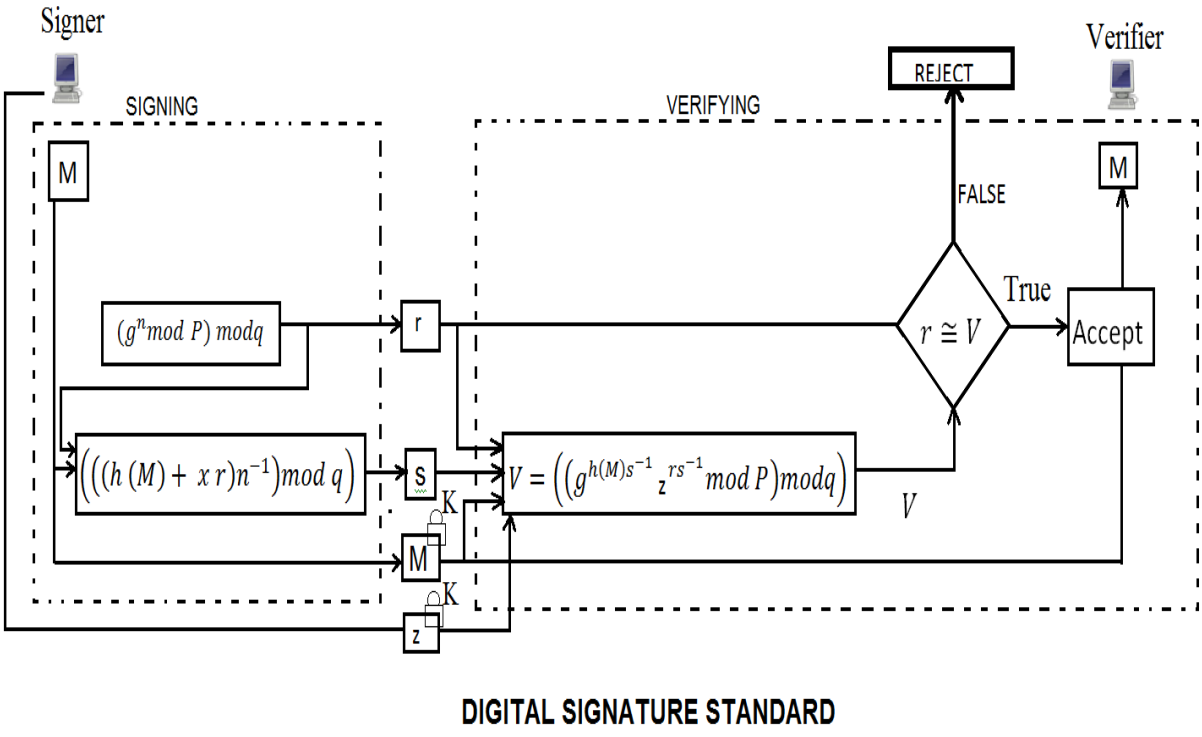

Figure 4: Digital Signature Standard

4.2.4 Providing services from cloud to user

- After verification from cloud manager cloud manager will directly provide service to user (except case of data uploading and downloading from data storage of server because in these case cloud manager will be involved for providing service).
- In case of uploading a File on cloud-

After getting this request cloud manager will randomly choose one of Asymmetric algorithm for file and store by using its Public/Private key for encryption.

Cloud manager will maintain a file in which it will have information about user data and corresponding encryption used on them and it has been locked by public key of cloud manager.

Every time if a user/owner requests for that file, cloud manager will decrypt it then provide a copy to user and after that again encrypt that file by randomly choosing an encryption algorithm. Only owner have the privilege to overwrite a file.

- In case of downloading a File-

Cloud manager will first de-obfuscate that file first and then provide it to user according to its users.

5. CONCLUSION

There are lots of security vulnerabilities and breaches in cloud computing, to deal with these breaches and vulnerabilities we have proposed a model in which by Station to Station Key Exchange Agreement a one to one medium is created between cloud server and user so as man in middle attack is completely eliminated by this, as session key is generated for fixed time interval, each session key is generated for one time use and a file is maintained that contains information of all users and corresponding session key provided to them, so by all this replay attack is eliminated and intruders can't use any users session key because for that a file has been maintained by cloud manager. Digital Signature Standard is used for authentication purpose. Cloud Manager will audit all users work on cloud and it will make files tamper resistant by using tamper resistant module. Cloud Manager performs lots of other functions also like encrypt files by using different encryption algorithm. So Cloud Manager improves privacy and security. Therefore we have used three different parts to enhance security of Cloud Computing.

6. ACKNOWLEDGMENTS

We would like to express our deepest gratitude to all the people who have supported and encouraged us during the course of this work without which, this work could not have been accomplished. We are deeply indebted to Dr. O. P. Verma, HOD, Computer Science, DTU for his immense support. We are grateful to Delhi Technological University for providing the right resources and environment for this work to be carried out.

7. REFERENCES

[1] Mr. Prashant Rewagad and Ms.Yogita Pawar "Use of Digital Signature with Diffie Hellman Key Exchange and AES Encryption Algorithm to Enhance Data Security in Cloud Computing" 2013 IEEE International Conference on Communication Systems and Network Technologies.

[2] Uma Somani, Kanika Lakhani, Manish Mundra "Implementing Digital Signature with RSA Encryption Algorithm to Enhance the Data Security of Cloud in Cloud Computing" 2010 IEEE 1st International Conference on Parallel, Distributed and Grid Computing (PDGC - 2010).

[3] Volker Fusenig and Ayush Sharma "Security Architecture for Cloud Networking" 2012 IEEE International Conference on Computing, Networking and Communications, Cloud Computing and Networking Symposium.

[4] Siani Pearson, Yun Shen and Miranda Mowbray "A Privacy Manager for Cloud Computing" HP Labs, Long Down Avenue, Stoke Gifford, Bristol BS34 8QZ, UK.

[5] Siani Pearson "Taking Account of Privacy when Designing Cloud Computing Services" HP Labs, Bristol, UK.

[6] Mandeep Kaur and Manish Mahajan "Using Encryption Algorithms to enhance the data security in Cloud Computing" 2013 International Journal of Communication and Computer Technologies Vol 1,issue 3,January 2013.

[7] Shabnam Sharma & Usha Mittal "Comparative analysis of various authentication techniques in Cloud Computing" International Journal of Innovative Research in Science, Engineering and Technology Vol. 2, Issue 4, April 2013.

[8] Jian Wang, Yan Zhou, Shuo Ziang & Jiajin Le "Providing Privacy Preserving in Cloud Computing" 2010 IEEE.

[9] Dave Shackleford "Cloud Security and Compliance: A Primer" SANS Whitepaper-August 2010.

[10] Joshua Browser "The Security Onion Cloud" SANS Whitepaper-2013.